FOOD ENGINEERING SERIES

Electronic Irradiation of Foods

An Introduction to the Technology

R. B. MILLER

Springer

ELECTRONIC IRRADIATION OF FOODS

An Introduction to the Technology

FOOD ENGINEERING SERIES

Series Editor

Advisory Board

Food Engineering Series

Jose M. Aguilera and David W. Stanley, *Microstructural Principles of Food Processing and Engineering*, Second Edition (1999)
Stella M. Alzamora, Maria S. Tapia, and Aurelio López-Malo, *Minimally Processed Fruits and Vegetables: Fundamental Aspects and Applications* (2000)
Gustavo Barbosa-Cánovas, Enrique Ortega-Rivas, Pablo Juliano, and Hong Yan, *Food Powders: Physical Properties, Processing, and Functionality* (2005)
P.J. Fryer, D.L. Pyle, and C.D. Rielly, *Chemical Engineering for the Food Industry* (1997)
Richard W. Hartel, *Crystallization in Foods* (2001)
Marc E.G. Hendrickx and Dietrich Knorr, *Ultra High Pressure Treatments of Food* (2000)
S.D. Holdsworth, *Thermal Processing of Packaged Foods* (1997)
Lothar Leistner and Grahame W. Gould, *Hurdle Technologies: Combination Treatments for Food Stability, Safety and Quality* (2002)
Michael J. Lewis and Neil J. Heppell, *Continuous Thermal Processing of Foods: Pasteurization and UHT Sterilization* (2000)
R. B. Miller, *Electronic Irradiation of Foods: An Introduction to the Technology* (2005)
Rosana G. Moreira, M. Elena Castell-Perez, and Maria A. Barrufet, *Deep-Fat Frying: Fundamentals and Applications* (1999)
Rosana G. Moreira, *Automatic Control for Food Processing Systems* (2001)
M. Anandha Rao, *Rheology of Fluid and Semisolid Foods: Principles and Applications* (1999)
George D. Saravacos and Athanasios E. Kostaropoulos, *Handbook of Food Processing Equipment* (2002)

ELECTRONIC IRRADIATION OF FOODS

An Introduction to the Technology

R. B. Miller
EBM, LLC
Albuquerque, New Mexico

Springer

Library of Congress Cataloging-in-Publication Data

Miller, R. B.
Electronic irradiation of foods: an introduction to the technology/R.B. Miller (author).
p. cm. — (Food engineering series)
Includes bibliographical references and index.
ISBN 0-387-23784-4
1. Radiation preservation of food. 2. Irradiated foods—Safety measures. 3. Ionizing radiation. I. Title. II. Series.

TP371.8.M48 2005
664′0288—dc22
2004063220

ISBN: 0-387-23784-4

Printed in the United States of America.

9 8 7 6 5 4 3 2 1

springeronline.com

Preface

Food irradiation, the use of ionizing radiation to destroy harmful biological organisms in food, is a safe, proven process that has many useful applications. To amplify this point, members of the World Health Organization's Food Safety Unit have described food irradiation as possibly the most significant contribution to public health to be made by food science and technology since the pasteurization of milk. Food irradiation has been endorsed by numerous health organizations and has now been approved for many applications by governments around the world. In spite of these facts, food irradiation has not yet been widely accepted and adopted for two primary reasons, both associated with the two important sources of ionizing radiation themselves, radioisotopes (Co^{60}) and electron accelerators.

Co^{60} is only produced in nuclear reactors, and irradiation facilities using this material are thus associated with the nuclear industry and its attendant problems of environmental waste, safe and secure handling and transportation of very radioactive material, licensing difficulties, etc. In fact, the most vocal opposition to food irradiation is usually attributed to the "anti-nuclear" lobby, with the expressed opinion that broad acceptance of food irradiation by the general public would lead to unacceptable nuclear proliferation and associated environmental risks and concerns.

The use of accelerator sources of ionizing radiation (electrons and x-rays) that use electrical "wall-plug" power would seemingly blunt much of this criticism, opening the way for a significant growth in food irradiation activity. However, such accelerator systems are often perceived as too "high-tech" with attendant problems of reliability and expense. In fact, in electron irradiation facilities using medium-power (<20 kW) electron accelerator systems, most maintenance and repair activities are now concerned with the mechanical material handling hardware components; system reliability will continue to improve as components and subsystem designs improve, and further cost reductions are to be expected.

It is somewhat ironic that the anthrax scare, and the US Postal Service's subsequent decision to begin processing limited quantities of mail with ionizing radiation, has increased public awareness and acceptance of the fact that ionizing radiation can kill harmful bacteria, and is thus beneficial. While the US Centers for Disease Control and Prevention estimates that roughly 100 people die each week in the US alone from food-borne illness, and ionizing radiation is a proven method for eliminating the adulterant *e. coli* O157:H7 bacterium in ground beef, waiting for governments to pass regulations mandating the use of food irradiation for safety reasons is not likely to be a successful strategy for food irradiation proponents. Instead, initial gains are most likely to occur for economic reasons; i.e, food irradiation provides an environmentally acceptable quarantine treatment that allows food processors access to expanded markets, or food irradiation extends the useful shelf life so that perishable foodstuffs can survive longer shipping times.

This viewpoint is a primary reason for this book. Food irradiation based on electron accelerator technology is now a practical food processing option with many useful applications, but there has been no single reference that describes all key aspects of the technology in any detail until now. This book emphasizes the physical science and technology aspects of food irradiation using machine (accelerator) sources of ionizing radiation. It provides significant technical depth for interested workers, yet offers much descriptive, introductory material that should help de-mystify the technology, allowing businessmen to make informed choices regarding important investment decisions, and governments around the world to make informed policy decisions.

The first introductory chapter explains why ionizing radiation is so effective in killing microorganisms, yet has relatively minor effects on the macro- and micro-nutrients of food, while the second chapter presents an overview of the key technology concepts, and includes a simple cost model. Chapters 3 and 4 describe in considerable detail the physical interaction mechanisms of electrons and x-rays, and how these ionizing radiations can be used effectively in food irradiation applications. Chapters 5–7 deal with electron accelerator technology. In particular, Chapter 5 compares and contrasts various electron accelerator approaches, leading to the identification of microwave accelerator technologies as generally being the most relevant for food irradiation applications. Chapter 6 summarizes the important physical principles associated with microwave accelerators, while Chapter 7 describes the important components and subsystems that must be integrated for successful system operation. Chapter 8 addresses electron beam transport in various magnetic field configurations, and presents several examples of how beams can be manipulated to address various processing objectives. With special thanks to the Material Handling Industry of America (MHIA), Chapter 9 describes and discusses various material handling system components and approaches that are commonly found in food irradiation facilities. Chapter 10 discusses the important topic of radiation safety, with special emphasis on the design of the x-ray shield, while Chapter 11 presents new material relating to the control of various accelerator parameters to ensure the integrity of the irradiation process.

The main text is supplemented with Appendices on various special topics. These include an overview of various dosimeter technologies, evaluated from the standpoint of usefulness in a food irradiation facility (App. A); recommendations for how depth-dose measurements can be reliably and routinely used to infer the kinetic energy of an electron beam (App. B); and ozone generation in air by electron beams and x-rays (App. D). Of special note is Appendix C, which discusses the topic of induced radioactivity. In particular, it is shown why induced activity is not of concern, and supports the recommendation that the kinetic energy limit for indirect x-ray irradiation can be safely raised from 5 to 7.5 MeV.

In writing this book I have benefited greatly from numerous interactions with friends and colleagues of the former SureBeam Corporation; this book is dedicated to them, with special thanks to Dr. C. Brian Williams. Special thanks are also due to former colleagues at the Los Alamos National Laboratory (in particular Jim Stovall, Jim Billen, Lloyd Young, Subrata Nath, Stan Schriber, Tom Wangler, Mike Lynch and Dan Rees) for insight into the design and operation of microwave accelerators, and to Gary Loda, Dan Shimer and Ken Prestwich for information concerning particular aspects of accelerator system design and usage.

I also wish to thank Dr. Gene Ray, Cheryl Barr, Esq., and the Titan Corporation for permission to use certain unpublished information, results, and concepts developed while I was employed by the SureBeam Corporation. Dr. Richard Ward of the MHIA also graciously gave permission for the use of several drawings as examples of material handling components.

Albuquerque, New Mexico *R. B. Miller*

Contents

CHAPTER 1

INTRODUCTION TO FOOD IRRADIATION

Food irradiation has generally come to describe the use of ionizing radiation (energetic charged particles such as electrons and alpha particles, or energetic photons such as gamma rays and x-rays) to decrease the population of, or prevent the growth of, undesirable biological organisms in food. Decades of research have conclusively shown that food irradiation can have myriad beneficial applications, including for example, the disinfestation of insects in fruits and grains,[1] the inhibition of sprouting in potatoes and onions,[2] the delayed ripening of fresh fruits and vegetables,[3] and the enhanced safety and sterilization of fresh and frozen meat products,[4] seafood,[5] and eggs.[6]

With special regard to the food safety applications, bacteria such as *Salmonella enteridis*, *Listeria monocytogenes*, *Campylobacter jejuni* and *Escherichia coli* serotype O157:H7 are the primary causes of food poisoning in industrialized countries.[7] In developing nations, parasitic diseases including trichinosis, taxoplasmosis and tapeworms are also of concern.[7] In 1999, food-borne illnesses were responsible for an estimated 5000 deaths in the USA alone,[8] with most of these occurring in relatively helpless population groups such as infants and young children, the elderly, and the immuno-compromised. It is now well-established that ionizing doses in the range of only 1–5 kilogray can readily reduce the population of these food-borne pathogens by several orders of magnitude, virtually eliminating these bacterial organisms from food, without negatively affecting the food's sensory and nutritional qualities, and without inducing radioactivity. Recognizing this fact, members of the World Health Organization's Food Safety Unit have described food irradiation as possibly the most significant contribution to public health to be made by food science and technology since the pasteurization of milk.[9]

The history of food irradiation dates to the discovery of x-rays by Roentgen in 1895, and radioactive substances by Becquerel in 1896. Following these discoveries there was much research examining the effects of these radiations on biological organisms. As a result, it became recognized in the early decades of the 20th century that ionizing radiation could have beneficial food irradiation applications.[10] However, the technology for delivering the required doses at affordable cost was not available.

Comparative research in the late 40s and early 50s examined the utility of five different types of ionizing radiation (ultraviolet light, x-rays, electrons, neutrons and alpha particles) for food preservation.[11] From these studies it was concluded that only electrons had the necessary characteristics of efficiency, safety, and practicality. The penetration depth for ultraviolet light and alpha particles is too limited, and x-rays were considered to be impractical because of the low generation efficiency. While neutrons have good penetration and are quite effective in destroying bacteria, they were eliminated from further consideration because of the potential for inducing radioactivity.

The first practical sources of ionizing radiation were particle accelerators that produced electron beams with energies up to 24 MeV.[12] Also in the late 40s, man-made radionuclides such as Co^{60} and Cs^{137} (which emit penetrating gamma rays) became available through the development of atomic energy.[13] With the availability of these sources of ionizing radiation, research was focused not only on issues associated with food preservation and safety, but also on the development of commercial food irradiation technology. This work has now resulted in the worldwide availability of reliable, commercially available food irradiation equipment, processes and facilities capable of contributing significantly to the supply of safe and wholesome food at costs of typically a few cents per pound.

While gamma rays from radioisotopes such as Co^{60} are effective for many food irradiation applications, facilities using accelerator sources of ionizing radiation are becoming relatively more prevalent, in part because of rising Co^{60} prices, but also because of public concerns related to the nuclear industry. Consequently, this book is devoted to an examination of the technologies and practical implementation techniques associated with food irradiation using accelerator sources of ionizing radiation, including electron beams and penetrating x-rays. These topics are treated in some detail in later chapters. To provide some background for this material we first discuss some elementary radiation chemistry, and summarize the effects of ionizing radiation on biological organisms, and the several groups of organic compounds that comprise foods. Various applications are also discussed as examples.

1.1. ELEMENTARY RADIATION CHEMISTRY

The particles comprising "ionizing radiation" (e.g., electrons and x-rays) are sufficiently energetic as to be capable of ejecting electrons from atoms and molecules. (The specific interaction mechanisms will be described in some detail in Chapters 3 and 4.) The overall process of forming chemically stable products after the absorption and redistribution of the excess energy of the ionizing radiation is termed radiolysis, and the resulting compounds are termed radiolytic products.

The primary effects produced when such energetic particles pass through matter are simplistically described by Eq. (1.1) for the case of a water molecule. The direct result of strong, ionizing collisions is the breaking of chemical bonds and the formation of cations and energetic secondary electrons; somewhat weaker interactions result in molecular dissociation. The cations and the dissociated daughter products are also termed free radicals, because they have an unpaired electron, as indicated by the dots in the equations. Still weaker interactions produce excited atoms and molecules, indicated by the asterisk. Ionization, dissociation and excitation effects are non-specific and random. That is, they will occur without preference for particular atomic or molecular structures.

$$\begin{array}{lcll} H_2O & \longrightarrow & {}^{\bullet}H_2O^+ + e^- & \text{ionization} \\ & \longrightarrow & {}^{\bullet}H + {}^{\bullet}OH & \text{dissociation} \\ & \longrightarrow & H_2O^* & \text{excitation} \end{array} \tag{1.1}$$

In addition to these primary effects, the chemically active free radicals produced during the primary events can combine either with themselves (recombination or dimerization), or with other atoms and molecules to produce secondary effects that depend on specific chemical structures. A substance that combines readily with a free radical is called a scavenger; substances that produce even more reactive radicals are sensitizers.

Since water is a large component of most foods its radiolysis warrants some specific attention. ${}^{\bullet}OH$, e^-, and ${}^{\bullet}H$ are very reactive species, and the only stable end products of water radiolysis are hydrogen and hydrogen peroxide (H_2O_2).[14] However, these are largely consumed through the reactions shown in Eq. (1.2).

$$\begin{array}{lcl} H_2O_2 + e^- & \longrightarrow & {}^{\bullet}OH + OH^- \\ H_2 + {}^{\bullet}OH & \longrightarrow & H_2O + {}^{\bullet}H \end{array} \tag{1.2}$$

Since the hydroxyl radical is a powerful oxidizing agent, and the hydrated electron is a strong reducing agent, the radiolysis of water can be expected to cause oxidizing and reducing reactions in foods through free radical attack.[15]

The summary equation for water radiolysis is

$$H_2O \longrightarrow {}^{\bullet}OH(2.7) + e^-(2.7) + {}^{\bullet}H(0.55) + H_2(0.55) + H_2O_2(0.71) + H_3O^+(2.7) \qquad (1.3)$$

H_3O^+ describes a hydrated proton, and is sometimes termed a hydronium ion. The quantities in parentheses in Eq. (1.3) are the numbers of the various species produced per 100 eV of energy absorbed; these quantities are termed "G values".

The effects of radiolysis necessarily depend on the amount of excess energy that is absorbed per unit mass of material; this quantity is defined as the absorbed dose. The unit of dose now in common usage is the gray (Gy), which corresponds to the absorption of one joule of energy in a mass of one kilogram. (1 Gy = 1 J/kg.) An older unit still found in the literature is the rad, which is defined as 100 ergs/g. The conversion factor is 1 Gy = 100 rad, or 1 Mrad = 10 kGy.

It is also of interest to estimate the amount of a particular daughter species N_m produced by radiolysis on a per molecule basis. This quantity is simply the product of the G value and the absorbed dose D (the amount of daughter product per kilogram), multiplied by the molecular weight of the original molecule M_w, and divided by Avogadro's number. Keeping track of the units, and with the dose expressed in kilogray, the result is[16]

$$N_m = 10^{-7}\, GM_wD(kGy) \qquad (1.4)$$

As an example, for water with a molecular weight of 18, and an assumed dose of 1 kGy, the probability of creating a hydroxyl radical from a single water molecule ($G = 2.7$) is only $N_m = 5 \times 10^{-6}$, which is quite small. It is therefore not surprising that macroscopic effects of water radiolysis are not observable unless the absorbed dose is very high. In fact, with reasonable precautions water can even be used as a radiation shielding material without the buildup of dangerous levels of hydrogen gas and hydrogen peroxide.

1.2. EFFECTS OF IONIZING RADIATION ON BIOLOGICAL ORGANISMS

1.2.1. Organisms of Interest

The biological organisms of primary interest for food preservation and safety include bacteria, yeasts and molds, viruses and other parasites, and insects and mites. Bacteria are single-celled organisms that generally exist as vegetative cells, growing and multiplying as external conditions permit. Some bacteria can also form "spores", essentially protective shells that enable these organisms to exist in a dormant stage and withstand extremely harsh conditions.

From the standpoint of food safety, bacteria are generally divided into three groups: (1) useful bacteria that are able to produce desirable products through sugar fermentation, (2) spoilage bacteria that are responsible for undesirable changes in the odor, color, flavor, texture and appearance of food, and (3) pathogenic (disease-causing) bacteria responsible for most of the outbreaks of food-borne illness. The latter category includes, for example, salmonella, listeria, clostridium botulinum, and e. coli (Figure 1-1).

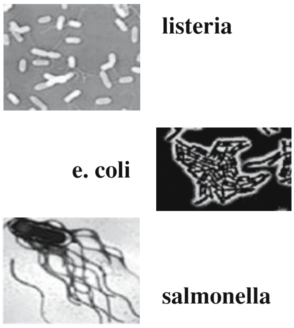

Figure 1-1. The appearance of various pathogenic bacteria. (Used with permission of the Titan Corporation.)

The pathogenic bacteria can cause disease in three basic ways: invasion, intoxication, and intoxification.[17] An example of an invading pathogenic bacterium is *Salmonella typhimuriam*, which produces salmonellosis following the consumption of contaminated poultry. This organism damages the lining of the small intestine resulting in diarrhea. Intoxications are the result of consuming food containing bacteria-produced toxins. Notable toxin-producing examples are *Staphylococcus aureus* and *Clostridium botulinum*. In particular, the latter organism produces the powerful neurotoxin in food that causes botulism. Intoxifications result from consuming food contaminated with bacteria that produce toxins once they are inside the body. An example of such an organism is *Clostridium perfringens*, the cells of which attach to the intestinal tract where they sporulate. The spore coat is believed to be the toxic agent.

Yeasts are also single-celled organisms, although they can aggregate into filaments called “hyphae”. Unlike bacteria that reproduce by cell division, yeasts reproduce by budding. Molds can be either single-celled or multicellular, and are usually found in decaying organic matter. Yeasts and molds can be pathogenic because of the poisonous toxins they produce. A common example is the mold *Aspergillus flavus* that produces the liver-damaging aflatoxin.

Viruses are not true cells, but are parasites that replicate by injecting their genetic material into a host cell, such as cells in the lining of the intestinal tract. Viruses do not grow in food, but can infect host bacteria. Infectious hepatitis and poliomyelitis viruses can be transmitted via raw milk and contaminated shellfish. There are many other parasites, particularly protozoa, tapeworms, and roundworms that also do not grow in food, but are nonetheless responsible for food-borne illness.

Insects, mites, and other such pests are higher-level, multicellular organisms responsible for considerable loss of fresh produce and grains. They can also serve as vectors for carrying pathogenic parasites and bacteria.

1.2.2. Effects of Ionizing Radiation

It is now well accepted that the biological effects caused by ionizing radiation are primarily the result of disruption of the deoxyribonucleic acid (DNA) molecules in the nuclei of cells.[6,18] The structural arrangement of DNA is that of a very long ladder twisted into a double helix. As indicated in Figure 1-2, the two backbones of the ladder are composed of sugar and phosphate molecules, while the rungs consist of nucleotide bases (cytosine, thymine, adenine and guanine) joined weakly in the middle by hydrogen bonds. The sequences of amino acids in the double-stranded helix chains of the DNA serve as a template for replication during cell division, and are responsible for the synthesis of essential proteins and enzymes that regulate cellular metabolism through the process of RNA transcription. Since there is only one (or at most a few copies) of the DNA molecule in

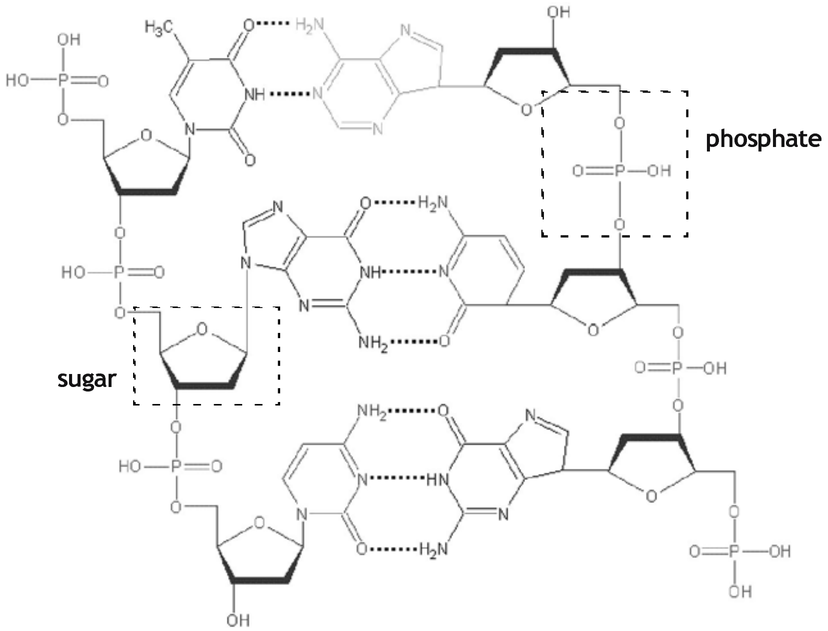

Figure 1-2. Structure of the DNA molecule.[19] The two backbones of the helix are composed of alternating phosphate and sugar molecules. The backbones are joined by weak hydrogen bonds (dashed lines) between the nucleotide bases cytosine and thymine, and adenine and guanine.

a cell, if it becomes damaged, by either primary ionizing events or through secondary free radical attack, the induced chemical and biological changes can prevent replication and can cause cell death.

An important reason for the comparatively high sensitivity of DNA to the effects of ionizing radiation is that DNA is much larger than the other molecular structures in a cell. As an example, the chromosomal DNA of e.coli consists of about 3.5×10^6 nucleotide base pairs, each with an average molecular weight of 660, for a total molecular weight of about 2×10^9. For an assumed G value of unity (typical for causing a lesion in a single-strand (backbone) of the DNA molecule), Eq. (1.4) suggests that an absorbed dose of one kilogray will produce approximately 200 such single-strand breaks per e. coli DNA molecule. While such single-strand breaks will usually not be lethal, they could result in mutations upon replication. The preponderance of evidence is that such mutations are weakened and more susceptible to environmental insult.[17] In addition, depending on the orientation of the molecule and incident direction of the ionizing radiation, it is also possible to produce double-strand lesions in which both backbones are severed simultaneously, thereby breaking the DNA molecule into two separate pieces. Such double-strand breaks are almost always lethal. The estimated G value for double-strand breaks is about 0.07.[6] A dose of 1 kGy would therefore correspond to 14 double-strand breaks in an e.coli DNA molecule, virtually guaranteeing the death of the cell.

For almost all biological organisms exposed to ionizing radiation, the time rate of decrease in population (dN/dt) is observed to depend linearly on the dose rate dD/dt and the population itself; i.e.,

$$dN/dt = -aN(dD/dt)$$

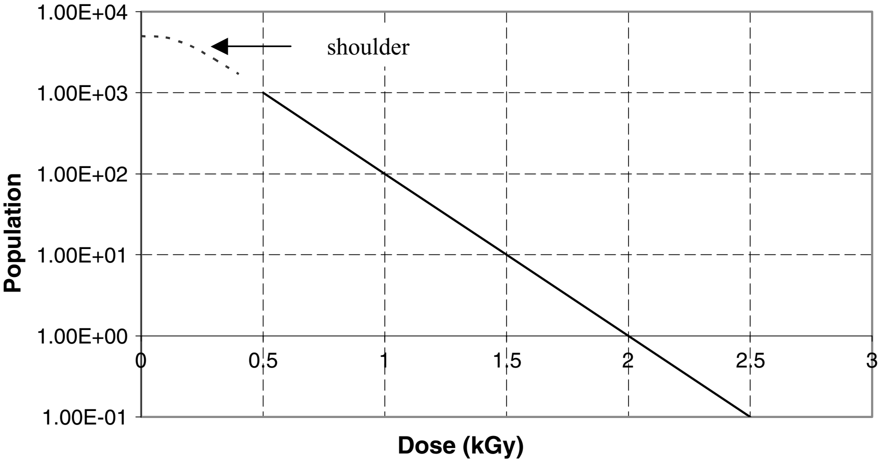

Figure 1-3. Typical bacterial population decreases with irradiation dose. For this example, a population reduction factor of ten is realized with a D_{10} dose of 0.5 kGy.

with a being a constant of proportionality.* Eliminating the time variable and performing the indicated integration gives

$$N = N_o e^{-aD} = N_o 10^{-(aD/2.3)} \tag{1.5}$$

with N_o being the initial population at the start of the irradiation and D being the accumulated dose. It is customary to take the logarithm of both sides and express the sensitivity of a particular organism to the effects of radiation in terms of a D_{10} dose, or often just the D-value (for decimal-value). This is the amount of dose required to reduce the initial population by a factor of 10. From Eq. (1.5) the D_{10} value is defined by

$$D_{10} = 2.3/a \tag{1.6}$$

The D_{10} value is usually determined by plotting the surviving population vs. dose on semi-log paper, as indicated in Fig. 1-3, and calculating the dose required for a factor of 10 reduction in population.

It should be noted that the population reduction curves for some organisms have a shoulder in the low dose range, as suggested in Fig. 1-3. The presence of such a shoulder usually indicates that the organism has a relatively effective DNA repair system. With increasing dose, the repair system becomes overwhelmed, and the population again decreases exponentially. For such cases a two-parameter model should be used to avoid underestimating the radiation resistance of the organism at low doses. With this caveat in mind, a representative list of the D_{10} values for several organisms of importance in food preservation and safety are summarized in Table 1.1. Much larger compilations are available in the literature.[6,21]

Since the size of the DNA molecule generally increases with the complexity of an organism,† viruses are generally more radiation resistant than bacteria, which are more resistant than insects, etc.[6] D_{10} values for viruses are typically several kGy, while D_{10} values for bacteria are typically a

---

* The available data suggest that a is a true constant, independent of the dose rate; i.e., there is no significant "dose rate effect."[20]

† Prions, the protein fragments believed to be responsible for "mad cow disease", have molecular weights much less than DNA, and are therefore more radiation resistant than even viruses.

Table 1.1. Estimated D_{10} Values for Representative Biological Organisms

Organisms	Medium	Temperature (°C)	D_{10} Value (kGy)
Viruses			
Hepatitis A	Clams, oysters	Ambient	4.8
Foot and Mouth	Aqueous solution	Ambient	2.0
Bacteria (NSF)[1]			
Campylobacter jejuni	Ground beef	Ambient	0.15
Shigella dysenteriae	Homog. shrimp	Frozen	0.22
Listeria monocytogenes	Poultry meat	12	0.49
Escherichia coli	MDCM[2]	10	0.23
Salmonella enteritidis	Low-fat ground beef	Ambient	0.7
Salmonella typhimurium	MDCM[2]	10	0.39
Salmonella paratyphi A	Homog. oysters	5	0.85
Staphylococcus aureus	Low-fat ground beef	5	0.75
Streptococcus faecium	Homog. shrimp	5	0.9
Bacteria (SF)			
Clostridium botulinum	Beef stew	Ambient	1.4
Clostridium perfringens	Water	Ambient	2.1
Yeasts and Molds			
Aspergillus flavus	Growth culture	Ambient	1.0
Rhizopus stolonifer	Colony	Ambient	1.2
Trichosporon cutaneum	Fresh sausage	Ambient	1.0
Protozoa			
Entamoeba hystolytica	Water, FFV[3]	Ambient	<0.1
Toxoplasma gondii	Pork	Ambient	<0.2
Cycsticercus bovis	Beef	Ambient	0.4
Trichina spiralis	Pork	Ambient	0.1
Insects			
Fruit fly	Fresh fruit	Ambient	0.15

[1] Non-Spore Forming
[2] Mechanically-Deboned Chicken Meat
[3] Fresh fruits and vegetables

few hundred Gy. However, there are many other factors that also affect radiation sensitivity. These include temperature, the composition of the cellular medium, and the growth cycle of the cell.[17] For example, it is usually (but not always) the case that radiation sensitivity decreases with decreasing temperature. The reasons for this effect are that lowering the temperature decreases the metabolism rate (simple H_2O activity), and decreases the formation and mobility of free radicals. Drying and freezing also generally decrease radiation sensitivity for the same reasons. Bacteria that can exist in a dormant spore stage are generally more radiation resistant as spores than as growing, vegetative cells.

Yeasts are generally more resistant to radiation effects than molds, typically having effective D_{10} values of a few kGy, while the D_{10} values for molds are generally 1 kGy or less. The mycotoxins generated by various molds have molecular weights much less than DNA and are therefore somewhat resistant to the effects of radiation.

The radiation dose required to kill an insect depends primarily on its age and stage of development, with eggs being the most sensitive, and adults being the most resistant. Doses in the range of 1–3 kGy will cause death for all stages in a few days, but sterilization is often as effective and occurs at much lower dose levels. For example, the sterilization dose for most adult insects lies between 50 and 150 Gy, and between 60 and 80 Gy for mites.

1.2.3. Minimum Required Dose

With the information in Table 1.1, food producers and distributors can specify the minimum required dose D_m that will decrease an assumed initial biological organism population by a desired amount. A common target level of population reduction for food safety applications is a factor of 10^5, or five D_{10} values.[21] For example, the D_{10} value of e.coli in fresh ground beef is about 0.25 kGy. Because of stringent sanitation conditions in meat packing plants, it is highly unlikely that an initial e.coli population would exceed 1000 organisms per 25 g of ground beef. For conservatism, a meat producer might therefore choose a minimum required dose of five D_{10}, or 1.25 kGy. Assuming such an initial population as a worst case, the probability of finding a single surviving e.coli organism in one pound of irradiated ground beef is less than 0.2, virtually guaranteeing the safety of the product.

The minimum required dose in this example application is considered to be a medium dose because (as discussed in Section 1.4) it lies in the range of 1–10 kGy. The temperature rise (obtained by dividing the dose by the specific heat) associated with such doses is minimal. Using the specific heat of water (1 cal/g-°C) as an example, the corresponding range of temperature rise is only 0.25–2.5 °C. Applications of medium range doses to control foodborne diseases are therefore sometimes referred to as "cold pasteurization," although this phrase is not generally accepted by the various regulatory agencies.

1.3. EFFECTS OF IONIZING RADIATION ON FOOD COMPONENTS

In addition to establishing the minimum required dose, it is also necessary to estimate the maximum acceptable dose. This need arises not only because government regulations establish a maximum upper dose limit (the maximum allowable dose) for a particular application, but also because high doses can have negative sensory effects on foods. To understand how such effects can arise, we briefly summarize the effects of ionizing radiation on the primary components of foods, including the carbohydrates, lipids and proteins, as well as some important micronutrients (vitamins). The molecules of interest are relatively large in comparison with water, although not nearly so large as DNA. For example, the simple sugar glucose has a molecular weight of 180. For such large molecules any excess energy is most likely to be absorbed in those parts of the molecule having the greatest electron density, or where bonds are relatively weak. Consequently, it is not surprising that the products of radiolysis are nearly identical to the products resulting from cooking, for example.[6]

1.3.1. Carbohydrates[6]

The carbohydrates (one water molecule per carbon atom), include sugars, starches and related substances, and are a major source of energy for the body. The simplest carbohydrate units are called monosaccharides, and have the general formula $(CH_2O)_n$, in which *n* is an integer larger than 2. The monosaccharides may in turn be divided into two sub-groups, the aldoses and the ketoses, depending on whether the main functional group is aldehydic or ketonic, respectively. The most common monosaccharides are glucose and fructose. The disaccharides, including sucrose, lactose, and maltose, are composed of two monosaccharide units, and have the general formula $C_n(H_2O)_{n-1}$, with *n* larger than 5. The chemical structure of lactose, containing both a galactose and a glucose unit, is shown in Figure 1-4, as an example. The polysaccharides include the starches and fibers, such as cellulose, glycogen and dextrin. They are giant molecules containing many monosaccharide units.

When subjected to ionizing radiation, the complex carbohydrates break down into the simpler sugars, while the monosaccharides break down into sugar acids and ketones. These are the same

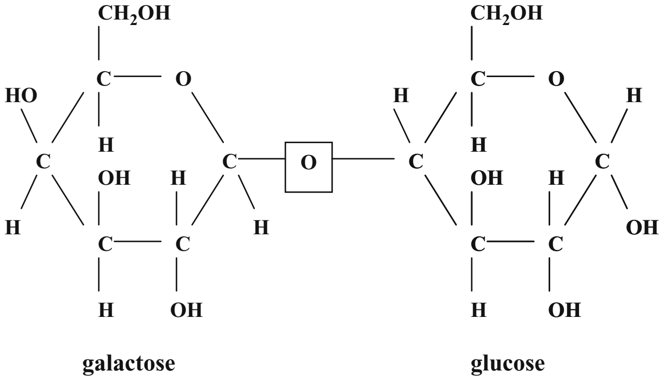

Figure 1-4. Structural representation of lactose, containing both galactose and glucose units.

compounds that result from ordinary hydrolysis. As a result, low and medium radiation doses have little effect on the nutritional value of carbohydrates. High radiation doses, however, can weaken fibrous plant cell wall material leading to a deterioration of texture and loss of quality.

1.3.2. Proteins[22]

Proteins are large compounds that contain nitrogen, in addition to carbon, hydrogen and oxygen. Some proteins also contain iron, phosphorus and sulfur. Proteins are also called polypeptides, because they consist of long chains of amino acids connected by peptide bonds (the carboxyl group of one amino acid is linked to the amino group of another). The general structure of an amino acid is shown in Figure 1-5. The molecular weights of proteins range from a few thousand to more than a million. They are the predominant ingredients of cells, making up more than 50% of the dry weight of animal tissue. Protein molecules range from the long, insoluble fibers that make up connective tissue and hair to the compact, soluble enzymes that can pass through cell membranes and catalyze metabolic reactions essential for life. The function of a protein molecule is largely determined by its three-dimensional structure. The fibrous proteins such as collagen and the muscle proteins actin and myosin are essentially parallel strands of amino acids linked by various side groups. In contrast, the globular proteins such as the enzymes, albumin, and myoglobin have highly irregular, twisted structures.

While amino acids by themselves are relatively sensitive to free radical attack following irradiation, they are much less sensitive when buried in the rigid structure of a protein molecule. Consequently, low and medium doses cause only a minor breakdown of food proteins into lower molecular weight protein fragments and amino acids. In fact, experimental evidence suggests that such treatments cause less protein degradation than steam heat sterilization. At high doses, however,

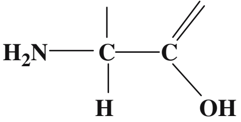

Figure 1-5. Structure of an amino acid. There are a total of twenty amino acids, which differ according to the structure of the variable R group.

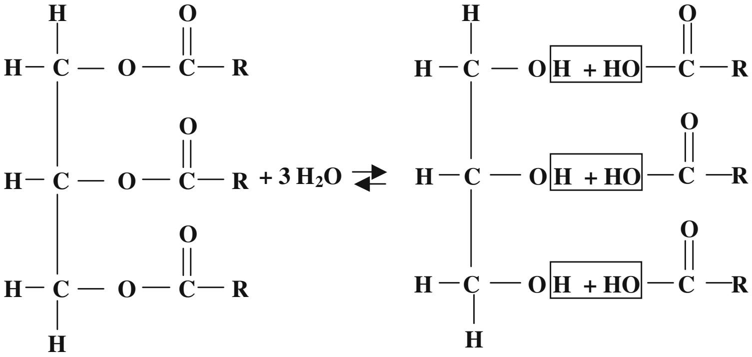

Figure 1-6. A triglyceride is produced by the hydrolysis of a fat molecule.

irradiation can result in protein denaturation (unfolding of the protein structure), with resulting loss of food quality.

1.3.3. Lipids[6]

Lipids are fats and oils composed of the same elements (carbon, hydrogen, and oxygen) as carbohydrates. The lipid portion of foods consists primarily of the triglycerides, in which the three hydroxyl groups of simple glycerol are replaced with long fatty acid side chains. The hydrolysis of a fat molecule to produce a triglyceride is schematically indicated in Figure 1-6. When a side chain (R) is fully bonded with hydrogen along its length, it is said to be "saturated". Saturated triglycerides are usually solid at room temperature, and are usually of animal origin. Unsaturated triglycerides are usually of plant origin and usually liquid at room temperature. Lipids are an efficient energy storage medium, yielding approximately 9500 calories per gram on oxidation, which is approximately twice that of carbohydrates and proteins. The body not only oxidizes fats, but also synthesizes them from excess carbohydrates.

At low and medium doses, the effect of irradiation on the nutritional content of lipids is minimal. In addition, it is also important to note that such doses will not cause the formation of aromatic or heterocyclic rings, or the condensation of aromatic rings, all of which are considered to be carcinogenic, and are known to form at high cooking temperatures. However, the irradiation of lipids at high doses, and especially in the presence of oxygen, can lead to the formation of liquid hydroperoxides. While not necessarily harmful, these substances often have undesirable odors and flavors (rancidity). The unsaturated fatty acids are more prone to develop rancidity. Lipid oxidation can be significantly reduced by freezing, and/or by oxygen removal prior to irradiation.

1.3.4. Vitamins[23]

Vitamins are small molecules not found in abundance in foods that are nevertheless essential for proper body functioning. Severe dietary vitamin deficiencies frequently produce profound physiological effects. There are thirteen known essential vitamins. The water-soluble vitamins include thiamin (B1), riboflavin (B2), niacin (B3), pantothenic acid (B5), pyridoxine (B6), cyanocobalamin (B12), folacin, biotin, and ascorbic acid (C); the fat-soluble vitamins include retinol (A), cholecalciferol (D), tocopherol (E), and phylloquinone (K).

Being smaller molecules, the primary effects of radiation on vitamins at low and medium doses are not significant. However, the antioxidant vitamins can combine with free radicals generated during irradiation and lose some of their potency. Of the water-soluble vitamins, niacin and pyridoxine are relatively resistant to radiation effects, while ascorbic acid and especially thiamin are least resistant. (The principle byproduct resulting from radiation degradation of vitamin C has essentially the same level of activity as vitamin C, however.) Of the fat-soluble vitamins only vitamins A and E evidence any radiation sensitivity. The radiation-sensitive vitamins can be somewhat protected by the exclusion of oxygen and by irradiating at reduced temperatures.

1.3.5. Summary of the Effects of Ionizing Radiation on Foods

In summary, the macronutrients (carbohydrates, proteins, and lipids) are not appreciably affected by low- and medium-range ionizing doses with regard to their nutrient content and digestibility. In fact, heating, drying, and cooking may cause higher nutritional losses. Also, certain carcinogenic aromatic and heterocyclic ring compounds that are produced during cooking at high temperatures are not observed after irradiation. However, for medium-high and high radiation doses the structural properties of the fibrous carbohydrates can be degraded, and lipids can become somewhat rancid, leading to a loss of food quality. Of the micronutrients, only thiamine is of concern because of its relatively high sensitivity to the effects of radiation, and the foods that contain it (pork, for example) are excellent candidates for irradiation to improve food safety.

1.4. APPLICATIONS OF FOOD IRRADIATION

Having examined the effects of ionizing radiation on biological organisms and the macronutrients and micronutrients that comprise food, we next discuss a few representative examples of potentially important food irradiation applications. This discussion is by no means exhaustive.[6,24] Following the recommendations of the Joint FAO/IAEA/WHO Expert Committee, these applications are organized according to the range of delivered dose.[25] While it should be understood that there is no sharp dividing line, low-dose applications are generally less than 1 kGy, and are concerned with inhibition of sprouting, delaying of maturation, parasite disinfection, and insect disinfestations. Medium-dose applications in the range of 1–10 kGy are generally concerned with the control of food-borne diseases and retardation of spoilage. High-dose applications (>10 kGy) are associated with radiation sterilization of foods, and are only undertaken with certain precautionary conditions to preserve food quality (taste, appearance, etc.) A summary of petitions now approved by the United States Food and Drug Administration is presented in Table 1.2. There are also three important petitions under review that would permit irradiation of processed (ready-to-eat) foods (submitted by the National Food Processors Association (NFPA) in Aug. 1999), molluscan shellfish (submitted by the National Fisheries Institute (NFI) in Oct. 1999), and crustaceans (submitted by NFI in Feb. 2001). Finally, irradiated papayas and mangoes have been approved by the Animal and Plant Health Inspection Service (APHIS) for importation into the continental US from Hawaii.

1.4.1. Low-Dose (<1 kGy) Applications

a. Sprouting Inhibition

Storage durations of up to several months are often necessary in order to provide consumers a year-round supply of various sprouting foods, such as potatoes, yams, garlic and onions. Sprouting

Table 1.2. Approved Food Applications of Ionizing Radiation in the United States

Product	Purpose	Max. Dose (kGy)	Date
Any food	Disinfestation	1	1986
Fresh fruits and vegetables	Inhibition of growth and maturity	1	1986
Dry seasonings/spices	Control of foodborne pathogens	30	1986
Pork	*Trichinella* control	1	1985
Poultry	Control of foodborne pathogens	3	1992
Red meat* (fresh/frozen)	Control of foodborne pathogens	4.5/7	2000
Shell eggs	Control of foodborne pathogens	3	2000
Seeds for sprouting	Disinfestation	8	2000
Pet food and animal feed	Sterilization	50	2000

*Includes both beef and pork products

can be inhibited by refrigeration and the application of various chemicals such as maleic hydrazide (preharvest) and isopropyl chlorocarbamate (postharvest). However, refrigeration is expensive, and especially so in the tropical and subtropical zones of the world. While the chemical treatments are relatively cheap and effective, they do leave residues, and many countries have banned their usage for health reasons. In such instances irradiation can offer a reasonable alternative.

Sprouting of potatoes is effectively prevented at doses of only 100 Gy, and significantly delayed at doses as low as 30 Gy. Onions require a dose of 50–60 Gy to inhibit sprouting, while garlic bulbs require 100–120 Gy. Onions and garlic are best treated immediately after harvest. For potatoes, however, the irradiation treatment should not be given immediately after harvest, because it can diminish the ability of the potato to form periderm around sites of mechanical damage. Without the protective periderm, parasites can enter the tuber and cause spoilage. A practical waiting period between harvest and irradiation has been determined to be two weeks. Sprouting prevention and reduced rotting and weight loss have been observed in yams for doses in the range of 75–125 Gy. Irradiation of yams is potentially important because yams quickly deteriorate at temperatures below 12 °C, and chemical inhibitors are generally ineffective.

b. Insect Disinfestation

Excellent control of insects in grain and grain products can be achieved by using fumigants such as ethylene dibromide (EDB) or ethylene oxide (EtO). However, the use of these pesticides has been banned or severely restricted in most countries for health and environmental reasons. For example, EDB is recognized as a carcinogen, and its use was banned by the US Environmental Protection Agency in 1984. Other fumigants such as methyl bromide and hydrogen phosphide are not as effective, and are also considered harmful to the environment. Radiation processing has therefore been suggested as an alternative to fumigation. Practical experience suggests that the necessary radiation dose is in the range of 150–700 Gy. Sterility is characteristic of the lower end of the range, while doses in the upper end are required for killing adult insects. However, radiation is a more expensive treatment, and its increased costs must be justified by the value of the product. This factor can be problematic for grains.

A potentially more promising application is disinfestation of fresh fruits and vegetables (FFV). Major importing nations, including Australia, Japan and the United States require that such produce be certified as free of insect infestation (especially fruitflies), or that it undergo quarantine treatment prior to importation. Until 1984 fruits and vegetables from infested areas were fumigated with ethylene dibromide (EDB) to meet the quarantine regulations. Subsequent to the banning of EDB, treatments with other fumigants have been less successful. While heat and cold treatments are capable of insect disinfestation, they can also seriously degrade the taste and appearance of the produce. For some products irradiation therefore appears to be a useful alternative. A dose level of 250 Gy provides an effective quarantine treatment for fruitflies, while a dose of 500 Gy can control all stages of most other pests. Many fruits tolerate these dose levels quite well (papayas and mangoes are notable examples). However, avocados are especially sensitive to radiation and can develop skin blemishes and fruit discoloration at doses as low as 100–200 Gy.

1.4.2. Medium-Dose (1–10 kGy) Applications

a. Control of Foodborne Pathogens

Beef, pork, poultry, seafood, eggs, and dairy products are all recognized as major sources of foodborne illnesses. The most serious contaminants are e.coli serotype O157:H7, listeria and tapeworm for beef; pork can also be contaminated with these bacteria, as well as with pork tapeworm and the trichinella organism; for poultry and eggs, the predominant pathogens are salmonella and campylobacter; listeria is of most concern for milk and soft cheeses; seafood, especially shellfish, is often contaminated with salmonella, *Vibrio parahaemolyticus*, and *Shigella*. From the data of Table 1.1, excellent control of all these organisms can be achieved with doses in the range of 1–3 kGy.

As previously discussed, the minimum required dose for these food safety applications is established by the desired degree of reduction in the pathogenic organism population and the D_{10} value of the organism of concern. The maximum dose, however, is established by either government regulation (Table 1.2), or by the development of negative sensory characteristics. For example, for fresh ground beef with high fat content and for fatty pork products, the maximum dose should be less than 2.5 kGy to prevent rancidity due to excess lipid oxidation. Liquid and dry eggs can tolerate doses in excess of 3 kGy, but for shell eggs, a 2-kGy dose can cause deterioration of the yolk sac membrane. Milk develops an off-flavor at relatively low doses, but various cheeses show good tolerance at doses of 3 kGy. Seafood products that have low fat content, such as flounder, crab meat and oysters, can be irradiated at doses up to 5 kGy without significant loss of quality.

b. Shelf-Life Extension

The same dose levels appropriate for control of foodborne pathogens can also significantly extend the shelf life of the products just discussed by reducing populations of spoilage bacteria, molds and yeasts. For example, a dose of 2.5 kGy can extend the shelf life of chicken and pork by as much as a few weeks, while the shelf life of low-fat fish can be extended from typically 3–4 days without irradiation to several weeks with 5-kGy doses. In addition, the shelf life of various cheeses can be extended significantly by eliminating molds at doses of less than 0.5 kGy. Finally, shelf life extension for strawberries, carrots, mushrooms, papayas and packaged leafy vegetables also appears to be promising at dose levels of a few kGy or less.

c. Spice Irradiation

The fresh plants from which spices are derived are almost always contaminated by microorganisms from the soil and windblown dust, and by bird droppings. During the drying process, these microorganisms can grow to population densities exceeding 10^6 organisms per gram of material. When used as seasonings in the manufacture of processed foods for which the manufacturing process does not include a sterilizing step, these organisms can cause rapid food spoilage, and can lead to foodborne illness. Since moist heat treatment is not generally suitable for such dry products, spice producers in the past routinely used EtO for disinfestation. With EtO also being recognized as a carcinogen, producers are now increasingly turning to ionizing radiation. In fact, the commercial irradiation of spices has been approved and practiced in many countries for several years. In the US, the use of irradiation for this application has been approved at dose levels not to exceed 30 kGy. However, doses of 5–10 kGy usually give quite satisfactory results (elimination of bacteria, mold spores and insects) without negative impact on chemical or sensory properties.

1.4.3. High-Dose (>10 kGy) Food Sterilization

As discussed previously, some foods such as fresh fruits and vegetables deteriorate when subjected to high radiation doses (>10 kGy). However, other foods, including meat, poultry, and certain seafoods do maintain good quality, provided that certain precautions are taken. As a result, it is possible to effectively sterilize these foods with doses in the range of 25–45 kGy. To prevent off-flavors resulting from lipid oxidation, oxygen must be excluded by vacuum packaging, and the irradiation must be performed at low temperatures (−20 °C to −40 °C). A further mild blanching treatment at 70 °C is also required to inactivate autolytic enzymes if long-term shelf life without refrigeration is desired. While these additional procedures and high doses significantly increase costs, these products are nonetheless important for hospitalized patients with suppressed immune systems (and NASA astronauts).

1.5. SUMMARY

Food irradiation has generally come to describe the use of ionizing radiation to decrease the population of, or prevent the growth of, undesirable biological organisms in food. The elementary particles comprising "ionizing radiation" (e.g., electrons, x-rays, gamma rays, etc.) are sufficiently energetic as to be capable of ejecting electrons from atoms and molecules, resulting in the breakage of chemical bonds. The biological effects caused by ionizing radiation are primarily the result of disruption of the deoxyribonucleic acid (DNA) molecules in the nuclei of cells, either through primary (ionizing) events, or through secondary free radical attack following water radiolysis. The sensitivity of a particular organism to the effects of ionizing radiation is usually expressed in terms of the D_{10} value, which is the amount of dose that will decrease the organism population by a factor of ten. An important reason for the comparatively high sensitivity of DNA to the effects of ionizing radiation is that DNA is an enormous molecule. As a result, with relatively modest radiation doses (typically 1–5 kGy) it is possible to effectively destroy the organisms responsible for foodborne illness and spoilage without affecting the nutritional and sensory qualities of the carbohydrates, proteins, and lipids that comprise foods. In fact, heating, drying, and cooking may cause higher nutritional losses.

Applications of food irradiation are generally organized into three categories according to the range of delivered dose. These are (1) low-dose applications (generally less than 1 kGy), which are concerned with inhibition of sprouting, delaying of maturation, parasite disinfection, and insect disinfestations; (2) medium-dose applications in the range of 1–10 kGy, which are generally concerned with the control of food-borne diseases and retardation of spoilage; and (3) high-dose applications (>10 kGy), which are associated with radiation sterilization of foods. In the US, the FDA has already approved several petitions permitting the irradiation of fresh produce, spices, red meats, poultry and eggs for the control of foodborne pathogens and shelflife extension, as well as disinfestation applications for all foods. Important petitions for the irradiation of ready-to-eat foods and various types of seafood are now under review.

REFERENCES

1. See for example, M. Ahmed, “Disinfestation of stored grains, pulses, dried fruits and nuts, and other dried foods,” **Food Irradiation Principles and Applications**, R.A. Molins ed., Wiley Interscience, New York (2001), p.77.
2. See for example, P. Thomas, “Irradiation of tubers and bulb crops,” **ibid**., p. 241.
3. See for example, P. Thomas, “Irradiation of fruits and vegetables,” **ibid**., p. 213.
4. See for example, R.A. Molins, “Irradiation of meats and poultry,” **ibid**., p. 131.
5. See for example, M.B. Kilger, “Irradiation processing of fish and shellfish products, **ibid**., p. 193.
6. See for example, J.F. Diehl, **Safety of Irradiated Foods**, Marcel Dekker, Inc., New York (1995), p. 310.
7. “Enhancing food safety through irradiation,” report of the International Consultative Group on Food Irradiation (ICGFI), Joint FAO/IAEA Division of Nuclear Techniques, Vienna (1999).
8. P.S. Mead, L. Slutsker, V. Dietz, L.F. McCaig, J.S Bresee, C Shapiro, P.M. Griffin, and R.V. Tauxe, “Food-related illness and death in the United States,” Centers for Disease Control and Prevention **Vol. 5**, No. 5 (Sep.-Oct., 1999).
9. F. K. Kaperstein and G.G. Moy, “Public health aspects of food irradiation,” J. Public Health Policy **14**, 149 (1993).
10. H.E. Goresline, “Historical aspects of radiation preservation of food,” in **Preservation of Food by Ionizing Radiation**, Vol. I, E.S. Josephson and M.S. Peterson (eds.), CRC Press, Boca Raton, FL (1982).
11. W.T. Thayer, R.V. Lachica, C.N. Huhtanen, and E. Wierbicki, “Use of irradiation to ensure the microbiological safety of processed meats,” Food Technol. **40**(4), 159 (1986).
12. E.S. Josephson, “An historical review of food irradiation,” J. Fd. Safety **5**, 161 (1983).
13. S. A. Goldblinth, “Historical development of food irradiation,” in **Food Irradiation**, Proceedings Series, Int. Atomic Energy Agency, Vienna, 3 (1966).
14. V. Arena, **Ionizing Radiation and Life**, Mosby, St. Louis, MO (1971).
15. M.H. Stevenson, “Irradiation of meat and poultry,” in **The Chemistry of Muscle-Based Foods**, D.A. Ledward, D.E. Johnston, and M.K. Knight (eds.), Royal Society of Chemistry Special Publication 106, Cambridge, UK, 308 (1992).
16. A. Brynjolfsson, “Chemiclearance of food irradiation: its scientific basis,” in **Combination Processes in Food Irradiation**, Proceedings Series, IAEA, Vienna, 367 (1983).
17. E.A. Murano, “Microbiology of irradiated foods,” in **Food Irradiation, A Source Book**, E.A. Murano (ed.), Iowa State University Press, Ames, Iowa (1995).
18. C. von Sonntag, **The Chemical Basis of Radiation Biology**, Taylor and Francis, London (1987).
19. J.D. Watson and F.H.C. Crick, “A structure for Deoxyribose Nucleic Acid,” Nature **171**, 737 (1953).
20. H. Singh, “Dose Rate Effect in Food Irradiation,” **AECL-10343**, Atomic Energy of Canada Limited (1991).
21. See for example, J.S. Dickson, “Radiation inactivation of microorganisms,” in **Food Irradiation Principles and Applications**, R.A. Molins (ed.), Wiley Interscience, New York, 23 (2001).
22. W.M. Urbain, **Food Irradiation**, Academic Press, Orlando, FL (1986).
23. E.M. Stewart, “Food irradiation chemistry,” in **Food Irradiation Principles and Applications**, R.A. Molins (ed.), Wiley Interscience, New York, 37 (2001).
24. See for example, E.S. Josephson and M.S. Peterson, **Preservation of Food by Ionizing Radiation**, Vol.3, CRC Press, Boca Raton, FL (1983).
25. “Wholesomeness of Irradiated Food,” Technical Report Series 659, World Health Organization, Geneva (1981).

CHAPTER 2

OVERVIEW OF FOOD IRRADIATION TECHNOLOGY AND CONCEPTS

Having summarized the effects of ionizing radiation on biological organisms and the organic compounds that comprise foods, and having discussed a few notable food irradiation examples, we will now give a brief description of an accelerator-based food irradiation installation and discuss several important food irradiation concepts as an introduction to the following chapters. A simplified diagram of a typical installation is shown in Figure 2-1. Its key elements include an *accelerator system* to deliver the energetic beam, a *scanning system* to provide uniform beam coverage of the product, and a *material handling system* that moves the product through the beam in a precisely controlled manner. Auxiliary equipment for the accelerator system includes vacuum and cooling subsystems. Extensive shielding is necessary to reduce the external radiation exposure rates to acceptable levels, and a safety system is necessary to prevent accidental exposure of personnel during accelerator operation.

Since the primary objective of any irradiation facility is the delivery of the specified minimum required dose to all parts of the product without wasteful/harmful overdose, process parameters that affect the dose distribution must be continuously monitored and controlled with process control software. On-site dosimetry is also required for initial product qualification and process validation, and for periodic process monitoring.

The volumes of food that can be processed with a modest accelerator system can be quite large, and the facility must therefore have adequate warehouse space for both incoming and outgoing product. It is usually necessary to maintain both the warehouse and irradiation cell areas at reduced temperatures, implying a significant HVAC (heating, ventilation and cooling) capability. The incoming product area is usually physically separated from the out-going area by a fence or other physical barrier to prevent commingling of non-irradiated and irradiated product. In addition, ionizing radiation produces ozone in air, and some means for ozone elimination is usually required. The on-site electrical power subsystem must be adequate to support all of these functions. Considering all of the physical plant equipment and extensive shielding, the footprint of the accelerator system is typically a small fraction of the facility floor space.

2.1. DESCRIPTION OF KEY SYSTEMS

To avoid any issues associated with nuclear activation of foods, the kinetic energy of the electrons produced by the accelerator system is limited by regulation to 10 MeV for direct electron irradiation, and to 5 or 7.5 MeV for indirect irradiation using x-rays.[1,2] Since the penetrating power of an electron beam scales linearly with kinetic energy, and since the efficiency of x-ray generation also

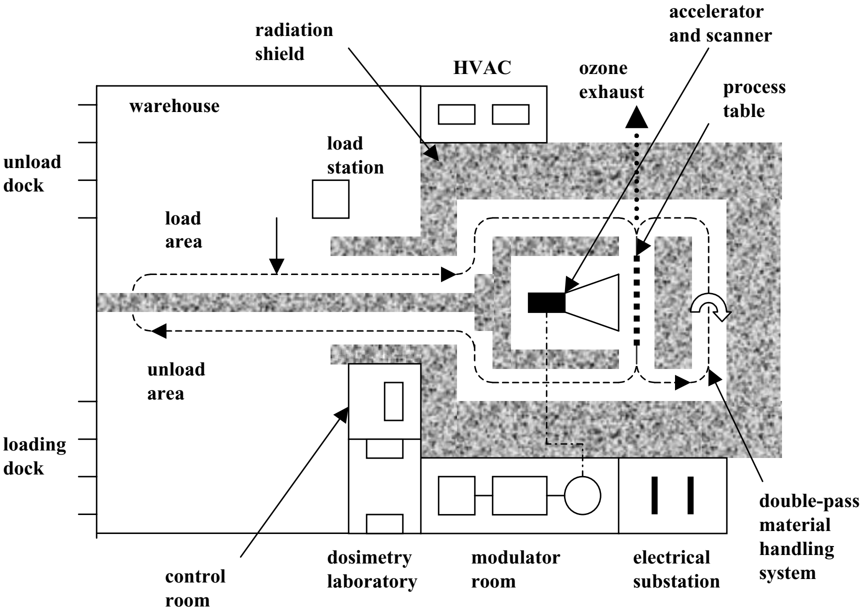

Figure 2-1. Simplified diagram of an accelerator-based food irradiation installation.

scales linearly with kinetic energy, it is usually desirable to operate the accelerator system near these maximum allowable limits. At these high kinetic energies, the most common accelerators found in the food irradiation industry are the microwave accelerators. Rather than developing a high voltage across a dielectric insulator, these devices accelerate electrons using alternating (rf) electric fields in evacuated, electromagnetic cavities. As a consequence, the average accelerating gradients of these devices can easily be 10 MeV/m, and these devices are therefore quite compact.

The energetic electron beam produced by a microwave accelerator generally has a beam radius that is much smaller than the physical dimensions of the product to be irradiated, and the beam must therefore be scanned in some fashion to provide uniform illumination. The scanning action is usually effected by a time-dependent magnetic deflection of the beam. If the product is to be directly treated with electrons, the accelerated beam emerges from the vacuum envelope of the accelerator through a thin titanium (usually) exit window at the end of the scan horn.

If x-ray irradiation is desired, the same accelerator and scanning systems are used, but the electron beam does not interact with the product. Rather, the beam is scanned across an x-ray converter made of a high-atomic-number metal such as tantalum or tungsten. When energetic electrons interact with the converter material they generate x-ray radiation by a process known as bremsstrahlung.

The product is moved through the scanned beam (either electrons or x-rays) by the material handling system. It is customary to operate the linac and scanning system at fixed parameters; the desired dose is therefore achieved by operating the conveyor system at the appropriate progression rate. We discuss a few details of these three key systems in the next sections.

2.1.1. Accelerator System

A block diagram of a typical standing-wave electron rf linac (a type of microwave accelerator) is shown in Figure 2-2.[3] Electrons are produced in an electron gun: they are thermionically emitted from a hot cathode, and formed into a pencil beam by the convergent electric fields between the gun

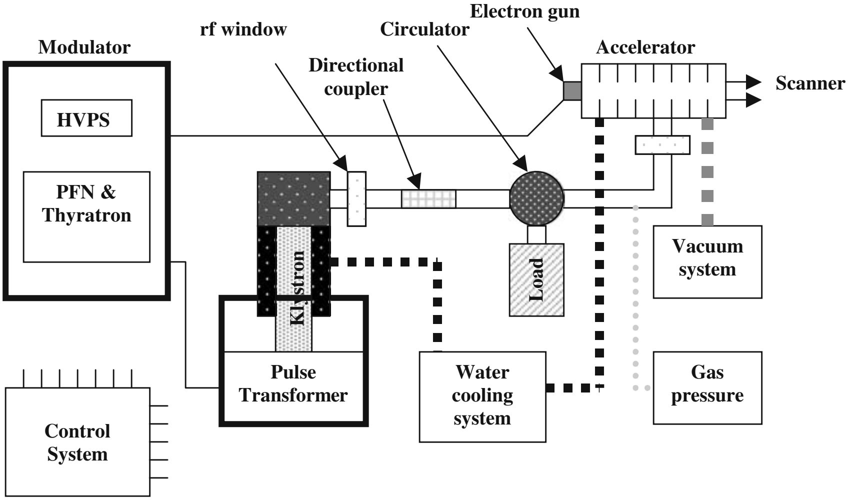

Figure 2-2. Simplified block diagram of a standing-wave rf linac accelerator system.

electrodes. The accelerating structure consists of one or more cavities that are electromagnetically resonant at microwave frequencies. Oscillating electric fields are established in the accelerating structure by coupling in microwave power from a suitable tube, such as a klystron or magnetron. The oscillating electric fields in the accelerating cavities form the steady electron stream from the gun into axial bunches, and accelerate the electron bunches to the desired kinetic energy. A circulator protects the tube from microwave power reflected by the accelerating structure. Auxiliary systems provide a high vacuum inside the accelerator, and cooling and temperature control of its conducting surfaces.

The klystron and gun are powered by a high voltage modulator, which converts ac power from the electrical mains into a repetitive stream of pulses that are stepped to high voltage using a pulse transformer. The microwave tube is usually mounted directly into the pulse transformer tank, and the tube socket and transformer are insulated using a suitable high-voltage dielectric fluid (transformer oil). The modulator typically employs a pulse-forming-network (PFN) and a gas-filled switch tube called a thyratron to form the pulses, although solid state switching components are becoming more prevalent. The PFN, comprised of discrete capacitors and inductors, has the characteristic behavior of a charged transmission line. Closure of the switch tube connects the PFN across the primary of the pulse transformer, and the capacitors discharge through the inductors to form a pulse that is stepped up in voltage by the pulse transformer. The switch tube arc extinguishes after the pulse has terminated, and the PFN capacitors can then be recharged by the power supply, usually through a diode string and a resonant charging choke.

For installations having an average beam power exceeding about 10 kW, the most common microwave tube is a klystron; for lower average power accelerator systems a magnetron tube is often used.[3] A magnetron consists of a series of resonant cavities arranged in circular form. Electrons emitted from the cathode by application of a high-voltage pulse are caused to pass through and excite the magnetron cavities by means of a transverse magnetic field. Magnetrons used to power linac systems are generally compact, efficient, and operate at voltages of no more than a few tens of kilovolts. Because the processes of emission, rf interaction, and spent beam collection occur in the same physical region, however, they are generally limited in their average power output by thermal considerations. A magnetron is an oscillator, and therefore does not require a

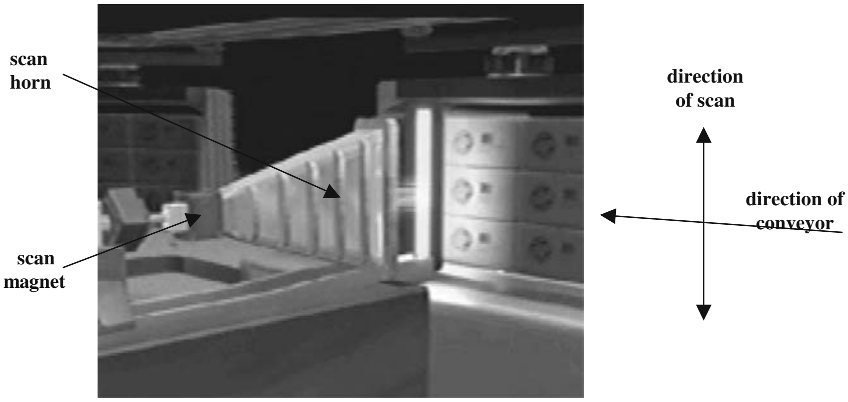

Figure 2-3. The beam from the linac is scanned in the vertical direction; the product is conveyed horizontally through the irradiation zone by the process conveyor of the material handling system. (Used with permission of the Titan Corporation.)

drive source. However, during system startup, the magnetron frequency can drift relative to the resonant frequency of the accelerator structure, unless an automatic frequency control (AFC) circuit is used. This circuit senses the resonant frequency of the linac structure and actuates a mechanical tuning plunger in the magnetron so that the frequency of the microwave power remains properly tuned.

A klystron is a linear beam device that uses the principle of velocity modulation to generate microwave pulses. Being a linear tube, the processes of beam generation, modulation, power extraction and spent beam collection occur in physically different regions, permitting high peak power and high average power operation. When used in a linac system for food irradiation, a klystron is usually operated at a voltage of the order of 100 kV, generating 5-MW pulses at average power levels in the range of tens to hundreds of kilowatts. A klystron is usually operated as an amplifier, with the input drive (a few hundred watts) being supplied by a solid-state oscillator.

2.1.2. Beam Scanning System

A uniform ionizing dose is delivered to the product by scanning the accelerated beam as the product is translated by a conveyor system through the irradiation zone, as suggested in Figure 2-3. The scanning action results from passing the beam through magnetic deflection coils driven by a time-varying current waveform.

Consider the schematic geometry of Figure 2-4. The radius of curvature R of an electron in a uniform transverse magnetic field of strength B is given by

$$\mathrm{BR} = 1.7 \times 10^{-3}\beta\gamma \text{ (Tesla-meters)} \tag{2.1}$$

where β and γ are the usual relativistic factors; if v represents the electron velocity, then $\beta = v/c$, and $\gamma = (1 - \beta^2)^{-1/2}$. If the transverse field has an effective length L, then the deflection angle of the beam as it exits the transverse field is given by

$$\theta = \sin^{-1}(\mathrm{L/R}) \tag{2.2}$$

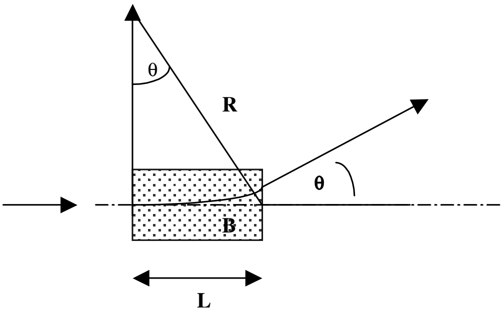

Figure 2-4. Schematic deflection geometry of the scanning magnet.

The beam scanning action is therefore created by varying the field strength between $-B_o$ and $+B_o$ as suggested by the waveform of Figure 2-5. As a numerical example, for 10 MeV electrons ($\beta\gamma = 20.5$), the scanning angle produced by a maximum deflection field of +/− 400 gauss (0.04 T) having an effective length of 25 cm is approximately +/− 16.7 degrees.

Since the beam produced by the rf linac is pulsed, the pulse repetition rate and scanning frequency must be appropriately chosen to ensure many overlapping beam spots in the direction of the scan, and many overlapping scanned-beam traces in the direction of the conveyor at the maximum conveyor speed. The beam expansion provided by scattering in the exit window helps in this regard, but magnetic beam expansion lenses may also be necessary for applications involving high-speed conveyors.

2.1.3. Material Handling System

The primary function of the material handling (or conveyor) system is to ensure that the food product moves through the irradiation zone in a precisely controlled, constant manner. There must be no slippage of material, and gaps between food packages or carriers, or variations in product depth (more precisely, areal density) are to be avoided in order to maximize throughput efficiency. The conveyor system must be able to turn corners within the maze of the radiation shield and to withstand the effects of the radiation. Conveyor speeds in the range of 0.1–100 ft per minute are of interest. Many material handling system approaches are available, including for example, belt conveyors, overhead power-and-free conveyors, chain and roller conveyors, gravity flow systems, turntables, and pallet handling systems.[4] The selection of a particular approach is largely guided by the type and packaging of the product and the type of radiation (e-beam, x-ray) to be used, in addition to the usual considerations of cost, reliability, maintainability, etc.

To examine the various aspects of a material handling system in somewhat more detail, consider the product flow for an x-ray irradiation facility (see Figure 2-1, for example). Packages of food

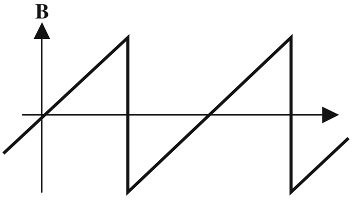

Figure 2-5. Time-varying field strength of the scanning magnet.

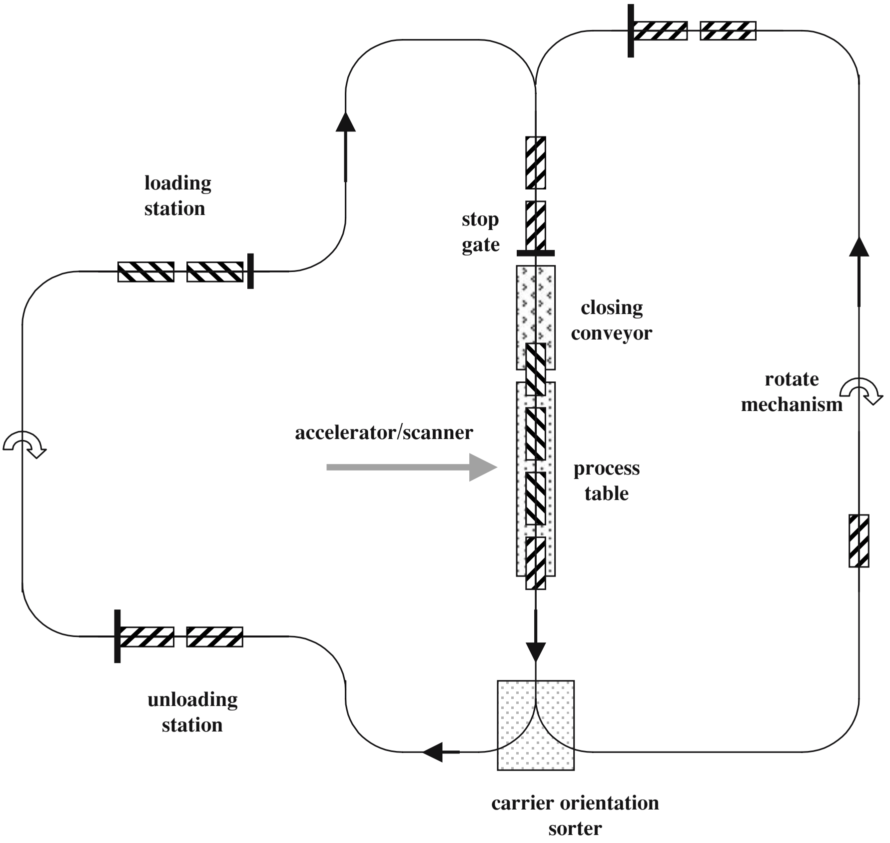

Figure 2-6. Schematic diagram of an overhead power-and-free, carrier-based conveyor system used to transport food products in an x-ray irradiation facility.

products are placed on carriers that are transported using a material handling system consisting of three different types of conveyors, all independently powered, as suggested in Figure 2-6. The three conveyors include (1) a process conveyor that moves carriers through the irradiation zone at a precise speed; (2) a high-speed, closed-loop, overhead power-and-free (OHPF) conveyor that moves carriers from a loading position in the warehouse to an accumulation station in the vicinity of the process conveyor, and then transports carriers from the exit end of the process conveyor to an unloading station in the warehouse; and (3) a closing conveyor that moves a carrier from an accumulation station (stop gate) to within a predetermined (small) separation distance from the previous carrier on the process conveyor. Programmable controllers and computers monitor and control the position of carriers throughout the system.

A power-and-free conveyor combines the powered rail of a continuous power line with a non-powered (free) rail that supports the weight of the carriers. The powered chain pushes the carrier on the free rail by means of a “pusher dog.” By mechanically controlling the pusher dog latching mechanism, carriers can be disengaged from the power chain for loading and unloading operations, accumulated at a stop gate for programmed release, and/or switched onto spurs as desired.

With the carrier weight still supported by the unpowered rail of the OHPF conveyor, a non-accumulating chain conveyor on the process table engages the bottom of a carrier and transports it through the irradiation zone at the desired speed (usually much slower than the speed of the OHPF conveyor). After a first carrier has moved past a particular position on the process table, a second carrier is released from the stop gate at the accumulation station, and the closing conveyor is actuated. The closing conveyor then engages the second carrier and moves it to the engagement point of the process conveyor. The speed of the OHPF conveyor is adjusted to minimize carrier transfer time, while the waiting time at the stop gate is determined by the speed of the process conveyor and the desired separation distance between carriers on the process table.

For x-ray irradiation it is almost always preferable to irradiate products from two sides to improve the dose uniformity and the mass throughput efficiency. This can be accomplished by either using two identical radiation beams, or by adding a carrier rotation loop to the material handling system of a single-beam configuration, as shown in Figure 2-6. Appropriate routing of carriers is easily achieved by introducing a physical asymmetry into the carrier design.

Since the process table lies in the high radiation zone, its components must use materials that are not susceptible to either radiation degradation processes or oxidation attack by ozone. This eliminates the use of essentially all organic compounds (plastics, rubber, certain organic lubricants, etc.), and usually requires use of stainless steels, or metals that form self-protecting oxidation layers, such as aluminum.

2.2. KEY FOOD PROCESSING CONCEPTS AND PARAMETERS

There are several key parameters that are necessary for an adequate description of the irradiation process. In addition to the absorbed dose itself, these include the uniformity with which the dose is applied, the efficiency with which the available radiation energy is utilized, the penetrating power of electrons and x-rays, and the estimated throughput rates that can be achieved under various processing assumptions. These key parameters are defined and discussed in the following paragraphs.

2.2.1. Dose Uniformity and Utilization Efficiency for Electron Beams

When energetic electrons pass through matter they lose energy via coulombic interactions with atomic and molecular electrons and nuclei. The ensuing radiation shower is schematically suggested in Figure 2-7. The primary electronic interactions are ionizing events that result in the ejection of secondary electrons, which then produce tertiary electrons, etc., until all of the kinetic energy of the primary electron has been absorbed. The nuclear interactions spread the beam via elastic scattering

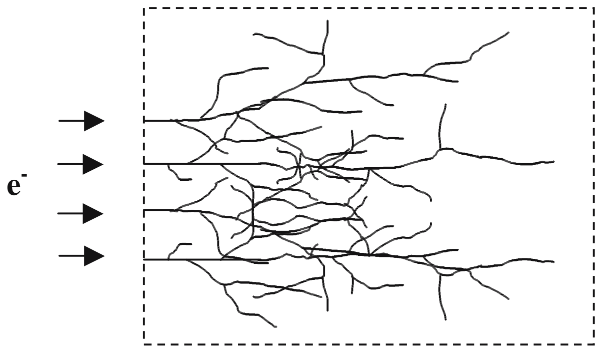

Figure 2-7. Schematic representation of the particle tracks of the primary, secondary, tertiary, etc. electrons in matter bombarded by high-energy electrons.

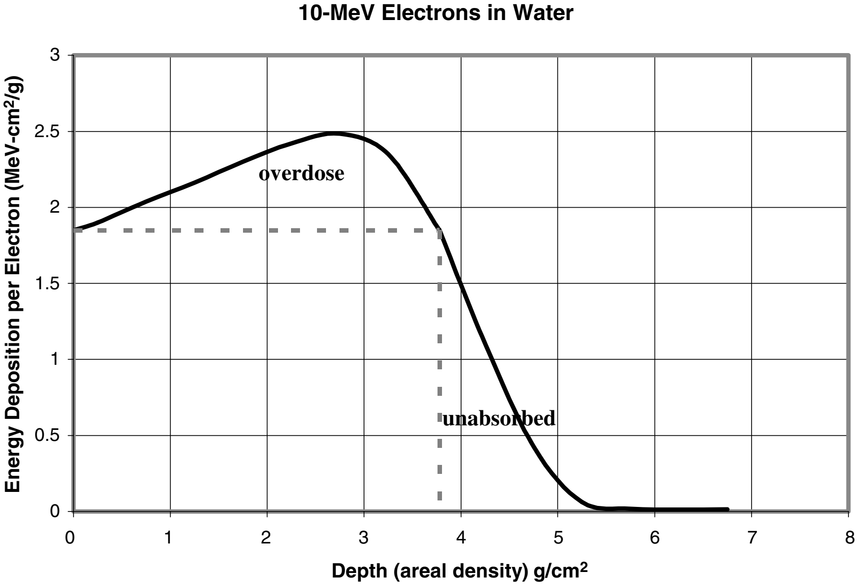

Figure 2-8. The characteristic energy deposition profile for 10-MeV electrons in water.

events, and can generate high energy x-rays, or bremsstrahlung. These processes will be described in some detail in later chapters. For present purposes, we will only consider the shape and magnitude of the energy deposition profiles in order to derive and discuss some fundamental parameters and concepts that are important for food processing.

The energy deposition profile produced by 10-MeV electrons normally incident onto the surface of a water absorber, as computed by the one-dimensional Monte Carlo computer code TIGER, has the characteristic shape shown in Figure 2-8.[5] The ordinate of this graph is the **specific energy deposited per incident electron**, ΔW_{sp}. The absorbed dose (energy absorbed per unit mass) at a particular depth d is obtained by multiplying the specific energy deposited by the number of incident electrons per square centimeter, which is equal to the current density j times the irradiation time t; i.e.,

$$D(d) = \Delta W_{sp}(d)\, jt \tag{2.3}$$

As a numerical example, for a current density $j = 10^{-6}$ amp/cm^2 incident on the surface for a time $t = 1$ s, the resulting surface dose is 1.85 kGy. (Recall that 1 kGy = 1 kJ/kg.)

Although the depth-dose profile of Figure 2-8 strictly pertains to a water absorber (density of 1 g/cm^3), it can be extended to absorbers having differing densities, provided that the penetration depth is measured in terms of the **areal density** A_d; this parameter is defined as the product of physical depth d and density ρ, as given by Eq. (2.4).

$$A_d = \rho d \tag{2.4}$$

Note that ΔW_{sp} increases from about 1.85 MeV-cm^2/g at the surface to a maximum of about 2.5 MeV-cm^2/g at a water depth of about 2.75 cm, before decreasing to essentially zero as the kinetic energy of the primary beam is dissipated. This characteristic profile is the result of the beam scattering processes and the non-zero range of the secondary and tertiary electrons. For a material having a density of 0.5 g/cm^3, ΔW_{sp} would have the same maximum value, but the maximum would occur at a physical depth of 5.5 cm.

Because the electron energy deposition is not constant, even in this one-dimensional case, there is a position in the product that will receive the minimum delivered dose D_{min}, and another position that will receive the maximum dose D_{max}. Consequently, one measure of the dose uniformity is the ratio D_{max}/D_{min}, known as the **max:min ratio**. Using the depth-dose profile of Figure 2-8 as an example, the dose increases with depth up to about 2.75 g/cm^2, and the max:min ratio therefore increases over this range to about 1.35. It then remains constant as the depth increases to about 3.8 g/cm^2 (the position of the vertical line). Beyond this depth, the minimum dose monotonically decreases below the surface dose (the horizontal line), and the max:min ratio rises accordingly.

An important additional consequence of this non-constant depth-dose distribution is a loss of efficiency in the utilization of the available electron beam energy. Referring again to Figure 2-8, note that for a product having a thickness d, the energy represented by the area of a box defined by D_{min} and d is that amount of energy that is usefully absorbed in the product. The product is not thick enough to absorb the residual energy represented by the area to the right of d, and the area above the D_{min} line represents energy that is wasted in overdosing the product. For this one-dimensional case, it is easy to see that the maximum efficiency will occur when the product depth is chosen such that the dose on the rear surface is equal to the front surface dose. The product of the minimum dose (1.85 MeV-cm^2/g) and the optimum depth of 3.8 g/cm^2 represents an effective absorbed energy of about 7 MeV; since the incident electron kinetic energy was 10 MeV, the maximum one-dimensional **utilization efficiency** is therefore about 70% for this case. The general variation of the utilization efficiency for this single-sided, electron beam irradiation scenario is presented in Figure 2-9, along with the dose max:min ratio as a function of the product depth measured in terms of the areal density.

When similar calculations are performed for electrons having differing kinetic energies, it is found that the depth at which the maximum throughput efficiency occurs varies nearly linearly with the kinetic energy according to

$$d_{opt}\,(g/cm^2) = 0.4\,E\,(MeV) - 0.2 \tag{2.5}$$

This optimum depth provides a useful measure of the electron **penetrating power**.

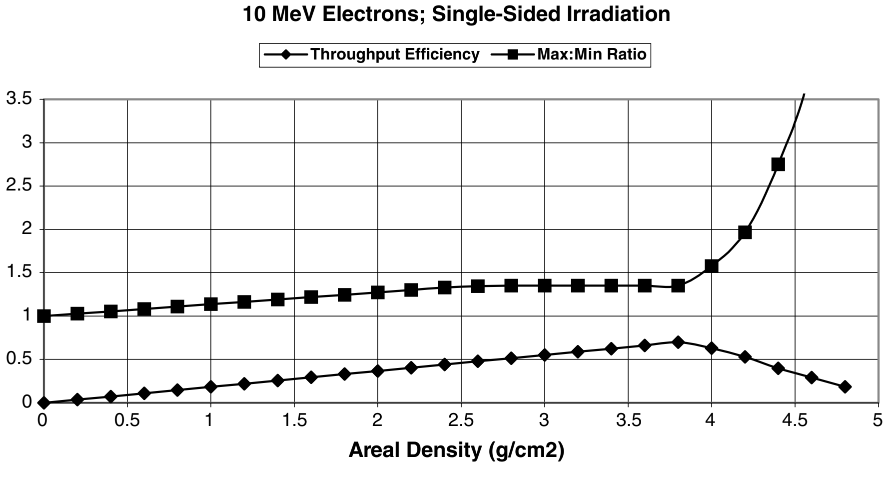

Figure 2-9. Utilization efficiency and dose max:min ratio for 10-MeV electrons.

Consideration of the data presented in Figures 2-8 and 2-9 indicates that the product thickness that can be effectively treated using a 10-MeV electron beam is limited to an areal density of about 4 g/cm^2, which is often overly restrictive. To circumvent this limitation we suppose that the product is irradiated from two sides with nominally identical electron beams. In this case the total dose profile will be given by

$$D_t(x, T) = D(x) + D(T - x) \tag{2.6}$$

where T is the product thickness, x is the depth into the product as measured from either surface, and D(x) is the single-sided depth-dose profile. It is apparent that the dose profile for double-sided irradiation must be symmetric about the midplane of the product.

The 10-MeV depth-dose profiles for a few selected product thicknesses are shown in Figure 2-10. Because of the rapid decrease in dose for depths greater than 3.8 g/cm^2, from Figure 2-9, the depth-dose profile for double-sided irradiation is quite sensitive to product thickness variation over the range of 7.5–10 g/cm^2. The corresponding max:min ratio and utilization efficiency constructed from these one-dimensional analyses are presented in Figure 2-11. The utilization efficiency attains a maximum value of about 0.8 for an areal density of 8.4 g/cm^2. Based on these data, the maximum product thickness that can be processed effectively with 10-MeV electrons is approximately 8.8 g/cm^2. For products requiring exceptional dose uniformity, utilization efficiencies in excess of 60% can be achieved if the product thickness can be restricted to an areal density <3 g/cm^2.

2.2.2. Dose Uniformity and Utilization Efficiency for X-Rays

Based on the analyses of the preceding section, products having areal densities of 3.8 g/cm^2 or less can be effectively treated by direct (single-sided) electron bombardment at electron kinetic energies of 10 MeV or less, and products with areal densities up to about 8.5 g/cm^2 can be processed by double-sided electron treatment. However, for areal densities exceeding about 8.8 g/cm^2, the ionizing dose must be provided by more penetrating x-ray radiation.

When energetic x-rays pass through matter they lose energy via three primary interaction mechanisms: (1) the photoelectric effect, (2) Compton scattering, and (3) pair production. These processes will be described in some detail in Chapter 4. For now, it is sufficient to note that all of these interactions produce energetic secondary electrons that subsequently lose their energy via the processes described in the previous section. Consequently, the radiation dose delivered by x-rays is identical in character to that delivered by a primary electron beam.

The energy deposition profile resulting from x-ray irradiation is usually described as an exponentially decreasing function of depth. For a monoenergetic x-ray beam of intensity I, the decrease in intensity dI in passing through a material thickness ds is proportional to the intensity multiplied by the incremental thickness. In equation form,

$$dI = -\mu I\, ds \tag{2.7}$$

The constant of proportionality, μ, termed the linear attenuation coefficient, represents the cumulative effect of the three interaction mechanisms. When the implied integration is performed, the intensity of this monoenergetic photon beam is found to decrease exponentially as

$$I = I_o\, e^{-\mu s} \tag{2.8}$$

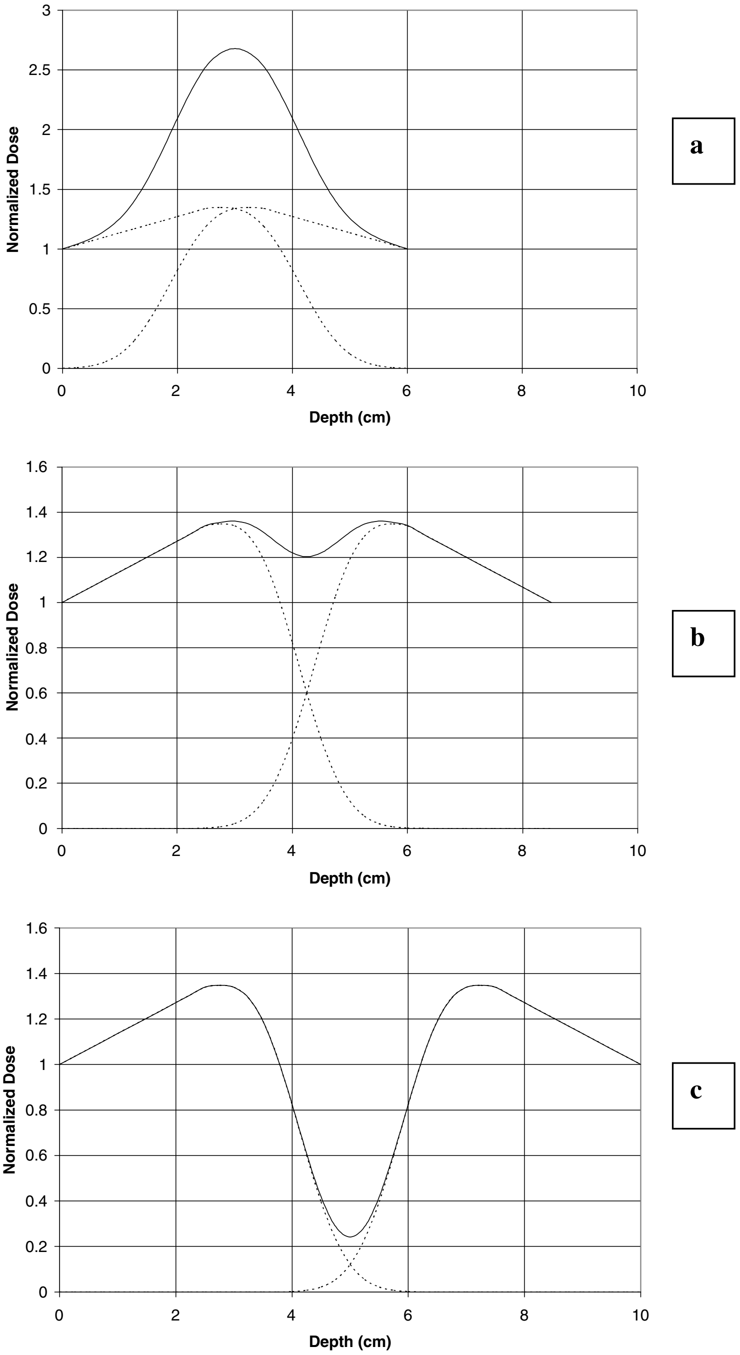

Figure 2-10. Double-sided irradiation depth-dose profiles in a unit density absorber for three different absorber thicknesses: (a) 6 cm, max:min = 2.7; (b) 8.5 cm, max:min = 1.35; (c) 10 cm, max:min = 5.4.

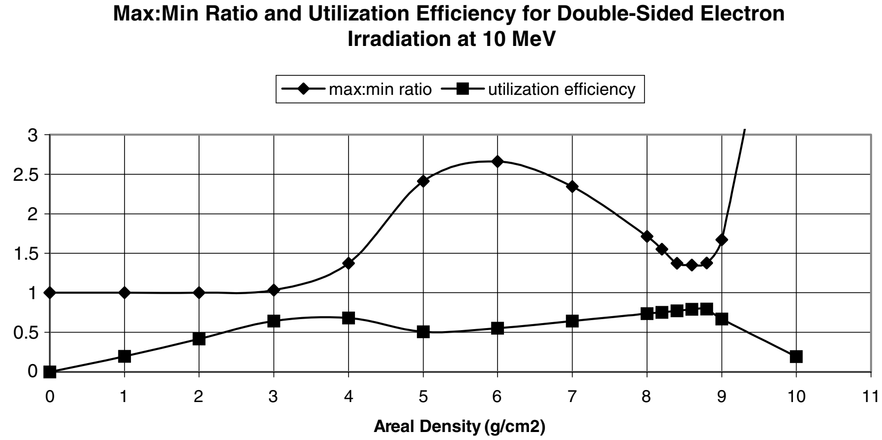

Figure 2-11. Max:min ratio and utilization efficiency for symmetric, double-sided irradiation using10-MeV electrons.

where I_o is the intensity at the front surface. Unfortunately, the bremsstrahlung x-ray energy spectrum is not monoenergetic, and the attenuation coefficient is energy dependent. In addition, the energy lost in an x-ray interaction is not deposited locally at the point of the interaction. In spite of these complications, an exponential model usually provides an adequate description of the deposition profile. Making this assumption, consider the diagram of Figure 2-12.

An x-ray flux F_o (joules/cm^2) is incident on product of thickness d. The x-ray energy is attenuated exponentially by absorption in the product by assumption, so that the flux at depth s is given by $F_o \exp(-\mu_m \rho s)$. The product density is designated by ρ(g/cm^3), while μ_m (cm^2/g) denotes the effective mass absorption coefficient. Multiplying the energy flux by the mass absorption coefficient therefore gives the dose at the depth s. In analogy to Figure 2-8, for the case of single-sided irradiation using electron beams, this x-ray depth-dose profile is shown in Figure 2-13.

For single-sided irradiation using x-rays, the maximum dose (μ_m F_o) always occurs at the front surface, while the minimum dose occurs at the rear surface ($s = d$), and is given by $\mu_m F_o \exp(-\mu_m \rho d)$. The max:min ratio is therefore trivially given by $\exp(\mu_m \rho d)$. The useful delivered dose corresponds to the rectangular area defined by D_{min} and the product depth d. Consequently, the efficiency with which the x-ray energy is utilized in delivering useful dose to the product is obtained by dividing $[F_o d \exp(-\mu_m \rho d)]$ by the total area under the exponential curve, which is given by $F_o/(\mu_m \rho)$. The

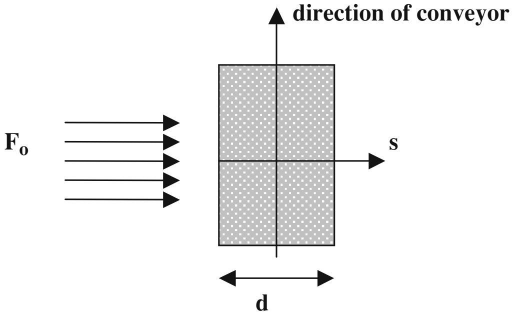

Figure 2-12. One-dimensional schematic drawing of the x-ray irradiation geometry.

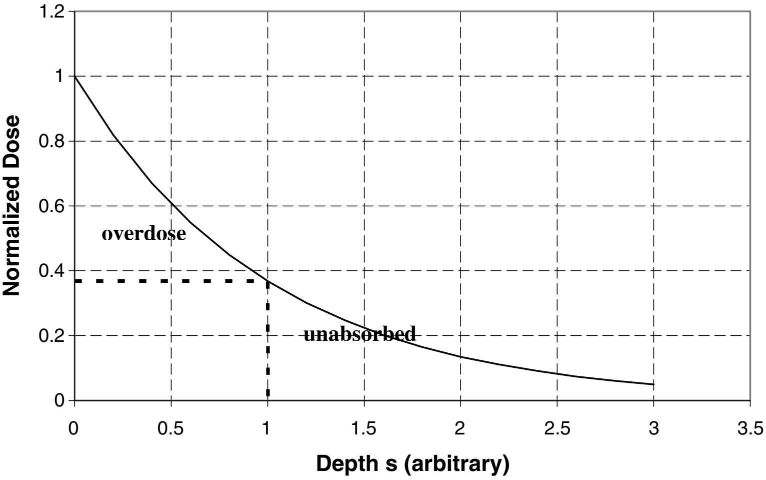

Figure 2-13. Depth-dose profile for single-sided x-ray irradiation.

x-ray utilization efficiency in this case is therefore given by

$$\eta_u = (\mu_m \rho d) \exp(-\mu_m \rho d) \tag{2.9}$$

This expression attains its maximum value of 0.368 at $\mu_m \rho d = 1$. The corresponding max:min ratio is 2.72, which is quite poor. The max:min ratio can only be improved by reducing the product thickness, which further reduces the utilization efficiency. As a result, single-sided x-ray treatment is almost never used for food irradiation. Instead, the product is either rotated for a second pass through the x-ray beam, or the product makes a single pass through two nominally identical x-ray beams, as suggested in Figure 2-14.

In this case, the dose distribution as a function of s is given by

$$D(s) = \mu F_o \left[e^{-\mu\rho s} + e^{-\mu\rho(d-s)}\right]$$

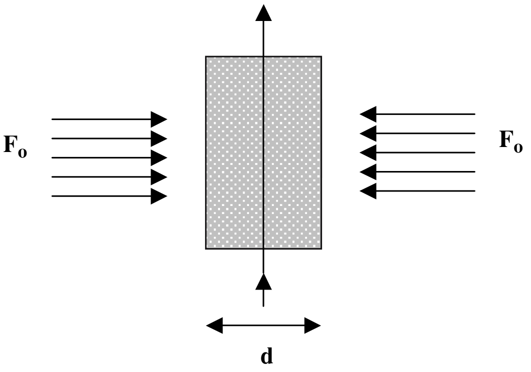

Figure 2-14. Schematic diagram of the double-sided x-ray irradiation configuration.

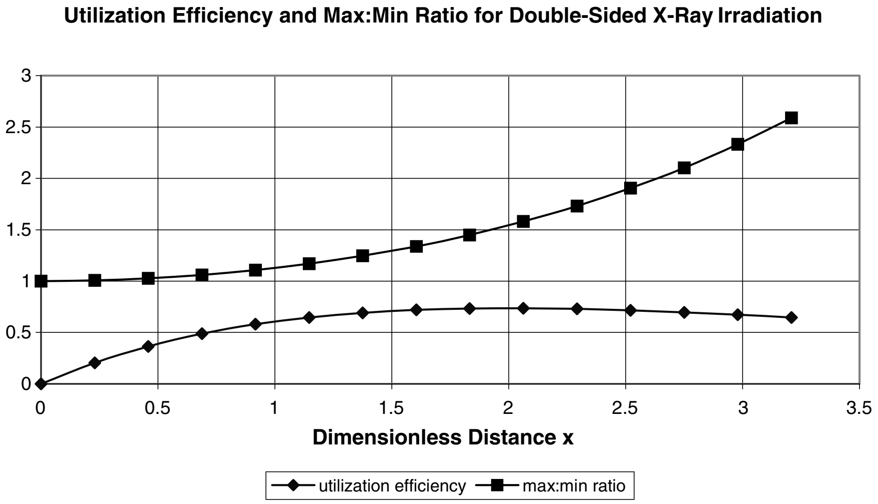

Figure 2-15. 1-D x-ray energy utilization efficiency, and max:min ratio for the double-sided irradiation configuration of Figure 2-14.

The maximum dose (at either surface) and the minimum dose (at $s = d/2$) are given by

$$D_{max} = \mu F_o(1 + e^{-\mu\rho d})$$
$$D_{min}(s = d/2) = 2\,\mu F_o \exp(-\mu\rho d/2) \tag{2.10}$$

The max:min ratio and the utilization efficiency are given as

$$D_{max}/D_{min} = 0.5[1 + e^{-\mu\rho d}]e^{\mu\rho d/2} \tag{2.11}$$
$$\eta_u = \mu\rho d\, e^{-\mu\rho d/2} \tag{2.12}$$

Eqs. (2.11) and (2.12) are graphed in Figure 2-15 as a function of the dimensionless depth variable $x = \mu\rho d$.[6] The utilization efficiency has a broad maximum of about 0.735 at $x = x_{opt} = 2.0$. The max:min ratio is 1.54 at x_{opt}.

2.2.3. Dose and Dose Rate Estimation

The dose and dose rate delivered to the product are determined by the operating parameters of the three key components of the processing system (accelerator, scanner and conveyor). In the next few paragraphs we illustrate how these quantities can be estimated for both electron beam and x-ray irradiation systems.

a. Electron Beams

Consider the schematic diagram of Figure 2-16. An electron beam is scanned uniformly in one dimension. Product is conveyed through the beam at right angles to both the scan direction and the beam direction. The beam is assumed to have a constant kinetic energy E and average current I. The scan width is designated by w, and the conveyor speed is v.

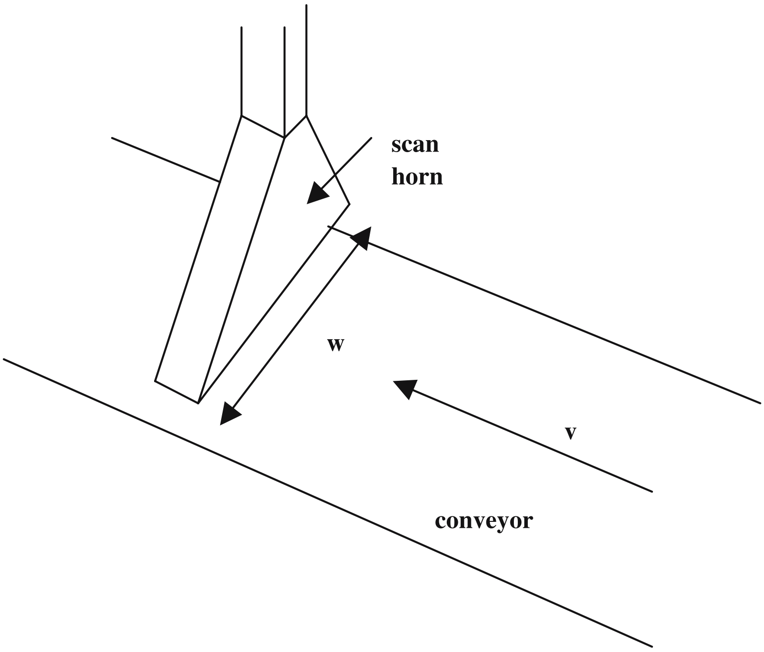

Figure 2-16. Schematic representation of the beam scanning configuration. Product is conveyed under the scan horn at a uniform velocity v. The width of the scan is w.

Writing the current density as j = I/A, Eq. (2.3) can be rewritten as

$$D(d) = \Delta W_{sp}(d)\ It/A$$

The quantity (A/t) can be identified as the area irradiated by the beam per unit time, which is equal to the product of the scan width and the conveyor speed; i.e.,

$$A/t = vw \tag{2.13}$$

Consequently, the dose delivered at the depth d into the product is given by

$$D(d) = \Delta W_{sp}(d)I/(vw) \tag{2.14}$$

As a numerical example, for a scan width $w = 100$ cm and a conveyor speed $v = 10$ cm/s, the front surface dose delivered by a 10-MeV, 1-mamp beam (having an average beam power of 10 kW) will be 1.85 kGy.

As discussed in Appendix A, the readings of certain dosimeters exhibit a dose rate dependence, and it is therefore useful to estimate the peak and average dose rates associated with electron irradiation configurations. The average dose rate for the process is simply found by dividing the delivered dose by the time t_p required for a slice of the product to move through the beam width W_b, as expressed in Eq. (2.15).

$$\langle dD/dt \rangle = D/t_p = Dv/W_b \tag{2.15}$$

From Eq. (2.14) the front surface dose is approximately given by

$$D_{fs} = 1.8 \times 10^6\, I_a/(vw)$$

where I_a is the average beam current and w is the width of the scan. Therefore, an estimate of the dose rate at the front surface of the product is

$$\langle dD_{fs}/dt \rangle = 1.8 \times 10^6\, I_a/(wW_b) \tag{2.16}$$

The scattering of the beam by the titanium exit window is considered in Chapter 3. Assuming 10-MeV electrons from a 15 kW machine (1.5 mamps average current) traversing a 5-mil Ti window, and a distance of 30 cm between the window and the front surface, then the beam width is approximately 6 cm. If the scan width is 120 cm, then the average dose rate for the process is approximately 3.75 kGy/s.

While this average dose rate is quite high, it should also be realized that most microwave accelerators operate in a pulsed manner, producing macropulses of duration T_m at the modulator repetition frequency F (see Chapter 5). As an example, for 20 microsecond pulses at a repetition rate of 250 Hz, the duty cycle is 0.5%. Consequently, for an average dose rate of 3.75 kGy/s, the peak macropulse dose rate is 750 kGy/s.

Finally, within the macropulse are individual micropulses that typically occur at the microwave frequency f. Since the peak current associated with a micropulse can be nearly an order of magnitude higher than the average macropulse current, the peak micropulse dose rate in the above example could exceed 5000 kGy/s!

b. X-Ray Systems

Developing accurate dose estimates for an x-ray system is considerably more difficult than for electrons because of the angular dependence of the x-rays produced in the converter target. As a first step, the total electron beam energy Q_b incident on the converter is multiplied by the x-ray conversion efficiency η_c to obtain the total forward-going x-ray energy. η_c scales linearly with kinetic energy; a useful approximate expression is

$$\eta_c = E(\mathrm{MeV})/60 \tag{2.17}$$

Therefore, at 5 MeV , $\eta_c = 0.08$, and $\eta_c = 0.12$ at 7.5 MeV. Using the 5-MeV case as an example

$$Q_x = 0.08\, Q_b = 0.08Pt \tag{2.18}$$

where P is the power of the electron beam incident onto the converter. This energy will be incident onto an (minimum) area given by the product of the scan width, the conveyor speed and the irradiation time. Therefore, the x-ray flux F_o at the front surface of the product is estimated as

$$F_o = Q_x/A = 0.08\, P/(v\, w) \tag{2.19}$$

From the previous section the dose at the product surface is obtained by multiplying the expression for F_o by the x-ray mass absorption coefficient μ_m, as

$$D = \mu_m F = 0.08\,[\mu_m P/(vw)] \tag{2.20}$$

For a 5-MeV x-ray spectrum, the mass absorption coefficient has an average value of about 0.03 cm^2/g. As a numerical example, for a scan height of 60 cm (about 24 inches), a conveyor speed of 0.5 cm/s (about one foot per minute) and an average beam power of 15 kW, Eq. (2.20) gives a predicted front surface dose of about 1.2 kGy.

The estimate provided by Eq. (2.20) usually underestimates the observed surface dose by a small amount (15%), depending somewhat on the distance from the x-ray converter to the front surface of the product. This discrepancy is the result of the large angular spread of the x-ray emission. This large angular spread also results in a more rapid decrease of dose with depth into the product than use of the average mass absorption coefficient would suggest. An adequate description of these features requires the more detailed treatment presented in Chapter 4.[6] Nonetheless, with the beam power in kilowatts, the scan speed in cm/sec, and the scan width in centimeters, a useful practical estimate for the front surface dose (in kGy) resulting from a 5-MeV x-ray irradiation is

$$D_{fs} = 2.7\,P/(vw) \tag{2.21}$$

The decrease in dose with depth is modeled by an effective absorption coefficient that depends on density according to $\mu_e = 0.045 + 0.01/\rho$.

The dose rate for x-ray irradiation can be estimated in the same manner as for electrons, but the beam width is considerably larger because of the scattering processes in the converter (see Chapter 4). As an order of magnitude estimate, assume $W_x = 20$ cm. For a conveyor speed of 1 cm/s, the irradiation time t_x for a particular slice of product is 20 seconds. For a machine power of 100 kW and a scan width of 1 meter, the front surface dose is estimated to be 2.7 kGy. Dividing this dose by 20 seconds, the surface dose rate is therefore 135 Gy/s, which is considerably less than the dose rates produced by the electron irradiation examples.

2.2.4. Throughput Estimates for Electrons and X-Rays

For irradiation using either energetic electron beams or more penetrating x-rays, the mass throughput of product through the system is essentially determined by the average beam power P divided by the minimum required dose. If dM/dt represents the mass throughput of product in units of kg/s, then

$$dM/dt = \eta_t\, P(kW)/D_m(kGy) \tag{2.22}$$

with the beam power in kilowatts and the minimum dose in kilogray. η_t is termed the **throughput efficiency**. Note that the throughput rate does not depend directly on the kinetic energy of the electrons produced by the accelerator system. For electron irradiation the throughput efficiency must account for the utilization efficiency resulting from the non-uniform depth-dose distribution (0.6–0.8), the amount of overscanning to ensure full dose coverage at the edges of the product (0.8–0.9), and the efficiency with which product is arranged on the conveyor (0.6–0.8). Taking all of these factors into consideration, a typical value of the throughput efficiency is 0.45.

The throughput efficiency for x-rays must take into account these same factors, plus the low x-ray conversion efficiency. As a result, a typical value for the throughput efficiency is only 0.03 at 5 MeV, increasing to 0.045 at 7.5 MeV.[6]

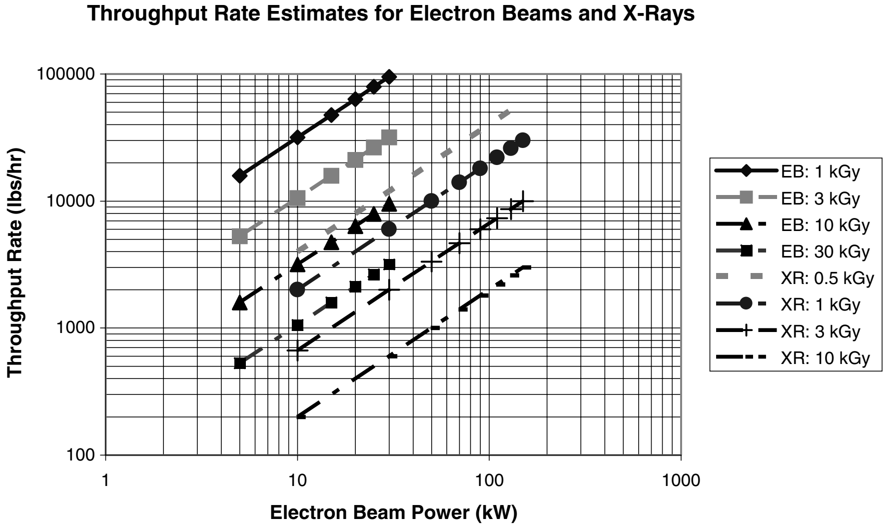

Figure 2-17. Estimated throughput rates for electron beam and 5 MeV x-ray systems as a function of the electron beam power produced by the accelerator. (For x-ray processing at 7.5 MeV, the throughput rates will increase by approximately 50%)

Using these throughput efficiency estimates, the throughput rates (in pounds per hour) that might be anticipated for both electron beam and x-ray systems are graphed in Figure 2-17 versus electron beam power for several different values of the minimum required dose. For doses typical of food safety applications (1–2 kGy), modest electron beam systems are capable of throughput rates in the range of 10,000–100,000 lbs/hr, which is quite impressive. For disinfestation applications (0.5 kGy), throughput rates of up to 10,000 lbs per hour are reasonable with modest x-ray systems. However, for irradiation of spices (5–10 kGy), very large x-ray systems are necessary to achieve reasonable throughput rates (>1000 lbs/hr).

2.3. COST ANALYSES AND UNIT PRICING

The amount of food currently produced worldwide on a yearly basis is estimated to approach two quadrillion pounds, broken down into five key areas as indicated in Table 2.1.[7] Even modest consumer acceptance of irradiated food products could result in an eventual demand for worldwide processing facilities that could amount to hundreds of billions of pounds per year. However, installation of the processing capacity to address this potential market will require significant amounts of investment capital, and some of the opportunities suggested by Table 2.1 will not generate sufficient return-on-investment to represent sustainable businesses.

To address these issues of economic viability we present a simplified model for the annual costs associated with building and operating a food irradiation facility, and use the model together with the results of the previous section to estimate breakeven unit pricing for several application examples.[*] The annual costs are conveniently divided into fixed and variable costs.[8] Fixed costs are essentially unchanged when product output varies. For example, once the conveyor and accelerator hardware

---

[*] This simplified model does not take into account various tax code provisions such as depreciation, investment tax credits, and deductibility of interest payments; such considerations will vary from firm to firm, country to country, and state to state.

Table 2.1. Estimated Worldwide Food Production Volume (millions of pounds)

Product	US	International	Total
Ground Beef	9,000	10,000	19,000
Poultry	35,000	100,000	135,000
Processed Meats	25,000	N/A	25,000
Seafood	12,000	250,000	262,000
Fruits/Vegetables	65,000	1,300,000	1,365,000
Total	146,000	1,660,000	1,806,000

necessary to process a particular level of throughput have been installed, the costs associated with the purchase of these items will not decrease if the output is reduced. On the other hand, variable costs depend on how much the facility is used. In particular, utilities and hourly labor will be directly related to the output volume. The breakeven unit cost is given by dividing the total annual cost (the sum of fixed and variable expenses) by the estimated yearly output.

2.3.1. Elements of Fixed Cost

The two largest fixed cost elements are the yearly amortization of the capital investment and fixed labor costs for salaried employees. The major capital costs are for construction and installation of the accelerator system, the radiation shielding, and the material handling equipment. For service center facilities, the costs of new building construction (or improvements to an existing building) and the land (if necessary) on which the facility is sited can also be quite significant.

For rf linacs in the kinetic energy range of 5–10 MeV, the accelerator system cost is essentially independent of kinetic energy, but generally increases with average beam power capability.[†] The dependence is much slower than linear, however; accordingly, we adopt a logarithmic estimate given by

$$C_{\text{linac}}(\$K) = 10^3 \log_{10}[P(kW)] \tag{2.23}$$

Installation costs, including mechanical and electrical installation and dose verification, are assumed to be 20% of the accelerator system cost. The concrete shield and air-handling system required for venting ozone to the atmosphere also scale with linac power, and are assumed (together) to be 30% of the linac cost.

Material handling equipment includes not only the conveyor system, but also forklifts for loading and unloading operations, as well as plastic wrapping machines and perhaps even depalletizing and repalletizing machinery for large facilities. Although the material handling system for an x-ray facility is probably somewhat more expensive because it must handle larger packages, we assume a flat cost of $250 K for each.

In addition to space for the accelerator, material handling system, and radiation shield, building space is also required for offices, the control room, the dosimetry laboratory, the warehouse floor, and truck docking. If perishable or frozen products are to be irradiated, then refrigerated storage space is also required. As a starting point for a stand-alone processing facility, we assume 40,000 sq. ft. of floor space at an average cost of $70 per sq. ft., for a total estimated building cost of $2.8 M. (This total is also assumed to include the cost of land.)

[†] Similar economic analyses have been performed for Rhodotron accelerator systems; see Ref. 9 for details.

Finally, costs associated with the design and engineering of the plant equipment, the radiation shield, the overall facility layout, the system utilities, product flow, etc., are assumed to be 10% of the total facility cost, less the costs of the accelerator hardware and accelerator installation. With these assumptions, the total capital cost (TC) is given by

$$\mathrm{TC}(\$\mathrm{K}) = 3350 + 1660 \log_{10} \mathrm{P}(\mathrm{kW}) \tag{2.24}$$

The annual amortization payment (yearly cost of the investment) is estimated from Eq. (2.25), where i is the interest rate (assumed to be 8%), and n is the number of years of useful life (assumed to be 15 years).

$$\mathrm{C}_{\mathrm{inv}} = \mathrm{TC}\{\mathrm{i}(1+\mathrm{i})^{\mathrm{n}}/[(1+\mathrm{i})^{\mathrm{n}} - 1]\} = 0.117\,\mathrm{TC} \tag{2.25}$$

Other fixed costs include labor and maintenance. Fixed labor costs must include the salaries of key employees (plant manager, radiation safety officer/quality control person, maintenance personnel, and clerical help). This total, including benefits, is assumed to be $300 K per year at current labor rates. Finally, annual fixed maintenance costs are assumed to be 5% of the total cost of the accelerator and material handling systems.

2.3.2. Elements of Variable Cost

Variable costs include utilities (primarily electrical power), labor (costs of a shift supervisor/plant operator and product handling personnel), and incremental maintenance. Electrical power is required to run the accelerator, the material handling system, the heating and cooling systems, and other miscellaneous facility equipment. The overall efficiency of an rf linac (wall plug to electron beam) is typically no greater than 20–25%, implying a power grid usage multiple of at least 4–5. To account for the additional power consumption of the other facility equipment, we assume that the total electrical power consumed by the facility is a factor of eight times the average electron beam power produced by the accelerator. In recent years, the cost of electrical power has varied considerably from locality to locality. For estimation purposes, we assume an average electricity cost of $0.08 per kilowatt-hour. Designating the number of production hours per year by U, the total estimated yearly cost of electricity is given by

$$\mathrm{C}_{\mathrm{elect}}(\$\mathrm{K}) = 8\,\mathrm{P}(\mathrm{kW}) \times 0.08 \times (\mathrm{U}/1000) = 6.4 \times 10^{-4}\,\mathrm{P}(\mathrm{kW})\,\mathrm{U}(\mathrm{hrs}) \tag{2.26}$$

Variable labor costs include the yearly wages and benefits paid to a shift supervisor and material handling personnel. At current labor rates, these are estimated at $140 K per year per shift. Assuming that a shift corresponds to 2000 hours per year, the yearly variable labor costs are given by

$$\mathrm{C}_{\mathrm{labor}}(\$\mathrm{K}) = 0.07\,\mathrm{U}(\mathrm{hrs}) \tag{2.27}$$

Variable maintenance costs depend on both the power level of the accelerator system, and the yearly usage. For estimation purposes this yearly cost is assumed to be 5% of the cost of the accelerator and material handling systems, multiplied by the number of shifts. With this assumption, the total yearly maintenance costs (fixed plus variable) for a facility operated for one shift is 10% of the capital cost of the accelerator and material handling equipment.

The yearly cost estimates given by this model using the stated assumptions are summarized in Table 2.2 for two different accelerator systems: a modest 15 kW machine used for electron beam

Table 2.2. Yearly Cost Estimates for Food Irradiation Facilities ($K), based on 2000 hours per year

Cost Element	15 kW	150 kW
Fixed Costs		
Capital Items		
Accelerator	1176	2176
Installation	235	435
Shielding	353	653
Mat'l Handling	250	250
Building	2800	2800
Engineering	340	370
Total Capital	**5169**	**6834**
Investment Expense	604	798
Labor	300	300
Maintenance	71	121
Total Fixed Costs	**975**	**1220**
Variable Costs		
Electricity	19	192
Labor	140	140
Maintenance	71	121
Total Variable Costs	**230**	**453**
Total Yearly Costs	**1206**	**1673**

irradiation, and a robust 150 kW machine used for x-ray irradiation. Each machine is assumed to have single shift usage (2000 hours per year).

2.3.3. Breakeven Unit Pricing

The amount of yearly throughput depends on the throughput rate, as given by Eq. (2.20), multiplied by the facility usage (in hours) per year. The unit cost is then found by dividing the total yearly cost by the total throughput; i.e.,

$$\text{Unit cost} = \text{TC}/[\text{U}(\text{dM}/\text{dt})] \tag{2.28}$$

As an example of the utility of the cost model, we will use it to estimate the breakeven unit pricing (cost per pound of product irradiated) for three different examples: (1) a 15-kW, 5-MeV x-ray facility used for insect disinfestation of fresh produce, assuming a minimum required dose of 0.5 kGy; (2) a 15-kW electron beam facility used to ensure the safety of fresh ground beef products, assuming a minimum required dose of 1.5 kGy; and (3) a 150-kW, 5-MeV x-ray facility used for shelf-life extension of spices, assuming a minimum dose of 6 kGy. The unit costs for these three assumed applications are graphed as a function of usage in Figure 2-18. The usage range is from half-shift operation (1000 hours per year) to a maximum of three shifts (6000 hours/yr).

Although this economic model is grossly simplified and can be criticized on several grounds, it does indicate many key points. First, these facilities are capital intensive; the largest single cost item is investment expense. Approaches for decreasing the high capital costs merit consideration. For example, assuming that market conditions are favorable, housing multiple irradiators (i.e., an electron beam and an x-ray irradiator) in a single facility, with a shared radiation shield if possible, will significantly decrease the required capital outlay compared to the capital required for two separate facilities.

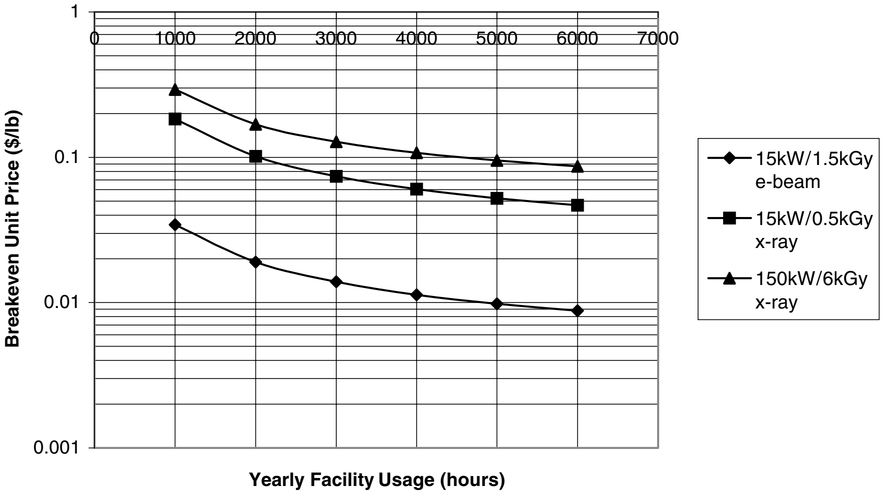

Figure 2-18. Breakeven unit price ($/lb) versus yearly facility usage for three representative food irradiation applications.

To generate sufficient cash flow to offset the high expenses, these facilities must not sit idle, and should be operated no less than one full shift averaged over a year. Because of the poor x-ray conversion efficiency, electron beam processing is always favored over x-ray processing, unless product packaging prohibits electron usage because of penetration limitations. Similarly, throughput scales inversely with the minimum required dose. The use of x-rays for applications with high minimum required doses is therefore prohibitively expensive unless high power accelerators are used. Assuming the existence of sufficient market demand, higher power installations are always favored because income scales linearly with power, while many cost items vary less rapidly with power.

The data of Figure 2-18 suggest that with the proper technological approach and reasonable usage factors, most food products can be irradiated at a unit price in the range of 1–10 cents per pound. For products with high intrinsic value (meat products, seafood, tropical fruits, etc.), this economic analysis indicates that the business prospects for such applications should be quite favorable.

2.4. SYSTEM ANALYSIS AND TECHNOLOGY SELECTION

The selection of a specific technological approach for a particular food irradiation application is governed by many factors. In addition to cost considerations, the several parameters that characterize the product lead naturally to certain processing requirements, which in turn dictate various technology choices, as schematically described in the information flow diagram of Figure 2-19. In the following paragraphs we discuss various aspects of this process, and give a few examples of the technological choices that are suggested.

The decision to use electron beam or x-ray processing is largely determined by the required penetration depth of the ionizing radiation, and the acceptable range of max:min ratios. The penetration depth depends on the areal density range of the product, and can be estimated knowing the package dimensions and the product density, as previously discussed in Section 2.2. The max:min ratio (MMR) is calculated knowing the minimum required dose (determined by the D_{10} value and the desired population reduction factor for the biological organism of concern) and the maximum desirable dose. The dose maximum is the smaller of the maximum allowable dose (established by regulation) and the maximum dose tolerated by the product.

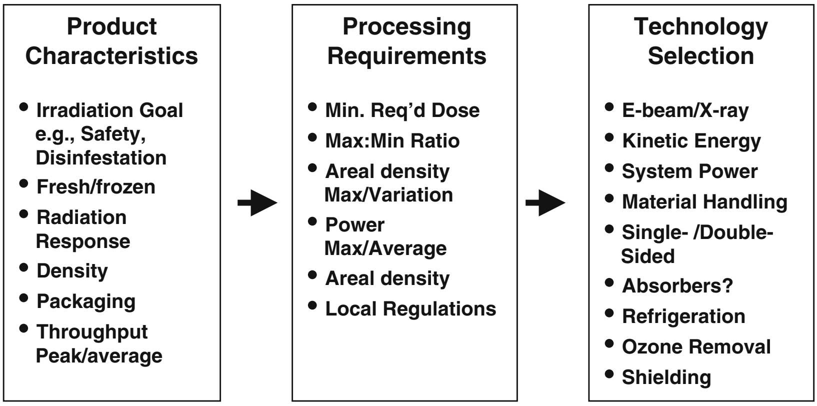

Figure 2-19. General information flow diagram leading to technology choices for particular food processing applications.

A simplified logic flow chart addressing this choice of processing approach is presented in Figure 2-20. The first question that must be answered is whether or not the product can be effectively processed at all. Since x-rays are more penetrating than electrons, this question can be addressed by referring to Figure 2-15. As a rough guideline, if the maximum areal density of the product exceeds 50 g/cm^2, and the MMR must be less than 3, then the product is not suitable for radiation processing, unless special steps are taken that can drastically decrease the throughput efficiency.

Assuming that the product can be effectively processed, the first technology decision to be made is whether or not electron beams can be used. The low x-ray conversion efficiency and a consideration of the electron beam energy utilization efficiency curve of Figure 2-11 indicate that the most effective approach for food irradiation is double-sided electron beam treatment for products having an areal density of approximately 8.4 g/cm^2. This approach will give the highest throughput rates (Figure 2-17) and lowest breakeven processing costs (Figure 2-18). However, the max:min ratio can be no better than 1.35, from Figure 2-11. If the product can be configured such that its nominal areal density is approximately 8.4 g/cm^2 ($+/-5\%$), and if max:min ratios in the range of 1.35–1.7 are acceptable, then double-sided electron beam processing using 10-MeV electrons is always the preferred approach.

If this special circumstance does not apply, then additional checks must done. In particular, if the areal density exceeds about 8.9 g/cm^2, or if the areal density exceeds 3.8 g/cm^2 and the MMR must be less than 1.35, then inefficient, but flexible, x-ray processing must be used. Otherwise, the product can be efficiently processed using electron beams, with the particular approach depending on the areal density and the MMR. For example, if the maximum areal density lies in the range of 3.8 g/cm^2 to 8.4 g/cm^2, then absorbers can be used to bring the combined areal density into the range of 8.4 g/cm^2. (Products having a large, unpredictable variation in areal density represent a special case and will be considered in Chapter 3.)

The required system power level is determined by the minimum required dose, the throughput rate and the type of ionizing radiation, as estimated using Eq. (2.22). For products whose processing rates necessarily fluctuate with time (seasonal fruits and vegetables, for example) the installed power capacity must be adequate to process at the peak throughput rate. This peak power level is important because it drives requirements for the radiation shield and the ozone exhaust system (which are subject to state and local regulations), the accelerator cooling requirements, and the size of the electrical substation; it is therefore an important factor in determining the capital cost of an installation, as previously discussed. Operating costs and revenues, however, generally depend on the average throughput rates and average power at which the facility is operated.

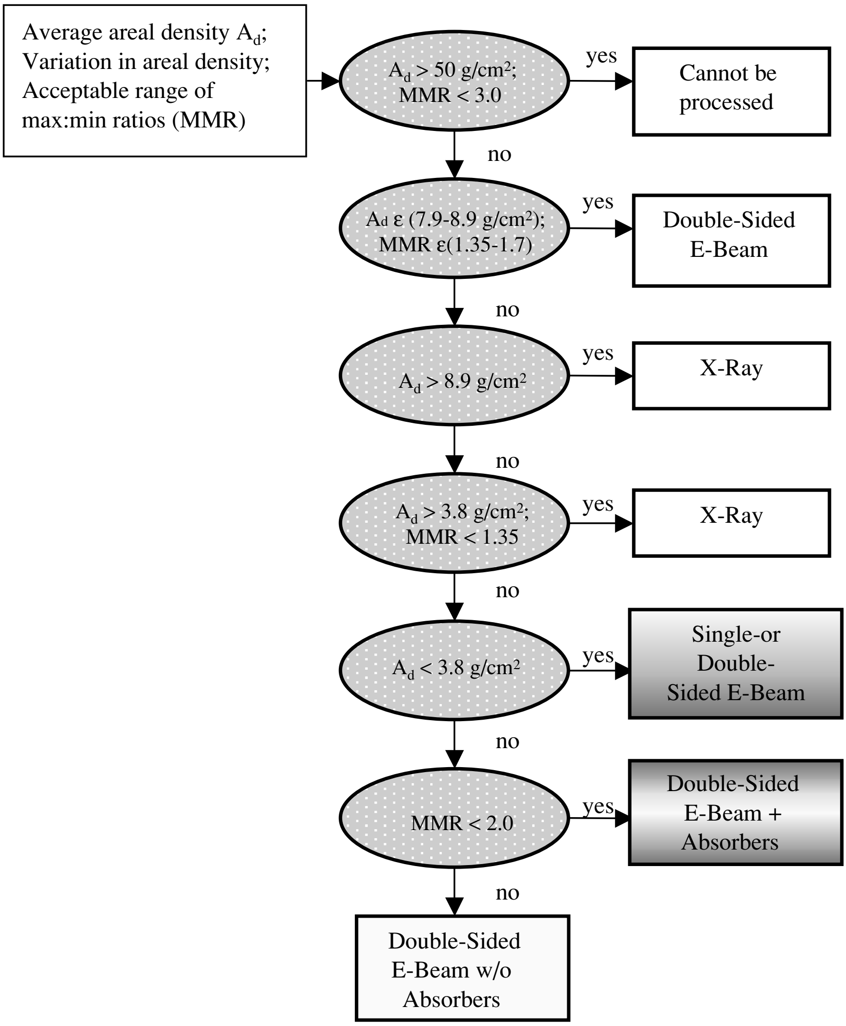

Figure 2-20. Decision tree for selecting the appropriate irradiation approach.

The choice of material handling system is largely governed by the choice of ionizing radiation. Since the penetration depth of electrons is limited (about 3.5 inches for double-sided irradiation of red meat products, for example), it is usually most convenient to irradiate with electron beams oriented vertically, and with product packages arrayed in flat fashion on a belt or roller conveyor. For products that require double-sided irradiation but cannot be flipped, the approach must use either two accelerators or else special split-beam-scanner hardware with a single accelerator. For more penetrating x-rays on the other hand, horizontal irradiation allows packages of products to be optimally arranged on a carrier that might be transported by a power-and-free conveyor system to a chain conveyor that moves the carriers through the irradiation zone.

For unpackaged foods (fluids and grains, for example) the material handling system will typically use gravity to provide a freely flowing stream of material through the irradiation zone. If single-sided electron irradiation is possible, a simple turntable system can offer a low-cost alternative. If double-sided electron irradiation is preferable or necessary, there must usually be a gap in the process conveyor region to provide an unimpeded path for the upward-directed beam to reach the product. Fresh produce is usually transported via pallets whose dimensions necessitate x-ray irradiation. Consequently, special pallet handling systems involving rotation mechanisms have been devised to permit effective irradiation of these foodstuffs.[10,11]

At present most food irradiation facilities are housed in service centers that provide custom irradiation of food products for many different customers. These facilities must therefore have sufficient flexibility to process a wide variety of products, which usually mandates an x-ray capability, as well as a large, refrigerated warehouse area with plenty of truck dock space. However, as food irradiation becomes more widely accepted as a routine food processing technology, it can be anticipated that some high volume food producers will require irradiation facilities located not only in-plant, but even incorporated directly into particular food production lines. In such circumstances considerable attention must be given to the product flow within the plant and to redundancy in the irradiation equipment to ensure that neither periodic maintenance nor unexpected downtimes results in a serious drop in production.

2.5. PROCESS VALIDATION

Following the construction of the facility and the installation of the equipment, there are several steps that must be completed before food products can be processed on a routine basis. As detailed in Reference 12, these include installation qualification, dose mapping, process qualification, and establishing routine process control parameters. A well-established dosimetry capability is essential for performing these tests (see Appendix A).

Following the initial installation (or any significant equipment alteration) the performance of the accelerator system must be determined under well-defined operating conditions. The necessary measurements include a determination of the electron kinetic energy, the height (width) and uniformity of the scan, the uniformity of the dose in the direction of conveyor motion, and a determination of depth dose distributions throughout the irradiation volume using homogeneous (phantom) absorbers with densities that correspond to the range of densities of the products to be processed. These tests necessarily ensure that the material handling system is working reliably according to its performance specifications, and that the software responsible for monitoring and controlling the process, as well as the several auxiliary systems that support accelerator operation, are operating reliably without spurious system faults.

Once the performance characteristics of the irradiation equipment and software have been determined, it is necessary to perform detailed dose-mapping studies of representative product samples to determine the positions of minimum and maximum dose. An additional goal is to establish the reproducibility of the process. These data can then be used to determine how the product should best be configured on the conveyor system for highest throughput efficiency, while consistently satisfying minimum and maximum dose criteria.

The final step is to establish routine process parameters based on the data gathered in the installation qualification and dose mapping steps. An important feature of this step is to set limits on the key process parameters so that the integrity of the process is ensured, while minimizing the occurrence of spurious and nuisance faults. This topic is discussed in some detail in Chapter 11.

2.6. SUMMARY

In this chapter we have discussed many important characteristics of food irradiation in a general way, in order to lay the foundation for more detailed treatments of specific technology aspects in later chapters. For an accelerator-based irradiator, the three systems that determine the dose are the accelerator, the beam scanner, and the material handling (conveyor) system. The same technology permits either direct electron beam irradiation (by allowing the scanned beam to emerge through a thin metallic window), or indirect x-ray irradiation (by impinging the scanned beam onto a high-atomic-number x-ray converter).

The amount of product that can be processed by an accelerator-based irradiator is determined by the beam power divided by the minimum required dose, and multiplied by a throughput efficiency factor. The throughput efficiency is essentially determined by the efficiency with which the beam energy is used to provide the minimum required dose, which depends on the depth-dose (energy deposition) profile. For x-rays, the throughput efficiency is further reduced by the low x-ray conversion efficiency.

Regardless of the type of beam, the in-product dose profile is not constant. This dose nonuniformity is usually characterized by the ratio of the maximum dose to the minimum dose. Various strategies, such as double-sided irradiation, can be used to reduce the max:min ratio to acceptable levels, and to increase the throughput efficiency. The particular processing approach usually depends on various such processing requirements, and the details of the product packaging. Electrons have limited penetrating power, but deliver energy efficiently. X-rays are much more penetrating, and this flexibility permits a wider array of treatment options. However, the low x-ray conversion efficiency usually implies the use of electron beams for economic reasons whenever possible.

REFERENCES

1. USFDA, Federal Register **21 CFR Part 179** (1986) 13376.
2. Codex Alimentarius General Standard on Food Irradiation (1983).
3. C.J. Karzmark, C.S. Nunan and E. Tanabe, **Medical Electron Accelerators**, McGraw-Hill, N.Y. (1993).
4. **The Essentials of Material Handling**, R.E. Ward, editor-in-chief, Material Handling Institute, Charlotte, NC (1996).
5. **ISO/ASTM 51649:2002(E)**, Practice for Dosimetry in an Electron Beam Facility for Radiation Processing at Energies between 300 keV and 25 MeV, ASTM International (2002).
6. R.B. Miller, "Food irradiation using bremsstrahlung X-rays," Rad. Phys. and Chem. **68**, 963–974 (2003).
7. Food and Agriculture Organization (FAO) of the United Nations Production Yearbook (1999).
8. R.M. Morrison, An Economic Analysis of Electron Accelerators and Cobalt-60 for Irradiating Food, Tech. Bull. 1762, US Dept. of Agriculture (1989).
9. M.R. Cleland, A.S. Herer and A. Cokragen, "Economics of Machine Sources for Irradiation of Food," Int'l. Conf. On Ensuring the Safety and Quality of Food through Radiation Processing, P. Loaharanu and P. Thomas, eds., Technomic Publishing Co., Inc., Lancaster, PA (2001). P. 159.
10. Y. Jongen and F. Stichelbaut, "The palletron: an X-ray high dose uniformity pallet irradiator," Proc. 17th Int'l. Conf. Appl. Accel. in Res. and Ind., Denton, TX (2002).
11. R. B. Miller, "X-Ray Pallet Processing System," SureBeam Patent Disclosure (2002).
12. **ISO/ASTM 51431:2002(E)**, Practice for Dosimetry in Electron and Bremsstrahlung Irradiation Facilities for Food Processing.

CHAPTER 3

FOOD IRRADIATION USING ELECTRON BEAMS

A brief introduction to food irradiation using energetic electrons has been given in Section 2.2. In this chapter we will consider this subject in much more detail. Beginning with a theoretical summary of electron-matter interactions, we will then discuss depth-dose profiles, and we will develop max:min ratios and energy utilization efficiency estimates for both single- and double-sided irradiation assuming one-dimensional, homogeneous media. This treatment is then extended to the important cases of standardized, homogeneous products of irregular shape, and products with randomly distributed areal densities. Finally, we will consider various edge effects, derive criteria for the uniform illumination of the front surface, and discuss methods for ensuring dose uniformity at air-product interfaces.

3.1. ELECTRON INTERACTIONS IN MATTER

As energetic electrons pass through matter they undergo Coulombic collisions with atomic electrons and nuclei, for each of which there are many possible energy losses and angular changes.[1] For incident electrons with energies in the range of 1–10 MeV, the relativistic mass is significantly greater than the mass of an atomic electron, but very small in comparison with the mass of an atomic nucleus. From purely kinematic considerations therefore, a scattering collision with a massive nucleus will not result in significant energy transfer, but will appreciably alter the incoming electron trajectories, and the abrupt accelerations can produce x-ray radiation (bremsstrahlung). In contrast, collisions with the atomic electrons can result in significant energy transfer, leading to ejection of these electrons from their atomic orbitals (ionization). In turn, these energetic secondary electrons, sometimes called knock-ons or delta rays, can also undergo Coulombic collisions, producing tertiary electrons, etc., until the kinetic energy of the incident electron is nearly completely absorbed (minus the energy of the escaping x-rays).

From the standpoint of understanding the variation in absorbed energy with depth (the depth-dose distribution shown in Figure 2-8, for example), the important processes are therefore, (1) energy loss of the primary particle as the result of inelastic collisions with atomic electrons; (2) the generation of energetic secondary, tertiary, etc. electrons (with non-zero range) as the result of these inelastic collisions; (3) angular deflections resulting from multiple nuclear elastic scattering collisions which produce transverse beam spread, and (4) bremsstrahlung radiation (x-rays), primarily from nuclear collisions. We discuss each of these processes in more detail in the following paragraphs.

3.1.1. Inelastic Scattering from Atomic Electrons

The essential features of the interaction between an energetic incident electron and an electron "free" of binding forces can be found in the classical treatments of Thomson and Bohr. Consider the interaction diagram of Figure 3-1. An energetic electron with velocity v moves past an atomic

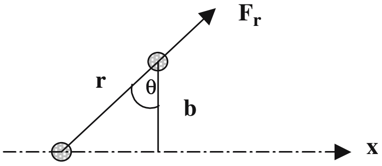

Figure 3-1. Schematic diagram of the collision between an energetic incident electron and an atomic electron.

electron. The distance of closest approach between the particles, termed the impact parameter, is designated as b. The differential change in momentum dp imparted to the atomic electron in a time dt is equal to the electric force F between the particles, which is given by e^2/r^2 (cgs units). e is the electronic charge and r is the instantaneous distance between the electrons. Assuming that the energy transferred, ΔE, is a relatively small fraction of the incident electron energy E, and that the direction of the incident electron does not change appreciably during the collision, the total change in momentum Δp of the atomic electron is given by the time integral of the perpendicular component of the force. Since $dt = dx/v$, the integral yields

$$\Delta p = (e^2/v)\int \cos\theta(dx/r^2) = 2e^2/(bv) \tag{3.1}$$

The energy lost by the incident electron, ΔE, is just $(\Delta p)^2/(m)$, with m being the electron rest mass. Evaluating this expression yields

$$\Delta E = 2e^4/(mv^2b^2) \tag{3.2}$$

If N is the density of atoms with atomic number Z, then there are $(2\pi bdb)$ NZ Δs atomic electrons per incremental length Δs that have an impact parameter between b and b + db (see Figure 3-2). Therefore, the average collisional energy loss per unit path length of the incident electron, $(\Delta E/\Delta s)_{coll}$, is calculated by integrating over all possible values of the impact parameter, as given by

$$-(\Delta E/\Delta s)_{coll} = 4\pi\, NZ(e^4/mv^2)\int (db/b) = 4\pi\, NZ(e^4/mv^2)\ln(b_{max}/b_{min})$$

Since the incident and target particles are both electrons, the maximum energy transfer is E/2; the minimum impact parameter can then be evaluated from Eq. (3.2). The maximum value of the impact parameter must account for the fact that the atomic electrons are not really free, but are bound in various atomic states. On the basis of a statistical model of the atom an average energy of

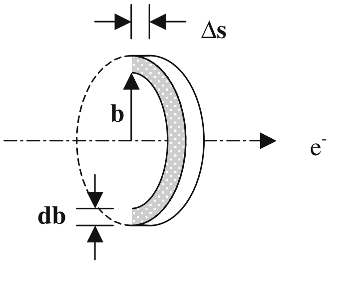

Figure 3-2. An incident electron transfers energy ΔE to each electron in the cylindrical volume element $(2\pi bdb)\Delta s$.

excitation and ionization I_{av} can be defined such that

$$-(dE/ds)_{coll} = 4\pi\, NZ(e^4/mv^2)\ln(E/I_{av}) \tag{3.3}$$

in the differential limit. I_{av} is approximately proportional to the atomic number of the material, with the constant of proportionality being of the order of the Rydberg energy, 13.5 eV. Note that at nonrelativistic electron energies, $E = mv^2/2$, and the collisional stopping power therefore decreases approximately as E^{-1}. At relativistic energies, however, the velocity v is nearly equal to the speed of light, and the stopping power increases logarithmically with energy.

3.1.2. Secondary Electron Generation

The spectrum of the secondary electrons generated as a result of the collision process can be obtained by noting that the differential interaction probability $d\sigma$ must scale as $2\pi b db$. Taking differentials of Eq. (3.2) indicates that the energy spectrum varies as

$$d\sigma/d(\Delta E)\ \alpha\ (\Delta E)^{-2}$$

The spectrum is therefore strongly weighted toward lower energies; for electrons with energies less than about 10 keV, the energy is usually considered as being deposited locally. However, the more energetic secondary electrons will leave the immediate vicinity of the collision, and will give rise in turn to other electrons. This process of energy degradation is nearly instantaneous, with the electrons finally reaching thermal energies and being either captured or escaping by conduction.

3.1.3. Multiple Nuclear Scattering

We now consider the collision of a relativistic electron with a massive nucleus of charge Ze, as schematically shown in Figure 3-3.

In analogy with Eq. (3.1), the change in momentum Δp of the incident electron is $2Ze^2/(bc)$. The scattering angle resulting from this interaction is just

$$\theta = \Delta p/p = 2Ze^2/(bcp) \tag{3.4}$$

As an electron beam penetrates into matter the individual electrons will undergo many such deflections, with the cumulative effect being a transverse spreading of the beam. While the most probable value of the average scattering angle is necessarily zero (the collisions are incoherent), it is possible to obtain a relation for the average mean square scattering angle $\langle\theta^2\rangle$ by integrating the square of Eq. (3.4) over the permissible range of impact parameters. Assuming the changes in p are small, this

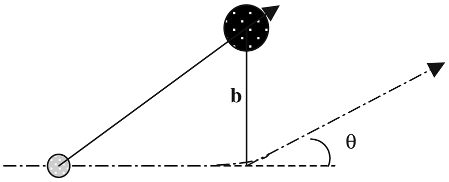

Figure 3-3. Schematic diagram of the collision between an incident electron and a massive nucleus of charge Ze.

integration gives

$$\langle\theta^2\rangle = 8\pi x\, NZ^2[e^4/(c^2p^2)]\ln(b_{max}/b_{min}) \tag{3.5}$$

with x being the penetration depth into the absorber.

The effective charge in this formula must actually be a function of the impact parameter b, because of screening of the nuclear charge by the atomic electrons. This fact is usually accounted for by the proper choice of b_{max}. However, the mean square scattering angle is not very sensitive to the actual values of either maximum or minimum impact parameter because they appear only in the logarithmic term.

Since (cp) is twice the electron kinetic energy, a crude approximation for the mean square scattering angle is $\langle\theta^2\rangle = a(Z/E)^2x$, with a being a constant. For water, a useful approximate expression is

$$\langle\theta^2\rangle = 6x(\mathrm{cm})/[E(\mathrm{MeV})]^2 \tag{3.6}$$

3.1.4. Bremsstrahlung Radiation

For small impact parameters, the collision between an energetic electron and a nucleus can be quite violent, producing an abrupt acceleration (deflection) of the electron. This abrupt deceleration is accompanied by the emission of bremsstrahlung x-rays. (The meaning of the German word "Bremsstrahlung" is "braking radiation".) The radiation probability depends on the effective distance from the electron to the nucleus because of the screening effect of the atomic electrons. For incident electron energies less than 35 MeV, the bremsstrahlung cross section is approximately given as

$$\sigma(E,\nu) = (4Z^2/137\nu)r_o^2\ln(2.8E) \tag{3.7}$$

where ν is the frequency of the radiated photon, and $r_o = e^2/mc^2 = 2.82 \times 10^{-13}$ cm is the classical electron radius. In analogy with the case of electron-electron collisions, it is possible to develop a stopping power formula for the case of bremsstrahlung. Since the number of photons emitted with frequency in the range of ν to $\nu + d\nu$ is $N\sigma(E,\nu)d\nu\, ds$, when an electron of energy E traverses a distance ds, the average energy loss by radiation per unit path length is given by

$$-(dE/ds)_{rad} = N\int h\nu\, \sigma(E,\nu)d\nu$$

Since an electron cannot radiate more energy than its kinetic energy, an upper limit on the integral is $h\nu_{max} = E$, with h being Planck's constant. While the cross section diverges at low photon energy, the total energy loss does not diverge since the quantity $h\nu\, \sigma(E,\nu)$ is approximately constant; the lower limit can be zero. The integral is thus evaluated as

$$-(dE/ds)_{rad} = (4NZ^2/137)E\, r_o^2\ln(2.8E) \tag{3.8}$$

The bremsstrahlung energy loss is therefore proportional to Z^2, and increases somewhat faster than linearly with incident electron energy. At non-relativistic electron energies, the bremsstrahlung emission is nearly isotropic. At relativistic energies, however, the emission is primarily forward directed with an average emission angle given by

$$\theta = [2E(\mathrm{MeV})]^{-1} \tag{3.9}$$

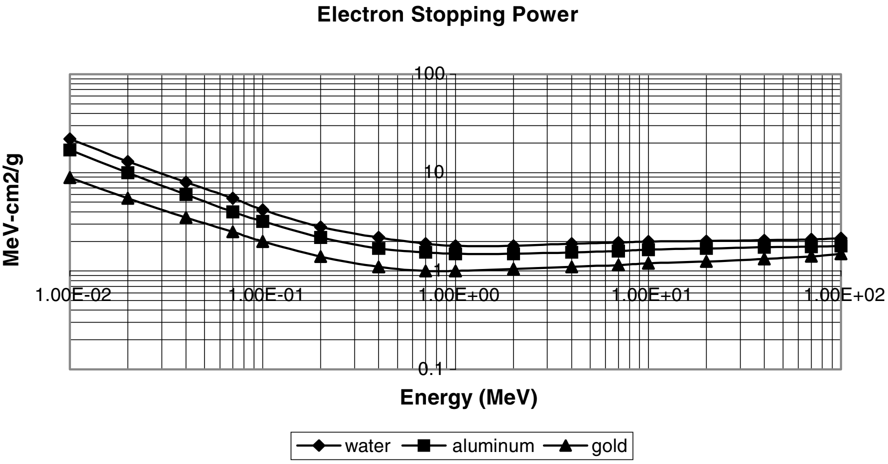

Figure 3-4. Electron stopping power in water, aluminum, and gold.

3.1.5. Stopping Power, Energy Straggling and CSDA Range

A comparison of Eq. (3.3) with Eq. (3.8) for mildly relativistic electrons indicates that, apart from weak logarithmic factors, the ratio of the radiative loss to the collisional loss scales approximately as

$$[(dE/ds)_{rad}]/[(dE/ds)_{coll}] = [ZE(MeV)]/800 \tag{3.10}$$

For food irradiation, $Z < 8$ and $E < 10$ MeV, indicating that collisional energy losses always dominate bremsstrahlung losses.

From Eq. (3.3), the collisional stopping power depends on the electron density (NZ) of the stopping medium. For foodstuffs that are primarily composed of the light elements, the electron density is roughly proportional to the physical density ρ. In this case it is convenient to use the collisional mass stopping power, defined as $(dE/ds)_{coll}/\rho$, for estimation purposes. The variation of the collisional mass stopping power with electron kinetic energy is shown in Figure 3-4 for a few different materials.[2] For energies in excess of about 200 keV, the mass stopping power is nearly independent of energy, depending only weakly on the atomic number Z of the material. Consequently, the energy loss of energetic electrons in foods is often simplistically described by

$$(dE/ds)_{coll}/\rho = 2.0\,\text{MeV-cm}^2/\text{g} \tag{3.11}$$

The energy loss predicted by Eq. (3.11) is only an average value, however. For each electron the actual value fluctuates, with two consequences. For a given path length, the energy loss fluctuates, and for a given energy loss, the path length fluctuates. This behavior is called straggling. Since an electron can lose up to half of its energy in a single collision with an atomic electron, electron energy straggling can be quite significant, reaching values of the order of 20% of the total energy loss.

The stopping power expression can also be used to define a range by performing the integration indicated in Eq. (3.12):

$$R_{CSDA} = -\int dE/(dE/ds) \tag{3.12}$$

R_{CSDA} is termed the continuous slowing down approximation (CSDA) range; it gives a reasonable estimate of the average path length of an electron in a material. It is not, however, the average axial penetration depth, owing to nuclear scattering collisions and straggling. An approximate estimate of R_{CSDA} can be obtained by substituting Eq. (3.11) into Eq. (3.12) to yield

$$R_{CSDA} = E(MeV)/[2\rho(g/cm^2)] \tag{3.13}$$

3.2. ENERGY DEPOSITION PROFILES

Although the mass stopping power is nearly constant for electron energies greater than about 200 keV, the energy deposition profile will not be a uniform function of penetration depth because of the complicated scattering processes, the non-zero path lengths of the secondary electrons, and energy straggling. Some of the important contributing features can be demonstrated by a few simple trajectory calculations. Guided by Eq. (3.6), we model the square of an average trajectory angle as $\theta^2 = \alpha x$, with $dr = \theta\, dx$. The incremental arc length is then given by $ds = dx(1 + \theta^2)^{1/2}$, and the energy deposition rate with depth is given by $dE/dx = (dE/ds)(ds/dx)$. Assuming an initial kinetic energy of 10 MeV, the results for three sample trajectories ($\alpha = 0, 0.06, 0.24$) are shown in Figure 3-5.

As the average scattering angle increases, the rate of energy loss with depth increases, and the penetration depth decreases for geometrical reasons. Also, the rate of energy loss increases dramatically at the end of the electron range because of the 1/E dependence in the stopping power expression. The case of $\alpha = 0.06$ corresponds to the mean square scattering angle from Eq. (3.6) for 10 MeV electrons. For a narrow pencil beam, the beam will therefore expand to a maximum diameter of about 3 centimeters. Most of the primary electrons will come to rest in a depth interval corresponding to about 80% of the maximum penetration depth.

Apart from such simplistic analytical models, two techniques have been developed for solving the complete electron transport problem. The first uses a method of moments approach[3] for solving the transport equation under the continuous slowing down approximation. Accurate results have been obtained, but only for restrictive geometries with somewhat artificial boundary conditions. As a

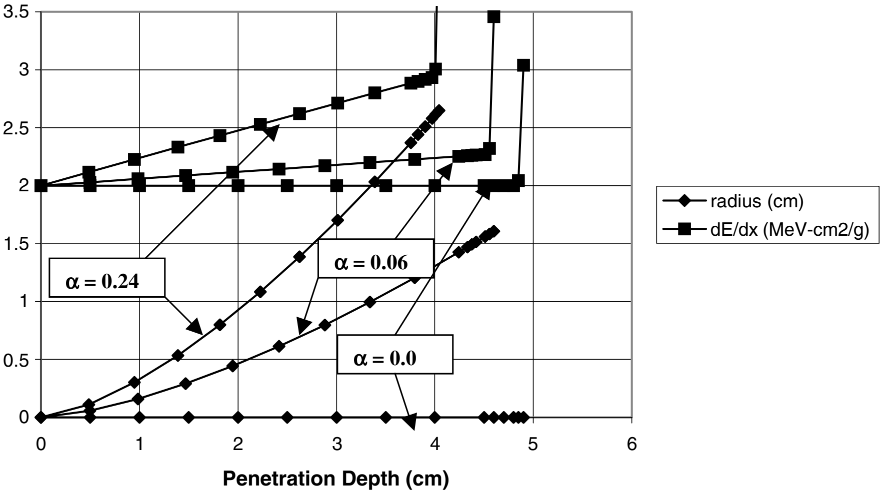

Figure 3-5. Energy deposition as a function of penetration depth for three different assumed electron trajectories. The initial electron kinetic energy was 10 MeV.

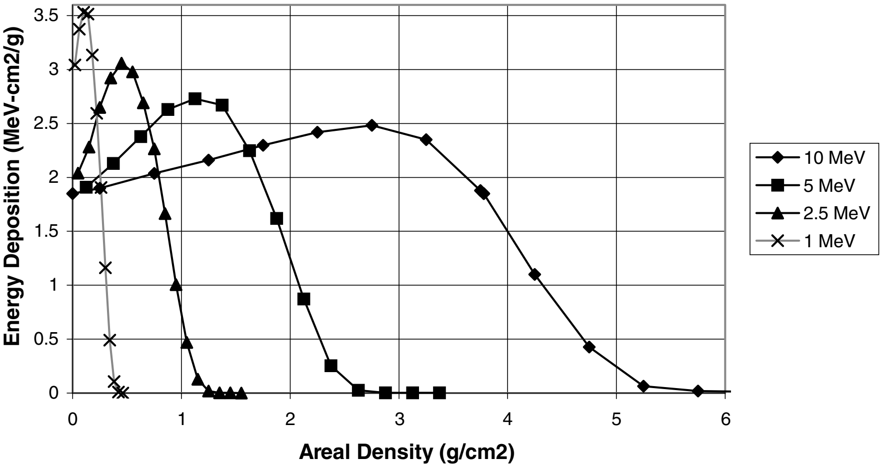

Figure 3-6. Energy deposition profiles for energetic electrons of differing energies. An exit window of 0.003″ titanium was used for each case.

result, most calculations of the energy deposition profiles are now performed using statistically-based "Monte Carlo" computer codes.[4] In principle, this approach can provide a complete description of the entire collision history of an electron. In practice, individual collisions are not treated. Instead, analytic results describing various aspects of the transport processes are used to describe large numbers of single collisions as a single segment of the calculation; the computation then proceeds through the electron history segment by segment. A major advantage of this approach is flexibility in specifying the problem geometry and the selection of boundary conditions.

The depth-dose profiles in water for several different electron kinetic energies, as computed using the one-dimensional Monte Carlo code TIGER, are shown in Figure 3-6. These results agree quite well with experimental measurements of the depth-dose profiles for monoenergetic electron beams. The most notable features of these profiles are a peak dose that increases with depth up to a maximum value, followed by an approximately linear decrease. The penetration depth increases approximately linearly with increasing energy as expected, because the stopping power is reasonably constant over the energy range of 200 keV to 10 MeV. The peak dose increases with decreasing energy, primarily because of the increase in scattering angle with decreasing energy (Eq. 3.6). In addition, note that the dose does not fall to zero abruptly. This result is a consequence of scattering, energy straggling, and a bremsstrahlung background for the higher kinetic energies.

To examine some of these features in more detail consider the additional TIGER data presented in Figures 3-7 through 3-11, pertaining to the penetration of 10-MeV electrons in water. The individual contributions of the secondary (knock-on) electrons and bremsstrahlung x-rays to the energy deposition profile are presented in Figure 3-7. Both contributions are relatively small in comparison with the energy deposition of the primaries. The x-ray contribution increases monotonically with depth; the contribution of the secondaries is somewhat more complicated, being negative near the surface because these electrons transport energy from the surface to greater depths. The degradation of the (initially monoenergetic) electron energy spectrum with depth is shown in Figure 3-8. The effects of multiple scattering and energy straggling are readily apparent. The deposited electron charge is shown in Figure 3-9. As suggested by the analytical calculation exhibited in Fig. 3-5, there is an accumulation of deposited charge at a depth of approximately 80% of the maximum penetration depth. Note that the surface will be charged slightly positive because secondary electrons are predominantly

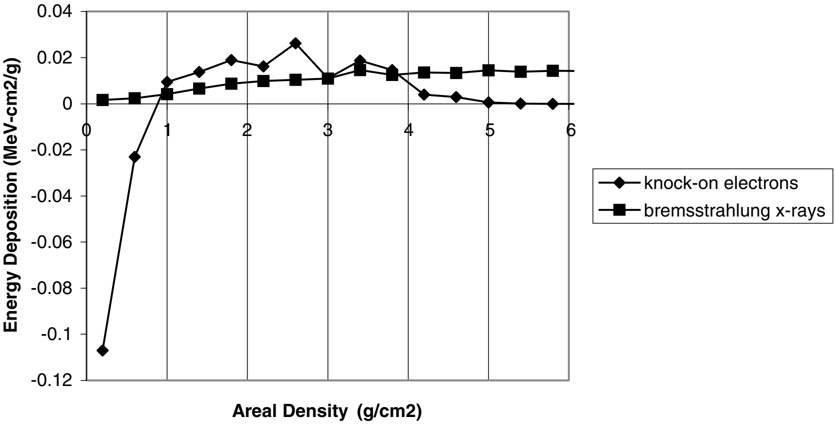

Figure 3-7. Contributions of the secondary (knock-on) electrons and bremsstrahlung x-rays to the energy deposition profile, as calculated by TIGER for monoenergetic 10-MeV electrons normally incident on a water absorber.

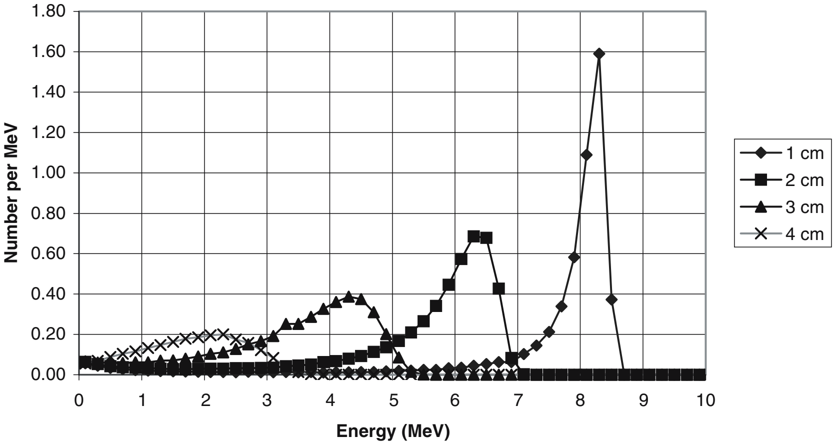

Figure 3-8. Degradation of the electron energy sprectrum with depth of penetration, as calculated by TIGER for initially monoenergetic 10-MeV electrons normally incident on a water absorber. The low-energy tail evident at small depths represents lower-energy secondary electrons.

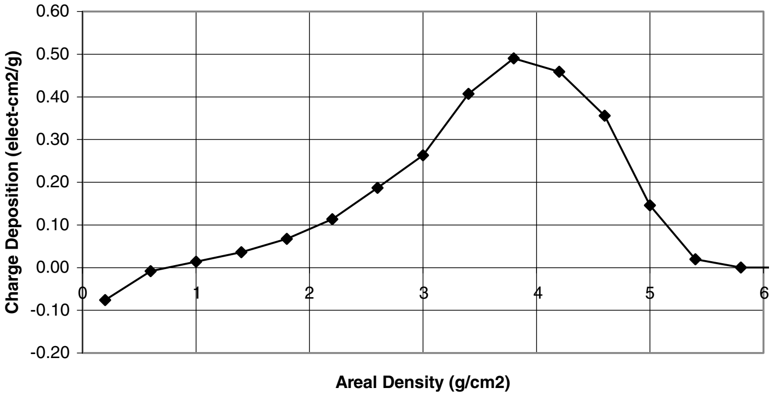

Figure 3-9. Deposited charge as a function of depth in water for the case of 10-MeV electrons, as calculated by TIGER. Note the negative region near the surface, corresponding to secondary electrons being scattered primarily in the forward direction.

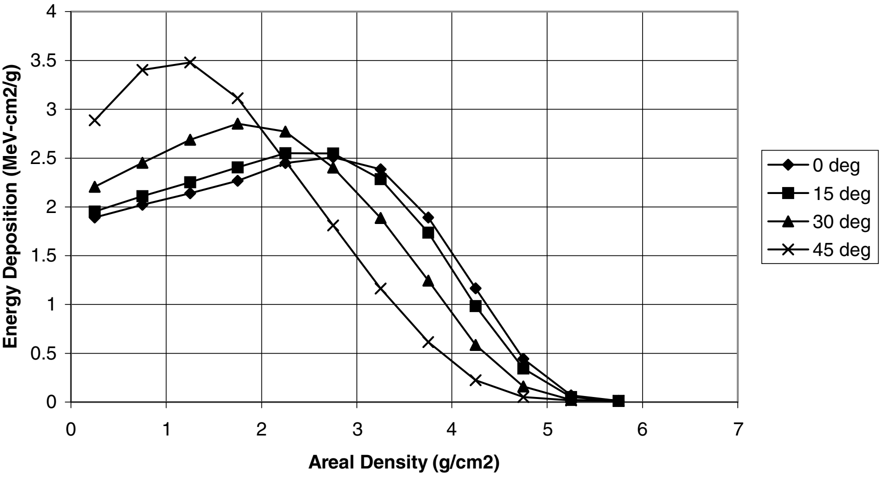

Figure 3-10. Energy deposition profiles for monoenergetic 10-MeV electrons with differing angles of incidence.

scattered into the forward direction. The energy deposition profiles for different angles of incidence are shown in Figure 3-10. The profiles are not greatly different until the incident angle exceeds about 15 degrees.

Also of interest is the expansion of a narrow pencil beam of electrons. The energy deposition of such a 10-MeV beam, as calculated by the three-dimensional Monte Carlo code ACCEPT (one of the Integrated TIGER Series codes[4]), is shown in Figure 3-11. The corresponding variation in the mean radius of the beam is shown in Fig. 3-12. The increase in beam radius is quite similar to that shown in Fig. 3-5 with $\alpha = 0.06$.

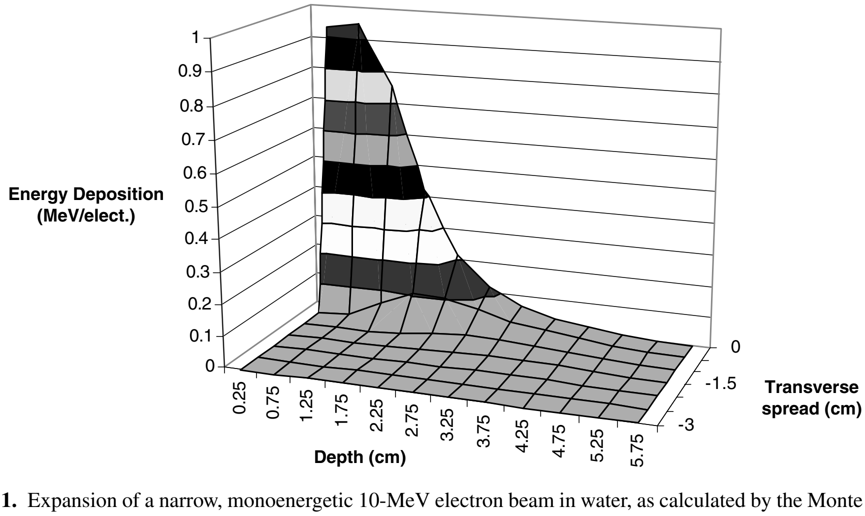

Figure 3-11. Expansion of a narrow, monoenergetic 10-MeV electron beam in water, as calculated by the Monte Carlo code ACCEPT. Note the rapid decrease in energy deposition on axis.

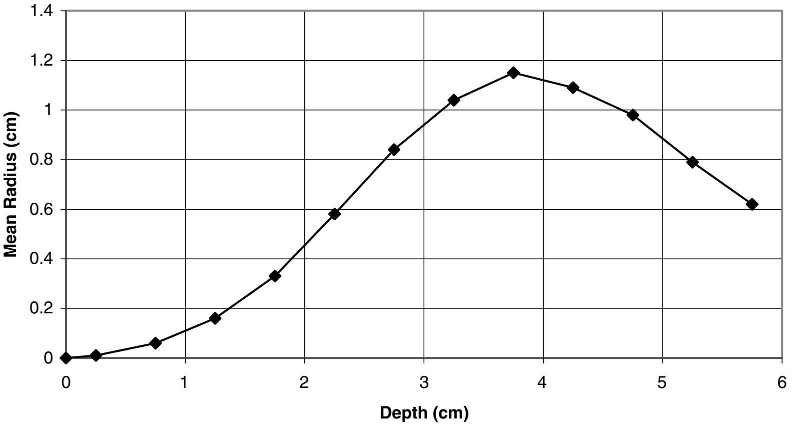

Figure 3-12. Average beam radius of a narrow, pencil beam of 10-MeV electrons normally incident onto a water absorber.

3.3. MAX:MIN RATIOS AND ENERGY UTILIZATION EFFICIENCY

Since the specific energy deposition varies with depth, there will always be a maximum delivered dose and a minimum delivered dose.[5,6] While the minimum dose must exceed the minimum dose requirement as specified by the processing protocol, it is usually desirable to limit the maximum delivered dose in order to minimize possible negative sensory effects in the product. A useful measure of the dose uniformity is the ratio of the maximum dose to the minimum dose, termed the max:min ratio. An important additional consequence of the dose variation with depth is a loss of efficiency in using the available beam energy. These issues will be examined in further detail in the following paragraphs in which we develop estimates of the max:min ratio and the one-dimensional utilization efficiency for both single-sided and double-sided irradiation scenarios.

3.3.1. Single-Sided Irradiation

Referring again to Fig. 3-6, for monoenergetic, normally-incident 10-MeV electrons the specific energy deposition at the front surface is about 1.84 MeV-cm^2/g, rising to about 2.48 MeV-cm^2/g at an areal density of 2.75 g/cm^2. It may be verified that a good parametric fit to the TIGER data is provided by Eq. (3.14):

$$\begin{aligned}\Delta W_{sp}(\text{MeV-cm}^2/\text{g}) &= 1.84 + 0.25d, \quad 0 < d < 2.5\\ &= 2.48\exp(-0.27|d-2.75|^{2.7}), \quad 2.5 < d < 6.5 \qquad (3.14)\end{aligned}$$

The integral under the curve gives a total absorbed energy of 9.61 MeV/electron. (Approximately 46 keV/electron is deposited in an assumed 3-mil titanium exit window; the remainder corresponds to escaping bremsstrahlung x-rays.)

We now suppose that a certain minimum dose must be delivered to all portions of the product. If a portion of the product receives more than this minimum dose, then energy is wasted, apart from any deleterious effects on food quality.[7] We thus define the utilization efficiency in the one-dimensional approximation as

$$\eta_u = d/d_{max} \qquad (3.15)$$

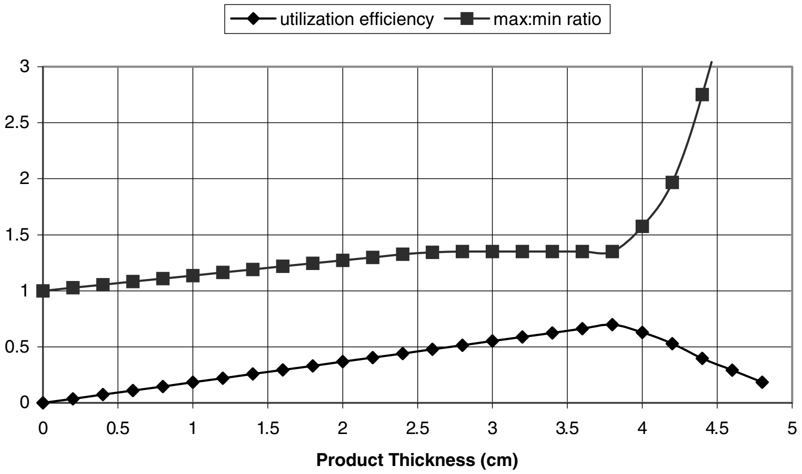

Figure 3-13. Utilization efficiency and dose max:min ratio for 10-MeV electrons in water.

with d_{max} corresponding to the maximum thickness of material that could be processed at the minimum required dose if all the available electron energy were utilized. Since the specific energy deposition (see also Eq. (2.3)) in Figure 3.6 is given in units of MeV-cm^2/g per electron, d_{max} is given as

$$d_{max} = E/(\rho\, \Delta W_{min}). \tag{3.16}$$

The minimum dose (or equivalently, the specific energy deposition) occurs at either the front surface for thin products, or at the rear surface, $d = d_r$, for thick products; i.e.,

$$\Delta W_{min} = \min[\Delta W(0), \Delta W(d_r)] \tag{3.17}$$

With the aid of these equations and the specific energy deposition profile, we can estimate the throughput efficiency and max:min ratio for the case of single-sided irradiation. As an example, the results for the case of single-sided irradiation using 10-MeV electrons in water are summarized in Figure 3-13. Since the dose increases with depth up to a thickness of 2.75 cm, the max:min ratio increases from unity to about 1.35 over this same range, then remains constant at this level until $d = 3.8$ cm. For $d > 3.8$ cm, the minimum dose falls below $\Delta W(0)$, and the max:min ratio increases rapidly with increasing depth.*

For the utilization efficiency, we again note that $\Delta W(0) = \Delta W(d_r) = 1.84$ MeV-cm^2/g at $d = d_r = 3.8$ cm. Consequently, from Eq. (3.16) we have $d_{max} = 5.43$ cm, since $E = 10$ MeV. The utilization efficiency increases linearly with product thickness for depths up to 3.8 cm. When the product thickness exceeds 3.8 cm, however, ΔW_{min} decreases sufficiently rapidly that d/d_{max} is also a decreasing function. The maximum utilization efficiency is therefore about 70%, and it occurs at a water depth of about 3.8 cm; i.e., the depth at which the specific energy deposition equals the front surface value.

---

* If the material thickness is less than the maximum range of the electrons, then the dose at the exit surface can be affected by scattering from the backing material. In particular, from Section 3.1.3, backing materials of higher atomic number will generate more scattering resulting in enhanced dose. Some care must therefore be exercised if low-Z food materials are placed directly on a stainless steel conveyor belt, for example. For double-sided irradiation of thicker materials, this effect is almost never an issue. See Reference 5 for more details.

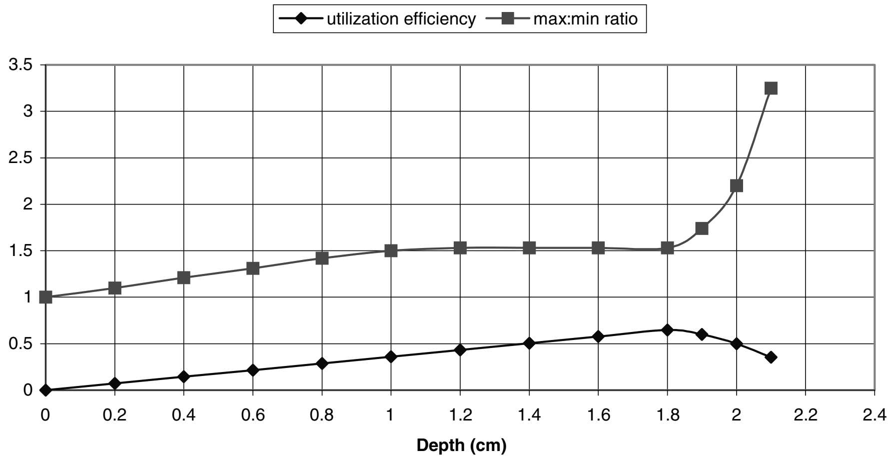

Figure 3-14. Utilization efficiency and dose max:min ratio for 5-MeV electrons in water.

Using similar analyses, results for the max:min ratios and utilization efficiencies for single-sided irradiation using 2.5 MeV and 5 MeV electrons are also presented in Figures 3-14 and 3-15. Using such data, the optimum water thickness for achieving the maximum throughput efficiency in a single-sided irradiation configuration is shown in Figure 3-16 as a function of electron energy. For electron energies in excess of about 1 MeV, the optimum water thickness follows the linear equation

$$d_{opt}(cm) = 0.4\,E(MeV) - 0.2 \tag{3.18}$$

The density of water is of course unity. For low atomic number materials of different density ρ, the optimum depth is therefore obtained by dividing by the material density; i.e.,

$$d_{opt\text{-}mat} = d_{opt\text{-}water}/\rho \tag{3.19}$$

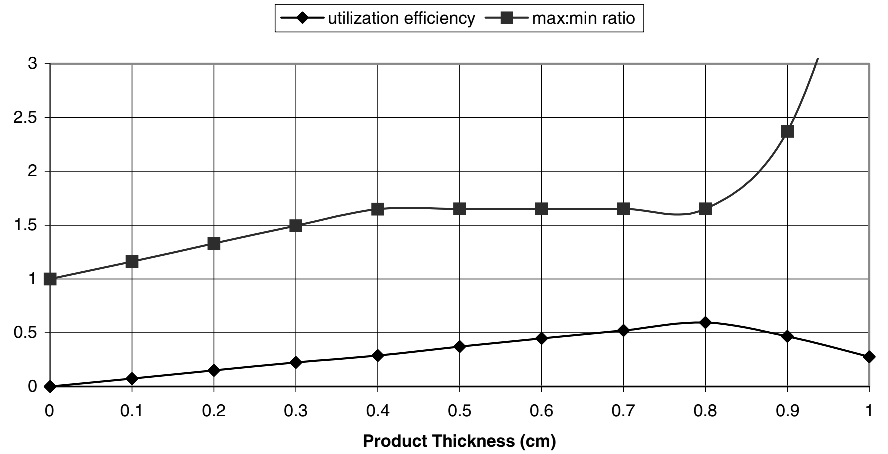

Figure 3-15. Utilization efficiency and dose max:min ratio for 2.5-MeV electrons in water.

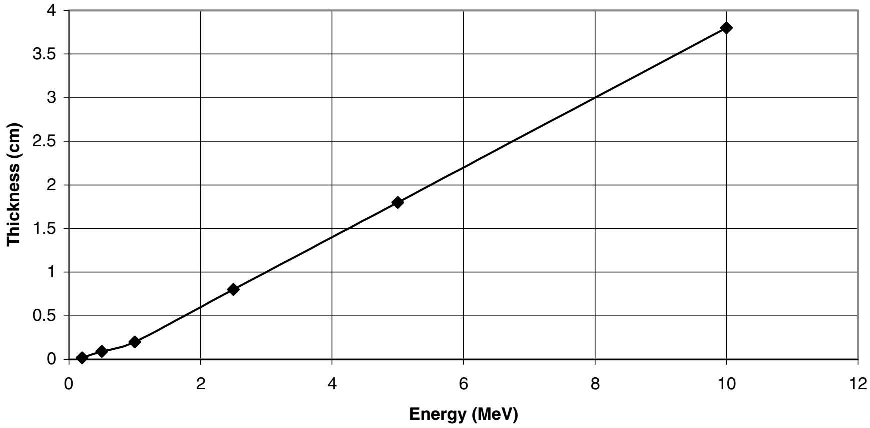

Figure 3-16. Optimum water thickness for maximum throughput efficiency as a function of electron energy.

3.3.2. Double-Sided Irradiation

We now imagine that the product is irradiated from two diametrically opposed sides with nominally identical electron beams. In this case the specific energy deposition profile will be given by

$$\Delta W_t(x, T) = \Delta W(x) + \Delta W(T - x) \tag{3.20}$$

where T is the product thickness, x is the depth into the product as measured from either surface, and $\Delta W(x)$ is the single-sided energy deposition (depth-dose) profile. It is apparent that the dose profile for double-sided irradiation is symmetric about the midplane of the product. As an example, the 10-MeV depth-dose profiles for product thicknesses ranging from 0 to 10 cm are shown in Figure 3-17.

For this case of double-sided irradiation we define the utilization efficiency in the one-dimensional approximation as

$$\eta_u = T/d_{max} \tag{3.21}$$

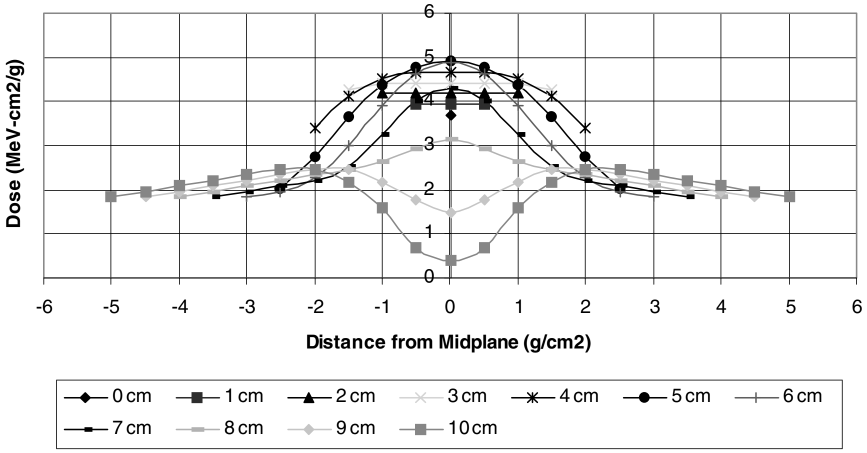

Figure 3-17. Depth-dose profiles for product thicknesses ranging from 0 to10 cm. x = 0 corresponds to the mid-plane of the product.

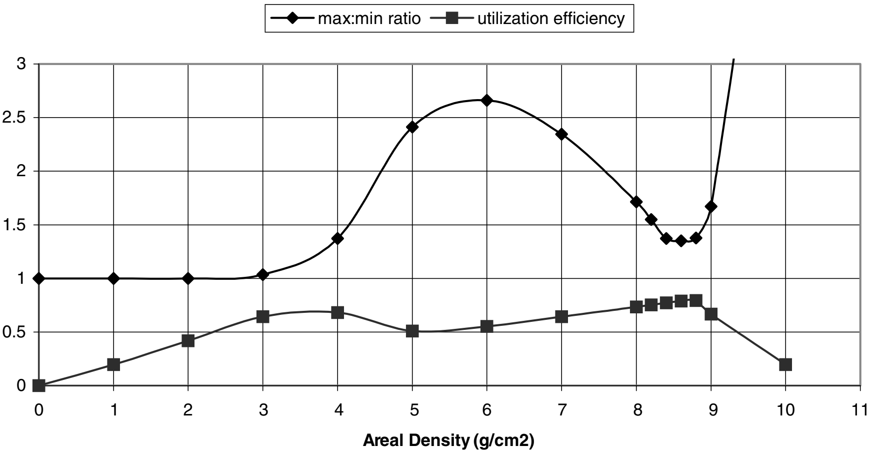

Figure 3-18. Max:min ratio and utilization efficiency for symmetric, double-sided irradiation of water using 10-MeV electrons.

$$d_{max} = 2E/(\rho\,\Delta W_{min}). \tag{3.22}$$

The factor of 2 results from the use of two equal beams.

Based on these depth-dose profiles, the max:min ratio and the utilization efficiency for this double-sided irradiation case at 10 MeV are shown in Figure 3-18.

It is quite apparent from these data that the dose uniformity for double–sided irradiation is excellent for areal densities less than 3.5 g/cm^2, and is acceptably good in the region between 8 and 9 g/cm^2, but is somewhat high otherwise. The utilization efficiency has one maximum of about 0.64 at a water thickness of about 3.8 cm, and a second maximum of about 0.79 at a thickness of about 8.6 cm. The max:min ratio has a minimum of 1.35 at about 8.6 cm of water, also. For products in which exceptional dose uniformity is required (nominally unity), utilization efficiencies in excess of 60% can still be achieved if the product thickness can be constrained to an areal density <3 g/cm^2.

Max:min ratios and utilization efficiencies for electrons of other energies can be developed using similar analyses. Based on such calculations, the optimum water thickness for achieving the maximum utilization efficiency in a double-sided irradiation configuration is shown in Figure 3-19 as a function of electron energy. For electron energies in excess of about 1 MeV, the optimum areal density follows the linear equation

$$d_{opt}(g/cm^2) = 0.9\,E(MeV) - 0.4 \tag{3.23}$$

3.4. ELECTRON BEAM IRRADIATION OF IRREGULAR PRODUCTS

The electron energy deposition analyses and results presented thus far have pertained to uniform, homogenous media. However, real food products are necessarily packaged in a variety of shapes and sizes, and may be homogeneous or non-homogeneous within the package. In this section, we consider various issues associated with electron beam irradiation of such irregular products. In the first case we analyze homogeneous products that have a constant, but irregular shape; in the second case, we analyze products having a significant variation in areal density. In general, such products can be effectively treated with acceptable dose uniformity, but at the expense of energy utilization efficiency.

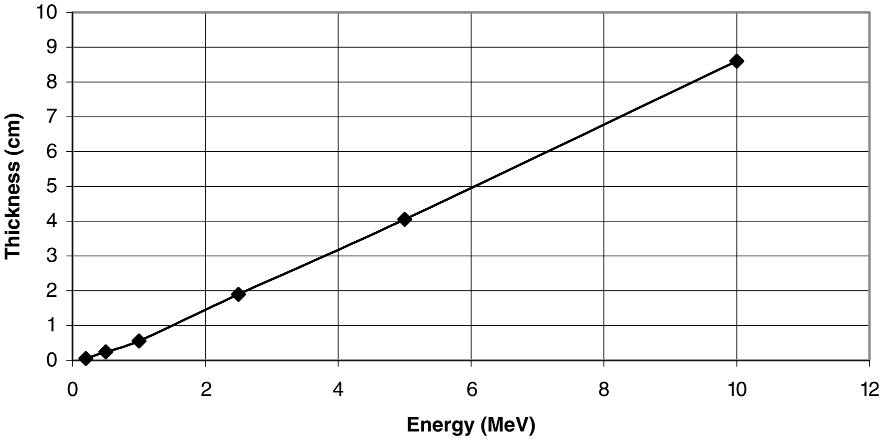

Figure 3-19. Optimum water thickness for maximum utilization efficiency as a function of electron energy for double-sided irradiation.

3.4.1. Products of Irregular but Consistent Shape

There are a variety of essentially homogeneous food products that are contained in well-defined packages with very little variation from package to package. Important examples include ground beef "chubs", and a variety of different processed meat products. To prevent negative sensory effects (browning and rancidity) in these products it is usually necessary to tightly control the dose uniformity. In this section we will discuss the design of special absorbers that can limit the max:min ratio to acceptable levels, and we will discuss the impact of such absorbers on the energy utilization efficiency.

To illustrate the process of designing suitable absorbers we will use the case of the irradiation of ground beef chubs to eliminate *e. coli* as an example.[8] *E. coli* is a surface contaminant (it does not reside in muscle) that can be killed with elevated temperatures. Rare beefsteaks can be eaten safely, provided the outer surfaces are seared. However, unirradiated ground beef products must never be undercooked, because the grinding process causes intermingling of outer surfaces. Even the handling of raw ground beef by food service personnel can spread *e. coli* contamination to other foodstuffs.

The consumption of undercooked ground beef contaminated by only a few viable *e. coli* O157:H7 cells has been unambiguously responsible for some severe outbreaks of food-borne illness leading to the deaths of several young children. As a result, the US Food Safety Inspection Service (FSIS), as regulatory policy (September, 1994), regards raw ground beef containing *e. coli* O157:H7 to be adulterated, and has instituted a testing program to inspect raw ground beef prepared at federally inspected establishments and at the retail level. Any product that tests positive is subject to Class I recall procedures, including the issuance of a press release. To avoid such consequences, some meat producers are investigating the practicalities of irradiating ground beef in its various packaging configurations.

Chubs (Figure 3-20) are essentially large, cylindrical, ground beef "sausages" encased in a thin plastic wrap; they constitute the greatest volume of the ground beef sold by processing plants. Chubs may be produced using a KartridgePak (KP) machine.[9] This device forces the ground beef into a cylindrical, heat-sealable film, seals the ends of the film with metal clips (applied two at a time), and simultaneously cuts the film between the clips. (These seals are not hermetic.) The chubs are then (typically) manually loaded into shipping cases for delivery directly to customers, distribution centers, or factory warehouses for temporary storage.

Figure 3-20. Chubs are cylindrical volumes of ground beef encased in a thin plastic wrap. The ends are sealed with metal clips. (Reprinted with permission of the Titan Corporation.)

Chubs are shipped in fresh, frozen or crusted (a lightly frozen shell) states. (Freezing stops the growth of *e. coli*, but does not kill it; the organism will again grow when warmth and nutrients are reintroduced.) *E. coli* is relatively susceptible to the effects of radiation. For fresh ground beef, the D_{10} value is about 0.25 kGy, and the minimum dose is usually chosen to be in the range of 1–1.3 kGy (four to five D_{10} values). For frozen ground beef the D_{10} value is slightly higher, about 0.35 kGy, and the minimum dose is usually chosen to be about 1.6 kGy. A dose of 2.6 kGy is a maximum upper limit for both fresh and frozen ground beef to avoid browning and rancidity, but it is desirable to remain below 2 kGy, especially for products having high fat content.

The KP machine dies can be adjusted to produce chubs of various diameters. For example, depending on their designated markets (retail or food service), chubs have traditionally had diameters ranging from 1.5 inches to 4.25 inches. Since the density of the ground beef in a chub is generally in the range of 0.88–0.92 g/cm^3, the corresponding range in areal density is therefore 3.43–9.7 g/cm^2. From Figure 3-18, the maximum areal density (in terms of producing both an acceptable max:min ratio and an energy utilization efficiency) for processing using two-sided electron beam irradiation is about 8.6 g/cm^2, corresponding to a maximum chub diameter of about 9.5 cm (3.75 inches). However, based on the one-dimensional results of the previous section, the max:min ratio for the double-sided irradiation of such large cylindrical chubs might be expected to be as high as 2.7. In practice, the results are not quite as bad because of detailed three-dimensional scattering effects, but they are still generally unacceptable. The dose map obtained using a bare 3.5-in dia. high-density polyethylene (HDPE) chub phantom is shown in Figure 3-21 as an example.[8] The edge regions in which beam overlap occurs receive doses that are typically a factor of two higher than the lowest dose delivered to any other region of a chub. With a minimum required dose in the range of 1.25–1.6 kGy, such a large max:min ratio can result in unacceptable product sensory qualities.

Various absorber approaches[10,11] can be devised to reduce the max:min ratio to acceptable levels for such large chubs.* The simplest conceptual approach is to surround the chub both top and

---

* For chubs having areal densities of <4 g/cm^2, (roughly 1.75 inches for a density of 0.9 g/cm^3) double-sided irradiation at 10-MeV will yield excellent max:min ratios without using absorbers.

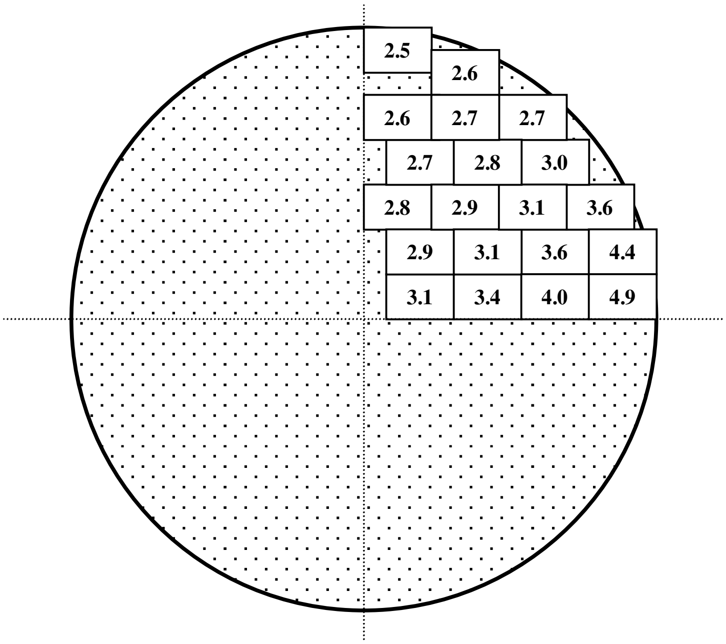

Figure 3-21. Dose map for a 3.5″ diameter, unit density, bare chub phantom, irradiated top and bottom. The values listed are absorbed doses in kilogray.

bottom with conformal absorbers having a density essentially equal to that of the chub (HDPE, for example). This approach will result in a best max:min ratio of approximately 1.35, assuming that the areal density of the assembly (absorbers plus chubs) is uniformly in the range of 8.4–8.6 g/cm^2.

While guaranteed to produce acceptable max:min ratios, this approach has several drawbacks. It requires that every chub be placed into a fixture containing a bottom layer of conformal absorbers, and then covered with a second layer of conformal absorbers. After irradiation, the chubs must be removed from the absorber fixtures and repackaged for shipping. These tasks are labor intensive and time-consuming, and therefore expensive. In addition, HDPE and most other suitable plastics can become quite brittle after suffering radiation damage, necessitating frequent absorber replacement.

There are (at least) two alternate approaches for processing chubs that can significantly decrease handling requirements, but they generally require the food processor’s cooperation in supplying the chubs in a suitable configuration. For the first approach, it is assumed that the chubs are arranged in single-layer fashion in stackable, removable inserts within a larger, multi-layer package. Each removable insert has a bottom and sides, but no top. The inserts can be placed directly onto the conveyor, with a suitably designed absorber placed over the layer of chubs. For the second approach, it is assumed that the chubs are supplied with a consistent orientation inside single-layer boxes. A suitably designed absorber is then externally affixed to the box prior to irradiation. Absorber designs for these two approaches are discussed in the following paragraphs.

a. Absorbers for Single-Layer Chub Inserts

This approach is illustrated in Figure 3-22. A single layer of chubs is close-packed within an insert (a topless cardboard box). A single conformal absorber is placed inside the insert on top of the layer of chubs, and the insert is placed on the (roller) conveyor for top and bottom irradiation by two nominally identical electron beams. The absorber consists of conformal HDPE, backed by a suitable

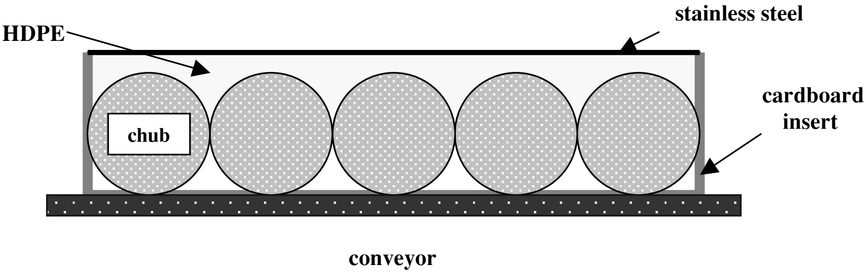

Figure 3-22. Schematic absorber approach for chubs packed in a cardboard insert.

thickness of stainless steel sheet. The bottom beam passes unimpeded through a break between rollers.

This approach should work quite well, provided that along the vertical diameter of the chub the individual areal densities of any absorbers, plus that of the chub, plus that of the exit windows, plus that of the insert, should sum to approximately 8.6 g/cm^2. Thus,

$$(\rho d)_{\text{chub}} + (\rho d)_{\text{insert}} + (\rho d)_{\text{HDPE}} + (\rho d)_{\text{SS}} + 2(\rho d)_{\text{window}} = 8.6 \text{ g/cm}^2 \tag{3.24}$$

As a check on this absorber design approach an ACCEPT calculation was performed for chubs having a diameter of 2.375 inches and a density of 0.87 g/cm^3. The dose map for this calculation is shown in Figure 3-23; the max:min ratio is 1.36. Experimental measurements using this approach give max:min ratios of typically 1.4.

b. External Absorbers for Single-Layer Chub Boxes

To combat the effects of HDPE embrittlement, small stainless support bars could be placed in the thickest portions of the HDPE absorbers (between the chubs) in the design of Figure 3-22. However, it would be preferable to make absorbers entirely of a metal such as aluminum or stainless steel. Also, handling could be reduced if the chubs were supplied in single layer boxes, to which the metal

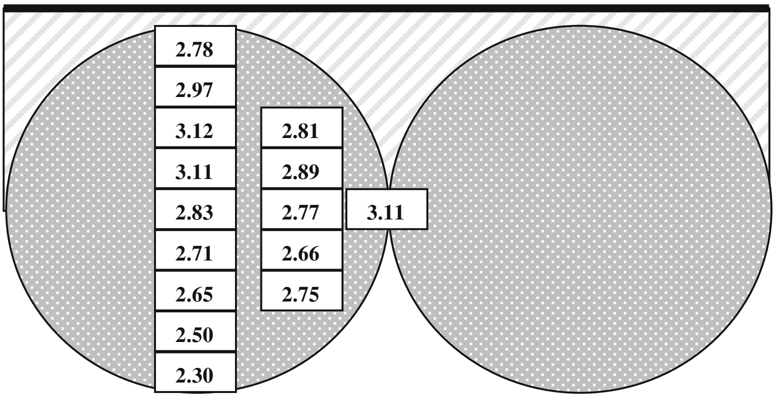

Figure 3-23. ACCEPT dose map corresponding to the absorber approach of Fig. 3-22.

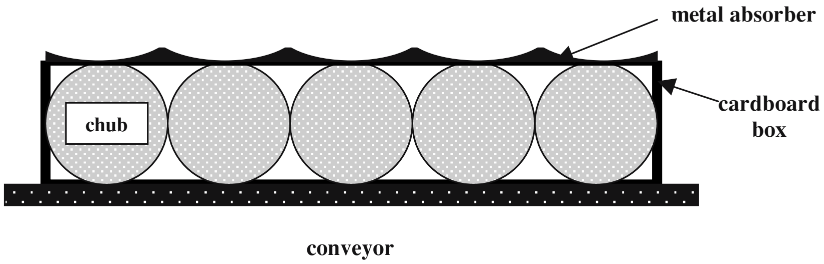

Figure 3-24. Schematic absorber approach for chubs packed in a cardboard box.

absorbers could be externally affixed prior to irradiation. This approach is schematically shown in Figure 3-24.

The approximate shape of the single external metallic absorber can be obtained using an initial estimate based on the one-dimensional depth-dose profile (Figure 3-6), followed by confirmation obtained using the three-dimensional Monte Carlo ACCEPT code. To illustrate the process, consider Figure 3-25. A cylindrical chub of density ρ_c and radius r is irradiated from top and bottom by nominally identical 10-MeV electron beams. The bottom beam is unimpeded, while the top beam passes through a metallic absorber of density ρ_m, the thickness t of which depends on the transverse coordinate x. Guided by Figure 3-6, it is assumed that both top and bottom beams should have passed through an areal density of approximately 4.2 g/cm^2 at the boundary defined by the circle

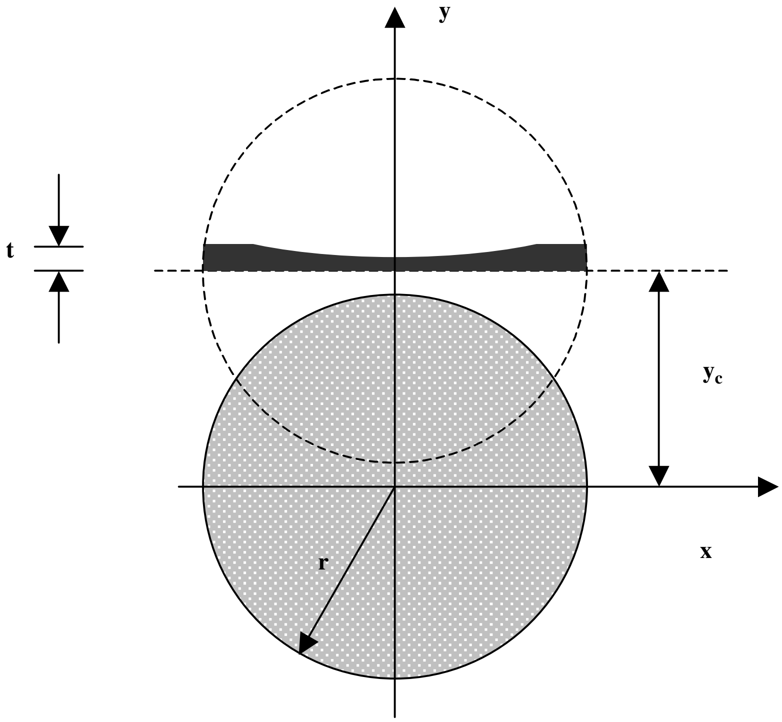

Figure 3-25. Schematic geometry for determining the shape of the single metallic absorber for double-sided irradiation of chubs.

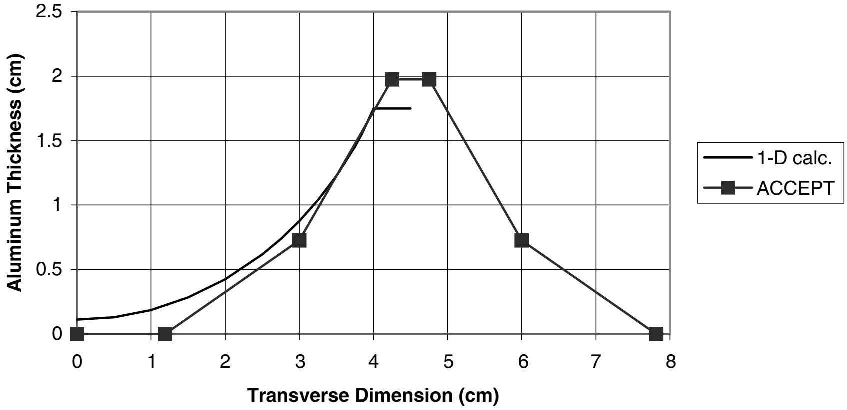

Figure 3-26. The single, one-dimensional, aluminum absorber thickness for double-sided irradiation of 9-cm diameter chubs with 10-MeV electrons. Both the result from Eq. (3.25) and the approximation used in the ACCEPT calculation are shown.

$(y-y_c)^2 + x^2 = r^2$ (the bottom of the dashed circle in Figure 3-25). The metal thickness corresponding to this assumption is given by

$$t = [8.4 - 2\rho_c(r^2 - x^2)^{1/2}]/\rho_m \tag{3.25}$$

The offset y_c is determined from $y_c\rho_c = 4.2$ g/cm^2.

For illustration purposes, Eq. (3.25) is graphed in Figure 3-26 for the case of a 9-cm diameter chub of density 0.9 g/cm^3 and an aluminum absorber of density 2.7 g/cm^3. Also shown in Figure 3-26 is the absorber shape used in the ACCEPT code calculation, the dose map from which is presented in Figure 3-27. The max:min ratio is approximately 1.65. While this result is considerably better than that with no absorber, it is not as good as that obtained with the conformal HDPE absorber.

Experimental measurements using this single external absorber configuration are in general agreement with the ACCEPT code results. If this max:min ratio is too large for the specific product being treated, use of two external metal absorbers, one on top and the other on the bottom can decrease the max:min ratio to approximately 1.4.

c. Utilization Efficiency Reduction

In summary, there are a number of absorber approaches that can be used to produce acceptable max:min ratios in consistently irregular products, such as ground beef chubs. The electron energy utilization efficiency must necessarily decrease, however. Recall that for double-sided, 10-MeV irradiation of products with a uniform areal density, the one-dimensional utilization efficiency η attains a maximum value of about 0.79 at an areal density $A_d = \rho$ d= 8.4 g/cm^2. The reduction in utilization efficiency resulting from the non-optimal product configuration can be estimated by multiplying this efficiency maximum by the ratio of the chub area to the area of the optimum configuration, according to

$$\eta_u = \eta_{max}\left\{\left(\pi r_c^2\right)/[(8.4/\rho_c)(2r_c)]\right\} = 0.146\,\rho_c r_c \tag{3.26}$$

For the chub example of Figure 3-27, ($\rho_c = 0.9$, $r_c = 4.5$ cm), the utilization efficiency is reduced to approximately 0.59. The implication of this decreased efficiency is an increase in the

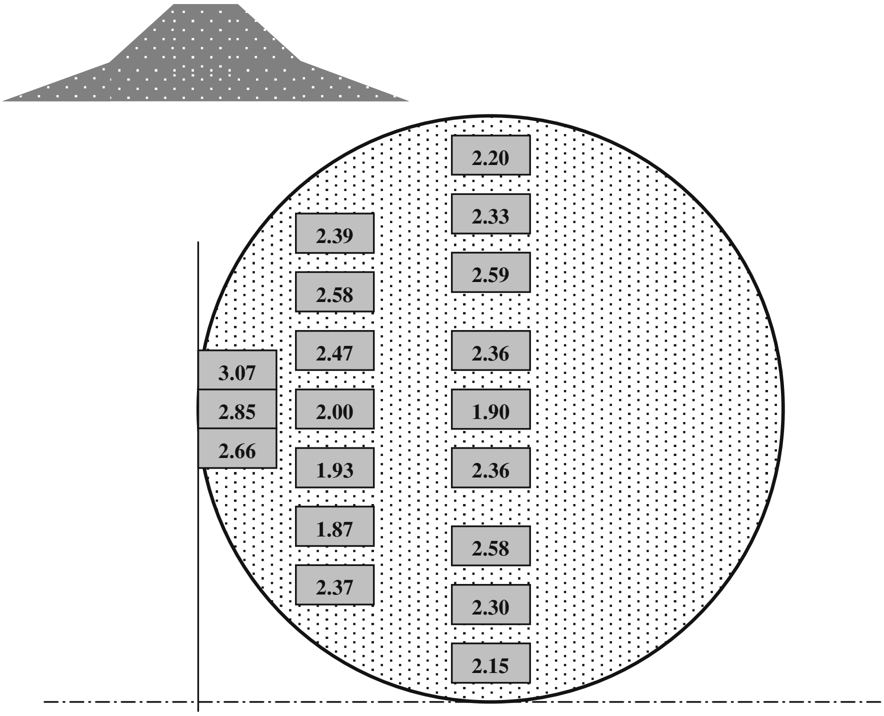

Figure 3-27. ACCEPT calculation dose map for the single aluminum absorber design of Figure 3-26. The approximate shape of the absorber is indicated.

breakeven processing price of about 32% in this case. Faced with such higher processing costs, producers are sometimes (but not always) willing to consider repackaging their products in configurations better suited for radiation processing.

3.4.2. Products with Random Variations in Areal Density

In contrast to the previous problem of processing products with consistent variation in areal density, there are also large classes of products that have essentially random variations in areal density. These variations may result from variations in thickness, density or both. Such products include a wide variety of fresh produce items, as well as bone-in chicken parts, for example. These products present special difficulties in ensuring the delivery of the minimum required dose to all portions of the product, while maintaining satisfactory max:min ratios and acceptable processing efficiencies.

When faced with the prospects of processing such products it is necessary to establish the approximate areal density distribution, in addition to establishing the minimum required dose and the maximum allowable max:min ratio. Since there is always a maximum product thickness, there is always a maximum areal density (the areal density distribution is truncated). If this maximum areal density is approximately 5 g/cm^2 or less, the distribution can be determined by first measuring the ratio of front and rear surface doses at many different representative positions of the product following a single-sided irradiation. These data can then be inverted using Figure 3-28 to obtain the areal densities. Since the areal density is a double-valued function of the surface dose ratio, the ambiguity can be removed by performing a second irradiation using an absorber of known areal density. A thickness of 2.75 g/cm^2 is most convenient.)

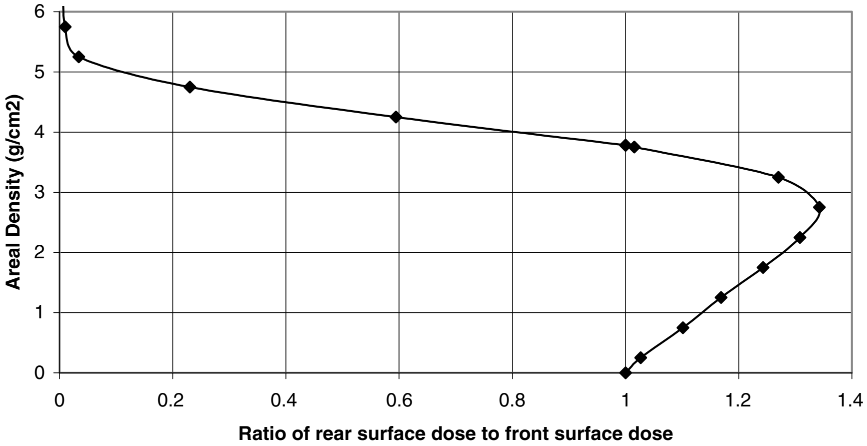

Figure 3-28. Variation of areal density with the ratio of the rear surface dose to the front surface dose for single-sided irradiation using 10-MeV electrons. The double-valued ambiguity can be removed by performing a second irradiation using an absorber of known areal density.

If the maximum areal density exceeds 5 g/cm^2, determining the areal density distribution is more difficult. In fact, if access to the interior of the product cannot be gained, the areal density variation must be measured using more penetrating radiation, such as x-rays. This technique will be discussed in the next section. If access to the interior of the product can be gained, the most straightforward approach is to measure the ratio of the midplane dose to the surface dose at several positions on the product. This ratio is presented in Figure 3-29 as a function of areal density. Since this function is also double-valued, the ambiguity can be removed by examining the magnitude of the surface dose. As an example, the ratio of the surface dose obtained in the double-sided irradiation to the surface dose from a single-sided irradiation is also shown in Figure 3-29.

Once the areal density distribution has been determined for the particular product of interest, it is possible to estimate several other parameters associated with the irradiation processing of the product. The usual case is that in which we must deliver a minimum required dose to all portions of the product, and we are then interested in the resulting energy utilization efficiency and the probability

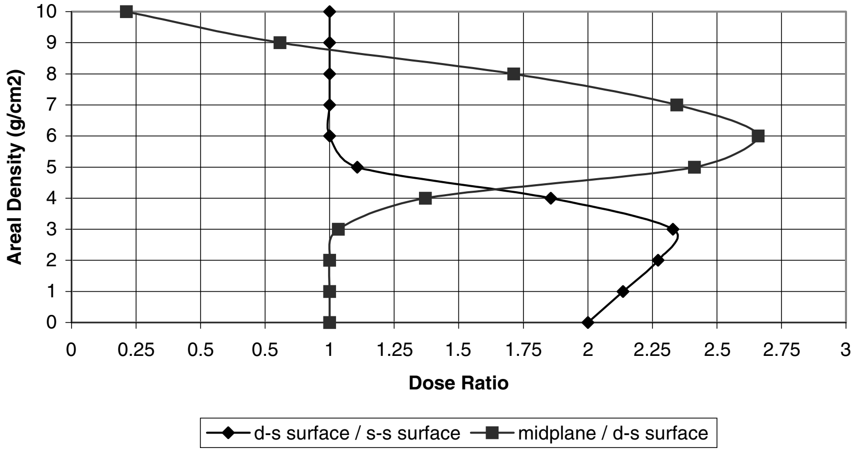

Figure 3-29. Areal density versus various dose ratios for double-sided irradiation using 10 MeV electrons.

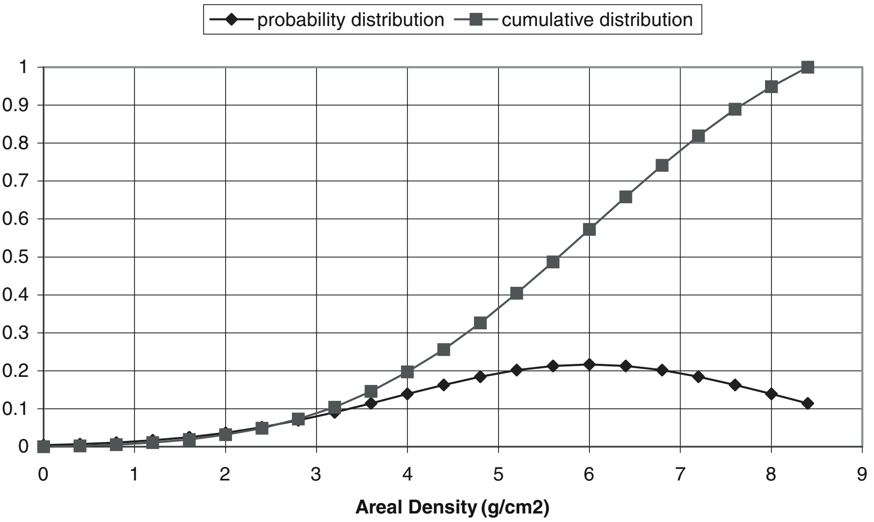

Figure 3-30. Normalized areal density probability distribution and the corresponding cumulative probability distribution, as determined from Eq. (3.27) with $x_m = 8.4\ g/cm^2$, $m = 6.0\ g/cm^2$, and $k = 0.33\ cm^2/g$.

that the max:min ratio will exceed a certain desired limit. To illustrate these calculations, we will assume the truncated gaussian distribution illustrated in Figure 3-30 and described by the following formula:

$$\begin{aligned} P(x) &= (k/\pi^{1/2})\exp[-k^2(x-m)^2], \quad 0 < x < x_m \\ &= 0, \quad \text{otherwise} \end{aligned} \tag{3.27}$$

The variable x is the areal density; m is the most probable value, x_m is the maximum, and k describes the width of the distribution. The normalization of this distribution is provided by integrating P(x) over the range $(0,x_m)$, which yields

$$S(x_m) = 0.5\{\mathrm{erf}(km) + \mathrm{erf}[k(x_m - m)]\} \tag{3.28}$$

with erf(x) defined as the error function. The average areal density is obtained by integrating xP(x) over the range $(0,x_m)$, and dividing by $S(x_m)$. If m is much larger than zero and x_m is much larger than m, the average areal density is also equal to m.

For our first example we assume values of $x_m = 8.4\ g/cm^2$, $m = 6\ g/cm^2$, and $k = 0.33\ cm^2/g$. In this case, $S(x_m) = 0.87$, and the average areal density is approximately 5.7 g/cm^2. With the assumed value of x_m, this product must be processed using double-sided electron irradiation (or with x-rays). From Figure 3-17, the minimum dose during treatment will occur on either surface; if the minimum required dose is exceeded on the surface, it will also be exceeded everywhere within the product. However, an examination of Figure 3-18 clearly indicates that irradiating this product in this manner will result in a max:min ratio well in excess of two for a significant portion of the product. We can estimate the percentage of time this condition will occur by referring to the cumulative distribution, also plotted in Figure 3-30. For example, from Figure 3-18, for all portions of the product having areal densities in the range of 4.6–7.6 g/cm^2, the midplane dose will exceed the surface dose by at least a factor of two. From the cumulative distribution of Figure 3-30, this condition will occur about 60% of the time. Performing similar calculations as a function of an assumed max:min criterion

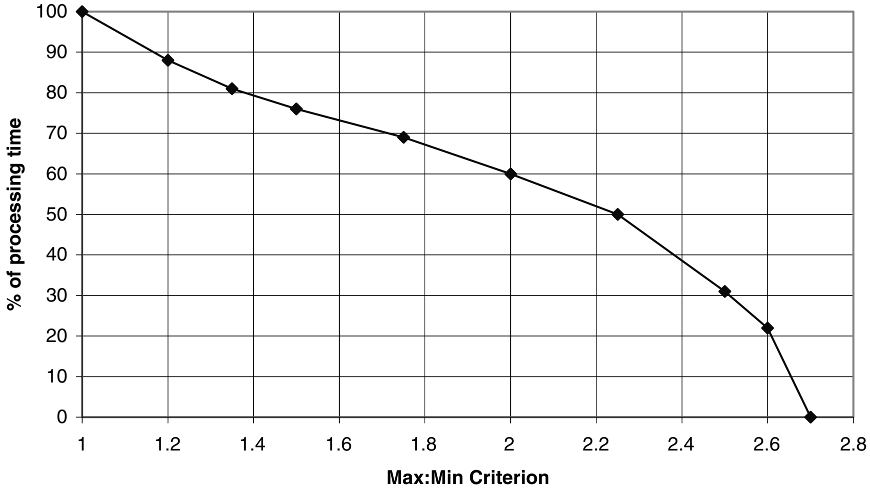

Figure 3-31. Percentage of time that the processed product will have a max:min ratio that exceeds a particular criterion, for the assumed areal density distribution of Figure 3-30.

leads to the curve of Figure 3-31, which estimates the percentage of time that the processed product will have a max:min ratio in excess of a particular value.

Since the minimum dose occurs on the surface, the energy utilization efficiency is simply determined by the average areal density. Referring again to Figure 3-18, the utilization efficiency for an areal density of 5.7 g/cm^2 is about 55%.

As a second example, we assume that this same product can be configured in such a fashion that its height can be divided by a factor of two, giving a probability distribution now characterized by $x_m = 4.2$ g/cm^2, $m = 3$ g/cm^2, and $k = 0.66$ cm^2/g. This distribution is therefore identical in shape to that of Fig. 3-30, but with the areal density divided by two. $S(x_m) = 0.87$ as before, but the average areal density is now 2.85 g/cm^2.

With this reduced value of x_m, we can now consider processing with either single- or double-sided irradiation, and we will examine the various performance factors for both cases. This comparison is facilitated with Figures 3-32 and 3-33 that compare the max:min ratios and energy utilization efficiencies for the two cases for areal densities up to 5 g/cm^2. From Figure 3-32, the max:min ratio increases monotonically with areal density for both cases, rising more rapidly when the areal density exceeds approximately 3.8 g/cm^2, and much more rapidly in the case of single-sided irradiation. For the case of single-sided irradiation, the choice of system parameters must ensure that the rear surface dose for the maximum areal density will exceed the minimum required dose. In contrast, for double-sided irradiation, the minimum dose will occur on either surface, and the maximum dose will always occur at the midplane of the product (see Figure 3-17).

With the reduced product thickness, the processing quality, in the sense of much reduced max:min ratios, is greatly improved. The estimated percentage of time that the processed product will have a max:min ratio in excess of a particular value is shown in Figure 3-34 for both single- and double-sided irradiation. Now, with single-sided irradiation, the max:min ratio will be 1.35 or less nearly 90 percent of the time, and for double-sided processing, the max:min ratio will be less than 1.2 nearly 85% of the time. In fact, for double-sided processing the max:min ratio will not exceed 1.6, and for single-sided processing the max:min ratio will not exceed 1.9.

The energy utilization efficiency for the case of single-sided irradiation can be estimated noting that the efficiency assuming a uniform product with an areal density of 4.2 g/cm^2 is about 54% from

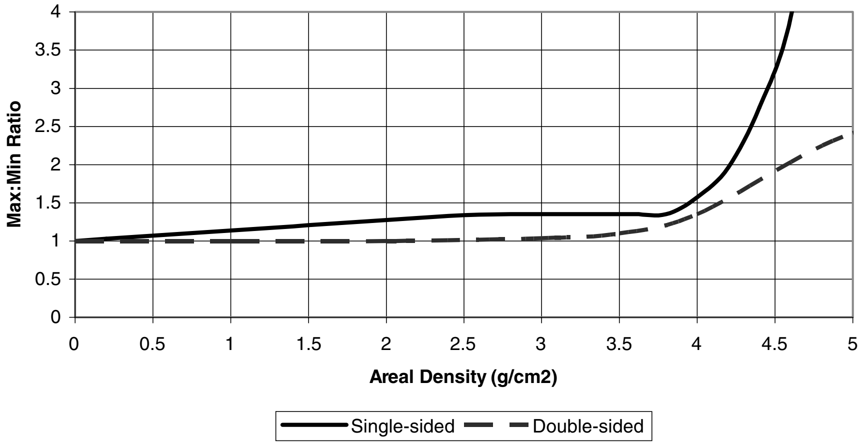

Figure 3-32. Comparison of the max:min ratio for single- and double-sided irradiation of uniform product as a function of areal density.

Figure 3-33. This must be reduced by the ratio of the average areal density (2.85) to the maximum (4.2), giving about 37%. The situation is somewhat better for double-sided irradiation because the efficiency for uniform product with an areal density of 4.2 g/cm^2 is about 66%. Using the same one-dimensional reduction factor now gives an efficiency of 45 %. These efficiencies are significantly less than that achievable with double-sided irradiation of the product with a maximum areal density of 8.4 g/cm^2, but the overdose condition is much better for the reduced areal density cases.

For this fictional product having the assumed areal distribution shape of Figure 3-30, there are thus three possible choices for the electron irradiation configuration, assuming that the height of the product (and maximum areal density) is selectable:

1. *Double-sided irradiation with the maximum areal density equal to 8.4 g/cm^2.* This condition will give the maximum energy utilization efficiency (approximately 55% for an areal

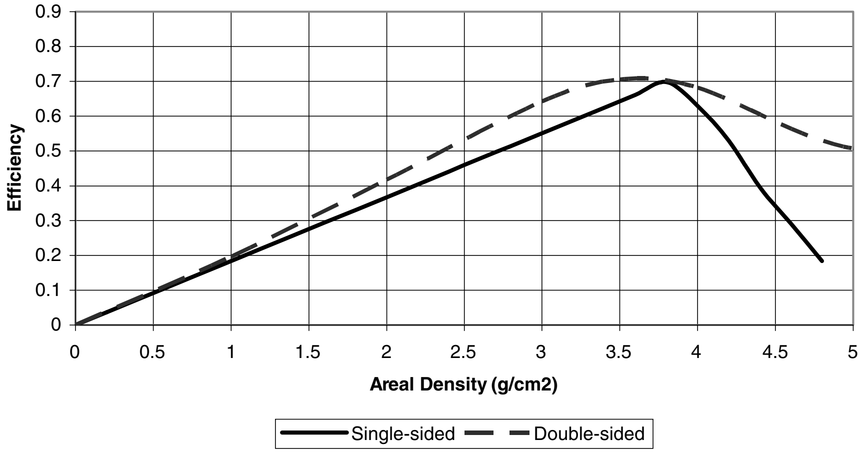

Figure 3-33. Comparison of the energy utilization efficiency for single- and double-sided irradiation of uniform product as a function of areal density.

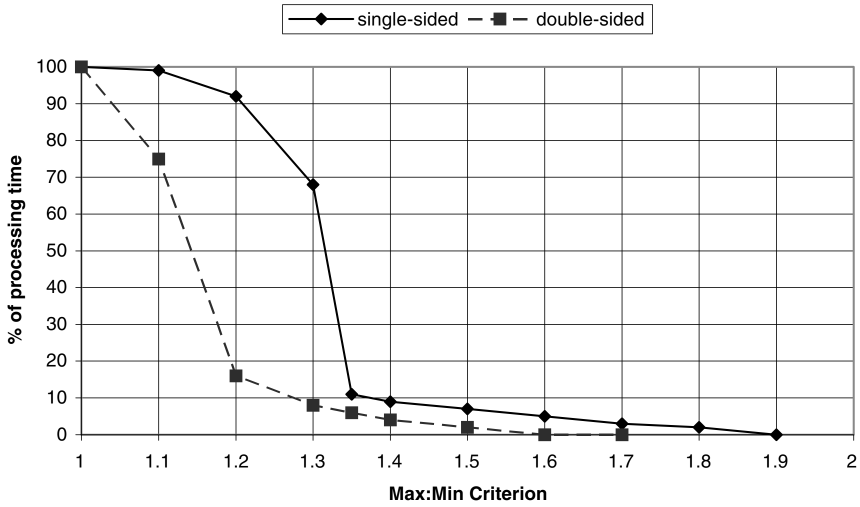

Figure 3-34. Percentage of time that the processed product will have a max:min ratio that exceeds a particular criterion, for the assumed areal density distribution shape of Figure 3-30, but with a maximum areal density of 4.2 g/cm^2.

distribution having the shape indicated in Figure 3-30), but a significant amount of the product will be overdosed.

2. *Double-sided irradiation with the maximum areal density chosen to be 3.7 g/cm^2.* This condition will ensure that the max:min ratio will never exceed 1.2 (highest quality), and the one-dimensional energy utilization efficiency (assuming the same distribution shape) will be approximately 48%.
3. *Single-sided irradiation with the maximum areal density chosen to be 3.8 g/cm^2.* This condition will presumably be lowest cost, in the sense of initial capital outlay. The max:min ratio will never exceed 1.35, and the utilization efficiency (47.5%) is essentially the same as that of the half-height, double-sided irradiation case.

If it is not possible to choose the maximum areal density because of packaging constraints, and the max:min ratio must be relatively low because of negative product sensory effects, it may be necessary to process such products using more penetrating x-rays.

3.5. FRONT SURFACE DOSE UNIFORMITY

The electron deposition analyses presented thus far have assumed that the electrons are uniformly incident on the surface of the product. However, almost all electron beams used in food irradiation are scanned, and most beams (from rf linacs) are pulsed. In this section we develop criteria for ensuring front surface dose uniformity using such beams.

To describe these situations, consider Figures 3-35 and 3-36 that illustrate the scanning waveform and the resulting beam centroid traces at the surface of the product, resulting from product motion on the conveyor. The time-dependent variation of the deflecting magnetic field has a characteristic sawtooth shape with a period T_s, as shown in Figure 3-35. For dc machines, the duration of the flyback portion of the pulse is usually small compared to the scan period. For pulsed machines, two approaches are in use. The more common approach is to use a slow scan encompassing many pulses, followed by a rapid flyback in the short duration between pulses. Less common is to scan during

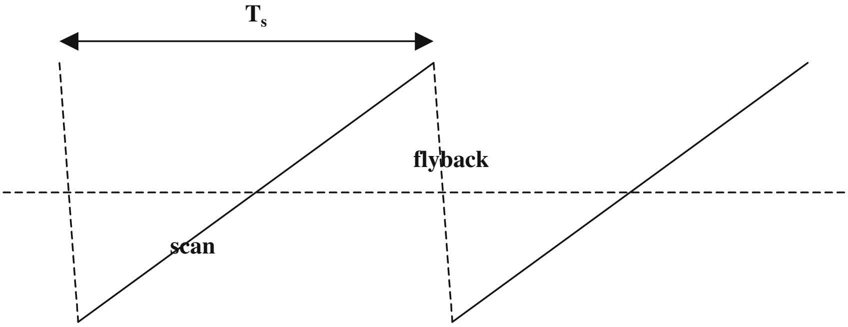

Figure 3-35. Time-dependent variation of the magnetic deflecting field in the scan magnet.

the pulse. During the period of the scan waveform, the product will move a distance $s = vT_s$, with v being the speed of the conveyor. The centroids of the beam traces resulting from these various approaches are illustrated in the diagrams of Figure 3-36.

To ensure uniform irradiation the lateral width S of the beam trace at the front surface of the product must be a few times larger than the separation between the centroids of adjacent traces. A reasonably conservative statement of this criterion is

$$vT_s < S/3 \tag{3.29}$$

In addition, for the case of a slowly scanned, pulsed beam (Figure 3-36(b)), the individual beam spots must overlap in the direction of the scan. If S also characterizes the beam spot size in the scan direction, and F is the pulse repetition rate of the linac, then this criterion is stated as

$$v/F < S/3 \tag{3.30}$$

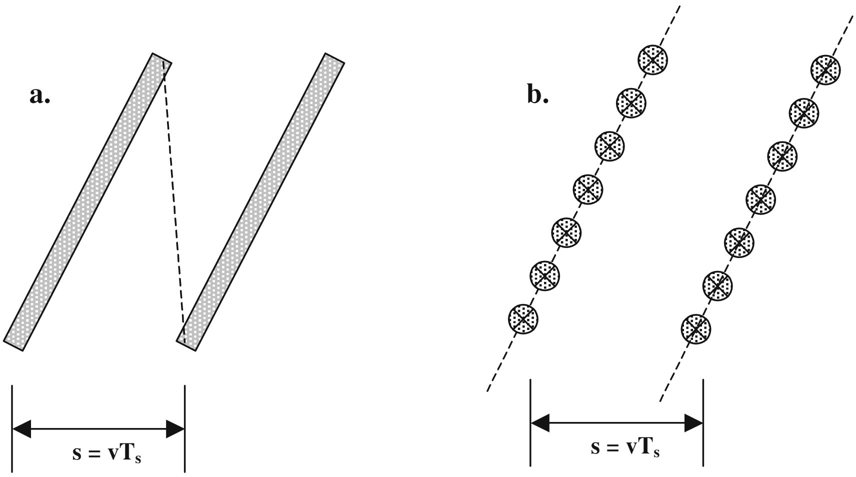

Figure 3-36. Beam trace centroids on the product surface. (a) dc beam or pulsed beam with the scan occurring during the pulse. The dashed line indicates some beam irradiation during the flyback portion of the scan waveform for the dc beam. (b) pulsed beam with many pulses per single scan.

The product throughput rate (dM/dt) is related to the beam power P, the dose D and the throughput efficiency through Eq. (2.22) as

$$dM/dt = \eta P/D$$

Assuming a scan height H and an areal density $A_d = \rho d$, to achieve the throughput rate in Eq. (2.22) requires a conveyor speed determined by

$$v = (dM/dt)/(HA_d) \tag{3.31}$$

Solving for (dM/dt) and substituting the expression for v into Eq. (3.29) gives the trace width criterion as

$$S > (3T_s\eta P)/(DHA_d) \tag{3.32}$$

Similarly, Eq. (3.30) can be rewritten as

$$S > (3\eta P)/(FDHA_d) \tag{3.33}$$

As a numerical example, we assume a pulsed beam at a repetition rate of 250 Hz, a scan height of 125 cm, and 50 pulses per scan ($T_s = 0.2$ s). We further assume an average beam power of 10 kW, a required dose of 1 kGy, a maximum areal density of 4 g/cm^2, and a throughput efficiency factor of 0.5. Evaluation of Eq. (3.33) gives $S > 0.08$ cm, which is easily satisfied; however, evaluation of Eq. (3.32) gives $S > 6$ cm, which is considerably larger than the beam diameter in a typical rf linac. Consequently, it would be necessary to expand the beam in the direction of conveyor motion.

There are at least two ways to produce sufficient overlap of the individual spots and traces at the product: (1) magnetic defocusing, and (2) scattering in the exit window, with enough distance between the window and product for sufficient beam expansion. Since scattering always occurs, we consider it first.

For titanium, a convenient expression for the mean-square scattering angle is

$$\langle\theta^2\rangle = 80\,x(\mathrm{cm})/[E(\mathrm{MeV})]^2 \tag{3.34}$$

in which x is the thickness of the exit window. For a 5-mil Ti foil ($x = 0.0127$ cm), 10-MeV electrons will therefore have an average scattering angle θ of 0.1 radian, or about 5.7 degrees. Assuming a narrow pencil beam, geometrical considerations indicate that the distance between the exit window and the front face of the product must exceed

$$S/(2\tan\theta) = 31.2\,\mathrm{cm} = 12.3\,\mathrm{inches} \tag{3.35}$$

to allow sufficient space for beam expansion. This distance is large, but reasonable.

However, if the required dose were only 0.5 kGy (typical of disinfestation doses) and/or the linac power were higher, the distance between window and product would have to increase proportionately. This could significantly increase the volume of the irradiation cell and would certainly increase ozone production. In such cases it may be desirable to use either a solenoid or a quadrupole lens to defocus the beam to produce the desired dose uniformity.

3.6. AIR-PRODUCT INTERFACES

From the data presented in Figures 3-11 and 3-12 it is apparent that multiple scattering causes expansion of a narrow pencil beam. In the product interior, such scattering does not have a dramatic effect on the dose uniformity; loss of dose resulting from scattering out of the volume of interest is balanced by scattering into the volume. However, this symmetry will be violated at interfaces, such as an air-product boundary. The dose nonuniformity at such an interface can be estimated by performing numerical calculations using a three-dimensional Monte Carlo code such as ACCEPT.

The geometry of such calculations is schematically indicated in Figure 3-37. 10 MeV electrons pass through a thin exit window, travel through a void (air) region that is several centimeters in depth, and enter the product. The scan occurs in the vertical direction as the product passes through the beam in the horizontal direction.

To give an example of such calculations, we assume the product is a rectangular volume having a uniform density of 0.9 g/cm^3. The height and width of the volume are 60 cm each, with a depth of 9 cm (implying that double-sided irradiation would be used for processing). The product volume is further divided into 1-cm^3 cells, and the amount of electron energy deposited in each cell is tallied as the beam is scanned vertically over the window while the product is transported (numerically) through the beam.

Particular cells of interest lie along the middle of the top of the volume, and along the corners, as indicated in Figure 3-37. A comparison of the doses delivered to these cells by a beam passing normally through the exit window is presented in Figure 3-38. Also shown is the dose delivered to cells in the middle of the product volume. As expected, lack of "in-scatter" leads to a decrease in dose along the air-product interface, with the decrease being most pronounced along the corners of the product volume.

It should be understood that these results are worst case because no packaging material was assumed. Nevertheless, if detailed in-product dose mapping does indicate an underdose condition at interfaces, there are several ways to improve the situation. For example, the separation between product packages should be decreased as much as possible; this will also improve the energy utilization efficiency. In addition, to decrease the interface effect on the exposed surfaces of the product, a layer of HDPE, wood, or aluminum honeycomb (having a density comparable to that of the product) can be placed alongside the product. The thickness of this layer need be no greater than 2 centimeters. Over scanning the beam by a few centimeters will then essentially eliminate the underdose condition.

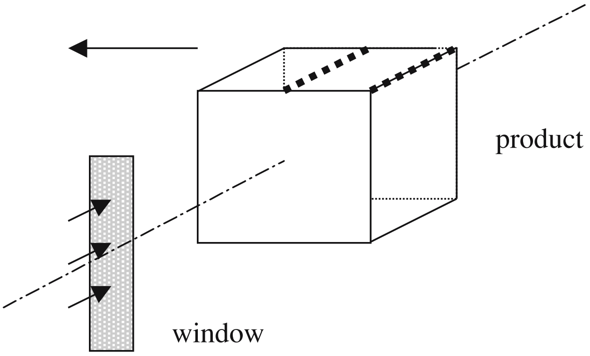

Figure 3-37. Schematic geometry of the air-product interface calculation. Regions of lower dose are expected in the top-middle and corner positions of the product volume.

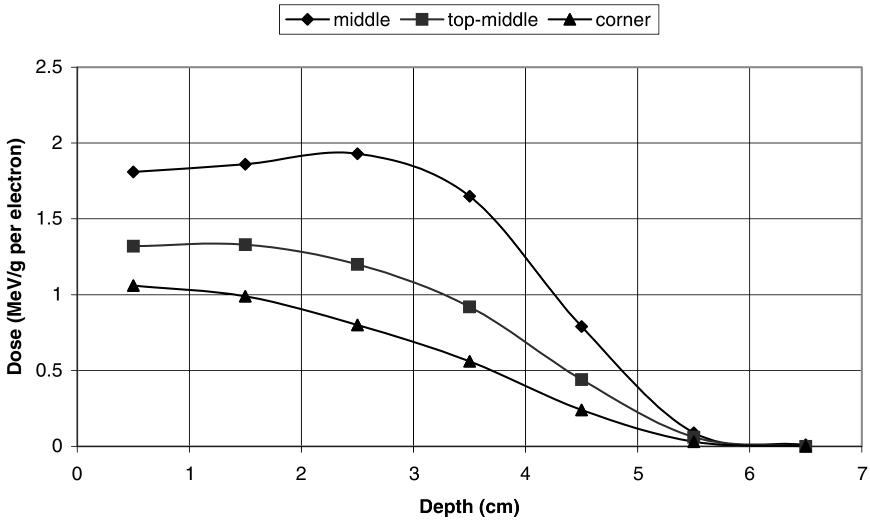

Figure 3-38. Depth-dose profile in one cubic centimeter cells arranged along the central axis of the product, along the top-middle of the product, and at the corner of the product volume. A 5-cm air gap was assumed between the window and the product volume.

3.7. SUMMARY

In this chapter we have discussed many aspects of food irradiation using energetic electron beams. The most important feature in the effective use of such beams is the characteristic depth-dose profile in uniform media. This distribution is determined by four primary electron interaction processes: (1) energy loss via inelastic collisions with atomic electrons; (2) the generation of energetic secondary, tertiary, etc. electrons as a result of these inelastic collisions; (3) multiple angular deflections resulting from elastic nuclear scattering collisions; and (4) bremsstrahlung (x-ray) generation, primarily through nuclear collisions.

Once the depth-dose distribution has been established, it can be used to estimate several parameters useful in describing the effectiveness of electron processing in a variety of scenarios. The two most important such parameters are the max:min ratio, which characterizes the dose uniformity, and the utilization efficiency, which represents the fraction of the electron energy that is absorbed as useful dose in the product. For single-sided irradiation of uniform material using monoenergetic 10-MeV electrons, the optimum areal density of 3.8 g/cm^2 gives a maximum one-dimensional utilization efficiency of about 70%. The max:min ratio for this condition is 1.35. When the areal density is increased beyond this optimum the max:min ratio rises rapidly, and the utilization efficiency falls sharply.

For double-sided irradiation using 10-MeV electrons, the utilization efficiency reaches its maximum value of about 79% at an areal density of about 8.5 g/cm^2; the max:min ratio is also about 1.35 in this case. For larger values of areal density, the max:min ratio rises rapidly and the utilization falls sharply. For smaller values of areal density, the energy utilization efficiency does not decrease below 50% until the areal density falls below about 2.5 g/cm^2. However, the max:min ratio exceeds two for areal densities in the range of 4.6–7.6 g/cm^2. Excellent dose uniformity (essentially unity) can be achieved if the areal density is less than 3 g/cm^2.

Real food products are necessarily packaged in a variety of shapes and sizes, and may be homogeneous or non-homogeneous within the package. Standardized products consisting of homogeneous material having a consistent, but irregular, shape can usually be effectively treated (i.e., with acceptable dose uniformity) using specially designed absorbers, albeit with a decrease in the energy utilization efficiency.

Products that have essentially random variations in areal density present special difficulties in ensuring the delivery of the minimum required dose to all portions of the product, while maintaining satisfactory max:min ratios and acceptable processing efficiencies. When faced with the prospects of processing such products it is necessary to establish the approximate areal density distribution, in addition to establishing the minimum required dose and the maximum allowable max:min ratio. Coupled with the depth-dose distribution, this information can be used to determine the possibility for successful electron beam treatment, or whether more penetrating x-rays must be used.

Multiple nuclear scattering will generally cause the dose distribution to be quite uniform in the bulk of the product being irradiated with electrons. However, asymmetries occurring at product interfaces can result in significant dose nonuniformity unless some care is taken. To ensure dose uniformity on the front surface of the product, consideration must be given to the scanning characteristics, conveyor speed, scattering in the exit window, and beam power and pulse characteristics, depending on the accelerator technology. In certain cases that require relatively low doses from a powerful machine, additional beam defocusing may be required.

REFERENCES

1. R.D. Evans, **The Atomic Nucleus**, McGraw-Hill, NY (1955).
2. **NIST Electron and Positron Stopping Powers of Materials Database**, US National Institute of Standards and Technology, Gaithersburg, Md.
3. N.D. Kessaris, “Calculated absorbed dose for electrons,” Radiation Research **23**, 630 (1964).
4. J.A., Halblieb, R.P. Kensek, T.A. Mehlhorn, G.D. Valdez, S.M. Seltzer, and M.G. Berger, ITS Version 3.0: The Integrated TIGER Series of Coupled Electron/Photon Monte Carlo Transport Codes, **SAND91-1634** (1992).
5. **ISO/ASTM 51649:2002(E)**, Practice for Dosimetry in an Electron Beam Facility for Radiation Processing at Energies between 300 keV and 25 MeV ASTM International (2002).
6. J.H. Bly, **Electron Beam Processing**, Int’l. Inform. Assoc., Yardley, PA (1988).
7. S. Humphries, Jr., “High-average-power electron accelerators for food processing,” in **High Brightness Accelerators**, A.K. Hyder, M.F. Rose and A.H. Guenther, eds. NATO ASI Series Vol. 178, Plenum (1986), p. 659–715.
8. R.B. Miller, E. Rubendall, A. Schnelle, K. Nanke, and A. Colangelo, “Absorbers for Electron Irradiation of Ground Beef Chubs,” **SB9999-53-0003.A1** (2001).
9. Packaging Technologies, Davenport, Iowa (USA).
10. G.K. Loda and R.C. Miller, “System for, and method of, irradiating opposite sides of an article with optimal amounts of cumulative irradiation,” US Patent No. 6,468,471 (2002).
11. J.T. Allen, G.M. Sullivan and C.B. Williams, “System for, and method of, irradiating articles,” US Patent Appl. 20030021722 (2003).

CHAPTER 4

FOOD IRRADIATION USING X-RAYS

The irradiation of food using energetic x-rays was previously introduced in Section 2.2. X-rays are generated using the same technology that produces electron beams, but afford considerably more flexibility in food processing applications because of their greater penetrating power. Unfortunately, the x-ray generation efficiency is quite low, and obtaining product throughput rates comparable to those of electron beam systems requires accelerators with roughly an order-of-magnitude higher average power. In this chapter we will consider several aspects of food irradiation using x-rays. We begin with a theoretical summary of energetic x-ray interactions with matter. We then return to the bremsstrahlung process of Chapter 3 in order to optimize the x-ray generation efficiency, and to accurately characterize the x-ray flux emitted from the converter. Detailed results are given for both 5 and 7.5 MeV systems. We then discuss x-ray depth-dose profiles, and develop max:min ratios and energy utilization efficiency estimates for a variety of irradiation scenarios. We conclude with an estimation of product throughput efficiencies that can be achieved using x-ray irradiation systems.

4.1. X-RAY INTERACTION PROCESSES

Of the many possible x-ray/matter interaction mechanisms, there are only three processes of significance for energies in the range of interest, namely 0.01–10 MeV. These are (1) the photoelectric effect, (2) Compton scattering, and (3) pair production.[1] In the photoelectric effect, the atomic electron cloud absorbs an x-ray of energy $h\nu_o$, resulting in the ejection of an electron from an inner atomic shell. The photoelectric effect is the primary absorption mechanism for medium- and high-Z materials for photon energies less than about 0.1 MeV. For energies comparable to the electron rest mass energy ($m_oc^2 = 0.511$ MeV) the dominant interaction is relativistic scattering of the photon by an electron, known as Compton scattering. The characteristic feature of this mechanism is a partial energy transfer from the photon to the electron, with the exact amount being a function of the scattering angle. If the photon energy exceeds twice the electron rest mass energy, the photon can disappear entirely, with the simultaneous appearance of an electron-positron pair whose total energy is $h\nu_o$. In the following paragraphs of this section we discuss the salient features of these interaction mechanisms.

4.1.1. Photoelectric Effect

The photoelectric effect is schematically illustrated in Figure 4-1. An incident photon is absorbed by the electron cloud of an atom, resulting in the ejection of an inner shell electron (usually K or L)

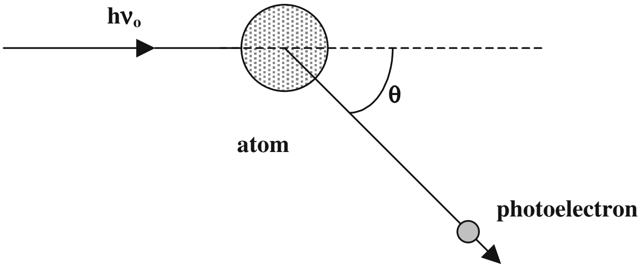

Figure 4-1. Schematic diagram of the photoelectric effect.

with a kinetic energy T given by

$$T = h\nu_o - E_b \tag{4.1}$$

E_b is the binding energy of the ejected electron; it reappears in the form of characteristic x-rays (fluorescence) and low-energy Auger electrons that are emitted as the atomic electron cloud relaxes and the inner shell vacancy is filled. At low photon energies, the photoelectron is emitted at right angles to the direction of incidence (in the direction of the electric vector of the incident radiation). At higher energies, the photoelectrons become more forward directed. Because of its rest mass, the momentum of the ejected electron must greatly exceed the momentum ($h\nu_o/c$) of the incident photon. Recoil of the entire residual atom is thus required for momentum conservation.

Theoretical treatments of the photoelectric effect are quite complicated because they necessarily use the relativistic Dirac equation for a bound electron. A crude but useful approximation for the atomic cross section for the photoelectric effect is given by

$$\sigma_{pe} = \text{const } Z^n (h\nu_o)^{-3} \tag{4.2}$$

with Z being the atomic number. The exponent n increases from about 4 to 4.6 as $h\nu_o$ increases from 0.1 to 3 MeV. However, there are jumps in the cross section, corresponding to the binding energies of the atomic orbitals.

4.1.2. Compton Scattering

The scattering of very low energy photons by free electrons is adequately described by the nonrelativistic classical theory (Thomson scattering). However, when the photon energy is comparable to the electron rest mass energy, the momentum of the incident photon is not negligible and must be conserved between the struck electron and the outgoing scattered photon. The energy of the scattered photon must therefore be less than that of the incoming photon. Consider the schematic diagram of Figure 4-2. An incident photon of energy $h\nu_o$ and momentum $h\nu_o/c$ is scattered by a free electron. The collision imparts energy T and momentum p to the electron, which emerges at angle ϕ with respect to the incoming photon. The scattered photon emerges at angle θ with reduced energy $h\nu$ and momentum $h\nu/c$. From energy conservation,

$$h\nu_o = T + h\nu \tag{4.3}$$

Conservation of momentum in the direction of the incident photon gives

$$h\nu_o/c = (h\nu/c)\cos\theta + p\cos\phi \tag{4.4}$$

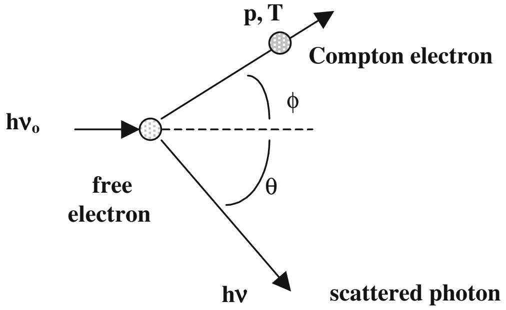

Figure 4-2. Schematic diagram of Compton scattering.

while momentum conservation in the normal direction gives

$$(h\nu/c)\sin\theta - p\sin\phi = 0 \tag{4.5}$$

The relativistically correct relationship between the momentum and energy of the electron is

$$(pc)^2 = T(T + 2m_oc^2) \tag{4.6}$$

These equations can be solved to yield

$$(h\nu)^{-1} = (h\nu_o)^{-1} + (1 - \cos\theta)(m_oc^2)^{-1} \tag{4.7}$$

The resulting energy of the scattered photon is plotted in Figure 4-3 as a function of incident photon energy for several different scattering angles. While low energy photons undergo only a moderate decrease in energy, high-energy photons generally suffer a large loss. Backscattered photons ($\theta = 180°$) can have energies no greater than 0.25 MeV, which is an important factor in radiation shield design.

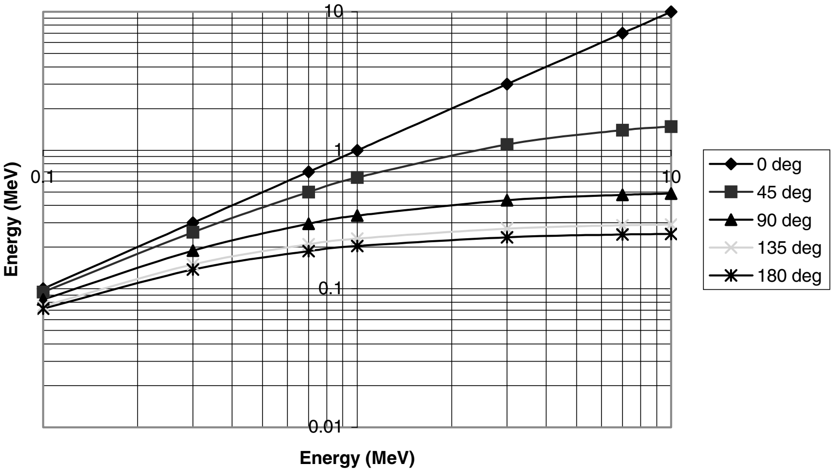

Figure 4-3. Variation of the energy of the scattered photon as a function of the energy of the incident photon for several values of the exit angle of the scattered photon.

The results presented thus far are based on general conservation laws and must be satisfied regardless of the details of the interaction. However, the probability of scattering at a particular angle does depend on the details. Using Dirac's relativistic theory of the electron, Klein and Nishina developed a treatment of Compton scattering that is correct in quantum-mechanical detail. The results of this theory are in excellent agreement with experimental data. According to this model the differential collision cross section per electron for incident, unpolarized radiation is given by

$$d_e\sigma_c = \left(r_o^2/2\right)d\Omega(\nu/\nu_o)^2[\nu_o/\nu + \nu/\nu_o - \sin^2\theta] \tag{4.8}$$

where the photon is scattered into the solid angle $d\Omega = 2\pi \sin\theta\, d\theta$, and $r_o = e^2/m_oc^2 = 2.82 \times 10^{-13}$ cm is the classical electron radius. The total collision cross section per electron ${}_e\sigma_c$ is obtained by integrating Eq. (4.8) over all angles θ between 0 and π. The result is

$$\begin{aligned} {}_e\sigma_c = 2\pi r_o^2\{&[(1+\alpha)/\alpha^2][2(1+\alpha)/(1+2\alpha) - [\ln(1+2\alpha)]/\alpha] \\ &+ [\ln(1+2\alpha)]/(2\alpha) - (1+3\alpha)/(1+2\alpha)^2\} \end{aligned} \tag{4.9}$$

The parameter α is the incident photon energy divided by the electron rest mass energy, $\alpha = h\nu_o/m_oc^2$. ${}_e\sigma_c$ has dimensions of square centimeters per electron. ${}_e\sigma_c$ thus represents the probability that a photon of energy $h\nu_o$ is removed from a collimated beam that passes through an absorber containing one electron/cm^2. Since there are Z electrons per atom, the atomic cross section for Compton scattering is given by $\sigma_c = Z_e\sigma_c$.

Although the photon is removed from the collimated beam, its energy is not absorbed locally. To account for this fact, it is customary to define average Compton scattering and absorption cross sections as follows:

$$\begin{aligned} \sigma_{sc} &= (\langle h\nu\rangle/h\nu_o)\sigma_c \\ \sigma_{ab} &= (\langle T\rangle/h\nu_o)\sigma_c \end{aligned} \tag{4.10}$$

with the brackets denoting average values.

4.1.3. Pair Production

A photon with energy exceeding twice the electron rest mass energy (1.02 MeV) can be completely absorbed in the Coulomb field of (primarily) a nucleus or (more rarely) an electron, with the simultaneous creation of an electron-positron pair, as suggested in the schematic diagram of Figure 4-4. The presence of the third charged particle is necessary for conservation of both energy and momentum in the transformation.

The pair production process is described well using the Dirac theory of the electron, in which the solution of Eq. (4.6) for the electron energy T can have either positive or negative values for the same particle momentum. All negative energy states are fully occupied, but unobservable. Elevating an electron out of a negative energy state to an observable positive energy state requires a minimum energy of $2m_oc^2$. The vacancy in the negative energy states is observed as a hole having the same properties as the electron, but with opposite charge; i.e., a positron. Described in this fashion, pair production must be intimately related to bremsstrahlung, in which the electron undergoes a similar transition, but from a higher positive energy state to a state of lower positive energy, being accompanied by the emission of a photon. In fact, the mathematical treatments of the two processes are nearly identical, and the nuclear pair production cross section is observed to have the same Z^2

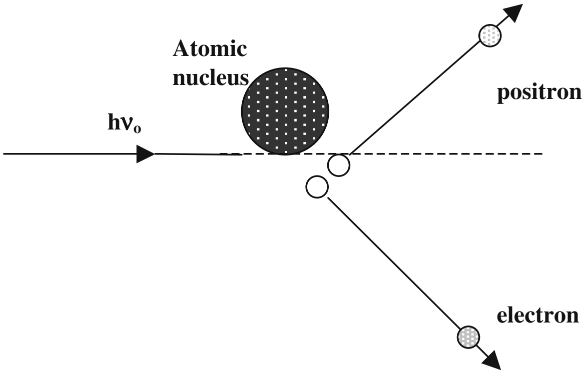

Figure 4-4. Schematic diagram of pair production.

dependence. The pair production cross section increases approximately logarithmically with photon energy; i.e.,

$$\sigma_{pp} = \text{const}\, Z^2 \ln(h\nu_o) \tag{4.11}$$

4.1.4. Attenuation and Absorption Coefficients

When a collimated beam of primary photons of intensity I photons per square centimeter with energy $h\nu_o$ passes through a thin foil of thickness dx having N atoms per cubic centimeter, the change in intensity of the photon beam dI depends on the sum of the three atomic cross sections as given by

$$\begin{aligned} dI/I &= -N(\sigma_{pe} + \sigma_c + \sigma_{pp})dx = -(N\sigma_{pe} + N\sigma_c + N\sigma_{pp})dx \\ &= -(\mu_{pe} + \mu_c + \mu_{pp})dx = -\mu dx \end{aligned} \tag{4.12}$$

The parameters μ_{pe}, μ_c, and μ_{pp} are linear attenuation coefficients, and μ is the total linear attenuation coefficient, with units of cm^{-1}. Integrating Eq. (4.12) gives

$$I = I_o e^{-\mu x} \tag{4.13}$$

Thus, the fraction of uncollided primary photons of energy $h\nu_o$ decreases exponentially with foil thickness.

However, not all of the energy represented by the interacting photons $(I_o - I)h\nu_o$ is deposited in the foil. In particular, the average energy of the Compton electrons is $(\sigma_{ab}/\sigma_c)h\nu_o$, and the total kinetic energy of the positron-electron pair is $(h\nu_o - 2m_oc^2)$. Taking into account these considerations, the differential energy absorption per square centimeter dF in a foil thickness dx is (assuming the energy of the charged particles is deposited in the foil)

$$dF = h\nu_o(dI_a) = h\nu_o\, I[\mu_{pe} + \mu_c(\sigma_{ab}/\sigma_c)h\nu_o + \mu_{pp}(h\nu_o - 2m_oc^2)]dx = \mu_a F dx \tag{4.14}$$

$F = I\, h\nu_o$ is the energy fluence, and μ_a is thus defined as the linear absorption coefficient. The energy absorption per unit volume in a thickness Δx, $\Delta F/\Delta x$, is simply the fluence F at depth x multiplied by μ_a.

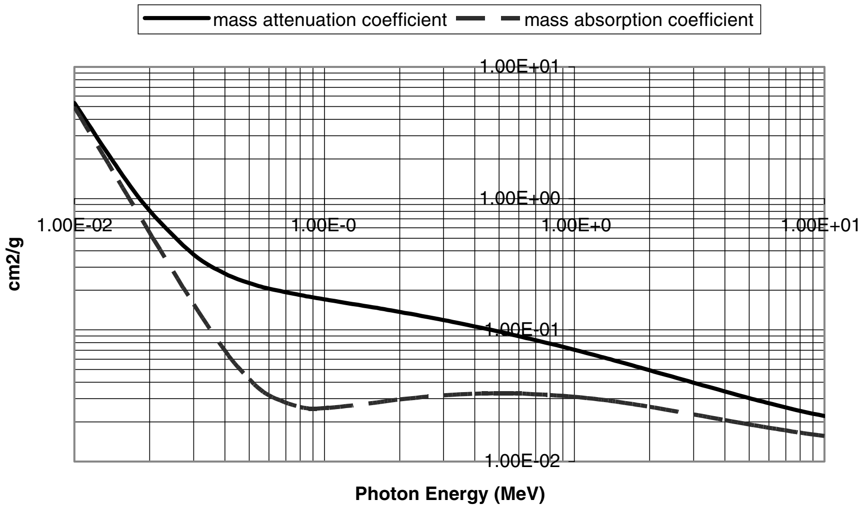

Figure 4-5. Mass attenuation and absorption coefficients for photons in water.

Finally, the energy absorbed per unit mass, or the absorbed dose, is obtained by dividing $\Delta F/\Delta x$ by the density ρ of the material. Thus

$$D = \mu_a F/\rho = \mu_{ma} F \tag{4.15}$$

μ_{ma} is termed the mass absorption coefficient; it has units of cm^2/g.

For materials comprised of a mixture of elements whose mass absorption coefficients are μ_{ma1}, $\mu_{ma2}, \ldots$, the overall mass absorption coefficient of the mixture is given by

$$\mu_{tot} = \mu_{ma1} w_1 + \mu_{ma2} w_2 + \ldots \tag{4.16}$$

where $w_1, w_2, \ldots$ are the weight fractions of the elements comprising the mixture.

The mass attenuation and absorption coefficients for water are presented in Figure 4-5 for the energy range of 10 keV – 10 MeV.[2] The rapid rise below about 30 keV is due to the photoelectric effect. Also, because of the Z^2 dependence, pair production is not important for water until the photon energy exceeds about 5 MeV. Consequently, over the energy range of interest for food irradiation with x-rays (7.5 MeV or less), the dominant x-ray interaction mechanism is Compton scattering. While the mass attenuation coefficient monotonically decreases with energy, the mass absorption coefficient is nearly constant at about 0.03 cm^2/g over the energy range of 50 keV to 2 MeV.

4.2. CONVERTER OPTIMIZATION

When processing with x-rays, the throughput efficiency depends on the efficiency of utilizing the available x-ray energy, and the efficiency of generating the x-ray fluence. In this section we analyze the design of the x-ray converter with the intent of optimizing the x-ray generation efficiency and characterizing the resulting fluence for use in later analyses.

Most x-ray converters are designed using Monte Carlo transport codes. Before turning to the results of such calculations, we discuss a few general features that could reasonably be expected. As presented in Section 3.1.4, the thin-target bremsstrahlung cross section scales as the square of the atomic number of the target material. Therefore, the converter should be made of a high-Z material, but one with good thermal conductivity and a high melting point because most of the electron energy will be deposited in the material, eventually appearing as heat. The most commonly used converter materials are tantalum, tungsten and gold, with Z = 73, 74 and 79, respectively. (In the US, tantalum and gold have been approved for use up to 7.5 MeV.) Since the radiative stopping power scales linearly with electron energy, the electron kinetic energy should be as high as permitted, 5 or 7.5 MeV, to maximize the yield. Finally, the converter must be sufficiently thick to stop all the primary electrons; otherwise, the surface of the product would receive a low-energy electron overdose.

4.2.1. Thick-Target Bremsstrahlung Yield

From Eq. (3.10) the ratio of the energy loss via bremsstrahlung to the energy loss due to collisions in a thin, high-Z target is nearly 50% for a kinetic energy E_o of 5 MeV. However, as the thickness of the high-Z layer is increased to increase the total x-ray yield, the electron energy (and x-ray conversion efficiency) decreases as a function of penetration depth. The net result is that the thick-target bremsstrahlung yield is far less than 50% at 5 MeV.

An analytical estimate of the thick-target bremsstrahlung yield can be obtained starting from Eq. (3.10) as

$$\begin{aligned}(dE/dx)_{tot} &= (dE/dx)_{rad} + (dE/dx)_{coll} = (dE/dx)_{coll}[1 + ZE(\mathrm{MeV})/800] \\ &= \alpha(1 + \beta E) \qquad (4.17)\end{aligned}$$

with $\beta = 0.09\ \mathrm{MeV}^{-1}$ and $\alpha = 2\rho = 35$ MeV/cm for a suitable high-Z material. Ignoring the difference between pathlength and depth, Eq. (4.17) can be integrated to yield a crude expression for the electron energy as a function of depth x into the converter; the result is

$$E = \beta^{-1}[(1 + \beta E_o)e^{-\alpha\beta x} - 1] \qquad (4.18)$$

The maximum penetration depth is found by setting E = 0, which gives

$$x_m = (\alpha\beta)^{-1} \ln(1 + \beta E_o) \qquad (4.19)$$

The total bremsstrahlung yield per electron (ΔE) is then found as a function of converter depth by integrating $(dE/dx)_{rad}$, using Eq. (4.18) for the electron energy as a function of depth; i.e.,

$$\begin{aligned}\Delta E &= \int (dE/dx)_{rad}\, dx = \alpha\beta \int E\, dx \\ &= \beta^{-1}(1 + \beta E_o)(1 - e^{-\alpha\beta x}) - \alpha x \qquad (4.20)\end{aligned}$$

For $E_o = 5$ MeV and the assumed values of α and βgiven above, $\Delta E = 0.87$ MeV per electron (maximum conversion efficiency of 17%) at the maximum depth. The variation of bremsstrahlung yield with depth, as given by Eq. (4.20), is plotted in Figure 4-6. Almost 80% of the maximum yield is achieved at half the maximum depth.

Although low to begin with, this crude conversion efficiency estimate is high for three important reasons. First, the depth is always less than the pathlength because of multiple electron scattering. Second, the yield was not reduced by x-ray self-absorption in the converter. Since the absorption cross sections generally increase with atomic number, a backing layer of lower-Z material is suggested.

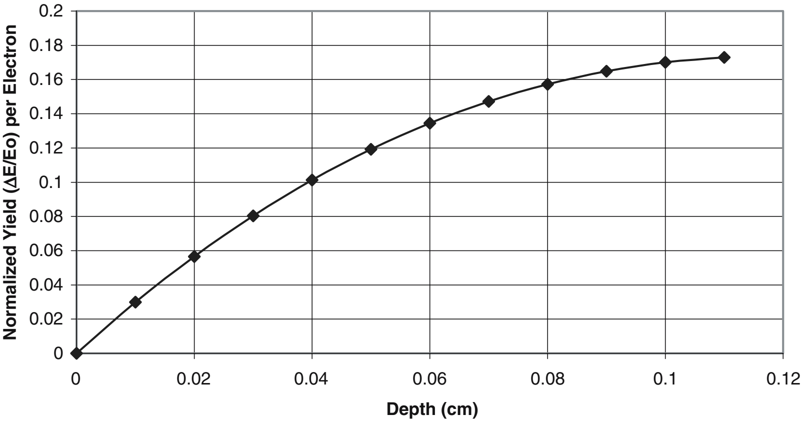

Figure 4-6. Analytical estimate of the thick-target bremsstrahlung conversion efficiency for a 5-MeV electron beam incident onto a high-Z converter, as given by Eq. (4.20).

Third, only those x-rays leaving the converter in the forward direction will be useful in treating product. As will be seen in the next section, consideration of these factors decreases the useful x-ray yield by about a factor of two from the Eq. (4.20) estimate.

4.2.2. Monte Carlo Simulation Results

Guided by the results of the previous section, a reasonable approach for designing the x-ray converter is to use a thin layer of high-Z material backed by a thicker layer of a lower-Z material.[3] The thickness of the high-Z layer that maximizes the forward-going x-ray fluence, including the effects of self-absorption, is first determined; then, the thickness and material of the second layer are chosen such that x-ray self-absorption is minimized, yet all primary electrons are stopped. These calculations are most easily performed using Monte Carlo codes such as those of the Integrated TIGER Series (ITS).[4] Detailed results are presented here for a 5-MeV converter. The corresponding results for a 7.5-MeV converter are then summarized for comparison purposes.

(a) 5-MeV

The variation with tantalum thickness of the total forward-going x-ray fluence, as calculated by the one-dimensional TIGER code, is shown in Figure 4-7.[5] Monoenergetic 5-MeV electrons were normally incident onto a bare tantalum converter having a density of 16.65 g/cm^3. (The CSDA range of tantalum is 0.22 cm.) The x-ray energy rapidly increases as the radiation shower forms, then saturates as the electron kinetic energy degrades and self-attenuation becomes significant. The x-ray energy fluence has a relatively broad maximum of about 9.7% of the initial electron kinetic energy over the range of 0.08–0.10 cm of tantalum, or a little more than one-third of the CSDA range.

Pertinent additional information is provided by the electron and photon energy spectra shown in Figures 4-8 and 4-9. The electron kinetic energy spectrum rapidly degrades through multiple scattering and energy straggling processes. At a depth of 0.08 cm, a peak in the spectrum is barely discernible at 3 MeV. The most energetic photons are generated in the very surface layer of the tantalum. Lower energy photons are then generated in abundance as the electron kinetic energy degrades and the shower forms. The effect of photoelectric self-absorption is apparent at energies below 0.5 MeV.

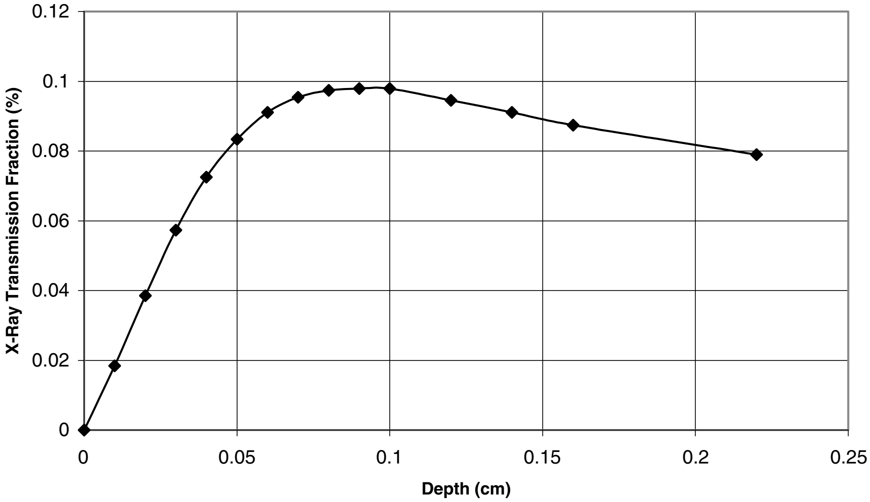

Figure 4-7. The fraction of the initial electron energy (5 MeV) converted into forward going x-rays as a function of tantalum thickness.

Based on these results, the optimum thickness of the high-Z tantalum layer should be in the range of 0.08–0.1 cm. Although the electron energy spectrum is badly degraded at these depths, the energy content is still significant, and these electrons must be prevented from reaching the product to avoid a serious surface overdose condition. The required thickness of the backing layer can be estimated by requiring the total converter thickness to exceed one CSDA range for 5-MeV electrons; i.e.,

$$(\mathrm{d}/\mathrm{R}_{\mathrm{csda}})_{\mathrm{Ta}} + (\mathrm{d}/\mathrm{R}_{\mathrm{csda}})_{\mathrm{B}} > 1.0 \tag{4.21}$$

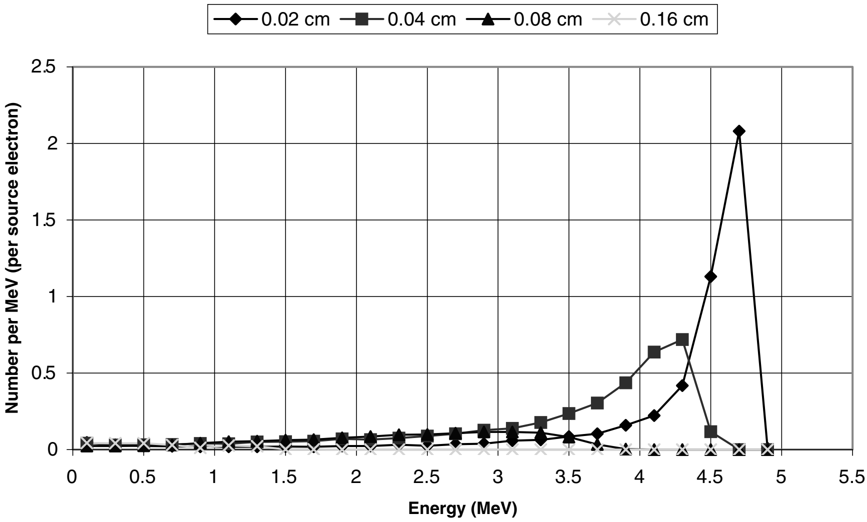

Figure 4-8. Electron energy spectra at various depths into the tantalum converter. The incident beam was monoenergetic at 5 MeV.

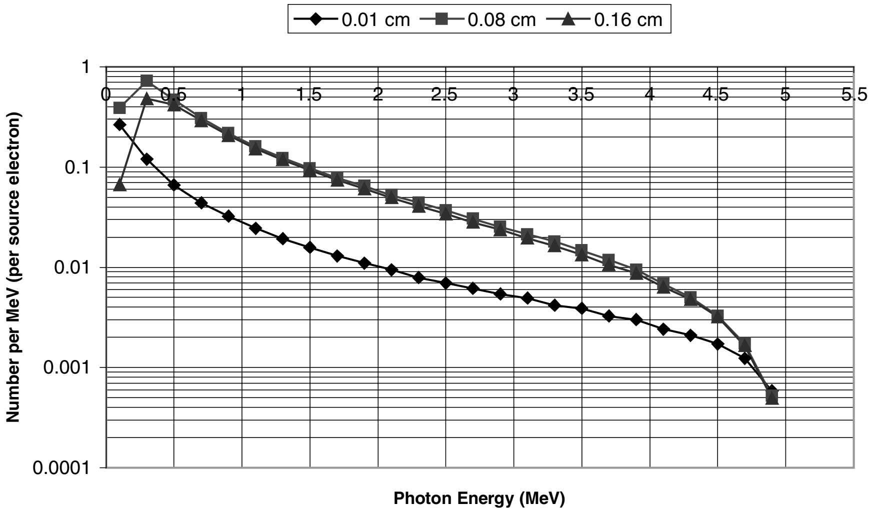

Figure 4-9. Photon energy spectra at various depths into the tantalum converter.

The backing material should have reasonably good thermal properties, and should be relatively transparent to the forward-going x-rays. The mass absorption coefficients for water, aluminum, iron and tantalum are compared over the energy range of 0.5–5 MeV in Figure 4-10.[2] Except for tantalum at low energies (the higher photoelectric effect cross section for high Z materials), there is not a great deal of difference in these absorption coefficients. Of the elements considered, aluminum has a low absorption coefficient over the energy range of a few hundred keV to a few MeV (only iron is lower); it also has good thermal conductivity and is relatively cheap. Consequently, aluminum is usually the backing material of choice. In addition, an aluminum backplate can easily be cooled with flowing water for high-power installations.

The CSDA range for 5-MeV electrons in aluminum is approximately 1.15 cm. Assuming a tantalum layer thickness of 0.08 cm, the thickness of the aluminum layer must exceed 0.73 cm from Eq. (4.21), to ensure that all primary electrons are stopped in the converter. For conservatism,

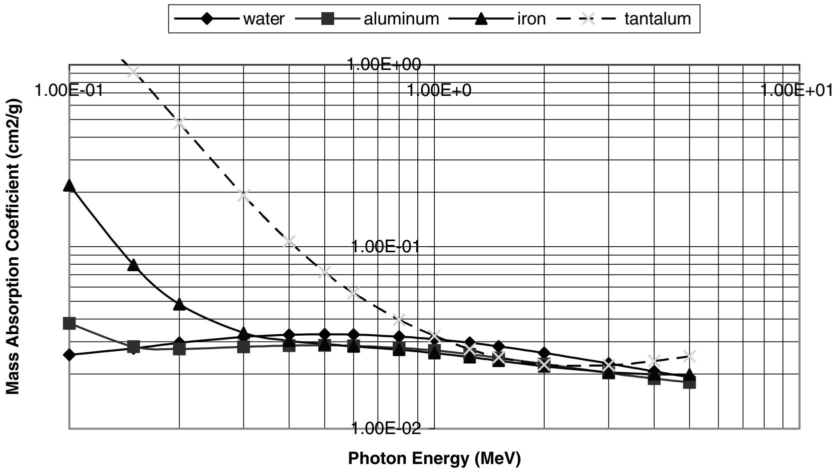

Figure 4-10. A comparison of mass absorption coefficients for various elements.

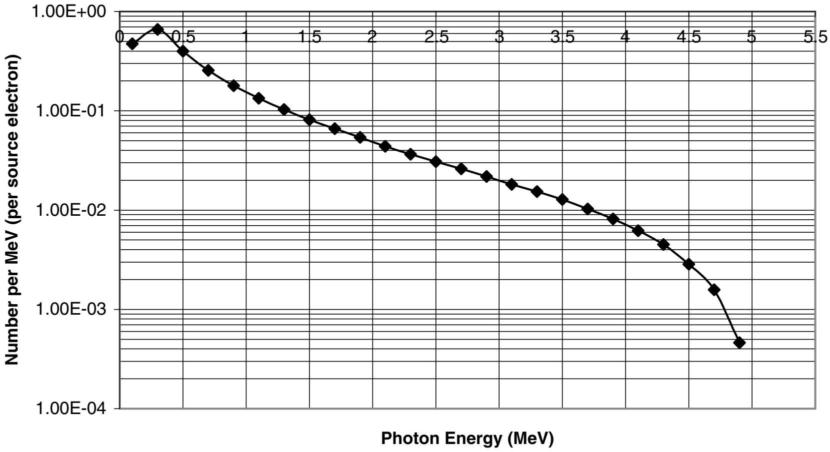

Figure 4-11. Energy spectrum of the forward-going x-ray fluence produced by monoenergetic 5-MeV electrons normally incident onto a compound converter consisting of a 0.08-cm layer of tantalum, backed by 1 cm of aluminum. (E_{avg} = 0.77 MeV.)

a backing plate of 1-cm-equivalent aluminum (including any water jackets) is typically used. The thickness of this converter is 1.23 times the total CSDA range, according to the TIGER code. The resulting spectrum, as calculated by TIGER, of the forward-going x-ray fluence for this compound converter is presented in Figure 4-11. The shape of the spectrum is essentially unchanged from the spectrum at 0.08 cm of tantalum (Figure 4-9), but the total forward-going x-ray fluence has been reduced from 9.7% to 8.4% of the incident electron energy. (Assuming a simple exponential decrease with an absorption coefficient of 0.03 cm^2/g would give a predicted decrease to 8.9%.) The average energy of the spectrum is 0.77 MeV.

There are several additional results from this calculation that are of interest. First, although all primary electrons are stopped in the converter, there are a significant number of low-energy Compton electrons that are emitted from the converter in the forward direction. The fractional energy carried by these electrons is only about 0.04% of the incident electron energy, however. In contrast, 16% of the incident electron energy is reflected backward by the converter; 12% is carried by backscattered electrons, and the remaining 4% is borne by photons. The backscattered photon spectrum is quite soft because of the Compton scattering kinematics, although there is a spectral peak at 0.511 MeV resulting from positron annihilation.

Dividing the transmitted photons into 15° angular bins, the energy vs angle and the total photon energy emitted into the six solid angle segments are presented in Figure 4-12.

With a normalization such that

$$\int_0^{\pi/2} f(\theta) 2\pi \sin\theta \, d\theta = 1 \tag{4.22}$$

an approximate functional dependence for the variation of x-ray energy with angle is provided by (with the angle in radians)

$$\begin{aligned} f(\theta) &= 0.644(1 - 1.13\theta); \quad && 0 < \theta < 0.15\pi \\ & 0.433(1 - 0.637\theta); && 0.15\pi < \theta < \pi/2 \end{aligned} \tag{4.23}$$

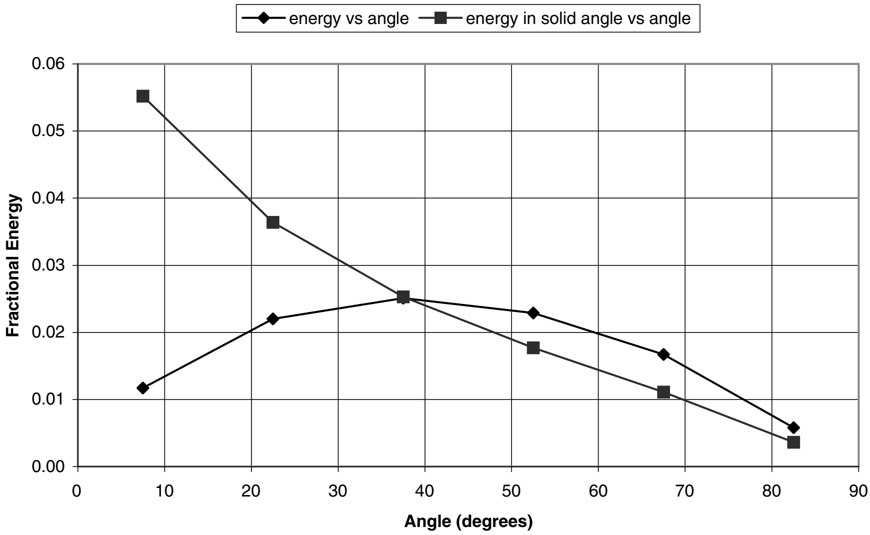

Figure 4-12. The x-ray energy per steradian and the total energy per source electron emitted into 15-degree solid angle segments ($2\pi \sin\theta\, d\theta$) versus the emission angle for 5-MeV electrons normally incident onto the compound x-ray converter.

While the flux is peaked on axis, there is significant emission at large angles, primarily because of electron elastic scattering in the converter. The resulting energy half-angle is nearly 40 degrees, which is more than five times as large as the thin-target prediction for 5-MeV electrons (see Eq. (3.9)). This result has important implications for the shape of the irradiation zone, which will be considered in detail later in this chapter. The corresponding energy spectra for the six emission angles are presented in Figure 4-13. As expected, the energy spectrum is somewhat harder in the forward direction.

The energy spectrum of an electron beam produced by a radio-frequency linac is not necessarily monoenergetic, and this can affect the forward-going x-ray generation efficiency. This quantity is

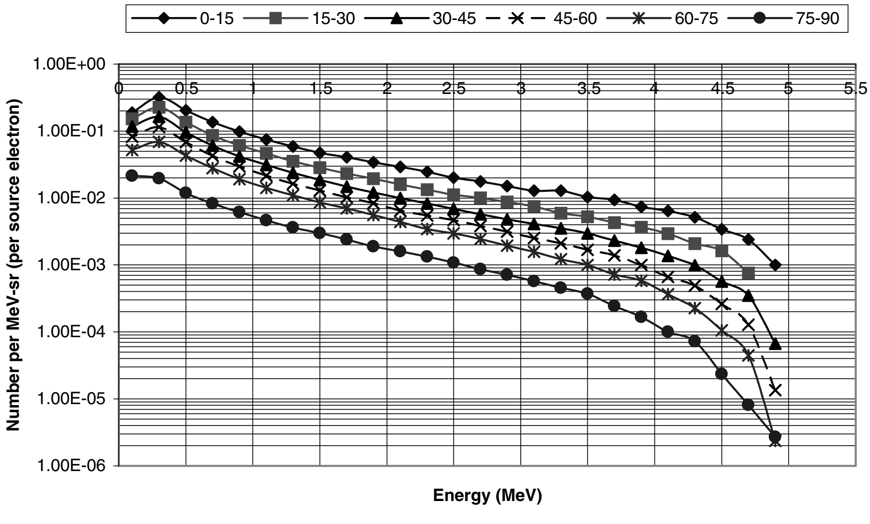

Figure 4-13. Energy spectra of the forward-going photon flux for several different angular bins.

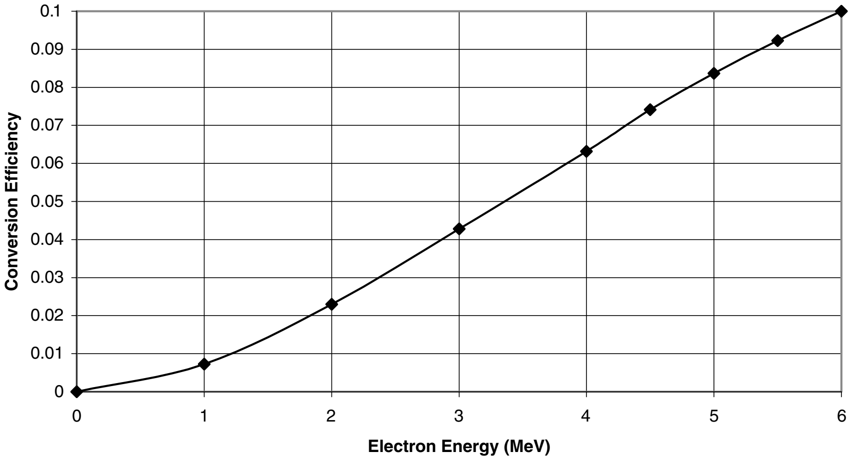

Figure 4-14. Variation of the x-ray conversion efficiency with electron kinetic energy for a fixed converter design optimized for 5-MeV electrons. The total converter thickness is approximately 1.05 times the CSDA range for 6 MeV electrons.

presented in Figure 4-14, assuming use of the 5-MeV compound converter described previously. The converter is too thick for low energy electrons, and the high-Z layer is not thick enough for optimum yield for electron energies in excess of 5 MeV. A useful estimate for the x-ray conversion efficiency for electrons with energies in the vicinity of 5 MeV is $\eta_g = (E/60)$, with E in MeV.

The low conversion efficiency implies that most of the electron beam energy is absorbed in the converter, which must therefore be water-cooled for high-power operation. The minimum flow rate can be estimated from

$$dm/dt = (1 - \eta_g - \eta_s)P/(c\Delta T) \tag{4.24}$$

c is the specific heat of water (1 cal/g-°C), η_g is the x-ray conversion efficiency, η_s is the backscattered energy fraction, ΔT is the allowed change in water temperature, and P is the electron beam power incident onto the converter. For example, for $\eta_g = 8\%$, $\eta_s = 16\%$, a 100 kW beam, and an allowable temperature rise of 10 °C, the required coolant flow rate is 1.8 liters/s, or about 27.5 gallons per minute.

(b) 7.5 MeV

The low x-ray generation efficiency at 5 MeV is a serious limitation to the economical irradiation of many products. The International Atomic Energy Agency[6] has recommended that the upper limit on electron energy for x-ray processing of food products be raised to 7.5 MeV, and the USFDA has recently approved this limit.* This higher kinetic energy improves the x-ray generation efficiency, and the radiation becomes somewhat more forward directed. Using a compound converter design of 0.12 cm of tantalum backed by 1.25 cm of aluminum, the forward-going x-ray conversion efficiency is 12.5% for 7.5 MeV electrons, an increase of about 50% over the 5-MeV result. Also, the average energy of the transmitted photon spectrum increases to 1.1 MeV.

---

* The topic of induced radioactivity resulting from x-ray irradiation is considered in Appendix C.

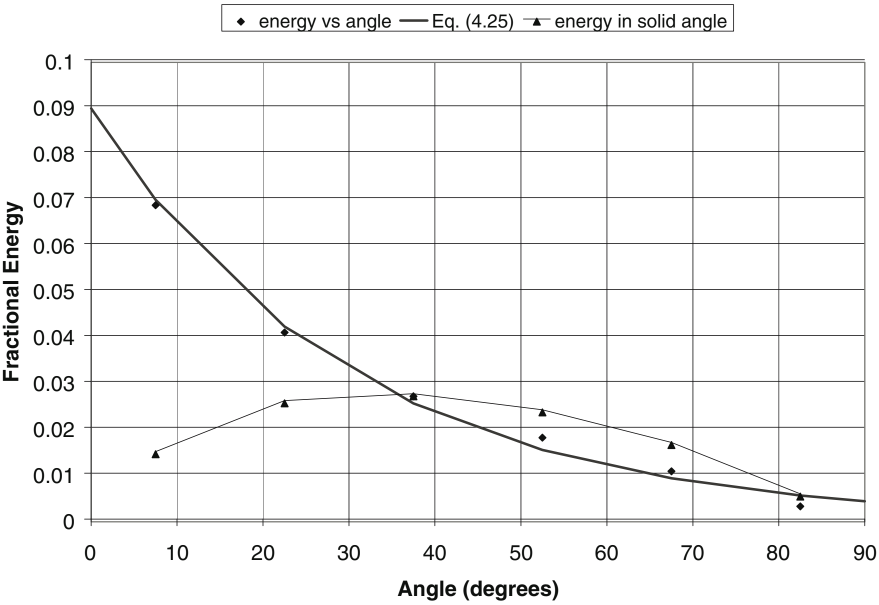

Figure 4-15. The x-ray energy per steradian and the total energy per source electron emitted into 15-degree solid angle segments ($2\pi \sin\theta\, d\theta$) versus the emission angle for 7.5-MeV electrons normally incident onto the compound x-ray converter. Also shown for comparison purposes is the functional dependence of Eq. (4.25)

The fractional amount of energy reflected by the converter decreases to 11.4%; 4% is still carried by photons, but the amount carried by backscattered electrons decreases to 7.4%.

Dividing the transmitted photons into 15° angular bins, the photon energy fraction data are presented in Figure 4-15 vs angle. In comparison with the 5-MeV results, the radiation is more forward directed at 7.5 MeV, although the difference is not large. Substantial x-ray energy is still emitted at angles in excess of 40 degrees. An approximate (normalized) functional dependence for the variation of x-ray energy with angle is provided by (with the angle in radians)

$$f(\theta) = 0.82e^{-6\theta/\pi} \qquad 0 < \theta < \pi/2 \tag{4.25}$$

This functional dependence is also plotted in Figure 4-15 for comparison purposes.

4.3. CHARACTERIZATION OF THE FREE-FIELD IRRADIATION ZONE[5]

The angular distribution of the emitted x-rays has a significant impact on the efficient treatment of food products. Before analyzing the x-ray energy deposition profiles, we consider the free-field irradiation zone (no absorbing materials) in some detail, taking into account the angular dependence of the x-rays emerging from the converter. A schematic diagram of this configuration is shown in Figure 4-16. The x-ray source is a straight line of height H in the y-direction at $x = z = 0$, generated by a scanned electron beam striking the converter in the y-z plane. The angle of incidence relative to the x-z plane is denoted by ϕ. If the average electron beam power is P watts, the x-ray source strength is S_l watts per unit length, with $S_l = \eta_g P/H$, and $\eta_g = 8\%$ for 5-MeV electrons, and 12% for 7.5 MeV.

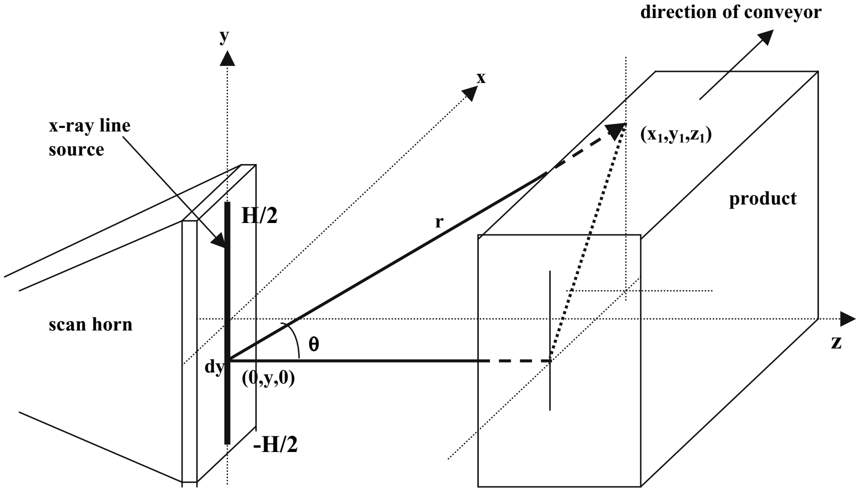

Figure 4-16. Schematic diagram for calculating the free-field x-ray intensity produced by a line bremsstrahlung source.

At a distance r from a source point the x-ray flux will geometrically decrease as ($1/r^2$). Thus, the incremental contribution dP_x to the x-ray power per unit area at point (x_1, y_1, z_1) due to the incremental source length dy at (0, y, 0) is $dP_x = [S_l\, f(\theta)/r^2]\, dy$, with r and θ given by

$$r^2 = \left[x_1^2 + (y_1 - y)^2 + z_1^2\right]; \quad \cos\theta = [(y_1 - y)\sin\phi + z_1\cos\phi]/r \tag{4.26}$$

For the case of normal incidence ($\phi = 0$), $\cos\theta = z_1/r$. The total power per unit area at point (x_1, y_1, z_1) is found by integrating along the line from −H/2 to H/2; i.e.,

$$P_x = S_l \int_{-H/2}^{H/2} [f(\theta)/r^2]dy \tag{4.27}$$

The results of evaluating the integral in Eq. (4.27) are most easily interpreted in terms of the transverse beam spread (in the x_1 dimension) for various heights (y_1) above the converter midplane, at various axial distances (z_1) from the converter. As an example, the transverse beam spread (the numerical value of the integral in Eq. (4.27)) at an axial depth $z_1 = 10$ cm is shown in Fig. 4-17 for several different values of y_1, assuming a uniform line source with H = 60 cm, and normally-incident 5-MeV electrons. The FWHM beam width at this distance from the converter is about 15 cm. This width increases nearly linearly with distance from the converter, as shown in Figure 4-18. Also shown for comparison in Figure 4-18 are the results of a 3-D ACCEPT[4] Monte Carlo code calculation, assuming a distance from the converter of 30 cm. The ACCEPT calculation mimicked the numerical integration parameters; i.e., 5-MeV electrons were normally incident onto the same compound converter. The contributions from beamlets positioned every centimeter along the 60-cm converter were then added in accumulation cells at 30 cm from the exit of the converter. (Both sets of data have been normalized to an electron beam power of 1 kW.) The agreement is excellent, indicating the validity of Eq. (4.23) for describing the angular distribution of the photons at an electron kinetic energy of 5 MeV.

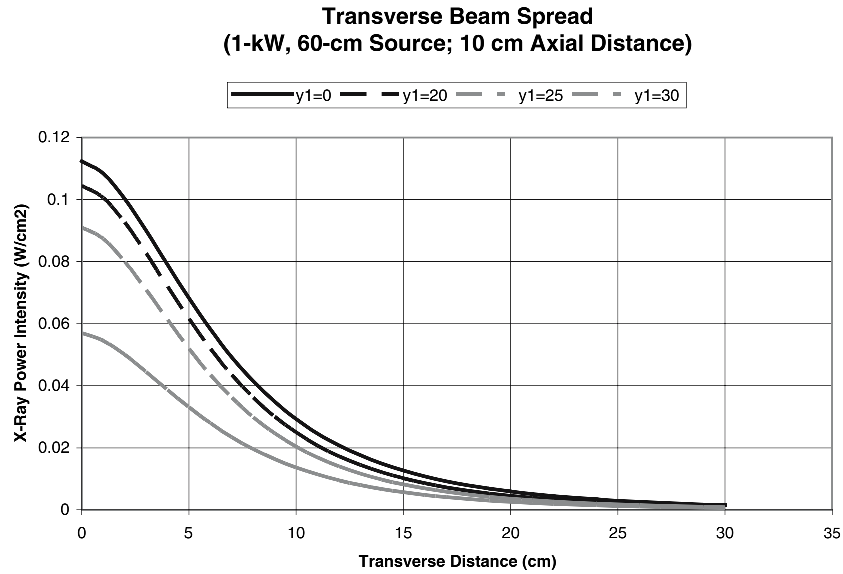

Figure 4-17. Variation in the x-ray beam intensity at 10 cm from the converter as a function of transverse distance from the plane of the converter for several different heights above the centerline of the converter. The x-ray line source was assumed to be 60 cm in height, the electron beam power was 1 kW, and the beam kinetic energy was 5 MeV.

The conveyor system is assumed to move product through the x-ray region in the transverse (x_1) direction. Assuming a uniform conveyor speed v, the x-ray energy density F_x delivered to a particular height y_1 above the midplane of the converter is obtained by integrating P_x according to

$$F_x = \int_{-\infty}^{\infty} P_x\,dt = \left[\int P_x\,dx_1\right]/v = (S_l/v)\int_{-\infty}^{\infty} dx_1 \int_{-H/2}^{H/2} \left[f(\theta)/r^2\right]dy = \left[\eta_g P/(vH)\right] I \qquad (4.28)$$

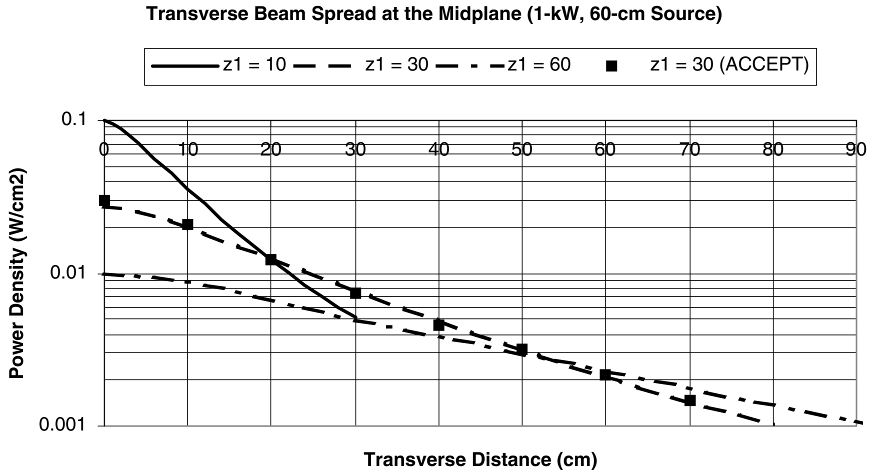

Figure 4-18. Variation in the x-ray beam intensity on the converter midplane with transverse distance from the plane of the converter, for several different distances from the converter. The x-ray line source was generated by a 1-kW, 5-MeV electron beam uniformly scanned over 60 cm.

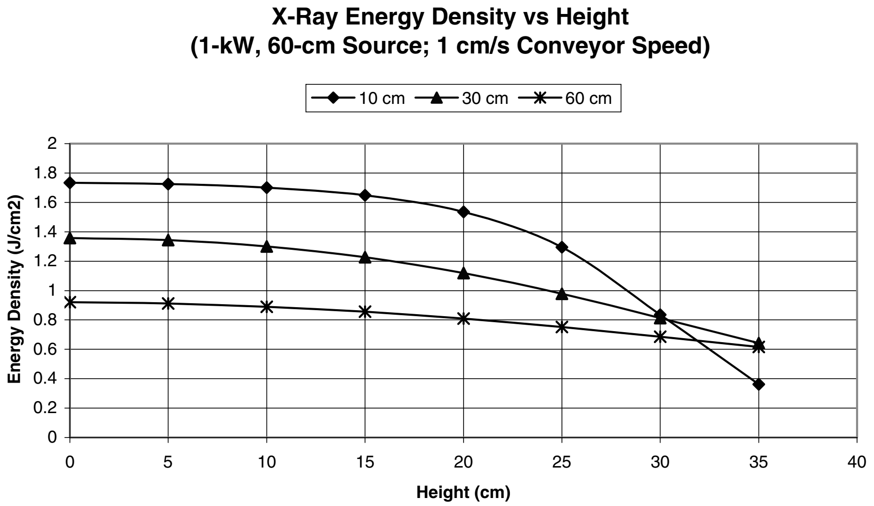

Figure 4-19. Variation of the x-ray energy density with height above the converter midplane at several distances from the converter. The x-ray source is a uniform line 60 cm in length produced by a uniform, normally-incident, 1-kW, 5-MeV electron beam. The assumed conveyor speed is 1 cm/s.

where I is the numerical value of the double integral. From Eq. (4.15), multiplying the free-field energy density by the average mass absorption coefficient μ of the product therefore gives the front surface dose at a particular distance from the converter z_1; i.e., $D = \mu F_x$.

The variation of the double integral of Eq. (4.28) with height above the midplane is shown in Figure 4-19 using the 5-MeV angular distribution for $z_1 = 10$, 30 and 60 cm from the converter. These results were obtained for a uniform scan over a total source height H of 60 cm, assuming normal incidence. As a numerical example, the effective average absorption coefficient μ for water is about 0.03 cm^2/g. Assuming 20 kW of electron beam power at the converter, and a conveyor speed of 0.5 cm/s (about 1 ft/min), the estimated front surface dose at the converter midplane for product placed 10 cm from the converter is about 2 kGy for this source configuration. We will return to these dose calculations in Section 4.4.

It is apparent from the data of Fig. 4-19 that the x-ray energy density decreases with distance from the converter. This decrease is explicitly shown in Fig. 4-20 on the midplane of the converter. Over the range of distances shown, the variation is well-modeled by a decreasing exponential function with an effective attenuation coefficient of 0.015 cm^{-1}; i.e.,

$$F_x \propto \exp[-0.015 z_1(\text{cm})] \tag{4.29}$$

The variation of the free-field energy density with height above the converter midplane (Fig. 4-19) merits additional discussion. At axial distances comparable to or greater than the height of the line source, the energy density decreases relatively slowly with height. However, close to the line source the energy density decreases sharply near the top and bottom of the source. At a height equal to the half-height of the source the energy density is approximately half of the value at the midplane. As discussed in Section 4.7, the minimum absorbed dose limits the throughput rate of product, and there are several strategies that can be used to increase the minimum delivered dose. One technique, illustrated in Figure 4-21, is to modify the sawtooth magnetic field waveform of the scan magnet in order to increase the dwell times at the top and bottom extremes.[7] To

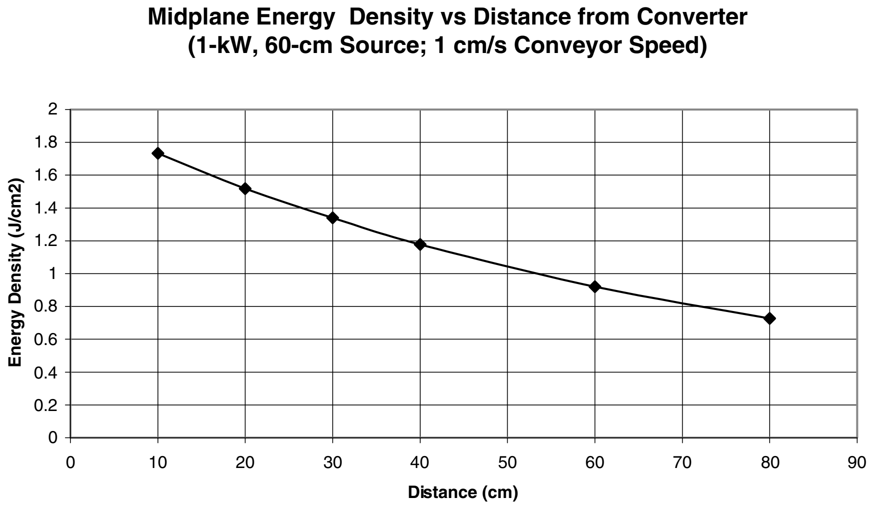

Figure 4-20. Variation of the x-ray energy density on the converter midplane with distance from the converter. The x-ray source is a uniform line 60 cm in length produced by a 1-kW, 5-MeV electron beam. The assumed conveyor speed is 1 cm/s.

illustrate the effect of this source intensity variation, we assume that the electron intensity at the converter, holding the total power constant, can be simply described by the weighting function (see Section 8.4.2)

$$w(y) = 0.9\{1 + \exp[0.3(y - H/2)]\},\ y > 0 \qquad (4.30)$$
$$0.9\{1 + \exp[-0.3(y + H/2)]\},\ y < 0$$

Evaluating the integrals over y (see Eq. (4.28)) and x_1 for an axial distance $z_1 = 10$ cm, and assuming $H = 60$ cm, yields the x-ray energy density profile as a function of height (y_1) shown in Figure 4-22, assuming a conveyor speed of 1 cm/s, a total electron beam power of 1 kW, and a kinetic energy of 5 MeV. Also shown for comparison are the weighting function and the corresponding energy density profile for the uniform source. The decrease in free-field intensity near the converter with the weighted source intensity reduces the effective attenuation coefficient of Eq. (4.29) slightly.

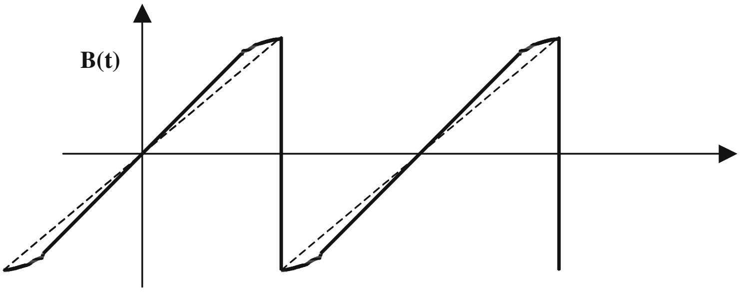

Figure 4-21. Schematic modification of the scan waveform to increase the effective beam intensity at the extremes of the scan.

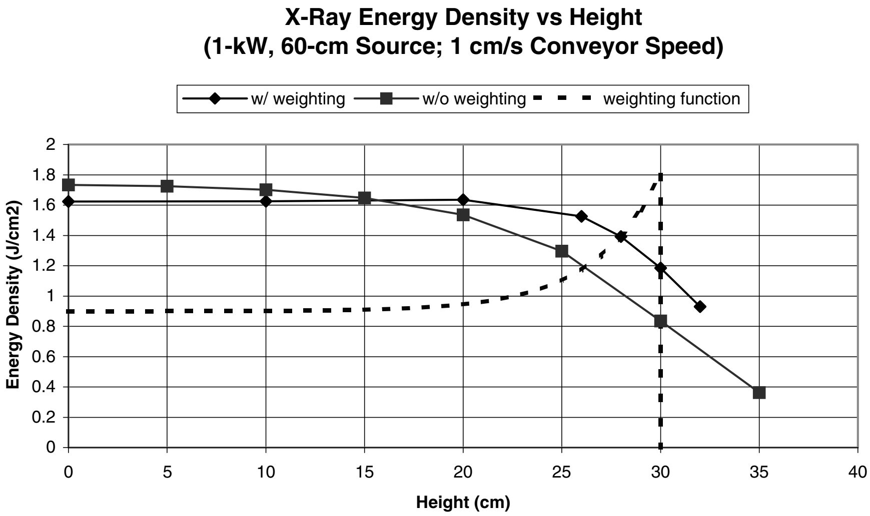

Figure 4-22. A comparison of the x-ray energy density vs height above the converter midplane for a uniform source and a source having the weighting function shown (and described by Eq. (4.30)). The axial distance was 10 cm from the converter.

4.4. X-RAY ENERGY DEPOSITION PROFILES[5]

Having described the x-ray irradiation zone produced by a line bremsstrahlung source in some detail, we now consider the absorption of the x-ray energy in products that are conveyed through the irradiation zone. We begin this discussion by first examining the one-dimensional case of an infinite line source/water absorber, before turning attention to the three-dimensional aspects of the process.

4.4.1. One-Dimensional X-Ray Energy Deposition

In the limit of large source and product heights, the depth-dependent energy deposition profile on the midplane near the converter is very nearly that of an infinite, one-dimensional absorber. Analytically, this case can be modeled by modifying Eq. (4.27) as

$$P_x = S_l \int [f(\theta)/r^2] e^{-\mu\rho r}\, dy \tag{4.31}$$

The presence of product is represented by the exponential absorption term, in which μ is the mass absorption coefficient and ρ is the density. (We initially assume there is no air gap between converter and product.) From Figure 4-10 we ignore any energy variation in the absorption coefficient, assuming a constant value of 0.03 cm^2/g for water. For a uniform, normally-incident, 5-MeV electron beam source of strength equal to 1 kW/cm, a conversion efficiency of 0.08, and a conveyor speed of 1 cm/s, evaluation of the integral in Eq. (4.31) at $y_l = 0$ for $z_l \ll H$ gives the depth-dependent dose at the midplane shown in Figure 4.23.

To corroborate these results, the one-dimensional TIGER Monte Carlo code was also used to compute the depth-dependent energy deposition profile. (The output of TIGER is given in units of MeV-cm^2/g. The conversion factor is 200 kGy/(MeV-cm^2/g), assuming a 5-MeV electron beam with an intensity of 1 kW/cm, and a conveyor speed of 1 cm/s.) The TIGER data are also shown

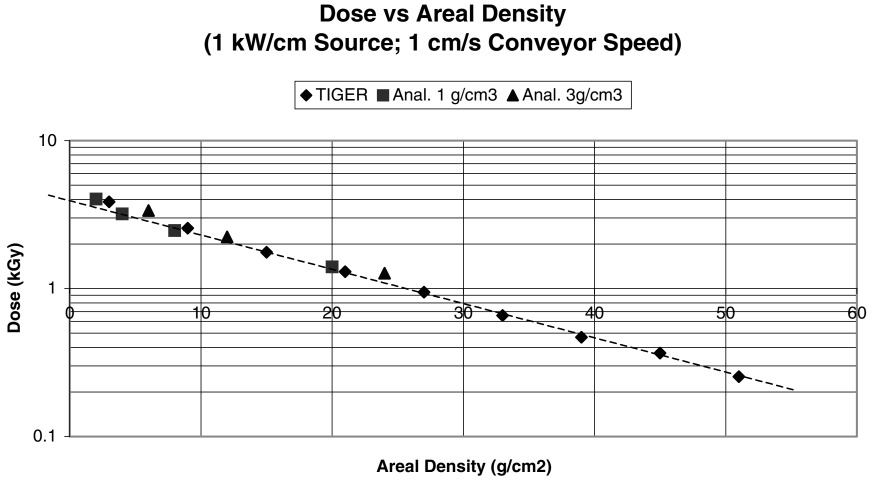

Figure 4-23. Variation of the x-ray energy deposition with depth for a 5-MeV bremsstrahlung spectrum and a water absorber. The effective absorption coefficient corresponding to the dashed line is approximately 0.05 cm^2/g.

in Figure 4-23 for comparison; the agreement is quite good. The decrease in deposited energy with areal density is nearly exponential with an effective mass absorption coefficient of about 0.05 g/cm^2.

Also of interest are the photon energy spectra at various depths into the absorber. As calculated by TIGER, these are shown in Figure 4-24 for several representative depths. The spectra harden slightly with depth, as expected from the absorption coefficient data of Figure 4-10, but the differences are not large.

Based on these results, spectrum hardening is relatively unimportant, and the reason for the slight surface dose enhancement and the larger effective mass absorption coefficient must be the significant angular spread of the x-rays emitted from the converter. This is clearly seen by examining the angular dependence of the energy deposition profiles of 1 MeV photons using the TIGER code. The results, presented in Figure 4-25, indicate significant geometrical surface dose enhancement for incident angles greater than 30 degrees. Since the energy content of the photons emitted from the converter at angles in excess of 30 degrees is more than 50% of the total energy, surface dose

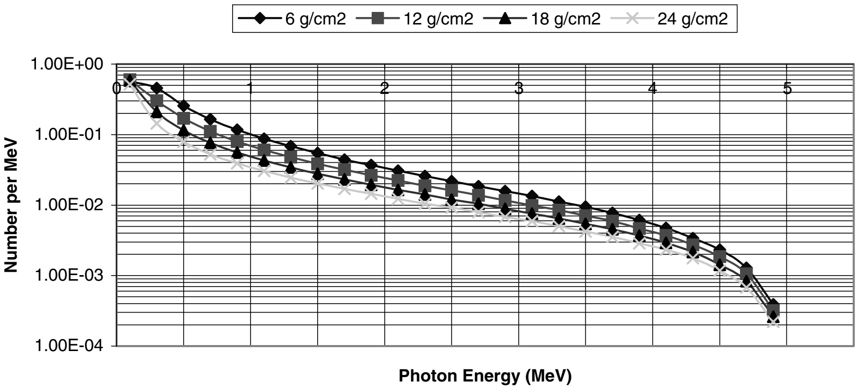

Figure 4-24. Variation of the photon energy spectrum with areal density into the water absorber, as computed by the TIGER code.

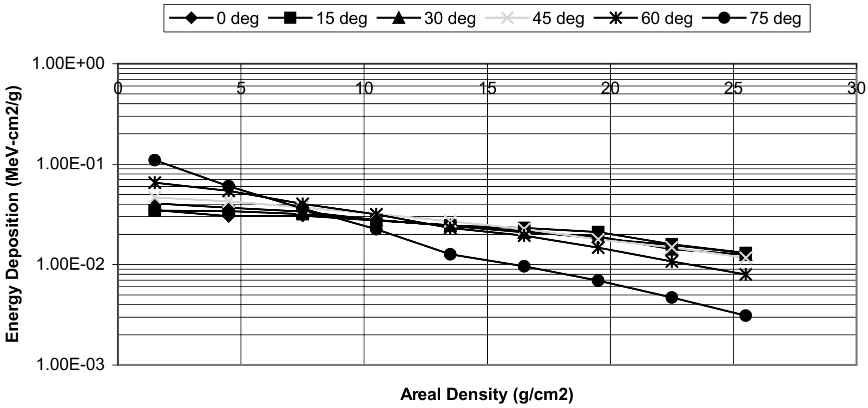

Figure 4-25. Energy deposition profiles for a 1-MeV photon beam for various angles of incidence onto a water absorber.

enhancement and a more rapid decrease in the energy deposition profile with depth into the absorber are to be expected.

4.4.2. Three-Dimensional X-Ray Energy Deposition Profiles

The close agreement between the analytical treatment using the simple exponential absorber model and the 1-D (but comprehensive) TIGER code calculation also suggests that beam broadening in the absorber is relatively unimportant, in contrast to the case for electron deposition. This behavior can be demonstrated by examining the spread of a monoenergetic (1-MeV), monodirectional photon beam using the ACCEPT code. The results of this calculation are shown in Figure 4-26 assuming a water absorber with unit density. Despite Compton scattering being the dominant interaction mechanism, the decrease in dose with distance from the axis of the pencil beam is quite pronounced, even at significant depths. For example, at a depth of about 20 cm (for which the on-axis dose was about 30% of its value near the surface), the dose at 4 cm from the axis was about a factor of 20 less than the on-axis value. An important consequence of this lack of in-product beam broadening is that in

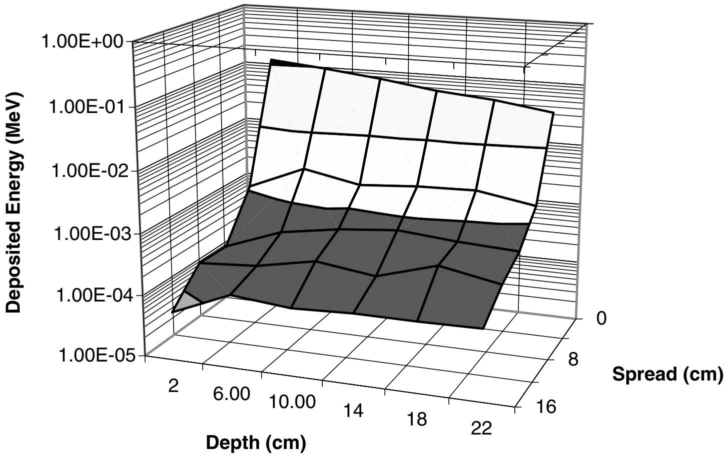

Figure 4-26. Only minimal spread is observed for a monodirectional, 1-MeV photon beam in a unit density water absorber.

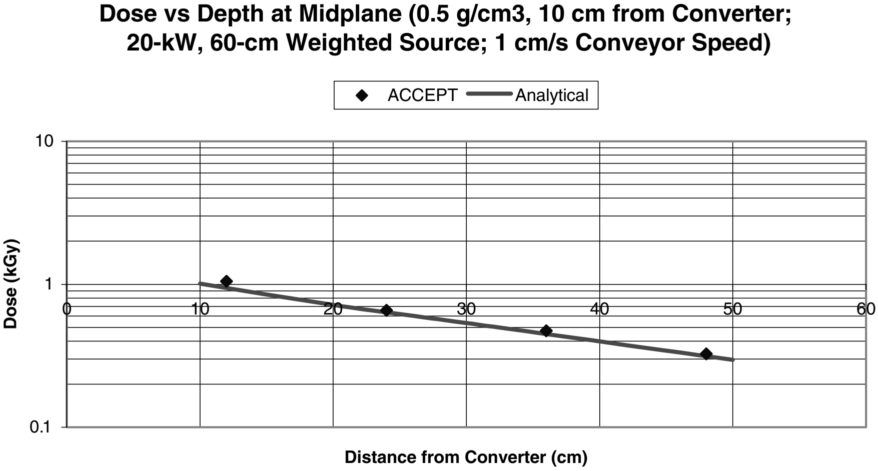

Figure 4-27. Comparison of the depth-dose profiles for a 0.5 g/cm^3 water absorber, as calculated using the 3-D ACCEPT Monte Carlo code and the analytical model of Eq. (4.32), assuming $\mu = 0.03$ cm^2/g. A normally-incident 5-MeV, 60-cm line source was assumed, with a 10-cm air gap.

almost all cases an adequate description of x-ray deposition can be obtained by taking into account the electron beam intensity at the converter, the distance between the converter and the product, and the product height, depth and density; i.e., the problem essentially reduces to two dimensions.

Assuming that the front surface of the product (absorber) is separated from the converter by a distance z_a, and allowing an electron beam intensity variation along the converter in order to improve the throughput efficiency, the x-ray power density integral becomes

$$P_x = S_l \int [f(\theta)/r^2] w(y) \exp(-\mu\rho r_1)\, dy \tag{4.32}$$

As before, w(y) denotes the beam intensity weighting function, and the absorber is modeled by the exponential term. However, to account for the air gap, r_1 represents the portion of the distance r from the source point to an observation point that lies inside the absorber. From simple geometrical considerations

$$r_1/r = (z_1 - z_a)/z_1 \tag{4.33}$$

To illustrate the procedure, we first consider the case of a 5-MeV, 60-cm line source, assuming normal incidence and the beam intensity weighting formula of Eq. (4.30). Evaluating the integral of Eq. (4.32) on the midplane of the converter ($y_1 = 0$), and performing the subsequent transverse integration associated with the conveyor motion leads to the depth-dose profile shown in Figure 4-27. The indicated values of dose assumed a beam power of 20 kW, a conveyor speed of 1 cm/s, and an air gap of 10 cm. The conversion efficiency was 8% for 5 MeV. The density of the absorber was 0.5 g/cm^3, and an average value of $\mu = 0.03$ cm^3/g (corresponding to water) was assumed. Also shown for comparison are the results of a full 3-D ACCEPT Monte Carlo code calculation for the same conditions. The agreement is quite good.

Depth-dose profiles for other absorber densities and air gaps have been computed holding all other parameters constant, and the results are presented in Figure 4-28. Ignoring the slight differences

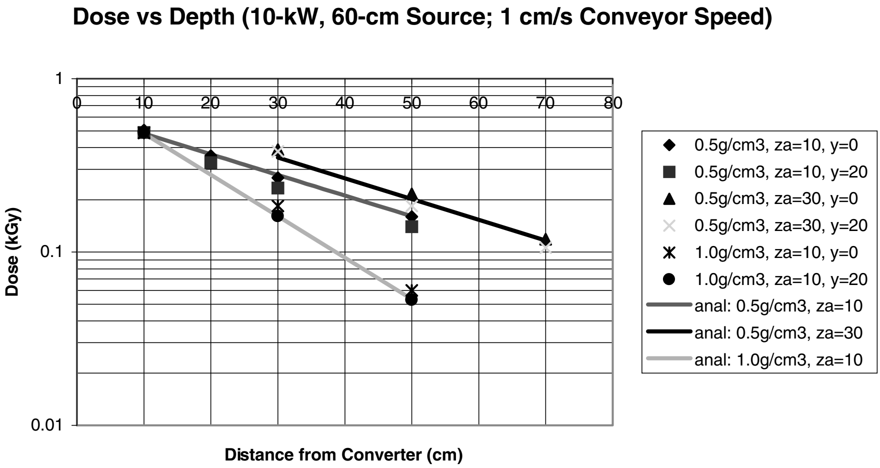

Figure 4-28. Depth-dose profiles for water absorbers of various densities and air gap separations from the converter, as calculated using the analytical model of Eq. (4.32), assuming $\mu = 0.03$ cm^2/g. Also shown for comparison is Eq. 4.34, evaluated for the same conditions.

between the values at the midplane and at a height 20 cm above the midplane, and the slight dose enhancement at the surface, the decrease in dose with depth is approximately exponential, with the slope varying nearly linearly with the absorber density. In addition there is also a decrease in dose with air gap. As suggested by the results of Figures 4-20 and 4-23, these depth-dose profiles can be modeled reasonably well using an empirical relationship of the form

$$D(\mathrm{kGy}) = 3.4\{P(\mathrm{kW})/[v(\mathrm{cm/s})H(\mathrm{cm})]\}e^{-0.012z(\mathrm{cm})}e^{-0.045\rho(\mathrm{g/cc})[z(\mathrm{cm})-z_a(\mathrm{cm})]} \tag{4.34}$$

which is also graphed in Figure 4-28 for the various conditions. The first exponential term is independent of the absorber material and models the decrease in free-field x-ray intensity with distance from the converter. The second term is nearly identical to the decrease in dose observed in the case of the infinite one-dimensional absorber geometry.

Eq. (4.34) can be rewritten as

$$D(\mathrm{kGy}) = D_{fs}e^{-\mu_e\rho(z-z_a)} \tag{4.35}$$

in which the front surface dose $D_{fs} = [3.4P/(vH)]e^{-0.012z_a}$. The effective mass absorption coefficient μ_e therefore varies with material density according to

$$\mu_e = 0.012/\rho + 0.045 \tag{4.36}$$

Note that μ_e is significantly larger than the average absorption coefficient of water and decreases with increasing density. Consequently, the decrease in dose with depth for low-density products is much more rapid than might be expected because of the geometrical decrease in the x-ray flux with distance from the converter.

4.5. MAX:MIN RATIOS AND X-RAY ENERGY UTILIZATION EFFICIENCY[5]

Eq. (4.35), augmented as necessary to account for beam divergence at the converter, has been compared in some detail with experimental data.[5,9] It tends to underestimate the surface dose, and it somewhat overestimates the dose at medium depths. Nonetheless, it does appear to give useful estimates for absorbers having densities in the range of 0.2–1 g/cm^3. While this empirical formula was derived for only one specific source scan height, weighting function and kinetic energy, similar exponential relationships can be anticipated for other source configurations, assuming that the specific conditions give reasonable dose uniformity at each depth. Consequently, in this section we use an exponential depth-dose relationship to develop max:min ratios and energy utilization estimates for several irradiation scenarios. In particular, we will examine a number of configurations involving single and multiple passes of product in front of one or multiple accelerator systems.

We first consider the case of a single pass of product in front of a single accelerator system for illustrative purposes (see also Section 2.2.2). The geometry is shown in Figure 4-29. We designate the thickness of the product as d, and distance into the product measured from the initial front face as s. We will assume an effective mass absorption coefficient μ(cm^2/g) that depends on the product density ρ(g/cm^3), as given by Eq. (4.36).

The resulting depth-dose profile is given by Eq. (4.35), with $s = z - z_a$, and is shown in Figure 4-30, with $x = \mu\rho s$. The minimum dose occurs at $s = d$, and is given by

$$D_{min}(s = d) = D_{fs}\exp(-\mu\rho d) \tag{4.37}$$

The max:min ratio is simply $D_{fs}/D_{min} = \exp(\mu\rho d)$. Assuming that we must deliver a minimum required dose, Eq. (4.37) therefore specifies the maximum product thickness for a given material density and front surface dose.

The total amount of x-ray power PX_{tot} absorbed in the product can be estimated by integrating Eq. (4.37) according to

$$\begin{aligned} PX_{tot}(W) &= D_{fs}\,\rho\,H\,v\int e^{-\mu\rho s}\,ds \\ &= (D_{fs}/\mu)\,H\,v(1 - e^{-\mu\rho d}) \\ &= P(kW)\{(3.4/\mu)e^{-0.012z_a}(1 - e^{-\mu\rho d})\} \end{aligned} \tag{4.38}$$

with the electron beam power P in kilowatts, and we have used Eqs. (4.35) for the front surface dose. Dividing both sides by the beam power therefore gives the x-ray absorption efficiency; i.e.,

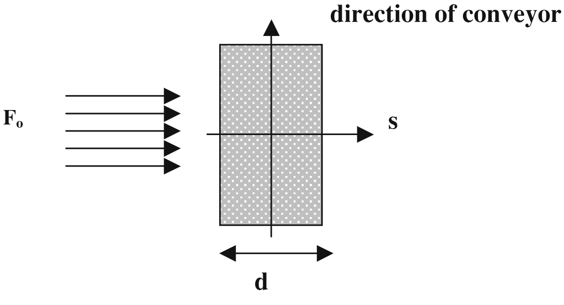

Figure 4-29. Schematic drawing of the single-gun, single-pass configuration.

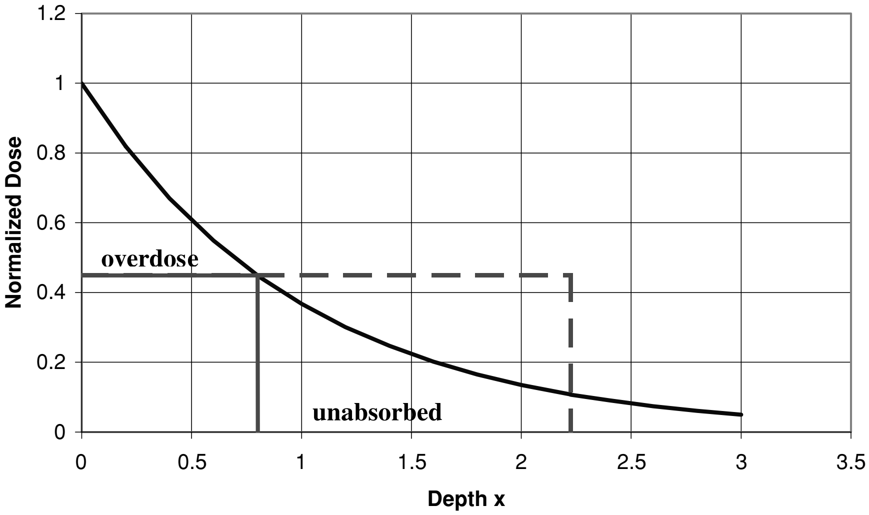

Figure 4-30. Depth-dose profile for single-sided x-ray irradiation. The minimum dose occurs at the product depth d. If the x-ray energy were uniformly deposited, the minimum dose could be delivered to a much larger depth, d_{max}.

the amount of x-ray power absorbed in the product per unit of electron beam power delivered to the converter. As a numerical example, for an effective mass absorption coefficient of 0.08 cm^2/g, corresponding to an average density of 0.34 g/cm^3, and $z_a = 10$ cm, the quantity in curly brackets has a maximum value of 36.8. The maximum absorption efficiency can therefore be no greater than about 3.7% in this case; less than half the x-ray power generated by the electron beam is absorbed in the product.

Unfortunately, not all of the x-ray power absorbed in the product is effectively utilized, as seen by examining Figure 4-30. In addition to perhaps being harmful to the product, delivered dose in excess of the minimum dose is wasteful. To illustrate this point further, suppose that all of the available x-ray energy were uniformly deposited at the level of the minimum dose to a maximum depth d_{max}, defined by

$$D_{min} d_{max} = D_{fs} \int e^{-\mu\rho s} \, ds = D_{fs}/(\mu\rho) \tag{4.39}$$

Then the efficiency with which the available x-ray energy is utilized is just

$$\eta_u = d/d_{max} = \mu\rho d \, e^{-\mu\rho d} \tag{4.40}$$

The power effectively absorbed in this example is therefore given as (using Eq. 4.35)

$$\begin{aligned} PX_{eff}(W) &= (D_{fs}\rho) H \, v \, d \, e^{-\mu\rho d} \qquad (4.41) \\ &= P(kW)[3.4/\mu] e^{-0.012 z_a} (\mu\rho \, d e^{-\mu\rho d}) \\ &= \eta_u P(kW)[3.4/\mu] e^{-0.012 z_a} \end{aligned}$$

The one-dimensional utilization efficiency η_u for this single-sided irradiation scenario has a maximum value of only $\exp(-1) = 0.37$, which occurs at $\mu\rho d = 1$. In other words, only 37%

of the 3.7% is effectively utilized in delivering the minimum dose. In addition, the max:min ratio corresponding to this condition is exp(1) = 2.72, which is quite large. For this simple case, getting sufficient product thickness to absorb a large fraction of the x-ray energy is more important than having a uniform dose, in the sense of optimizing x-ray energy usage.

Because of these poor performance parameters, single-sided x-ray irradiation is almost never used. However, based on this example, the prescription for finding the maximum utilization efficiency for other configurations is seen to consist of the following steps: (1) evaluate D_{min}; (2) substitute this result into the expression (d/d_{max}); (3) differentiate (d/d_{max}) with respect to d; (4) set the derivative to zero to find the optimum value of d; and (5) evaluate the utilization efficiency at this optimum product thickness. We will perform this procedure for a few other simple irradiation configurations.

4.5.1. Single-pass, Two-gun Configuration

In this configuration product is irradiated by two identical, diametrically opposed accelerator systems, as schematically indicated in Figure 4-31. The dose distribution as a function of s is now given by

$$D(s) = D_{fs}\left[e^{-\mu\rho s} + e^{-\mu\rho(d-s)}\right] \tag{4.42}$$

with D_{fs} denoting the front surface dose delivered by a single accelerator system. By symmetry, the minimum dose occurs at $s = d/2$, and is given as

$$D_{min}(s = d/2) = 2D_{fs}\exp(-\mu\rho d/2) \tag{4.43}$$

and the max:min ratio is given as

$$D_{max}/D_{min} = 0.5[1 + e^{-\mu\rho d}]e^{\mu\rho d/2} \tag{4.44}$$

With Eq. (4.43), the utilization efficiency is given as

$$\eta_u = d/d_{max} = \mu\rho d\, e^{-\mu\rho d/2} \tag{4.45}$$

where we have recognized that $d_{max} = 2\,D_{fs}/(\mu\rho D_{min})$ because there are two equal accelerators.

Eqs. (4.44) and (4.45) are graphed in Figure 4-32 as a function of the dimensionless depth variable $x = \mu\rho d$. Note that the max:min ratio monotonically increases with x, while the utilization

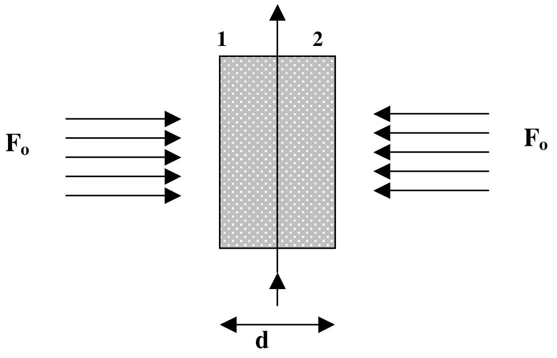

Figure 4-31. Schematic diagram of the two-gun, single-pass configuration.

Figure 4-32. 1-D x-ray energy utilization efficiency and max:min ratio for the two-gun, single-pass configuration of Figure 4-31.

efficiency has a broad maximum of about 0.735 around $x = x_{opt} = 2.0$. The max:min ratio is 1.54 at x_{opt}. These represent considerable improvements over the single-sided irradiation configuration considered previously. Even for $x = 2.5$, the max:min ratio is still less than two. For products having densities of about 0.5 g/cm^3, the effective mass absorption coefficient is approximately 0.07 cm^2/g, giving an optimum areal density of 29 g/cm^2. This areal density is more than three times as large as the maximum areal density that can be treated by double-sided 10-MeV electron irradiation, and affords considerable processing flexibility.

There are additional configurations that are essentially identical to the configuration of Figures 4-31, in terms of x-ray utilization efficiency. One such configuration, shown in Figure 4-33, uses two accelerator systems, but the accelerators are situated on the same side of the product line, and the conveyor rotates the product by 180 degrees between the two converters. Another common configuration uses two passes and a single gun, with a rotation step between the passes.

4.5.2. Double-pass, Two-gun Configuration

In the preceding paragraphs we have seen that treating product from two-sides instead of one dramatically improves the maximum utilization efficiency (about a factor of two), and markedly reduces the max:min ratio for the optimum utilization condition (by almost 50%). It is therefore reasonable to expect some further improvement in these quantities using the configuration shown in Figure 4-34. There are now two accelerator systems, and the product makes two passes in front of each, using a single bend and a single rotation in the conveyor system as shown.

For this configuration, the dose distribution as a function of s is given by

$$D(s) = D_{fs}\left[e^{-\mu\rho s} + e^{-\mu\rho(d+s)} + e^{\mu\rho(s-d)} + e^{-\mu\rho(2d-s)}\right] \tag{4.46}$$

By symmetry, the minimum again occurs at $s = d/2$, and is given as

$$D_{min}(s = d/2) = 2D_{fs}[\exp(-\mu\rho d/2) + \exp(-3\mu\rho d/2)] \tag{4.47}$$

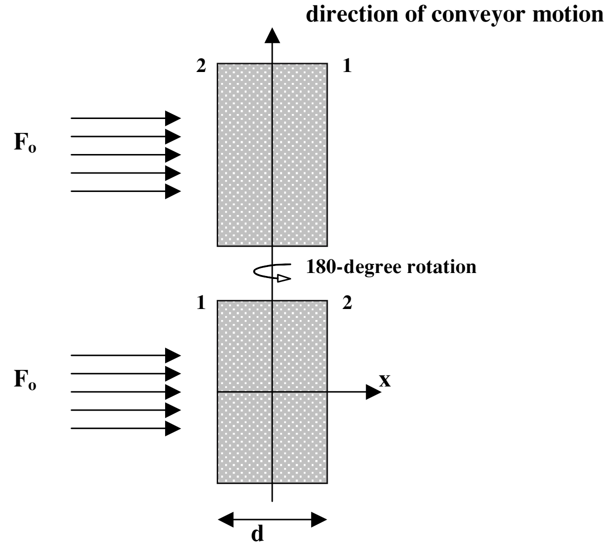

Figure 4-33. Two-gun, single-pass configuration using a 180-degree rotation between guns.

while the maximum dose occurs on either surface of the product. In terms of the dimensionless variable x, the max:min ratio is given as

$$D_{max}/D_{min} = 0.5[1 + 2e^{-x} + e^{-2x}]/\left(e^{-x/2} + e^{-3x/2}\right) \tag{4.48}$$

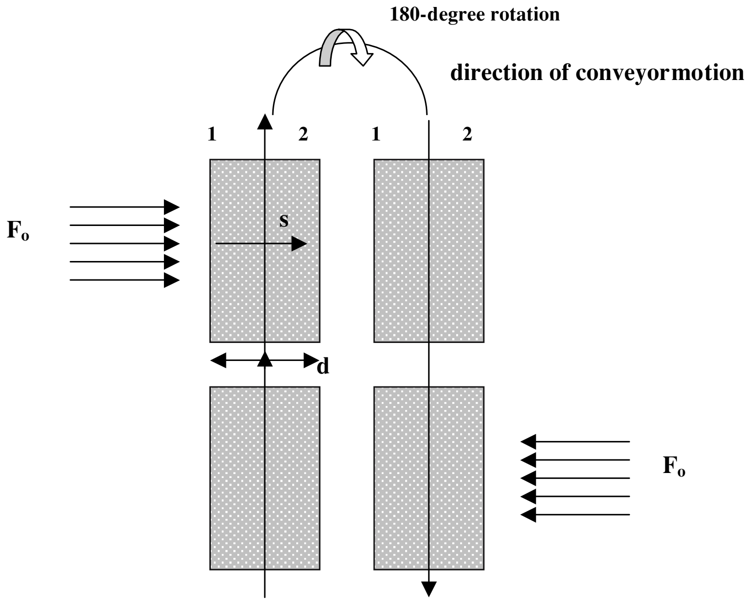

Figure 4-34. Schematic diagram of the double-pass, two-gun configuration.

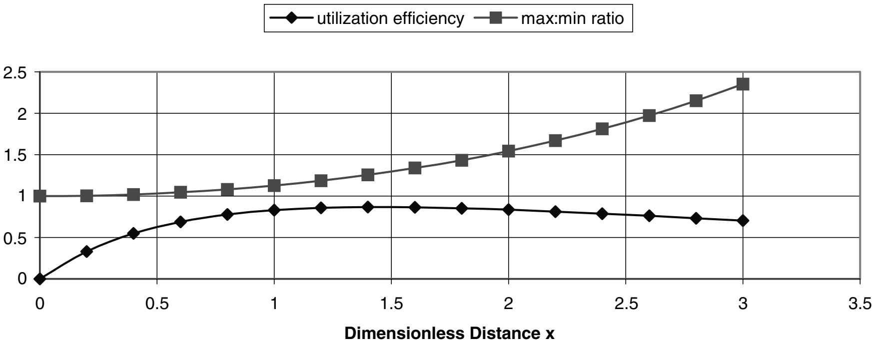

Figure 4-35. 1-D x-ray utilization efficiency and max:min ratio for the two-gun, two-pass configuration of Figure 4-34.

and the utilization efficiency is

$$\eta_u = d/d_{max} = x\left(e^{-x/2} + e^{-3x/2}\right) \tag{4.49}$$

Eqs. (4.48) and (4.49) are graphed in Figure 4-35 as a function of the dimensionless depth variable x. Note that the utilization efficiency has a broad maximum of about 0.87 around $x_{opt} = 1.4$. The max:min ratio for this optimum condition is about 1.25, which is quite good. The dose distribution in the product (as a function of s) for this optimum condition is shown in Figure 4-36.

We also note that there are several other configurations that are equivalent to that of Figure 4-34, in terms of the one-dimensional dose distribution. These include a four-gun, single-pass configuration and an equivalent four-pass, single-gun configuration. Even more complicated configurations involving three separate product conveyor lines have also been proposed.

4.6. THROUGHPUT EFFICIENCY ESTIMATES FOR X-RAY PROCESSING[5]

Using the analyses presented thus far it is possible to estimate various efficiencies for particular x-ray processing scenarios. To illustrate the methodology we return to the common case of a symmetric two-sided irradiation, as discussed in Section 4.5.1. From Section 4.4.2, the optimum depth for

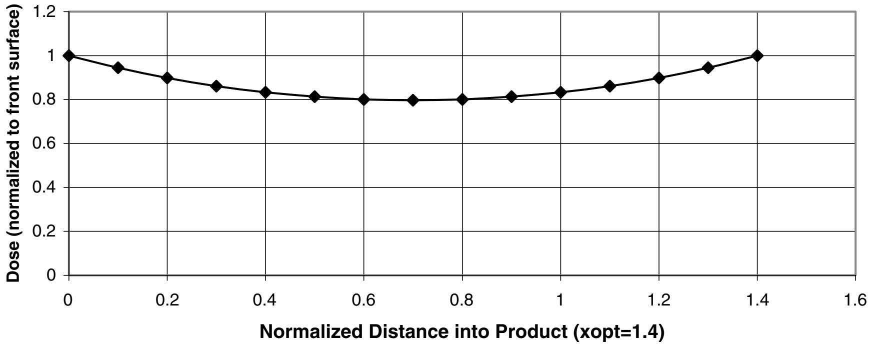

Figure 4-36. The depth-dose profile in the product for the two-gun, two-pass configuration at the product thickness corresponding to optimum utilization efficiency ($x_{opt} = 1.4$).

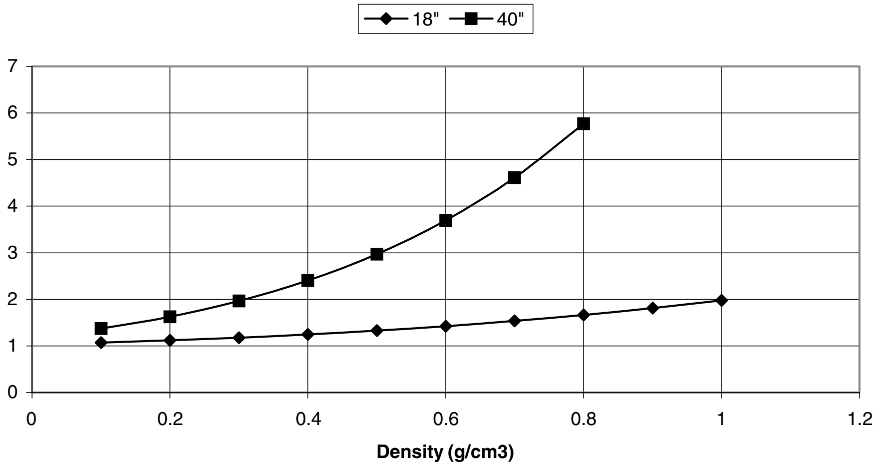

Figure 4-37. Variation of the max:min ratio with density for fixed carrier widths of 18 and 40 inches.

maximum utilization efficiency, assuming normal incidence at the converter, is obtained from Eq. (4.36) as

$$d_{opt} = 2.0(0.012 + 0.045\rho)^{-1} \tag{4.50}$$

As an example, for an average density of 0.5 g/cm^3, the maximum utilization efficiency is achieved when the product thickness is about 60 cm. However, the more usual case is that in which the product has a maximum fixed depth; for example, it is either placed on a carrier of a certain width, or the product is loosely contained in a pallet. For these cases the max:min ratio and the utilization efficiency are functions of the product density through Eqs. (4.36), (4.44) and (4.45). Representative results for carrier widths of 45.7 cm (18 inches) and 102 cm (40 inches) are shown in Figures 4-37 and 4-38. For the 18-in case, products with densities up to unity can be processed with good utilization efficiency, although the max:min ratio climbs to approximately two at 1 g/cm^3. On

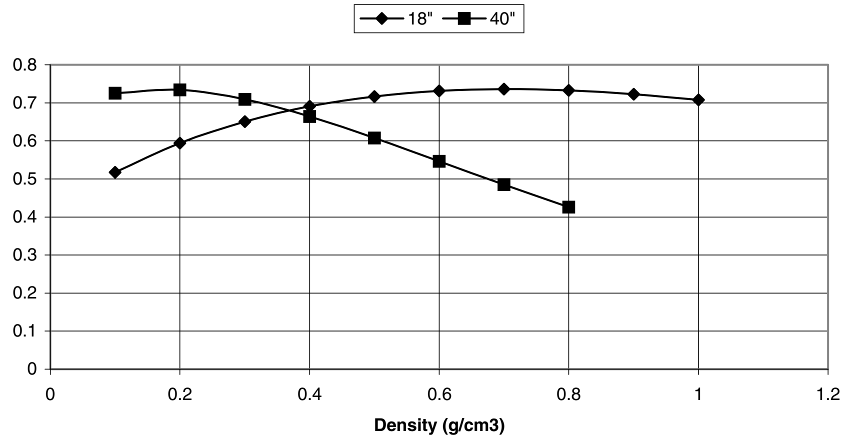

Figure 4-38. Variation of the utilization efficiency with density for fixed carrier widths of 18 and 40 inches.

the other hand, for the 40-in case, the max:min ratio climbs rapidly above two as the product density exceeds 0.3 g/cm^3.

In addition to the x-ray absorption efficiency and the utilization efficiency, the amount of product processed per unit time (dm/dt) can be expressed in terms of the throughput efficiency η_t, defined through Eq. (4.51) as

$$dm/dt = \eta_t P/D_{min} \tag{4.51}$$

With the beam power in kilowatts and the minimum dose in kilogray, the throughput is in units of kg/s. Assuming a steady stream of uniform product, then

$$dm/dt = 10^{-3}(\rho dvH) \tag{4.52}$$

with the density in units of g/cm^3. Solving Eqs. (4.51) and (4.52) for the throughput efficiency, and recalling Eqs. (4.34) and (4.40) yields

$$\eta_t = 3.4 \times 10^{-3}(\eta_u/\mu_e)e^{-0.012z_a} \tag{4.53}$$

Eq. (4.53) is graphed in Figure 4-39 using an air gap of $z_a = 10$ cm. The throughput efficiency attains its maximum value at the optimum density given by $\rho_{opt} = (0.0225d)^{-1}$. For high-density products arrayed uniformly on an 18-in carrier, the throughput efficiency has a maximum value of about 3.75%. However, increasing the carrier width to 40 inches decreases the maximum throughput efficiency to approximately 2.7%. The geometric decrease in dose with distance from the converter is the primary reason for this behavior.

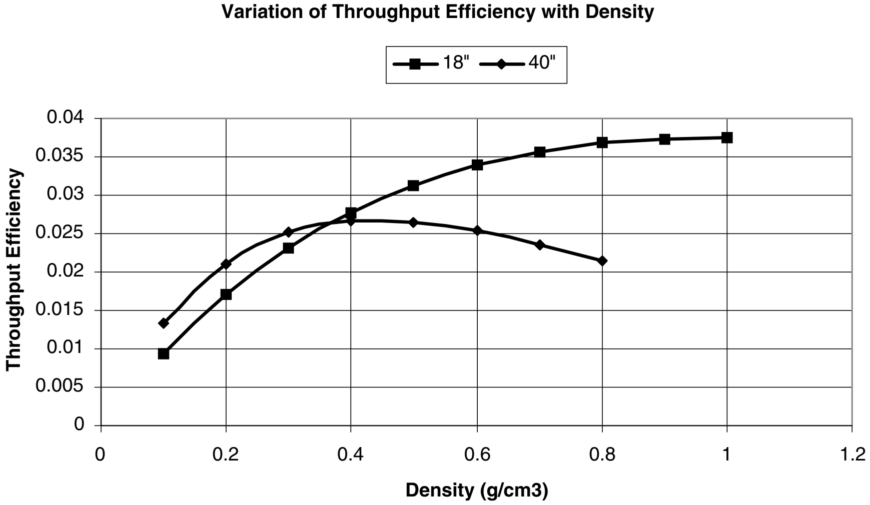

Figure 4-39. Mass throughput efficiency as a function of density for two different carrier widths.

4.7. THROUGHPUT EFFICIENCY IMPROVEMENTS AT 5 MeV

For product having a total depth of 60 cm and an average density of $0.5 g/cm^3$, Eq. (4.53) predicts a throughput efficiency of about 3.2%, assuming that $z_a = 10$ cm. However, a detailed examination of the dose with height above the converter centerline in the middle of this product shows that the dose at the top (and bottom) will be low by almost 17% relative to the predicted dose given by Eq. (4.34), even with the assumed weighting of Eq. (4.30). Since the conveyor speed must be adjusted to give the minimum required dose to all regions of the product, the throughput efficiency for this assumed irradiation configuration must be reduced by about 17%, to 2.65%.

In this section we examine the effectiveness of several techniques for improving the throughput efficiency, assuming an electron kinetic energy of 5 MeV. Specifically, we wish to increase the product throughput rate for a specified minimum required dose using a machine of constant power. The primary goal is to increase the minimum dose in the middle of the product. In particular, we will examine the effectiveness of (1) increasing the height of both source and product, (2) overscanning, with the source height exceeding that of the product, (3) varying the intensity profile of the electron beam at the converter (weighting), and (4) varying the electron angle of incidence at the converter. The effectiveness of these techniques for an electron kinetic energy of 7.5 MeV is examined in the following section.

4.7.1. Overscanning

As just discussed, the minimum dose delivered to any position in the product will limit the mass throughput rate. To develop a baseline for comparison, we assume a product density of $\rho = 0.4 g/cm^2$ and $d = 66$ cm (corresponding to nearly the optimum throughput condition of the previous section). We further assume that the product is increased in height to 100 cm ($y_{1max} = 50$ cm), and that the source height H is also 100 cm. For the case of normally incident electrons, a uniform scan (no weighting), and a distance from the converter to the front face of the product of $z_a = 10$ cm, the dose variations (actually, the value I of the double integral of Eq. (4.32) – see also Eq. (4.28)) are shown in Figure 4-40 as a function of height (y_1) at the front face of the product ($z_1 = 10$ cm) and in the middle of the product ($z_1 = 43$ cm). As expected, the minimum value of the double integral occurs in the middle of the product ($s = d/2$). Denoting $I_{min} = \min\{I(d/2)\}$, the value $I_{min} = 0.38$ would correspond to a minimum dose of 0.91 kGy, assuming $P/H = 1$ kW/cm ($P = 100$ kW), and $v = 1$ cm/s.

Assuming a symmetric, two-sided irradiation, the dose will be a minimum in the middle of the product at top and bottom, and the maximum throughput efficiency will be limited by this minimum dose. To illustrate this point, the mass throughput in this instance will be given by

$$dm/dt = \rho d(2y_{1max})(v/2) = \eta_t (P/D_{min}) \tag{4.54}$$

where y_{1max} denotes the maximum height of product above the converter centerline. From Eq. (4.28), the minimum dose for the double-sided irradiation configuration will be given by

$$D_{min} = [2\mu\eta_g(P/H)/v]I_{min} \tag{4.55}$$

Solving Eqs. (4.54) and (4.55) for η_t yields

$$\begin{aligned}\eta_t &= 2\rho\, d\, y_{1max}(\mu\eta_g)[I_{min}/H] \\ &= 0.127 y_{1max}[I_{min}/H]\end{aligned} \tag{4.56}$$

assuming $\rho = 0.4 g/cm^3$, $d = 66$ cm, $\mu = 0.03 cm^2/g$, and $\eta_g = 0.08$ for 5 MeV.

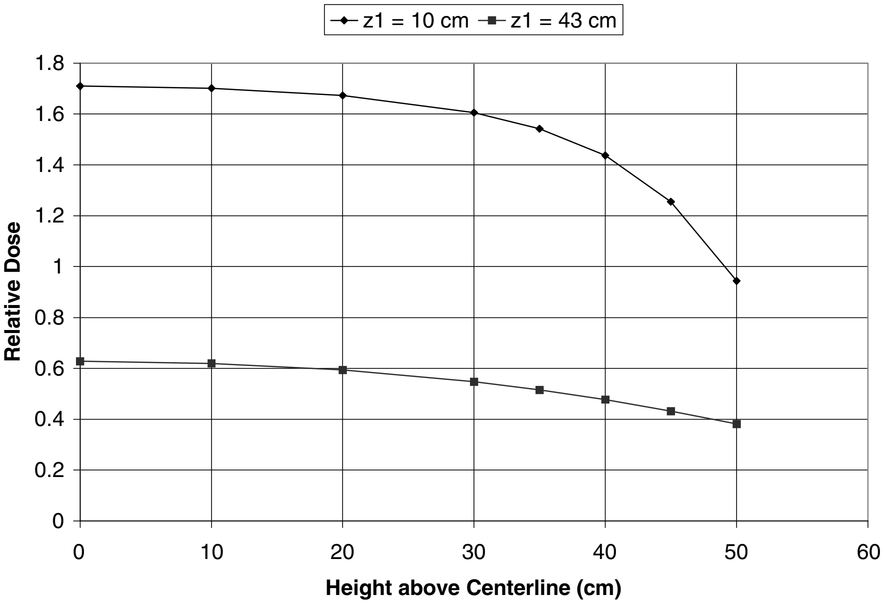

Figure 4-40. Dose profiles at the front face and middle of the product for a normally incident 5-MeV electron beam. The x-ray and product heights were both equal to 100 cm.

From Figure 4-40, $I_{min} = 0.38$ for $y_{1max} = H/2 = 50$ cm, and η_t is evaluated to be 2.4%, which is quite low. In fact, by decreasing y_{1max} to 40 cm, I_{min} improves to 0.48, which yields slightly higher throughput efficiency from Eq. (4.56). This suggests that a significant improvement might be gained by simply overscanning, i.e., making the source height H greater than the product height $2y_{1max}$. As a measure of the effectiveness of this approach, the quantity

$$I_m^* = (100\,\mathrm{cm}/H)\,I_{min} \tag{4.57}$$

(holding the beam power constant as the source height is varied) is graphed in Figure 4-41 as a function of H. The improvement is dramatic; increasing the source height to 140 cm (20 cm of overscan at both top and bottom) has increased I_m^* to 0.475, an increase of about 25%. The throughput efficiency, now given by

$$\eta_t = 1.27 \times 10^{-3}\, y_{1max}\, I_m^* \tag{4.58}$$

has increased to approximately 3%.

The dose variations for this overscan condition are shown in Figure 4-42 as a function of height at the front face and in the middle of the product. Note the decrease in front surface dose on axis in comparison with Figure 4-40 (nearly equal to the factor of $100/H = 0.71$), and the improvement in dose uniformity as a function of height at both depths. Also, the minimum dose now occurs just below the top surface. X-rays emitted from the converter at a height above the product, but emitted downward toward the product, are not attenuated before reaching the top surface. Consequently, the material handling system must not have significant absorbing material above and below the product to take full advantage of this overscan approach.

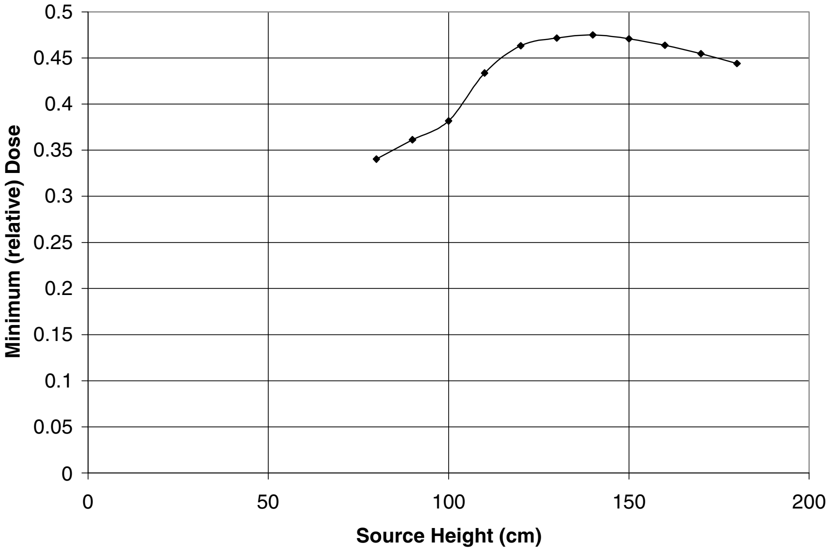

Figure 4-41. Variation of the minimum dose (I_m^*) in the middle of the product, as a function of x-ray source height, while holding the total electron beam power constant. The product height was fixed at 100 cm.

4.7.2. Increased Height of Both Product and Source

Even with the overscanning condition, consideration of Figure 4-42 indicates that the minimum dose still occurs near the top and bottom of the product. By increasing the height of both product and source, these low-dose regions will become a smaller fraction of the total product height, resulting in increased throughput efficiency. This is in fact seen by increasing the product height to 140 cm,

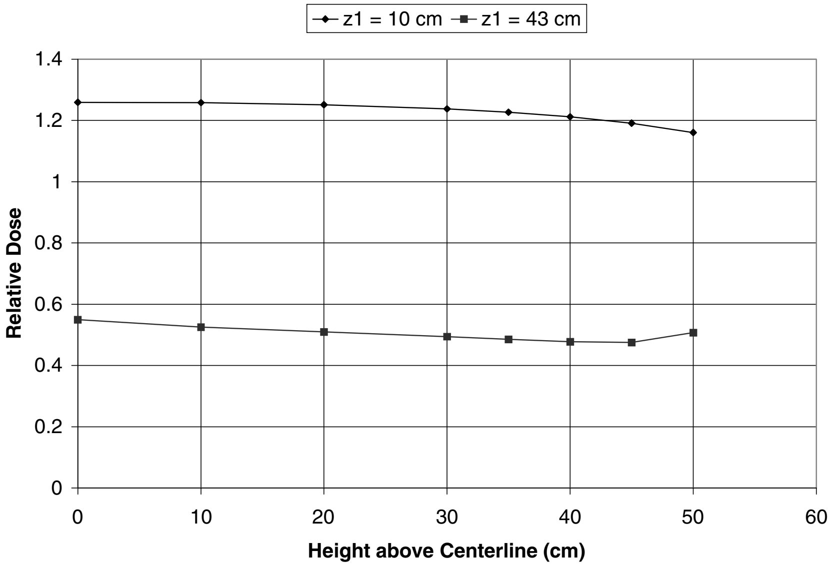

Figure 4-42. Dose profiles (I) at the front face and middle of the product for a normally incident 5-MeV electron beam. The product height equals 100 cm, but the source height has increased to 140 cm.

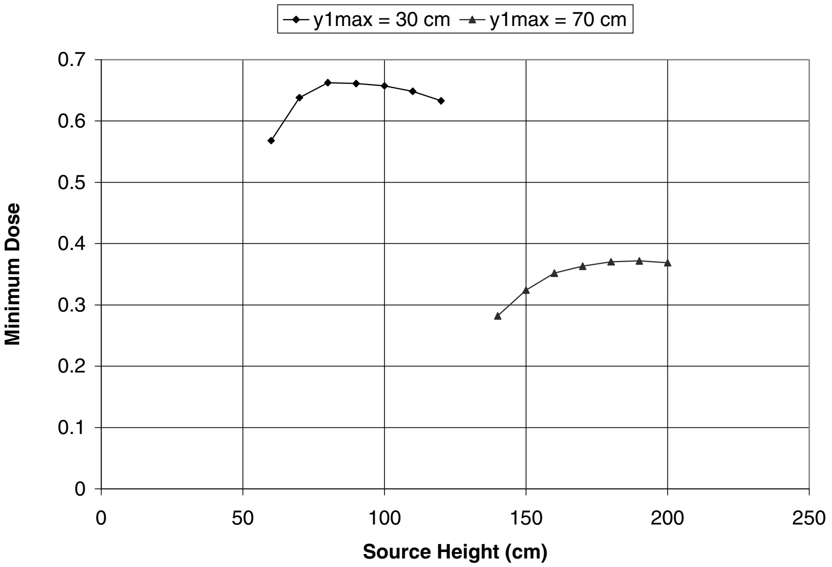

Figure 4-43. Variation of the minimum relative dose (I_m^*) in the middle of the product, as a function of x-ray source height, while holding the total electron beam power constant. The two product heights are 60 and 140 cm.

and using the overscan approach. The minimum relative dose data for this case are presented in Figure 4-43. With the increased source height, I_m^* decreases to 0.37 (for $H = 180$ cm), but this is more than offset by the increase in $y_{1\max}$ to 70 cm; the throughput efficiency improves to 3.3%. Also shown for comparison are the minimum relative dose data for a reduction in product height to 60 cm, which was considered previously. The throughput penalty is quite apparent with a decrease in throughput efficiency to 2.5% for the optimum overscan condition.

4.7.3. Converging/Diverging Beams

The calculations presented thus far have assumed that the electrons are normally incident on the x-ray converter. To produce this condition it is usually necessary to use either a “bow-tie” magnet or a “Panofsky lens” in conjunction with the scan magnet, as discussed in Chapter 8. For some installations, the expense of this additional magnet system is judged to be unnecessary, and it is of interest to know the effect of diverging electron rays at the converter; alternatively, it is also of interest to examine the combined effects of overscanning with converging rays at the converter. For the case of a 100-cm product height, the minimum dose in the middle of the product is shown in Figure 4-44 for diverging and converging beams. (The normally-incident case is also shown for comparison.) The angle of electron incidence at the converter was chosen to be either linearly increasing or decreasing with height above the converter midplane according to

$$\phi = ay/y_{1\max} \tag{4.59}$$

The data presented in Figure 4-44 are for $a = 0.2$ rad (diverging with an angle of about 11.5 degrees at $y = y_{1\max} = 50$ cm), $a = -0.2$ rad (converging), and $a = 0$ (normal incidence). Note the improvement obtained with significant overscanning (30 cm top and bottom); the maximum throughput efficiency for this case is 3.2%. The maximum convergence angle in this case was about

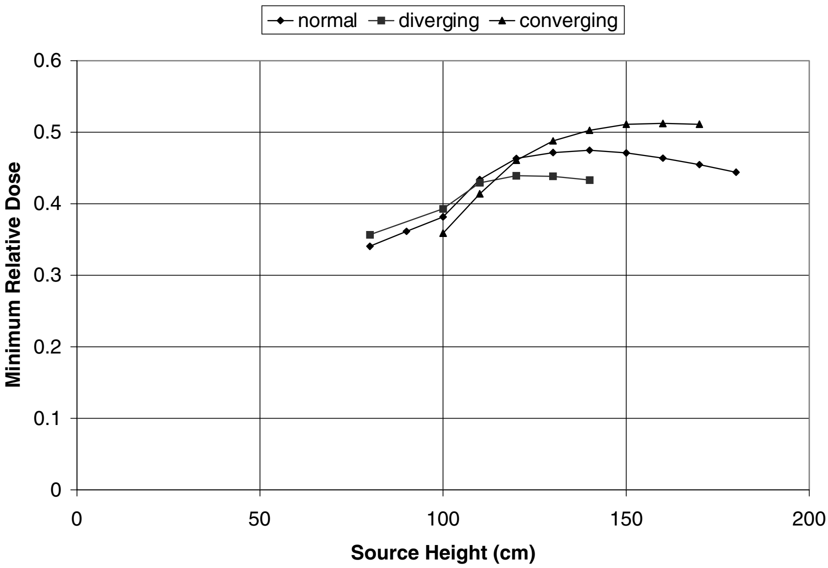

Figure 4-44. Variation of the minimum relative dose (I_m^*) in the middle of the product, as a function of x-ray source height, for diverging and converging beams at the converter. (The case of normal incidence is also shown for comparison.) The product height was 100 cm.

18 degrees. Note also that if the source height is less than the height of product, the throughput efficiency will be slightly better for the diverging beam. The maximum throughput efficiency for the diverging beam is 2.8%.

4.7.4. Weighting

The use of overscanning to improve the throughput efficiency requires a larger scan horn and converter, and may imply a change of hardware for existing facilities. It is therefore of interest to examine what improvement might result from simply changing the scan magnet waveform to vary the electron intensity at the converter (see Section 8.4.2). Various intensity profiles that have been previously considered include modified sinusoids, parabolas, and exponential functions (as discussed in Section 4.3). For the purposes of this section we assume a very simple weighting function that consists of a constant intensity c_1 over an intermediate region of the scan ($|y| < h/2$), and a higher constant intensity $c_2 = \alpha c_1$ over the outer portions of the scan ($h/2 < |y| < H/2$). With this assumed weighting scheme

$$c_1(\alpha - 1)/(\alpha c_1 - 1) = H/h \tag{4.60}$$

Referring to Figure 4-40, the dose decreases significantly in the top 15 cm of product when the source height and product height are equal. Guided by this result, h/2 was set to 35 cm, and the minimum dose in the middle of the product was computed as a function of the intensity ratio α. For normal incidence with $H/2 = y_{1\max} = 50$ cm the results indicate that while the minimum relative dose increases monotonically with α, the throughput efficiency increases to only 2.7% for $\alpha = 2$, indicating that weighting without overscan is not particularly effective. Consequently, the source height was increased to $H = 130$ cm, but with $h/2 = 35$ cm as before. In this case the dose in the middle of the product was highest for $\alpha = 1.6$ ($c_1 = 0.783$, $c_2 = 1.253$), as shown in Figure 4-45.

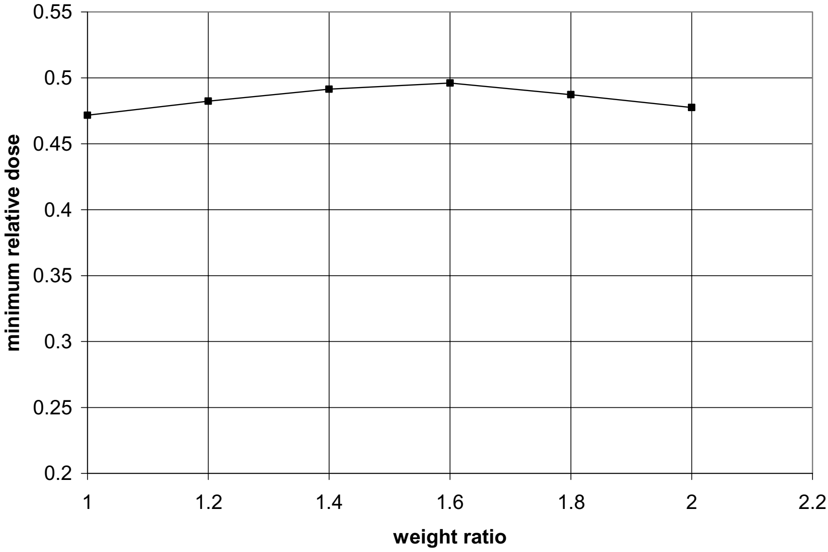

Figure 4-45. Variation of the minimum relative dose (I_m^*) in the middle of the product, as a function of the weight ratio parameter α for h/2 = 35 cm. The product height was 100 cm, but the source height was increased to 130 cm.

The throughput efficiency has improved to 3.1%. The dose profiles for this case are shown in Figure 4-46. The dose in the middle of the product is nearly constant, but there is some dose enhancement at the top and bottom on the front surface.

As a final calculation using weighting, beam convergence (a = −0.2) was added to the previous case with h/2 = 35 cm, H = 130 cm and α = 1.6. The product height was 100 cm. The relative

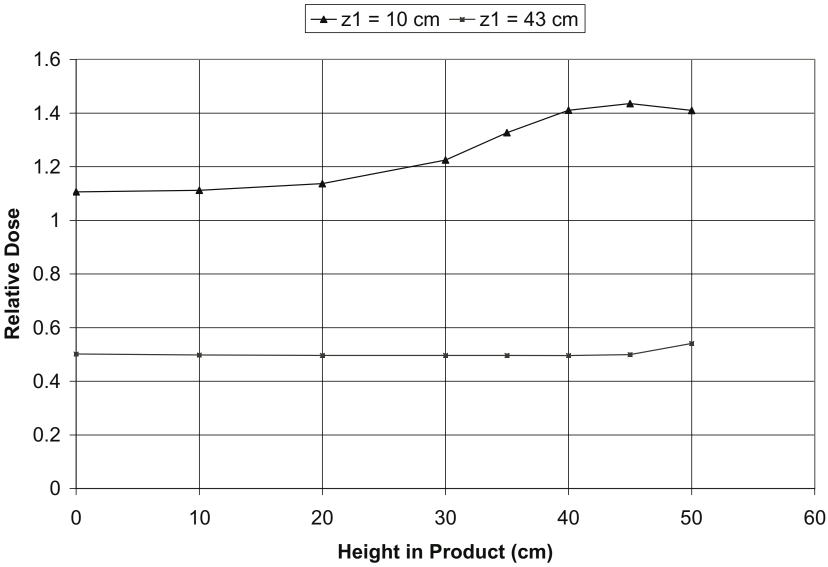

Figure 4-46. Dose profiles (I) at the front face and middle of the product for h/2 = 35 cm, H = 130 cm and α = 1.6. The product height was 100 cm. The beam was normally incident on the converter.

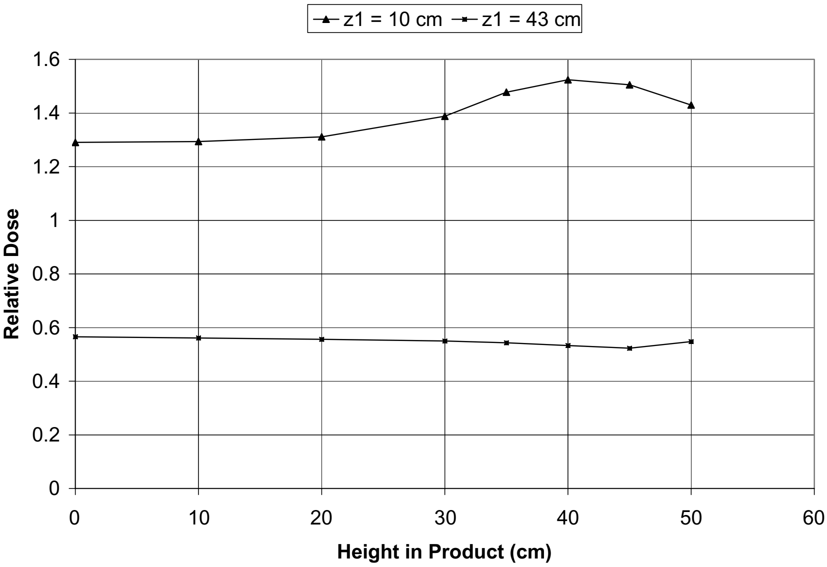

Figure 4-47. Dose profiles (I) at the front face and middle of the product for $h/2 = 35$ cm, $H = 130$ cm and $\alpha = 1.6$. The product height was 100 cm. The beam was convergent on the converter with $a = -0.2$.

dose minimum (I_m^*) in the middle of the product increased to 0.523, corresponding to a throughput efficiency of 3.3%. The dose profiles for this case with convergence are shown in Figure 4-47.

4.7.5. Efficiency Enhancement Summary for 5 MeV

A summary of the various cases is provided in Table 4.1. The single technique that provides the most benefit is overscanning, i.e., the height of the source exceeds the height of the product (in a symmetric fashion). However, taking full advantage of this approach requires some care in the design of the material handling system. Intensity enhancement (weighting) near the extremes of the scan, and increasing the height of both source and product also provide significant improvements. A combination of approaches provides small additional gains.

4.8. THROUGHPUT EFFICIENCY ENHANCEMENTS AT 7.5 MeV

The recent action by the USFDA approving an increase in the kinetic energy limit to 7.5 MeV for x-ray food irradiation applications significantly improves the economic prospects for this irradiation mode, with essentially no nuclear activation consequences (see Appendix C). Accordingly, throughput efficiency calculations similar to those performed in the previous section for 5 MeV have been extended to 7.5 MeV. The results are summarized in this section.

4.8.1. Overscanning for Various Product Heights

Variations in the quantity I_m^* (see Eq. (4.57)) are summarized in Figure 4-48 as a function of the overscan condition for three different product heights, $y_{1max} = 30$, 50 and 70 cm for the case of 7.5-MeV electrons normally incident onto an optimized converter with uniform intensity along the

Table 4.1. Summary of Throughput Efficiency Calculations (d = 66 cm, $\rho = 0.4$ g/cm^3) at 5 MeV

Case	Condition	H (cm)	$2y_{1\,max}$ (cm)	Con/div $\phi = ay/y_{1\,max}$	Weighting α	Weighting h (cm)	η_t (%)	max:min[1]
1	basic	100	100	a = 0	1	–	2.4	4.25
2	overscan	140	100	a = 0	1	–	3.0	2.7
3	overscan	80	60	a = 0	1	–	2.5	3.1
4	overscan	180	140	a = 0	1	–	3.3	2.6
5	diverge+oversc	120	100	a = 0.2	1	–	2.8	2.9
6	converg+oversc	160	100	a = −0.2	1	–	3.2	2.4
7	weighting	100	100	a = 0	2	70	2.7	4.25
8	weight+oversc	130	100	a = 0	1.6	70	3.1	2.8
9	wght+ovsc+conv	130	100	a = −0.2	1.6	70	3.3	2.8

[1] The max:min ratio of this column is the ratio of the maximum dose on the surface to the minimum dose in the middle of the product for a single pass. This ratio will decrease by nearly a factor of two for a symmetric double-pass treatment.

scan. As before, the total depth of the product was 66 cm, and the front face of the product was separated from the converter by 10 cm. Taking into account the increased efficiency for generating x-rays at 7.5 MeV, the throughput efficiency is now given by

$$\eta_t = 0.19 \times 10^{-3}\, y_{1max}\, I_m^* \tag{4.61}$$

Thus, from Figure 4-48 increasing the product height from 60 cm to 140 cm improves the throughput efficiency from 3.6% to 4.7%, assuming the optimum overscan condition for each height.

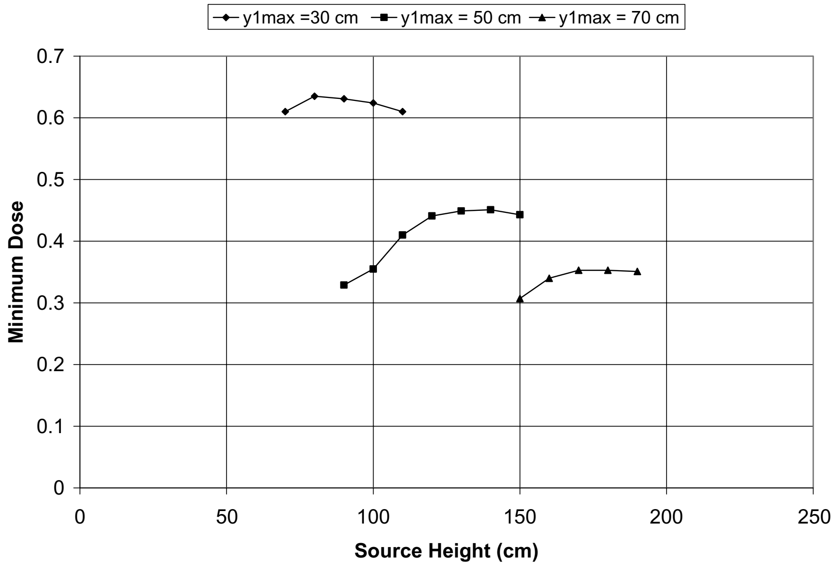

Figure 4-48. Variation of the minimum dose (I_m^*) in the middle of the product, as a function of x-ray source height, while holding the total electron beam power constant. The three different product heights were 60, 100 and 140 cm.

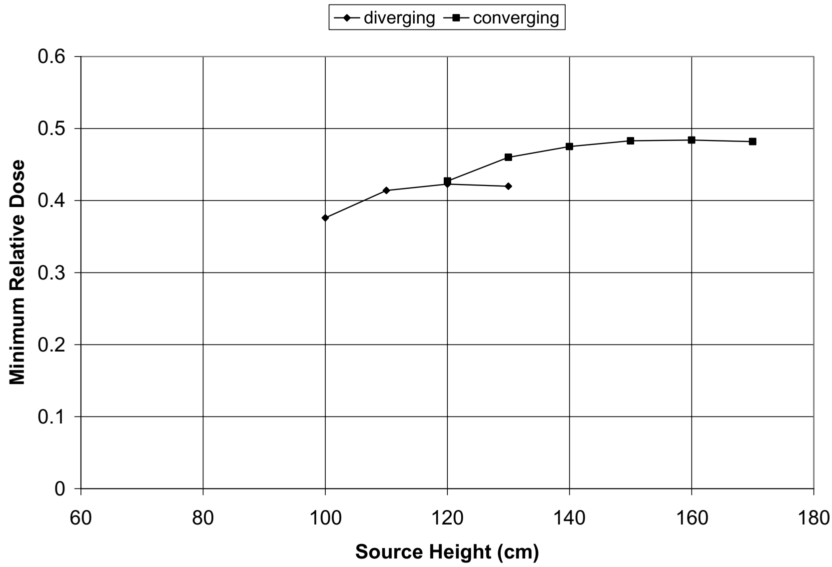

Figure 4-49. Variation of the minimum relative dose (I_m^*) in the middle of the product, as a function of x-ray source height, for diverging and converging beams at the converter. The product height was 100 cm.

4.8.2. Converging/Diverging Beams

Holding the product height fixed at 100 cm, the variation in I_m^* with source height is shown in Figure 4-49 for diverging and converging beams. The angle of electron incidence at the converter was chosen to be either linearly increasing or decreasing with height above the converter midplane according to Eq. (4.59), with $a = +/- 0.2$. Note the improvement again obtained with significant overscanning (30 cm top and bottom) using a converging beam; the maximum throughput efficiency for this case is 4.6%. The maximum convergence angle was about 18 degrees.

4.8.3. Weighting

The use of weighting with overscanning gives a modest improvement in the throughput efficiency. Again, we assume a very simple weighting function that consists of a constant intensity c_1 over an intermediate region of the scan ($|y| < h/2$), and a higher constant intensity $c_2 = \alpha c_1$ over the outer portions of the scan ($h/2 < |y| < H/2$), as described by Eq. (4.60). In particular, for a source height of $H = 130$ cm and $h/2 = 35$ cm, the minimum dose in the middle of the product is highest for $\alpha = 1.4$ ($c_1 = 0.844$, $c_2 = 1.182$). The dose profiles for this case are shown in Figure 4-50. The dose in the middle of the product is nearly constant. The throughput efficiency is about 4.5% for this case.

As a final calculation using weighting, beam convergence ($a = -0.2$) was added to the previous case with $h/2 = 35$ cm, $H = 130$ cm and $\alpha = 1.4$. The product height was 100 cm. The relative dose minimum (I_m^*) in the middle of the product increased slightly to 0.488, corresponding to a throughput efficiency of 4.65%.

4.8.4. Efficiency Enhancement Summary for 7.5 MeV

A summary of the various cases examined in the previous sections is provided in Table 4.2. The overall features are quite similar to those observed at 5 MeV; the only significant difference is the improvement resulting from the increased x-ray generation efficiency.

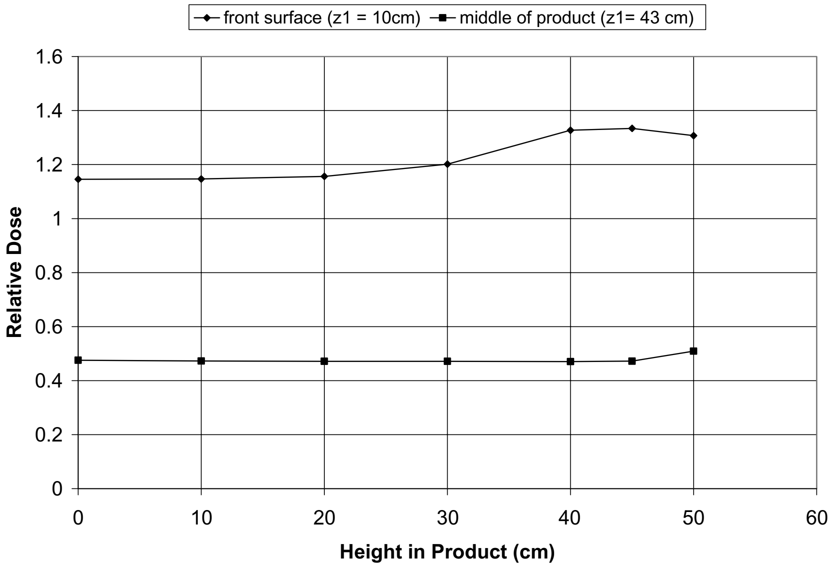

Figure 4-50. Dose profiles (I*) at the front face and middle of the product for h/2 = 35 cm, H = 130 cm and $\alpha = 1.4$. The product height was 100 cm. The 7.5-MeV beam was normally incident on the converter.

4.8.5. Depth-Dose Profiles at 7.5 MeV

According to Eq. (4.28) the dose delivered in a single pass of product through the irradiation zone will depend on the value I of the double integral over the scan (y) and the conveyor direction (x_1) according to

$$D = \mu \eta_g (P/H)(I/v) \tag{4.62}$$

Using $\mu = 0.03\ \text{cm}^2/\text{g}$ and $\eta_g = 12\%$ for 7.5 MeV, we have D = 0.0036 (P/H) (I/v). Depth-dose calculations have been performed for difference product densities and air gaps corresponding to Case 8 of Table 4.2. Representative results (values of I) are shown in Figure 4.51 for a height in product corresponding to the midplane of the converter ($y_1 = 0$). It is apparent from this figure that

Table 4.2. Summary of Throughput Efficiency Calculations (d = 66 cm, $\rho = 0.4\ \text{g/cm}^3$) at 7.5 MeV

					Weighting			
Case	Condition	H (cm)	$2y_{1\,\max}$ (cm)	Con/div $\phi = ay/y_{1\,\max}$	α	h (cm)	η_t (%)	max:min[1]
1	basic	100	100	a = 0	1	–	3.4	4.6
2	overscan	140	100	a = 0	1	–	4.3	2.7
3	overscan	80	60	a = 0	1	–	3.6	3.1
4	overscan	180	140	a = 0	1	–	4.7	2.8
5	diverge+oversc	120	100	a = 0.2	1	–	4.0	3.1
6	converg+oversc	160	100	a = −0.2	1	–	4.6	2.4
7	weighting	100	100	a = 0	2	70	3.8	4.4
8	weight+oversc	130	100	a = 0	1.4	70	4.5	2.8
9	wght+ovsc+conv	130	100	a = −0.2	1.4	70	4.65	2.9

[1] The max:min ratio of this column is the ratio of the maximum dose on the surface to the minimum dose in the middle of the product for a single pass. This ratio will decrease by nearly a factor of two for a symmetric double-pass treatment.

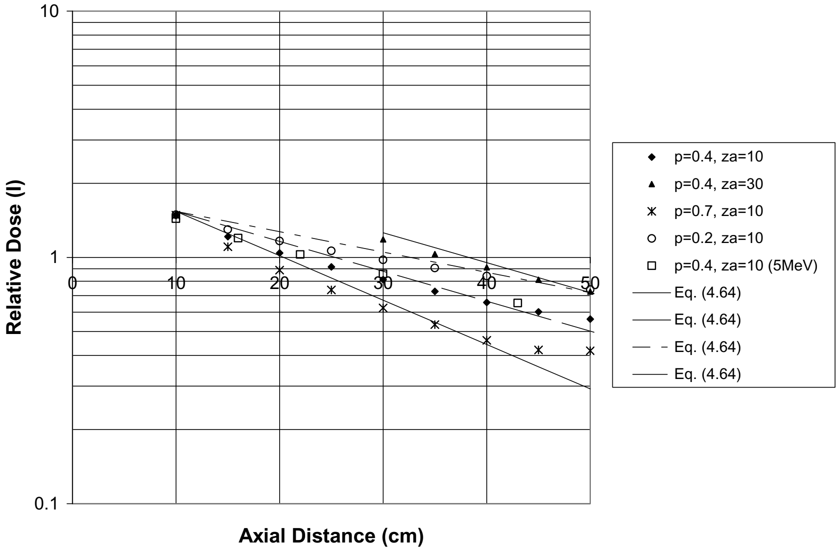

Figure 4-51. Depth-dose data (the values of the double integral I) for Case 8 of Table 4.2 on the midplane of the converter. Shown for comparison are the values of Eqs. (4.64) and (4.65). Also shown is the depth-dose profile for Case 8 of Table 4.1 (5 MeV).

the decrease with dose at this height is not exactly exponential, and from Figure 4-50, the depth-dose profiles must also vary with height. Despite these observations, it is nevertheless quite useful to have a simple formula that permits quick estimates of throughput efficiency and max:min ratios. An empirical formula that very approximately models the depth-dose behavior in Figure 4-51 is

$$I = 1.7e^{-0.01z_a}\, e^{-\mu_e \rho (z_l - z_a)} \tag{4.63}$$

$$\mu_e = 0.01/\rho + 0.045 \tag{4.64}$$

Eq. (4.63) is graphed in Figure 4-51 for comparison purposes with the various calculation results.

Also plotted in this figure is the depth-dose profile of Case 8 from Table 4.1 (at 5 MeV). The differences between the results at 5 and 7.5 MeV are not particularly significant. The only factor that slightly changes the rate of decrease of dose with depth is increasing the air gap between the converter and product. However, this beneficial effect is more than offset by the overall decrease in throughput efficiency with distance from the converter. Based on these results, an empirical estimate of the dose given by a single pass of product through the irradiation zone is given by

$$D = [6.1P/(vH)]\, e^{-0.01z_a}\, e^{-\mu_e \rho (z_l - z_a)}; \quad (7.5\,\text{MeV}) \tag{4.65}$$

$$D = [4.1P/(vH)]\, e^{-0.01z_a}\, e^{-\mu_e \rho (z_l - z_a)}; \quad (5.0\,\text{MeV}) \tag{4.66}$$

For both energies the effective mass absorption coefficient is given by Eq. (4.64)

In comparison with the analysis of Section 4.4.2, the increased numerical coefficient and the smaller exponential factors for the 5-MeV prediction are the result of the larger product and scan heights and the more favorable dose distributions with scan height. When the heights of source and product are not identical, Eq. (4.53) must be modified to include the multiplicative term $(2y_{1\max}/H)$.

From Eqs. (4.65), (4.66) and (4.64), the throughput efficiencies are estimated as

$$\eta_t = 6.1 \times 10^{-3}(2y_{1\,max}/H)(\eta_u/\mu_e)e^{-0.01z_a}; \quad (7.5\,\text{MeV}) \tag{4.67}$$

$$\eta_t = 4.1 \times 10^{-3}(2y_{1\,max}/H)(\eta_u/\mu_e)e^{-0.01z_a}; \quad (5.0\,\text{MeV}) \tag{4.68}$$

The maximum values still occur at

$$\rho_{opt} = (0.0225d)^{-1} \tag{4.69}$$

For $d = 66$ cm, $\rho = 0.4$ g/cm^3, $z_a = 10$ cm and $(2y_{1max}/H) = 100/130 = 0.77$, Eq. (4.67) gives a throughput efficiency of 4.4%; this generally agrees with the results of Table 4.2. The same calculation using Eq. (4.68) for 5 MeV gives 3.0%. The optimum density for a product depth of 66 cm for both energies is $\rho_{opt} = 0.67$ g/cm^3. In this case the throughput efficiency has a maximum value of 5% at 7.5 MeV, and 3.4% at 5 MeV.

4.9. PALLET PROCESSING CONCEPTS

Many food products, especially fresh produce, are routinely transported using pallets; typical pallet footprint dimensions are 1 m × 1.2 m (40″ × 48″). From Figure 4-35 it is apparent that with a conventional double-sided irradiation configuration the max:min ratio can become excessively large, depending on the average density of the product. In order to process higher density pallets it is necessary to increase the time that interior regions of the pallet are exposed to the x-ray source, while decreasing the dose to surface regions. A conceptual solution to this problem is provided by the approach used in cancer radiation therapy. By movement of the electron accelerator, well-collimated x-ray beams are caused to overlap in the region of a tumor. In this way a lethal dose can be delivered to the tumor while the dose to healthy tissue is minimized.[10]

Two topologically similar solutions better suited to food irradiation applications are indicated in Figures 4-52 and 4-53. In the first approach,[11] the pallet is rotated in a time-dependent fashion while it is being scanned vertically. For the highest density pallets collimation is also used to prevent x-rays emitted at large angles from reaching the product. This decreases the surface dose enhancement,

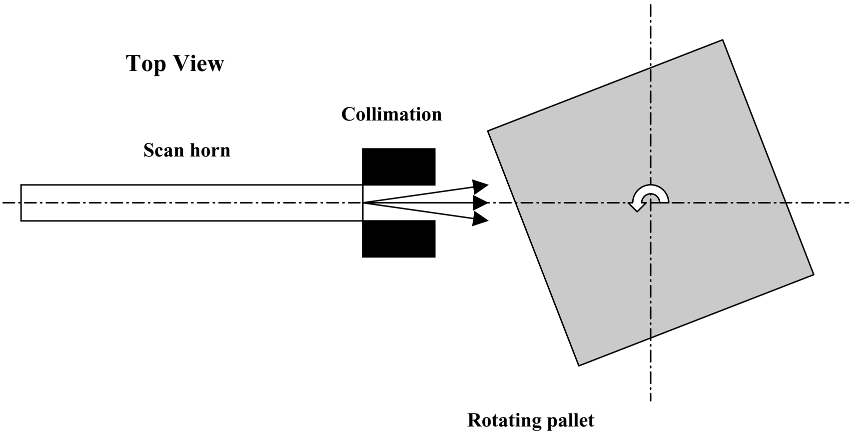

Figure 4-52. Schematic diagram of the Palletron concept. Acceptable dose uniformity for high density pallets of product is achieved by a combination of time-dependent pallet rotation and collimation of the x-ray flux.

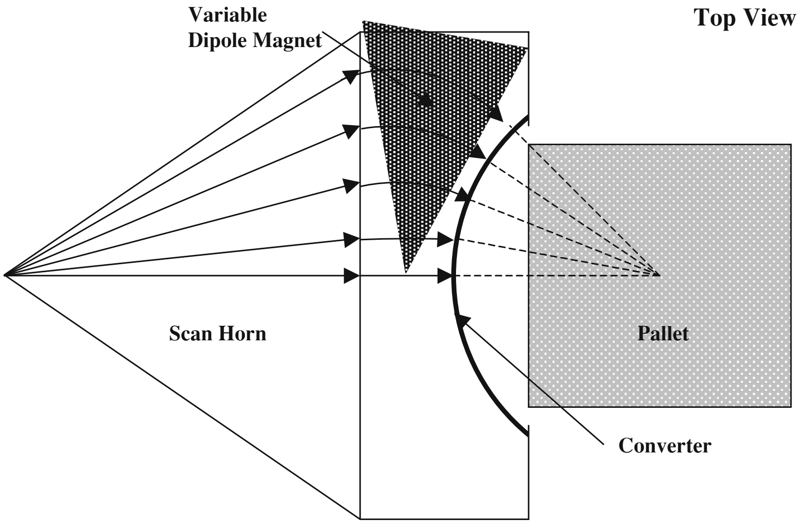

Figure 4-53. Schematic diagram of an alternate pallet irradiator concept. All beamlet rays incident on the converter converge at the center of the pallet.

and effectively improves the penetration depth. Using this approach, max:min ratios of 1.5 or less are claimed for products having average densities up to 0.9 g/cm^3. The mass throughput efficiency decreases at the higher densities to about 2%, however.

The second approach[12] uses beam manipulation rather than time-dependent pallet rotation to achieve improved dose uniformity. In particular, the beam is scanned horizontally while the pallet is raised or lowered. Magnetic lenses (see Section 8.4.4) cause the electron beamlets to be incident onto the converter such that all the rays would converge at the center of the pallet. If irradiated from only one side, the pallet is raised and lowered through the beam a total of four times, with the pallet being rotated by 90 degrees between irradiations. If two machines are available (placed on opposite sides of the pallet, for example), the pallet is lowered through the beams, rotated by 90 degrees and raised through the two beams to complete the processing.

The analytical x-ray model discussed previously can also be used to analyze the performance of this system. The specific configuration of the calculation is shown in Figure 4-54. The air-gap

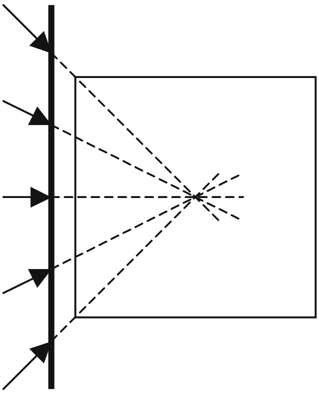

Figure 4-54. Schematic diagram of the pallet irradiation configuration for calculating the depth-dose profile.

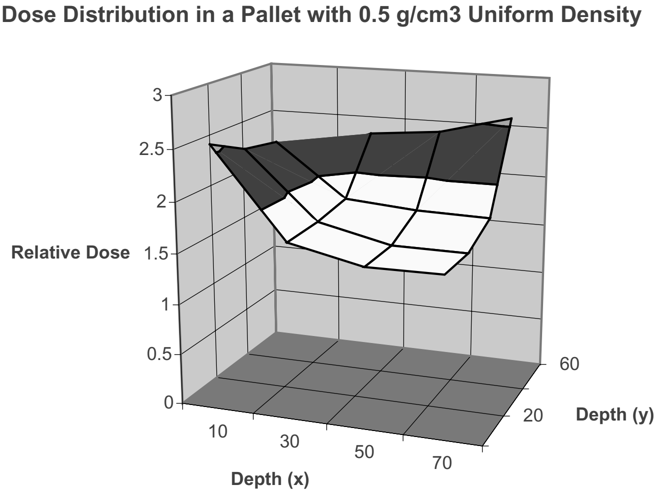

Figure 4-55. Dose distribution in a pallet quadrant with symmetric, four-sided irradiation using the configuration of Fig. 4.53. For a uniform density of 0.5 g/cm^3, the max:min ratio is about 1.6, with no collimation and a uniform intensity scan.

distance between the converter and pallet was assumed to be 10 cm, and the pallet footprint was 120 cm by 120 cm. No collimation was used. The electron intensity was uniform at the converter, but the incidence angle varied linearly from zero at the midplane to a maximum of $+/-$ 45 degrees at the extremes of the scan ($-/+$ 70 cm). Assuming symmetric four-sided irradiation at 5 MeV, the results for a quadrant of a pallet containing a uniform product with an average density of 0.5 g/cm^3 are shown in Figure 4-55. With no collimation there is still some surface dose enhancement, and the max:min ratio is approximately 1.6. However, with a symmetric double-sided treatment the max:min ratio for such a pallet would have been about four. The improvement is dramatic. In addition, further improvement could be realized by varying the intensity as a function of position at the converter. With higher densities, however, collimation is still essential for achieving max:min ratios less than two, at the expense of mass throughput efficiency.

4.10. SUMMARY

In this chapter we have discussed several important features of irradiating food using the x-rays produced by energetic electron beams. The best x-ray converter designs invariably consist of a thin, high-Z layer, typically a little greater than one-third of a CSDA range, backed by a layer of a lower-Z material that is sufficiently thick that none of the primary beam electrons can reach the product. Even in the best circumstances, little more than 8% of the primary electron energy is converted into forward-going x-ray energy for an incident electron kinetic energy of 5 MeV, increasing to about 12% at 7.5MeV. While the emerging x-ray flux is peaked in the forward direction, there is considerable energy emitted at larger angles, primarily as a result of electron scattering in the high-Z layer.

The free-field irradiation zone (the spatial distribution of the x-ray intensity, in the absence of absorbers) can be accurately characterized by considering the x-ray source as a line produced by the scanned electron beam. The x-ray intensity at any position is then found by integrating the incremental intensity contributions along the line source. Since the motion of the conveyor system through the irradiation zone effectively integrates over the x-ray intensity in this direction, the resulting integrated intensity distribution varies only with axial distance from the converter and in the third direction perpendicular to the motion of the conveyor (usually the direction of the scan).

Through various techniques, it is usually possible to essentially eliminate significant variations in the integrated intensity in this third direction, so that the integrated intensity only varies with axial distance from the converter over the region normally occupied by product.

As product is conveyed through the irradiation zone, energy is deposited as the result of three primary x-ray interaction mechanisms. These are (1) the photoelectric effect, (2) Compton scattering, and (3) pair production. For the low-Z elements predominantly comprising foods, the most important x-ray interaction mechanism is relativistic Compton scattering. Regardless of the particular mechanism however, the salient feature of each process is the generation of energetic charged particles (electrons and positrons) that are subsequently slowed by Coulombic interactions; the actual energy deposition processes for x-ray irradiation are therefore identical to those considered in the electron irradiation of food.

The x-ray energy deposition profile can be calculated by integrating along the line source, with the integrand exponentially decreased because of absorption in the product. The exponent is equal to the product of the mass absorption coefficient (0.03 cm^2/g is a good approximation for foods) and the areal density of the portion of product lying along the line between the source point and the deposition point. Assuming that the free-field x-ray intensity varies only with distance from the converter, the energy deposition essentially varies only with distance from the converter, also. This energy deposition profile can be approximated by a decreasing exponential function whose exponent is the product of the areal density corresponding to depth as measured normally from the front surface and an effective mass absorption coefficient that depends on the product density. The value of this effective mass absorption coefficient is typically a factor of 2–3 times larger than the mass absorption coefficient of water because of the significant amount of x-ray emission at large angles, as well as the geometrical decrease in the free-field intensity.

With the x-ray energy deposition profile being effectively characterized as a decreasing exponential function, it is relatively straightforward to calculate the max:min ratio and the one-dimensional x-ray energy utilization efficiency for particular irradiation scenarios of interest. In particular, such calculations indicate that single-sided x-ray irradiation always has very poor energy utilization efficiency, and is therefore almost never used. With uniform double-sided irradiation, the utilization efficiency has a broad maximum for areal densities in the range of 25–35 g/cm^2, with a corresponding max:min ratio of approximately 1.5. Pallets of products having even larger areal densities (75 g/cm^2) can still be effectively processed using special irradiation geometries and pallet handling techniques.

The large range of areal densities that can be effectively treated using x-ray processing affords considerable flexibility in food irradiation applications. However, the price for this increased flexibility is a significant loss in throughput efficiency, primarily as the result of inefficient x-ray generation. While throughput efficiencies of 40–50% are commonly realized using electron processing, the throughput efficiency for symmetric, double-sided x-ray processing is generally of the order of only 3% at 5 MeV and 4.5% at 7.5 MeV, even with the use of various efficiency enhancement techniques such as overscanning, intensity weighting, electron convergence, etc. The average power of an x-ray system must therefore be roughly an order-of-magnitude higher to achieve mass throughput rates comparable to those available with an electron beam system.

REFERENCES

1. E. Segre, **Nuclei and Particles**, Benjamin, NY (1965).
2. J.H. Hubbell and S.M. Seltzer, Tables of X-Ray Mass Attenuation Coefficients and Mass Energy-Absorption Coefficients, Nat'l. Inst. Standards and Tech. **NISTIR 5632** (1996).
3. J. Meissner, M. Abs, M.R. Cleland, A.S. Herer, Y. Jongen, F. Kuntz, and A. Strasser, "X-Ray Treatment at 5 MeV and Above," Rad. Phys. and Chem. **57**, 647–651 (2000).

4. J.A., Halblieb, R.P. Kensek, T.A. Mehlhorn, G.D. Valdez, S.M. Seltzer, and M.G. Berger, ITS Version 3.0: The Integrated TIGER Series of Coupled Electron/Photon Monte Carlo Transport Codes, **SAND91-1634** (1992).
5. R.B. Miller, "Food irradiation using bremsstrahlung X-rays," Rad. Phys. and Chem. **68**, 963–974 (2003).
6. Report of the Consultant's Meeting on the Development of X-Ray Machines for Food Irradiation, Food and Agriculture Organization, International Atomic Energy Agency (1995).
7. G. Loda, and R. Smith, Private Communication (2000).
8. V. Auslender, Private Communication (2001).
9. M.R. Cleland, C.C. Thompson, H. Kato, M. Odera, R.F. Morrissey, C.M. Herring, M.T. O'Neill, T.R. Wilcott, J. Masefield, J.M. Hansen, M.C. Saylor, and D.P. Sloan, "Evaluation of a New X-Ray Processing Facility," Nucl. Inst. Meth. in Phys. Res. **B56/57**, 1242–1245 (1991).
10. C.J. Karzmark, C.S. Nunan and E. Tanabe, **Medical Electron Accelerators**, McGraw-Hill, NY (1993).
11. Y. Jongen and F. Stichelbaut, "The Palletron: An X-Ray High Dose Uniformity Pallet Irradiator," 17th Int'l. Conf. Appl. Accel. in Res. and Ind., Denton, TX (2002).
12. R.B. Miller, "X-Ray Pallet Processing System," SureBeam Patent Disclosure (2002).

CHAPTER 5

OVERVIEW OF ELECTRON ACCELERATOR SYSTEMS

The energetic electrons and x-rays that deliver ionizing dose to food products are provided by an electron accelerator system. Its two essential features are (1) an electron source, and (2) an accelerating electric field. The electron source is almost always a thermionic gun, the cathode of which is raised to a sufficiently high temperature that electrons are "boiled" from the surface. In contrast, there are many different techniques for creating the accelerating electric field. In this chapter we will first summarize the general requirements for the accelerator system for various food irradiation applications. We will then discuss the attributes of the several acceleration approaches in light of these requirements, identifying microwave accelerator approaches as those most generally appropriate. In the following two chapters we will discuss the general operating principles of microwave accelerators, and more specific details including the function and integration of the key components.

5.1. GENERAL CONSIDERATIONS AND REQUIREMENTS

Essential factors in selecting the appropriate accelerator technology for a particular food irradiation application are the required penetration depth and the peak throughput rate. Additional important factors include size, cost, operating efficiency, ease of maintenance, and reliability. We briefly discuss each of these factors.

5.1.1. Penetration Depth and Kinetic Energy Considerations

As discussed in previous chapters, the maximum areal density that can be processed using electrons is limited to about 8.9 g/cm^2 (double-sided irradiation at 10 MeV). Products exceeding this limit must be processed using inefficient, but more penetrating x-rays. If electron processing can be used, the optimum kinetic energy depends on the areal density according to

$$\mathrm{E_{opt}(MeV)} = 2.5\,\mathrm{A_d(g/cm^2)} + 0.50; \quad \text{(single-sided)} \tag{5.1}$$

$$\mathrm{E_{opt}(MeV)} = 1.1\,\mathrm{A_d(g/cm^2)} + 0.45; \quad \text{(double-sided)} \tag{5.2}$$

To put these equations into perspective, a quarter-inch-thick burger patty will have an areal density of about 0.6 g/cm^2, implying a minimum electron kinetic energy of 2 MeV for single-sided processing. For a stack of fourteen such burgers (with a total height of approximately 3.5 inches), 10-MeV electrons are required for double-sided processing. If the application demands that x-rays be used, it is almost always desirable to operate at the maximum permissible limit (5 or 7.5 MeV) for two reasons: (1) the generation efficiency scales linearly with kinetic energy, and (2) the angular divergence scales inversely with kinetic energy. Therefore, although there may be some food products for which only a surface treatment (at the few hundred keV level) will suffice, processing the bulk of food products will require accelerators capable of producing electron beams with kinetic energies in the general range of 2–10 MeV.

5.1.2. Throughput and Average Power

The required average power of the electron beam produced by the accelerator system depends linearly on the minimum required dose and the maximum required mass throughput rate, and inversely with the throughput efficiency according to

$$P(\mathrm{kW}) = D(\mathrm{kGy})\,[dM/dt(\mathrm{kg/s})]/\eta \tag{5.3}$$

The throughput efficiency for electron beam processing is typically in the range of 0.4–0.5; for x-rays, the throughput efficiency is typically in the range of 0.025–0.035 for 5 MeV, and 0.04–0.05 for 7.5 MeV. Average power levels depend on processing demands, and typically range from a few kilowatts for small e-beam installations to a few hundred kilowatts for x-ray processing of high-dose products such as spices.

5.1.3. Capital and Operating Costs

Capital costs and operating expenses are always important considerations, as are ease of maintenance and reliability. At present, because of their large installed base, microwave-based linear accelerator systems are the standard by which other accelerator technologies and approaches must be judged for food irradiation applications. A very approximate rule of thumb is that the yearly amortization expense for a relatively low-voltage (<10 MeV) microwave linac is

$$C_{\mathrm{am}}(\$\mathrm{K}) = 100\log_{10}[P(\mathrm{kW})] \tag{5.4}$$

Klystron-powered microwave linacs have a wallplug-to-beam efficiency of typically 0.2–0.25. Assuming two-shift operation (4000 hours per year), and a nominal electricity cost of \$0.08 per kilowatt-hour, yearly power consumption costs associated with operating the linac are estimated as

$$C_{\mathrm{el}}(\$\mathrm{K}) = 1.6\,P(\mathrm{kW}) \tag{5.5}$$

Consequently, for low-power systems (10 kW or less), linac capital amortization costs are significantly higher than yearly electricity costs, and technologies that require lower capital outlays are of interest. On the other hand, for high-power installations (>100 kW), electricity costs can be comparable to linac amortization costs, and technologies that offer improvements in operating efficiency are of interest, assuming that capital costs remain approximately equivalent.

5.1.4. Size and Shielding

While the size of the accelerating structure is less important for food irradiation than for other applications (medical linacs used for radiation therapy, for example), the accelerator configuration usually establishes the minimum footprint of the radiation shield. Since the accelerating gradient of a microwave linac is typically of the order of 10 MeV/m, the accelerating structures are short (one meter or less) and have a diameter of less than 30 cm. Also, the modulator and microwave tube can be placed outside of the shield, further reducing the shield footprint.

5.1.5. Maintenance and Downtime

Almost all foodstuffs are perishable, and many require refrigeration both before and after irradiation. Combined with the very large processing rates that can be anticipated, food processing applications cannot tolerate lengthy downtimes or maintenance periods for the acceleration system. Thus, accelerator approaches that are modular, with key components that can be replaced in at most a few hours if necessary are favored.

5.2. ACCELERATOR SYSTEM APPROACHES

The several electron acceleration approaches in common usage can be generally grouped into three categories: (1) direct methods, in which the accelerating field results from the direct application of a high potential difference across an insulating column; (2) induction methods, in which the accelerating field results from a time-changing magnetic field; and (3) microwave (or radio-frequency) acceleration methods, in which acceleration results from oscillating electromagnetic fields established in a resonant microwave cavity structure. In the following paragraphs we discuss these general approaches, giving a few specific examples of each. For more detailed information, excellent reviews are available with extensive references.[1–7]

5.2.1. Direct Acceleration Methods

Examples of systems using direct acceleration methods include transformer-rectifier units, resonant transformers, Dynamitrons, and various electrostatic approaches, including the Van de Graaff accelerator and the Pelletron. The common feature of these approaches is the generation of a high potential difference across a graded insulating column, which also serves as the vacuum interface. The voltage gradient that can be sustained along the insulator column depends somewhat on the time duration of the applied voltage. For constant (DC) voltages, the maximum gradient is limited to about 30 kV/cm (on the vacuum side of the insulator), and gradients in the range of 10–20 kV/cm are more typical. In high-voltage versions of these direct accelerators, the insulating column is usually placed inside a large pressure vessel filled with a suitable insulating gas (sulfur hexafluoride, for example). Consequently, these units tend to be quite large.

Electrostatic Accelerators

Perhaps the simplest direct acceleration method to visualize is that of the electrostatic accelerators. These approaches establish a large potential difference by physically transferring charge to a high voltage terminal, as schematically shown in Figure 5-1. The resulting voltage is determined according to $V = Q/C$, where Q is the net transferred charge, and C is the capacitance between the high voltage terminal and ground. In the case of the Van de Graaff accelerator,[8] the charge transfer is accomplished by means of a moving belt placed externally to the insulator column. The Pelletron[9] is a more recent version of the Van de Graaff concept in which the continuous belt is replaced by a "charging chain" consisting of alternating insulating and conducting "pellets" that are charged and discharged inductively. This configuration is somewhat less susceptible to electrical breakdown, and the charging chain is more resistant to wear. Voltages of several million volts can be achieved using these electrostatic approaches, and such machines can operate at high power levels (up to a few hundred kilowatts) with good efficiency. They are quite large, however. Also, maintaining the insulating column and repairing the charge transfer apparatus can be time-consuming, involving

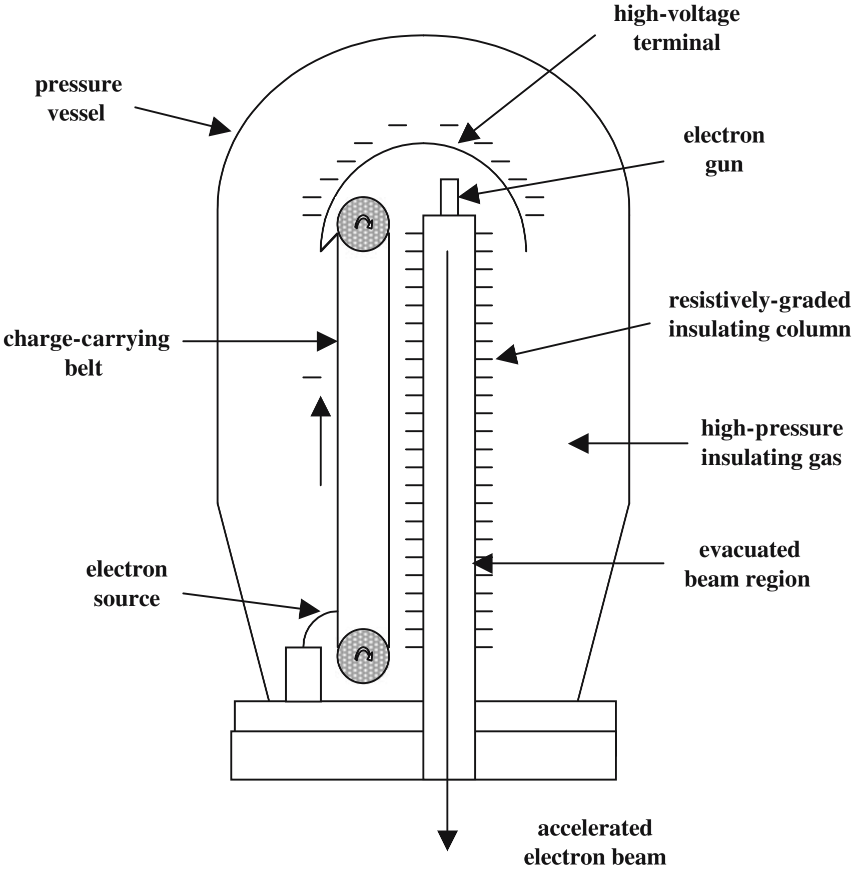

Figure 5-1. Schematic diagram of a Van de Graaff accelerator.

discharge and storage of the insulating gas, re-evacuation of the insulating volume, re-charging the gas, and high-voltage conditioning of the high-voltage terminal to reduce corona and breakdown effects.

Transformer-Rectifiers

In the case of the transformer-rectifier units, the output voltage of an iron-core, step-up transformer is rectified and applied directly across the accelerating column. A low-voltage example of this approach is the common dental x-ray machine, in which the x-ray tube itself can act as a self-rectifier, as suggested in the simple circuit diagram of Figure 5-2. Voltages in excess of one megavolt have been achieved by cascading such units (Cockcroft-Walton cascade generator[10]), but these are quite large and bulky. Commercial units seldom exceed 300 kV.

Resonant Transformers

Many industrial radiation-processing applications use accelerators based on resonant transformers. This device is in essence a half-wave, self-rectified, high-voltage source. The primary winding is driven at the resonant frequency (typically 100 Hz to1 kHz), and multiple secondary windings are

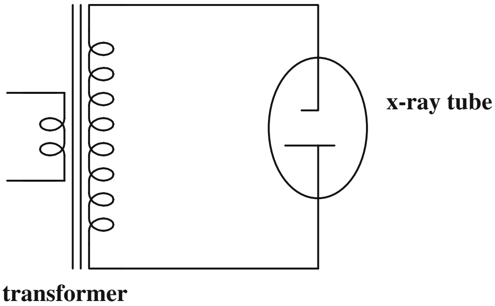

Figure 5-2. Simple transformer-rectifier circuit, in which the x-ray tube acts as a self-rectifier.

connected at multiple points along the accelerating column to maintain a constant voltage gradient. Feedback is usually necessary to stabilize the output voltage, beam current, and driving frequency. An elegant version of this type of accelerator is the nested high voltage generator (NHVG).[11] Resonant transformer units are relatively efficient and can operate at high average power. Also, the overall volume can be reduced by placing the insulating column inside the secondary winding in a coaxial arrangement. Nonetheless, the peak output voltages are typically limited to a few million volts, and the accelerating columns are often several meters in length.

Dynamitrons

The Dynamitron[12] is somewhat similar to the resonant transformer approach, but uses a radiofrequency generator instead of a resonant transformer. In essence, it uses capacitive coupling of a low-frequency (approximately 100 kHz) rf source to power a rectifier chain consisting of the equipotential rings of the insulating column themselves. The use of rf frequencies allows the output voltage to have only a small ripple without the use of smoothing capacitors. Output voltages of up to a few million volts can be obtained at relatively high average power levels (hundreds of kilowatts), and Dynamitrons have been used quite successfully for industrial radiation-processing applications.

5.2.2. Induction Acceleration Methods

The primary drawback of the direct acceleration methods for generating electron beams with kinetic energies in excess of a few MeV is the development of the total potential difference across a single long insulating column. An alternative approach is to pass a beam many times through relatively smaller accelerating sections. So that the exterior of the accelerator can remain at ground potential, these smaller accelerating increments should be “induced” by time-changing magnetic fields. Two practical embodiments of the induction acceleration principle are the linear induction accelerator and the betatron.

Linear Induction Accelerators

An induction linac[13] consists of a linear series of inductively coupled accelerating cavities, usually loaded with a ferromagnetic material such as ferrite, laminated iron, or (more recently) metallic glass.[14] A single such induction cell is schematically shown in Figure 5-3. The voltage pulse from a modulator, usually consisting of a pulse-forming network (PFN) switched by a thyratron, is applied to the cavity, usually by means of symmetric coaxial feeds. The magnetization of the ferromagnetic

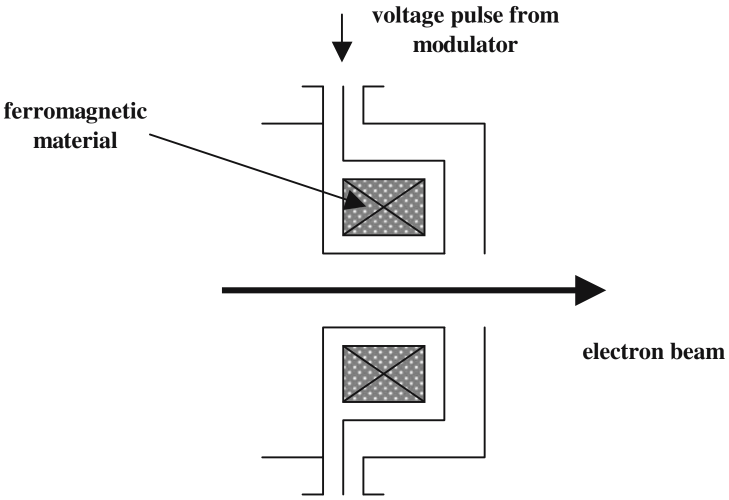

Figure 5-3. Schematic diagram of an accelerating cavity in a linear induction accelerator containing a toroidal core of ferromagnetic material.

material is pre-set in reverse saturation prior to the arrival of the pulse, and therefore prevents the pulse from being shorted over the time required for the magnetization to saturate in the forward direction. Thus, the cavity essentially functions as a single-turn transformer with the electron beam constituting the secondary winding.

The accelerating voltage seen by the beam can be expressed as the time rate of change of magnetic flux density in the ferromagnetic core as the magnetization changes in response to the applied voltage pulse. From the integral form of the third Maxwell equation, the voltage on the accelerating gap is

$$V_g = -\int (d\mathbf{B}/dt)\mathbf{x}\, d\mathbf{s} \tag{5.6}$$

with the surface integral taken over the cross section of the core. If dB/dt is constant over the cross-sectional area A for a time τ, then the integral can be simply evaluated as

$$V_g\tau = A\Delta B \tag{5.7}$$

The area of the core and the total flux swing therefore determine the maximum “volt-seconds” of acceleration that can be applied.

A simple example illustrates the important characteristics of the induction linac approach. Let L be the length of a core, with r_0 and r_1 denoting its inner and outer radii. Then the cross-sectional area of the core is $A = L(r_1 - r_0)$. The mass of the core material of density ρ is given by $M = \rho L\pi(r_1^2 - r_0^2)$, and the accelerating gradient can be no greater than $G = V_g/L$. Since the weight (and expense) of the core material scales as the square of the radius, some accelerating gradient is usually sacrificed in favor of smaller cavity radii. We assume that $L = 25$ cm, and that $r_1 = 30$ cm and $r_0 = 10$ cm, so that $A = 0.05\ m^2$. Assuming a total flux swing of 0.6 T, then the maximum volt-seconds of acceleration is given by Eq. (5.7) as 0.03 V-s. As an example, this core would allow a constant accelerating voltage pulse of 300 kV to be applied for 100 ns. To achieve 5 MeV, approximately seventeen such cells would be required, implying an accelerator length in excess of 4 meters (at an accelerating gradient

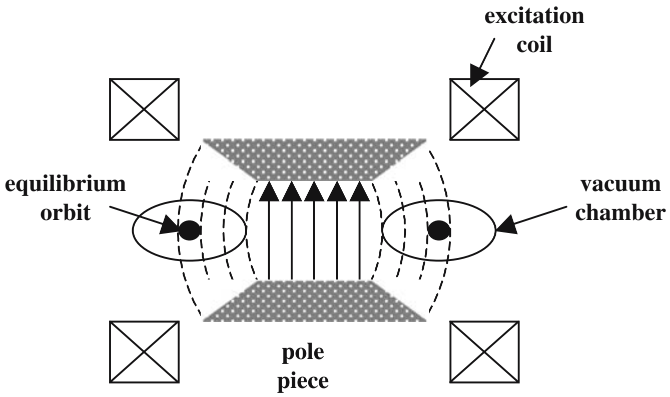

Figure 5-4. Schematic diagram of a betatron magnet and vacuum chamber, showing a central region of strong magnetic field, and a weaker field at the orbit radius.

of <12.5 kV/cm). Assuming an average core density of 5 g/cm^3, the weight of a single core would be 310 kg, and the weight of core material in the total linac would be 5300 kg. The overall diameter of the linac would approach one meter.

Induction linacs are inherently low impedance devices, and can efficiently accelerate beam currents of several kiloamperes, assuming a good beam transport system, and some care in cavity design to avoid high-current beam instabilities. Assuming 4 kA of beam current, the energy per pulse would be 2 kJ. At a pulse repetition rate of 100 Hz, the average beam power would be 200 kW. For applications in which high instantaneous beam power is required, induction linacs have significant advantages over other acceleration approaches. They are also modular, which permits rapid troubleshooting and quick replacement of components in the event of a failure. However, high instantaneous power is not a particular advantage for food processing, and the expense of the short pulse modulators and the ferromagnetic material itself, plus the size and weight of the accelerator proper make induction linac technology less advantageous for food irradiation applications, unless very high average power operation is essential (approaching 1 MW).[15]

Betatrons

A second inductive acceleration approach is used in the betatron.[16] A schematic diagram of this device is shown in Figure 5-4. Electrons execute circular orbits in an evacuated toroidal acceleration chamber under the action of an axial magnetic field produced by an electromagnet. When the magnet current is increased, an azimuthal electric field is induced by the time-changing magnetic flux density linking the electron orbits. The energy gained by an electron in one revolution is therefore equal to the induced voltage in a one-turn coil, if the coil were located at the radius of the electron orbit.

The fundamental issue in betatron operation is maintaining a constant orbit radius during the acceleration cycle. This condition can be summarized in the form of Eq. (5.8), known as the 2:1 rule

$$\Delta\Phi = 2\pi r^2 B(r) \tag{5.8}$$

In words, the flux change within the orbit radius r must be twice the value that would result if the flux density were uniform and equal to the flux density at the electron orbit radius. This means that there must be a strong central field, and a weaker field at the orbit, with both fields increasing proportionally with time.

The betatron is usually powered by an ac supply, with acceleration occurring over typically one-quarter of the cycle. Electrons are injected at low energy when the guiding field is small. At the end of the acceleration phase they are diverted from the equilibrium orbit using a second "peeler" magnet, resulting in one short beam pulse per ac cycle. Space charge effects during injection impose a serious limit to the circulating current in a betatron. This limit scales as $(\beta\gamma)^3$, with these relativistic factors referring to the electron kinetic energy at injection.[17] For an injector voltage of 100 keV, the circulating current limit is about 0.7 A. For a betatron diameter of 60 cm, the period of a revolution ($T = \pi D/c$) is about 2π ns; therefore, the total amount of circulating charge ($Q = IT$) is only 4.4 nC. At a magnet excitation frequency of 240 Hz, the limit on the average extracted beam current would be only 1 μA, and the average beam power (at 5 MeV) would be only 5 W. This average power level is too low to be of interest for nearly all food irradiation applications.

5.2.3. Microwave Acceleration Approaches

The common feature of the several microwave (or radio-frequency) accelerator approaches is electron acceleration by the oscillating electric fields established in an electromagnetic cavity structure that is driven at resonance by a suitable microwave or radio-frequency power source. (We will use the terms "microwave" and "radio-frequency" interchangeably.) The accelerating structure can consist of either a single cavity or multiple coupled cavities, and the beam can make either a single pass or multiple passes through the accelerating structure. The simplest microwave accelerator concept consists of a single accelerating cavity through which the beam passes a single time. The most common microwave accelerator approach is to pass the beam through a linear series of such accelerating cavities that are electromagnetically coupled, i.e., a microwave or rf linac. Other approaches of interest recirculate the beam through a single or multiple cavities several times. We will discuss a few illustrative examples.

ILU Accelerators

An ILU accelerator is schematically shown in Figure 5-5.[18] It consists of a single accelerating cavity that is essentially the output cavity of an rf power tube operating at a frequency $f = 175$ MHz. The cavity is operated in the TM_{010} mode, and has a diameter of about 1.2 meters. Electrons are produced in a gridded-gun arrangement and are injected into the acceleration region over the proper phase angle for acceleration to high kinetic energy. The kinetic energy gain is therefore limited by the maximum electric field that can be sustained on the cavity "electrodes" and the maximum drift angle of the electrons in the accelerating gap.

For a sinusoidal electric field, the maximum phase angle over which acceleration can occur is approximately 60 degrees, so that the useful acceleration period is $T = (6f)^{-1}$. Assuming a velocity of nearly the speed of light, this corresponds to a distance between electrodes of $d = cT = c/(6f) = 28.6$ cm. The maximum average electric field gradient is limited by breakdown to about 100 kV/cm. Consequently, these assumptions lead to a maximum kinetic energy of approximately 3 MeV. In fact, with proper surface preparation and extensive rf conditioning, kinetic energies of nearly 5 MeV have been achieved at average beam powers of a few tens of kilowatts using this single cavity approach.

Microwave Linacs

Higher kinetic energies could be realized with the single-cavity, single-pass approach by operating at a lower frequency. However, since the cavity dimensions increase inversely with frequency, it is

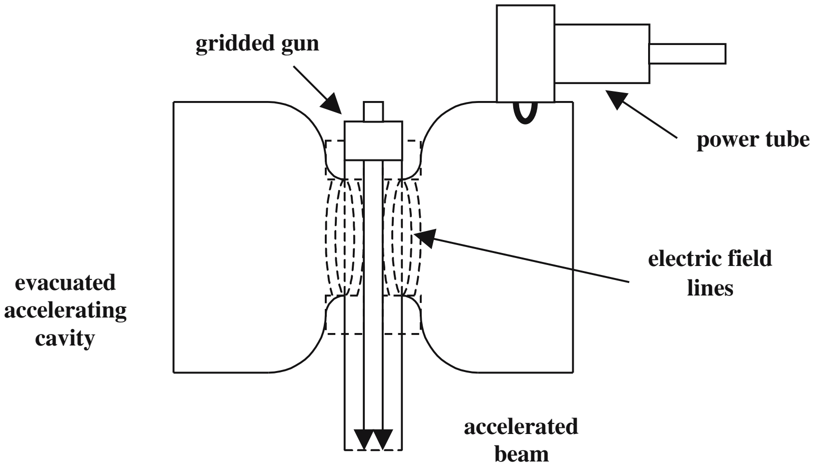

Figure 5-5. Schematic diagram of the ILU-series of single-cavity microwave accelerators.

usually more convenient to arrange for the beam to perform multiple passes through a single cavity, or to pass the beam through a series of cavities, as in a microwave linac.[19] We will briefly describe the general features of the linac approach here; we will examine it in considerably more detail in the following chapters.

A schematic diagram of a microwave linac system was shown in Figure 2-2. The linac, consisting of a series of coupled cavities, is powered by a suitable microwave source, such as a klystron or a magnetron. The system is modular with components that can be quickly replaced in the event of failure. The microwave source usually operates in pulsed mode, with the high-voltage pulses provided by a modulator/pulse transformer combination. A typical pulse structure is shown in Figure 5-6. The microwave source supplies output pulses (macropulses) of duration τ at the modulator repetition frequency F. Application of a macropulse to the linac produces a stream of electron pulses (micropulses) at (usually) the frequency of the microwave radiation f.

The power from the microwave source establishes oscillating electromagnetic fields in the resonant cavities of the accelerator structure. Electron bunches arriving at the proper time (or phase angle) are accelerated by these fields. According to the laws of electromagnetism, the fields must be

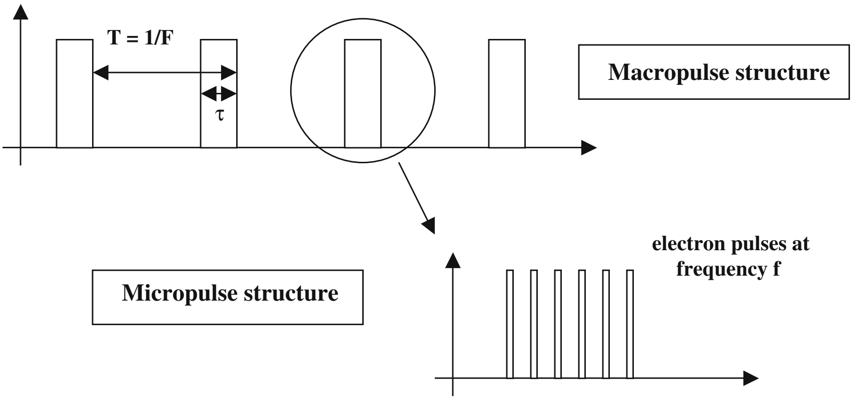

Figure 5-6. Typical macropulse and micropulse structure of a microwave linac.

self-consistently supported by currents flowing on the interior surfaces of the cavities; these currents give rise to dissipative losses. For a well-matched structure (negligible reflected power), the efficiency η of transferring microwave power P_t into electron beam power P_b is therefore given by

$$\eta = P_b/P_t = P_b/(P_c + P_b) \tag{5.9}$$

with P_c denoting the cavity losses. The beam power is simply the product of the beam voltage V and the macropulse beam current I_b, while the cavity loss term can be written as V^2/R_s, with R_s being the total shunt resistance of the structure. It is customary to introduce two additional parameters; these are the accelerating gradient, $E_g = V/L$, and the shunt impedance per unit length, $Z_l = R_s/L$, with L being the length of the accelerating structure. With these definitions, the efficiency can be written as

$$\eta = [1 + E_g/(Z_l I_b)]^{-1} \tag{5.10}$$

For modern well-designed structures, the shunt impedance per unit length generally has a value in the range of 50–100 megohms per meter (MΩ/m). Consequently, such structures can have excellent efficiency, even with accelerating gradients in excess of 10 MeV/m, provided that the beam current is a significant fraction of one ampere. However, this amount of beam loading requires high microwave power (typically 5 MW for 5–10 MeV electron kinetic energies), which is the reason that the microwave source is usually pulsed. As a numerical example, we assume $Z_l = 75$ MΩ/m, $E_g = 10$ MeV/m, and $I_b = 0.3$ amps. The efficiency of the structure is therefore 69%, and the peak source power required to produce a 10 MeV beam is 4.35 MW. At a duty cycle of 3% (100 μs pulses at a pulse repetition rate of 300 Hz), the average electron beam power would be 90 kW for an average source power of 130 kW. With modest changes as necessary, these parameters are well-suited for a wide variety of food irradiation applications.

Microwave sources having these peak and average power capabilities can generally be found in the frequency range of 1–3 GHz. Consequently, the accelerating structures are quite compact, typically having diameters of only a few inches and lengths of one meter or less. Klystrons generally have higher peak and average power capabilities with efficiencies in the range of 40–50%. Magnetrons generally have somewhat higher efficiency, but are more limited in peak and average power. Consequently, the overall efficiency (including modulator losses) of microwave linear accelerator systems designed for food irradiation applications is generally of the order of 25%.

Microtrons

The microtron is an electron accelerator that uses recirculation of the beam through a suitable accelerating structure to achieve the desired kinetic energy. There are two primary versions of the microtron. In the original circular microtron concept,[20] Fig. 5-7(a), electrons are constrained to move in circular orbits between the pole tips of an electromagnet, as in the betatron, but the field of the electromagnet is held constant. Regardless of radius, all of the circular orbits have one point in common. A single microwave cavity placed at this position is driven in the TM_{010} mode, and accelerates the electrons once per revolution. In the more recent "racetrack microtron," Figure 5-7(b), the magnet is split into two halves. A linear accelerator placed between these halves then provides a higher energy gain per revolution than could be realized with the single cavity.[21] In either case, the key feature of microtron operation is that the orbit period must be a multiple of the microwave period. Achieving and maintaining this condition requires careful control of the cavity fields and the field strength of the electromagnet.

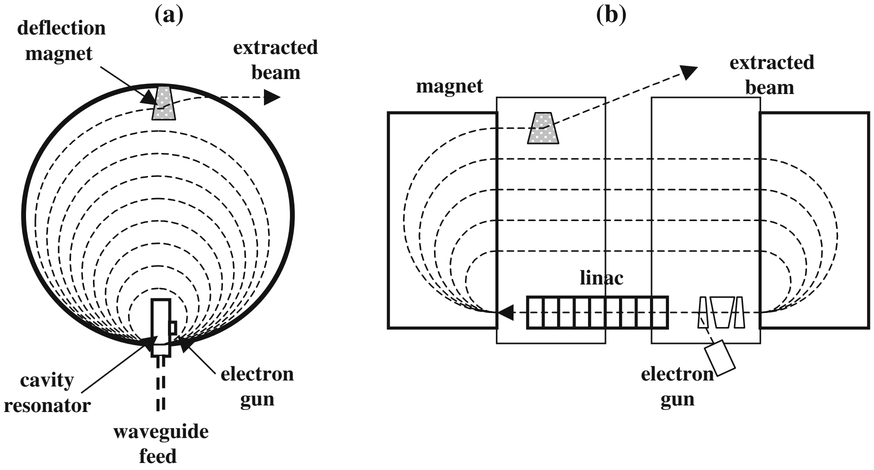

Figure 5-7. Schematic diagrams of (a) the circular microtron, and (b) the racetrack microtron.

Circular microtrons have been used to generate electron beams with kinetic energies in the range of 5–50 MeV at pulsed currents of typically several tens of milliamperes. The pole tip diameter is generally in the range of 0.5–1 meter. These accelerators are therefore relatively compact, and have found application in various research endeavors, as well as in medical radiation therapy. They may have applicability for low-power food irradiation applications. Because of the kinetic energy gain in relatively modest linacs, racetrack microtrons are better suited for applications requiring kinetic energies of a few tens of MeV or more.

The Rhodotron

The Rhodotron[22] also uses recirculation of the beam through a single coaxial cavity, but the cavity is driven at resonance in the lowest-order TEM mode. Consequently, electron acceleration is in the radial direction between inner and outer conductors of the coaxial cavity. The electron orbits are described in Figure 5-8. The beam from an external gun is injected toward the inner conductor through an opening in the outer wall. After a first acceleration, the beam passes through the inner conductor. When the beam re-emerges on the other side, the radial field has reversed sign, and the beam is accelerated a second time toward the outer wall of the cavity. The beam exits the cavity, is bent through an angle of 198°, and then re-enters at the proper phase of the rf cycle for a third acceleration. The Rhodotron derives its name from these rose-petal orbits; rhodos means rose in Greek.

In normal operation the cavity fields are adjusted to provide approximately 1 MeV of kinetic energy gain for one traversal of a cavity diameter. The ten transits shown in Figure 5-8 therefore give a maximum kinetic energy of 10 MeV, but a 5-MeV beam could also be easily generated, for example, by deactivating the appropriate external magnet. To avoid beam loss due to aiming errors, the magnets must be accurately aligned, and the magnetic field strengths and the cavity field amplitude must be precisely controlled. Assuming that these conditions can be met, the emerging beam will have a narrow energy spread.

The transit time of an electron across the device is equal to the microwave period. At an operating frequency f of 107.5 MHz, the device diameter is therefore approximately

$$D = c/f = 2.8 \text{ meters} \tag{5.11}$$

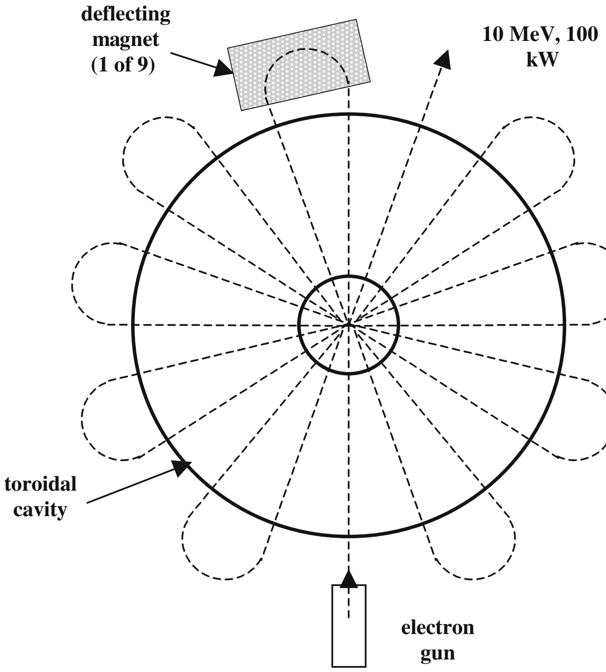

Figure 5-8. Schematic diagram of the Rhodotron electron accelerator.

The lowest TEM mode of the coaxial cavity is characterized by a wavelength that is equal to twice the height of the cavity. Therefore, the height is half the diameter, or about 1.4 meters. The device is therefore relatively large compared to a microwave linac.

Unlike the microwave linac, the Rhodotron can operate in a continuous wave (CW) mode, with power being provided by a high-average-power tetrode. At an operating voltage of less than 20 kV, such a tube can provide 200 kW of power with an efficiency of nominally 75%. At the accelerating fields appropriate for 10-MeV operation, the efficiency of the accelerating cavity is nominally 50%, implying an average beam power capability of 100 kW. Operating in CW mode, the losses in the high-voltage section will be small. Consequently, the overall efficiency of the Rhodotron system should exceed 30%, which is somewhat higher than that of a microwave linac of comparable average power. For these reasons, Rhodotrons are expected to be best suited for food processing applications that require high average power operation (e.g., x-ray irradiation of spices).

5.2.4. Comparison of Accelerator Approaches for Food Irradiation Applications

A summary of the salient features of the accelerator approaches described in the previous sections is presented in Table 5.1, with emphasis on those aspects of most interest for food irradiation applications. Crude value judgments have been made by the author, with N standing for neutral or acceptable; U meaning unacceptable, or at least unfavorable; and F meaning favorable.

The direct acceleration methods are generally deemed less favorable for food processing applications for two primary reasons: (1) the large size of the equipment for generating electron kinetic energies up to 10 MeV; and (2) the significant downtime required for repair or replacement of a high-voltage insulating column. For foodstuffs that are non-perishable, and that can be treated in a thin stream, these unfavorable aspects become much less important. For example, direct acceleration methods could process huge quantities of grain streams quite successfully.

Table 5.1. Comparison of Accelerator Approaches

Accelerator Approach	KE 2–10 MeV	Power 5–200 kW	Cap. Cost	Oper. Cost	Size	Maint.	Down-Time
Van de Graaff	N	F	N	F	U	F	U
Pelletron	N	F	N	F	U	F	U
Trans. Rectifier	U	N	F	F	U	N	U
Res. Transformer	U	F	F	F	U	N	U
Dynamitron	N	F	N	F	U	F	U
Induction Linac	F	F	U	N	U	N	F
Betatron	F	U	F	N	F	N	N
ILU Cavity	N	F	F	N	F	N	F
Microwave Linac	F	F	F	N	F	N	F
Circular Microtron	F	N	F	N	F	N	F
Rhodotron	F	F	N	N	N	N	F

Of the induction methods, the average power of the betatron appears to be too low to be of use. In contrast, the average power of the induction linac approach can be quite high, but use of this expensive technology would only be warranted for applications requiring very high processing rates and/or high doses.

Apart from the circular microtron, which has limited average power capability, the various microwave accelerator approaches have the flexibility to process almost every type of food product in an efficient, effective manner in facilities of reasonable size and cost. In the next two chapters we will examine key features of these approaches in more detail.

5.3. SUMMARY

For almost all food irradiation applications, the required kinetic energy lies in the range of 2–10 MeV, while the required average power generally lies in the range of a few kilowatts to a few hundred kilowatts. In addition to these basic requirements, other important considerations in the choice of an accelerator system include size, cost, operating efficiency, ease of maintenance, and reliability.

The several electron acceleration approaches that might be considered for food irradiation can be generally grouped into three categories: (1) direct methods, in which the accelerating field results from the direct application of a high potential difference across an insulating column; (2) induction methods, in which the accelerating field results from a time-changing magnetic field; and (3) microwave (or radio-frequency) acceleration methods, in which acceleration results from oscillating electromagnetic fields established in a resonant microwave cavity structure.

The direct acceleration methods are generally deemed less favorable for food processing applications because of their large size and the significant downtime required for repair or replacement of the high-voltage insulating column. Of the induction methods, the average power of the betatron is too low, while the induction linac approach is quite expensive. However, several microwave accelerator approaches appear to have the flexibility to process almost every type of food product in an efficient, effective manner in facilities of reasonable size and cost.

REFERENCES

1. M. S. Livingston and J. P. Blewett, **Particle Accelerators**, McGraw-Hill, NY (1962).
2. W. Scharf, **Particle Accelerators and Their Uses**, Harwood Academic, NY (1985).
3. S. Humphries, Jr., **Principles of Charged Particle Acceleration**, John Wilely and Sons, NY (1986).

4. C. J. Karzmark, C. S. Nunan and E. Tanabe, **Medical Electron Accelerators**, McGraw-Hill, NY (1993).
5. S. Humphries, Jr., "High-average-power electron accelerators for food processing," in **High Brightness Accelerators**, A. K. Hyder, M. F. Rose and A. H. Guenther, eds. NATO ASI Series Vol. 178, Plenum (1986), p. 659–715.
6. "Options Analysis: Machine Sources for Food Irradiation," CH2M Hill, **DE-AC04-87AL37414** (US Dept. of Energy) (1988).
7. J. H. Bly, **Electron Beam Processing**, Int'l. Inform. Assoc., Yardley, PA (1988).
8. R. J. Van de Graaff, K. T. Compton and L. C. van Atta, Phys. Rev. **43**, 149 (1933).
9. R. G. Herb, "Pelletron accelerators for very high voltage," Nucl. Instr. Meth. **122**, 267–276 (1974).
10. J. D. Cockcroft and E. T. S. Walton, Proc. Roy. Soc. (London) **A136**, 619 (1932).
11. R. J. Adler, "Nested high voltage generator/particle accelerator," U.S. Patent No. 5,124,658 (1992).
12. C. C. Thompson and M. R. Cleland, Nucl. Instr. Meth. Phys. Res. **B40/41**, 1137 (1989).
13. N. C. Christofilos, "The ASTRON Concept", **UCRL-52000-78-5**, 1 (1978).
14. D. L. Goodman, D. L. Birx, and V. R. Dave, "High Energy Electron Beam Processing Experiments with Induction Accelerators," Nucl. Instr. Meth. Phys. Res. **B79**, 865 (1993).
15. C. R. McClenahan, L. E. Martinez, G. E. Pena, and G. J. Weber, "Repetitive, Electron-Beam Diode Development, **SAND93–01796** (1993).
16. D. W. Kerst, Phys. Rev. **60**, 47 (1941).
17. A. I. Pavlovskii, G. D. Kuleshov, A. I. Gerasimov, V. O. Klementev, V. A. Kuznetsov and A. D. Tarasov, Sov. Phys. Tech. Phys. **22**, 218 (1977).
18. V. L. Auslender, A. A. Bryazgin, B. L. Faktorovich, V. A. Gorbunov, M. V. Korobeinikov, S. A. Maksimov, V. E. Nekhaev, A D. Panfilov, V. O. Tkachenko, A. A. Tuvik, and L. A. Voronin, Vestnik "Radtech Euroasia" **N2(10)**, Novosibirsk (1999).
19. E. L. Ginzton and C. S. Nunan, Int. Journal Rad. Onc. Biol. Phys. **11**, 205 (1985).
20. S. P. Kapitsa and V. N. Melekhin, **The Microtron**, Harwood Academic, London (1978).
21. J. Schwinger, Phys. Rev. **75**, 1912 (1949).
22. Y. Jongen, M. Abs, F. Genin, A. Nguyen, J. M. Capdevila and D. Defriese, Nucl. Instr. Meth. in Phys. Res. **B79**, 865 (1993).

CHAPTER 6

PRINCIPLES OF ELECTRON ACCELERATION IN MICROWAVE ACCELERATORS

In this chapter we discuss the essential concepts involved in the generation and acceleration of electron beams in microwave accelerator structures. Specifically, we discuss the motion of electrons in dc and oscillating fields, the formation of a beam in an electron gun, the properties of resonant electromagnetic cavities and coupled-cavity linac structures, and methods for coupling power from a microwave source into an accelerating structure.* Finally, with the aid of numerical simulations we illustrate explicitly how the confined microwave fields are used to accelerate electrons.

6.1. ELECTRON ACCELERATION

The time rate of change of the momentum **p** of a particle subject to a force **F** is given by Newton's second law according to $d\mathbf{p}/dt = \mathbf{F}$. For a particle of charge q, the force is given by the Lorentz law as

$$\mathbf{F} = q(\mathbf{E} + \mathbf{v} \times \mathbf{B})$$

in which **E** and **B** denote the electric and magnetic field vectors, and **v** is the particle velocity vector. For an electron, $q = -e$, with the unit electron charge equal to 1.6×10^{-19} coulombs. Electrons have a small rest mass m of 9.1×10^{-31} kg. Consequently, they become relativistic with only modest acceleration, and it is necessary to use the relativistic particle momentum in describing their motion, with **p** related to the electron velocity by $\mathbf{p} = \gamma m\mathbf{v}$. $\gamma = (1-\beta^2)^{-1/2}$ and $\beta = |\mathbf{v}|/c$ are the usual relativistic factors. The relativistic equation of motion for an electron is therefore

$$d(\gamma m\mathbf{v})/dt = -e(\mathbf{E} + \mathbf{v} \times \mathbf{B}) \tag{6.1}$$

It is instructive to take the vector dot product of the electron velocity with both sides of Eq. (6.1). The result is that

$$d(\gamma mc^2)/dt = -e\,\mathbf{v}\cdot\mathbf{E} \tag{6.2}$$

From the special theory of relativity the quantity in parentheses is identified as the total energy of the electron. Since the rest mass energy of the electron is $mc^2 = 0.511$ MeV, the energy associated

---

* Only normally conducting structures will be considered. At the present time, the high capital cost of superconducting technology is not justified for the low electron kinetic energies appropriate for food irradiation.

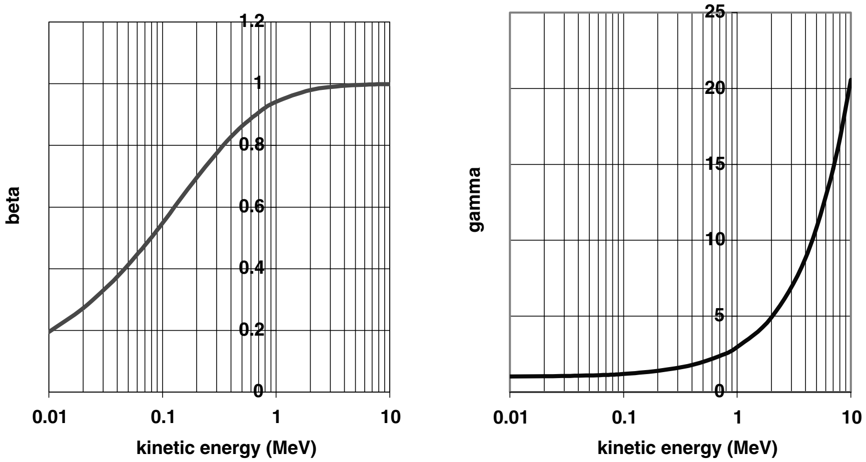

Figure 6-1. Variation of the relativistic beta and gamma factors with electron kinetic energy.

with the electron motion, the kinetic energy, must be $(\gamma - 1)mc^2$. The variation of γ and β with electron kinetic energy are shown in Figure 6-1. Note also that only an electric field in the direction of the electron motion can change its kinetic energy. Since the vector formed by $\mathbf{v} \times \mathbf{B}$ is necessarily perpendicular to the velocity, a static magnetic field can only deflect an electron.

6.1.1. Acceleration in a Constant, Uniform Electric Field

We first consider the acceleration of an electron in an acceleration gap of width d to which a constant voltage V_o has been applied. The geometry is schematically shown in Figure 6.2. The electron is assumed to enter the gap at time $t = 0$ with an initial velocity v_o (and kinetic energy $(\gamma_o - 1)mc^2$) in the direction opposite the electric field vector of magnitude $E_o = V_o/d$. Eq. (6.1) therefore becomes

$$d(\beta\gamma)/dt = (e/mc)E_o$$

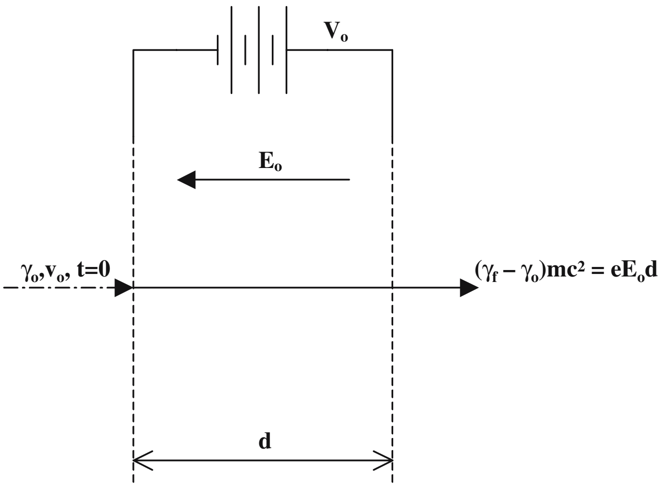

Figure 6-2. Electron acceleration in a constant, uniform electric field.

Performing the indicated integration yields

$$\beta\gamma = \beta_o\gamma_o + (e/mc)E_ot \tag{6.3}$$

When relativistic effects are important, it is the quantity $\beta\gamma = (\gamma^2 - 1)^{1/2}$ that increases linearly with time, not the electron velocity.

Recognizing that the kinetic energy gain on crossing the gap is eE_od, Eq. (6.3) can be used to determine the electron transit time. If the electron enters the gap with an initial kinetic energy in excess of 1 MeV, the transit time τ is essentially d/c. At the other extreme, if the initial velocity is nearly zero, then the transit time is approximately

$$\tau = (d/c)[1 + 2mc^2/(eE_od)]^{1/2} \tag{6.4}$$

6.1.2. Acceleration in Oscillating Fields

We now consider the case in which the applied voltage is oscillatory, and the electric field amplitude can be represented as

$$E_z = E_o \sin \omega t \tag{6.5}$$

Assuming that the electron velocity does not change appreciably while crossing the gap, then the kinetic energy gain (or loss) from Eq. (6.2) depends on the entry and exit times t_o and t_l according to

$$\Delta\gamma mc^2 = (evE_o/\omega)[\cos \omega t_l - \cos \omega t_o] \tag{6.6}$$

Referencing t_o and t_l to the time t_c that the electron is at the center of the cavity, we have $t_o = t_c - d/(2v)$ and $t_l = t_c + d/(2v)$, and the term in square brackets can be written as

$$\cos(\omega t_c + \theta_g/2) - \cos(\omega t_c - \theta_g/2)$$

with the gap transit angle defined as $\theta_g = \omega d/v$. Using the trigonometric identity $\cos(a + b) = \cos(a)\cos(b) - \sin(a)\sin(b)$, Eq. (6.6) can be written as

$$\Delta\gamma mc^2 = eE_odT \sin(\omega t_c) \tag{6.7}$$

with T, the transit time factor of the gap, defined as

$$T = [\sin(\theta_g/2)]/(\theta_g/2) \tag{6.8}$$

Maximum acceleration occurs when $\omega t_c = \pi/2$, which can nearly always be arranged for electrons; however, because of the transit time factor, the energy gain in the sinusoidally varying electric field is less than the energy gain (eE_od) in the corresponding dc field. The transit time factor is plotted versus (θ_g/π) in Figure 6-3. As a numerical example, for a 3-GHz pillbox cavity having a width of 5 cm, the transit angle for a relativistic electron is equal to π, and the transit time factor has a value of only 0.64.

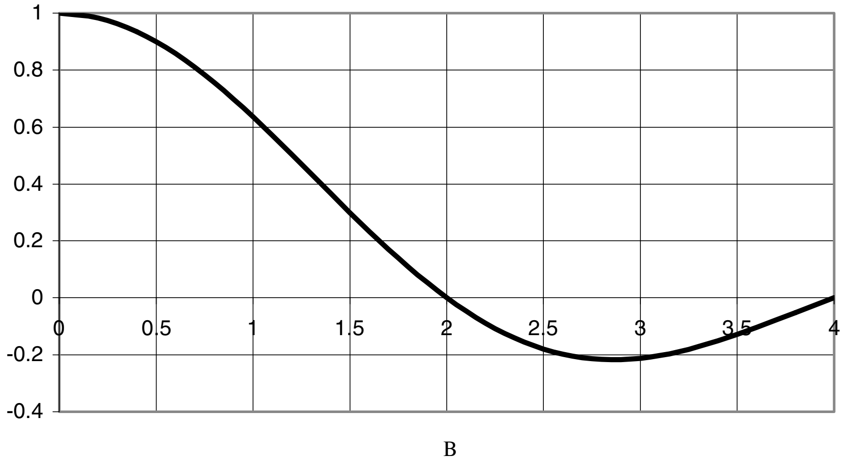

Figure 6-3. Transit time factor as a function of normalized transit angle.

6.2. ELECTRON BEAM GENERATION[1]

The beam current in a microwave accelerator is relatively modest (typically of the order of one ampere or less), and is therefore almost always supplied by a thermionic cathode in a cylindrically symmetric electron gun configuration, as schematically shown in Figure 6-4. Electrons emitted from the cathode surface are accelerated by an applied voltage of typically several tens of kilovolts and geometrically focused through an aperture in a grounded anode. If it is necessary to control the beam current without varying the anode-cathode (A-K) voltage, a control grid may be interposed between the cathode and anode.

The factors that are primarily responsible for determining the cathode emission characteristics include the energy band structure of the material, the temperature, the magnitude of an applied electric field, and the influence of the electron space charge in the diode region. The details of the resulting electron flow depend on the diode geometry, the applied voltage and the presence or absence of a

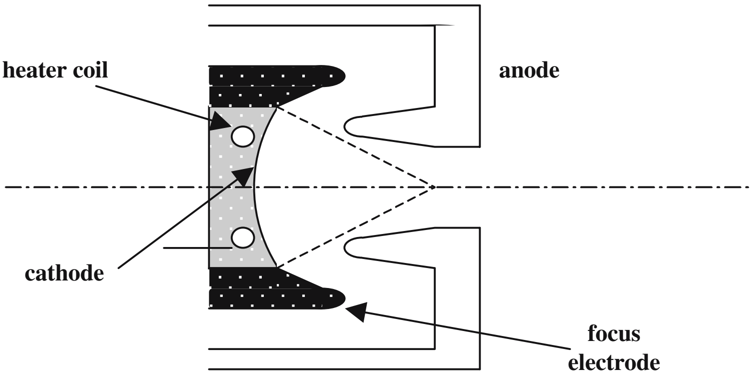

Figure 6-4. A cross-sectional view of a Pierce-type convergent diode electron gun[2] consisting of a spherically shaped cathode with an embedded heater coil, a focus electrode, and a specially-shaped anode with a central aperture. The angle between the outermost electron trajectory and the focus electrode is 67°.

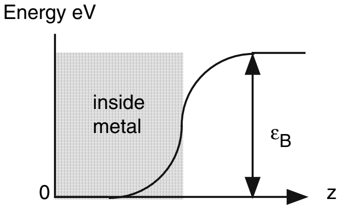

Figure 6-5. The metal interior can be conveniently regarded as an equipotential volume, with the zero energy level corresponding to the bottom of the conduction band. The potential barrier of height ε_B prevents electron emission from the surface. The magnitude of ε_B equals the sum of the Fermi level plus the work function.

magnetic field. In this section we briefly summarize the important features of the emission process, operation in temperature-limited and space-charge limited regimes, and the resulting electron flow.

6.2.1. Thermionic Emission

It is convenient to consider the interior of a metal as an equipotential volume with a potential barrier at the surface, as suggested in Figure 6-5. Since only differences in potential have physical meaning, we can assume that the zero energy level represents the bottom of the conduction band. The kinetic energies of the free electrons in the conduction band are therefore always positive with respect to this level.

Since electrons obey the Pauli exclusion principle, the probability that an electron has a particular energy ε is specified by the Fermi-Dirac distribution function given by

$$f(\varepsilon) = \{1 + \exp[(\varepsilon - \varepsilon_f)/kT]\}^{-1} \tag{6.9}$$

in which $k = 1.38 \times 10^{-23}$ J/°K is the Boltzmann constant, T is the absolute temperature (°K), and ε_f is termed the Fermi level.

The energy difference between the Fermi level and the barrier height is called the work function ε_w; ε_w lies in the range of 2–6 eV for most metals. Emission of an electron from the surface can occur if the electron kinetic energy exceeds $\varepsilon_B = \varepsilon_f + \varepsilon_w$. At temperatures above absolute zero there are always some electrons having energies greater than ε_f. With sufficient heating it is therefore possible to create a significant electron population with energies in excess of $\varepsilon_w + \varepsilon_f$.

The current density j produced by heating the metal can be computed by integrating the electron flux incident on the metal surface from the interior over all energies exceeding the surface potential barrier. The result is

$$\begin{aligned} j &= -(4\pi emk^2/h^3)T^2 \exp(-\varepsilon_w/kT) \\ &= -1.2 \times 10^6\, T^2 \exp(-\varepsilon_w/kT) \text{ amps/m}^2 \end{aligned} \tag{6.10}$$

This equation is known as the Richardson-Dushman equation for thermionic emission. In practice it is found that the temperature dependence of thermionic emission closely follows Eq. (6.10), but that the value of the numerical constant is typically a factor of two to four lower. This decrease is usually attributed to two factors: (1) a variation of the work function over the emission surface, and (2) a variation in the work function with temperature.

Eq. (6.10) indicates that obtaining high electron emission rates requires high temperatures and low work functions. Unfortunately, the pure metals that have low work functions are unusable because they also have low melting temperatures. It is possible, however, to reduce the work functions of some high-melting-temperature metals, such as tungsten and osmium, by introducing surface impurities such as barium and oxygen. While complex, the surface chemistry responsible for reducing the work function is now reasonably well understood. The oxides most often used are BaO, SrO, and CaO. To make these coating materials suitable for use they must first be "activated", i.e., heated to a temperature somewhat higher than the normal operating temperature. During this process, the oxides are partially reduced giving rise to free barium.

Such metal oxide cathodes have proven to be quite useful, delivering current densities on the order of 1 amp/cm^2 at relatively low temperatures (800 °C), but they do have drawbacks: (1) the coating is usually quite resistive, (2) they tend to blister, (3) they can be destroyed by back-bombardment, and (4) they can be easily poisoned by residual gases. These limitations have led to the development of the so-called dispenser cathode. Although there are many varieties of dispenser cathode, the common feature is a porous tungsten matrix through which barium can diffuse to the surface. For example, in the Philips B-type cathode the porous tungsten is impregnated with a compound of BaO, CaO and Al_2O_3 in the ratio of 5:3:2. With a mix of 4:1:1, the cathode is known as an S-type cathode. These cathodes are rugged, and can provide an emission density of several tens of amps/cm^2 when operated at temperatures of about 1100 °C. The lifetime of a dispenser cathode depends on the availability of free barium that can migrate to the surface, which in turn depends on the cathode temperature. A thin surface overcoating of osmium, iridium, or ruthenium can lower the work function by almost 20%. This reduces the operating temperature for a given current density by almost 100 °C, resulting in extending the cathode life by about a factor of ten.

6.2.2. Space-Charge-Limited Operation

The characteristic variation of the current density from a thermionic cathode is plotted as a function of temperature in Figure 6-6. At low temperatures the current increases with temperature according to the Richardson-Dushman law and is said to be temperature-limited (TL). As the temperature is further increased, however, the current becomes nearly independent of temperature. The phenomenon that limits the current is the electron space charge in the diode. Electron guns in microwave accelerators are almost always operated in this space-charge-limited (SCL) mode because it eliminates the need for precise temperature and work function uniformity over the cathode surface. It also eases voltage and current stability requirements for the cathode heater.

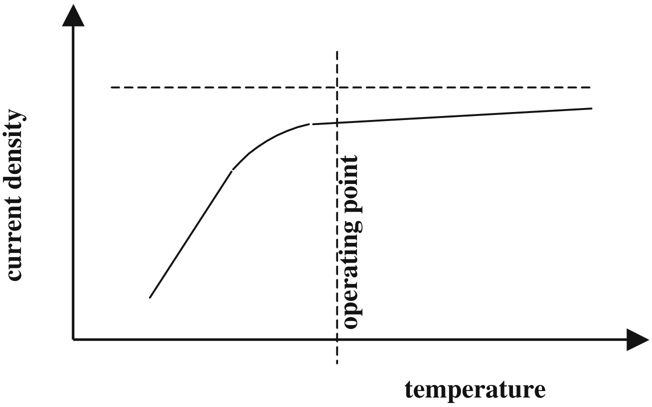

Figure 6-6. Variation of the emission current density from a thermionic cathode as a function of temperature. The operating point is usually chosen to be in the flat, space-charge-limited region of the curve.

The space-charge-limiting current for a particular electron gun geometry can be derived by assuming that the electric field *vanishes* at the cathode surface, and that the emitted electrons have zero initial velocity. The velocity of an electron at any position between the electrodes can then be determined from energy conservation. Solving Poisson's equation for a one-dimensional, planar, non-relativistic electron gun, the resulting current density is given as

$$\begin{aligned} j &= -(4/9)\varepsilon_o(2e/m)^{1/2}(V^{3/2}/d^2) \qquad (6.11)\\ &= -2.33\times10^{-6}(V^{3/2}/d^2)(\text{amps}/\text{m}^2) \end{aligned}$$

Eq. (6.11) is the familiar one-d Child-Langmuir law; it is accurate to within 10% for voltages up to approximately 1 MeV.

6.2.3. Electron Gun Design

Multiplying Eq. (6.11) by the effective cathode emission area A, the Child-Langmuir equation is commonly written in the form

$$I = PV^{3/2} \qquad (6.12)$$

with $I = jA$. P, the diode perveance, is a numerical factor that depends only on the diode geometry. For the low current guns used in microwave accelerators, the gun is usually based on a convergent design due to Pierce, in which the electron flow is assumed to occur between an outer sphere (the cathode) and an inner sphere (the anode nose cone). Let the radius of curvature of the cathode be R_c, and the equivalent radius of the anode nose cone be R_a. Further, let θ denote the half-angle arc of the spherical cathode. Then the perveance is approximately given by

$$P = 14.7\times10^{-6}(1-\cos\theta)\alpha^{-2} \qquad (6.13)$$

where $\alpha = a + 0.3a^2 + 0.075a^3$, and $a = \ln(R_c/R_a)$. As a numerical example, if $\theta = 12$ degrees and $R_a = 0.4R_c$, then $P = 2.1\times10^{-7}$. An applied voltage of 25 kV would therefore yield a beam current of about 0.84 amps.

A numerical solution using the EGUN code[3] for the electron trajectories in an electron gun with geometrical parameters similar (but not identical) to those above is shown in Figure 6-7. The beam current is 1.33 amps at an applied voltage of 32.5 kV, giving a perveance of 2.3×10^{-7}.

6.3. RESONANT ELECTROMAGNETIC CAVITIES

Electromagnetic radiation is characterized by frequency f and wavelength λ, with the two parameters being related by the speed of light c according to $f = c/\lambda$. With $c = 3\times10^8$ m/s, the wavelength in centimeters is given by $\lambda = 30/f$, with f in gigahertz (GHz). The several regions of the electromagnetic spectrum are described in Figure 6-8, according to frequency and wavelength, and origin.

The longest wavelengths (radio waves) are produced by oscillating electric currents, while infrared wavelengths (heat) are produced by molecular vibrations. The term "microwave" generally describes that portion of the short radio waves having frequencies ranging from about 300 MHz to about 100 GHz. The narrow visible and ultra-violet wavelengths are produced by a rearrangement of the electrons in outer atomic shells. X-rays can be produced by rearrangements of electrons in

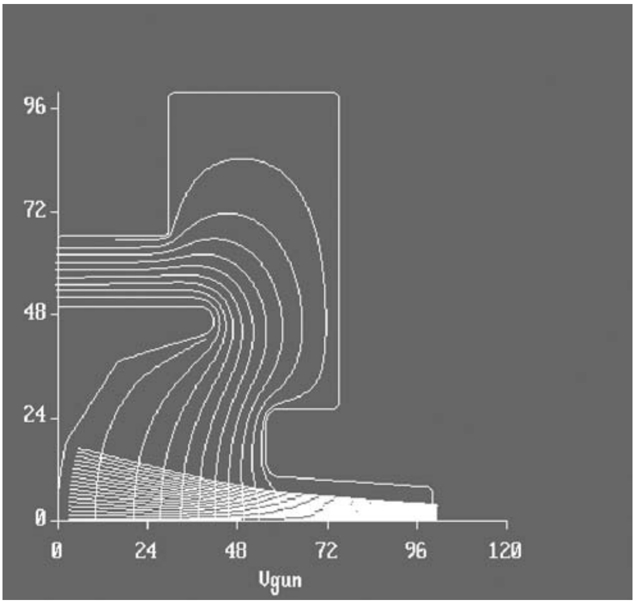

Figure 6-7. Electron flow trajectories in a space-charge-limited electron gun, as computed by the EGUN code. With 32.5 kV applied voltage, the gun generates 1.33 amps.

the inner atomic shells and by the abrupt slowing of energetic electrons (bremsstrahlung, or braking radiation). Gamma rays are produced by the de-excitation of radioactive nuclei.

Electromagnetic waves in the radio-frequency range can be confined in metallic cavities, and this fact permits the construction of radio-frequency (rf) accelerators. This is achieved using resonant electromagnetic cavities and coupled-cavity linac structures. In the remainder of this section we consider resonant cavities; in the following section we will consider coupled-cavity linac structures.

6.3.1. Maxwell's Equations

The underlying principle of electromagnetic radiation is that a time-changing magnetic field will induce an electric field, and a time-changing electric field will induce a magnetic field. The mathematical expression of this symmetry is embodied in the time-dependent Maxwell equations. Assuming vacuum conditions and no free charges or currents, the differential form of these equations is given below, with bold-faced type denoting vector quantities:[4]

$$\nabla \times \mathbf{E} + \partial \mathbf{B}/\partial \mathrm{t} = 0 \tag{6.14}$$

$$\nabla \times \mathbf{H} - \partial \mathbf{D}/\partial \mathrm{t} = 0 \tag{6.15}$$

The variables in these equations are identified as follows:

E is the electric field intensity in volts/meter,
D is the electric displacement in coulomb/meter^2,
B is the magnetic induction in weber/meter^2, and
H is the magnetic field intensity in amperes/meter.

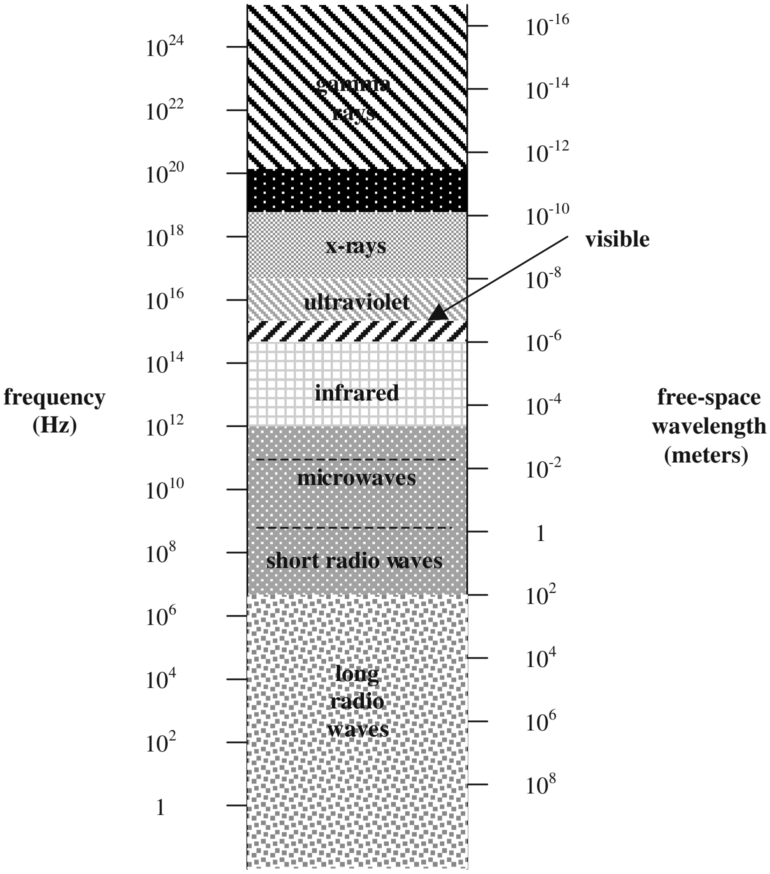

Figure 6-8. The electromagnetic spectrum.

In a vacuum, these fields are related according to $\mathbf{D} = \varepsilon_o\mathbf{E}$, and $\mathbf{B} = \mu_o\mathbf{H}$, with $\varepsilon_o = 8.85 \times 10^{-12}$ farads/meter being the permittivity of free space, and $\mu_o = 1.26 \times 10^{-6}$ henry/meter being the permeability of free space. It may be verified that the speed of light $c = (\varepsilon_o\mu_o)^{-1/2} = 3 \times 10^8$ m/s.

Assuming a time dependence of the fields in the form of $e^{j\omega t}$, the time derivative can be replaced by $j\omega$. In the frequency domain, Maxwell's equations then become

$$\nabla \times \mathbf{E} = -j\omega\mu_o\mathbf{H}$$

$$\nabla \times \mathbf{H} = j\omega\varepsilon_o\mathbf{E}$$

Taking the curl of Eq. (6.14) on both sides, and using Eq. (6.15) for the curl of **H** gives

$$\nabla \times \nabla\mathbf{E} = -j\omega\mu_o\nabla \times \mathbf{H} = \omega^2(\varepsilon_o\mu_o)\mathbf{E} \tag{6.16}$$

The vector identity for the curl of the curl of the electric field vector is expressed by

$$\nabla \times \nabla \times \mathbf{E} = -\nabla^2\mathbf{E} + \nabla(\nabla \cdot \mathbf{E}) \tag{6.17}$$

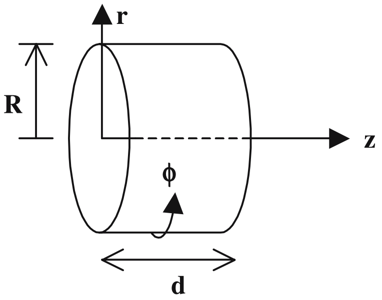

Figure 6-9. Coordinate system for a cylindrical cavity resonator.

In free space there is no free charge density and the latter term is zero. Therefore, the wave equation for the electric field becomes

$$\nabla^2 \mathbf{E} = -\omega^2(\varepsilon_o \mu_o)\mathbf{E} = -(\omega/c)^2 \mathbf{E} \tag{6.18}$$

A similar equation can be derived for the magnetic field intensity.

6.3.2. Normal Modes of a Pillbox Cavity[5]

These electromagnetic waves can be confined in high-conductivity cavities, with wave energy being continuously interchanged between the magnetic and electric fields. There are normal modes of oscillation that depend on the boundary conditions, and each mode has a definite resonant frequency. Consider the cylindrical (pillbox) cavity shown in Figure 6-9, having radius R and width d. In cylindrical coordinates, the "del squared" operator of Eq. (6.18) becomes

$$\nabla^2 = r^{-1}\frac{\partial}{\partial r}\left(r\frac{\partial}{\partial r}\right) + r^{-2}\frac{\partial^2}{\partial \phi^2} + \frac{\partial^2}{\partial z^2} \tag{6.19}$$

Of particular interest for particle acceleration are those normal modes having an electric field that is a maximum along the axis of symmetry. Solutions to Eq. (6.18) for the axial component E_z that satisfy the boundary condition $E_z = 0$ at $r = R$ are the Bessel functions J_n of the first kind of order n. Sinusoidal functions satisfy the differential operator in the axial and azimuthal coordinates. It may be verified that the functions given in Eq. (6.20) are solutions of Eq. (6.18). It may also be verified that for these solutions the axial component of the magnetic field is zero; these modes are therefore designated as transverse magnetic, or TM_{npq} modes. There is a complementary set of TE modes.

$$E_z = E_{oz}\, J_n(x_{np} r/R)\cos(n\phi)\cos(q\pi z/d) \tag{6.20}$$

where

$n = 0,1,2,\ldots$ is the number of the periodicity in the azimuthal direction
$p = 1,2,3,\ldots$ is the number of zeros of the field in the radial direction
$q = 0,1,2,\ldots$ is the number of zeros of the field in the axial direction
E_{oz} = amplitude of the electric field

Table 6.1. p^{th} Zeros of $J_n(x_{np}r/R)$ for TM_{np} Modes

p	n = 0	1	2
1	2.405	3.832	5.136
2	5.520	7.106	8.417
3	8.645	10.173	11.620
4	11.792	13.324	14.796

The resonant frequencies of the TM normal modes are determined by substituting Eq. (6.20) into Eq. (6.18). The result is (recall that $\omega = 2\pi f$)

$$(x_{np}/R)^2 + (q\pi/d)^2 = (\omega/c)^2 \quad \text{or,}$$
$$f = (c/2\pi)[(x_{np}/R)^2 + (q\pi/d)^2]^{1/2} \tag{6.21}$$

The lowest zeros of the $J_n(x_{np}r/R)$ Bessel functions are summarized in Table 6.1. Of special interest are those TM modes having no variation in either the azimuthal or axial directions ($n = q = 0$). The TM_{010} mode, for which E_z is zero only at $r = R$, has the lowest frequency of these modes; from Table 6.1, it is given by

$$f_{010}(\text{Hz}) = 2.405c/(2\pi R) = 1.15 \times 10^{10}/R(\text{cm}) \tag{6.22}$$

It is easily shown from Eq. (6.16) that the other field components of the TM_{010} mode are given as $E_r = E_\phi = H_r = H_z = 0$, and

$$H_\phi = jE_{oz}(\varepsilon_o/\mu_o)^{1/2} J_1(x_{01}r/R) \tag{6.23}$$

These field distributions are shown schematically in Figure 6-10.

For a cavity oscillating in a particular normal mode the electric and magnetic energies are equal and in time quadrature, meaning that when the electric energy is a maximum, the magnetic energy is zero, and vice versa. The total electromagnetic energy stored in the cavity can be obtained by integrating either the electric or magnetic energy density over the cavity volume. For the TM_{010} mode of the pillbox cavity this integration gives

$$U = (\pi\varepsilon_o/2)E_{oz}^2(dR^2)\, J_1^2(x_{01}r/R) \tag{6.24}$$

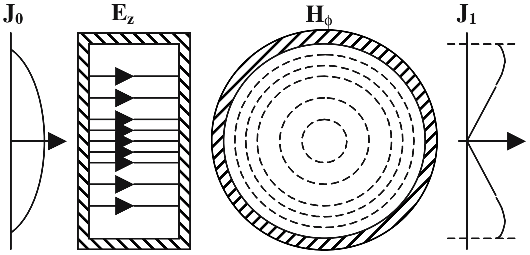

Figure 6-10. TM_{010} electric and magnetic field distributions in a cylindrical cavity.

Metals at room temperature have finite conductivity. A practical consequence is that the fields (and the surface currents that support them) can penetrate into the surface a characteristic distance, termed the "skin depth", giving rise to resistive losses. This average power loss can be evaluated by integrating the magnetic power density over the inner surface of the conductor. For the TM_{010} mode of the pillbox cavity this yields

$$P_c = \pi R(d + R)(\varepsilon_o/\mu_o)\rho_s E_{oz}^2 J_1^2(x_{01}r/R) \tag{6.25}$$

with ρ_s denoting the surface resistivity. A measure of the relative energy damping of a resonant cavity is the term "Q", or quality factor, defined as follows:

$$Q = \omega \times (\text{stored energy/average power loss})$$

From Eqs. (6.24) and (6.25), the Q of the pillbox resonator is therefore given by

$$Q = (\mu_o \pi f R)/[\rho_s(1 + R/d)] = 1.2\mu_o c/[\rho_s(1 + R/d)] \tag{6.26}$$

The cavities of practically all microwave accelerators are made of high-conductivity copper which has a surface resistivity approximately given by $\rho_s = 2.61 \times 10^{-7} f^{1/2}$, with ρ_s in ohms for f in Hz.[6] Therefore, the Q of a copper pillbox cavity resonating in the TM_{010} mode is approximately given as

$$Q = 1.73 \times 10^9 f^{-1/2}(1 + R/d)^{-1} \tag{6.27}$$

For practical dimensions, Q is of the order of 10,000. Q always increases with increasing d. Also, since the frequency varies inversely with radius, the quality factor increases with frequency for large R/d. However, for R/d comparable to unity or less, Q slowly decreases with frequency. As a numerical example, we assume a frequency of 3 GHz, with a corresponding cavity radius of 3.83 cm. For a cavity width of 5 cm,* which would correspond to a nominal voltage gain of 500 kV at an average field stress of 100 kV/cm, the resulting quality factor is approximately 17,900. While this value is reasonably high, it can be further increased by shaping the cavity surfaces, as discussed in Section 6.3.4.

6.3.3. Circuit Model of a Resonant Cavity[5]

The oscillating character of the energy stored in the electric and magnetic fields in the cavity is closely analogous to the oscillations in a resonant LC circuit in which energy is alternately stored in the magnetic field of an inductor and the electric field of a capacitor. In fact, for a cavity oscillating in a single mode, the simplest model for describing the behavior of a resonant cavity is provided by a parallel RLC circuit driven by a current source, as schematically shown in Figure 6-11. The driving current I(t) produces a voltage V(t) across the parallel combination of inductance L, capacitance C, and shunt resistance R, that can be identified with the axial voltage ($E_o d$) in the cavity.

Equating voltages and summing the currents leads to the second order circuit equation

$$dI/dt = V/L + (dV/dt)/R + C(d^2V/dt^2) \tag{6.28}$$

---

* 5 cm is also the distance a relativistic electron will travel in half the oscillation period.

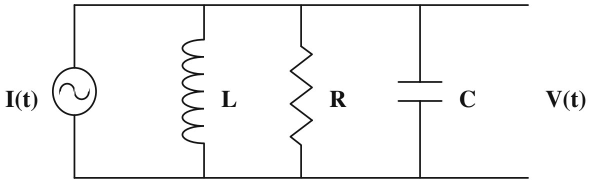

Figure 6-11. Parallel RLC model of a resonant cavity driven by a current source.

We note that the stored energy of the circuit is given by $U = CV_o^2/2$, while the dissipated power is $P = V_o^2/(2R)$, with V_o denoting the peak voltage.* Therefore, the Q of this circuit is just $Q = \omega_o RC$, with the resonant frequency defined as $\omega_o = (LC)^{-1/2}$.

Assuming a harmonic time dependence of the form $e^{j\omega t}$, Eq. (6.28) can be rewritten as

$$V = j\omega CI/[(\omega_o^2 - \omega^2) + j\omega\omega_o/Q]$$

and the shunt impedance of the circuit can be written as

$$Z = V/I = R(e^{j\phi})(1 + y^2)^{-1/2} \tag{6.29}$$

where $\phi = -\tan^{-1}y$, and the "detuning factor" y is defined by

$$y = Q(\omega/\omega_o - \omega_o/\omega) \tag{6.30}$$

The normalized shunt impedance Z/R is graphed in Figure 6-12, assuming $Q = 20{,}000$ and $\omega_o/2\pi = f_o = 3$ GHz.

The width of the resonance is defined as the difference between the frequencies at which the voltage falls to $2^{-1/2}$ of its maximum (the half-power points), which occurs when $y = 1$. Let $\delta\omega = |\omega - \omega_o|$ be the frequency difference corresponding to the half-power points. In the limit of large Q, y is approximately equal to $2Q\,(\delta\omega/\omega_o)$. Therefore, the resonance width $\Delta\omega$ can also be written in terms of the quality factor as

$$\Delta\omega = 2\delta\omega = \omega_o/Q \tag{6.31}$$

Consequently, measuring the resonant response of a microwave cavity provides a convenient method for determining the quality factor. For the example of Figure 6.12, the resonance width of the unloaded cavity is 150 kHz.

The general solution of Eq. (6.28) is the sum of a homogeneous solution and the particular solution, and can be written as[7]

$$V(t) = (ae^{j\omega_1 t} + be^{-j\omega_1 t})e^{-\omega_o t/(2Q)} + ZI(t) \tag{6.32}$$

where a and b are constants determined from the initial conditions, and

$$\omega_1 = \omega_o[1 - (2Q)^{-2}]^{-1/2}$$

---

* The accelerating cavity shunt impedance is usually defined as $R_s = 2R$.

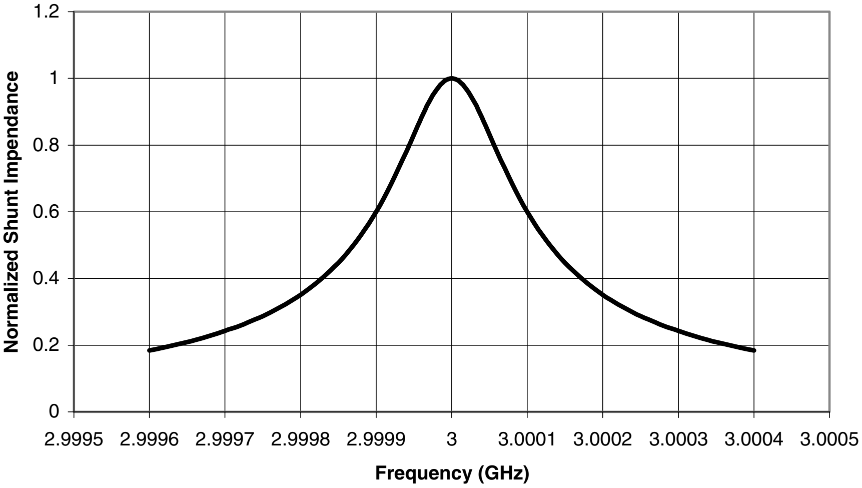

Figure 6-12. Response curve of a resonant cavity with $f_o = 3$ GHz and $Q = 20{,}000$.

At resonance, $y = \phi = 0$, and in the limit of large Q, $\omega_1 = \omega_o$. If a driving current I_o is applied at $t = 0$, when the voltage is initially zero, then $a = b = -RI_o/2$. Taking the real part of Eq. (6.32), the voltage is given by

$$V(t) = RI_o[1 - e^{-t/\tau}]\cos(\omega_o t) \tag{6.33}$$

with the time constant of the resonator being defined by $\tau = 2Q/\omega_o$. The voltage is oscillatory, and the amplitude of the oscillation increases over a few time constants to the value RI_o. If the driving current is abruptly reduced to zero, the voltage will also decrease to zero with the characteristic time constant τ.

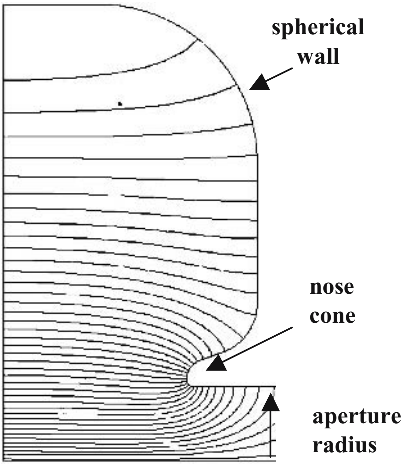

Figure 6-13. Generic shape of an accelerating cavity "half-cell" with the field lines as calculated by SUPERFISH.

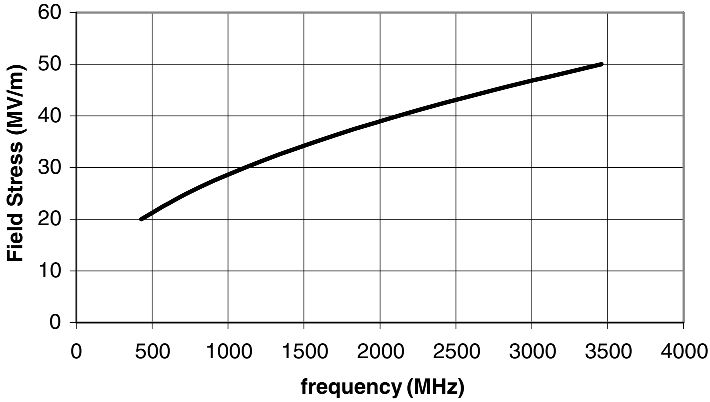

Figure 6-14. The limiting electric field stress, as given by the Kilpatrick criterion, Eq. 6.35.

6.3.4. Accelerating Cavity Design Issues

There are several factors to consider when designing resonant cavities for particle acceleration. In addition to resonating in the correct mode at the desired frequency, the transit time factor, shunt impedance, and peak field stress are all important design parameters. Recall that the shunt impedance is a measure of the effectiveness of producing an axial voltage $V = E_o d$ for a given power dissipation. For particle acceleration it is usually more important to maximize the particle energy gain per unit of power dissipation. Since the shunt impedance is defined in terms of the cavity power loss and voltage as $R = V^2/P$, the effective shunt impedance can be obtained by replacing V by (VT) to yield

$$R_e = (VT)^2/P = RT^2 \tag{6.34}$$

The effective shunt impedance per unit length is similarly given as $Z_e = ZT^2$.

The general shape of an accelerating cavity is shown in Figure 6-13. Beginning with the simple pillbox geometry, nose cones are added to concentrate the fields in the gap region, thereby increasing the transit time factor. Also, the outer walls are given a spherical shape, corresponding to the smallest surface area for a given volume, in order to increase the quality factor and the shunt impedance. The aperture of the nose cone must be large enough to guarantee low beam loss, although the transit time factor decreases with increasing aperture.

To avoid electrical breakdown (sparking) on the nose cones, it is necessary to limit the peak electrical stress. The Kilpatrick criterion,[8] given as Eq. 6.35 with the frequency f in MHz and E_k the limiting field stress in MV/m, is often used for this purpose.

$$f = 1.64 E_k{}^2 e^{-8.5/E_k} \tag{6.35}$$

The Kilpatrick criterion is graphed in Figure 6-14. Note that E_k increases with frequency. The peak design stress level is usually expressed as $E_s = bE_k$, with b termed the “bravery factor.” Since the Kilpatrick criterion is based on older experimental data obtained under relatively poor vacuum conditions (by today’s standards), b is typically 1.5 or greater, especially for pulsed systems with

Table 6.2. Typical SUPERFISH Cavity Design Output Data

Parameter	Value
Resonant Frequency	1318.35 MHz
Transit Time Factor (T)	0.80
Quality Factor (Q)	25861
Shunt Impedance per Unit Length	84.45 MΩ/m
ZT^2	54.5 MΩ/m
Peak to Average Field Ratio	3.82

macropulses less than one millisecond. Thus, for operation at 1.3 GHz, the design field stress is typically 45 MV/m, increasing to perhaps 65 MV/m at 3 GHz.*

Values of the key cavity design parameters can be obtained by solving Maxwell's equations subject to the appropriate boundary conditions, and there are now several good computer programs that perform these calculations, e.g., SUPERFISH.[9] As an example, the SUPERFISH output for a 1.3-GHz version of the cavity shown in Figure 6-13 is summarized in Table 6.2. Coupling slots (discussed in the next section) would lower the operating frequency by about 18 MHz. In practice, the quality factor as calculated by SUPERFISH is usually reduced by about 15% to account for surface irregularities, coupling slots, etc. In addition, a rule-of-thumb is that the shunt impedance will decrease by about 3% for every 1% increase in the coupling constant.

The nose cone shape used in Figure 6-13 produces a peak-to-average field ratio of 3.82. Assuming $b = 1.5$, and using a Kilpatrick limit of 32 MV/m from Figure 6-14, the maximum design field stress for this cavity is 48 MV/m, implying an average accelerating field of 12.5 MV/m. Multiplying by the transit time factor $T = 0.8$ from Table 6.2 gives a maximum effective gradient of 10 MV/m.

6.4. MULTIPLE-CAVITY ACCELERATING STRUCTURES

Multiple-cavity accelerators can be constructed from a series of independent cavities, with each driven by its own separate microwave source. Provided that the phase of the fields in each cavity can be independently adjusted so as to maintain phase synchronism of the fields with the accelerated bunches, such an approach allows for very flexible, and perhaps, high-average-power operation. With one accelerating gap per cavity, the cavity spacing in such an accelerator is simply $d = cT/2$ for relativistic electrons, with T being the microwave period. In fact, such independent-cavity linacs have been built, primarily for heavy ion acceleration (the UNILAC,[10] for example).

6.4.1. Comparisons of TW and SW Structures

With the powerful, pulsed microwave sources now available, however, it is usually far simpler to construct linear accelerating sections consisting of many coupled cavities, with each section driven by a single microwave source. There are two such structures in common usage: the traveling-wave (TW) linac, and the standing-wave (SW) linac. The TW structure consists of a cylindrical waveguide that is periodically loaded with conducting disks, as schematically shown in Figure 6-15. The microwave

---

* A resonant breakdown phenomenon termed electron "multipactoring" (implying multiple electron impacts) is almost never an issue for the accelerating cavities in high-gradient electron microwave accelerators, but it can be a problem in the low energy sections of ion accelerators, and in the low-field coupling cavities of electron linacs. It has been noted that the Kilpatrick voltage limit is approximately 2000 times the electron multipactor condition, suggesting that proton multipactoring might be the limiting mechanism in high-voltge rf breakdowns. See Reference 18 for more details.

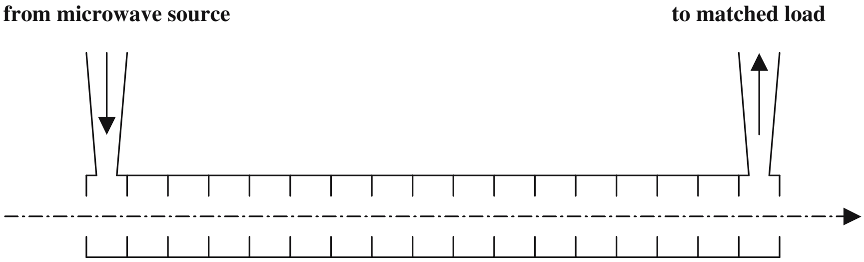

Figure 6-15. Schematic representation of a traveling wave linear accelerator.

power travels in one direction, from input to output. Internal reflections from the periodic disks reduce the wave phase velocity below the speed of light, enabling particle acceleration as the waves and particle bunches travel synchronously down the structure. The unused microwave power at the high-energy end is usually coupled into a matched resistive load. TW linacs can be designed to operate in either constant impedance or constant gradient modes. If the accelerating cavities defined by the disks are identical, then the impedance per unit length is constant, and the accelerating gradient decreases as the transmitted power droops. If a constant gradient is desired, the diameter of the disk apertures is gradually decreased down the structure. For modern TW linacs, the phase advance per cavity is chosen to be $2\pi/3$ (i.e., three cavities per wavelength).

In a SW linac both ends of the structure are effectively shorted, so that electromagnetic waves are reflected back and forth resulting in a standing wave pattern (as in a single resonant cavity). Both TW and SW structures can be thought of as series of individual resonators that are electromagnetically coupled. A TW linac is capacitively coupled through the disk apertures, which must be large and thin to obtain adequate coupling. In contrast, the SW linac uses inductive coupling through peripheral slots from one cavity to its neighbors. The spatial concentration of the electric field at the electron bunch is therefore better in the SW structure, and the transit time characteristics are usually somewhat more favorable. As a result, the rf efficiency is significantly higher for a SW waveguide for the same accelerating gradient, although the SW cavity surfaces must be machined with greater precision.

The TW structure is somewhat less complex, and usually less expensive per unit length to fabricate. It does not require an isolator or circulator, since it is a matched device, but it does require both input and output couplers. The larger radius apertures permit a somewhat higher beam current. On the other hand, since the cavities are much more tightly coupled, the SW accelerator is much more stable in phase with respect to temperature variations, and has much less tuning sensitivity. For applications in which physical space and rf power efficiency are important, and beam stability is essential, the SW accelerator offers a number of advantages, and it has become the linac structure of choice for most food irradiation applications. In the remainder of this section we discuss SW structures in some detail. For more details on TW structures, there are several excellent references for the interested reader.[6,7,11]

6.4.2. Inductively-Coupled Linac Structures

Most of the important features of an inductively coupled SW structure can be understood by extending the circuit model developed for the resonant cavity to the case of $N + 1$ coupled oscillators, with the currents in each oscillator corresponding to the fields in a cavity. To demonstrate the use of this model, consider the case of three coupled oscillators, shown in Figure 6-16.[7] The center oscillator (cavity or cell) has a total inductance of $2L_o$ and capacitance C_o, and a resonant

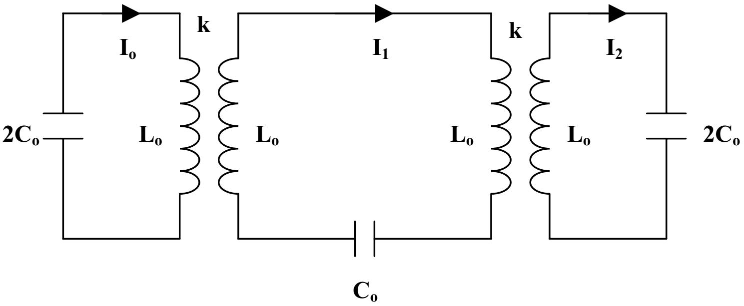

Figure 6-16. Modeling of three coupled cavities by three coupled resonator circuits.

frequency $\omega_o = (2L_oC_o)^{-1/2}$. The end oscillators (cavities) have half the inductance, but twice the capacitance.* The inductive slots that couple the cavities are modeled by a coupling constant $k = M/L_o$, with M being the mutual inductance.

Normalizing the current (field) I_n in the n^{th} oscillator according to $i_n = (2L_o)^{1/2}I_n$, and assuming a harmonic time dependence of the form $e^{j\Omega t}$, Kirchoff's equations for the three coupled circuits are

$$i_o(1 - \omega_o^2/\Omega^2) + i_1k = 0 \tag{6.36}$$

$$i_1(1 - \omega_o^2/\Omega^2) + (i_o + i_2)(k/2) = 0 \tag{6.37}$$

$$i_2(1 - \omega_o^2/\Omega^2) + i_1k = 0 \tag{6.38}$$

These three coupled equations can be written in matrix form as $AX_m = \Omega_m^{-2} X_m$, with the matrix operator A given as

$$A = \begin{bmatrix} 1/\omega_o^2 & k/\omega_o^2 & 0 \\ k/(2\omega_o^2) & 1/\omega_o^2 & k/(2\omega_o^2) \\ 0 & k/\omega_o^2 & 1/\omega_o^2 \end{bmatrix} \tag{6.39}$$

The eigenvectors X_m are given as

$$X_m = \begin{pmatrix} i_o \\ i_1 \\ i_2 \end{pmatrix} \tag{6.40}$$

and Ω_m^{-2} denote the corresponding eigenvalues. The three normal mode eigenfrequencies and their normalized eigenvectors are given by (in order of increasing frequency)

(1) m = 0; the zero mode, in which all oscillators have the same phase

$$\Omega_o = \omega_o(1 + k)^{-1/2}; \quad X_o = \begin{bmatrix} 1 \\ 1 \\ 1 \end{bmatrix} \tag{6.41}$$

---

* In an accelerating structure the end oscillators would correspond to "half-cells" with conducting planes placed at the symmetry plane of a full accelerating cavity, as suggested in Figure 6-13.

(2) m = 1; the π/2 mode, with a π/2 phase shift from oscillator to oscillator; note that the center oscillator is unexcited

$$\Omega_1 = \omega_o; \quad X_1 = \begin{bmatrix} 1 \\ 0 \\ -1 \end{bmatrix} \tag{6.42}$$

(3) m = 2; the π mode, with a π phase shift from oscillator to oscillator

$$\Omega_2 = \omega_o(1 - k)^{-1/2}; \quad X_2 = \begin{bmatrix} 1 \\ -1 \\ 1 \end{bmatrix} \tag{6.43}$$

This same calculation can be extended in straightforward fashion to a system of N + 1 coupled oscillators, consisting of N − 1 identical internal oscillators with half-cells on each end. In this case, the relative magnitudes of the eigenvector elements of the m^{th} mode in the n^{th} oscillator are

$$X_{m,n} = \cos(\pi mn/N); \quad n = 0, 1, \ldots, N \text{ (oscillator) and } m = 0, 1, \ldots N \text{ (mode)} \tag{6.44}$$

and the eigenfrequency of the m^{th} mode can be expressed by the dispersion relation

$$\Omega_m = \omega_o[1 + k\cos(\pi m/N)]^{-1/2} \tag{6.45}$$

The argument of the cosine is the phase advance per oscillator. The frequency of the zero mode is $\omega_o(1 + k)^{-1/2}$, while the π mode (m = N) has the highest frequency $\omega_o(1 - k)^{-1/2}$. The frequency of the m = N/2 mode, the π/2 mode, is always ω_o. Note that the difference in frequency between the zero mode and the π mode depends only on the coupling constant k. As the number of cavities increases, the normal mode frequencies become more closely spaced. The frequency separation between next nearest modes is always largest for the π/2 mode. The dispersion relation and the relative field amplitudes are shown in Figures 6-17 and 6-18 for the case of N = 6.

The coupled oscillator model can also be used to examine the effects of resistive power flow losses in the cavities. When such losses are included in the analysis, they introduce a relative phase shift (the power-flow phase shift) between adjacent oscillators for all modes except the π/2 mode. This phase shift depends inversely on the product of the quality factor Q and the coupling constant k. In the π/2 mode, however, the power flow does not produce this phase shift; rather, it produces a first-order excitation of the normally unexcited resonators, and a second-order decrease in amplitude in the excited resonators that increases with distance from the driven cavity. This power flow droop explicitly depends on $(kQ)^{-2}$.

When accelerating structures are manufactured, machining tolerances inevitably lead to slight variations in the resonant frequencies of individual cavity resonators. The effects of such frequency errors can be examined using perturbation theory, with the results being expressed in terms of an unperturbed eigenvector for a particular mode, plus small corrections from the other unperturbed eigenvectors, that depend on the magnitude of the errors and the coupling constant. The results of such perturbation calculations indicate that frequency errors lead to first-order corrections in the magnitudes of the cavity fields for all modes except the π/2 mode. In contrast, frequency errors for this mode give rise to first-order field corrections in only the resonators that are normally unexcited. The field errors in the normally excited resonators are of second order.

In summary, the π/2 mode has several attractive features for particle acceleration. These include power flow insensitivity, insensitivity to frequency errors, and good mode separation. However, if all

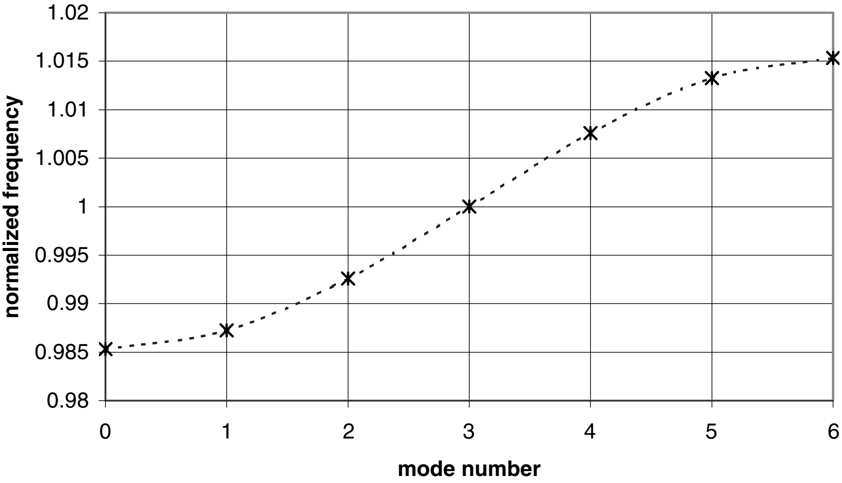

Figure 6-17. Dispersion relation for the case of N + 1 coupled oscillators with N = 6 and a coupling constant k = 0.03. The resonant frequency is normalized to f_o.

the cavity resonators are identical, either the gradient or the shunt impedance must decrease because the accelerating fields exist in only half the available length of the structure (Figure 6-18).

A practical way of implementing the π/2 mode is to form a biperiodic chain of cavities in which the geometry of the excited cavities is optimized for high shunt impedance, while the unexcited (coupling) cavities are designed to occupy a small amount of axial space (but still have the same resonant frequency). The two most popular such accelerator structures are the on-axis coupled linac[12] and the side-coupled linac,[13] shown schematically in Figure 6-19. For the on-axis structure the coupling cavities simply have a very short axial length; in the side-coupled structure, the coupling cavities are displaced from the axis. Both structures use magnetic coupling through slots cut in the cavity walls.

The coupled circuit model can also be used to analyze this biperiodic structure. Assuming N coupling cavities with resonant frequency ω_c interspersed in alternate fashion with N + 1 accelerating cavities with resonant frequency ω_a, the resulting dispersion relation can be written as[7]

$$k^2 \cos^2(m\pi/2N) = [1 - (\omega_a/\Omega_m)^2][1 - (\omega_c/\Omega_m)^2];\ m = 0, 1, \ldots, 2N \tag{6.46}$$

k is now the coupling constant between a coupling cell and an accelerating cell, and Ω_m is the frequency of the mth normal mode. For the π/2 mode (m = N), the right-hand-side of Eq. (6.46) is zero, and there are two solutions: $\Omega_N = \omega_a$, corresponding to excited accelerating cells; and $\Omega_N = \omega_c$, corresponding to excited coupling cells. Since this latter mode would correspond to unexcited end cells, it is not allowed for physical reasons.

The normal mode spectrum of a coupled cavity structure is obtained by exciting the structure with a swept-frequency signal and detecting the field in an end cell. A typical result for $\omega_c < \omega_a$ is shown in Figure 6-20 for a biperiodic structure consisting of seven accelerating cavities and six coupling cavities. The corresponding dispersion relation is shown in Figure 6-21. The frequency ranges above and below the discontinuity are termed the upper and lower pass bands. The region between ω_a and ω_c is termed the stopband, within which there are no solutions.

This case of $\omega_a > \omega_c$ is usually to be avoided because it can lead to thermal instability. The stopband can be eliminated by designing (or tuning) the cavities such that $\omega_a = \omega_c$, a condition

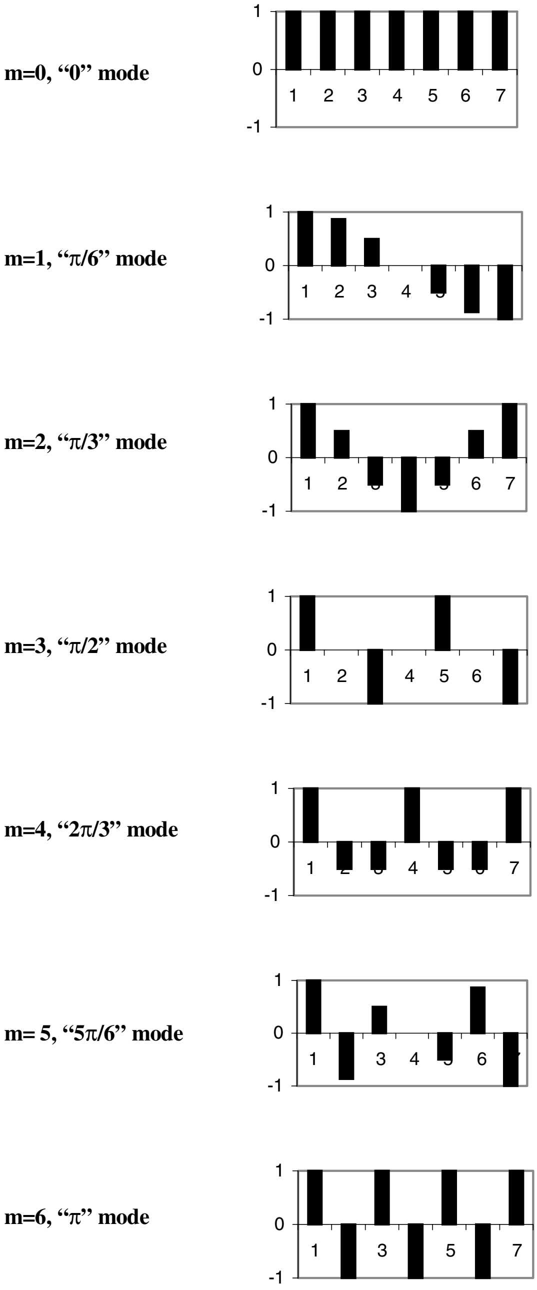

Figure 6-18. Relative amplitudes of the axial fields in a linac structure consisting of seven coupled cavities.

termed confluence. When this occurs, the slope of the dispersion curve increases to a maximum in the vicinity of the $\pi/2$ resonance, and the power-flow phase shift again vanishes. The dispersion relation for a biperiodic structure with 12 coupling cells and 13 accelerating cells in confluence is shown in Figure 6-22.[14]

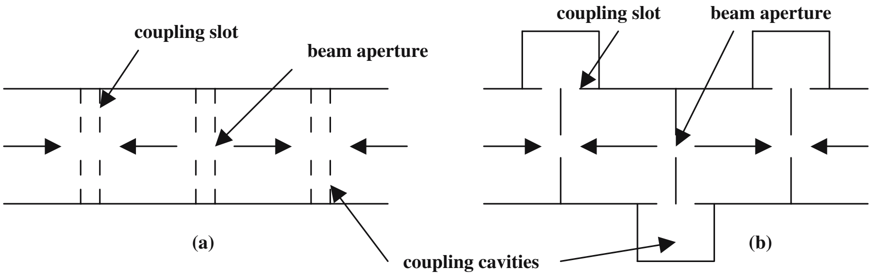

Figure 6-19. Schematic diagram of biperiodic SW accelerating structures: (a) axial-cavity coupling; (b) side-cavity coupling.

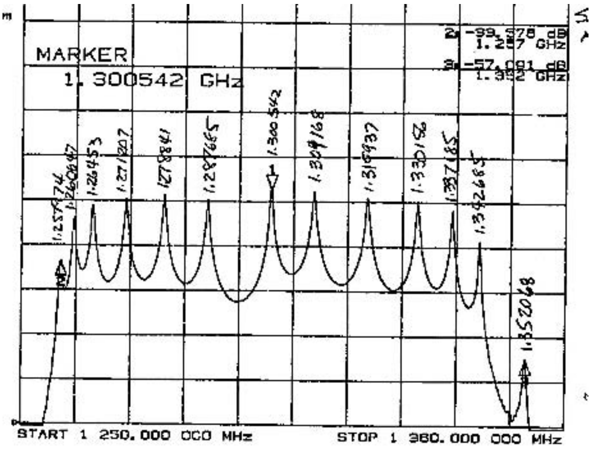

Figure 6-20. Normal mode spectrum for a 13-cell biperiodic structure with $\omega_c < \omega_a$.

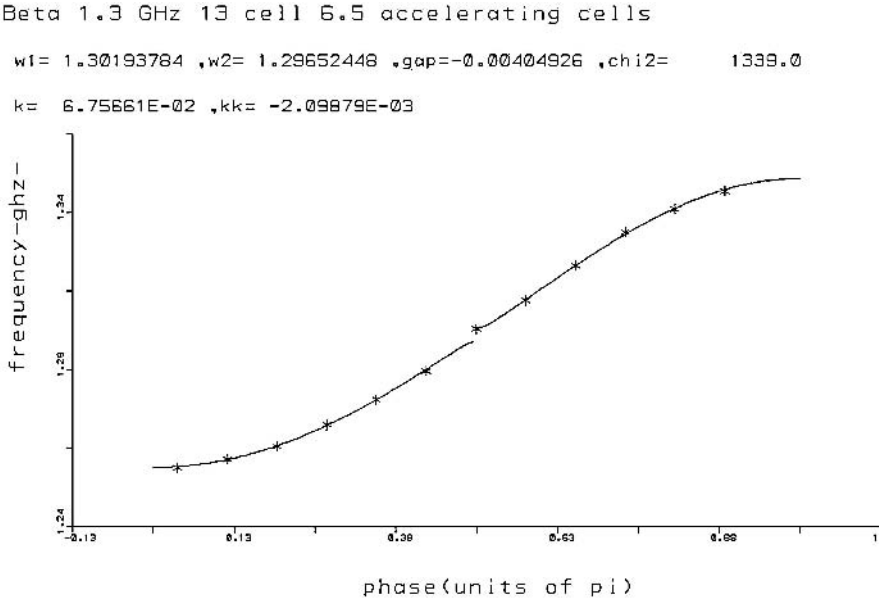

Figure 6-21. Dispersion relation for the 13-cell structure of Figure 6.20 with $\omega_c < \omega_a$. Note the 4-MHz stopband; the coupling constant is approximately 6.7%. The coupling constant between adjacent accelerating cells is only 0.2%.

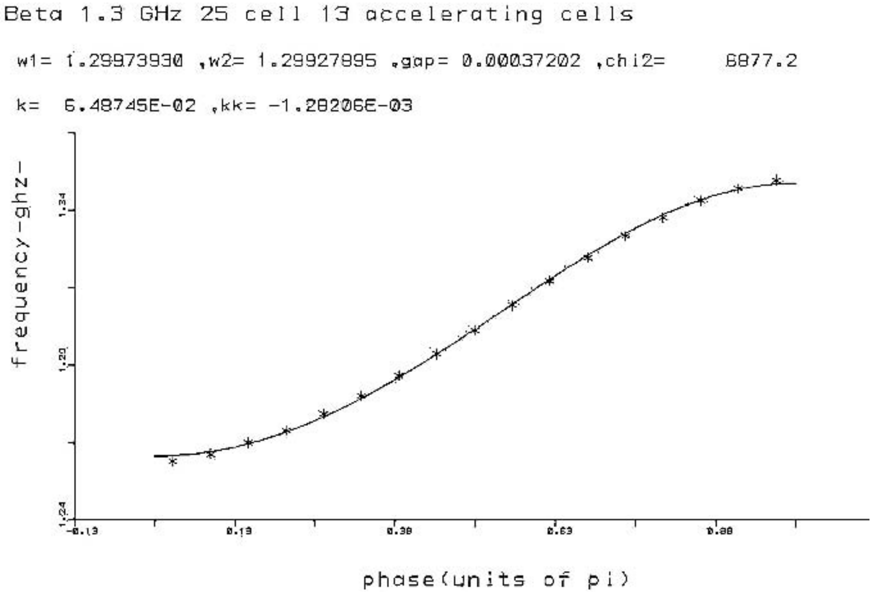

Figure 6-22. Dispersion relation for a 25-cell biperiodic structure that has been brought into confluence by tuning ($\omega_c = \omega_a$). There is no stopband, and the slope of the dispersion relation is largest in the vicinity of the $\pi/2$ resonance.

For relativistic SW structures the wave phase velocity (determined by the length of an accelerating/coupling cavity pair) is essentially equal to the speed of light. However, the group velocity is determined from the slope of the dispersion curve at the operating frequency. Since the group velocity is the velocity with which microwave energy propagates down the structure, operating in the $\pi/2$ mode with a large coupling constant leads to rapid energy propagation. Consequently, when power is coupled into a SW linac, the fields in all cavities tend to increase nearly simultaneously, rising to the saturated value in a fill time approximately determined by

$$\tau_{\text{fill}} = 2Q/\Omega_{\pi/2} \tag{6.47}$$

Practical embodiments of the two most common types of coupled cavity linac structures are shown in Figure 6-23.[6,14] The length of a complete acceleration block, consisting of a single accelerating cell and coupling cell, is equal to the distance that an electron travels in one-half the microwave period. Such blocks are brazed together to form accelerating structures of the desired length. The side-coupled linac typically has higher shunt impedance, but the axially-coupled structure is usually less expensive to fabricate. The axially-coupled linac can have a larger coupling coefficient and is therefore more stable and more easily tuned.

6.5. COUPLING TO RESONANT ACCELERATOR STRUCTURES[7]

The three methods for introducing radio-frequency power into a cavity are schematically shown in Figure 6-24. These include (1) a magnetic coupling loop, (2) an electric coupling antenna at the end of a coaxial transmission line, and (3) an iris opening in the cavity wall to which a waveguide is attached. For rf accelerators, the magnetic coupling loop is most commonly used for low-frequencies, while the waveguide iris is most common at microwave frequencies. While not usually used for

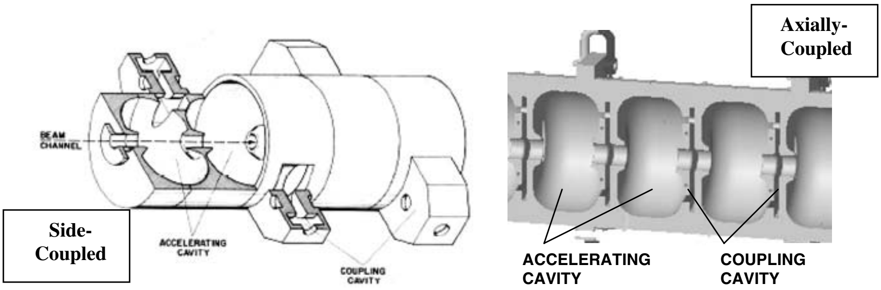

Figure 6-23. Perspective drawings of side-coupled and axially-coupled SW accelerator structures. (The drawing of the side-coupled structure is reprinted courtesy of the Los Alamos National Laboratory.)

acceleration (because the probe would normally occupy the region of the beam), electric field coupling is nevertheless quite useful for determining resonant frequencies and quality factors under cold-test (low-power, no beam) conditions.

6.5.1. Coupling with Minimal Beam Loading

The external circuit that drives the cavity and the cavity itself can be described by extending the parallel RLC circuit model to include an external driving circuit consisting of a matched current generator, a transmission line with characteristic impedance Z_o, and a coupling mechanism represented by a transformer with a turns ratio of 1:n. This analysis is especially useful for the loop coupling method. For a resonant structure coupled to a waveguide, it is more conventional to define a general parameter β_o that is a measure of the waveguide-to-cavity coupling strength in the absence of any beam loading. This parameter is given by

$$\beta_o = Q_o/Q_{ex} = P_{ex}/P_c \tag{6.48}$$

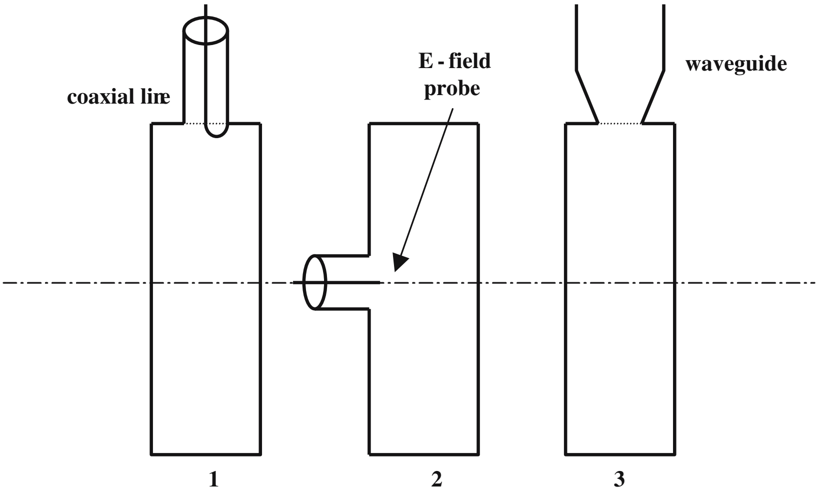

Figure 6-24. Techniques for coupling rf power to cavities: (1) loop coupling (magnetic) from a coaxial cable; (2) antenna (electric) coupling from a coaxial cable; and (3) waveguide-iris coupling.

As before, P_c is the power loss in the cavity; the external power P_{ex} is the power that would be absorbed in the driving circuit if the microwave source were turned off. The quality factor associated with P_c is termed the external Q, Q_{ex}. With the generator turned off, the external circuit loads the cavity, and the average power dissipated is $P = P_{ex} + P_c$. Consequently, the loaded Q is defined as

$$Q_L = \omega_o U/(P_{ex} + P_c) = Q_o Q_{ex}/(Q_o + Q_{ex}) = Q_o/(1 + \beta_o) \tag{6.49}$$

For a cavity driven at resonance, the load impedance of the driving circuit is $Z_L = \beta_o Z_o$, and the resulting reflection coefficient of the input coupler is given as

$$\Gamma = (Z_L - Z_o)/(Z_L + Z_o) = (\beta_o - 1)/(\beta_o + 1) \tag{6.50}$$

If P_t is the total incident power from the generator, then the power reflected from the input coupler backward toward the generator is

$$P_r = \Gamma^2 P_t = [(\beta_o - 1)/(\beta_o + 1)]^2 P_t \tag{6.51}$$

and the power delivered to the cavity through the input coupler is

$$P_c = P_t\left(1 - \Gamma^2\right) = 4\beta_o P_t/\,(1 + \beta_o)^2 \tag{6.52}$$

When $\beta_o = 1$, the cavity is critically coupled to the generator and $P_c = P_t$.

The voltage associated with the steady-state power loss in the cavity can be considered to be produced by the sum of a forward-going voltage wave V_+ and a backward going wave V_-, with $V_- = \Gamma V_+$. Assuming that V_+ is constant at $t = 0$, then we can introduce the known time dependence of the cavity voltage from Eq. (6.33), and the time-dependent reflection coefficient can be written as

$$\Gamma(t) = V_-(t)/V_+ = [2\beta_o/(1 + \beta_o)]\left(1 - e^{-t/\tau}\right) - 1 \tag{6.53}$$

with τ now defined in terms of the loaded Q as $\tau = 2Q_L/\omega_o$. The variation of Γ^2 with time is graphed in Figure 6-25. If $\beta_o = 1$, then Γ^2 monotonically increases to 0, at which time there is no backward-going wave. To reach the maximum steady-state cavity voltage, the input voltage must be longer than typically 2τ. For the undercoupled case, $\beta_o < 1$, the reflected power again decreases monotonically, but to a non-zero value in the steady state. When $\beta_o > 1$, the system is overcoupled; the reflected power first decreases to zero, then increases to its steady-state value. Also note that at $t = 0$, $\Gamma = -1$ always, implying that all of the incident power is reflected. To prevent damage to the generator, even for a well-matched system, it is usually desirable to insert a circulator or other isolator device between the cavity and the generator so that any reflected power is diverted into a resistive load.

6.5.2. Optimum Coupling with Beam Loading

It is usually desirable to design the input coupler geometry to minimize reflected power in the steady-state. However, when significant current is accelerated, the passage of the beam through the structure can induce fields comparable to those produced by the microwave source, and the net accelerating field is the superposition of the source field and the beam-induced field. This beam loading effect is especially important in ion accelerators for which longitudinal focusing is necessary, implying that the synchronous phase angle (between the beam bunches and the peak of the accelerating field)

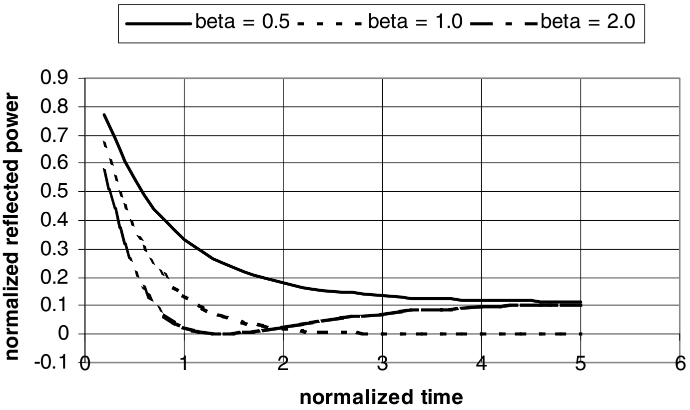

Figure 6-25. Reflected power versus time for different values of the coupling factor β_o.

is not zero. In this case it is also necessary to detune the frequency of the source from that of the accelerating structure to achieve minimum reflected power.

For relativistic electron accelerators, longitudinal focusing is not required, and the electron bunches can be accelerated at the crest of the accelerating field for maximum energy gain. In this case the structure is driven at its resonant frequency, the cavity impedance seen by the source is purely real, and the source power is increased to offset the voltage reduction induced by the beam. The input coupler geometry must therefore be designed to account for the increased power flow.

To account for beam loading we can modify Eq. (6.48) as

$$\beta = P_{ex}/(P_c + P_b) \tag{6.54}$$

in which P_b represents the power that goes into the beam. Eliminating P_{ex} gives

$$\beta = \beta_o(1 + P_b/P_c)^{-1} \tag{6.55}$$

The total power required from the source P_t is defined from energy conservation as

$$P_t = P_r + P_b + P_c \tag{6.56}$$

with the reflected power $P_r = \Gamma^2 P_t$. To minimize the required generator power at full beam loading we should choose $\beta = 1$, or from Eq. (6.55)

$$\beta_o = 1 + P_b/P_c \tag{6.57}$$

The efficiency with which an accelerating structure delivers microwave power to the beam is simply P_b/P_t. As a numerical example, we will assume that the structure efficiency is 75% when the input coupler is matched, implying that $P_b = 3P_c$. Minimum reflected power will then occur when the input coupler has an unloaded coupling factor of $\beta_o = 4$.

We now assume that the input coupler has been brazed to the accelerating structure, but that the beam current is not equal to the design value. Taking into account beam loading, the reflection

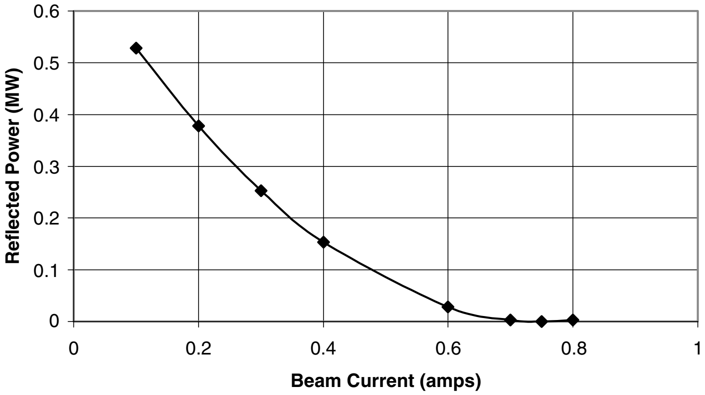

Figure 6-26. Reflected power vs beam power for a 5-MeV linac assuming a coupling parameter $\beta_o = 4$, and fixed cavity losses of 1.25 MW.

coefficient Γ is now given in terms of the beam-loaded β as

$$\Gamma = [(1 - \beta)/(1 + \beta)] \tag{6.58}$$

and the reflected power is given by

$$P_r = [\Gamma^2/(1 - \Gamma^2)](P_b + P_c) \tag{6.59}$$

The microwave power reflected from the coupler as a function of the beam current is shown in Figure 6-26 for the case corresponding to $\beta_o = 4$, $P_c = 1.25$ MW, and a fixed kinetic energy of 5 MeV, as an illustrative example. A perfect match corresponds to the case of 0.75 amps and a beam power of 3.75 MW. The match is quite good over a beam current variation of more than 100 mamps, however.

6.5.3. Measurement of the Coupling Parameter

The coupling parameter β_o can be measured by detecting the reflected signal when power is launched through the waveguide toward the coupler. The results are usually displayed on a "Smith chart," which consists of a set of constant impedance (constant β) circles that pass through the point $(-1, 0)$.[15] The radii of these circles are given by $R_Z = 1/(1 + Z_L/Z_o) = 1/(1 + \beta)$. The outer circle of the Smith chart is defined by $R_Z = 1$, corresponding to $\beta = 0$, which defines a short circuit. For a matched load, $\beta = 1$ and $R_Z = 0.5$.

If the frequency of the input power is swept through a resonance of the structure under test, then a "resonance circle" will appear inside the short circuit impedance circle of the Smith chart. The radius r_c of the resonance circle determines the coupling parameter for the measurement according to

$$\beta_m = r_c/(1 - r_c) \tag{6.60}$$

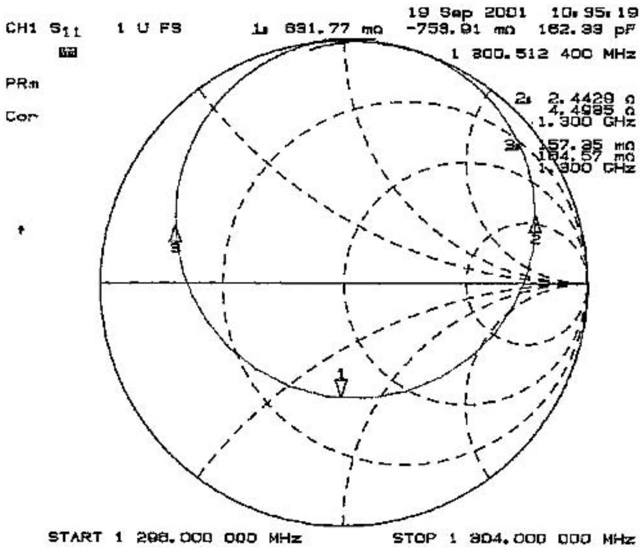

Figure 6-27. Smith chart measurement of the coupling beta for a waveguide-to-cavity transition. The radius of the resonance circle is approximately 0.74, giving $\beta_m = 2.8$.

The unloaded coupling parameter is then inferred from the measured value by correcting for the loaded quality factor, according to

$$\beta_o = [\beta_m/(1 + \beta_m)](Q_o/Q_L) \tag{6.61}$$

An example of this procedure is shown in Figure 6-27. For a loaded Q_L of 3645, the measured coupling parameter was $\beta_m = 2.8$. With an unloaded Q_o estimate of 17000 (from measurements and Superfish calculations), β_o was inferred from Eq. (6.61) to be 3.44.[14]

6.5.4. Load Line of a SW Structure

Representing the beam power as $P_b = VI_b$, with I_b the beam current, and $P_c = V^2/R$, with R being the total shunt impedance of the structure, Eq. (6.55) can be written as

$$\beta = \beta_o(1 + RI_b/V)^{-1} \tag{6.62}$$

Solving Eq. (6.58) for Γ^2 and substituting the result into Eq. (6.56) gives an expression for the load line of the structure[6]

$$V = [2(\beta_o RP_t)^{1/2} - I_b R]/(1 + \beta_o) \tag{6.63}$$

The kinetic energy of the accelerated beam therefore increases with the square root of the power from the source, and decreases linearly with the accelerated beam current. As a numerical example, we assume $\beta_o = 4$, a shunt impedance per unit length of 75 MΩ/m, and a structure length of one meter. Then R = 75 MΩ, and Eq. (6.63) becomes

$$V = 6.93 \times 10^3 P_t^{1/2} - 1.5 \times 10^7 I_b$$

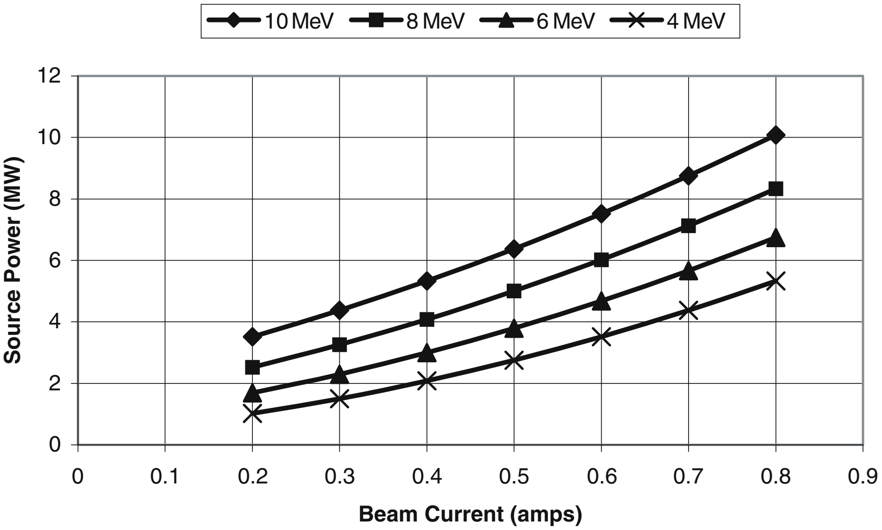

Figure 6-28. Source power required to produce a particular beam kinetic energy as a function of accelerated beam current, for $\beta_o = 4$ and $R = 75\ M\Omega$.

Lines of constant kinetic energy for this load line are shown in Figure 6-28 versus source power and beam current. For a 5-MW source, and a macropulse current of 0.5 amps, the beam kinetic energy would be approximately 8 MeV for this linac.

6.6. SINGLE-CAVITY RF ACCELERATORS

Having discussed several essential concepts used in microwave accelerators, we will next illustrate their use with numerical simulation examples. In this section we will examine the simplest microwave accelerator consisting of an electron gun and a single accelerating cavity through which the beam makes a single pass. The results will therefore be somewhat representative of an ILU accelerator (see Section 5.2.3).[16] In the following section we will examine the case of a multiple-cavity microwave linac.

We assume the cavity is driven in the TM_{010} mode by a high-power triode at a frequency of 175 MHz, and adopt nominal design goals of 50 kW of average beam power at a maximum beam kinetic energy of 5 MeV, implying an average beam current of 0.01 amps. With an assumed peak power of 1 MW from the triode, and assuming a cavity efficiency of 50% ($P_b = P_c$), the peak macropulse beam current should be 0.1 amp, which implies a 10% duty cycle, e.g., 1 msec at 100 Hz.

The accelerating cavity will be a full cavity, with halves of the general shape shown in Figure 6-13; the electron gun is placed in one of the nose cone apertures. From Eq. (6.22), the outer radius of the cavity will be approximately 65 cm. The accelerating gap design should have the highest transit time factor consistent with the maximum field stress from the Kilpatrick criterion, Eq. (6.35). At $f = 175$ MHz, $E_k = 14$ MV/m. Because of the millisecond pulse duration, we assume a bravery factor of only 1.25, implying that the peak field stress should not exceed 17.5 MV/m on the nose cones. A cavity shape satisfying these criteria is shown in Figure 6-29. The distance between electrodes is 38 cm, and the outer cavity radius is 59 cm. The ratio of the peak field on the nose cone to the average field over the 70-cm length of the cavity is 2.98.

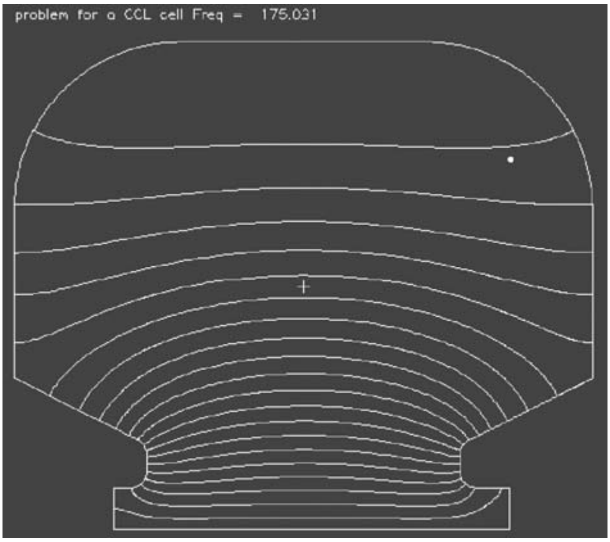

Figure 6-29. Design of the single acceleration cavity with a resonant frequency of 175 MHz. The outer cavity radius is 59 cm and the total cavity length is 70 cm. The distance between nose cones is 38 cm, and the nose cone aperture radius is 5 cm. The ratio of the peak field on the nose cone to the average field over the 70-cm length is 2.98.

With a constant voltage applied to the gun, we might expect the sinusoidal accelerating fields of the cavity to capture approximately one-half of the emitted current, implying that the total gun current should be about 0.2 amps. It is instructive to examine the capture and acceleration processes in some detail. The phase space trajectories of test electrons crossing the acceleration gap are plotted in Figure 6-30, assuming a sinusoidally varying electric field with amplitude of about 15 MV/m. The test electrons were emitted uniformly in time over one complete rf cycle ($-\pi$, π). A gun voltage of 15 kV was assumed.

Only those electrons emitted with relative phase angles in the range of (-0.25, 2.34) cross the gap, implying a capture efficiency of a little more than 40%. Those electrons emitted with relative phase angles around zero tend to be axially focused, forming a sharp leading edge of the accelerated

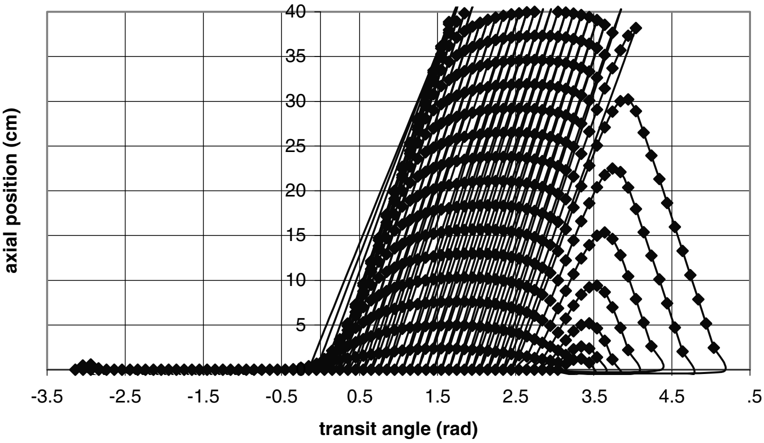

Figure 6-30. Phase space trajectories of trial electrons crossing the accelerating gap of the cavity shown in Figure 6-29.

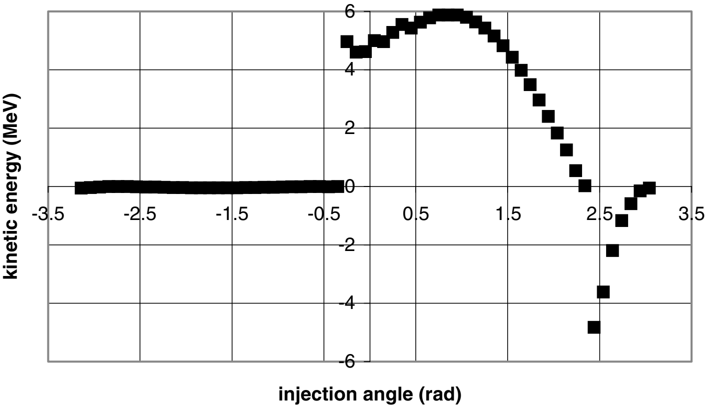

Figure 6-31. Kinetic energies of transmitted and reflected electrons as a function of their injection phase angle relative to the sinusoidal accelerating field.

bunch. The kinetic energies of the transmitted and reflected electrons are plotted as a function of relative phase angle at entry to the gap in Figure 6-31. (Negative energies denote electrons reflected backward.) There is a large energy spread in the transmitted electrons (0–6 MeV), and some of the reflected electrons will impact the cathode with considerable energy.

To avoid these problems of excessive cathode back-bombardment and a poor kinetic energy spectrum, single cavity rf accelerators almost always use some form of gridded-gun arrangement that permits control of the gun conduction angle. That is, electrons are only emitted when they can be efficiently captured and accelerated by the cavity fields.*

6.7. MULTIPLE-CAVITY RF ACCELERATORS

To illustrate the interplay of various multiple-cavity linac parameters, we will next examine an S-band linac at 2.856 GHz having the nominal performance parameters summarized in Table 6.3. The peak kinetic energy is 10 MeV, with an average beam power of 15 kW at a duty cycle of nominally 0.5% (e.g., 20 μsec at 250 Hz). Assuming an average kinetic energy of 9.5 MeV, the average beam current should be approximately 1.6 mamps, and the beam current during the macropulse should be in the range of 0.3–0.35 amperes, corresponding to a useful peak beam power of approximately 3 MW. Assuming a capture efficiency of 0.4–0.5 from a standard diode gun, the gun current should be in the range of 0.6–0.8 amperes. Beam power losses due to reflection and nose cone interception are estimated at 10% of the useful beam power, or 0.3 MW. If the structure efficiency is 70%, then the copper power losses will be approximately 1.4 MW, and the input coupler should therefore have an unloaded coupling parameter of $\beta_o = 3.35$. A klystron with a peak power rating of 5 MW should be sufficient. With a gradient of 10 MeV/m, the structure should be approximately one meter in length. At 2.856 GHz, the accelerating block length for a relativistic electron is approximately 5.25 cm, implying that there should be about 19 accelerating cavities.

To simulate the performance of this hypothetical linac we will use a fixed-frame version of Parmela.[17] Required inputs include the gun design (from EGUN), the suitably scaled fields of the accelerating cavities (from SUPERFISH), and (if necessary) any magnetic fields to assist beam

---

* In fact, the ILU accelerators use a unique gridded gun configuration in which some of the cavity fields are deliberately allowed to leak into the space between cathode and grid.[16]

Table 6.3. Multiple-Cavity Linac Parameter Goals

Parameter	Value
Maximum kinetic energy	10 MeV
Average energy	9.5 MeV
Macropulse current	0.32 amps
Efficiency (microwave to e-beam)	70%
Duty cycle (pulse duration x rep rate)	0.005
Average e-beam power	15 kW
Accelerating gradient	10 MeV/m

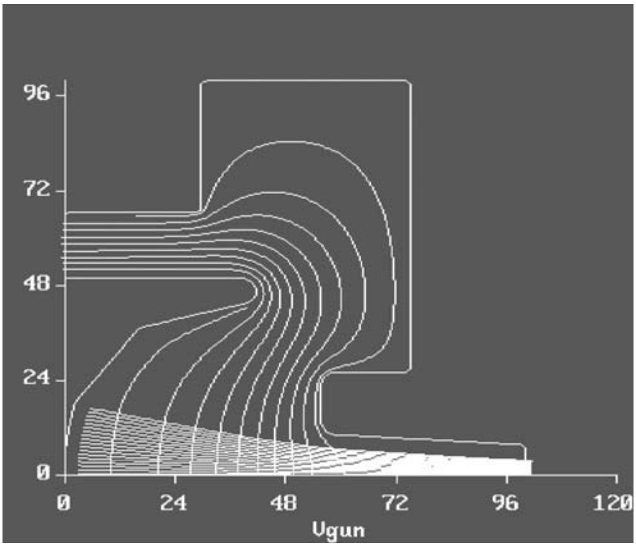

Figure 6-32. Electron flow trajectories for the electron gun. With 25 kV applied voltage, the gun generates 0.8 amps.

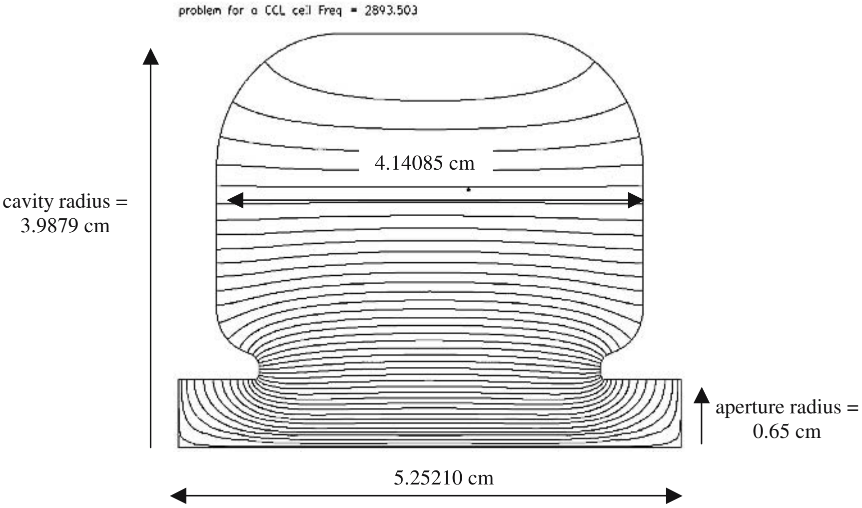

Figure 6-33. Relativistic accelerating cavity design for the 2.856-GHz linac.

Table 6.4. SUPERFISH Relativistic Cavity Output Data

Parameter	Beta = 1	Half-cell	Int. Beta = 0.85
Transit Time Factor (T)	0.77	0.82	0.81
Quality Factor (Q)	18331	9827	15207
Shunt Impedance per Unit Length	142.5 MΩ/m	40.9 MΩ/m	110.3 MΩ/m
ZT^2	84.0 MΩ/m	27.8 MΩ/m	72.2 MΩ/m
Peak to Average Field Ratio	3.45	5.80	3.83

transport (from POISSON). Assuming a capture efficiency of 40%, the gun must supply 0.8 amps. An EGUN calculation for a gun design having a perveance of 2×10^{-7} is shown in Figure 6-32. The required voltage is 25 kV.

At a frequency of 2.856 GHz, the center-to-center length of an accelerating/coupling cavity block for a relativistic electron is 5.2521 cm. Assuming that such a cavity provides an average energy gain of about 0.5 MeV, the average field is about 10 MV/m. Since the Kilpatrick criterion is $E_k = 46$ MV/m at 2.856 GHz, the peak-to-average field stress could exceed six with even a low bravery factor. A cavity design satisfying these modest criteria is shown in Figure 6-33. The interior cavity width of 4.14085 cm permits use of axial coupling cavities, if desired.

The half-cell used to capture the beam from the gun is shown in Figure 6-34. Since the energy gain from this half-cell will be no greater than about 0.2 MeV, a cavity design similar to that of Figure 6-33, but for an intermediate electron velocity of 0.85c, is used as the second cavity. A summary of the SUPERFISH output parameters for these three cavity designs is presented in Table 6.4.

The transit time factors apply to the entire cavity length; e.g., the transit time factor for the gap region of the relativistic cavity between the nose cones is about 0.85. Assuming 5% coupling, the shunt impedances are reduced by 15% to compute the copper power loss.

The simulation used a total of 6000 macroparticles uniformly injected over four complete rf cycles. Summary results of the simulation (based on the middle two rf cycles) are given in Table 6.5; they are very nearly equal to the nominal performance goals. Various frames from the simulation are

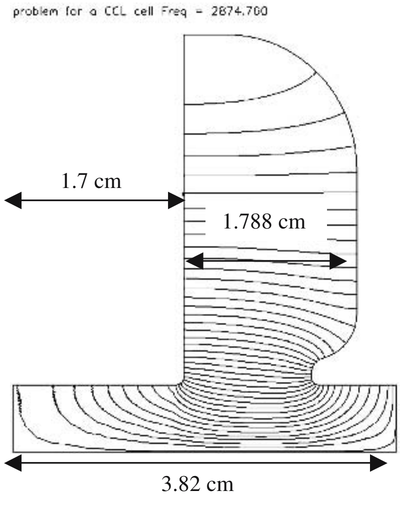

Figure 6-34. Half-cell design for the S-band linac.

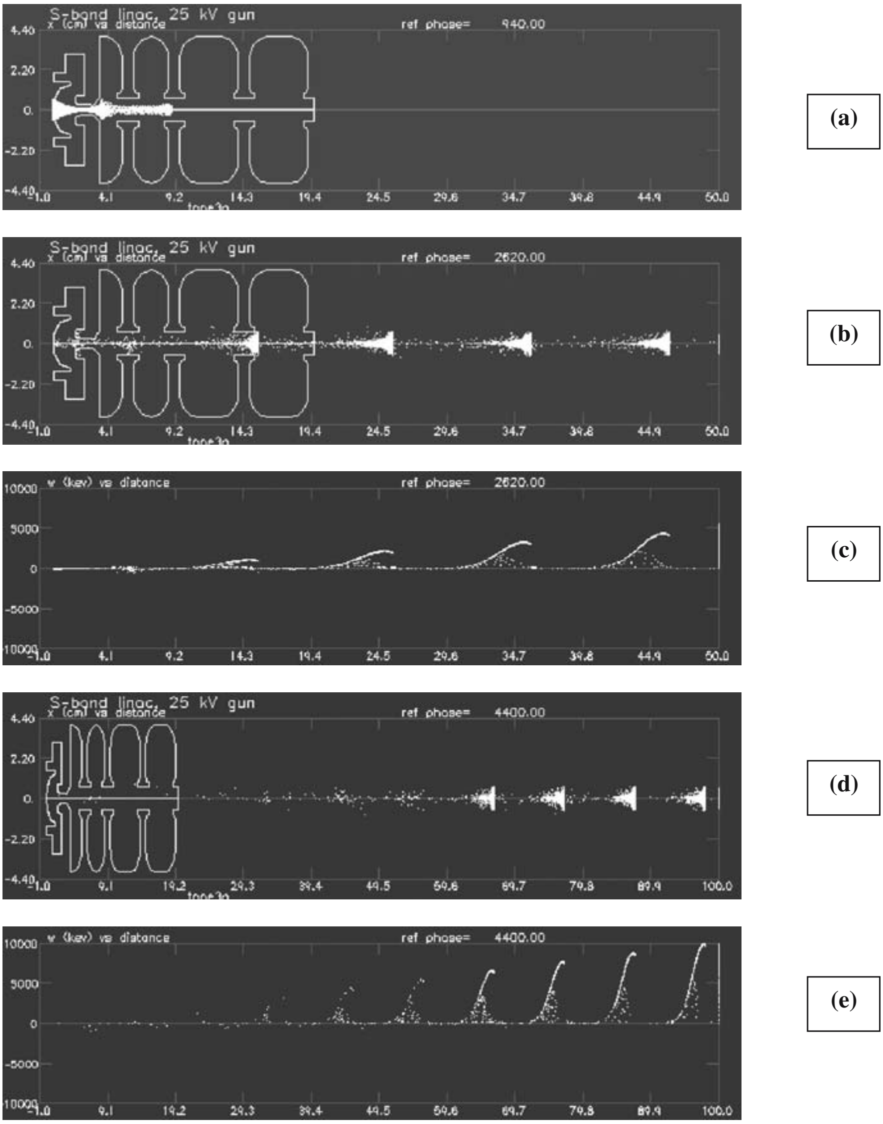

Figure 6-35. Frames from the numerical simulation of the S-band linac. (a) first half (50 cm) of the linac at relative phase 940 showing electron reflection at the half-cell; (b) first half of the linac at relative phase 2620 showing four well-formed bunches; (c) energy vs axial position for the first half of the linac; (d) full linac at relative phase 4400; (e) energy vs axial position for the full linac. (The final 15 accelerating cells are not shown.)

shown in Figures 6-35 and 6-36. Note the focusing of the beam from the gun into the first half-cell, and the increased radius of the charge at the time of reflection from the half-cell. Somewhat later there are four well defined bunches; each bunch has a sharp leading edge (also suggested by Figure 6-30 for the single cavity), with the highest kinetic energy occurring just behind the leading edge. The axial profile of a bunch remains constant after the first two accelerating cells as it is systematically accelerated down the linac; the peak kinetic energy at the exit is nearly 10 MeV.

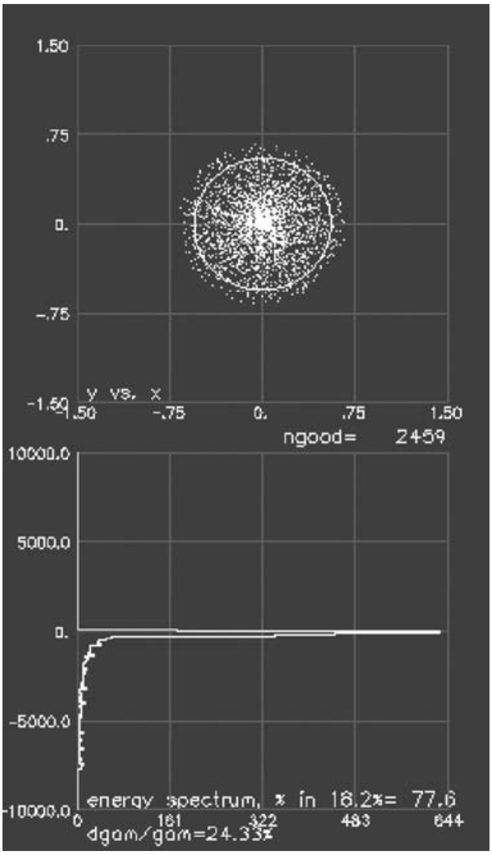

Figure 6-36. Beam x-y coordinate plot and kinetic energy spectrum at the end of the linac.

The x-y coordinates of the particles and the beam kinetic energy spectrum (relative to a synchronous particle in the bunch) at the linac exit are shown in Figure 6.36. The beam kinetic energy is sharply peaked at 9.85 MeV. The beam spot is not well defined and is essentially a truncated Gaussian. In fact, a tight beam spot with very high current density on axis is not desirable for foil heating and dose uniformity reasons. Similarly, very low beam emittance is not particularly important for food irradiation applications.

Table 6.5. Summary Simulation Results of the Hypothetical S-Band Linac

Parameter	Value
Maximum kinetic energy	9.91 MeV
Average kinetic energy	9.60 MeV
Beam current	0.32 amps
Beam power	3.1 MW
Total beam loading	3.4 MW
Copper power	1.5 MW

6.8. SUMMARY

In this chapter we have examined the essential concepts associated with the generation and acceleration of electron beams in microwave (radio-frequency) accelerators. The frequency range of interest is typically 100 MHz to 10 GHz, because electromagnetic waves with the corresponding wavelengths of 3 meters to 3 centimeters can be readily confined in metallic cavities of physically convenient size.

The electron beam in a microwave accelerator is almost always generated in a Pierce-type electron gun, using a thermionic cathode operated in a space-charge-limited mode. However, there are several particular types of accelerating structures, including both single and multiple-cavity designs (capacitively-coupled traveling wave and inductively-coupled standing wave linacs).

The individual cavities in these structures are usually designed to minimize resistive losses (as expressed by the shunt impedance) subject to electrical breakdown constraints. Shunt impedances in the range of 50–100 MΩ/m are now commonly achieved in standing-wave linacs, and this type of structure has become the standard microwave accelerator approach for food irradiation applications because of its compact size, efficiency, and stability.

The analysis of electromagnetic accelerating structures is facilitated by the use of resonant electrical circuit models. In particular, such models clearly indicate the advantageous properties of the $\pi/2$ mode for standing wave linacs. A practical method for operating in the $\pi/2$ mode is to construct a biperiodic structure consisting of accelerating cells designed for high shunt impedance, with alternating coupling cells that occupy minimum axial length.

Because the accelerating fields in microwave accelerators are sinusoidal, the kinetic energy gain of an electron depends on its phase angle with respect to the oscillating field and its transit time through the accelerating gap of the cavity. The important features of electron capture, bunch formation, and kinetic energy spread can be readily demonstrated and analyzed using numerical particle simulation techniques.

REFERENCES

1. A. S. Gilmour, Jr., **Principles of Traveling Wave Tubes**, Artech House, Boston (1994).
2. J. R. Pierce, **Theory and Design of Electron Guns**, 2nd ed., Van Nostrand, N.Y. (1954).
3. W. B. Herrmannsfeldt, "EGUN, An Electron Optics and Gun Design Program," **SLAC-331** (1988).
4. J. D. Jackson, **Classical Electrodynamics**, John Wiley and Sons, N.Y. (1962).
5. S. Y. Liao, **Microwave Devices and Circuits**, Prentice-Hall, Englewood Cliffs, N.J. (1990).
6. C. J. Karzmark, C. S. Nunan and E. Tanabe, **Medical Electron Accelerators**, McGraw-Hill, N.Y. (1993).
7. T. P. Wangler, **Principles of RF Linear Accelerators**, John Wiley and Sons, N.Y. (1998).
8. T. J. Boyd, Jr., "Kilpatrick's Criterion," Los Alamos Group AT-1 Report **AT-1:82-28**, (February 12, 1982).
9. J. H. Billen and L. M. Young, POISSON/SUPERFISH, Los Alamos National Laboratory Report **LA-UR-96-1834** (rev. December, 1997).
10. D. Bohne, Proc. 1976 Linear Accel. Conf., Chalk River, Canada, **AECL-5677**, 2 (1976).
11. G. A. Loew and R. B. Neal, in **Linear Accelerators**, P. M. Lapostolle and A. L. Septier, Wiley and Sons, N.Y., 39 (1970).
12. S. O. Schriber, Proc. 1976 Linear Accel. Conf., Chalk River, Canada, **AECL-5677**, 405 (1976).
13. E. A. Knapp, B. C. Knapp and J. M. Potter, Rev. Sci. Instrum. **39**, 979 (1968).
14. R. B. Miller, G. Loda, R. C. Miller, R. Smith, D. Shimer, C. Seidt, M. MacArt, H. Mohr, G. Robison, P. Creely, J. Bautista, T. Oliva, L. M. Young, and D. DuBois, "A High-Power Electron Linear Accelerator for Food Irradiation Applications," Nucl. Instrum. Meth. in Sci. Res. B, **211**, 562–570 (2003).
15. P. H. Smith, "Transmission Line Calculator," Electronics **12**, 29–31 (1939).
16. V. L. Auslender, A. A. Bryazgin, B. L. Faktorovich, V. A. Gorbunov, M. V. Korobeinikov, S. A. Maksimov, V. E. Nekhaev, A. D. Panfilov, V. O. Tkachenko, A. A. Tuvik, and L. A. Voronin, Vestnik "Radtech Euroasia" **N2(10)**, Novosibirsk (1999).
17. L. M. Young, "Parmela," Los Alamos National Laboratory Report **LA-UR-96-1835** (Revised January 3, 2003).
18. S. Humphries, Jr., **Principles of Charged Particle Acceleration**, John Wiley and Sons, NY (1986).

CHAPTER 7

MICROWAVE ACCELERATOR SUBSYSTEMS AND COMPONENTS

Having discussed how electron beams are generated and accelerated in microwave accelerators, we now consider the important subsystems and key components necessary for proper operation of the accelerator system as a whole. Using the block diagram of a typical microwave linac system in Figure 2-2 as an example, microwave power is generated by a suitable source that is energized by a high-voltage modulator. The microwave power is transferred to the input coupler of the accelerating structure through sections of waveguide that are usually pressurized with SF_6 gas to inhibit electrical breakdowns. A circulator isolates the linac from the source, diverting any reflected power into a water load. Both the linac structure and the microwave source must be highly evacuated for proper functioning; ceramic windows are used to separate these high-vacuum regions from the pressurized waveguide.

The frequency of the microwave source must be precisely matched to the resonant frequency of the accelerating structure for efficient power transfer to the beam. However, rf heating of the microwave cavity surfaces causes thermal expansion that decreases the resonant frequency. Proper control of the linac is typically achieved using a combination of two techniques. First, the temperature of the structure is held approximately constant by a temperature-controlled water circulation system. Second, an automatic frequency control (AFC) system monitors the reflected power and/or the cavity fields and provides a suitable drive signal to the microwave source to maintain the resonance condition.

In this chapter we review and discuss the design and function of these key microwave accelerator components and subsystems. We first discuss the various microwave tubes and the high-voltage systems used to drive them. We then discuss the design and function of various microwave engineering components. The automatic frequency control system and the manner in which it controls the accelerator are discussed next. Finally, we briefly consider the important auxiliary systems, including the cooling system, the vacuum and pressurized gas systems, and cooling of the exit window.

7.1. RF AND MICROWAVE POWER SOURCES

From Chapter 5, the average electron beam power required for a particular food irradiation application depends on the required throughput and the minimum required dose, and typically ranges from a few kilowatts for small e-beam installations to a few hundred kilowatts for x-ray processing of high-dose products such as spices. Taking into account accelerating cavity losses, reflection at the input coupler, etc., the average power required from the microwave tube will generally be in the range of 5 kW to 1 MW. In addition, for those accelerator approaches that operate in repetitive pulse mode, peak power requirements will generally lie in the range of 1–10 MW. There are three different types of rf (or microwave) sources that are used to satisfy these power requirements, depending on the specific application.

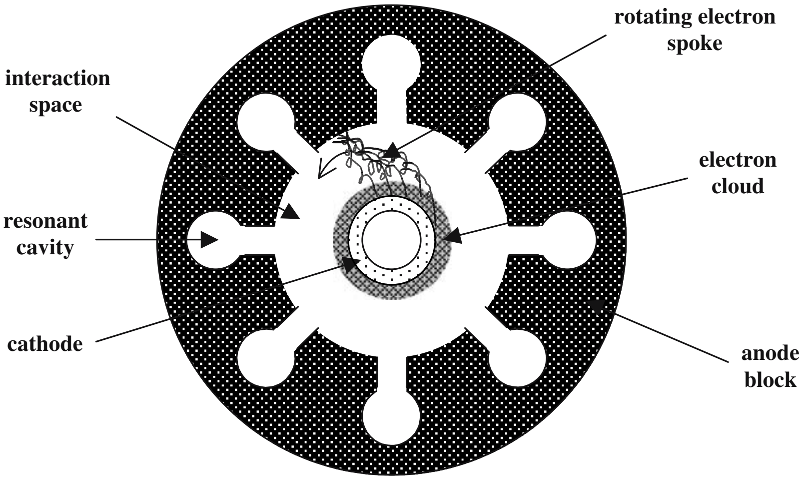

Figure 7-1. Schematic diagram of a cylindrical magnetron

For operating frequencies exceeding about 300 MHz, if the required average beam power exceeds about 10 kW, the most appropriate microwave tube is usually a klystron; for lower average power accelerator systems in this frequency range, it may be more economical to use a magnetron. For frequencies below about 300 MHz, conventional gridded power tubes (triode and tetrode amplifiers) are usually most appropriate. We discuss each of these power sources in the following sections.

7.1.1. Magnetrons[1]

A magnetron consists of a series of resonant cavities bored into an anode block arranged in circular form around a cathode, as shown in Figure 7-1. Electrons are emitted from the cathode when a high-voltage pulse is applied. A static magnetic field, oriented perpendicularly to the electric field, causes the electrons to circulate around the cathode. The cavities in the anode block constitute a slow-wave structure. By suitable adjustment of the applied voltage and the strength of the static magnetic field, the rotation velocity of the electron cloud about the cathode can be brought into synchronism with the phase velocity of a desired normal mode (usually the π mode) of the slow-wave circuit. The resulting interaction between the slow wave fields and the electron flow is unstable leading to large-scale disruption of the electron flow (spoke formation) and large amplitude electromagnetic fields.[2] In essence, electrons that are accelerated by the wave fields spiral into the cathode; in contrast, electrons that give up energy to the wave migrate across the anode-cathode gap and are collected on the anode block, having gained little kinetic energy. Effectively, the electrical potential energy of the applied voltage is efficiently converted directly into microwave energy.

A magnetron is an oscillator, and therefore does not require a drive source. However, because of the oscillator behavior, the operating frequency can vary with operating conditions, in particular, current flow to the anode (frequency pushing), and reflections from the load (frequency pulling). In addition, the magnetron frequency can drift appreciably during system startup. Consequently, when using a magnetron as an accelerator power source it must be isolated from the accelerating structure by a circulator, and an automatic frequency control (AFC) circuit is essential. The AFC senses the resonant frequency of the accelerator structure (usually by monitoring the reflected power), and actuates a mechanical tuning plunger in the magnetron so that the magnetron frequency remains in resonance with the accelerator frequency.

Table 7.1. Typical Operating Parameters for the Marconi MG6028 Magnetron

Parameter	Value
Heater voltage (V)	6.0
Magnetic field (kG)	1.5
Peak anode current (A)	200
Peak anode voltage (kV)	44
Pulse duration (μs)	4.0
Duty cycle (%)	0.075
Rate of voltage rise (kV/μs)	125
Peak output power (MW)	4.1
Efficiency (%)	47%
Average output power (kW)	3.1

The temperature rise associated with the cathode back-bombardment could result in a drastic decrease in cathode lifetime. However, since the back-bombardment power scales with the microwave output power, a cut-back circuit can be reliably used to decrease the cathode filament current, thereby avoiding excessive cathode overheating.

Magnetrons used to power accelerator systems are generally compact, efficient, and operate at voltages of no more than a few tens of kilovolts. Because the processes of electron emission, rf interaction, and spent beam collection occur in the same physical region, however, they are generally limited in their average power capability by thermal considerations, and in peak power by electrical breakdown in the strong rf fields. The nominal operating specifications of the Marconi MG6028 magnetron are summarized in Table 7.1 as an example.

7.1.2. Klystrons[3]

The microwave power source most commonly used for accelerator applications at frequencies above about 300 MHz is the klystron amplifier. A klystron is a linear microwave tube that uses the principle of velocity modulation to amplify a low-power microwave signal. The cross-section of a typical multi-cavity klystron amplifier is shown schematically in Figure 7-2. It consists of an electron gun, a "buncher" cavity that is driven by a low-power rf source, a series of amplifier cavities and an output cavity, all of which have nearly the same resonant frequency as that of the rf driver, and a beam collector. The beam is guided through the tube by a solenoidal magnetic field.

The rf driver is usually coupled to the buncher cavity using loop coupling. As the steady electron beam from the gun traverses the buncher, the low-amplitude electric field established by the driver alternately accelerates and decelerates some of the beam electrons, depending on the relative phase of the electric field at their time of passage. In particular, the velocity modulation corresponding to that portion of the rf cycle in which deceleration is followed by acceleration causes the accelerated electrons to overtake the decelerated electrons, resulting in the formation of electron bunches at the frequency of the drive signal. When the resulting rf current passes through the next cavity, it drives this cavity in resonance, inducing a higher level of rf excitation than in the buncher (i.e., amplification of the drive signal). These higher fields result in more bunching, which result in higher fields in the next cavity, etc. The fields induced in the final (output) cavity are sufficiently large that the electrons (in the bunches) undergo significant deceleration; they subsequently intercept the collector walls at low kinetic energy. Microwave power is coupled out of the final cavity using a cavity-to-waveguide coupling slot that is similar in design to a linac input waveguide coupler. The klystron cavity-to-cavity stage gain can be of the order of 10 dB, and high-power pulsed klystrons typically have total gains in the range of 40–50 dB.

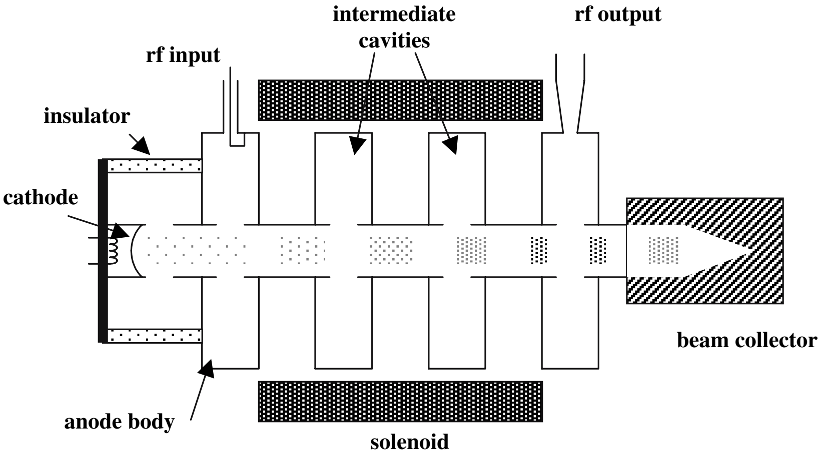

Figure 7-2. Schematic diagram of a multi-cavity klystron amplifier.

Being a linear tube, the processes of beam generation, modulation, power extraction and spent beam collection occur in physically different regions of the klystron, permitting high peak power and high average power operation. As a result, klystrons have been successfully designed to operate from a few hundred MHz to several tens of GHz, and have operated at pulse durations from one microsecond to CW. Output efficiencies of about 40% are typical for high-power pulsed klystrons, and efficiencies of nearly 60% have been achieved in CW operation. When used in a pulsed linac system for food irradiation, a klystron is usually operated at a voltage of the order of 100 kV, generating peak power pulses in the range of 5–10 MW at average power levels in the range of tens to hundreds of kilowatts. The nominal operating specifications of CPI's VKS-8262F pulsed klystron amplifier at 2856 MHz are summarized in Table 7.2, as an example.

7.1.3. RF Power Tubes[4]

For frequencies below about 300 MHz, high-power klystrons are physically quite large. In addition, the high-frequency effects that tend to limit the performance of gridded power tubes (interelectrode capacitance, large transit angles) are less worrisome. Consequently, conventional high-power triodes

Table 7.2. Typical Operating Parameters for the CPI VKS-8262F Pulsed Klystron Amplifier

Parameter	Value
Heater current (A-ac)	23.0
VYW-8262 electromagnet current (A)	35
Drive Power (W)	80
Peak anode current (A)	83
Peak anode voltage (kV)	125
Pulse duration (μs)	18.0
Duty cycle (%)	0.75
Peak output power (MW)	5.1
Efficiency (%)	48%
Gain (dB)	48
Average output power (kW)	38

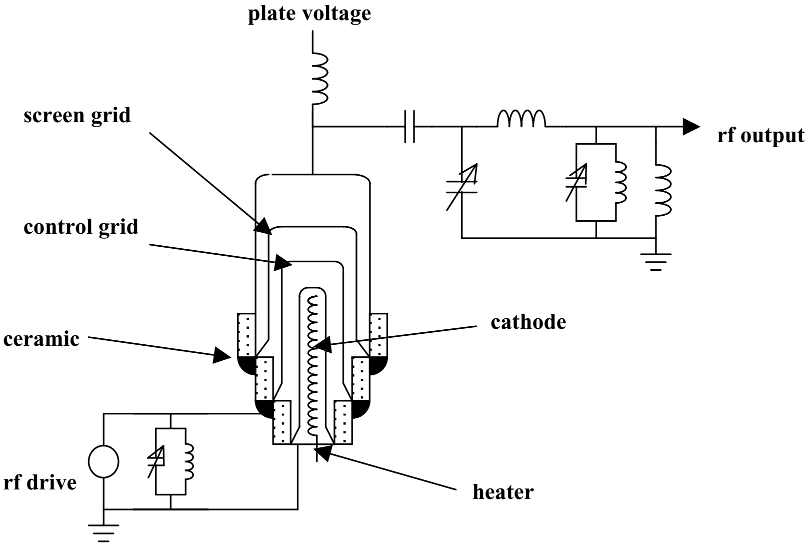

Figure 7-3. Simplified schematic diagram of a grounded-cathode, tetrode amplifier.

and tetrodes are usually the preferred rf tubes for low-frequency accelerator applications. These tubes are invariably cylindrical, having the internal arrangement indicated in Figure 7-3.

A triode tube has three elements: a cathode to generate electrons, a plate (anode) that attracts the electrons, and a grid that controls the electron current that passes between the cathode and the plate. A tetrode has a second grid (the screen grid) that acts as a shield between the input and output circuits of the tube. When operated as a power amplifier, a varying voltage applied between the (control) grid and cathode of the triode (tetrode) produces a larger variation in the plate voltage.

The triode grid (or tetrode control grid) is a highly transparent wire mesh that is usually biased negative with respect to the cathode. It functions as an imperfect electrostatic shield allowing some of the electric field lines from the anode to leak through its wires. Under space-charge-limited conditions, the current is determined almost solely by the electrostatic field near the cathode, and is given in terms of the plate and grid voltages (V_p and V_g, relative to the cathode voltage) as

$$I = K(V_g + V_p/\mu)^{3/2} \tag{7.1}$$

The constant K is essentially the perveance of the tube, while the constant μ, the amplification factor, depends on the specific design and placement of the control grid within the anode-cathode drift space. For a particular tube the amplification factor is determined by

$$\mu = -(dV_p/dV_g)_I \tag{7.2}$$

i.e., the change in plate voltage divided by the change in grid voltage, holding the current constant. The μ values of triodes generally range from 5 to 200.

In a similar manner, the total current in a tetrode is determined from

$$I = K(V_c + V_s/\mu_s + V_p/\mu_p)^{3/2} \tag{7.3}$$

where V_c is the voltage on the control grid, V_s is the voltage on the screen grid, and μ_s and μ_p are the screen and plate amplification factors, respectively.

Using the triode as an example, it is apparent from Eq. (7.1) that if the negative grid voltage exceeds V_p/μ, no current flows and the tube is said to be "cut-off." However, it is also apparent that small changes in grid voltage can produce large changes in plate current, depending on the amplification factor. This change in plate current with grid voltage is termed the transconductance, usually denoted by G_m. Thus, an oscillating signal introduced between cathode and grid can be greatly amplified. Such amplifiers are generally classified according to the four primary operating modes summarized below:

Class A – the grid signal is amplified nearly linearly; the maximum efficiency for this mode of operation is 50%.
Class B – the amplifier is operated just outside its linear transfer characteristic, providing improved efficiency at the expense of some waveform distortion; Class AB has a transfer characteristic between Class A and Class B.
Class C – the amplifier is operated significantly outside its linear transfer characteristic, resulting in a pulsed output at high efficiency; this mode is used extensively as a power amplifier.
Class D – the device is used as a switch, pulsed either on or off.

The various classes of operation depend on the conduction angle of the current. For example, in Class A operation electron current flows continuously, while in Class C, the tube is cut off 50% of the time.

Because of its high efficiency (typically 65–85%), a Class C amplifier is usually used for applications requiring large amounts of rf power. Most tetrodes are operated with the grid negatively biased with respect to the grounded cathode. The rf input uses a tuned circuit for impedance matching, and the pulsed plate current drives a tuned output circuit at resonance. When a triode is operated in this manner, it is necessary to cancel the large plate-to-grid interelectrode capacitance, an adjustment termed "neutralization." An alternate configuration convenient for triodes is that of the grounded grid, in which the grid acts as a shield between the input and ouput circuits, and neutralization is not normally required. The input signal is coupled to the cathode using a matching circuit, and the plate output feeds a π network through a blocking capacitor.

High-power triodes and tetrodes are now available with output power capabilities exceeding 1 MW at VHF frequencies. The input and output circuits of these tubes are transmission line cavities. In particular, the grid/cathode circuit is a transmission line terminated by the rf resistance of the electron current flow between the cathode and grid. The output circuit is a $^1/_4$-wavelength transmission line in which the plate position is foreshortened, making the line inductive so that it resonates with the tube's output capacitance and provides the correct plate impedance (typically 600–800 ohms).

A recent extension of the tetrode is the so-called diacrode.[5] Its operating principle is essentially the same as that of the tetrode; however, the diacrode includes an electrical extension of the output circuit structure to an external cavity. This configuration produces two current maxima, at the base of the tube, and above the tube at the cavity short-circuit. Consequently, the rf power capability of the diacrode is essentially double that of the equivalent tetrode having the same applied voltages. The Thales TH628 diacrode has successfully operated at 200 MHz, producing a peak power of 3 MW at 20% duty, and over 1 MW in cw mode.

In comparison with klystrons, these conventional gridded tubes operate at lower impedance, decreasing the difficulties associated with high voltage. In addition, a solenoid and its attendant power supply are not required, decreasing costs. However, these gridded tubes have much lower gain, and therefore require significant power at the input circuit. For example, the diacrode is usually driven by the Thales TH781 tetrode, which itself can provide up to 140 kW of power. Also, these tubes have lifetimes of typically $<10{,}000$ hours, as compared with lifetimes now routinely in excess of 20,000 hours for high-power klystrons.

7.2. PULSE MODULATOR SYSTEMS

While some rf accelerator approaches can operate in cw mode (low-gradient linacs and the Rhodotron, for example), most approaches require high peak power pulses (up to 10 MW) from the microwave source. The high-voltage pulses necessary to drive the source are provided by the pulse modulator system. The conventional pulse modulator, termed a line-type modulator, uses capacitive energy storage in a lumped-element transmission line that is switched into the load (a high-voltage pulse transformer) by a thyratron closing switch. However, the rapid development of solid-state switching technology has fostered several newer modulator approaches that offer distinct advantages for high average power operation. We discuss examples of each approach in the following sections.

7.2.1. Conventional Line-Type Modulator[6]

The traditional method of high-voltage pulse generation uses a pulse-forming network (PFN) of either the voltage-fed or current-fed type. It is termed a line-type modulator because the energy storage and pulse-shaping functions are performed using a lumped-element transmission line (the PFN). A block diagram of this modulator approach is shown in Figure 7-4. The PFN consists of several inductors and capacitors arranged in well-known configurations. The capacitors of the PFN are charged by a dc high-voltage power supply through a charging inductor to a few tens of kilovolts. When fully charged, the PFN is switched into the load (a step-up pulse transformer) by triggering a gate-controlled thyratron closing switch. The pulse transformer steps up the voltage by a factor of several, applying a high-voltage pulse of typically 120 kV to the anode-cathode gap of a klystron, for example.

The typical dc power supply is a three-phase transformer-rectifier. A silicon-controlled rectifier (SCR) supplies three-phase AC power from the facility power grid to the primary of a rectifier transformer. The level of AC power is controlled by the phase angle at which the SCR fires. The output voltage of the transformer is rectified by a diode string and filtered by high-voltage capacitors. The output, at typically 10 kV DC, is delivered to the PFN through a charging inductor supported by a high-voltage diode stack.

The capacitors of the PFN are resonantly charged to twice the voltage of the dc power supply. When the desired charging level is reached, the charging cycle is often terminated by closing a

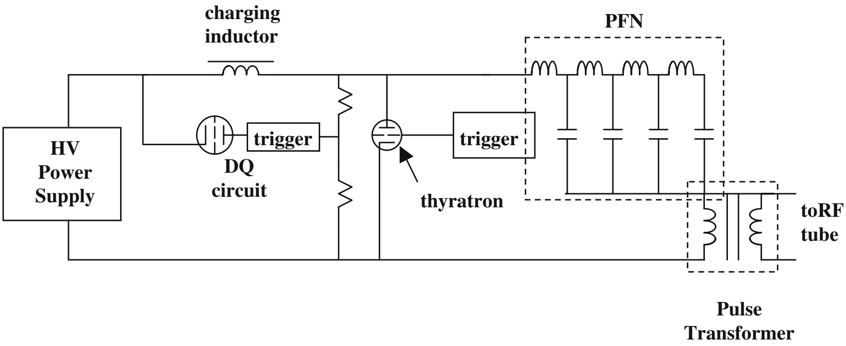

Figure 7-4. Simplified circuit diagram of a line-type pulse modulator.

"deQing" switch, which causes the residual energy in the charging inductor to be dumped into a resistor, effectively reducing the quality factor of the charging circuit.

The characteristic impedance of the PFN is designed to be equal to the load impedance for maximum energy transfer efficiency. As a numerical example, we assume a high-power klystron having a gun perveance of 2×10^{-6}. At a voltage of 125 kV, the klystron current is therefore 88 amperes, corresponding to an impedance $Z = 1400\ \Omega$. Assuming a step-up pulse transformer having a turns ratio of $n = 10$, the design value of the characteristic PFN impedance would be $Z_o = Z/n^2 = 14\,\Omega$.

The characteristic PFN impedance Z_o is determined by the total PFN inductance L_t and capacitance C_t according to

$$Z_o = (L_t/C_t)^{1/2} \tag{7.4}$$

The total PFN inductance is just the sum of the individual inductors, L_i, and the total capacitance is the sum of the individual capacitors, C_i. If the PFN consists of N essentially identical stages, then $L_t = NL_i$, $C_t = NC_i$, and $Z_o = (L_i/C_i)^{1/2}$. When the thyratron is fired, the PFN is connected across the primary of the pulse transformer. The PFN capacitors discharge sequentially resulting in a current pulse being supplied to the load that has a duration T equal to twice the electrical transmission length of the PFN, or

$$T = 2(L_tC_t)^{1/2} = 2N(L_iC_i)^{1/2} \tag{7.5}$$

A very rectangular pulse can be produced by properly tuning the capacitor and inductor stages.

The thyratrons used in conventional line modulators have limited lifetimes and their maximum pulse repetition rates are usually less than 1000 Hz. Also, the pulse lengths of line modulators are typically limited to a few tens of microseconds. The reason is that in the event of a load arc, the PFN continues to discharge for the entire pulse length. For long-pulse applications this can damage the load. Consequently, typical line modulator duty cycles are usually limited to about 1% or less (e.g., 20 microseconds at 500 Hz).

7.2.2. Current-Fed Solid State Modulator[7]

To obtain higher average power operation it would be desirable to lengthen the pulse. However, to avoid damage to the load in case of an arc, a reliable means of terminating the pulse is necessary. With a capacitive storage system and a series switch, this would require the reliable opening of the switch at the time of peak current flow (the arc), which is generally difficult. An alternate approach would be to use inductive storage, with the pulse being generated by opening a solid-state switch under well-defined, controlled conditions. In the event of an arc, the inductor would limit the peak current, and the switch could be rapidly and reliably triggered to its normally closed condition, limiting the current flow to the load and allowing the arc to extinguish. This is the conceptual approach used in the current-fed solid-state modulator, schematically shown in Figure 7-5. Its main components include a high current dc power supply, the energy storage inductor, the solid-state switch, and a pulse transformer. Supporting components include a clamp circuit, a droop compensation network, a dc blocking circuit, open load and arc load protection, and controls.

The heart of the modulator is the solid-state switch, consisting of a series stack of Integrated Gate-Commutated Thyristors (IGCTs). These devices have low conduction losses, and can be turned on and off using gate control. When the modulator is energized, the IGCTs are gated on, and the dc power supply establishes controlled direct current in the energy storage inductor; the on state of the switches causes the current to bypass the primary of the pulse transformer. To generate an

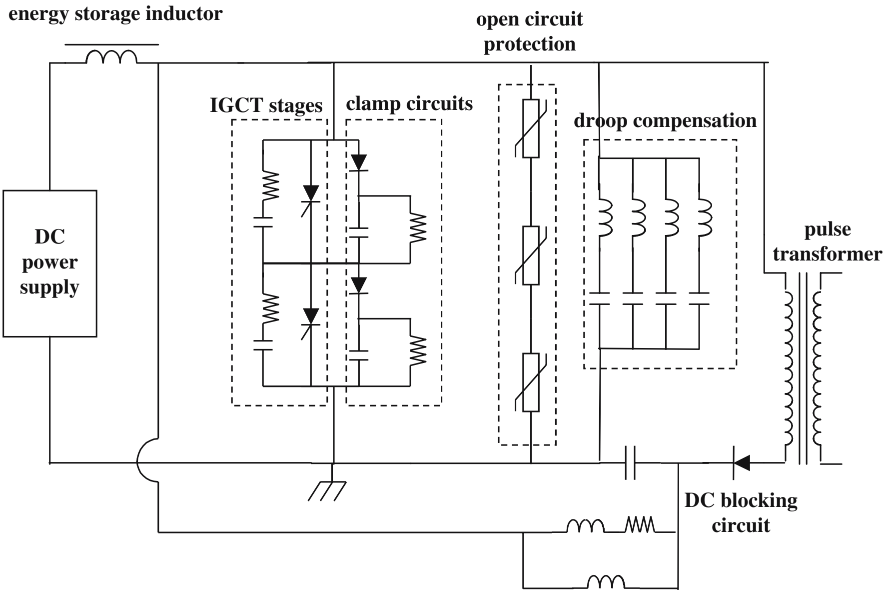

Figure 7-5. Simplified circuit diagram of the current-fed solid-state pulse modulator.

output pulse, the switches are gated off, causing a transfer of current into the transformer primary. The output pulse terminates when the switches are again gated on.

The clamp circuit balances the voltages across the individual IGCTs and limits the voltage across the series string during turn-off when the current is transferred to the load. The droop compensator approximately cancels the L/R sag in the inductor current by extracting current from the circuit during the first half of the pulse and injecting it back into the circuit during the second half of the pulse. The droop compensator network is much smaller than the PFN used in a conventional line modulator.

The dc blocking circuit, consisting of a large capacitor, diode, and damped inductor, prevents dc voltage from appearing at the transformer primary, and provides the voltage necessary to drive the magnetizing current to zero between pulses. Open load circuit protection is provided by a series set of varistors and a current sensor. The current sensor turns the IGCT switches on if the varistor current exceeds a certain threshold; the varistors limit the voltage during the few microseconds of delay before switch turn-on. A voltage sensor on the transformer primary provides the load arc protection by turning on the IGCTs if the voltage is below a threshold. The current remains nearly constant during the arc and the short turn-on delay time of the switch because of the large storage inductor.

This type of solid-state switch modulator has operated quite successfully,[8] producing a peak output power of 13 MW. With a maximum duty cycle of nearly 5% (a pulse repetition rate of approximately 330 Hz, and pulse duration of 150 μsec), the average power output exceeded 600 kW. A 14:1 step-up pulse transformer provided a nominal peak voltage pulse of 140 kV into a 1500-ohm load (a klystron).

7.3. MICROWAVE ENGINEERING COMPONENTS

For low-frequency, single-cavity accelerating structures (the Rhodotron and the ILU accelerators, for example) the rf tube is physically much smaller than the cavity and is essentially co-located using a direct coupling loop structure between the rf tube and the cavity. For linac structures driven by a klystron, however, the klystron and the pulse transformer tank are usually larger than the linac, and are located outside the x-ray shield with the modulator cabinets. In this case power transmission from the source to the linac is accomplished using common elements of microwave engineering, i.e., waveguides, windows, directional couplers, circulators, etc. In this section we briefly describe these components and illustrate their functions.

7.3.1. RF Transmission Waveguide[9]

Microwave power is transmitted from the microwave source to the accelerating structure through conventional rigid, rectangular, microwave waveguide sections. Such waveguides support two classes of normal modes, each infinite in number. In one class, the magnetic field has a component parallel to the guide axis, but the electric field is always transverse to the axis; these modes are called transverse electric modes (TE). Modes of the second class have a magnetic field always transverse to the axis and are thus designated as TM modes. Such waveguides will only transmit electromagnetic energy if the frequency of the radiation exceeds a certain limiting (cutoff) value. The mode having the lowest cutoff frequency f_c is called the dominant mode. For rectangular waveguide having transverse interior dimensions of a and b (see Figure 7-6), the cutoff wavelength is given by

$$[\lambda_c]_{mn} = 2[(m/a)^2 + (n/b)^2]^{-1/2} \tag{7.6}$$

The integers m and n denote the number of half-period variations in transverse field intensity in the a and b dimensions, respectively. If $a > b$, then the TE_{10} mode will be the dominant mode with a cutoff wavelength of

$$[\lambda_c]_{10} = 2a = c/f_c \tag{7.7}$$

The wavelength of the radiation in the guide is related to the cutoff wavelength and the free-space wavelength λ according to

$$\lambda_g = \lambda(1 - (\lambda/\lambda_c)^2)^{-1/2} \tag{7.8}$$

λ_g is always greater than λ.

In the United States, the Electronic Industry Association designations for rectangular waveguide use the larger transverse dimension (in inches). For example, WR650 is rectangular waveguide having a larger (interior) transverse dimension of 6.5 inches. The smaller dimension is usually a factor of two less than the larger. Several characteristics of standard EIA waveguide sizes are summarized in

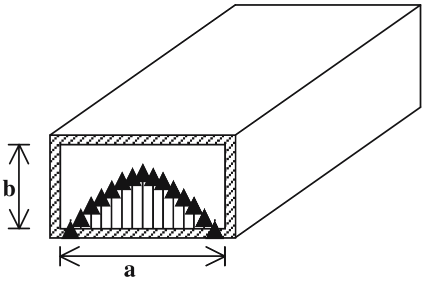

Figure 7-6. Rectangular microwave waveguide; the electric field profile of the TE_{10} mode is illustrated.

Table 7.3. Characteristics of Standard Rectangular Waveguides

Designation WR( )	Width (in.)	Height (in.)	Cutoff Frequency (GHz)	TE_{10} Mode Range (GHz)
2300	23.0	11.5	0.257	0.32–0.49
2100	21.0	10.5	0.281	0.35–0.53
1800	18.0	9.0	0.328	0.41–0.62
1500	15.0	7.5	0.394	0.49–0.75
1150	11.5	5.75	0.514	0.64–0.98
975	9.75	4.875	0.606	0.76–1.15
770	7.70	3.85	0.767	0.96–1.46
650	6.50	3.25	0.909	1.14–1.73
510	5.10	2.50	1.158	1.45–2.20
430	4.30	2.15	1.373	1.72–2.61
340	3.40	1.70	1.737	2.17–3.30
284	2.84	1.34	2.079	2.60–3.95
229	2.29	1.145	2.579	3.22–4.90
187	1.872	0.872	3.155	3.94–5.99
159	1.590	0.795	3.714	4.64–7.05
137	1.372	0.622	4.304	5.38–8.17
112	1.122	0.497	5.263	6.57–9.99
90	0.900	0.400	6.562	8.20–12.5
75	0.750	0.375	7.874	9.84–15.0

Table 7.3. For accelerator applications the waveguide is almost always selected such that radiation can only be transmitted in the dominant TE_{10} mode. For S-band operation at 2.856 GHz, the appropriate waveguide is WR284; for L-band at 1.3 GHz, WR650 is the usual choice.

The maximum power that can be transmitted through a waveguide depends on the maximum electric field strength permitted by breakdown considerations. For rectangular waveguide in the dominant TE_{10} mode, the transmitted power P (in watts) is related to the peak electric field E_p (in volts per centimeter) in the center of the guide according to

$$P = 6.63 \times 10^{-4}\, ab(\lambda/\lambda_g)E_p^2 \tag{7.9}$$

with a and b in centimeters.

For air-filled guides at STP, the breakdown limit is about 30 kV/cm. As a numerical example, for WR 284 waveguide transmitting radiation at a frequency of 2.856 GHz, $\lambda = 10.5$ cm, $\lambda_c = 14.4$ cm, and $\lambda_g = 15.3$ cm; the maximum peak power that can be transmitted according to Eq. (7.9) is about 10 MW at STP. However, if the waveguide must transmit significant average power, the waveguide walls can become quite hot, and the breakdown strength of the air can decrease appreciably. Consequently, it is standard practice to pressurize the waveguide with the electronegative gas sulfur hexafluoride (SF_6) to increase the dielectric breakdown strength. The peak power capability of pressured SF_6 relative to atmospheric dry air is shown in Figure 7-7. At STP the breakdown strength of SF_6 is approximately three times that of dry air, implying nine times the peak power capability; at 25 psi of SF_6, the power transmission capability of the waveguide will be increased by a factor of approximately 25.[6]

For microwave linac systems, the waveguide runs may be several tens of feet in length, usually involving directional changes. These are accomplished using waveguide bends and twists. To keep reflections low, the radius of curvature R of an E-plane bend (the electric field changes direction) should be $R > 1.5b$, while the radius of curvature of an H-plane bend should be $R > 1.5a$. The length of a 90° twist should exceed 4 λ_g.

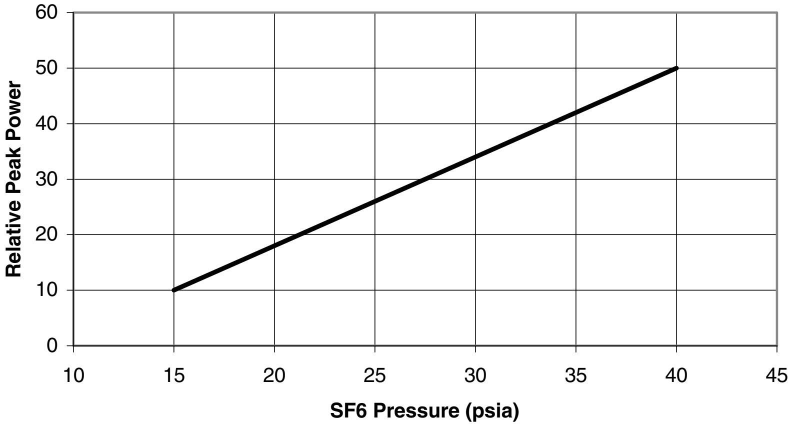

Figure 7-7. Relative peak power breakdown threshold for pressured SF_6.

The waveguide assembly may also incorporate small lengths of flexible waveguide to allow for minor mechanical misalignments. Small sections of flexible waveguide are also used to reduce mechanical stress on rf windows at the accelerator and source.

7.3.2. Waveguide Windows[11]

Waveguide windows made of a suitable dielectric material are used to separate the pressurized waveguide region from the high-vacuum envelopes of the microwave source and the accelerator structure. Such windows usually consist of a disk of high-purity alumina (Al_2O_3) that is brazed into a thin cylindrical copper sleeve. The sleeve is brazed to copper flanges that are, in turn, brazed to an outer cylinder of (usually) stainless steel, thereby forming a pillbox cavity, as schematically shown in Figure 7-8.

Window failures, while now rare, usually result from excessive localized heating of the window material due to electrical breakdown, multipactoring, dielectric loss in the alumina, etc. The thin sleeve allows relief of stresses resulting from thermal expansion differences between the ceramic and the metal, and the vacuum surface of the alumina is sputter-coated with a thin layer of titanium nitride to suppress secondary electron emission, thus preventing multipactoring (Section 6.3.4). Water-cooling is usually provided in the region between the stainless housing and the flexible copper

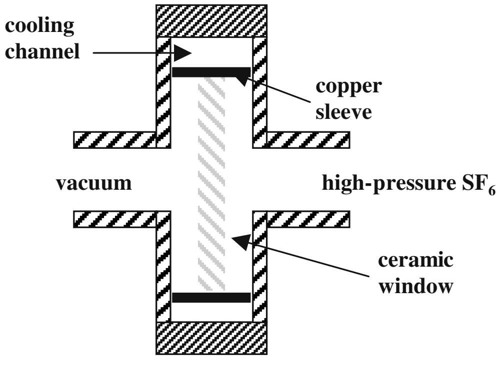

Figure 7-8. Schematic design of a ceramic waveguide window.

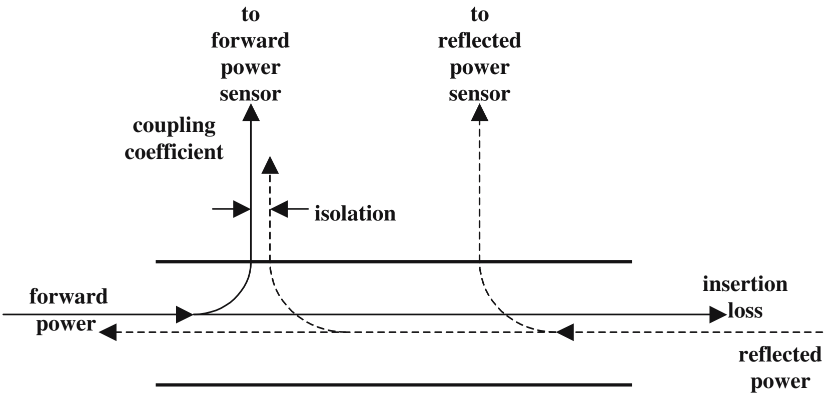

Figure 7-9. Schematic diagram of a directional coupler.

sleeve, and the dimensions of the pillbox are carefully chosen to avoid excessive electrical field stress.

7.3.3. Directional Couplers[3]

A directional coupler is a device that transfers a fraction of the power flowing in one direction in a transmission line to a second transmission line, as illustrated in Figure 7-9. The parameters that are used to characterize the directional coupler are the insertion loss, the coupling coefficient, and the isolation. The insertion loss measures the power loss in the first transmission line due to the presence of the coupler. The coupling coefficient measures the ratio of the power coupled into the second line to the power flowing in the desired direction of the first transmission line. The isolation measures the ratio of the output power coupled into the second line for power flow in the first line in the desired direction to that observed for an equal power flow in the opposite direction in the first line.

When inserted into the waveguide between the microwave source and the accelerator structure, the directional coupler can be used to determine the forward-going power from source to accelerator, as well as the power reflected backward from the accelerator toward the source. The insertion loss is typically less than 0.5 dB, while the coupling coefficient is typically in the range of 50–60 dB. The isolation is typically better than 20 dB.

7.3.4. Circulators

To avoid serious damage and/or deterioration in performance, the rf source must be protected against high-power reflections from the accelerator. The device that diverts power reflected from the accelerator structure into a water load is called a circulator. It is so named because a signal applied to one port can only circulate to the next port. This unidirectional property results from magnetization of a ferrite alloy inside the device.[12]

Ferrite is a non-linear material that exhibits a phenomenon called Faraday rotation when placed in a dc magnetic field. The relative permeability of ferrite changes with the applied field, causing the wave in the ferrite to be circularly polarized. The length of the ferrite slab and the strength of the magnetic field therefore give rise to a phase shift of the outgoing wave with respect to the input wave. Since the saturation magnetization of the ferrite is temperature sensitive, control of the biasing field of an auxiliary electromagnet can be used to stabilize circulator performance at high power levels.

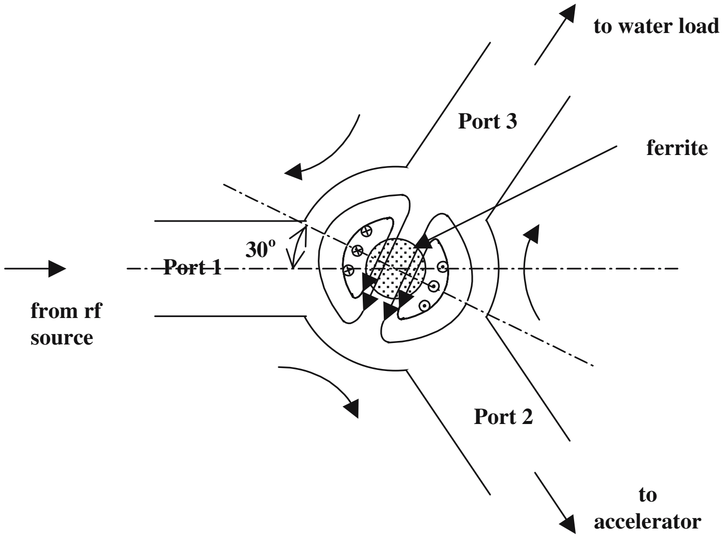

Figure 7-10. A three-port Y circulator showing the H-plane TM_{110} mode pattern of the ferrite.

In the three-port Y-junction circulator, schematically illustrated in Figure 7-10, the phase shift causes port 1 (the source) to couple to port 2 (the accelerator), port 2 to couple to port 3 (the water load), and port 3 to couple to port 1. If the water load is well matched, then any energy reflected from the accelerator is completely absorbed, and no signal will enter port 1 from port 3; effectively, the source is isolated from the accelerator.

The conceptual behavior of a common four-port circulator design is illustrated in Figure 7-11. It consists of two "magic tees" and a ferrite gyrator that produces a phase shift of 180° for wave propagation in one direction, but not the other. The magic tee (Figure 7-12) is a combination of an E-plane junction and an H-plane junction that has several unique properties, as summarized below:[3]

1. A wave fed into the H-arm will divide into two equal waves propagating in the a and b waveguides.
2. A wave fed into the E-arm will produce waves of equal amplitude but opposite phase in the a and b waveguides.
3. When two waves having equal amplitude and phase are fed into the a and b waveguide ports, they add constructively in the H-arm, and destructively in the E-arm (no signal).

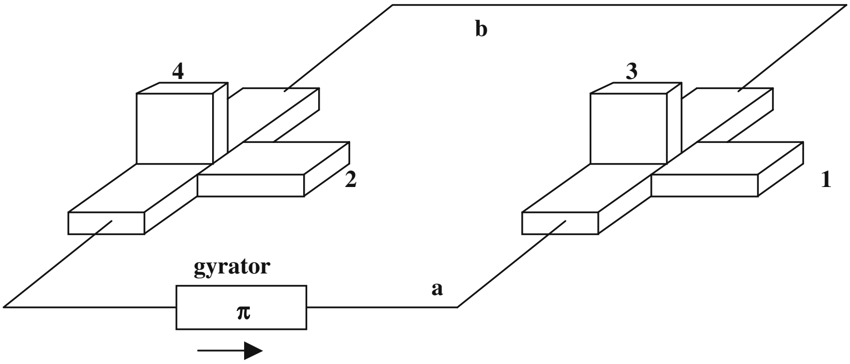

Figure 7-11. Conceptual behavior of a four-port circulator.

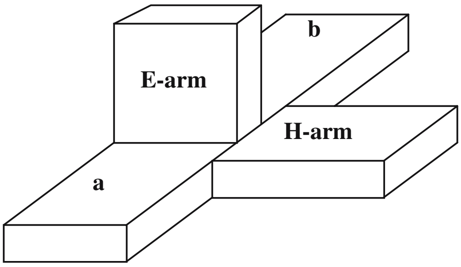

Figure 7-12. The "magic tee" hybrid coupler.

4. When two waves having equal amplitude but with opposite phase are fed into the a and b waveguide ports, they add constructively in the E-arm, and destructively in the H-arm.

Returning to Figure 7-11, a wave incident at port 1 (from the source) is split into two equal waves in waveguides a and b with no power delivered to port 3 (the high-power water load). These waves combine in phase at port 2 (the accelerator) since the gyrator does not affect the phase of the wave in waveguide a. A reflected wave from the accelerator input at port 2 will also be split into two waves, but the wave in the a leg is phase shifted 180° relative to that in the b leg. Consequently, the two waves cancel at port 1 (the source), but combine in phase at port 3 (the water load). (A low-power load is usually placed at port 4 also, to ensure proper terminations.)

7.3.5. Water Loads

The circulator diverts the reflected power from the accelerator into a water load that absorbs the power with minimal reflection. For food irradiation applications the water load can remain in a fixed position. Also, the average reflected power can reach levels in excess of a few kilowatts. Consequently, the water load for food irradiation applications usually has the "water-filled" design indicated in Figure 7-13.

The reflected power enters the water section via a ceramic window. To provide an ideal match between the pressurized waveguide and the water, the dielectric constant ε of the window is given by

$$\varepsilon = (\varepsilon_{\text{water}}/\varepsilon_{\text{gas}})^{1/2} \tag{7.10}$$

Since $\varepsilon_{\text{gas}} = 1$ and $\varepsilon_{\text{water}} = 80$, the desired dielectric constant of the window is approximately 9, which also happens to be the dielectric constant of alumina (the ceramic waveguide window material). To minimize reflections, the optimum thickness Δ of the alumina should be one-quarter of the waveguide

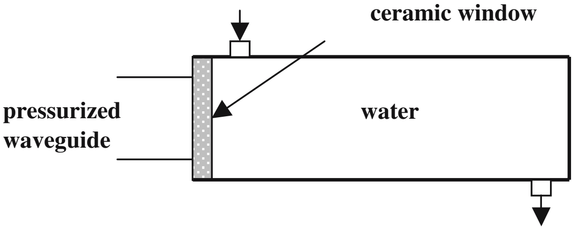

Figure 7-13. Cross-section of a water-filled load.

wavelength λ_g at the particular operating frequency. I.e.,

$$\Delta = \varepsilon^{-1/2}(\lambda_g/4) = \lambda_g/12 \qquad (7.11)$$

The power-handling capability of the water-filled load design can easily exceed 10 kW.

7.3.6. Arc Detector

The circulator is the primary protection device for the microwave source. However, the output window of the source is usually highly stressed, and excessive arcing could result in permanent damage. Consequently, as a second level of protection, a fiber optic arc detector monitors the condition of the window. The arc detector is positioned in a waveguide bend attached to the source such that the ceramic window can be viewed directly through a small sight glass. In the event of a window arc, the light emitted from the flash triggers a fault detection circuit that terminates modulator operation.

7.4. AUTOMATIC FREQUENCY CONTROL SYSTEM

An Automatic Frequency Control (AFC) circuit is used to keep the operating frequency of the rf source tuned to the resonant frequency of the accelerating waveguide, which can drift because of temperature fluctuations. To gain an appreciation for the magnitude of the frequency drifts, consider a 10-MeV S-band linac consisting of 20 accelerating cells and 19 coupling cells with a coupling constant of 5%. If the cells are tuned in confluence to 2.856 GHz, then the frequency separation between the $\pi/2$ mode and its next nearest neighbors is (from Eq. (6.46)) approximately 5.6 MHz.

The resonant frequency of an accelerating cell scales approximately inversely with the inner cavity radius (see Eq. (6.22)), and the coefficient of thermal expansion for copper is 16.6×10^{-6} per °C. Assuming that the water skid regulates the inlet temperature of the cooling water to an accuracy of +/−1°C, the frequency fluctuations under steady-state conditions are expected to be no worse than +/−47.4 kHz. By comparison, the resonance width of a structure having an unloaded quality factor of 20,000 is about 144 kHz.

More serious is the situation at start-up, when rf power is first introduced into the structure. Assuming a nominal structure efficiency of 70% and an average source power of 40 kW, then the copper power losses will be approximately 12 kW. The temperature rise produced by this rf heating can be estimated from

$$\Delta T = P_c/(Fc) \qquad (7.12)$$

where F is the water flow rate in g/sec, and $c = 4.2$ J/g-°C is the specific heat of water. Assuming a flow rate of 12 gallons per minute (800 g/sec), the increase in temperature of the structure following a cold start will be approximately 3.6 °C, corresponding to a frequency decrease of about 170 kHz, which is significant. A typical thermal equilibration time constant for this decrease in frequency is 10 seconds.

For relativistic electron accelerators the electron bunches can be accelerated at the crest of the accelerating field for maximum energy gain. It is therefore desirable to drive the accelerating structure at its resonant frequency, in which case the cavity impedance seen by the source is purely real.[13] The optimum operating condition therefore corresponds to maximum cavity fields and minimum reflected power. The consequence of a mismatch between the source frequency and the resonant frequency of the structure is an increase in the reflected power and a change in relative phase between the input

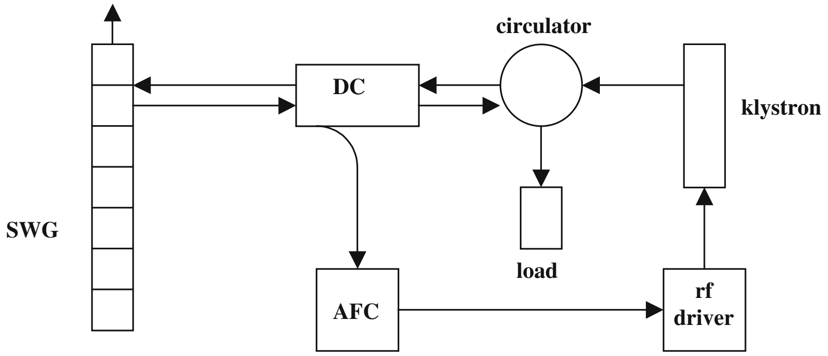

Figure 7-14. A schematic drawing of the rf control system for a klystron-based standing-wave linac.

power and the reflected power. These properties are used by the AFC to generate an error correction signal that realigns the frequency of the source with the resonant frequency of the structure. Several different logical approaches can be used. For example, a delay line can be used to null the phase difference between the SWG forward and reflected signals when the accelerator structure is driven by a low-power signal at resonance. A 3-dB hybrid coupler can then be used to generate an error signal proportional to the phase difference when the system is in high-power operation. In this case, the AFC is designed to minimize the phase error signal. Alternatively, the AFC can be designed to directly minimize the reflected power signal.

For klystron amplifier-based accelerator systems, the error signal from the AFC is applied to the frequency control port of the rf driver, as schematically shown in Figure 7-14. This device is essentially a solid-state oscillator/amplifier that provides a very frequency-stable output of adjustable amplitude and pulse duration. The heart of the driver is a voltage-controlled oscillator (VCO) whose frequency can be varied very precisely over a narrow range (typically $+/-1$ MHz) by the error signal supplied by the AFC. The frequency stability of the VCO to temperature variations is typically less than 10^{-5} MHz/°C. The output power of the VCO is amplified internally by a factor of perhaps 50–55 dB, resulting in a driver output power of a few hundred watts.[10] This signal is then amplified by the klystron.

For magnetron-based systems, the situation is somewhat different because it is necessary to control the resonance condition of the magnetron oscillator. In particular, it is necessary for the AFC error signal to adjust a mechanical tuner in the magnetron. This adjustment can be made by a servomotor, or by controlling the current through an electromagnet.

7.5. AUXILIARY SYSTEMS

7.5.1. Water Cooling System

The water cooling system removes excess heat from critical accelerator system components (e.g., the rf source, various electromagnets, circulator, rf driver, rf load, pulse transformer, etc.), and maintains the inlet cooling water to the accelerating structure at a nearly constant temperature to avoid excessive drifting of the resonant frequency. The cooling system consists of a submersible water circulation pump enclosed in a reservoir tank, a heater, a heat exchanger, a controllable flow valve, various manifolds, hoses, temperature and pressure gauges, and temperature control circuitry.[10] Several of these elements are usually mounted together on a "water skid."

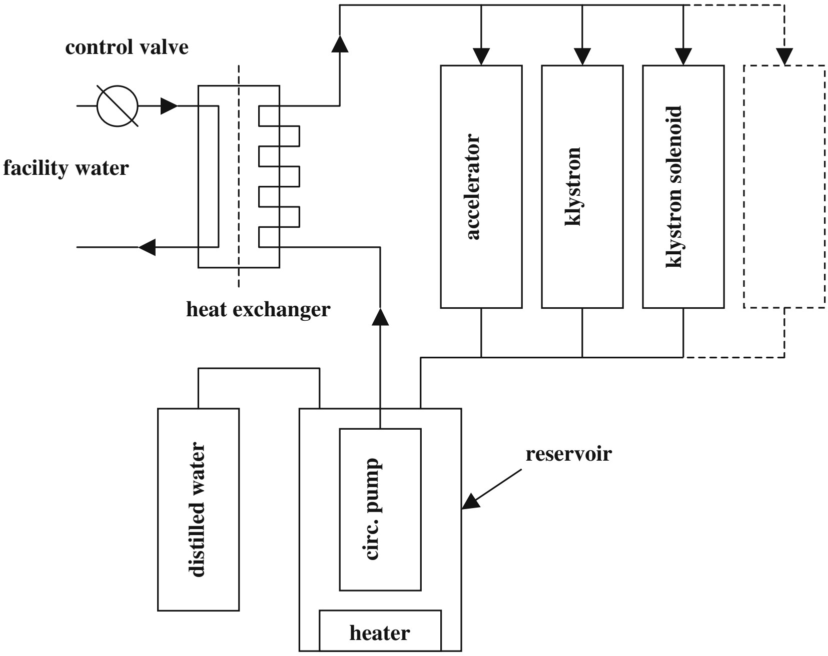

Figure 7-15. Block diagram of the water cooling system.

A block diagram of the water-cooling system is shown in Figure 7-15. The heat exchanger isolates the facility cooling water from the closed circulation loop of the accelerator system. Filtered, distilled water is used in the closed loop to limit corrosion and scale build-up. The temperature of the water leaving the heat exchanger is monitored and controlled by opening and/or closing the facility water flow valve, and by turning on or off the water heater. Temperature control to $+/-1$ °C is now commonly achieved. Use of a water heater is typically necessary only at start-up; alternatively, the water may be warmed to the operating temperature by the heat generated in the klystron collector prior to the application of rf drive.

7.5.2. Vacuum System

High vacuum conditions ($<10^{-7}$ torr) are necessary to maintain proper operation of the rf source and accelerator structure. However, even in leak-free systems surface heating, caused by the high rf fields and electron interception, results in gas desorption (outgassing) from internal surfaces, and it is usually necessary to continuously pump on these structures. The so-called vacion pumps are used for this purpose.[14] In these devices a nominal 5-kV potential difference is applied to a diode configuration consisting of a highly transparent, multi-cell anode sandwiched between two titanium cathode plates, as schematically shown in Figure 7-16. A magnetic field of 1–3 kG is provided by a permanent magnet, with the field lines oriented parallel to the applied electric field. The low energy (<5 keV) electrons tightly spiral around the magnetic field lines, and are effectively prevented from reaching the anode. Consequently, they oscillate backward and forward in the potential well formed by the opposing cathodes. These long electron pathlengths result in a high probability for dissociating and ionizing collisions with residual gas molecules. The resulting positive ions are accelerated toward the titanium cathodes where they can be buried, cause sputtering of the titanium, and/or release more secondary electrons.

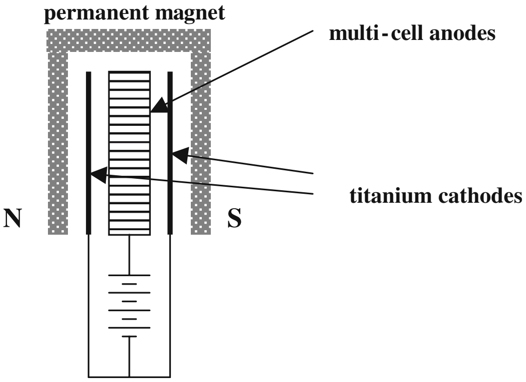

Figure 7-16. Schematic diagram of a diode vacion pump.

The actual pumping process itself depends on the specific nature of the gas. For example, hydrogen is initially buried in the titanium and diffuses into the metal forming a hydride. In addition to ion burial, active gases such as oxygen and nitrogen are also pumped by chemically bonding to the sputtered titanium. After first being dissociated, organic gases are pumped by adsorption and precipitation. Since inert gases do not react chemically with the titanium they are pumped less efficiently, usually by being covered with sputtered titanium on the pump walls (at the anode potential).

The pumping speed of a vacion pump depends on the surface areas of the cathodes, anode and pump walls. Small vacion pumps used for small electron guns may have pumping speeds of only 2–8 liters/sec, while large vacion pumps used on large scan chambers may have pumping speeds of several hundred liters/sec. Since the molecular ionization rate depends linearly on the background density (i.e., pressure), the ion current intercepting the cathode is an accurate indication of the pressure in the structure. The lifetime of a vacion pump is typically limited by the sputter lifetime of the titanium cathodes; 50,000 hours at 10^{-6} torr is a typical value.

Since vacion pumps cannot be used until the pressure is less than about 10^{-4} torr, the initial pumpdown is usually accomplished with an oil-free turbo-molecular pump that reduces the pressure from one atmosphere to the 10^{-5}–10^{-6} torr range. After starting the vacion pumps, it is then common to heat (bake) the structures at elevated temperatures to remove loosely adsorbed gases from surfaces prior to applying rf power and initiating electron flow. After bake-out, peak and average power levels are slowly increased as the vacuum improves and the surfaces become conditioned to the high rf fields. This process is lengthy, often taking a few weeks to condition the structures to their full operating parameters, even with adherence to strict cleanliness standards.

The actual pumping speed of a vacuum system depends not only on the pump, but also on the system conductance. For cylindrical structures in the molecular flow region, the conductance varies as the cube of the diameter. Consequently, for SW structures with small nose-cone apertures, the actual pressure internal to the structure can be an order of magnitude higher than the pressure measured at the pump.

7.5.3. Pressurized SF_6 System

As discussed in Section 7.3.1, the breakdown threshold of the waveguide can be increased significantly by pressurizing it with the electronegative gas sulfur hexafluoride (SF_6). This gas is usually sold in liquid form in medium pressure tanks at 320 psi. For an initial fill, the residual air in the waveguide is first exhausted with a small mechanical vacuum pump attached to the vent connection of the SF_6 gas manifold. SF_6 is then introduced into the waveguide from its pressurized tank through manual valves and a single-stage regulator. A waveguide pressure of 25 psi is typical. A pressure relief valve guards against an overpressure condition that might damage the ceramic windows (typically rated for 30 psi). SF_6 is not toxic, but it is heavier than air and can cause asphyxiation if inhaled. Also, if electrical discharges have occurred, some of the SF_6 breakdown products are quite reactive (fluorine). Consequently, SF_6 should always be vented to the facility exterior.

7.5.4. Exit Window Cooling

In most installations the accelerated electron beam is extracted through a thin (3–5 mil) titanium window. In the absence of cooling, the time-dependent temperature rise in the foil ΔT is governed by

$$\Delta T = Q/(mc) = (c\rho)^{-1}(dE/dx)(I/A)t \tag{7.13}$$

where Q is the amount of energy deposited in mass m having specific heat c and density ρ. I denotes the beam current incident on area A for duration t, and (dE/dx) is the electron stopping power. For estimation purposes, the mass stopping power can be considered as a constant, $[(dE/dx)/\rho] = 2$ MeV-cm^2/g. The specific heat of titanium is approximately 0.5 J/g-°C, and its melting temperature is 1660 °C.

As a numerical example, for a 15-kW/5-MeV accelerator the average current is 3 mamps. Assuming a duty cycle characterized by 20 microsecond pulses at a pulse repetition frequency of 250 Hz, the average macropulse current is 600 mamps. For an S-band linac, a typical beam diameter is 0.5 cm, so that the area of a beam spot is approximately 0.2 cm^2. Thus, the estimated temperature rise in the foil generated by a single beam pulse is approximately 240 °C; the foil would reach its melting temperature in only six pulses, if the beam were not scanned over the foil, and the foil were not cooled.

Assuming that the beam is scanned over a 60-cm length, then the average current density is 3-mamps over approximately 30 cm^2, for 0.1 ma/cm^2. In this case, Eq. (7.13) predicts that the foil will reach its melting temperature in only 3.5 sec, ignoring radiative and convective cooling processes. Consequently, it is usually necessary to cool the exit window, typically by a thin stream of high-pressure air that is directed across the window by an "air knife" over the full height of the scan. Even if the flow is laminar,[15] it is quite effective in limiting the temperature rise of the foil.

7.6. SUMMARY

In this chapter we have discussed the design and function of the key microwave accelerator components and subsystems that must be successfully integrated for proper accelerator system function. Important topics have included the various microwave tubes, the high-voltage systems used to drive them, and the various microwave engineering components. Important auxiliaries include the vacuum, cooling and pressurized gas subsystems. Finally, an automatic frequency control system is essential to ensure that the microwave source is precisely tuned to the resonant frequency of the accelerator structure.

REFERENCES

1. G. B. Collins, ed., **Microwave Magnetrons**, McGraw-Hill, NY (1948).
2. R. B. Miller, **An Introduction to the Physics of Intense Charged Particle Beams**, Plenum, NY (1982).
3. S. Y. Liao, **Microwave Devices and Circuits**, Prentice-Hall, Inc., Engelwood Cliffs, NJ (1990).
4. J. C. Whitaker, **Power Vacuum Tubes Handbook**, CRC Press, Boca Raton, FL (1999).
5. G. Clerc, J. P. Ichac, and C. Robert, "A New Generation of Gridded Tubes for Higher Power and Higher Frequencies," Proc. Part. Accel. Conf., Vancouver, 2899–2901 (1997).
6. G. N. Glasoe and J. V. Lebacquz, Pulse Generators, McGraw-Hill, Inc., NY, 1948.
7. D. Shimer and G. Loda, SureBeam Patent Disclosure (2001).
8. R. B. Miller, G. Loda, R. C. Miller, R. Smith, D. Shimer, C. Seidt, M. MacArt, H. Mohr, G. Robison, P. Creely, J. Bautista, T. Oliva, L. M. Young, and D. DuBois, "A High-Power Electron Linear Accelerator for Food Irradiation Applications, Nucl. Instrum. Meth. in Sci. Res. **211**, 562–570 (2003).
9. T. Moreno, **Microwave Transmission Design Data**, Artech House, Norwood, MA (1989).
10. C. J. Karzmark, C. S. Nunan and E. Tanabe, **Medical Electron Accelerators**, McGraw-Hill, NY (1993).
11. G. E. Southworth, **Principles and Applications of Waveguide Transmission**, D. Van Nostrand Company, Princeton, NJ (1950).
12. R. F. Soohoo, **Theory and Applications of Ferrites**, Prentice Hall, Inc., Englewood Cliffs, NJ (1960).
13. T. P. Wangler, **Principles of RF Linear Accelerators**, John Wiley and Sons, NY (1998).
14. A. Guthrie, **Vacuum Technology**, John Wiley and Sons Inc., NY, 1963.
15. A. H. Shapiro, **The Dynamics and Thermodynamics of Compressible Fluid Flow**, The Ronald Press Company, NY (1953).

CHAPTER 8

MAGNETIC TRANSPORT AND BEAM SCANNING SYSTEMS

Beam manipulation using magnetic fields is an important feature of almost every food irradiation installation. For example, the energetic electron beam produced by the accelerating system generally has a beam radius that is much smaller than the physical dimensions of the product to be irradiated. The beam must therefore be scanned in some fashion to provide uniform coverage. This scanning action is usually the result of time-dependent magnetic deflection of the beam. In addition, solenoidal magnetic lenses and quadrupole magnets are quite useful in transporting the beam through the accelerator (in the case of a linac, for example), and in producing beam spots of particular dimensions to improve dose uniformity.

In this chapter we consider the general topic of electron motion in magnetic fields. Beginning with the single particle equations of motion we analyze the effect of dipole, quadrupole and solenoidal magnetic fields, and show how these fields can be used to manipulate the beam to beneficial advantage. We also present and discuss specialized split / scan and pallet irradiation concepts.

8.1. ELECTRON MOTION IN A UNIFORM DIPOLE MAGNETIC FIELD

As an introduction to electron motion in a magnetic field, consider Figure 8-1. An electron with velocity $\mathbf{v} = v_o\mathbf{u}_z$, where $\mathbf{u}_z$ is the unit vector along the z-axis, enters a region of constant, uniform magnetic field $\mathbf{B} = B_o\mathbf{u}_y$, which is perpendicular to the motion of the electron. From Eq. (6.2), the magnetic field will not change the electron kinetic energy, and the equation of motion, Eq. (6.1), can be written as

$$\gamma m(d\mathbf{v}/dt) = -e\mathbf{v} \times \mathbf{B} \tag{8.1}$$

Explicitly writing the x and z components of Eq. (8.1) gives

$$dv_x/dt = (\Omega/\gamma)v_z \tag{8.2}$$

$$dv_z/dt = -(\Omega/\gamma)v_x \tag{8.3}$$

The parameter $\Omega = eB_o/m$ is termed the cyclotron frequency. Differentiating Eq. (8.3) with respect to t, and substituting Eq. (8.2) for dv_x/dt gives

$$d^2v_z/dt^2 + (\Omega/\gamma)^2v_z = 0 \tag{8.4}$$

which has the solution

$$v_z = v_o\cos[(\Omega/\gamma)t] \tag{8.5}$$

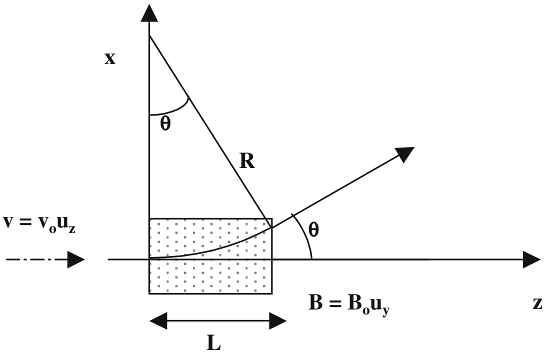

Figure 8-1. Electron motion in a static magnetic field oriented such that the field is perpendicular to the initial electron velocity.

Therefore, the electron executes circular motion with a radian frequency $\omega = \Omega/\gamma$, and period $T = 2\pi\gamma/\Omega$. By integrating Eq. (8.2), it can be verified that the radius R of the circular motion is given by

$$R = \gamma v_o/\Omega \tag{8.6}$$

Substituting for numerical constants, the radius of curvature R can be written as

$$B_oR = 1.7 \times 10^{-3}\beta\gamma \text{ (Tesla-meters)} \tag{8.6$'$}$$

where β and γ are the usual relativistic factors. If the magnetic field has an effective length L, then the deflection angle of the beam as it exits the field region is given by

$$\theta = \sin^{-1} (L/R), \quad \text{or} \tag{8.7}$$

$$\sin\theta = B_oL/(1.7 \times 10^{-3}\beta\gamma) \tag{8.8}$$

This deflection angle is graphed in Figure 8-2 as a function of electron kinetic energy for the case of $B_oL = 10^{-2}$ T-m (a one-kilogauss field acting over a length of 10 cm).

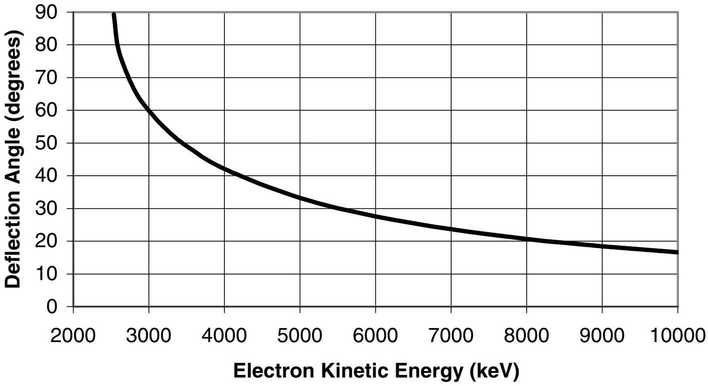

Figure 8-2. Electron deflection angle vs electron kinetic energy for $B_oL = 10^{-2}$ T-m.

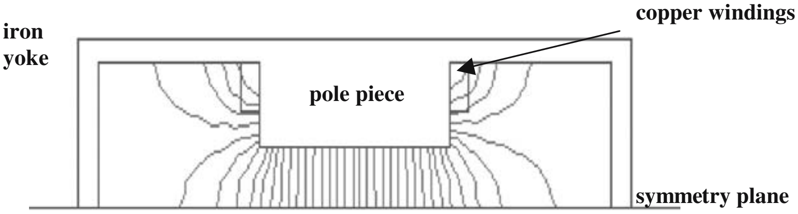

Figure 8-3. The magnetic field profile of a simple dipole magnet, as calculated using the Poisson code. The width of the pole piece is 10 cm; the gap between pole pieces is also 10 cm. The total current carried by the windings is 100 amperes.

If the beam is not monoenergetic, then the kinetic energy spectrum can be determined using such a dipole field. In addition, a tight beam spot will be smeared in the direction of the deflection. As a numerical example, for $B_0L = 10^{-2}$ T-m, the deflection angle for a 10-MeV electron is approximately 16 degrees. If the kinetic energy is 5% lower, the deflection angle is approximately 5% greater.

8.1.1. Design of a Simple Dipole Magnet

An example of a simple dipole magnet is shown in Figure 8-3. It consists of a central iron pole piece surrounded by copper windings. An iron yoke surrounding the pole piece and windings completes the magnetic circuit and confines stray fields. The field calculation was performed by the 2-D Poisson computer code.[1] With a 10-cm pole piece and a pole piece gap of 10 cm, the field is very constant over a 4-cm width in the center, as shown in Figure 8-4.

8.2. BEAM TRANSPORT IN A SOLENOIDAL MAGNETIC FIELD

In moving through an accelerating structure an electron beam will encounter transverse forces as well as axial accelerating fields, and will also tend to expand as the result of its self-fields. A solenoidal magnetic field is sometimes used to minimize transverse motion of the beam electrons. In addition, solenoidal lenses are also used to focus the beam into the linac, and to defocus the accelerated beam to avoid overheating the exit window and to improve front surface dose uniformity. In this section we first examine the equilibrium condition for an electron beam in a solenoidal magnetic field, showing

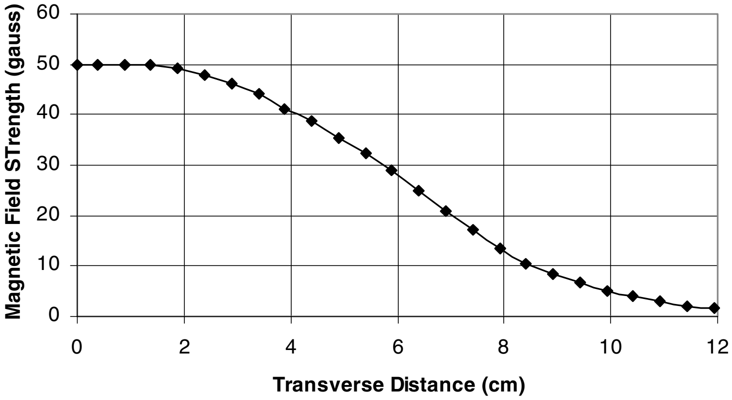

Figure 8-4. Magnetic field strength as a function of distance from the center of the pole piece at the symmetry plane for the simple dipole magnet of Figure 8.3.

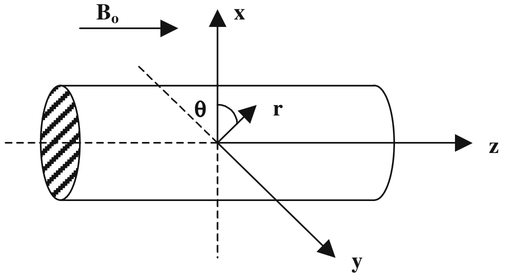

Figure 8-5. Cylindrically symmetric electron beam propagating parallel to a uniform externally generated magnetic field. The z-axis is the axis of symmetry. θ denotes the polar angle in the x-y plane, while $r = (x^2 + y^2)^{1/2}$ is the radial distance from the z axis.

that for the typical beams encountered in microwave accelerators, self-field effects are relatively unimportant. We will then analyze the focusing properties of solenoidal lenses.

8.2.1. Beam Envelope Equation[2]

The case of electron beam transport in a solenoidal magnetic field is schematically shown in Figure 8-5. Assuming that the beam axis and the axis of the solenoid are co-linear, and that the beam is cylindrically symmetric, it is convenient to decompose the electron velocity vector as

$$\mathbf{v} = v_r\mathbf{u}_r + v_\theta\mathbf{u}_\theta + v_z\mathbf{u}_z \tag{8.9}$$

where $\mathbf{u}_x$ denotes a unit vector in the x direction, for example.

It is further assumed that $v_r, v_\theta \ll v_z$, in which case $\gamma = (1 - v_z{}^2/c^2)^{-1/2}$. With the assumed cylindrical symmetry, the important field components are E_r, B_θ and B_z. We further assume that the axial magnetic field is generated by external field coils only, and that the field is constant and uniform across the radial profile of the beam; i.e., $B_z = B_o$. With these assumptions, the radial component of the equation of motion, Eq. (6.1), becomes

$$d^2r/dt^2 - v_\theta^2/r = -[e/(\gamma m)][E_r + (v_\theta B_o - v_z B_\theta)] \tag{8.10}$$

while the azimuthal component becomes a statement of conservation of canonical angular momentum P_θ. Assuming that the beam is born in a region free of axial magnetic fields, then $P_\theta = 0$, and

$$\gamma r v_\theta - \Omega r^2/2 = 0 \tag{8.11}$$

Restricting attention to a single electron at the outer radius r_b of the beam, and using Eq. (8.11) to eliminate v_θ, Eq. (8.10) becomes an equation for the radial envelope of the beam

$$d^2r_b/dt^2 + [\Omega/(2\gamma)]^2 r_b = -[e/(\gamma m)][E_r - v_z B_\theta] \tag{8.12}$$

The field components E_r and B_θ at the edge of the beam depend on the beam charge density n according to Gauss' and Ampere's laws.

$$\int \mathbf{E}\cdot d\mathbf{A} = -(e/\varepsilon_o)\int n\, dV \tag{8.13}$$

$$\int \mathbf{B} \cdot d\mathbf{l} = -e\mu_o \int n\mathbf{v} \cdot d\mathbf{A} \tag{8.14}$$

For a beam of constant density n_o out to the radius r_b, Eqs. (8.13) and (8.14) yield

$$E_r = -en_o r_b/(2\varepsilon_o) \tag{8.15}$$

$$B_\theta = -e\mu_o n_o v_z r_b/2 = \beta E_r/c \tag{8.16}$$

with $\beta = v_z/c$. Therefore,

$$-[e/(\gamma m)][E_r - v_z B_\theta] = -[e/(\gamma m)]E_r(1-\beta^2) = \omega_e^2 r_b/(2\gamma^3)$$

Note that the self-fields cancel to γ^{-2}. ω_e is identified as the plasma frequency, given by

$$\omega_e = [n_o e^2/(m\varepsilon_o)]^{1/2} \tag{8.17}$$

Eq. (8.12) can then be written as

$$d^2r_b/dt^2 + \left\{[\Omega/(2\gamma)]^2 - \omega_e^2/(2\gamma^3)\right\} r_b = 0 \tag{8.18}$$

The unneutralized beam self-fields therefore cause the beam to expand, while the applied magnetic field supplies a restoring force. These opposing forces cancel when

$$\Omega^2 = 2\omega_e^2/\gamma \tag{8.19}$$

The magnetic field strength required for this equilibrium condition is graphed in Figure 8-6 as a function of electron kinetic energy for a beam of one ampere having a radius of 0.5 cm. The plasma frequency for this beam is approximately equal to 1.8×10^9 sec^{-1}. At 1 MeV, the strength of the applied magnetic field required to balance the beam self-forces is only 44 gauss; the self-fields are essentially negligible. For the short accelerators and the low-current beams applicable for food irradiation applications, magnetic focusing is usually not required to control self-field

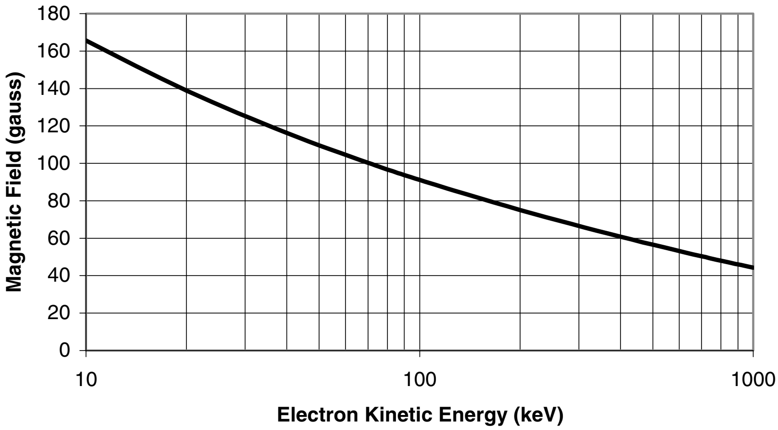

Figure 8-6. Equilibrium solenoidal magnetic field versus electron kinetic energy for a one-ampere, 0.5-cm radius electron beam.

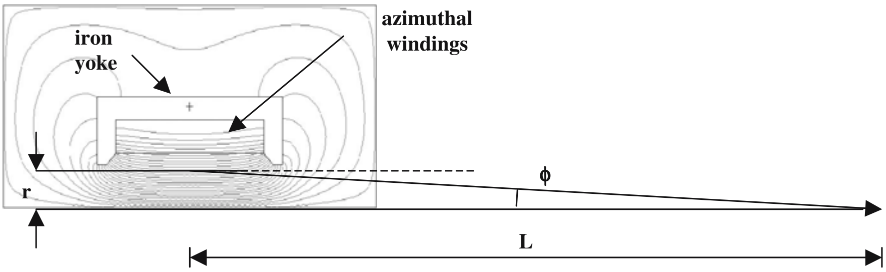

Figure 8-7. Schematic diagram of a solenoidal lens. The magnetic field lines were calculated using the Poisson code.

beam expansion, except possibly in the low energy injection region between the gun and the first accelerating cavity.

8.2.2. Solenoidal Magnetic Lens[3]

A solenoidal lens is illustrated in Figure 8.7. It consists of axisymmetric windings carrying azimuthal currents. Electrons enter the lens through a radial field region. The axial electron velocity crossed with this radial field gives an azimuthal Lorentz force that causes the electrons to rotate about the axis. In the interior of the lens, this rotation velocity crossed with the axial magnetic field gives rise to a radial focusing force. The focusing is therefore a second order effect.

In the previous section we saw that the self-fields can essentially be neglected for beams characteristic of microwave accelerators. In this limit, and recognizing that $d^2r/dt^2 = v_z\,(dv_r/dz)$, Eq. (8.10) can be written as

$$v_z(dv_r/dz) = v_\theta^2/r - \Omega v_\theta/\gamma \tag{8.20}$$

Solving Eq. (8.11) for v_θ and substituting into Eq. (8.20) yields

$$v_z(dv_r/dz) = -r(\Omega/2\gamma)^2 \tag{8.21}$$

The focal length of the lens can be obtained by performing the indicated integration over the axial coordinate as the electron passes through the lens. Assuming that r and v_z do not change appreciably (the thin lens approximation), this integration gives

$$v_z v_r = -r\int dz(\Omega/2\gamma)^2 \tag{8.22}$$

The focal angle ϕ is determined from

$$\tan\phi = v_r/v_z = r/L \tag{8.23}$$

where L is defined as the focal length of the lens. L is then explicitly given by

$$L = \left\{\int dz[\Omega/(2\gamma v_z)]^2\right\}^{-1} \tag{8.24}$$

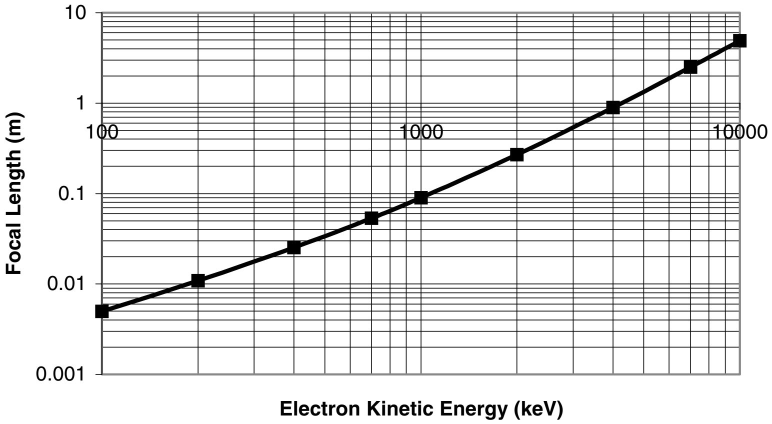

Figure 8-8. Approximate variation of focal length with electron kinetic energy for a 10-cm solenoidal lens having a strength of 1 kilogauss.

If B_o is the field strength in the uniform field region, and S is the length of the yoke, then Eq. (8.24) is approximately evaluated as

$$L = S^{-1}[2\gamma m v_z/(eB_o)]^2$$

The focusing power is therefore proportional to the square of the field strength, but inversely proportional to the square of the electron momentum. The focal length of a 1-kilogauss solenoidal lens that is 10 cm in length is graphed in Figure 8-8 as a function of electron kinetic energy.

8.3. BEAM TRANSPORT IN A MAGNETIC QUADRUPOLE LENS[3]

A magnetic quadrupole lens is illustrated in Figure 8-9. It consists of four hyperbolic pole pieces arranged such that like poles are diametrically opposed. In the coordinate system shown, the magnetic field components vary linearly with distance from the symmetry axis according to

$$B_x = B_o(y/a); \quad B_y = B_o(x/a) \tag{8.25}$$

where B_o is the field at the pole piece tip at a minimum distance a from the axis.

When these fields are substituted into the transverse equations of motion, the resulting equations become

$$d^2x/dt^2 = -(\Omega/\gamma a)v_z y \tag{8.26}$$

$$d^2y/dt^2 = (\Omega/\gamma a)v_z x \tag{8.27}$$

with $\Omega = eB_o/m$. Converting the time derivatives to axial derivatives ($dz = v_z dt$), Eqs. (8.26) and (8.27) can be rewritten as

$$d^2x/dz^2 = -ky$$

$$d^2y/dz^2 = kx$$

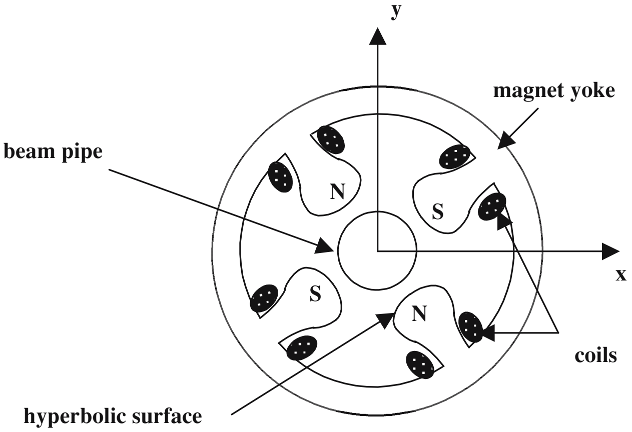

Figure 8-9. Cross section of a magnetic quadrupole lens.

with the parameter $k = \Omega/(a\gamma v_z)$. If the electron enters the lens with transverse coordinates (x_1,y_1), and with transverse velocity components that are zero, then the solutions of these equations can be simply written as

$$x(z) = x_1 \cos k^{1/2} z \tag{8.28}$$

$$y(z) = y_1 \cosh k^{1/2} z \tag{8.29}$$

$$dx/dz = -x_1 k^{1/2} \sin k^{1/2} z \tag{8.30}$$

$$dy/dz = y_1 k^{1/2} \sinh k^{1/2} z \tag{8.31}$$

The lens therefore acts to focus in x and to defocus in y. If the quadrupole is rotated by 90 degrees, it focuses in y and defocuses in x. It can be shown that the net effect of a focusing/defocusing quad pair is focusing, and such quadrupole lenses are used extensively for beam transport in high-energy particle accelerators. For the low-energy electron accelerators of interest here, however, the primary application is to defocus the beam in the direction of conveyor motion.

8.4. BEAM SCANNING AND TRANSPORT APPLICATIONS

Having examined the motion of electrons in a variety of magnetic field configurations, we now illustrate how the beam can be manipulated to produce beam patterns of specific interest for food irradiation applications. We begin with simple beam scanning, and then consider more specialized split/scan and pallet irradiation configurations.

8.4.1. Beam Scanning

If the dipole deflection angle (Eq. 8.8) is small, then $\sin\theta = \tan\theta$, and the transverse beam displacement at the exit of the dipole field depends linearly on the field strength. If the strength of the field is varied with time, as suggested by the waveform of Figure 8-10, the result is a scanning action that can be used to effectively spread the beam across the product as it is translated through the irradiation zone by the material handling system. The configuration is illustrated in Figure 8-11 for the case of x-ray irradiation.

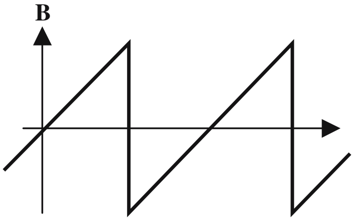

Figure 8-10. Time-dependent variation of the magnetic field in the scan magnet.

This scan rate is usually chosen in one of two ways, illustrated in Figure 8-12. Since it is convenient to mount the scanning dipole magnet outside of the beam pipe, the diffusion time for the field to penetrate through the pipe can limit the scan rate. For a pipe wall of thickness δ having conductivity σ and permeability μ, the characteristic magnetic diffusion time, $\tau_{m,}$ is given by[4]

$$\tau_m = \mu\sigma\delta^2 \tag{8.32}$$

For non-magnetic stainless steel ($\mu = \mu_o = 4\pi \times 10^{-7}$) having a conductivity of 1.39 mhos/m and a wall thickness of 0.4 cm, the characteristic magnetic diffusion time is about 32 μsec. Consequently, for pulsed machines with pulse durations of the order of 100 μsec or less, it is usually necessary to use a relatively slow scan rate with many pulses per scan. On the other hand, for longer pulse machines operating at lower pulse repetition rates, it may be necessary to provide a complete scan during the pulse. In the latter case, the distance between scan traces d_t at the product depends on the pulse repetition frequency (PRF) and conveyor speed v according to

$$d_t = v/(PRF) \tag{8.33}$$

For the short pulse / slow scan option let N be the number of pulses per scan. Then

$$d_t = Nv/(PRF) \tag{8.34}$$

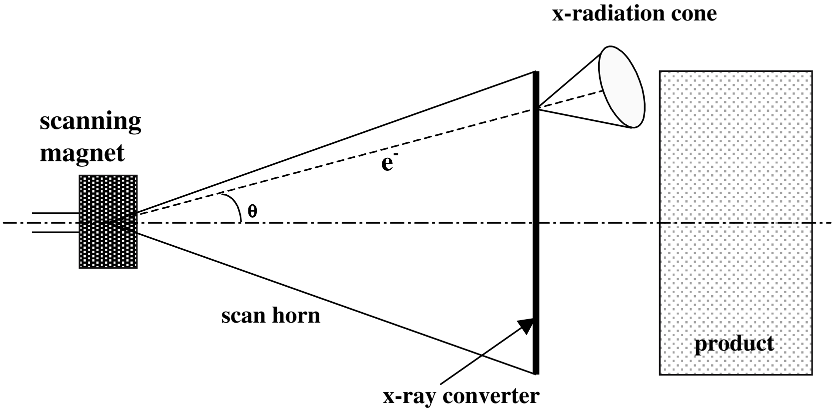

Figure 8-11. Schematic diagram of the scan geometry.

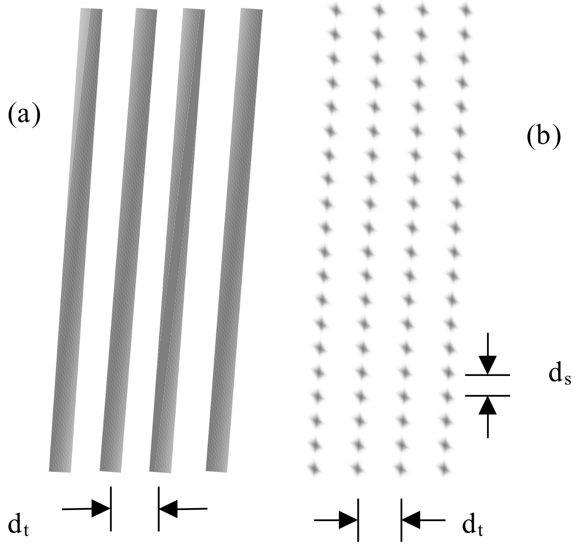

Figure 8-12. Different scan algorithms for (a) long pulse machines with a single continuous scan per pulse, and (b) short pulse machines with many pulses per scan. (The separations are exaggerated for illustration purposes.)

If H is the scan height, the centroid distance between beam spots in the direction of the scan is given by

$$d_s = H/N \tag{8.35}$$

The optimum conveyor speed in this case corresponds to $d_s = d_t$, which implies that

$$v_{opt} = H(PRF)N^{-2} \tag{8.36}$$

To assure a uniform front surface dose for electron beam irradiation, both the separation between scan traces and the separation between beam spots in the scan for the short pulse / slow scan option should be a fraction of the beam spot diameter at the product surface, as discussed in Section 3.5.

8.4.2. Non-Linear Scan Waveforms (S-Shaped Curves) for X-Ray Irradiation

In Chapter 4 it was shown that for x-ray irradiation one technique for improving the dose uniformity is to enhance the electron beam intensity at the extremes of the scan. A practical way of accomplishing this is to deflect the beam more slowly at the extremes of the scan, in comparison with the rate of deflection in the middle of the scan.

To analyze this procedure, we note that the average current density J(y) at a point y on the converter is just the incremental electron charge dQ divided by the incremental scan height dy, or

$$J(y) = dQ/dy = (dQ/dt)/(dy/dt) = I/(dy/dt) \tag{8.37}$$

where I is the average beam current and (dy/dt) is the scan rate at the point y. If the desired intensity profile J(y) is known, then the variation of the scan height with time, y(t), can be found by integrating

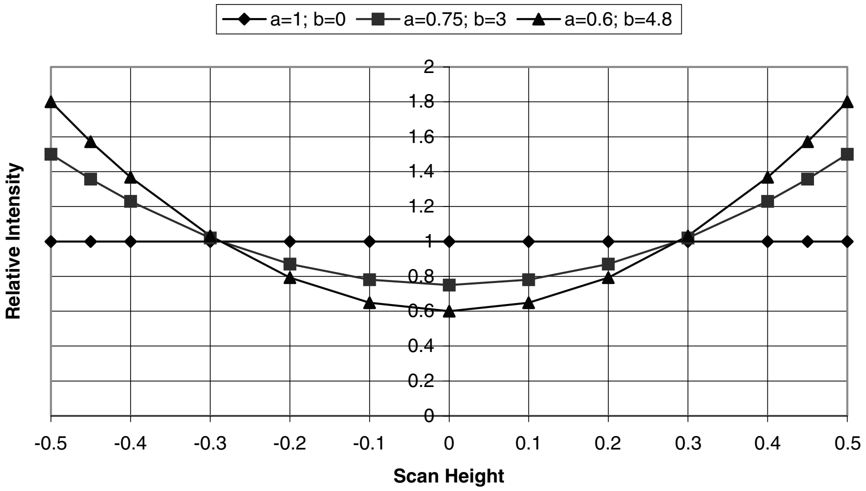

Figure 8-13. Variation of beam intensity at the converter for selected parabolic weighting functions.

Eq. (8.37) according to

$$\int J(y)dy = I \int dt \tag{8.38}$$

As an example of this procedure, consider the simple parabolic weighting function $J(y) = a + by^2$. For computational ease, the average power is normalized to unity, and symmetric, normalized integration limits are assumed such that $y = -\frac{1}{2}$ at $t = -\frac{1}{2}$, and $y = \frac{1}{2}$ at $t = \frac{1}{2}$. (I.e., the total scan height of unity is scanned in a total period of unity.) In this case, Eq. (8.38) yields

$$ay + by^3/3 = t \tag{8.39}$$

with a and b related according to $(a + b/12) = 1$. A few different parabolic intensity profiles and their corresponding scan waveforms are shown in Figures 8-13 and 8-14. The increased electron intensity at the extremes of the scan is produced by a waveform that has a characteristic "S-shape," corresponding to more dwell at the scan extremes.

8.4.3. Beam Trajectory Control at the Scan Horn Exit

In Chapter 4 it was also shown that a diverging electron beam at the x-ray converter results in a more rapid decrease in the depth-dose profile, and a loss of x-ray utilization efficiency. This situation could be improved by ensuring that the electrons would always impact the converter at normal incidence (or perhaps even at slightly converging angles). As a result, various magnetic field configurations have been devised to control the beam trajectories at the exit of the scan horn, as suggested in Figure 8-15. In the following paragraphs we consider two different examples that have been used successfully.

a. Bar Magnets (Panofsky Lens)[5]

The first configuration consists of two rectangular iron bars placed on either side of the scan horn as suggested in Figure 8-16. (This configuration is known as a Panofsky lens in the Russian literature.)

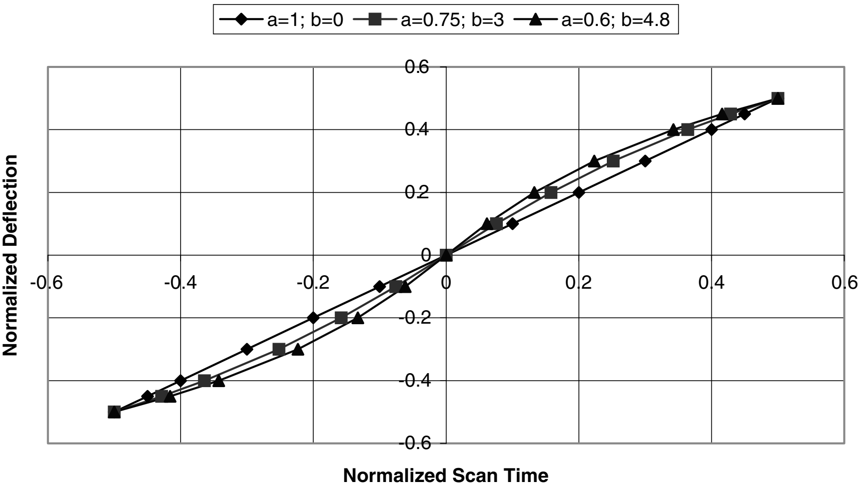

Figure 8-14. Scan waveforms corresponding to the various parabolic intensity weighting functions of Figure 8-13.

Current flows through uniform windings to produce poles at the extremes of the bars as shown. Provided that saturation does not occur in the bars, the transverse magnetic field between the bars is quite linear, as shown in Figure 8-17.

The geometry of interest for calculating the electron orbits is shown in Figure 8-18. A transverse magnetic field $B = B(y)$ is imposed over a small axial region Δz near the exit region of the scan horn of length L and full height H.

The radius of curvature required to cause electrons entering the magnetic field region at height y and angle $\theta = \tan^{-1}(y/L)$ to exit the field region parallel to the z-axis is given by $R = \Delta z/\tan\theta = \Delta zL/y$; the required field strength is therefore given by (from Eq. (8.6))

$$B = 1.7 \times 10^{-3}\beta\gamma\,[y/(L\Delta z)] \tag{8.40}$$

The maximum field strength is required at the maximum height $y = H/2$. Assuming for estimation purposes that $H = 60$ cm, $L = 3$ m, $\Delta z = 10$ cm, and a beam kinetic energy of 10 MeV, then

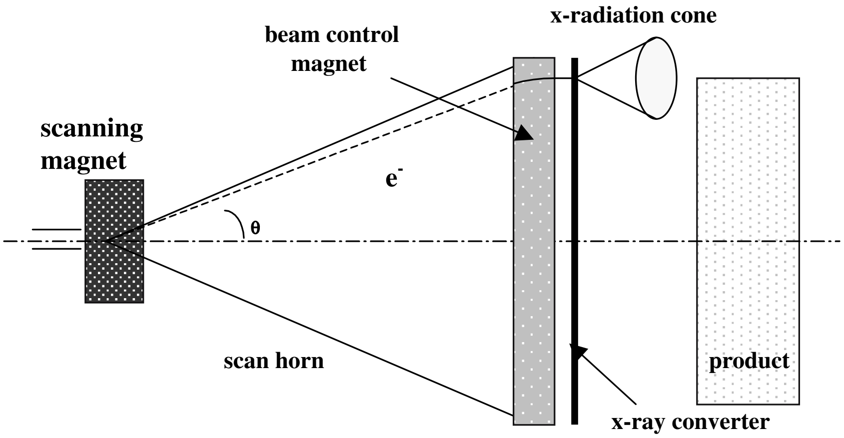

Figure 8-15. Schematic diagram of the scan geometry using trajectory control at the end of the scan horn.

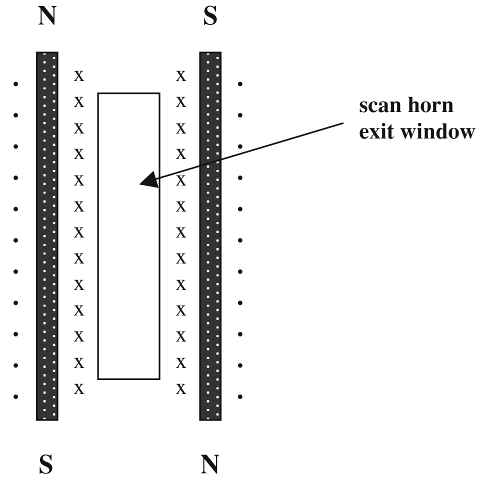

Figure 8-16. Schematic configuration of the Panofsky lens.

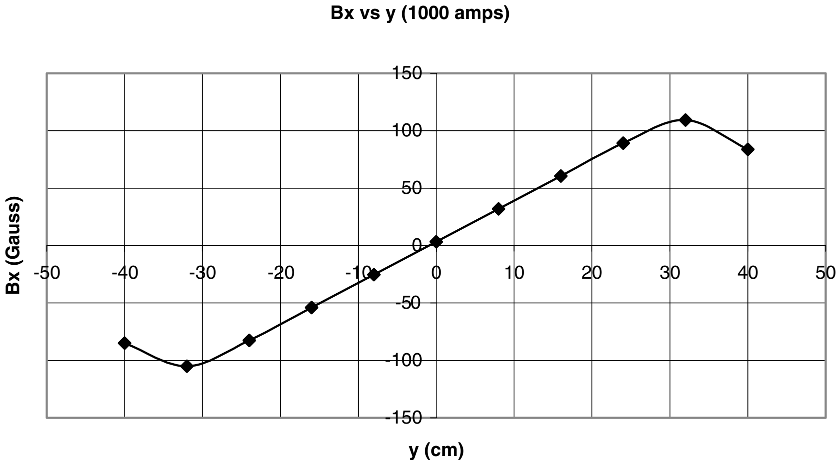

Figure 8-17. Transverse magnetic field strength for a Panofsky lens 70 cm in height with a bar separation of 10 cm, as calculated by Poisson. The current in each coil was 1000 ampere-turns.

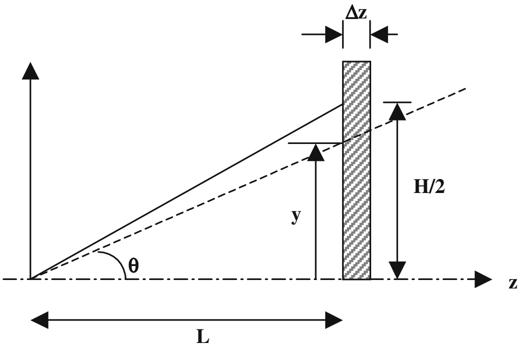

Figure 8-18. A transverse magnetic field region is imposed on the exit end of a scan horn.

$B_{max} = 0.035$ T = 350 gauss. From the calculation of Figure 8-15, the required exciting current would exceed 3000 ampere-turns. Unless care is taken in the design of the bars, these high currents can lead to saturation of the iron and a severe distortion of the field profile, especially at large aspect ratios ($H/\Delta z$).

b. Sector (Bow-Tie) Magnets

The reason that such high currents are required in the Panofsky lens is that the transverse field between the bars is essentially the fringing field of the coils. Instead of using a magnetic field profile that varies spatially, an alternate approach is to use a uniform magnetic dipole field over a well-defined region that varies in lateral extent, as suggested in Figure 8-19. Such a dipole is generally termed a sector magnet. These magnets are often used as thick lenses to give one-dimensional focusing of parallel beams, but they can also be inverted to create parallel beamlets.

There are many possible shapes for the pole pieces, but for reasons that will become apparent later, we will choose the exit plane of the magnet to be vertical, as illustrated in Figure 8-19. A mirror image of this pole piece combination is also placed below the axis, and coils are wound about both pole pieces in the form of a figure eight. With this characteristic shape, this sector magnet combination is often termed a "bow-tie" magnet.

To calculate the required shape of the beam entrance face of the dipole, we consider Figure 8-19 in more detail. A beamlet emerges from the scanner magnet at an angle θ, and enters the dipole field at position (x_1,y_1). When in the dipole field, the radius of curvature R is constant. The beamlet is required to emerge from the sector magnet in the horizontal direction. From simple geometrical considerations, we must have

$$\tan\theta = y_1/x_1 = s/(y_1 - \Delta y) \tag{8.41}$$

In addition, all electrons must emerge horizontally from the dipole at the same axial distance $L = x_1 + s$ from the scanner magnet. When the maximum deflection angle and scan height are selected, these constraints completely specify the problem.

As a numerical example, we assume a 5-MeV beam and a constant dipole field B = 0.05 T = 0.5 kG. From Eq. (8.6′) the radius of curvature is R = 36.7 cm. The maximum half-height of the scan is chosen to be H/2 = 60 cm, at a maximum scanner deflection angle $\theta_m = 22$ degrees. Therefore,

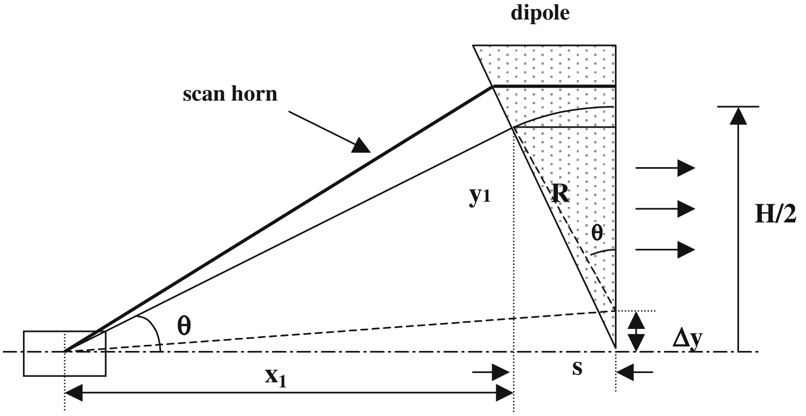

Figure 8-19. Schematic drawing of the sector magnet approach.

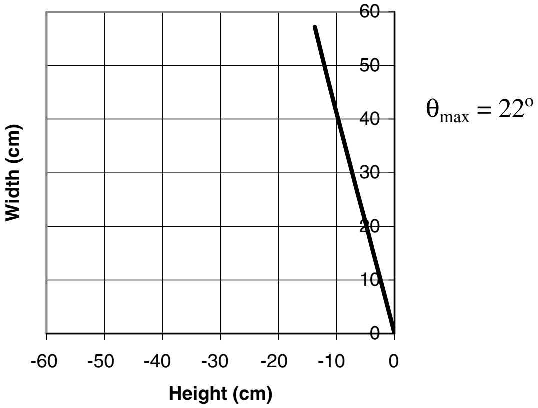

Figure 8-20. Entrance face of the dipole magnet for 5 MeV, 500 G, and H = 60 cm.

$s_m = R \sin\theta_m = 13.7$ cm. Since $\Delta y_m = H/2 - R = 23.3$ cm, then $y_{1m} = 57.2$ cm and $x_{1m} = 141.6$ cm, from Eq. (8.42), and $L = 155.3$ cm. Having specified these dimensions for the maximum deflection angle, the entrance face of the dipole can then be determined for all other deflection angles. The result is shown in Figure 8-20. For the small maximum deflection angle, the entrance face of the dipole is nearly linear.

8.4.4. Combined Beam Splitter / Beam Scanner Concept[6]

As discussed in Chapters 3 and 4 it is often beneficial to irradiate products in a symmetric, double-sided fashion. This could be achieved, for example, with a single pass of product through two identical accelerators placed on either side of the conveyor track, or by a single accelerator / double-pass conveyor system with a product rotation or translation stage (see Chapter 9). A third attractive option is to split the beam from a single accelerator into two equal halves that are directed to opposite sides of a single-pass conveyor track. There are many beam splitting concepts discussed in the patent literature. However, the results of the previous section suggest a simple, direct approach for realizing the split beam objective, as shown in Figure 8-21.

A single scanner magnet deflects the beam with a programmed, time-varying magnetic field pattern, such as that shown in Figure 8-22, resulting in a combined splitting / scanning action. Following the upper trajectories as an example, all beamlets are first directed horizontally by the upper half of a modified bow-tie magnet, and then perpendicularly onto the product by the fixed dipole magnet. Two sample electron trajectories are shown for illustrative purposes. This approach therefore uses only five magnets. The analysis of this system is nearly identical to that of the bow-tie magnet, and will not be repeated. The orientation of the dipole magnets as shown provides a magnification of the scanning action; a factor of two is typical.[7]

8.4.5. Alternative Pallet Irradiation Concept[8]

In Chapter 4 it was shown that even relatively dense products contained on pallets could be effectively processed using x-rays, provided that the pallet was rotated in front of the x-ray converter. Consideration of Figure 8-21 suggests an alternate approach that is topologically equivalent, but which uses beam manipulation rather than pallet rotation to achieve improved dose uniformity.

Refer back to the schematic diagram of Figure 4-53. The beam is scanned horizontally while the pallet is raised or lowered. Now, the use of back-to-back magnetic sector lenses, similar to those

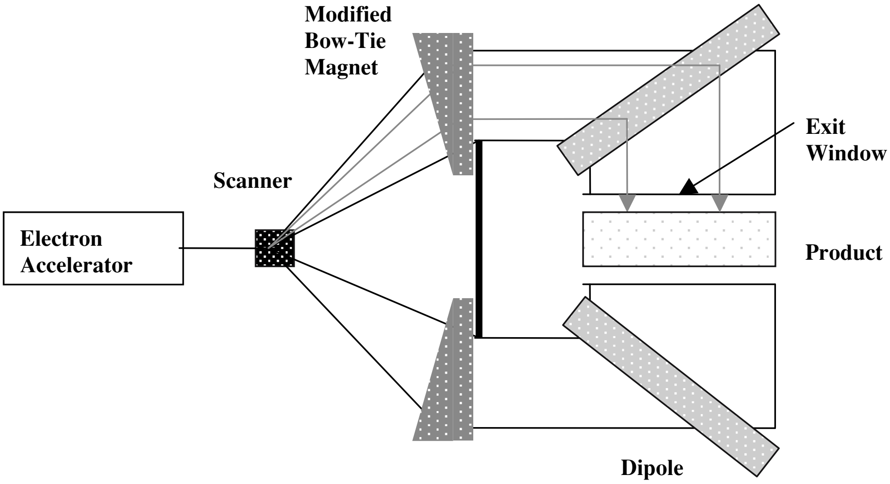

Figure 8-21. Schematic diagram of a combination beam splitter / beam scanner system.

considered previously, cause the electron beamlets to be incident onto the converter such that all the rays converge at the center of the pallet. If irradiated from only one side, the pallet is raised and lowered through the beam a total of four times, with the pallet being rotated by 90 degrees between irradiations. If two machines are available (placed on opposite sides of the pallet, for example), the pallet is lowered through the beams, rotated by 90 degrees and raised through the two beams to complete the processing.

The front part of the magnet can be thought of as a sector lens that causes all electron trajectories to become horizontal, while the exit portion of the magnet can be thought of as a sector lens that focuses all trajectories at the center of the pallet. The shape of this magnet can be determined using the previous analyses. For a 5-MeV beam, a maximum scan angle of +/−11.25 degrees, a product footprint of 120 cm by 120 cm, a 10 cm air gap, and an assumed field strength of 1 kG (giving a radius of curvature of about 18 cm), the shapes of the pole pieces are shown in Figure 8-23 (neglecting fringe field effects). Note that the angle of the entrance face is nearly constant; the angle of the exit face is not constant, however. The maximum excursion of an electron having the maximum scan angle is about 75 cm from the midplane. Thus, the total length of the modified bow tie dipole magnet

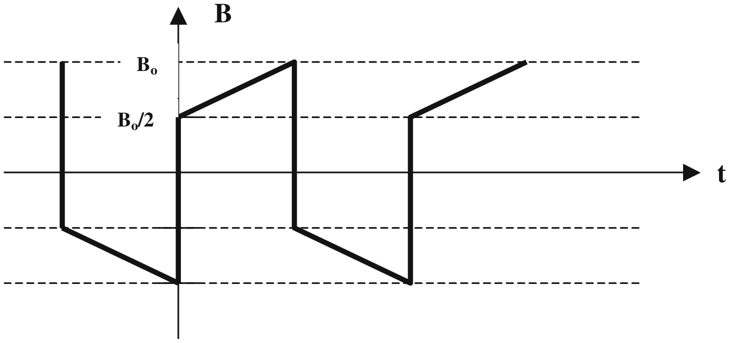

Figure 8-22. Scan magnet waveform for the combined beam splitter / scanner concept.

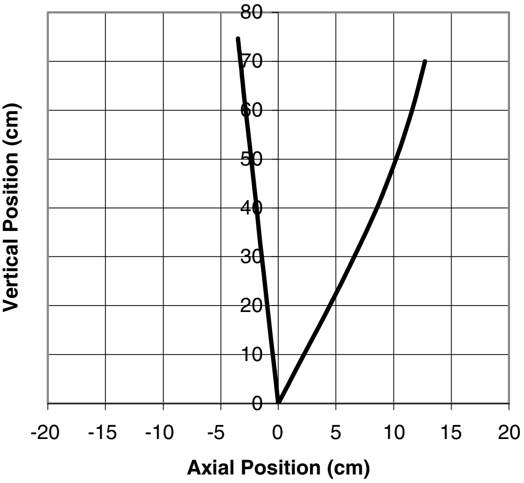

Figure 8-23. Approximate shape of the pole pieces for focusing all beam trajectories at the center of a 120 cm by 120 cm pallet.

will be of the order of two meters. With this shallow scan angle, the scan horn is rather long (about four meters). A larger scan angle would decrease the length of the scan horn, without appreciably changing the length of the dipole. The front face of the dipole would necessarily have a different angle, however.

8.5. SUMMARY

Almost every food irradiation installation uses magnets to manipulate the electron beam in one way or another. In this chapter we began by considering the motion of electrons in dipole, solenoid, and quadrupole magnets, developing the appropriate equations of motion to describe the trajectories. Using such analyses, we then examined several specific magnet applications, the most important of which is beam scanning. Since the energetic electron beam produced by the accelerating system generally has a radius that is much smaller than the physical dimensions of the product to be irradiated, the beam must be scanned across the product to provide uniform exposure. This scanning action can be generated by a time-dependent magnetic deflection of the beam in a dipole scanner magnet.

Since most accelerator systems are pulsed, care must be exercised when choosing the scan frequency to ensure a uniform front surface dose. For machines with pulse durations of the order of 100 μsec or less, it is usually necessary to use a relatively slow scan rate with many pulses per scan. On the other hand, for longer pulse machines operating at lower pulse repetition rates, it may be necessary to provide a complete scan during the pulse. For applications requiring high conveyor speeds, solenoidal and quadrupole lenses can be useful for producing beam spots of particular dimensions to improve front surface dose uniformity.

Once the beam has been scanned, special dipoles called sector magnets can be used in a variety of beneficial ways. These include directing the beam onto an x-ray converter at normal incidence, and creating convergent beamlets for irradiating thick pallets of products. Finally, with a suitable modification of the scanning waveform, it is possible to split the beam and scan it using a single magnet. When combined with sector magnets and simple dipoles, this approach facilitates the double-sided irradiation of products using a single conveyor lane.

REFERENCES

1. J. H. Billen and L. M. Young, POISSON/SUPERFISH, Los Alamos National Laboratory Report **LA-UR-96-1834** (rev. December, 1997).
2. R. B. Miller, **An Introduction to the Physics of Intense Charged Particle Beams**, Plenum, NY (1982).
3. S. Humphries, Jr., **Principles of Charged Particle Acceleration**, John Wiley and Sons, NY (1986).
4. J. D. Jackson, **Classical Electrodynamics**, John Wiley and Sons, NY (1962).
5. V. L. Auslender, A. A. Bryazgin, B. L. Faktorovich, V. A. Gorbunov, M. V. Korobeinikov, S. A. Maksimov, V. E. Nekhaev, A. D. Panfilov, V. O. Tkachenko, A. A. Tuvik, and L. A. Voronin, Vestnik "Radtech Euroasia" **N2(10)**, Novosibirsk (1999).
6. R. B. Miller, "System for, and method or, irradiating opposite sides of an article," US Patent Appl. Ser. No. 10/224,062 (2003).
7. R. S. Smith, et al. To be published.
8. R. B. Miller, "X-Ray Pallet Processing System," SureBeam Patent Disclosure (2002).

CHAPTER 9

MATERIAL HANDLING SYSTEMS AND COMPONENTS

The primary functions of the material handling system are to efficiently transport products to and from the irradiation zone, to move products through the irradiation zone in a precisely controlled manner, and in the case of service centers, to efficiently move food products into and out of the facility. In the irradiation zone itself there must be no slippage of material, and large gaps between food packages or carriers, and variations in product depth (more precisely, areal density) are to be avoided in order to maximize throughput efficiency. In this chapter we begin with a brief summary of the requirements for the material handling system for various representative applications. We then discuss several material handling systems of interest, including interface requirements and important components. Finally, we consider a few representative examples.

9.1. MATERIAL HANDLING SYSTEMS REQUIREMENTS

The process flow diagram for a typical service center irradiation facility is shown in Figure 9-1. Palletized food packages are off-loaded by fork truck from a transportation trailer and moved into the conveyor loading area. The packages are depalletized (either manually or by robot), and are loaded onto a suitable conveyor system, either directly or in totes or carriers. The conveyor system transports the material through the irradiation zone, and moves the material to an unloading/storage area. The irradiated packages are removed from the conveyor and repalletized, and the pallet is stretch wrapped in thin plastic film. The wrapped pallets are then moved by fork truck back onto the transportation trailer. The key elements of the material handling system (MHS) in this simple (but representative) example include the fork truck, depalletizer, various elements of the conveyor system, repalletizer, and the wrapping machine. In the following paragraphs of this section we discuss several general issues associated with food irradition, indicating how they influence the choice of material handling approach, and how requirements for the MHS are established.

The heart of the MHS is the conveyor. Considering the irradiation step in somewhat more detail, the conveyor system must ensure the precise motion of product through the beam(s), with minimum gaps between cartons or carriers, regardless of the material input rates at the load station. This usually requires different conveyor speeds in various regions of the product flow path, the accumulation of product at a stop gate, and precision release of product from the stop gate. For maximum throughput, the rate-limiting step for the process should be the irradiation of product; the material handling system design should eliminate other potential bottlenecks.

There are many different conveyor system approaches, including for example, belt conveyors, chain and roller conveyors, and overhead power-and-free conveyors, as well as specialized auxiliary equipment including turntables, transfer stations, rotate mechanisms, etc.[1–3] The selection of a particular approach, or combination of approaches, is largely guided by the type and packaging of the product (physical properties), the mode of radiation (e-beam, x-ray) to be used, and the required

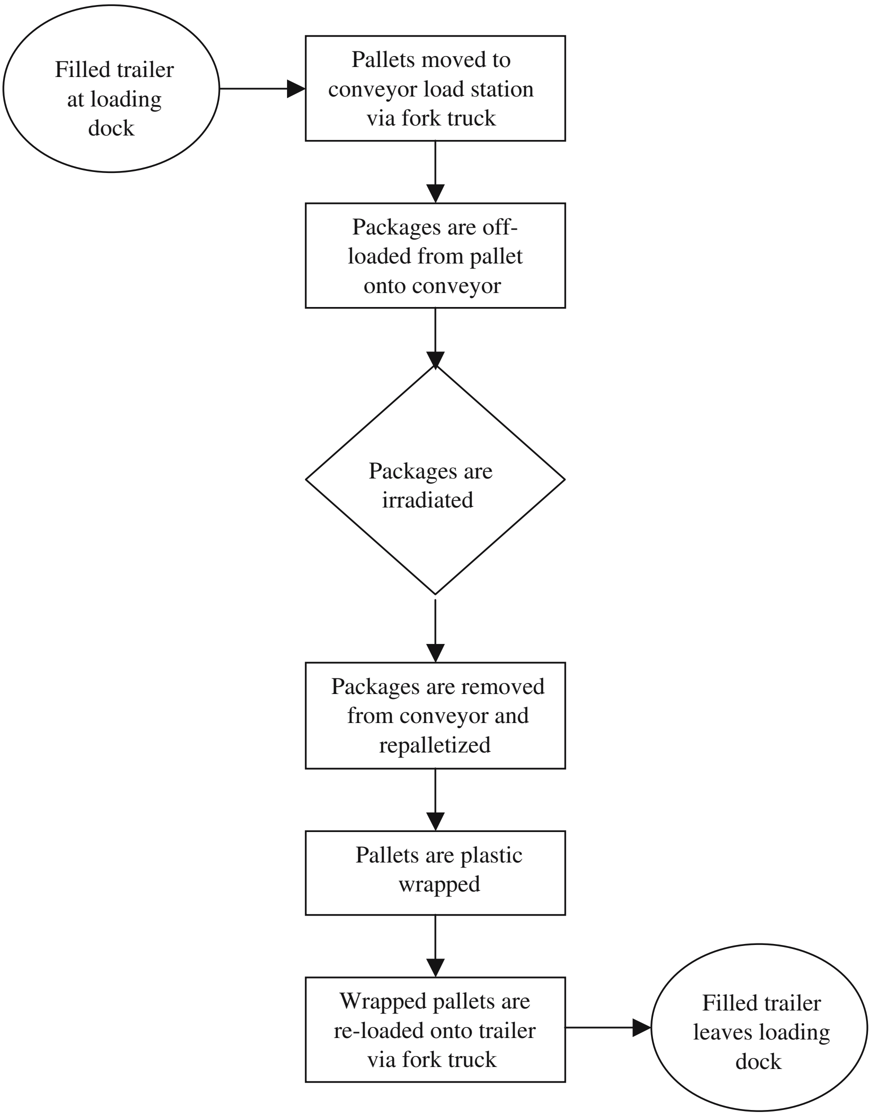

Figure 9-1. Process flow diagram for a typical service center food irradiation facility.

throughput rates, in addition to the usual considerations of cost, reliability, maintainability, noise, etc.

While an irradiation system installed in a food producer's facility might be required to treat only one type of product (spices processed in bulk, for example), service centers must be able to accommodate a wide variety of products. Since these products are shipped to the irradiation facility, they will be packaged in a number of different boxes, bags, pallets, etc., and it is important to know the package dimensions, shapes and unit weights, as well as the characteristics of any load surfaces that might interface with the conveyor system. If the product cannot be placed directly on the conveyor system, specially made totes or carriers are necessary. The design of these containers will depend largely on the physical characteristics of the products and the irradiation mode. For example, ground

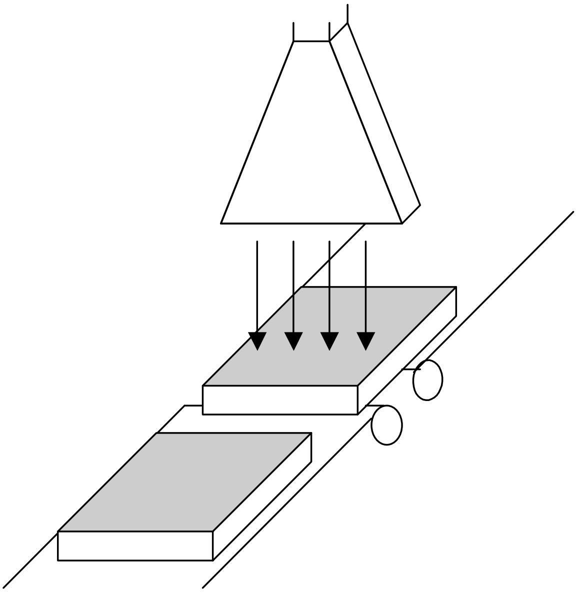

Figure 9-2. Typical electron irradiation configuration. Packages are placed flat onto a belt or slat conveyor. The beam is directed vertically downward and scanned horizontally across the product. A second beam may be directed vertically upward for double-sided irradiation.

beef chubs must usually be close-packed as a single layer into a cardboard tote for electron beam irradiation. For products that might be susceptible to recontamination, the packages must be sealed prior to the irradiation.

9.1.1. Radiation Mode

From Chapter 3, the maximum areal density that can be processed using electrons is about 8.9 g/cm^2 (double-sided irradiation using 10-MeV electrons). Since food products have densities generally in the range of 0.3–1.0 g/cm^3, the maximum product thickness that can be processed will be in the range of 9–27 cm. Since this dimension will almost always be the smallest product dimension, it is usually preferable to use vertically directed beams in the electron irradiation mode, from the standpoint of package stability and handling ease. Bulk products can be distributed in uniform fashion on a belt conveyor, and packaged products can either be placed directly on a belt conveyor on in totes on a roller conveyor, for example. The beams are then scanned across the products in the horizontal direction, as schematically shown in Figure 9-2.

On the other hand, it is usually preferable to use horizontally directed beams when processing in x-ray mode. Since it is always best to use (at least) double-sided irradiation when processing with x-rays, the optimum product thickness is approximately given by (from Eq. (4.50))

$$x_{\mathrm{opt}}(\mathrm{cm}) = 2(0.012 + 0.045\rho)^{-1} \tag{9.1}$$

As an example, for $\rho = 0.5$ g/cm^3, x_{opt} is 58 cm. To maximize throughput efficiency it is desirable to arrange product packages such that the total product thickness presented to the x-ray beam is nearly equal to x_{opt}. This is usually accomplished most easily by stacking product packages in symmetric fashion (for double-sided irradiation) to the desired horizontal thickness on a carrier

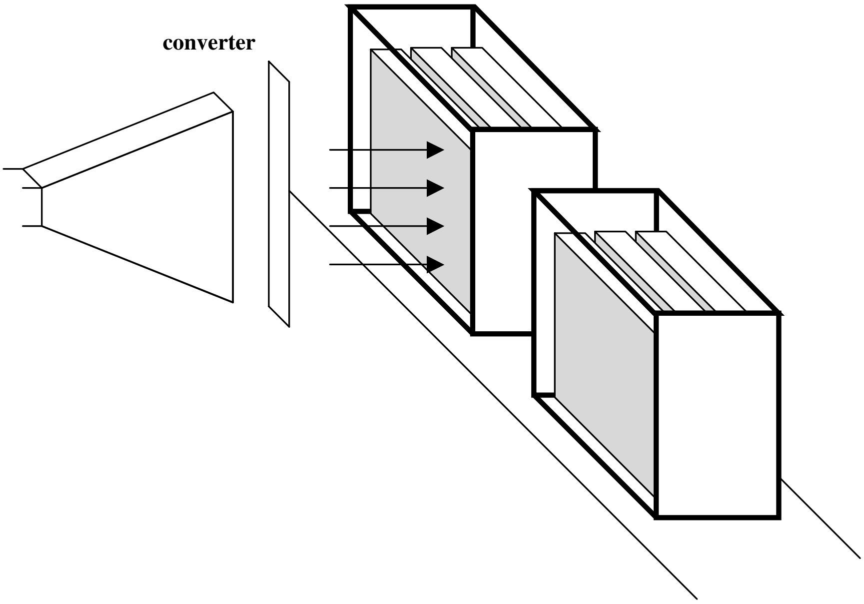

Figure 9-3. Typical x-ray irradiation configuration. Packages are loaded onto a carrier to a depth suitable for x-ray irradiation. The beam is directed horizontally and scanned vertically across the carriers. A second beam may be directed horizontally from the other side for double-sided irradiation, or the carriers may be rotated for a second pass.

of fixed dimensions, as schematically described in Figure 9-3. Such carriers can be conveniently transported to the irradiation cell using an overhead power and free system. Also, with a horizontal beam from only one accelerator, a rotation or transfer station can facilitate double-sided irradiation, as described in Chapter 2; with a single vertical beam, however, packages would have to be flipped, with the possible shifting of contents.

For some products that are normally transported by pallet, it may be important to minimize handling (for example, to avoid injury to fragile strawberries). In such cases it would be desirable to process the product on the pallet using x-ray irradiation. Considering Eq. (9.1) it may be necessary to use more sophisticated pallet rotation or beam manipulation approaches to achieve satisfactory dose uniformity ratios; i.e., conventional conveyor systems may not be appropriate.

9.1.2. Throughput Requirements

Processing speed requirements are estimated by the available beam power, the minimum required dose and the irradiation mode according to

$$\mathrm{dm}/\mathrm{dt} = \eta \mathrm{P}/\mathrm{D} \qquad (9.2)$$

The minimum required dose ranges from a low of about 250 Gy for disinfestation, to 6–10 kGy for preservation of freshness for spices, while the machine power ranges from several kilowatts to perhaps a few hundred kilowatts. The throughput efficiency is typically 0.4–0.5 for electron beam mode, but is usually no greater than 0.03 for x-ray irradiation at 5 MeV, and 0.045 at 7.5 MeV.

A few numerical examples serve to illustrate the range of processing speeds and unit weights that might be required of the material handling system.

(a) **E-beam disinfestation of tropical fruit with $P = 15$ kW, $D = 0.25$ kGy, $\eta = 0.5$:**
In this case Eq. (9.2) implies a mass throughput rate of 30 kg/s, which is relatively high. Assuming an average areal density of 6 g/cm^2 and a scan width of 120 cm, the implied conveyor speed is 41.7 cm/s, or about 83.3 feet per minute. If the product is arranged in cardboard totes having a tote footprint of six square feet, the total weight of product on a tote is about 33.4 kg.

(b) **X-ray processing of spices with $P = 30$ kW, $D = 6$ kGy, and $\eta = 0.03$ (5 MeV):**
In this case the mass throughput rate is only 0.075 kg/s. Assuming an average density of 0.5 g/cm^3, and that the product is stacked on a carrier to optimal thickness, the areal density is approximately 30 g/cm^2. With product filling a maximum scan height of 120 cm, the implied conveyor speed is therefore about 0.04 cm/s, or about 0.08 feet per minute. For a carrier length of 120 cm, the weight of product on a single carrier exceeds 400 kg.

(c) **X-ray processing of beef trimmings in a pallet, with $P = 300$ kW, $D = 1.5$ kGy, and $\eta = 0.025$ (5 MeV):**
In this case the mass throughput rate is approximately 5 kg/s. For pallet dimensions of 100 cm × 100 cm × 180 cm and an average density of 0.8 g/cm^3, the mass of product on a pallet is 1440 kg, and the average processing time for a single pallet is about 300 seconds. If the pallet is to be processed using rotation, the average rotation rate is 1.2 degrees per second.

From this brief discussion, conveyor systems should be capable of operating at speeds in the range of 0.1–100 feet per minute. The weight of product arranged in totes for electron beam processing will typically be a few tens of kilograms, while the weight of product on carriers for x-ray processing will typically be a few hundred kilograms. Full pallets may exceed a metric tonne.

9.1.3. Radiation Shielding and Ozone Considerations

The design of the x-ray radiation shield is examined in some detail in Chapter 10. When designing the shield there are generally two issues that must be considered. The first is the direct (line-of-sight) radiation; designing the shield to have sufficient attenuation for this radiation source is relatively straightforward. However, since products must enter and exit the irradiation zone, radiation that is scattered along the conveyor corridors can pose a severe hazard. This scattered radiation is decreased by minimizing the widths of corridors, and by building the shield in the form of a maze (and by having product on the carriers). Consequently, the conveyor and any product carriers or totes must be able to turn corners within the maze. Elevation changes can also be used to decrease hall widths.

From Chapter 1 excessive radiation dose can cause deterioration of organic compounds. In addition, the ozone generated by electron and x-ray propagation in air can cause rapid oxidation of bare steel and iron components. Since the process table lies in the high radiation zone, its components must use materials that are not susceptible to either radiation degradation processes or oxidation attack by ozone. This eliminates the use of essentially all organic compounds (plastics, rubber, certain organic lubricants, etc.), and usually requires use of stainless steels, or metals that form self-protecting oxidation layers, such as aluminum.

9.2. CONVEYOR SYSTEMS

Having summarized the general requirements that must be satisfied by the conveyor system, we next consider the various types of conveyors that are available. These are usually classified according to the mounting approach, i.e., overhead trolley or floor-mounted, and the type of load to be conveyed, i.e., bulk materials or unit packages.[4] Bulk materials, such as grain or raw spices could be conveyed via chutes or on belt conveyors, while fluids could be conveyed through pipes, troughs, or as exhaust from a chute. At the present time, processing of these bulk food materials is not common, and we will not consider them further. Unit materials such as cartons, bags, and/or packages stacked on pallets might be conveyed with belt, roller, and slat conveyors mounted on the floor, or borne by overhead trolleys. We will consider these various approaches in more detail.

9.2.1. Floor-Mounted Conveyor Systems

The primary distinction between the various floor-mounted conveyor systems is the method by which material proceeds along the flow path.[5] With simple gravity conveyors, the material moves under action of its own mass down sections of freely rotating rollers or skate wheels. With belt and slat conveyors, the material is transported along with the moving surface. On the other hand, with powered rollers loads are propelled by fixed rollers that are driven by belts or drive chains.

Gravity Conveyors[6]

Unpowered roller and wheel conveyors (see Figure 9-4), either inclined or horizontal, are usually termed gravity conveyors. These are usually the cheapest means of transferring food parcels, and are relatively easy to install and maintain. Although skate wheel conveyors are generally more economical than roller conveyors, they are limited to light-duty applications. For the medium loads more characteristic of food parcels (a few tens of pounds) rollers are preferred. In food irradiation facilities the primary location for a gravity conveyor is at the unload station. Also, if elevation has been used to reduce the corridor width in the radiation shield, a gravity conveyor provides a convenient method for bringing the irradiated products down to worker level for repalletization.

For wheel conveyors the number of wheels per foot of travel is typically equal to the width of the conveyor in inches; i.e., a conveyor that is 18 inches in width will have nominally 18 wheels per foot of travel. Standard wheels are 1 15/16 in. diameter with $^1/_4$ in. axles. For roller conveyors, the diameter of a roller is usually in the range of 1–3 inches. The roller pitch (the center-to-center spacing of the rollers) must ensure that at least three rollers are under the carrier or tote at all times, and six rollers are common.

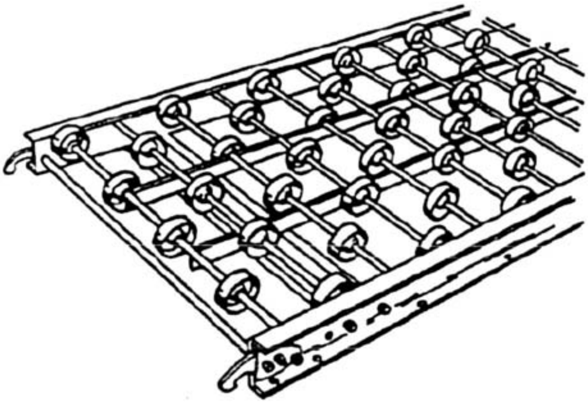

Figure 9-4. A section of skate-wheel gravity conveyor. Courtesy of the Material Handling Industry of America (www.mhia.org). (From "Supplement to An Overview of Basic Equipment;" all rights reserved.)

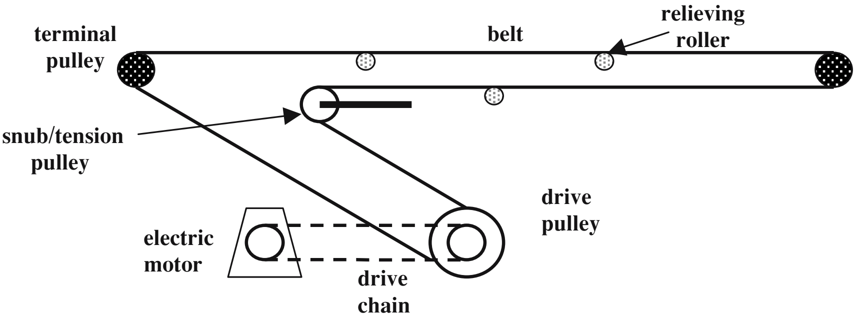

Figure 9-5. Schematic diagram of a belt conveyor, with underslung drive pulley. Courtesy of the Material Handling Industry of America (www.mhia.org). (From "Supplement to An Overview of Basic Equipment;" all rights reserved.)

The descending slope of the conveyor depends on the weight of the parcel. For normal use the slope should be of the order of 5% (6 inches of fall in a standard length of 10 feet) for packages weighing a few tens of pounds. Lighter packages require a steeper slope, and heavier packages require less steepness. A good cardboard carton is an ideal load for a gravity conveyor. If the cardboard has become softened by excessive radiation exposure or moisture however, a much steeper slope will be necessary. If the decline is curved, the slope should be increased by at least 75%. Guide rails should always be used in curves, and tapered rollers can improve the performance of curved sections.

Belt Conveyors[7]

A belt conveyor consists of a pulley driven belt that rides on either a slider plate or rollers. The belts themselves are usually made of either a solid weave or plies of canvas that are impregnated with rubber or plastic compounds to provide considerable friction with the load. Consequently, belt conveyors are especially useful for inclines and controlled declines, and as feed conveyors. However, the high friction prevents smooth accumulation, and organic belts cannot be used in the process corridor because of radiation degradation.

A typical belt conveyor configuration is shown schematically in Figure 9-5. A geared electric motor drives a chain that turns a drive pulley. The belt rides on terminal pulleys and relieving rollers placed periodically along the belt path. A snub pulley provides a means for adjusting the belt tension. Working belt tensions of approximately 100 lb-ft per inch of belt width are typical. For a given feed rate, higher belt speeds imply less weight per unit length, allowing the belt tension to be reduced. When used as an incline, the maximum elevation angle depends on the configuration and surface of the carton or tote, the type of belt used, and the method of feeding the incline. A slope of 25 degrees is a practical maximum for conveying most carton sizes.

Slat and Chain Conveyors[8]

Thin stainless steel belts are available and could be used to transport bulk materials through the irradiation zone. However, chain-driven slat (or bar) conveyors are preferred for food parcels or totes. A slat conveyor resembles a belt conveyor in that slats or bars are rigidly attached to a chain that is driven by a wheel or sprocket. The significant friction afforded by this design provides excellent control of the orientation and movement of product. Consequently, chain-driven slat or bar conveyors are well suited for moving products through the irradiation zone. In addition, the slats can be made of, or plated with, stainless steel to resist oxidation by ozone attack. A further extension of this

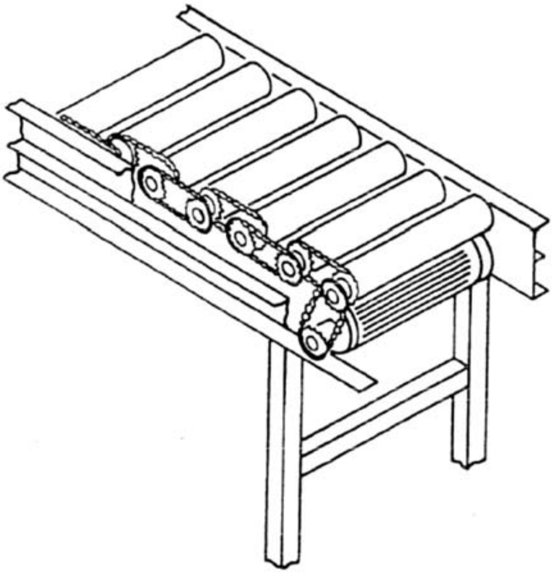

Figure 9-6. Roller to roller chain-driven live roller conveyor. Courtesy of the Material Handling Industry of America (www.mhia.org). (From "Supplement to An Overview of Basic Equipment;" all rights reserved.)

approach, especially useful for facilities using horizontal beams, is to specially design the bottom of the carrier to interlock with the slats, or even with the drive chain(s) itself. In most cases the chain does not have to support the load, but simply propels it along a roller bed or an overhead trolley.

Powered Roller Conveyors[9]

Live, or powered roller conveyors are very versatile, with applications including not only transport, but also accumulation, diverting, and turning. Practically any load having a rigid, smooth base can be moved on roller conveyors. Thus, cardboard boxes or cardboard totes containing food items are ideal for use with powered roller conveyors. Such conveyors are usually categorized by the mechanism used to turn the rollers. The most common approaches use drive belts and drive chains, either continuous or roller to roller. Belt driven units are nearly identical in layout to the belt conveyor of Figure 9-5 except that the top of the belt contacts the undersides of the rollers, causing the rollers to rotate and propel the load in the direction opposite that of belt motion. Very light loads can be transported by a continuous chain live roller conveyor, in which a single chain meshes with a sprocket at the end of each roller. A continuous cover plate maintains chain contact with the sprocket. A more versatile construction uses roller to roller drive chains. In this case there are two sprockets on the end of each roller. Individual chains connect pairs of rollers in a staggered pattern along the length of the conveyor, as schematically shown in Figure 9-6. Such conveyors can carry a wide variety of loads, and contact between chains and sprockets is ideal.

The roller width, diameter and pitch are typically determined by the size and weight of the parcels to be conveyed. As an example, a single bush-bearing steel roller with a diameter of $2^1/_4$ inches and a 5/8-in spindle diameter has a carrying capacity of nearly 150 pounds (68 kg). For vertically directed electron beam systems, the maximum weight per unit area is set by the areal density penetration limit of <10 g/cm^2. Therefore, for a roller width of 24 in (60 cm), the maximum allowed roller pitch from only load bearing considerations would exceed 100 cm. Thus, food parcels in this application are considered to be light loads, and the roller pitch is usually governed by maintaining adequate control of the parcels; as a result, 4″ and 6″ pitches are commonly used.

For roller conveyor curves, the outside conveying surface should turn faster than the inside surface to facilitate proper tracking. For articles such as cartons or totes, tapered rollers offer a good solution. The inside radius of a roller curve should be greater than the length of the longest article to be conveyed. Together with the conveyor width, this specifies the desired roller taper.

The required power of the drive motor depends on the total weight (M) of the material on the conveyor, the coefficient of friction (f) between the stationary boxes and rollers, the conveyor speed (v), and the drive efficiency ε, according to Eq. (9.3). (The product fM is usually termed the chain pull.) Assuming five 60-lb boxes on a 20-ft length of conveyor, and a coefficient of friction of 0.15, the total conveyor load is 300 lb, and the motor must have at least 900 lb-ft of starting torque. At an assumed conveyor speed of 60 ft/min and a drive efficiency of 0.5, the minimum required power of the drive motor is 5400 ft-lb/min, or about 0.16 hp.

$$\mathrm{P(hp)} = [\mathrm{fM(lbs)v(ft/m)}]/(33,000\varepsilon) \tag{9.3}$$

Special Conveyor Functions[10]

In addition to basic material transport, conveyors are used to perform several other material handling functions, including accumulation, merging, sorting, and transfer, to achieve appropriate material flow and control. We briefly discuss the accumulation and transfer functions in the following paragraphs.

Accumulation

Accumulation is a basic function that can help satisfy four different material handling needs: (1) absorbing surges in material flow; (2) providing backlog ahead of machines and processes; (3) providing accurate control of loads into transfers, merges, sizing stations, counters, etc.; and (4) reducing pressure so that loads may be removed from the middle of a line. There are many conveyor manufacturers who offer a variety of accumulation options, many of which are patented. However, for the purposes of discussion these can be generally grouped into three types: flexible accumulation, slug accumulation, and fixed accumulation. As the names suggest, with slug accumulation, a product queue is accumulated and moved simultaneously on release from a stop gate; fixed accumulation simply means one load in and one load out. Flexible accumulation is characterized by independent inputs and outputs. Since the irradiation itself is usually the rate-limiting step, and the input load rate can vary considerably, flexible accumulation is usually the approach of choice for food irradiation facilities. In this case, the stop gate acts as a buffer, allowing product backlog. Opening the gate releases a single load for the subsequent close packing of articles on the process conveyor.

Accumulation conveyors can be devised from roller, slat and belt conveyors. As an example, one common approach is to use a combination slat-and-roller conveyor, with articles being carried by free rollers acting as slats. When an article is stopped at a gate, the rollers simply roll underneath the article. Another common accumulation technique uses a belt-driven roller conveyor. When accumulation is necessary, a roller section is raised so that the rollers no longer contact the drive belt. Finally, with a Bosch-style conveyor,[11] work-piece platens ride on twin strands of belt, flat top chain or roller chain, allowing an open center for transfer, positioning, etc. Controlled sliding friction propels the platens until they encounter a stop gate or another platen. The platens can then accumulate by sliding on the low back-pressure strands.

Transfers

Articles are moved from one conveyor section to another at transfer stations or junctions. There are two important types of transfers. The first is simply the straight transfer of an article across a gap.

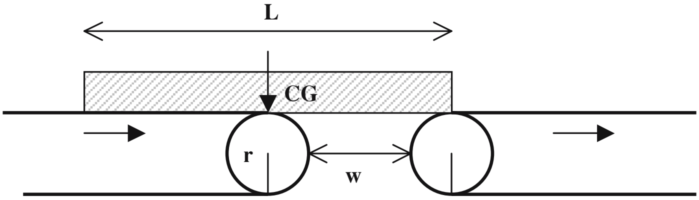

Figure 9-7. Transfer of an article across a gap of width w.

For example, if an article is to undergo electron irradiation from both top and bottom, there must be a gap in the conveyor to allow the upward-directed beam to pass unimpeded to the article. The width of the gap depends on the beam spot size, the sprocket radius, and the length of the articles to be irradiated. Referring to Figure 9-7, if a carton of length L is uniformly loaded such that the center of gravity is in the middle of the article, then the maximum gap width w_{max} is determined as

$$w_{max} = L/2 - 2r \tag{9.4}$$

where r is the radius of the sprocket. Smaller sprockets therefore permit larger gaps for a given package length. To allow for nonuniform loading, it is common practice to restrict the width of the gap to

$$w < L/3 - 2r \tag{9.5}$$

Another important reason for a transfer junction is to adjust the spacing between articles. Consider Figure 9-8. Efficient use of the available beam energy implies that packages should be closely packed as they move through the beam(s) on the process conveyor. With the process conveyor speed v_p being the rate-controlling factor, close packing could be achieved using a timed release of articles onto a feed conveyor running at a faster speed v_f. The arrival period between one article and the next must be the same on both conveyors, and equal to the release time T. Therefore, the separation s_p between articles on the process table must be related to the separation s_f on the feed conveyor according to

$$T = (s_p + L)/v_p = (s_f + L)/v_f \tag{9.6}$$

As a numerical example, if the packages are 50 cm in length, the desired separation between packages on the process table is 2 cm, and the process conveyor speed is 10 cm/s, then the release time is 5.2 seconds. If the feed conveyor is running at a speed of 20 cm/s, then the separation between packages on the feed conveyor is 54 cm.

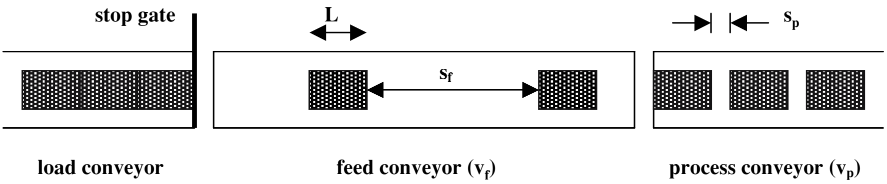

Figure 9-8. Control of the spacing between articles on the process conveyor.

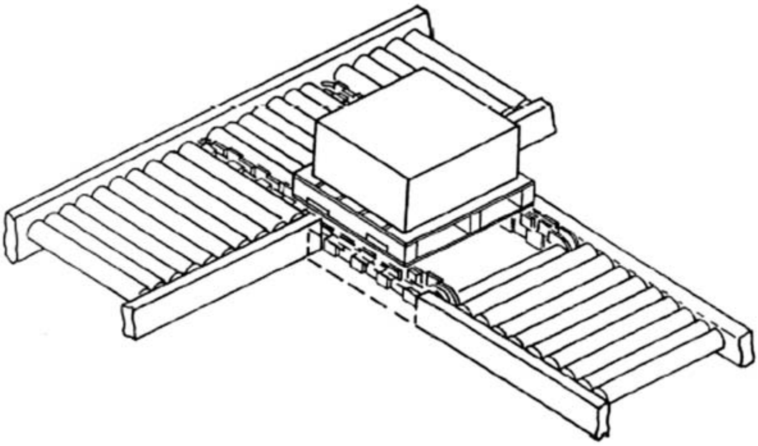

Figure 9-9. Two-strand chain conveyor used as a cross transfer device. Courtesy of the Material Handling Industry of America (www.mhia.org). (From "Supplement to An Overview of Basic Equipment;" all rights reserved.)

Eq. (9.6) assumes no slippage of articles on conveyors, and is therefore dependent on good friction between the cartons and conveyors. As a carton or tote moves across a junction, its speed is increasingly controlled by the downstream conveyor, but it generally cannot be considered to move at the speed of the downstream conveyor until its center of gravity has crossed the transfer gap.

For the transfer of an article from a faster conveyor section to a slower section, the slower section will act as a brake. If articles are misaligned at the transfer gap, the braking action will tend to increase the misalignment (i.e., the rotation angle), unless guard-rails or skirts are used. A so-called "herring-bone" configuration of the rollers can also be used to move articles of width less than the conveyor toward a particular side of the conveyor. This permits a smaller scan width and more efficient use of the beam energy.

The second important type of transfer is the cross transfer, which is used to transport an article or carrier perpendicularly from one conveyor to another. A common design, shown in Figure 9-9, uses two thin strands of chains or belts that fit between the rollers of two conventional roller conveyors. When the article is in the correct position on the first conveyor, the strands are raised, and the article is lifted and transported to the second conveyor. When the desired position is reached, the strands are lowered, depositing the article onto the second conveyor. Such transfer stations can be used to introduce an effective 180° translation for a double-sided irradiation application.

9.2.2. Overhead Trolley Conveyors[12]

Single Track Trolley Conveyors

A trolley consists of a wheel/bearing/bracket assembly that is used to support suspended loads or load-bearing elements (see Figure 9-10). An overhead trolley conveyor consists of a series of such trolleys supported from or within an overhead track. There are two primary types of trolley conveyor. The simplest consists of equally spaced trolleys simply connected by a single endless chain or cable. This type of conveyor has relatively low maintenance, low cost and can change directions both vertically and horizontally with relative ease. It is quite useful for paced flow applications, but it affords little versatility for operations that require frequent starting and stopping at load/unload stations, while other parts of the process are to be operated continuously.

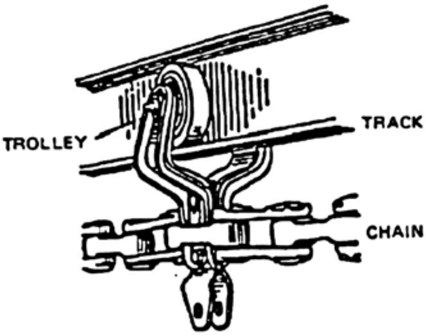

Figure 9-10. Trolley, track and chain of a simple overhead trolley conveyor. Courtesy of the Material Handling Industry of America (www.mhia.org). (From "Supplement to An Overview of Basic Equipment;" all rights reserved.)

Overhead Power and Free Conveyors[13]

Of more interest for food processing applications is the versatile overhead power and free (OHP&F) conveyor. In this system a second rail or track is added to the simple overhead conveyor. A continually moving power chain is carried by the upper track, while the load is suspended from a lower free track, as shown in Figure 9-11. Load carriers engage and are transported by the power chain by means of "pusher dogs" that usually engage the lead trolley. However, the trolley can easily be disengaged from the power chain to permit a variety of material handling operations, including line speed variation, route variation and accumulation.

An important capability of a power and free system is the movement of carriers from one powered section to another conveyor section that may be either powered or not. For example, this transfer function allows rapid transport to and away from the irradiation zone, while permitting the irradiation to occur at a slower, precisely controlled line speed. When combined with track switches, the automatic transfer capability also permits route variation, which can be especially useful for providing double-sided irradiation with a single horizontal beam. One commonly used design is the so-called push-across-dog method. After the lead trolley has separated from the power chain, the rear trolley (still in the power path) is subsequently engaged, propelling the front trolley into the new power path. Another important transfer method uses a paddle wheel. The delivery power chain wraps around a sprocket equipped with paddle arms that push the carrier across the transfer gap.

Track stops allow queing of multiple carriers in an accumulation bank. This feature allows precise release of carriers for close-packing through the irradiation zone, as well as storage on

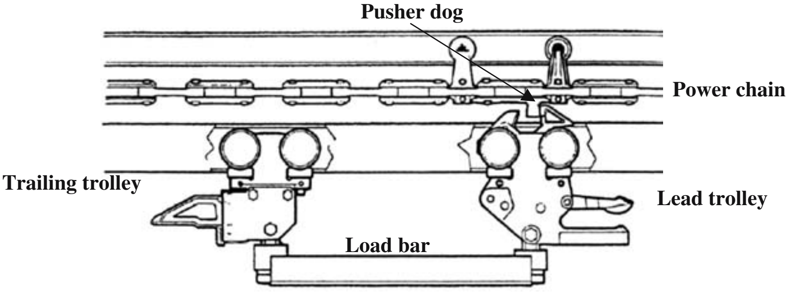

Figure 9-11. Overhead power and free conveyor with load bar and two trolleys. Courtesy of the Material Handling Industry of America (www.mhia.org). (From "Supplement to An Overview of Basic Equipment;" all rights reserved.)

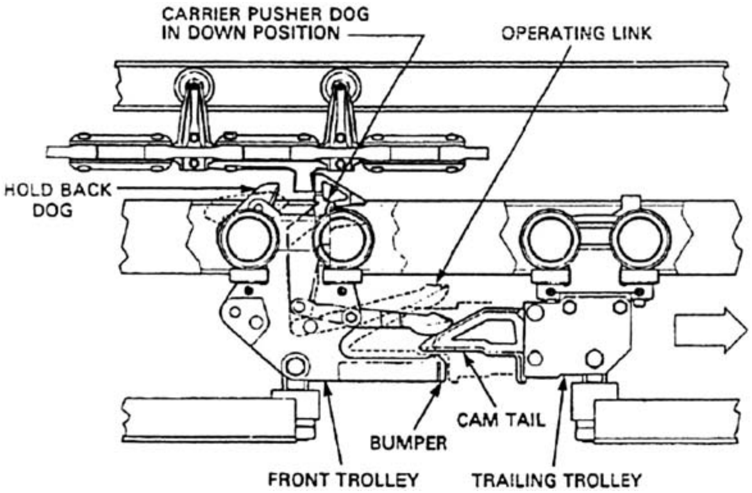

Figure 9-12. Overhead power and free conveyor illustrating a mechanism for self-accumulation. Courtesy of the Material Handling Industry of America (www.mhia.org). (From "Supplement to An Overview of Basic Equipment;" all rights reserved.)

loading and unloading spurs. The stop is normally a blade that is pneumatically inserted between the power track and the free track, causing disengagement of the lead trolley from the power chain, thereby stopping the carrier. Manufacturers have devised several approaches for causing subsequent carriers to accumulate statically while the power chain continues to move. The most common method is illustrated in Figure 9-12. An operating lever on the lead trolley of the trailing carrier engages the cam tail on the rear trolley of the first carrier. This lowers the carrier dog, disengaging the trolley from the power chain. The automatic transfer capability, when combined with track switches, stops and accumulation, also facilitates merges and multiple passes through the irradiation zone, as required.

The basic load-handling component of a power and free system is the load bar assembly to which the carrier is attached. The unit is specially designed for each system and has at least two trolleys. The separation of the trolleys by the load bar determines the radius for horizontal and vertical turns. In the absence of elevation changes, a typical two-trolley OHP&F system with a three-inch free track can transport maximum carrier loads of up to 2000 pounds. The required horsepower of the drive motor is given by Eq. (9.3). Assuming ten carriers of 400 pounds each, an effective coefficient of friction of 0.1, a conveyor speed v of 20 feet per minute, and a drive efficiency $\varepsilon = 0.5$, the required drive horsepower is approximately 0.5 hp.

9.3. MISCELLANEOUS MATERIAL HANDLING SYSTEM COMPONENTS

In addition to the various elements of the several conveyor systems, there are a number of other pieces of material handling equipment that have proven to be quite useful in food irradiation facilities. For service center operation, in which pallet unloading and re-loading onto transportation trailers is typically required, a counterbalanced rider forklift truck is nearly indispensable. Such trucks are usually battery powered to avoid noxious fumes inside the facility.

Service centers must usually be able to process a wide variety of products that are packaged in boxes or bags of various sizes and shapes. Consequently, it is usually best to manually de-palletize and re-palletize. If, however, products of predominantly only one size and shape are to be processed, automatic palletizing and depalletizing robots can be a time saving, cost-effective alternative.

For some products that are to be irradiated on the pallet, it may be necessary to seal the product prior to irradiation to avoid recontamination. In this case, shrink-wrapping with heat sensitive plastic film may afford the necessary protection. After the products have been irradiated and re-palletized, it is usually desirable to unitize the load on the pallet using either stretch- or shrink-wrapping. If the primary objective is to avoid recontamination (air permeable bags of spices, for example), shrink-wrapping is essential. If the primary objective is simply stabilization of the load on the pallet (with minor protection against dust and moisture), stretch-wrapping is a less expensive alternative.

Most irradiation examples considered thus far are best suited to the horizontal flow of articles. However, for some specialty applications (certain pallet irradiation schemes), it may be more desirable to move the product vertically. Lifts (elevators) using a constant velocity screw drive can be used for this application. The lifting platform can also be configured as a turntable to permit multiple-sided irradiation with a single accelerator system.

9.4. COMPUTER-ASSISTED PROCESS CONTROL

The explosion in reliable and inexpensive computer hardware and software has fostered a revolution in computer applications to material handling. Coupled with reliable electronic and mechanical sensors, computer-based control systems are widely used to control and monitor a number of important material handling functions, including the precise flow of product through the beam, controlling the release of stop gaps, tracking merges, etc. Most irradiation companies now have their own proprietary software packages specifically tailored to optimize the performance of their accelerator and material handling equipment, with the primary intent of reliably controlling the delivery of the requisite radiation dose at the maximum throughput efficiency.

9.5. REPRESENTATIVE MATERIAL HANDLING SYSTEM EXAMPLES

Having discussed various aspects and components of material handling technology, we will now apply this knowledge to develop material handling concepts for two hypothetical irradiation examples, one involving electron irradiation, and one for x-rays.

9.5.1. Electron Beam Irradiation of Ground Beef

As a first example, we will consider electron irradiation of a variety of fresh and frozen ground beef products, including for example, chubs of various weights and diameters, stacks of frozen ground beef patties, and 2-lb packages of fresh ground beef. A simplified product flow diagram is shown in Figure 9-13. The products are stacked on pallets and transported to an irradiation service center in refrigerated, 40,000-lb semi trailers. The pallets are removed from the trailer and transported to the load conveyor using a fork truck. Because of the many different types of products and packages, the pallets are manually unloaded from the pallet. Following irradiation, the packages are restacked on a pallet, which is subsequently stretch-wrapped and stored as necessary, before being returned by fork truck to the trailer.

It is assumed that all products can be configured in such a fashion that they can be treated using double-sided irradiation with 10-MeV electron beams oriented in the vertical direction. I.e., the height of all ground beef products on the process table does not exceed 3.5 inches. Ease of product

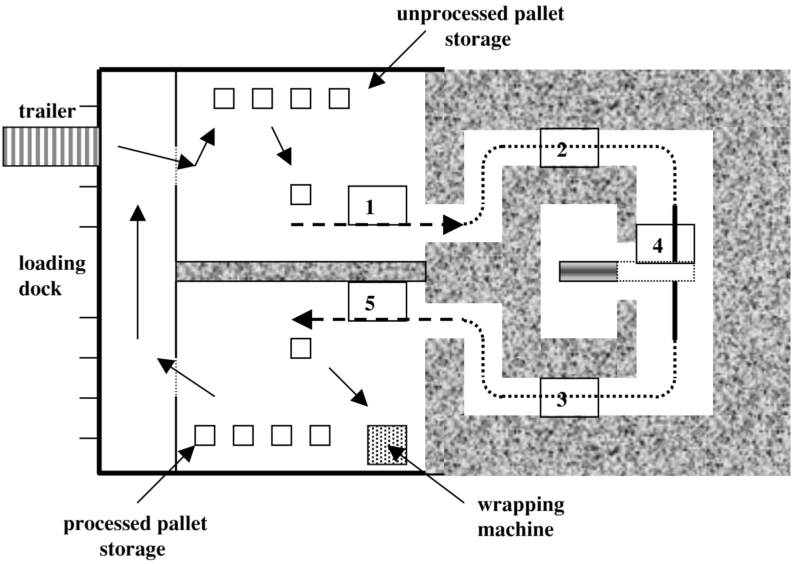

Figure 9-13. Simplified schematic diagram of the product flow in an electron beam service center facility.

handling and package stability therefore suggests the use of a material handling approach based on the use of floor-mounted conveyor units. A conveyor width of 24″ is assumed. In some cases, the products are boxed in such a fashion that they can be placed directly onto the conveyor; in other cases, the packages must be removed from their cartons and placed into special cardboard handling fixtures, or totes. In the case of chubs, special absorbers must be used to ensure dose uniformity.

It is further assumed that the two electron beams are generated with a single 10-MeV/15-kW electron accelerator, using the split-scan configuration discussed in Section 8.4.4. The minimum required dose is specified by the requirement for a 5-log reduction in the population of any e.coli O157:H7 that might be present. For fresh ground beef, the D-value for e.coli is 0.25 kGy, and for frozen product, the D-value is 0.35 kGy. The corresponding minimum required doses are 1.25 kGy and 1.75 kGy, respectively. With double-sided irradiation and the assumed product depths, the minimum dose will occur on the product surface. It is assumed that the maximum width of a box or tote is 22″, and that the scan width is chosen as 23″ to provide a slight overscan on either side of the product. From Eq. (2.14), the corresponding process conveyor speeds are estimated to be 36.4 ft/m and 26.0 ft/m for fresh and frozen products, respectively.

The conveyor system consists of five different sections: (1) a belt conveyor for the loading section, (2) and (3) two sections of powered roller conveyor for transport through the radiation shield maze, (4) a slat conveyor for the process table, and (5) a horizontal gravity conveyor for accumulation of processed product. The maximum length of a container or tote is assumed to be 30 inches, and the desired spacing between totes on the process table is assumed to be one inch. From Eq. (9.6), a container or tote of this maximum length containing fresh product will be released every 4.3 seconds from the stop gate at the load conveyor, and every 6 seconds for frozen product. If the roller conveyor is operated at a constant feed rate of 50 ft/m, the separation between totes of fresh product will be 12.6 inches, and 30 inches for frozen product. The minimum inside radius of a turn in the roller conveyor section should exceed 30 inches.

The process conveyor consists of two slat conveyor sections (see Fig. 9-14), separated by a gap that allows the upward-directed beam to reach the product. Assuming that the minimum length of a tote is 24 inches, and that the end sprockets of each slat conveyor section have a diameter of two

Figure 9-14. A possible configuration of a slat conveyor in the process corridor. A section of the scan horn form the downward-directed beam is shown. (Used with permission of the Titan Corporation.)

inches, the clear gap width is chosen as four inches, from Eq. (9.5). Transfer gaps between other conveyor sections will generally be less than this distance. The maximum possible weight of a tote is approximately 36 kg, implying a maximum average conveyor loading of about 22 lbs per linear foot. For a 50-ft section of roller conveyor, a coefficient of friction of 0.1, and a conveyor speed of 50 ft/m, the required power of the drive motor is about 0.2 hp.

The maximum throughput rate of the system is limited to approximately 67,000 lbs per hour of fresh product, and 48,000 lbs per hour of frozen product. However, these figures must generally be adjusted downward, sometimes by a considerable amount, depending on how the products are packaged within their boxes or totes, and on whether or not absorbers must be used to ensure dose uniformity. Nonetheless, one hour is a reasonable estimate for processing one trailer load (40,000 lbs) of such products.

9.5.2. X-Ray Irradiation of Boxes of Whole Chickens

As a second hypothetical example, we will consider x-ray irradiation of fresh and frozen whole chickens. The chickens are sealed in plastic bags and placed at random in cardboard boxes with dimensions of $20'' \times 12'' \times 10''$. The average density of such a box is assumed to be 0.5 g/cm^3, and the maximum areal density (in the minimum dimension) is assumed to be 15 g/cm^2. This product must therefore be treated using x-rays. The boxes are assumed to be stacked on pallets with overall dimensions of $40'' \times 48'' \times 60''$. We will consider two specific approaches: (1) a carrier-based system in which the boxes are manually removed from the pallet and placed on carriers that are transported to and from the irradiation zone by an overhead power and free conveyor system (in this section), and (2) a pallet-based system in which the pallets are processed directly (discussed in the next section).

The carrier platforms are assumed to have an open platform space of 48″ in length and height, with a depth of 24″. With a maximum density of approximately 0.6 g/cm^3, the product can be stacked to a depth of twenty inches on a 24″ carrier, assuming double-sided irradiation. The height of product on the carrier is 40″, and the carrier length of 48″ can be completely filled. The corresponding total weight of product on the carrier is nearly 700 pounds.

A process flow diagram for such a carrier-based system was schematically shown in Figure 2-6. The accelerator system is horizontally mounted, and the beam is scanned in the vertical direction. There are three different types of conveyors, all independently powered. These include (1) a chain conveyor on the process table that propels carriers through the irradiation zone at a precise speed; (2) a high-speed, closed-loop, overhead power-and-free (OHP&F) conveyor that moves carriers from a loading station in the warehouse to an accumulation station in the vicinity of the process conveyor, and then transports carriers from the exit end of the process conveyor to an unloading station in the warehouse; and (3) a chain-driven, variable-speed closing conveyor that moves a carrier from an accumulation station (stop gate) to within a predetermined (small) separation distance from the previous carrier on the process conveyor. Programmable controllers and computers monitor and control the position of carriers throughout the system.

With the carrier weight supported by the unpowered rail of the OHP&F conveyor, a non-accumulating chain conveyor on the process table engages the bottom of a carrier and transports it through the irradiation zone at the desired speed (usually much slower than the speed of the OHP&F conveyor). After a first carrier has moved past a particular position on the process table, a second carrier is released from the stop gate at the accumulation station, and the variable-speed closing conveyor is actuated. The closing conveyor engages a dog on the bottom of the second carrier and moves it to the engagement point of the process conveyor, matching the speed of the process conveyor at the end of its cycle. Double-sided irradiation is achieved by adding a carrier rotation loop, also based on use of an OHP&F conveyor (see Fig. 9-15). The load bar of the carrier is mounted onto a rotatable collar assembly that is attached to the two trolleys of the OHP&F conveyor. Appropriate routing of carriers is easily achieved by introducing a physical asymmetry (a limit switch striker tab) into the carrier design. A second stop gate in the rotation loop is necessary for a smooth merge.

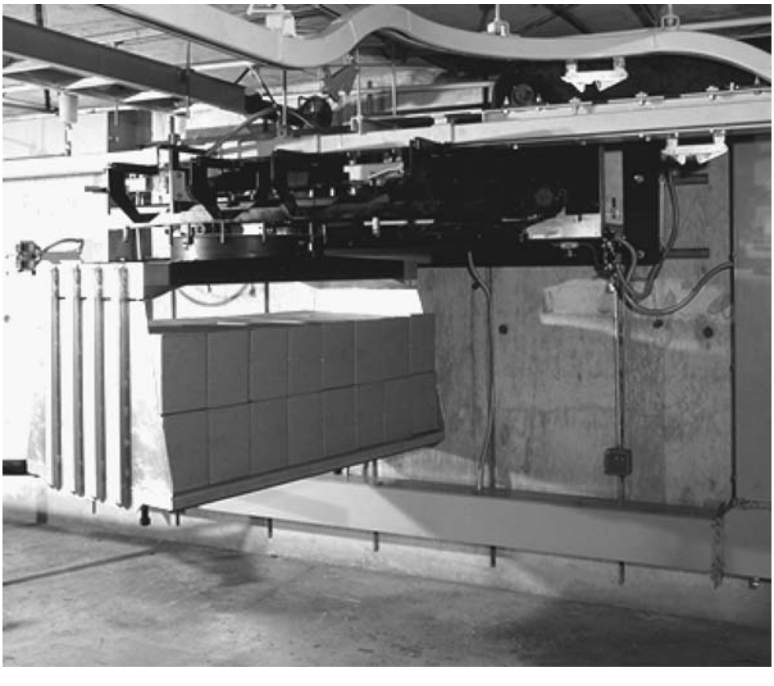

Figure 9-15. A 180° carrier rotation station incorporated into an OHP&F material handling system facilitates double-sided irradiation of product. (Used with permission of the Titan Corporation.)

The speed of the OHP&F conveyor is adjusted to minimize carrier transfer time, while the release time at the stop gate is determined by the speed of the process conveyor and the desired separation distance between carriers on the process table. The speed of the process conveyor can be estimated using Eq. (4.66) for 7.5 MeV, or Eq. (4.67) for 5 MeV. Assuming 100 kW at 5 MeV, a scan height of 100 cm, and a separation distance of 10 cm between the converter and the front surface of the product on the carrier, the dose in the middle of the product for a single pass through the irradiation zone is approximately given by

$$D(s = 10'') = 1.44\,\mathrm{kGy}/v(\mathrm{cm/s}) \tag{9.7}$$

Assuming a two-pass irradiation scenario and a minimum required dose of 2.5 kGy, the corresponding conveyor speed during a single pass is approximately 2.3 ft/m. Assuming a close-spacing distance of two inches between carriers on the process table, then the stop gate should release a carrier every 108 seconds. With two passes required per carrier, the maximum throughput rate is about 11,500 lbs/hr.

If the total number of carriers on the primary OHP&F system is 20, and the effective coefficient of friction is 0.1, then the total chain pull is 1400 lbs. For a drive efficiency of 0.5 and a conveyor speed of 20 ft/m, the power of the primary drive motor is 2 hp, from Eq. (9.3). The load (closing) conveyor transports one carrier at a time. Assuming a similar coefficient of friction and drive efficiency, but a maximum speed of the variable drive of 10 ft/m, the required power of the drive motor is only 0.04 hp. Assuming a maximum of three carriers on the process table, and a speed of 2.3 ft/m, the power of the process conveyor drive motor is a little over 0.025 hp.

9.5.3. X-Ray Irradiation of Pallets of Chicken

To avoid the labor associated with removing boxes from the pallet, placing them on the carriers, and then repalletizing following the irradiation, it may be more desirable to irradiate the pallets directly, if acceptable dose uniformity can be achieved. As discussed in Chapter 4, the total areal density associated with a pallet can be considerable (approximately 50 g/cm^2 in this example), and it may not be possible to achieve acceptable dose uniformity using a simple double-sided irradiation configuration. In this case, special techniques involving pallet rotation or beam manipulation can be used, as discussed in Section 4.9. For this example we will consider the configuration shown in Figure 9-16. The pallet is placed directly onto a rotatable elevator platform by a fork truck. The platform is driven by a precision, constant-speed screw lift. The platform is first lowered through the x-ray beams produced by diametrically opposed accelerator systems, each having an average power of 100 kW. After the entire pallet has been irradiated in this fashion, the platform is stopped, and rotated by 90 degrees. The platform is then raised through the beams, also at constant velocity. Following the irradiation, the pallet is removed from the platform by the fork truck, and another pallet is loaded into position.

The irradiation geometry for a single accelerator was schematically shown in Figure 4-53. The electrons impact the converter plate in converging fashion, with all electron rays having a focal point at the center of the pallet. From Section 4.9, the resulting dose uniformity ratio for a full pallet having an average density of 0.5 g/cm^3 will be approximately 1.5. The minimum dose will occur approximately in the center of the pallet, and for a single beam on a single pass, this minimum dose will be approximately given by (for 7.5 MeV)

$$D(\mathrm{kGy}) = 1.4\,P(\mathrm{kW})/[v(\mathrm{cm/s})w(\mathrm{cm})] \tag{9.8}$$

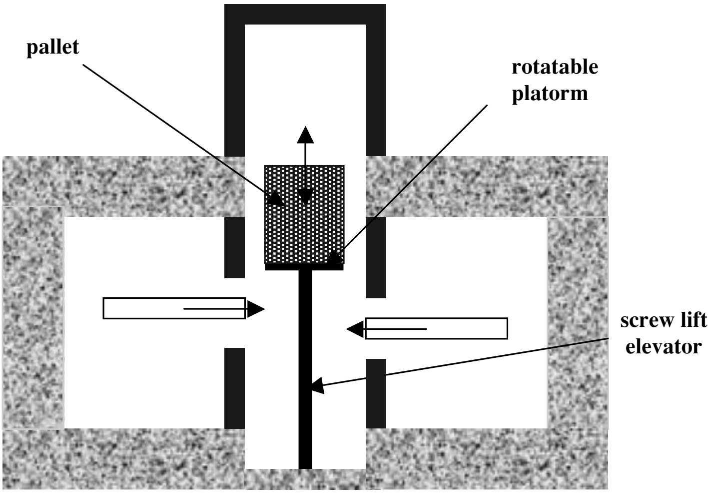

Figure 9-16. Schematic geometry for a pallet irradiation system. The pallet is loaded by fork truck onto a rotatable platform that is raised and lowered by a constant velocity screw lift.

For a pallet with a maximum width of 48″, the total scan width w will be approximately 150 cm. Assuming a minimum required dose of 2.5 kGy, the corresponding speed of the elevation change is approximately 1.5 cm/s, or about 3.0 ft/m. For the 60″ pallet height, the time for a descent or ascent is approximately 1.7 minutes. Including time for rotation, and loading and unloading operations, a single such pallet weighing approximately 2000 lbs could be processed in a cycle time of less than 6 minutes, corresponding to a throughput rate of about 21,000 lbs per hour. Thus, a single 40,000 lb trailer could be processed in less than two hours in this hypothetical application.

9.6. SUMMARY

The primary functions of the material handling system are to efficiently transport products to and from the irradiation zone, to precisely move products through the irradiation zone, and in the case of service centers, to efficiently move food products into and out of the facility. The heart of the MHS is the conveyor. Considering just the irradiation step, the conveyor system must ensure the precise motion of product through the beam(s), with minimum gaps between cartons or carriers, regardless of the material input rates at the load station. This usually requires different conveyor speeds in various regions of the product flow path, the accumulation of product at a stop gate, and precision release of product from the stop gate. For maximum throughput, the rate-limiting step for the process should be the irradiation of product; the material handling system design should eliminate other potential bottlenecks.

There are many different conveyor system approaches, as well as specialized auxiliary equipment including turntables, transfer stations, rotate mechanisms, etc. The selection of a particular approach, or combination of approaches, is largely guided by the type and packaging of the product (physical properties), the mode of radiation (e-beam, x-ray) to be used, and the required throughput rates, in addition to the usual considerations of cost, reliability, maintainability, noise, etc.

As a general rule, it is usually preferable to use vertically directed beams in the electron irradiation mode, from the standpoint of package stability and handling ease, while horizontally directed beams afford more flexibility when processing in x-ray mode. For food processing applications the speed at which the conveyor system must operate lies generally in the range of 0.1–100 feet per minute. The weight of product arranged in totes for electron beam processing will typically be a few tens of kilograms, while the weight of product on carriers for x-ray processing will typically be a few hundred kilograms. Full pallets may exceed a metric tonne.

The various types of conveyors that are available are usually classified according to the mounting approach, i.e., overhead trolley or floor-mounted, and the type of load to be conveyed, i.e., bulk materials or unit packages. Unit materials such as cartons, bags, and/or packages stacked on pallets might be conveyed with belt, roller, and slat conveyors mounted on the floor, or borne by overhead trolleys. The primary distinction between the various floor-mounted conveyor systems is the method by which material proceeds along the flow path.

With the versatile overhead power and free (OHP&F) conveyor a continually moving power chain is carried by an upper track, while the load is suspended from a lower free track. Load carriers engage and are transported by the power chain by means of "pusher dogs" that usually engage the lead trolley. However, the trolley can easily be disengaged from the power chain to permit a variety of material handling operations, including line speed variation, route variation and accumulation.

The explosion in reliable and inexpensive computer hardware has fostered a revolution in computer applications to material handling. Coupled with reliable electronic and mechanical sensors, computer-based control systems are used to control and monitor a number of important material handling functions, with the primary aim of reliably controlling the delivery of the requisite radiation dose at the maximum throughput efficiency.

REFERENCES

1. **The Essentials of Material Handling**, R. E. Ward, editor-in-chief, Material Handling Institute, Charlotte, NC (1996).
2. T. H. Allegri, Sr., **Materials Handling Principles and Practice**, Van Nostrand Rheinhold Co., NY (1984).
3. J. M. Apple, **Plant Layout and Material Handling, 3rd ed.**, Krieger Publishing Co., Malabar, FL (1991).
4. R. A. Kulwiec, **Basics of Material Handling**, Material Handling Institute, Charlotte, NC (1981).
5. **Materials Handling Handbook, 2nd ed.**, R. A. Kulwiec, ed., John Wiley and Sons, NY (1985).
6. D. K. Smith, **Package Conveyors: Design and Estimating**, Charles Griffin & Co., Ltd., London (1972). Ch. 2.
7. Ibid., Ch. 3.
8. Ibid., Ch. 4.
9. Ibid., Ch. 6.
10. W. K. Stubbs, "Light and Medium Load Conveyor Transportation Systems," 1980 Automated Mat'l. Hand. And Stor. Syst. Conf., Material Handling Institute, Charlotte, NC (1980).
11. Bosch Rexroth Corporation, Western Regional Center, Irvine, CA (USA).
12. **Materials Handling Handbook, 2nd ed.**, R. A. Kulwiec, ed., John Wiley and Sons, NY (1985), Ch. 9.
13. C. Kaltwasser, "Overhead Chain and Trolley Conveyors with Emphasis on the Evolution to Power and Free," 1980 Automated Mat'l. Hand. And Stor. Syst. Conf., Material Handling Institute, Charlotte, NC (1980).

CHAPTER 10

RADIATION SAFETY AND X-RAY SHIELD DESIGN

A food irradiation installation must be designed to process a wide variety of food products in an efficient, but extremely safe, manner. In particular, the design of the facility must not only limit the radiation exposure to facility occupants and transient visitors, but must also effectively eliminate the possibility of any significant exposure to the general public outside of the facility. In this chapter we will consider the general approach to radiation safety, with special emphasis on the design of the x-ray shield.

10.1. GENERAL SAFETY CONSIDERATIONS FOR A FOOD IRRADIATION INSTALLATION

10.1.1. Non-Radiation Hazards

In addition to the obvious radiation hazard, an accelerator-based irradiation facility will have many potential safety hazards that are commonly found in industrial settings, plus a few additional hazards that are specifically associated with accelerator operation. For example, the electrical wiring of the facility should satisfy accepted electrical building codes, and the material handling system and hardware items should satisfy accepted industrial safety codes. First aid materials and equipment must be readily available for treatment of minor injuries, and good housekeeping practices are essential to minimize the potential for accidents.

Those hazards specifically associated with accelerator operation frequently include high voltage, compressed gases, production of noxious gases, use of industrial solvents, fire, and confined space.[1] Using a microwave accelerator as an example, voltages of several tens of kilovolts or more are often required for operation of the microwave source, the waveguide is often filled with high pressure sulfur hexafluoride gas, the beam is accelerated in a hard vacuum, various gaskets and flanges are cleaned with industrial solvents, the accelerator may be sited in a vault that constitutes a confined space, the beam itself (especially with direct electron deposition) can generate a significant amount of ozone, and the rapid dose delivery can lead to a fire hazard if the conveyor system fails. It is important to identify, analyze, and develop risk mitigation steps for all of these potential hazards; e.g., a Hazards Analysis and Critical Control Point (HACCP) plan should be prepared for each facility and/or installation.

10.1.2. Radiation Hazard Considerations

Ionizing radiation produced by accelerators is generally classified as primary radiation, secondary radiation, stray radiation, and induced radioactivity.[1] The energetic electron beam produced by the accelerator system in a food irradiation facility is always considered the primary radiation. When the primary beam interacts with matter, secondary radiation is generated. Depending on the specific design of the accelerator system, there may be some small portion of the beam that is lost in the accelerator system (due to slight misalignments, dark currents, or backstreaming, for example). The secondary radiation produced when any beam is lost inside the accelerator system is termed stray radiation.

In most applications the electron beam emerges through a thin vacuum window before encountering either the product or an x-ray converter. The maximum range of an electron in air is roughly equal to the electron kinetic energy in MeV multiplied by five meters (50 m at 10 MeV!). Electrons are scattered by air and all materials they encounter. For conservatism, the kinetic energy in shielding calculations of any secondary electrons is assumed to be identical to the kinetic energy of the primary beam.

Because of the regulatory limits on the electron beam kinetic energy for food irradiation applications (<10 MeV electrons for direct electron processing and 5 or 7.5 MeV for x-ray processing), the secondary radiation is generally considered to consist only of electrons and x-rays; i.e., nuclear reactions are unimportant. Consequently, the neutron yield is insignificant, and there is no induced radioactivity.[2] The kinetic energy limitation therefore considerably simplifies the design of the radiation shield, as well as the radiation safety procedures to be followed around and inside the irradiation cell. The National Council on Radiation Protection and Measurements has specified the radiation protection guidelines to be used for such electron accelerator installations.[3]

10.1.3. Radiation Exposure Terms

There are several different terms that are used in the context of radiation safety, including absorbed dose, radiation exposure, and radioactivity. To avoid any confusion, these terms and their associated units are defined below:[4]

1. **Absorbed dose** is a measure of the energy absorbed per unit mass, regardless of the type of ionizing radiation. As discussed previously, the accepted unit is the Gray, defined as one joule per kilogram. An older unit, the rad (for radiation absorbed dose) is defined as 100 ergs per gram. It may be verified that $1\ \text{Gy} = 100$ rads. Dosimeters measure absorbed dose.
2. **Radiation exposure** is a measure of the ionization produced when x-rays or gamma rays traverse a particular quantity of air at STP. Hand-held survey meters (usually ionization chambers) measure radiation exposure. The unit of radiation exposure is the roentgen, which corresponds to the production of one electrostatic unit of charge, either positive or negative, in one cubic centimeter of air at 0 °C and 760 mm of Hg; this is equivalent to 2.58×10^{-4} coulombs per kilogram of air. Assuming 33.85 eV per electron-ion pair,[5] this is about 8.7 mJ/kg, or about 0.87 rads. Since air and water consist of elements that have atomic numbers that are nearly the same as that of soft tissue, an x-ray exposure of one roentgen in air is usually considered to produce one rad (0.01 Gy) of radiation dose in soft tissue.
3. The biological effects per unit of absorbed dose can be quite different, depending on the type of ionizing radiation, especially for massive nuclear particles. Consequently, the **radiation dose equivalent** is defined as the absorbed dose, multiplied by a **quality factor** (QF) that expresses the difference in **biological effectiveness** of various types of radiation, in comparison with x-rays. The old dose equivalent unit is the rem, for roentgen equivalent man. Since the quality factor for x-rays, gamma rays and electrons with a maximum energy of greater than 30 keV is unity, one rem equals one rad, and these terms are often used interchangeably for these types of radiation. The newer dose equivalent unit is the Sievert (Sv), which is equal to 100 rem.

4. For completeness, **radioactivity** describes the process by which an excited nucleus emits an ionizing particle. The new unit of radioactive source strength is the Bequerel (Bq), which is defined to be one nuclear disintegration per second. It has largely replaced the older unit, the Curie (Ci), defined as 3.7×10^{10} disintegrations per second.

For comparison purposes, an average person living in the United States receives an equivalent dose of about 360 mrem (3.6×10^{-3} Sv) per year resulting from background radioactivity, cosmic rays, and medical exposures. The single-exposure whole body dose that is lethal to 50% of the human adult population is generally considered to be in the range of 400–500 rads (only 4–5 Gy).[4]

10.1.4. Radiation Dose Limits

Permissible radiation dose limits are summarized in Appendix B of NCRP Report No. 51.[3] These include limits for various parts of the body, limits for fertile women, limits for students, etc. For food irradiation installations, however, there are two limits of primary importance: (1) a yearly limit of 5 R for radiation workers (for whom exposure records must be kept); and (2) a yearly limit of 0.1 R for any member of the general public (including students). It is usually assumed that a normal work shift is one in which the accelerator system is operated at maximum levels eight hours per day, five days per week, and 50 weeks per year, for a total of 2000 hours per year. Therefore, for the purpose of designing radiation shields, the maximum permissable limits are usually interpreted in terms of hourly dose rates as

Noncontrolled areas	<0.05 mrem per hour (<0.5 μSv/hr)
Controlled areas	>0.05 mr/hr, but <2.5 mr/hr (<25 μSv/hr)

Regardless of these maximum permissible exposure rates, a basic rule governing radiation safety is that all dose rates should be reduced ***as low as reasonably achievable***. This is the so-called “ALARA” doctrine.[6]

10.2. RADIATION SHIELDING ESTIMATION

While the klystron in a microwave accelerator system can be a source of 100-kV x-rays, these are relatively easily shielded by a lead or steel case. Of more concern for this chapter are the very penetrating x-rays produced by the accelerator system. As an introduction to determining the shielding required for this radiation, we consider Eq. (4.34) for the front surface dose produced by a 5-MeV, short-scan (H = 60 cm), x-ray installation, repeated here for convenience.

$$D_{fs}(\mathrm{kGy}) = \{3.4\,P(\mathrm{kW})/[v(\mathrm{cm/s})\,H(\mathrm{cm})]\}e^{-0.012z_c} \tag{10.1}$$

Assuming a 100 kW machine, a conveyor speed of 1 cm/s, and a scan height of 60 cm, the dose delivered to the front surface of product at ten centimeters from the converter is approximately 5 kGy. Since the half-angle of the radiation is approximately 40 degrees, half of this dose will be delivered in a time of approximately 7 seconds, corresponding to an approximate dose rate of 350 Gy/s, or about 1.25×10^8 R/hr. The total attenuation required to achieve the controlled area limit is 5×10^{10}, and 2.5×10^{12} for a noncontrolled area. To put these numbers into context, for a typical mass absorption coefficient of 0.03 cm^2/g, the estimated thickness of concrete (with a density of 2.35 g/cm^3) required to reduce the x-ray dose rate by a factor of ten is about 33 cm. Thus, the required x-ray shield is estimated to be of the order of 11–12 feet of concrete.

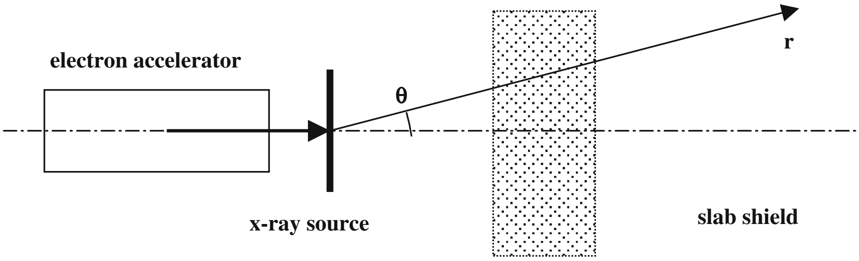

Figure 10-1. Schematic configuration for a slab radiation shield.

10.2.1. X-Ray Shielding Estimation Procedure for Electron Accelerators

In addition to source strength and shielding, the radiation exposure rate is affected by distance. Further, in the general case multiple source points and stray and scattered radiation must also be considered, including the energy dependence of the scattering cross-sections. This generally leads to a problem of considerable complexity. Fortunately, it has proven possible to design adequate radiation shields in a straightforward fashion using a considerably simplified approach based on empirical attenuation factors, as discussed in the following paragraphs.[3]

Consider the schematic diagram of Figure 10-1. From Chapter 4 the x-ray power per unit area (P_x) generated by an electron beam striking a point on a converter is given by

$$P_x = \eta P f(\theta)/r^2 \qquad (10.2)$$

where η is the energy-dependent conversion efficiency, $f(\theta)$ is the angular dependence of the emitted x-rays, and r is the distance from the converter to the observation point. $P = Ei$ is the electron beam power, with E being the kinetic energy and i being the current.

If an absorber (e.g., a dosimeter) is placed at the observation point, the dose rate (dD/dt) is given by

$$dD/dt = \mu P_x = \mu \eta E i\, f(\theta)/r^2 = (dD_i/dt) i/r^2 \qquad (10.3)$$

where μ is the mass absorption coefficient of the absorber. $(dD_i/dt) = [\mu \eta E\, f(\theta)]$ is variously termed the dose rate index, or the detector response function.[6] It is the dose rate that would be measured at $r = 1\text{m}$ from the converter per unit beam current; convenient units are [(rads/s)-m^2] / mamp.

Now suppose that a slab of shielding material is interposed between the point source and the detector, as indicated in Figure 10-1. Then the decreased dose rate can be written in terms of an attenuation factor B_f, termed the shielding transmission ratio, as[3,6]

$$dD/dt = (dD_i/dt) i\, B_f/r^2 \qquad (10.4)$$

The dose rate index has been measured and calculated for many different x-ray sources. From Eq. (10.3) it is seen to depend on the kinetic energy of the electrons striking the target, the observation angle relative to the electron angle of incidence, and the target characteristics. Various graphs describing these dependencies are available in the literature.[3] Consequently, given the source current and the permissible dose rate (dD_p/dt) (from Section 10.1.4), the required value of the shielding transmission ratio B_f can be determined from these data according to

$$B_f = (dD_p/dt) r^2/[i(dD_i/dt)] \qquad (10.5)$$

It is customary to describe the shielding transmission ratio in terms of tenth-value layers (TVL); a TVL is the shield thickness that will attenuate a broad x-ray beam by a factor of ten. If x is the thickness of the shield, then

$$B_f(x) = 10^{-x/TVL} \tag{10.6}$$

Therefore, the shield thickness necessary to reduce the exposure rate below a particular limit can be found from Eqs. (10.5) and (10.6) as

$$x > (TVL)\log_{10}[i\,(dD_i/dt)/[(dD_p/dt)r^2)] \tag{10.7}$$

10.2.2. Description of X-Ray Sources

If there is more than one source of x-radiation, the total exposure rate at the measurement point is just the sum over all sources (j), as given by

$$dD/dt = \sum i_j\,(dD_{ij}/dt)B_j r_j^{-2} \tag{10.8}$$

The various types of x-ray sources associated with an electron accelerator in a food irradiation facility are schematically indicated in Figures 10-2 and 10-3. For electron irradiators, x-rays are generated in the product, in a water-cooled beam collector in the absence of product, and internal to the accelerator system (stray radiation). For an x-ray system, the x-ray converter is the primary source, in addition to the small internal sources. The sum in Eq. (10.8) could also be extended to include sources of scattered radiation, in addition to the direct bremsstrahlung production. Estimating the contributions from reflected x-radiation will be described in a later section.

Measured values for the dose rate index at one meter from the target per milliampere of electron current normally incident onto a target are contained in the selected data presented in Appendix E of Ref. 3. Data from the cited references therein are plotted in Figure 10-4 over the energy range of 1–10 MeV. Excellent fits for the response functions over the kinetic energy range of 2–10 MeV, for emission in the forward (0 degrees) and side (90 degrees) directions for thick, high-atomic number targets ($Z > 73$), are given by Eqs. (10.9) and (10.10), with E in MeV. These equations are also

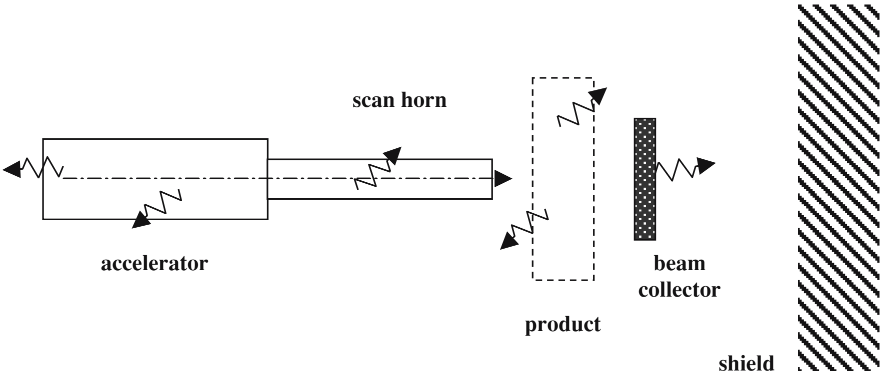

Figure 10-2. X-ray sources from an electron accelerator used for direct electron beam irradiation.

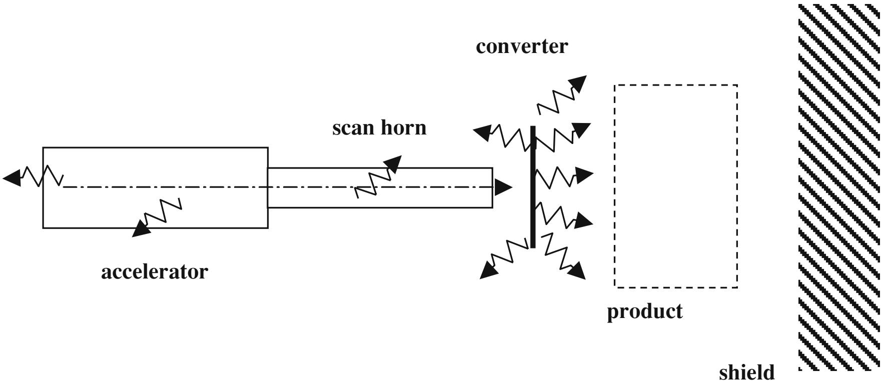

Figure 10-3. X-ray sources from an accelerator used for indirect x-ray irradiation.

plotted in Figure 10-4 for comparison purposes.

$$dD_i/dt(rads/s) = 1.15E^{2.85}; \qquad (0\ degrees) \qquad (10.9)$$

$$dD_i/dt(rads/s) = 2.37E - 1.87; \qquad (90\ degrees) \qquad (10.10)$$

The linear dependence on energy for emission at 90 degrees simply reflects the increased energy of a single electron. For emission in the forward direction, the nearly cubic dependence on energy is the result of two factors: (1) the linear increase in energy of a single electron; and (2) the approximately linear decrease with energy of the half-angle of the bremsstrahlung radiation cone.

The emission is nearly isotropic at 1 MeV, but becomes increasingly forward directed as the energy increases. The angular dependence of the response function in the forward half-space is shown in Figure 10-5 for 5- and 8-MeV electrons. At 5 MeV the intensity half-angle is approximately 23 degrees, decreasing to approximately 13 degrees at 8 MeV, roughly consistent with a 1/E variation.

The spectrum of the x-rays emitted at 90 degrees is somewhat softer than that emitted in the forward direction. To take this effect into account when determining TVLs, an equivalent electron

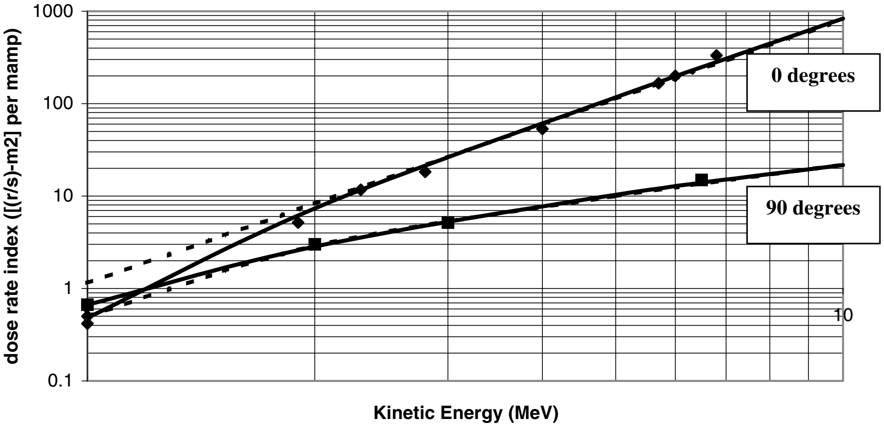

Figure 10-4. The dose rate index for the forward (0 degrees) and sideward (90 degree) directions as a function of incident electron kinetic energy over the range of 1–10 MeV. The analytical fits provided by Eqs. (10.9) and (10.10) are shown as dashed lines.

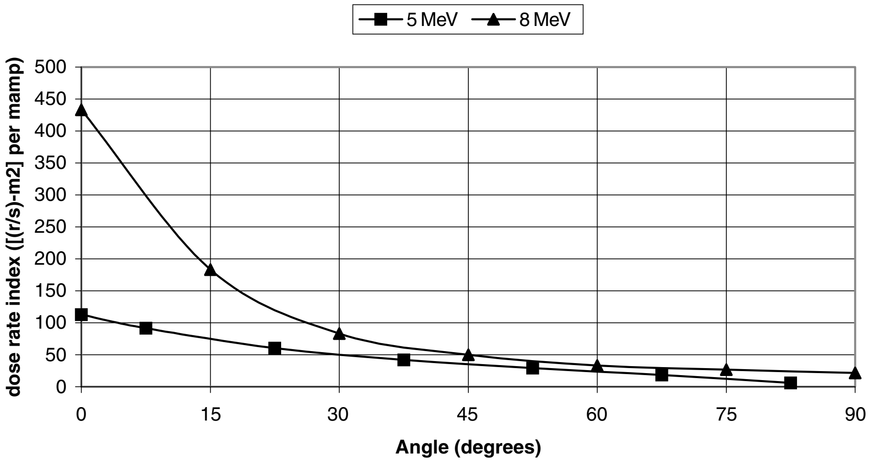

Figure 10-5. Variation of the response function with angle for thick, high-Z targets. The dip near 90 degrees for the 5-MeV data reflects self-absorption in the target. The 8-MeV data have been smoothed, masking this effect.

energy can be defined for the 90-degree direction that would produce x-rays with comparable transmission characteristics in the forward direction. Over the incident energy range of 1–10 MeV, an empirical equation that well describes this relationship is

$$E_{eq}(90^\circ) = 0.61\,E(0^\circ) + 0.12 \tag{10.11}$$

Finally, for lower atomic number targets the emission intensity is reduced relative to the data presented in Figures 10-4 and 10-5. The variation of the response function with atomic number Z is approximately proportional to $Z^{1/2}$ in the forward direction; in the sideward direction, the variation is more nearly linear with Z.

10.2.3. Shielding Transmission Ratios (Tenth-Value Layers)

The most common shielding materials found in an irradiation facility are concrete, steel and lead. Concrete is usually the material of choice for the primary shield. It has good structural properties, can be formed in complex shapes, and is much less expensive than other materials for comparable results. Steel plate is used for specific localized shielding regions in which space is at a premium, while lead is often packed in cracks and crevices to shield against scattered radiation.*

Mass absorption coefficients for these shielding materials are presented in Figure 10-6 over the photon energy range of 100 keV to 10 MeV. Lead is especially effective against softer scattered radiation because of its high photoelectric effect cross section. There is very little difference between the absorption coefficients for steel and concrete. Consequently, equivalent shielding thicknesses of these materials are in inverse proportion to their densities (2.35 g/cm^3 for concrete and 7.8 g/cm^3 for steel).

For photon energies below about 1 MeV, the mass absorption coefficient for either concrete or steel is roughly equal to 0.03 g/cm^2, and slowly decreases to approximately 0.02 g/cm^2 as the photon energy increases to 10 MeV. Thus, a TVL for concrete for forward directed radiation from a

---

* Lead should not be used as primary shielding for electron accelerators with energy in excess of about 6 MeV because of the possibility of neutron production and induced radioactivity.

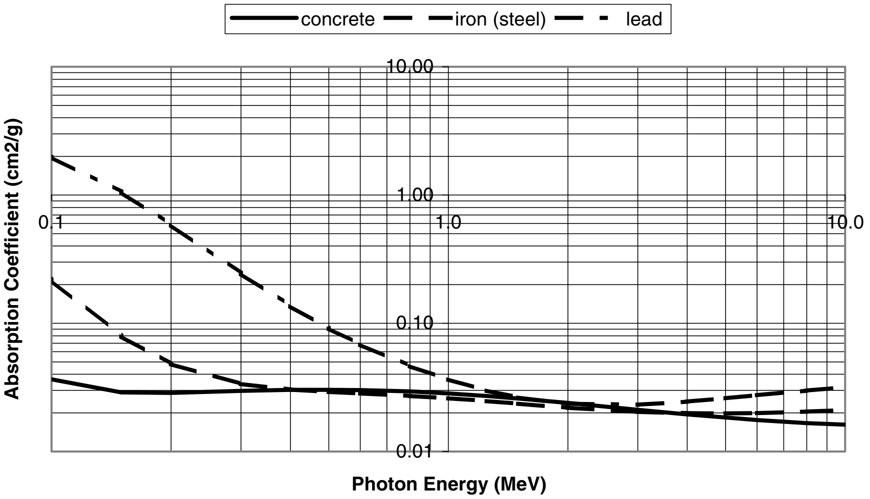

Figure 10-6. Mass absorption coefficients for concrete, iron(steel) and lead.

5-MeV electron accelerator should have a value of a little over 30 cm, while for a 10-MeV machine the TVL should increase to nearly 40 cm. In fact, experimental measurements of tenth-value layers are consistent with these expectations.[3] For concrete, an excellent fit to the "equilibrium" TVL data over the energy range of 1–10 MeV is provided by

$$\mathrm{TVL(cm)} = 26\log_{10}(3\mathrm{E}) \tag{10.12}$$

with E being the electron kinetic energy in MeV. (If the electron kinetic energy is less than approximately 3 MeV, Eq. (10.12) tends to underestimate the thickness of the first tenth value layer by approximately 10% owing to a radiation shower effect; this is also sometimes described in terms of a "build-up factor.")[6]

10.2.4. Reflected X-Ray Sources

The most common method for introducing products into the irradiation zone is via a maze (either horizontal or vertical). In addition, ducts and other shield penetrations are necessary for delivering power and cooling water to the accelerator system, for exhausting ozone, etc. When designing such mazes and ducts the problem of x-ray scattering must be given careful thought in the overall design of the radiation shield. Referring to Figure 10-7, important parameters in shield design for reflected x-rays include (1) the area of reflecting material illuminated by the x-ray beam (A_r), (2) the reflection coefficient (α_r) of the material, which depends on the reflection angle (θ_r), (3) the distance d from the scattering surface to the measurement point, and (4) the shielding transmission ratio (B_{fr}) for the scattered x-rays.

From Eq. (10.2) the x-ray power per unit area at the reflecting wall located a distance r_w from the converter is given by $P_x = \eta P f(\theta)/r_w{}^2$. Each position on the reflecting surface can be thought of as a point source of reflected radiation, so that the reflected x-ray power per unit area can be written as

$$P_{xr} = \left[\eta P f(\theta)/r_w^2\right](\alpha_r A_r/d^2) \tag{10.13}$$

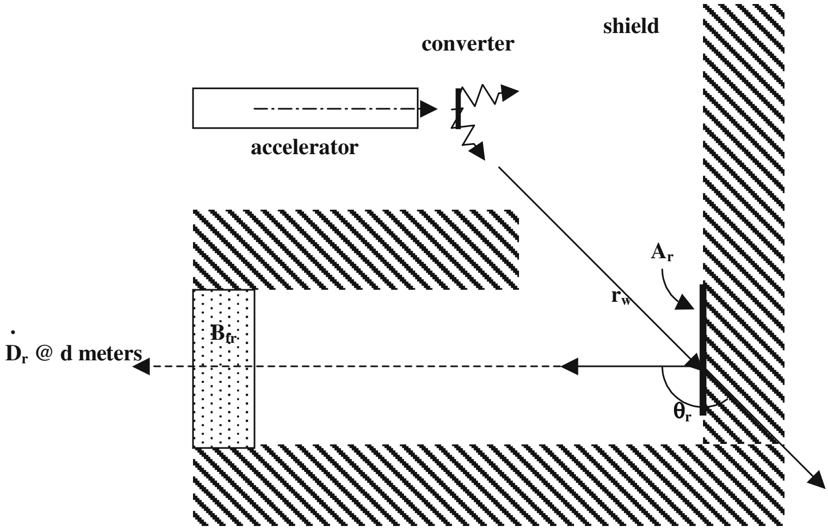

Figure 10-7. Schematic diagram for analyzing the dose rate contribution arising from scattered x-rays.

If a dosimeter is placed at the observation point behind a slab of shielding material, the recorded dose rate will be given by

$$dD_r/dt = \mu_r P_{xr} = \left[(dD_i/dt)/r_w^2\right] i\, B_{fr}(\alpha_r\, A_r/d^2) \tag{10.14}$$

where the difference in effective mass absorption coefficient (because of the softer spectrum) has been ignored. (dD_i/dt) is the dose rate index from Eq. (10.3), i is the beam current incident on the converter, and B_{fr} is the shielding transmission ratio for the reflected x-rays. In the case of multiple reflections, the term ($\alpha_r\, A_r/d^2$) can be appropriately repeated to account for each reflection.

For x-rays produced by electron kinetic energies of interest, the spectrum of the scattered x-rays is largely determined by Compton scattering kinematics, and pair production, both of which soften the spectrum. For monoenergetic photons normally incident onto concrete, the reflection coefficient varies nearly inversely with incident photon energy, being approximately 0.01 at 1 MeV for a reflection angle of 180°. The reflection coefficient decreases with decreasing reflection angle (because there is more opportunity for absorption in the reflecting wall). For equal angles of incidence and reflection, the reflection coefficient increases with shallower angle, and tends to be larger for higher energy photons. In all cases, a useful, conservative approximation is to assume a reflection coefficient of 0.02, and a decrease in the average photon energy of the scattered spectrum by a factor of two.

As a further point, it is conceivable that for some applications it might be desirable to house the irradiation equipment in a separate, isolated enclosure located some distance from other buildings. (One example is an accelerator system mounted on a transportable platform that could be moved from one field location to another to "follow the harvest.") In this case an immediate question is the magnitude of shielding required for the roof over the irradiation cell. An ordinary weather protection roof will only marginally attenuate any upward-directed radiation, and the (softer) radiation reflected downward from the atmosphere (so-called "skyshine") can pose a significant radiation hazard. This problem can also be addressed using the methods outlined in this section. See Reference 3 for more details.

10.3. SHIELDING CALCULATION EXAMPLES

The information contained in the previous section will now be used to analyze various shield designs to illustrate several important features. Before performing detailed calculations for a particular shield design, we first estimate the shield thicknesses associated with the minimum shield footprint by setting the thickness x equal to the distance r from the x-ray source in Eq. (10.7). The dose rate index is given by either Eq. (10.9) or Eq. (10.10), depending on the observation angle. For the 90° direction, the equivalent energy to be used in the TVL formula, Eq. (10.12), is given by Eq. (10.11). We examine two cases: (1) a 10-MeV, 1-mamp beam incident on food products, with $Z = 8$, and (2) a 5-MeV, 20-mamp beam incident onto a high-Z converter. The results for a concrete shield are summarized in Table 10.1, assuming a maximum permissible dose rate of 0.05 mr/hr $= 1.39 \times 10^{-8}$ r/s, corresponding to an uncontrolled area.

The values in Table 10.1 represent the maximum shield thicknesses for the assumed conditions; values for actual mazes and machines will differ depending on beam parameters and the atomic number of the target. Nonetheless, these results underlie two important general guidelines for shield design in food irradiation facilities: (1) eleven feet of concrete in the forward direction, and (2) eight feet of concrete in the sideward directions.

10.3.1. Shield Design for a 10-MeV Direct Electron Irradiation Facility

As a first detailed example, consider the hypothetical shield design for an electron irradiation facility pictured in Figure 10-8. Two 10-MeV/20-kW electron accelerators are oriented vertically to provide two-sided irradiation of products that are transported to and from the irradiation zone. The scan width is 48 inches (122 cm) to accommodate two 24-in roller lanes, and the accelerators are centered in a process corridor that is 96 inches wide, allowing 24 inches of clearance on either side of the process table. All other corridors of the maze are 96 inches wide. The primary shield walls are 96 inches of concrete, with an interior wall of 48 inches. Other shield walls, including that over the upward-pointed beam have the thicknesses shown.

Being an electron facility, x-rays are generated in food products, or when the beam is stopped in an aluminum beam collector. Positions of primary interest for estimating the dose rate contribution from direct radiation are those labeled A, B, F and G. For position C, the x-rays undergo a single reflection, and the reflected spectrum is shielded with six feet of concrete. For position D, there are two reflections and two feet of concrete shielding, and for position E, there are three reflections and no shielding.

Estimated dose rates for the four direct radiation positions are given in Table 10.2, along with other various quantities of interest. For these estimates it is assumed that x-rays are generated at the aluminum ($Z = 13$) beam collector, representing the worst case. Based on the estimated results, there are several issues that must be addressed for this design. First, the dose rate at position A (at the shield boundary) exceeds the permissible limit for the general public by about a factor of three. If this shield is near the property boundary, it should be increased by about one TVL to approximately

Table 10.1. Concrete Shield Thickness for Minimum Footprint

			D_i (r/s)		TVL (cm)		x(m)	
E (MeV)	i (mamp)	Z	0°	90°	0°	90°	0°	90°
10	1	8	269	2.39	38.4	33.0	3.53	2.48
5	20	73	113	10.0	30.6	25.4	3.13	2.38

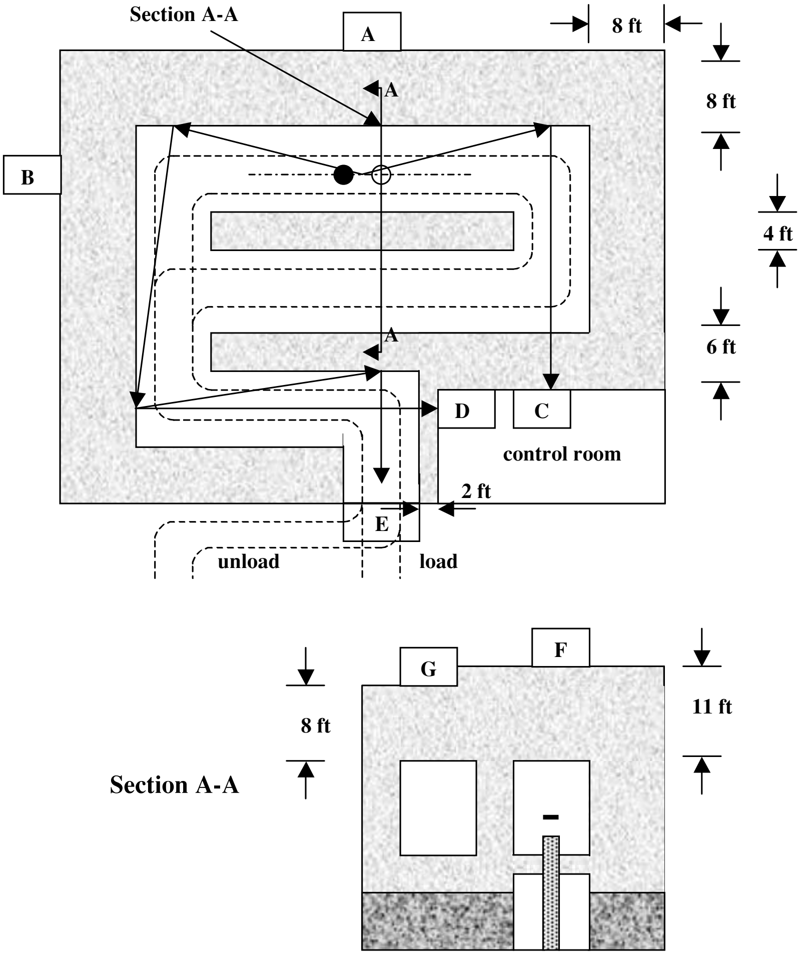

Figure 10-8. Hypothetical shield design for a 10-MeV, 40-kW electron beam irradiation facility. Various positions of interest for shielding calculations are illustrated with the letters A-G. The shield footprint is approximately 46 ft × 64 ft.

nine feet of concrete. For position B, although the shield thickness is the same as for position A, the additional distance through the process corridor to the outer shield boundary reduces the dose rate below the uncontrolled area limit.

The dose rates above the ceiling at positions G and F are just below the controlled area limit. There are several options, including the following extremes: (1) increasing the entire ceiling thickness

Table 10.2. Estimated Direct Radiation Dose Rates for the Shield Design of Figure 10-8

Pos.	Angle (deg)	D_i (r-m^2/s-ma)	E_{eq} (MeV)	TVL (ft)	x (ft)	B_f	i (ma)	r (ft)	D (mr/hr)
A	90	3.9	6.2	1.08	8	3.9×10^{-8}	4	12	0.16
B	90	3.9	6.2	1.08	8	3.9×10^{-8}	4	32	0.023
F	0	340	10	1.26	11	1.2×10^{-8}	2	16	0.185
G	30	68 (20%)	10	1.26	10	1.2×10^{-8}	2	18	0.195

Table 10.3. Estimated Reflected Radiation Dose Rates for the Shield Design of Figure 10-8

Pos.	D_i r-m^2/s-ma	r_w ft	i ma	d_1 ft	d_2 ft	d_3 ft	E_{eq} MeV	TVL ft	x ft	B_{fr}	D_r mr/hr
C	3.9	18	4	26			3.1	0.81	6	4.3×10^{-8}	2.6×10^{-4}
D	3.9	18	4	28	34		1.5	0.56	2	2.7×10^{-4}	6.4×10^{-4}
E	3.9	18	4	28	34	16	–	–	–	–	0.029

by one foot of concrete, which would reduce the entire area below the uncontrolled limit, and (2) simply posting the entire ceiling region as a controlled radiation area, and denying general public access to this region.

Dose rates resulting from reflected radiation are more difficult to estimate, and have significantly higher uncertainties. Estimated results for positions C, D and E are given in Table 10.3. For each reflection, values of $\alpha_r = 0.02$ and $A_r = 10$ m^2 were used with the appropriate distances indicated. The equivalent energy used in estimating TVLs was also decreased a factor of two on each reflection.

Note that estimated dose rates at positions C and D are quite low. However, it may be verified that reducing the shield thickness by two feet for point C leads to a dose rate that exceeds the uncontrolled area limit. The dose rate at position E is marginally less than the uncontrolled area limit.

10.3.2. Shield Design for a 5-MeV X-Ray Irradiation Facility

As a second detailed example, consider the hypothetical shield design for an x-ray irradiation facility pictured in Figure 10-9. One 5-MeV/150-kW electron accelerator is oriented horizontally. A rotation mechanism is used to provide two-sided irradiation of products that are moved into and out of the process corridor using an overhead power and free conveyor system. Most corridors of the maze are 72 inches wide. The primary shield walls are 96 inches of concrete, with an additional thickness of 36 inches in the forward direction. Other shield walls have the thicknesses shown.

It is assumed that X-rays are generated only in the high-Z converter. Positions of primary interest for estimating the dose rate contribution from direct radiation are those labeled A, B, D, E and G. For positions C and F, the x-rays undergo a single reflection, with the reflected spectrum being shielded with six and four feet of concrete, respectively. Also, for position E, there are three reflections and no shielding.

Estimated dose rates for the five direct radiation positions are given in Table 10.4, along with other various quantities of interest. This design appears to be quite conservative with respect to direct x-ray radiation.

Table 10.4. Estimated Direct Radiation Dose Rates for the Shield Design of Figure 10-9

Pos.	Angle (deg)	D_i (r-m^2/s-ma)	E_{eq} (MeV)	TVL (ft)	x (ft)	B_f	i (ma)	r (ft)	D (mr/hr)
A	0	113	5	1.0	11	1.0×10^{-11}	30	15	0.0058
B	90	10.0	3.2	0.84	8	3.0×10^{-10}	30	28	0.0044
D	150	10.0	3.2	0.84	9.2	1.0×10^{-11}	30	25	0.0002
E	180	10.0	3.2	0.84	8	3.0×10^{-10}	30	34	0.0032
G	30	56.5 (50%)	5	1.0	10	1.0×10^{-10}	30	18	0.020

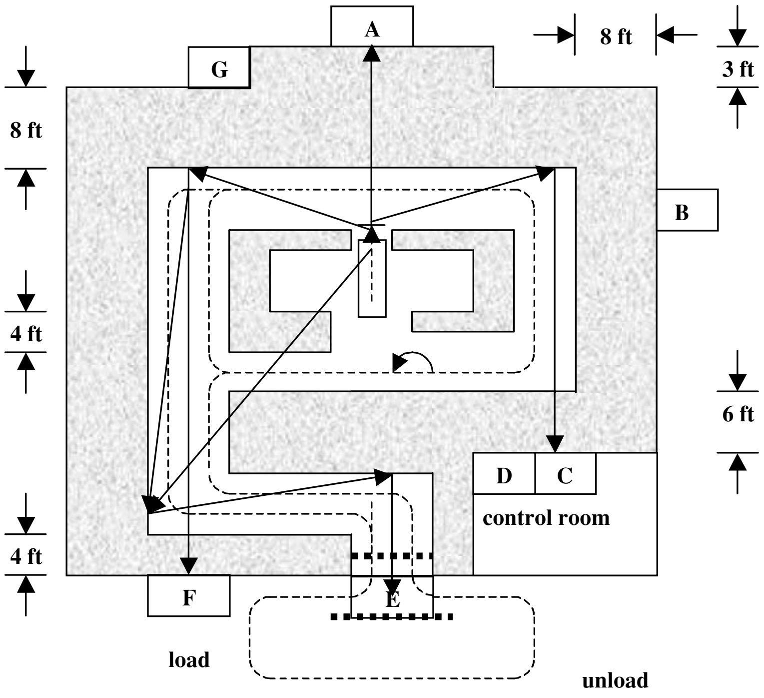

Figure 10-9. Hypothetical shield design for a 5-MeV, 150-kW x-ray irradiation facility. Various positions of interest for shielding calculations are illustrated with the letters A-G. The shield footprint is approximately 51 ft × 58 ft.

Estimated dose rates from reflected radiation for positions C, E and F are given in Table 10.5. For each reflection, values of $\alpha_r = 0.02$ and $A_r = 10\ \text{m}^2$ were used with the appropriate distances indicated. The equivalent energy used in estimating TVLs was also decreased a factor of two on each reflection.

Note that the estimated dose rate at position C is quite low, and the dose rate at position F is small. However, the estimated dose rate at position E resulting from unshielded reflected radiation exceeds the controlled area limit. While this estimate is considered to be conservative (high), it nevertheless emphasizes the importance of considering unshielded, reflected radiation in the design of the shield maze. Having scattered three times, this radiation will be relatively soft, and relatively easily shielded. Depending on the results of radiation surveys, it may be necessary to install additional thin shield walls (steel or lead sheet), placed as indicated by the dashed lines in Figure 10-9. This result, plus that of the previous section, leads to the third general shielding guideline for food irradiation facilities: any unshielded path for reflected x-rays should include at least three "bounces."

Table 10.5. Estimated Reflected Radiation Dose Rates for the Shield Design of Figure 10-9

Pos.	D_i r-m^2/s-ma	r_w ft	i ma	d_1 ft	d_2 ft	d_3 ft	E_{eq} MeV	TVL ft	x ft	B_{fr}	D_r mr/hr
C	10.0	18	30	28			1.5	0.61	6	1.5×10^{-10}	1.5×10^{-5}
E	10.0	18	30	32	28	12	0.4	0.3	–	–	4.2
F	10.0	18	30	38			1.5	0.61	4	2.8×10^{-7}	0.015

10.4. AUXILIARY RADIATION PROTECTION SYSTEMS AND PRACTICES

The accelerator systems used in food irradiation facilities are capable of delivering doses that are fatal to humans in a fraction of a second. In addition to the shield itself, additional precautions are required to prevent inadvertent or accidental entry into the shield. The simplest approach, that of sizing maze entry and exit ports to physically prevent entry, is usually not possible because of product packaging considerations and maintenance requirements. Consequently, safety interlocks and warning devices are essential features of every food irradiation installation.

A safety interlock consists of an electrical circuit that interrupts the delivery of electrical power to the accelerator system if a potentially hazardous condition arises. For example, radiation shields should be designed to have only a single personnel entrance. If the access door is opened when the machine is in operation, the entry interlock will cause the immediate termination of radiation production. In addition to the access door, it is good practice to build in redundancy using interlocked pressure mats, light curtains, motion sensors, etc. which can detect inadvertent intrusion into the maze.

All radiation safety interlocks should be designed to be "fail-safe" as much as possible, so that any defect or component failure in the interlock system will prevent accelerator operation. Also, each safety interlock subsystem should operate independently of all other safety interlocks. Finally, if a safety interlock is tripped, it should not be possible to resume accelerator operations until the interlock controls have been manually cleared at the position of the trip, as well as electrically at the main control console.

Following repair and/or maintenance operations inside the maze, the system operator must perform a "search and evict" walkthrough to ensure that there are no persons inside the maze prior to accelerator system startup. Nearly all accelerators now use a key activation switch in the control system. As part of the accelerator activation process it is good practice to place a key switch at the farthest point into the maze; accelerator startup is then impossible until the maze and access door switches are sequentially activated as part of the search and evict procedure.

All locations designated as radiation areas, high radiation areas, and exclusion areas must be equipped with appropriate warning devices, including flashing lights of appropriate colors and audible sirens or horns, and must be posted with appropriate signs. For example, a horn or siren should sound prior to initiating the accelerator start-up sequence. In addition, flashing lights should be used to designate the status of the accelerator system. For example, flashing yellow or amber lights might be activated both inside and outside the maze, in conjunction with an audible warning, following activation of the key switches of the search and evict procedure. Flashing red lights could then be used to indicate high-voltage modulator operation, and flashing magenta lights, interlocked to a radiation monitor, could be used to indicate the generation of ionizing radiation. These warning devices should be clearly visible and audible in the extremely unlikely event that a person was present in the maze when these were activated. As a final precaution, the radiation cell must be equipped with a "scram button" or other emergency interlock device (e.g., pull cords) that will cause immediate stoppage of accelerator function when activated.

Signs should be used to designate any areas in which hazardous conditions could exist. These areas must be determined by a thorough radiation survey conducted when the machine is in full power operation. A "radiation area" is generally defined as an area that is accessible to personnel, and in which a major portion of the body could receive a dose of 5 millirem in one hour, or a dose of 100 millirem could be received over five consecutive days. A "high radiation area" generally means any area accessible to personnel, and in which a major portion of the body could receive a dose of 100 millirem in one hour. For example, position E of Figure 10.9 should be clearly posted with a sign saying "Radiation Area when Magenta Light is Flashing."

As part of a comprehensive radiation protection program, facility personnel and frequent visitors to the facility should have a thorough training course covering all important aspects of radiation safety, as well as detailed instruction on the various accelerator activation procedures and the meanings of the various warning devices. Since ionizing radiation cannot be detected by human senses at the time of exposure,[4] it is good practice to provide personal radiation monitoring devices (film badges, or pocket dosimeters) to all facility employees and frequent visitors. Monthly personnel dose reports will help assure employees that they are working in a safe environment, and can provide the operating company cheap liability insurance against false or fraudulent claims of radiation safety negligence.

10.5. SUMMARY

In this chapter we have considered various problems of radiation safety, with emphasis on the design of the radiation shield. Since electron accelerators for food irradiation are limited to maximum kinetic energies of 10 MeV for direct electron irradiation, and 5 or 7.5 MeV for indirect x-ray irradiation, there is essentially no neutron production and no possibility of induced radioactivity. Consequently, the primary area of concern is providing protection against penetrating x-radiation.

The general problem of calculating the radiation dose at a particular location for a given shield design is quite complicated. Fortunately, it has proven to be possible to design adequate radiation shields using a simplified approach based on empirical source strengths and attenuation factors. The results of such analyses lead to three generally conservative guidelines for shield design in food irradiation facilities; these can be summarized as follows: (1) eleven feet of concrete in the forward direction; (2) eight feet of concrete in the side directions; and (3) any unshielded path for reflected x-rays should include at least three “bounces.” These guidelines should be used as the starting points. Once a preliminary facility design has been developed, more detailed calculations can then be performed using the techniques of this chapter, with shielding corrections to be made as necessary.

While this chapter has emphasized shield design, it should be noted that several additional precautions and procedures are required to prevent inadvertent or accidental radiation exposure. These include the use of safety interlocks, warning devices, appropriate radiation signs, training programs covering all important aspects of radiation safety, and monitoring of facility personnel.

REFERENCES

1. W.M. Brobeck and Associates, **Particle Accelerator Safety Manual,** MORP68-12, US Dept. HEW, Rockville, Md (1968).
2. American National Standard N433.1, **Radiological Safety in the Design and Operation of Particle Accelerators**, American National Standards Institute, NY (1978).
3. NCRP Report No. 51, **Radiation Protection Design Guidelines for 0.1-100 MeV Particle Accelerator Facilities**, NCRPM, Bethesda, Md (1977).
4. R.P. Gardner and R.J. Ely, Jr., **Radioisotope Measurement Applications in Engineering**, Reinhold Publishing Corp., NY (1967).
5. “Average Energy Required to Produce an Ion Pair,” **ICRU Rept. 31**, Int’l. Com. Rad. Units and Meas., Wash. DC (1979).
6. A.B. Chilton, J.K. Shultis and R.E. Faw, **Principles of Radiation Shielding**, Prentice-Hall, Inc., Engelwood Cliffs, NJ (1984).

CHAPTER 11

CRITICAL SYSTEM PARAMETERS AND PROCESS CONTROL

The primary objectives of any irradiation application are twofold: (1) ensuring the delivery of the minimum required dose to all positions in the product, and (2) limiting the maximum delivered dose in order to minimize adverse effects on the product and to increase the throughput efficiency. These factors naturally depend on the product configuration and how packages are arrayed on the material handling system. The maximum areal density and variations in areal density must be established by detailed dose mapping tests for each product application; in Chapters 3 and 4, the dose uncertainties that can arise from variations in areal density were examined in some detail.

It is also clear that dose uncertainties can arise if critical parameters associated with the three key system technologies, i.e., the accelerator system, the beam scanning system, and the material handling system, are not adequately stabilized. Consequently, much of the emphasis of this chapter is on the necessary amount of control of the critical process parameters, so that dose uncertainties are essentially the result of areal density variations, only. In particular, we will use the results of previous chapters to identify these critical system parameters, illustrating their interdependencies, and how they determine the delivered dose. We will also discuss allowable tolerances on variations in the critical parameters to assure stability of the three key system technologies, the consistency of the delivered dose (process integrity), and the implications for throughput. As a final topic we will consider the dose variations that can arise as the result of an unplanned interruption of the irradiation process.

11.1. CRITICAL PROCESS PARAMETERS

For direct electron irradiation, the three key technologies are linked by the front surface dose, D_{fs}, as given by Eq. (2.14), repeated here for convenience.

$$D_{fs} = 1.8 \times 10^{6}\, I_a/(wv) \tag{11.1}$$

If the average current I_a is given in amps, the scan width w in cm, and the conveyor speed v in cm/s, the front surface dose is given in kilogray. Note that the front surface dose does not depend on the electron kinetic energy. However, the shape of the depth-dose distribution does depend on the kinetic energy, and the implications of this dependence will be examined in the next section.

For indirect x-ray irradiation, the front surface dose depends on the kinetic energy and scan height. Using Eq. (4.34), but rewritten as given in Eq. (11.2) to emphasize the linear dependence of the conversion efficiency on the beam kinetic energy E (in electron volts),

$$D_{fs} = [6.8 \times 10^{-7}\, E^{2}\, I_a/(wv)] \tag{11.2}$$

(The exponential term accounting for the geometric decrease with distance from the converter has been omitted.) For x-rays, the depth-dose distribution is only weakly dependent on the electron kinetic energy through the detailed angular dependence of the bremsstrahlung cone.

Regarding Eqs. (11.1) and (11.2), it is apparent that the critical process parameters include the average beam current, the conveyor speed, the width of the scan, and the beam kinetic energy. While the conveyor speed is an independent variable, the other parameters are interdependent. In particular, for pulsed systems the average beam current is the product of the peak beam current I_p and the duty factor (repetition rate F times pulse width τ), as given by Eq. (11.3), while the beam kinetic energy also depends on the peak beam current through the accelerator load line. For microwave accelerators, the load line also depends on the square root of the microwave power P_s of the source, as given by Eq. (11.4).[1] Further, the scan width depends on the maximum deflection angle, which varies inversely with the kinetic energy, and linearly with the peak scan magnet current I_s, as given by Eq. (11.5).

$$I_a = I_p F\tau \tag{11.3}$$

$$E = aP_s^{1/2} - bI_p \tag{11.4}$$

$$w = \alpha I_s/E \tag{11.5}$$

a, b and α in Eqs. (11.4) and (11.5) are numerical proportionality constants that depend on the specific system design.

For process integrity with respect to dose, Eqs. (11.1)–(11.5) suggest that it is necessary to control the conveyor speed, the peak beam current, the pulse repetition rate, the pulse duration, the power of the microwave source, the scan magnet current, and (redundantly) the average beam current. (A useful (but redundant) measure of the beam kinetic energy could also be obtained from the microwave fields in an accelerating cavity of a microwave linac, following a suitable calibration.)

The electronic sophistication for controlling all of these parameters to deliver a particular desired dose probably exists now. However, it is traditional, and still much simpler to explain to an auditor, that all accelerator and scanning system (interdependent) parameters are held constant during processing, in which case the magnitude of the delivered dose depends only on the inverse of the conveyor speed, which is the one independent variable (apart from areal density variations).

Since the kinetic energy and dose are not continuously monitored, but are only checked periodically with dosimetry, it is important to understand how variations in the several parameters lead to variations in the dose and kinetic energy. With this knowledge it is then possible to establish limits on each critical performance parameter to guarantee the integrity of the process. By electronically interlocking these limits, the process will be interrupted in the event of an out-of-limit condition. There are two situations that typically arise in practice. The first is one in which a significant problem occurs that causes an abrupt change in a critical parameter. An example might be a failure of the scan magnet, caused by either an open or short circuit. Such a condition is easily sensed, and can be interlocked with rather loose limits. More problematic are slower drifts in parameter values resulting from thermal fluctuations and/or aging.

11.2. VARIATION OF THE DEPTH-DOSE PROFILE WITH KINETIC ENERGY FOR ELECTRON BEAM PROCESSING

For x-ray irradiation, the depth-dose profile is relatively independent of small changes in electron energy, with the magnitude of the dose being given by Eq. (11.2). For electron irradiation, however, the situation is quite different; although the front surface dose does not vary with changes in the electron

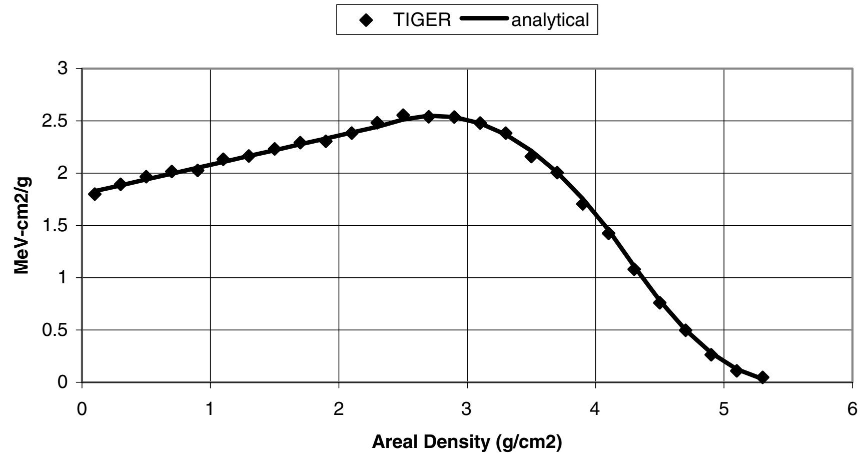

Figure 11-1. Depth-dose profile for 10-MeV electrons incident onto a uniform water absorber, as calculated by the one-dimensional Monte Carlo code TIGER. The solid line is the analytical fit of Eq. (11.6).

kinetic energy (except indirectly through the scan width variable), the depth-dose distribution does change. This effect can have important consequences for the dose uniformity and energy utilization efficiency, depending on the distribution of areal densities for the product.

The depth-dose profile that results when 10-MeV electrons are normally incident on a uniform water absorber has the characteristic shape shown in Figure 11-1. The specific energy deposition (dose) increases from about 1.8 MeV-cm^2/g to a maximum value of about 2.55 MeV-cm^2/g at a depth (areal density) of about 2.75 g/cm^2. The dose then monotonically decreases to a minimal bremsstrahlung background at about 5.5 g/cm^2. With x designating depth, a good approximation to this depth-dose profile is provided by

$$\begin{aligned} D(\text{MeV-cm}^2/\text{g}) = {} & 1.80 + 0.28x; && 0 < x < 2.4 \\ & 2.55 - 0.60(x - 2.75)^2; && 2.4 < x < 4.4 \\ & 0.78(5.5 - x)^2; && 4.4 < x < 5.4 \end{aligned} \tag{11.6}$$

Two quantities of interest in radiation processing are (1) the dose uniformity ratio (UR), given by dividing the maximum dose D_{max} at any depth by the minimum dose D_{min}, and (2) the energy utilization efficiency η_u, which is the efficiency of delivering the minimum required dose to all portions of the product. A convenient expression for the utilization efficiency is

$$\eta_u = x/x_{max} = xD_{min}/E \tag{11.7}$$

where E is the incident electron kinetic energy. From Figure 11-1, the minimum dose is given by the smaller of the doses at either the front or rear surfaces.

Graphs of the dose uniformity ratio and the energy utilization efficiency are shown in Figure 3-13 as a function of depth (areal density). The maximum utilization efficiency is about 0.68, occurring at the optimum depth of 3.8 g/cm^2, where the dose equals the front surface dose. The uniformity ratio has a value of about 1.4 for this condition, but rapidly increases with greater depth.

The depth-dose profile (especially in an aluminum absorber) is commonly used to infer the kinetic energy of an incident electron flux (see Appendix B).[2] In particular, empirical relations have been developed that give the kinetic energy as a linear function of the R_{50} range; i.e., the depth at which the dose has decreased to 50% of its maximum value. Guided by this observation, it is assumed that a relatively small change in kinetic energy dE will produce a new depth-dose profile D′(x), with the property that

$$D'(x') = D(x) \tag{11.8}$$

for $x' = x(1 + dE/E)$. As an example of the implied procedure, consider the linear portion of Eq. (11.6). Writing $D(x) = mx + b$, and $D'(x) = m'x + b'$, then Eq. (11.8) gives

$$D'(x') = m'x(1 + dE/E) + b' = mx + b$$

Collecting like orders of x gives

$$m' = m(1 + dE/E)^{-1}, \quad b' = b$$

When this procedure is applied to all of Eq. (11.6), the result for the new dose profile produced by a small change dE in kinetic energy is

$$\begin{aligned} D'(x) = 1.8 + 0.28(1 + dE/E)^{-1}; \quad & 0 < x < 2.4(1 + dE/E) \\ 2.55 - 0.6(1 + dE/E)^{-2}[x - 2.75(1 + dE/E)]^2; \quad & 2.4(1 + dE/E) < x < 4.4(1 + dE/E) \\ 0.78(1 + dE/E)^{-2}[5.5(1 + dE/E) - x]^2; \quad & 4.4(1 + dE/E) < x < 5.4(1 + dE/E) \end{aligned} \tag{11.9}$$

The validity of this approximation is assessed in Figure 11-2, in which the predictions of Eq. (11.9) are compared with the depth-dose profiles as calculated by the TIGER[3] code for incident energies of 9.5 and 10.5 MeV (dE/E = +/−5%). The agreement is quite good.

11.2.1. Single-Sided Irradiation

Having validated Eq. (11.9), it is relatively easy to estimate the change in dose at a particular depth x resulting from a small energy change dE by computing D′(x) − D(x). For the single-sided irradiation

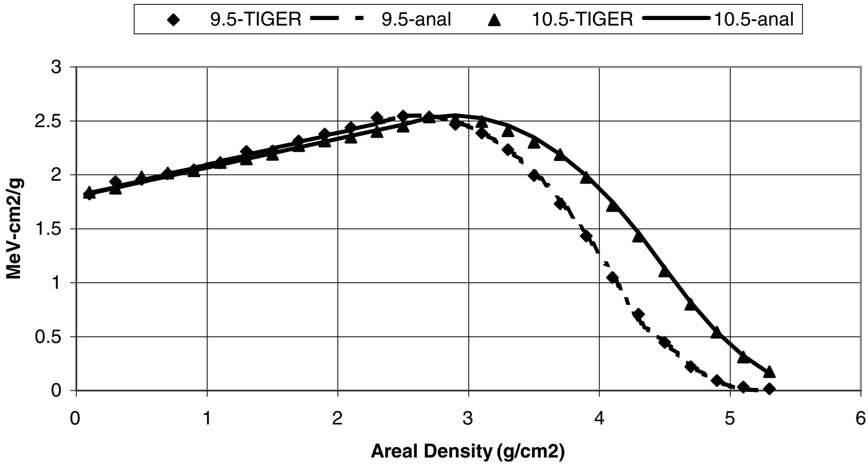

Figure 11-2. Comparison of the analytical approximation of Eq. (11.9) with detailed TIGER results for incremental energy changes of +/−5% from 10 MeV.

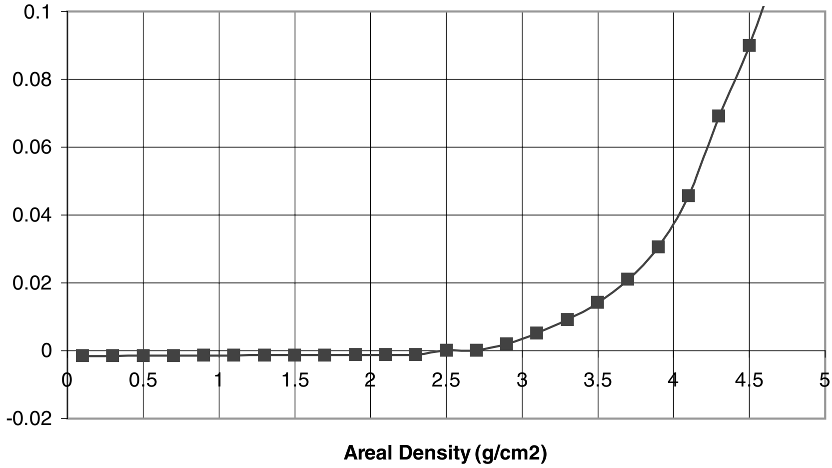

Figure 11-3. Fractional change in dose resulting from a 1% change in electron energy.

configuration, the linearized result is

$$\begin{aligned}(dD/D) &= -(0.28/D)\,(dE/E); && 0 < x < 2.4\\ &\ [1.2x(x-2.75)/D]\,(dE/E); && 2.4 < x < 4.4 \qquad (11.10)\\ &\ [1.56x(5.5-x)/D]\,(dE/E); && 4.4 < x < 5.4\end{aligned}$$

Eq. (11.10) is graphed in Figure 11-3 as a function of depth, assuming $dE/E = 1\%$. Dose differences resulting from energy changes are quite small until the depth nears $x = x_{opt} = 3.8$ g/cm^2; at this depth a 1% change in kinetic energy causes a dose change of about 2.7%. As the depth increases to about 4.4 g/cm^2, for which the dose is about half the front surface dose, a 1% change in kinetic energy produces a dose change of about 8%.

The dose uniformity ratio and the energy utilization efficiency are shown in Figures 11-4 and 11-5 for several different areal densities around the optimum depth of 3.8 g/cm^2. For depths less

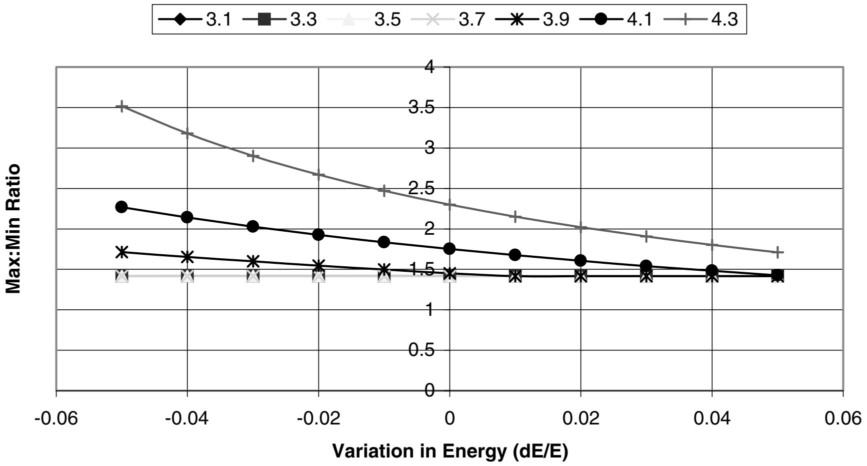

Figure 11-4. Variation of the dose uniformity ratio with variation in the electron kinetic energy (about 10 MeV) for the single-sided irradiation scenario. The results for several different areal densities are shown.

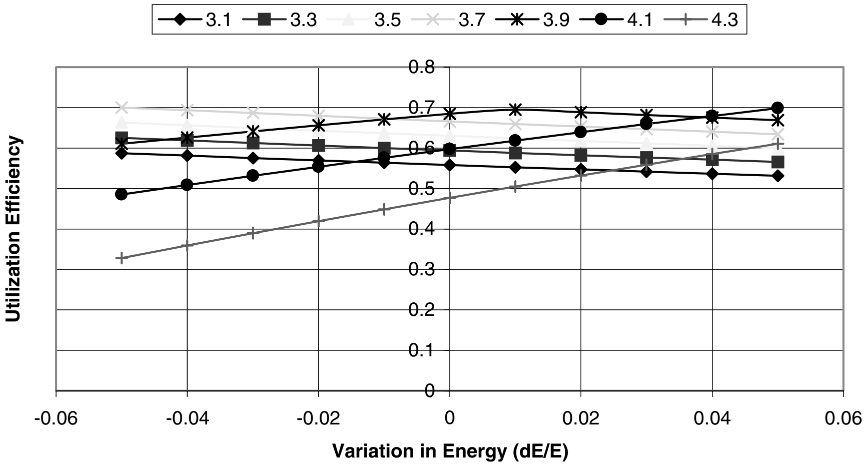

Figure 11-5. Variation of the throughput efficiency with variation in the electron kinetic energy (about 10 MeV) for the single-sided irradiation scenario. The results for several different areal densities are shown.

than the optimum, the effect of an energy variation on the dose uniformity is negligible. For depths greater than the optimum, an increase in kinetic energy improves the dose uniformity, but a decrease in kinetic energy worsens the dose uniformity. For depths less than the optimum, an increase in kinetic energy marginally decreases the throughput efficiency. For depths greater than the optimum, an increase in energy marginally improves the throughput efficiency, but a decrease in energy worsens the throughput efficiency. In brief summary, for single-sided irradiation, with a maximum product thickness limited to the optimum areal density for 10-MeV electrons, the allowed variation in energy that still results in a high-integrity irradiation is nearly +/−5%.

11.2.2. Double-Sided Irradiation

The results of the previous section can also be used to deduce the variation in the depth-dose profile with a variation in the electron kinetic energy for the symmetric, double-sided irradiation configuration by noting that

$$D(x, L) = D(x) + D(L - x) \tag{11.11}$$

where L is the thickness of the product. The calculated dose uniformity ratio and throughput efficiency for a symmetric, double-sided, 10-MeV irradiation are presented in Figure 11-6 as a function of the areal density (refer also to Chapter 3). The maximum energy utilization efficiency is about 0.8, and occurs at an optimum areal density of about 8.8 g/cm^2, corresponding to a narrow minimum of about 1.4 in the the max:min ratio. Note also that the dose uniformity ratio increases to nearly 2.7 at an areal density of 6 g/cm^2.

The dose profiles obtained using Eqs. (11.9) and (11.11) for doubled-sided irradiation are shown in Figure 11-7 for an absorber thickness of 8.8 g/cm^2, assuming energy variations of zero and +/−5% around 10 MeV. The dose in the middle of the absorber is clearly quite sensitive to energy. Based on the single-sided irradiation result of Eq. (11.10), a −5% change in kinetic energy will produce a 40% change in dose in the center of the absorber (4.4 g/cm^2), in excellent agreement with the depth-dose profile results.

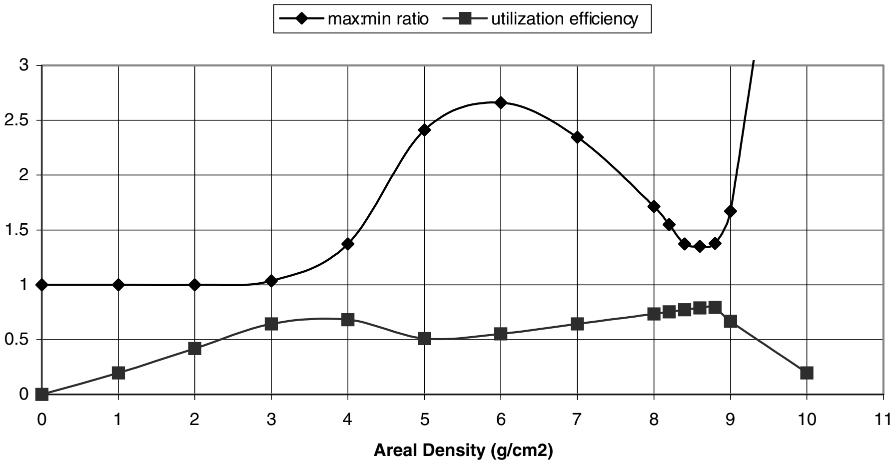

Figure 11-6. Dose uniformity ratio and utilization efficiency as a function of product depth (areal density) for symmetric, double-sided irradiation of water using 10-MeV electrons.

This dose sensitivity for the double-sided irradiation configuration has important implications for the dose uniformity and utilization efficiency parameters, especially for kinetic energy changes in the negative direction. These parameters are graphed in Figures 11-8 and 11-9 as a function of the percent energy change for several different values of absorber thickness.

For dose consistency in the high throughput efficiency range of the areal density parameter, it is more important to limit variations in areal density than it is to tightly control the electron kinetic energy. For example, for areal densities in the range of 8.0–8.8 g/cm^2, variations in kinetic energy of -3% to $+3\%$ cause (usually) acceptable variations in dose uniformity (max:min ratio <2) and utilization efficiency. However, tightening the energy limits to $+/-2\%$ provides only a marginal increase in areal density range to 7.9–8.9 g/cm^2.

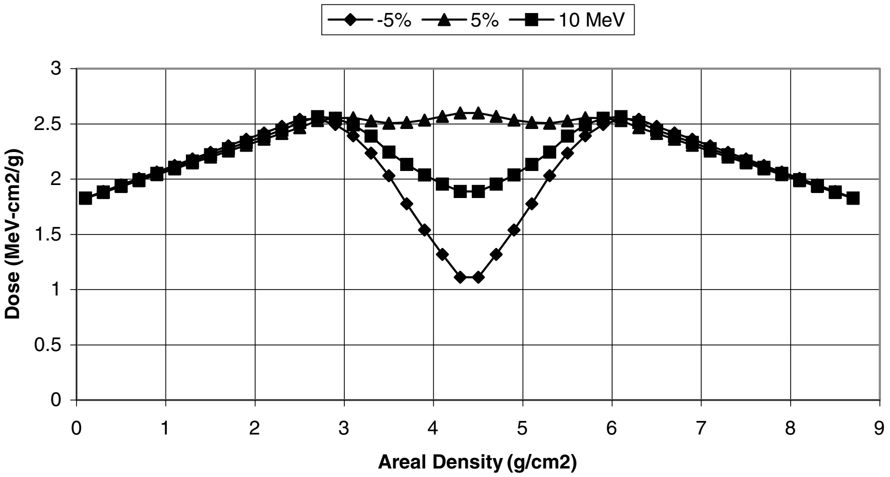

Figure 11-7. Depth-dose profiles for a total absorber thickness of 8.8 g/cm^2 for the symmetric, double-sided irradiation scenario. The results for a kinetic energy change of 0 and $+/-5\%$ about 10 MeV are shown.

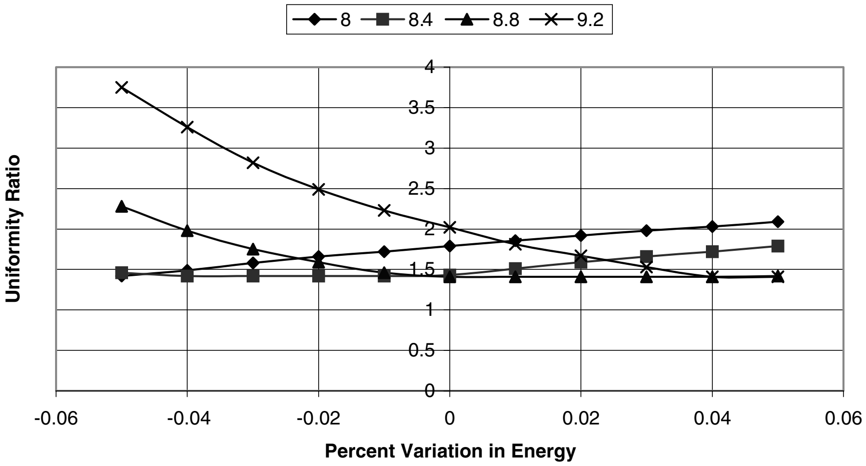

Figure 11-8. Variations in the max:min ratio with variations in electron kinetic energy (about 10 MeV) for several different absorber thickness values.

11.3. ENERGY CONTROL

Having seen the consequences that small variations in electron kinetic energy can have on the depth-dose profile for electron irradiation, we next examine the parameters that control the beam kinetic energy, using a microwave linac as an example. Assuming small variations about the operating point, the differential limit of the load line Eq. (11.4) is given as

$$dE = (a/2)P^{-1/2}\,dP - b\,dI$$

or, dividing both sides by E,

$$(dE/E) = [aP^{1/2}/(2E)](dP/P) - [bI/E](dI/I) \qquad (11.12)$$

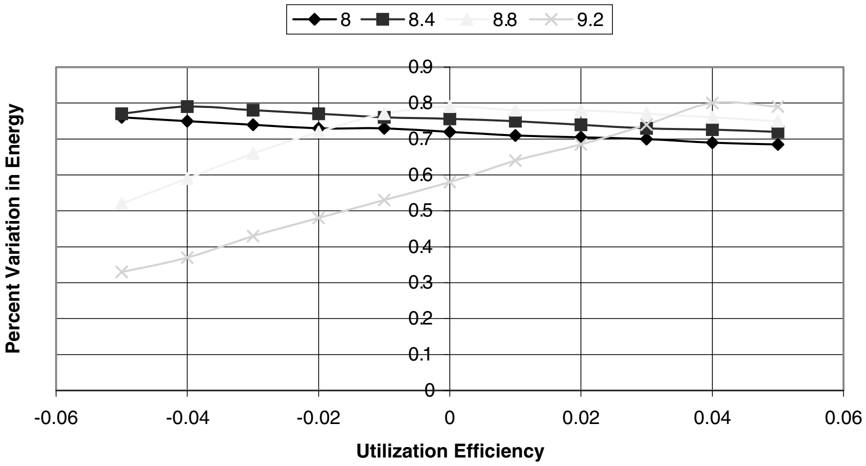

Figure 11-9. Variations in the energy utilization efficiency with variations in electron kinetic energy (about 10 MeV) for several different absorber thickness values.

Thus, the relative variation in the beam kinetic energy can be related to the relative variations in the klystron power and the beam current, once the coefficients of these terms are evaluated at the nominal operating point.

As an example, for the accelerator reported in Reference 4, the load line is given as

$$E = 3.69 \times 10^3 P^{1/2} - 4.38 \times 10^6 I \tag{11.13}$$

Assuming a nominal operating point of 5 MeV at an input power of 5 MW, implying a macroscopic peak beam current of 0.74 amps, Eq. (11.12) becomes

$$(dE/E) = 0.825(dP/P) - 0.648(dI/I)$$

If the power is held constant, a 5% variation in beam current will give rise to a 3.2% variation in kinetic energy, while a 5% variation in microwave power will result in a 4.1% change in kinetic energy. This level of stability is usually satisfactory for most food applications, but for other applications (e.g., high dose-rate radiotherapy using electrons) it is insufficient. As a result, servo-feedback control mechanisms have been developed to independently stabilize the beam current (using the signal from either a current transformer that directly monitors the beam current, or an ionization chamber that monitors the dose rate), and to stabilize the kinetic energy by controlling the modulator voltage (which controls the klystron power).[1] An implicit assumption for this approach is that variations in beam current and klystron power are not correlated. This usually implies the use of a triode electron gun. We will analyze the situation for a diode gun energized from a tap on the pulse transformer in Section 11.5.

If it is imperative that variations in kinetic energy must be tightly controlled (perhaps certain electron beam configurations in which constancy of the depth-dose profile is critical), then the gun current must be controlled independently to compensate for source power variations, as suggested by Eq. (11.12). In such cases it is possible in principle to maintain a nearly constant dose by feedback control of the conveyor speed, as suggested by Eq. (11.1).

11.4. DOSE CONTROL

The variations in dose arising from variations in the various critical process parameters can be deduced from Eqs. (11.1)–(11.5). The cases for electron irradiation and x-ray irradiation are examined separately in the following paragraphs.

11.4.1. Direct Electron Irradiation

The average current depends on the duty factor through Eq. (11.3). For all practical purposes, the pulse width, pulse repetition rate and the conveyor speed can be considered as constants. Consequently, in the differential limit Eq. (11.1) becomes

$$dD/D = (dI/I) - dw/w \tag{11.14}$$

However, from Eq. (11.5), $dw/w = -dE/E$. Using the differential load line Eq.(11.12), Eq. (11.14) becomes

$$dD/D = (1 - bI/E)(dI/I) + (0.5aP^{1/2}/E)(dP/P)$$

As an example, assuming load line values of $a = 6.40 \times 10^3$ and $b = 14.3 \times 10^6$, with a nominal operating point of 10 MeV at an rf power of 5 MW (and a beam current of 0.3 amps), then Eq. (11.14) becomes explicitly

$$dD/D = 0.715(dP/P) + 0.429(dI/I)$$

A 5% variation in microwave power will result in a dose variation of 3.6%, and a 5% variation in beam current will give a dose variation of 2.9%. This dose variation is separate from that resulting from the change in the dose profile produced by the change in electron kinetic energy.

11.4.2. Indirect X-Ray Irradiation

The differential limit of Eq. (11.2) is

$$dD/D = 2(dE/E) + (dI/I) - dw/w \tag{11.15}$$

As an example, using the differential form of the load line of Eq. (11.3), Eq. (11.15) becomes

$$dD/D = 2.475(dP/P) - 0.944(dI/I) \tag{11.16}$$

A 5% variation in beam current will result in a 4.7% variation in dose, but a 5% variation in microwave power will produce a 13.4% change in dose. Although there is little profile variation with energy changes for x-ray irradiation, the magnitude of the dose can vary significantly with microwave power because of the squared energy dependence.

11.5. DOSE AND ENERGY VARIATION WITH MODULATOR VOLTAGE

As previously mentioned, for some accelerator applications, especially electron radiotherapy, precise control of both the kinetic energy (penetration) and beam current (dose) is essential. This control is facilitated by the use of a triode gun that permits control of the beam current independent of the modulator voltage. However, for most food irradiation applications such precise dose control is not usually required, and it is common to produce the beam current with a diode gun that is energized by a tap off the high voltage pulse transformer. In this case, the beam current and the rf forward power are necessarily correlated, and it is important to understand how changes in the modulator voltage will affect both the electron kinetic energy and the delivered dose.

Assuming the use of a high-power klystron microwave source, the rf power is given by $P = \eta I_k V_k$; the klystron current I_k is determined by the klystron perveance p_k according to $I_k = p_k V_k^{3/2}$, and η is the klystron rf efficiency. Thus, the klystron power can be related to the voltage according to

$$P = \eta p_k V_k^{5/2} \tag{11.17}$$

Similarly, the linac gun current is determined by the gun perveance p_g according to $I_g = p_g V_g^{3/2}$. Since the gun voltage is a fraction f of the klystron voltage, $V_g = fV_k$. If the accelerator is being operated at near its nominal operating point, the linac beam capture efficiency ε is nearly constant. Therefore, the beam current is given by

$$I = \varepsilon p_g (fV_k)^{3/2} \tag{11.18}$$

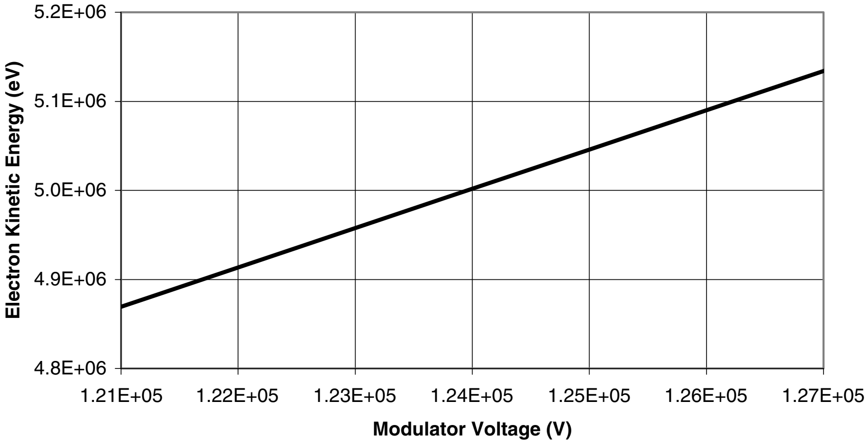

Figure 11-10. Variation of the electron kinetic energy with modulator voltage for a simple diode gun configuration.

Taking differentials of Eqs. (11.17) and (11.18), a 1% change in modulator voltage will cause a 2.5% change in the klystron power and a 1.5% change in the beam current. Therefore, for variations due to changes in the modulator voltage

$$\mathrm{dP/P} = (5/3)\,\mathrm{dI/I} \tag{11.19}$$

As a numerical example, suppose the klystron power is 5 MW at a voltage of 125 kV, so that $P = 9 \times 10^{-7}\,V_k^{5/2}$. Also, assume that the beam current is given by $I = 1 \times 10^{-7}(fV_k)^{3/2}$, with $f = 0.30$. When these quantities are substituted into the load line Eq. (11.13), the result is

$$E = 3.50\,V_k^{5/4} - 0.44(fV_k)^{3/2} \tag{11.20}$$

This equation is graphed in Figure 11-10 as a function of the klystron (modulator) voltage.

Taking differentials of Eqs. (11.20) and evaluating the coefficients at the nominal 5 MeV operating point gives

$$\mathrm{dE/E} = 1.09\,\mathrm{dV_k/V_k} \tag{11.21}$$

Thus, near the nominal operating point, a 1% change in modulator voltage (about 1.25 kV) should produce a kinetic energy change of a little over 1% in the beam kinetic energy. From Eq. (11.16) the change in dose is given by

$$\mathrm{dD/D} = 3.18\,\mathrm{dI/I} = 1.91\,\mathrm{dP/P} = 4.78\,\mathrm{dV_k/V_k} \tag{11.22}$$

Therefore, a 1% change in modulator voltage will cause a 1.1% change in beam kinetic energy, a 1.5% change in beam current, a 2.5% change in klystron power, and a 4.8% change in dose. To limit variations in dose to nominally +/−10%, the modulator voltage of this hypothetical system should be controlled to +/−2%.

11.6. DOSE VARIATIONS RESULTING FROM A PROCESS INTERRUPT

From the analyses of the previous sections it is apparent that certain critical parameters must be tightly controlled to ensure the dose integrity of the irradiation process. However, if these limits are set too tightly, the possibility for machine faults produced by spurious signals (noise) can rise dramatically. Such nuisance faults can be costly if product on the process table at the time of the fault must be discarded because of large uncertainties in the delivered dose. In this section we consider the problem of a "process interrupt," and derive estimates for the dose variations that can result.

Consider the schematic diagram of Figure 11-11. The conveyor system moves product at a constant speed v_o through a beam of lateral width L. The beam current (or power) is constant until a fault occurs, at which time it drops abruptly to zero. However, the conveyor cannot stop immediately. The control system must sense that the fault has occurred and remove power from the drive motor of the process table. Once drive has been removed, the conveyor will continue to move a small amount because of its inertia. Consequently, there will be some portions of the product that will receive a lower dose.

After the fault has been cleared, start signals are sent to both the accelerator system and the conveyor system. The accelerator can restart nearly instantaneously, but there will be a non-zero lag time for the drive motor to accelerate the process conveyor to its constant speed. Depending on this time lag, some of the product can receive a higher or lower dose than normal; the actual dose given to product depends on its position in the beam at the time of the fault, the beam width, and the various time constants and time delays for conveyor stopping and restarting. In the following paragraphs we discuss a simple electron irradiation example to illustrate the important points.

Consider the simplified situation in which the beam intensity is constant over L. In this case, the dose delivered to a position in the product simply depends on the time that the particular product position is in the region of the beam with the beam on. To explicitly illustrate this time dependence, Eq. (11.1) is rewritten as

$$D_{fs} = [1.8 \times 10^6/(wL)] \int I\,dt \tag{11.1'}$$

The dose delivered to a particular position in the product depends on its time of entry into the beam region, relative to the time that accelerator operation is interrupted. To be specific, we assume the time-dependent beam current and conveyor speed profiles shown in Figure 11-12. In particular, the entry time is designated by t_1, and the fault is assumed to occur at the fixed time t_2. The conveyor velocity decreases linearly (constant deceleration), reaching zero at the time t_3, at which time the restart command is given. While the beam current is restored instantaneously, the conveyor velocity increases linearly (constant acceleration), reaching v_o at the time t_4.

The parameter t_1 is assumed to vary over the range $[0, t_4]$, and the interrupt occurs at $t_2 = L/v_o$. The conveyor deceleration rate is designated by a_1; therefore, the conveyor velocity following the interrupt is given by $v = v_o - a_1(t - t_2)$, and the time t_3 is equal to $(t_2 + v_o/a_1)$. The conveyor

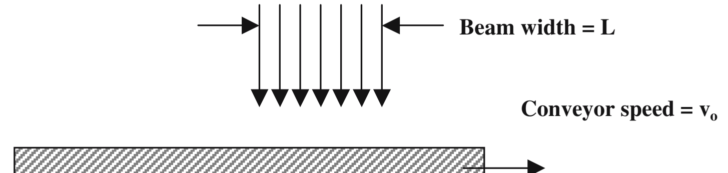

Figure 11-11. Product is conveyed through the beam of lateral width L at a constant conveyor speed v_o.

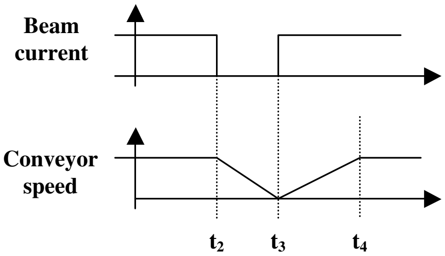

Figure 11-12. Assumed time-dependent behavior of the beam current and conveyor velocity associated with a process interrupt event.

acceleration rate is designated by a_2; the conveyor speed following the restart is therefore given by $v = a_2(t - t_3)$, and the time t_4 is equal to $(t_3 + v_o/a_2)$.

For a particular entry time t_1, the time of exit from the beam region, designated as t_5, is found by integrating the equation of motion for the assumed conveyor velocity profile of Figure 11-12. From Eq. (11.1′), the dose delivered to a particular product position simply depends on the time differences as given by Eq. (11.23)

$$\begin{array}{ll} (t_2 - t_1); & t_2 < t_5 < t_3 \\ (t_5 - t_1) - (t_3 - t_2); & t_5 > t_3 \end{array} \tag{11.23}$$

As a specific numerical example, we assume that $L = 5$ cm, $v_o = 10$ cm/s, and $a_1 = 100$ cm/s^2. In this case, $t_2 = 0.5$ s, and $t_3 = 0.6$ s. In the 0.1-second interval between t_3 and t_2, the conveyor moves 0.5 cm without the beam being on. Since this distance is 10% of the beam width, the largest dose decrease will also be 10%, which occurs for $t_5 = t_3$ at $t_1 = 0.05$ s.

For $t_5 > t_3$, the delivered dose depends on the conveyor restart profile. If the conveyor restart were instantaneous, then $t_4 = t_3$, and the dose would remain 10% low until $t_1 = t_4$, at which time it would increase abruptly to its normal value. This low-dose region would correspond to 5.5 cm of product. If the acceleration rate were equal to the deceleration rate, then the acceleration time is also 0.1 second, and the conveyor would move a total distance of 0.5 cm at reduced speed. The corresponding difference in entry times is 0.1 second; at the nominal conveyor speed of 10 cm/s, the region of disrupted dose would therefore correspond to only 1 cm of product. If the acceleration rate were half the deceleration rate, then $t_4 - t_3 = 0.2$ seconds. A significant portion of the product will therefore remain in the beam 10% longer than usual, and the dose will be 10% higher than usual, until $t_1 = t_4 = 0.8$ sec, at which time the dose would abruptly decrease to the usual value. The high-dose region would correspond to 6.5 cm of product. These various cases are illustrated in Figure 11-13.

Based on the results of this simple example, a general conclusion is that the maximum percent decrease in delivered dose is roughly equal to the distance that the conveyor moves following the beam interruption, divided by the beam width. As a consequence, for the larger beam widths and slower conveyor speeds associated with x-ray irradiations, dose variations resulting from a process interrupt are usually not a problem. For example, for $L = 20$ cm, $v_o = 1$ cm/s and $a_1 = 100$ cm/s^2, the distance that the conveyor moves following a beam interruption is only 0.005 cm. Therefore, the maximum percent decrease in dose is estimated to be only 0.025%.

For situations in which the product is costly, and it is imperative that there be no decrease in delivered dose, there are various strategies that can be considered to reduce the dose deficiency, depending on the capabilities of the conveyor and control systems. For example, it might be possible to operate the process conveyor in reverse for a certain desired distance prior to beam restart. Also,

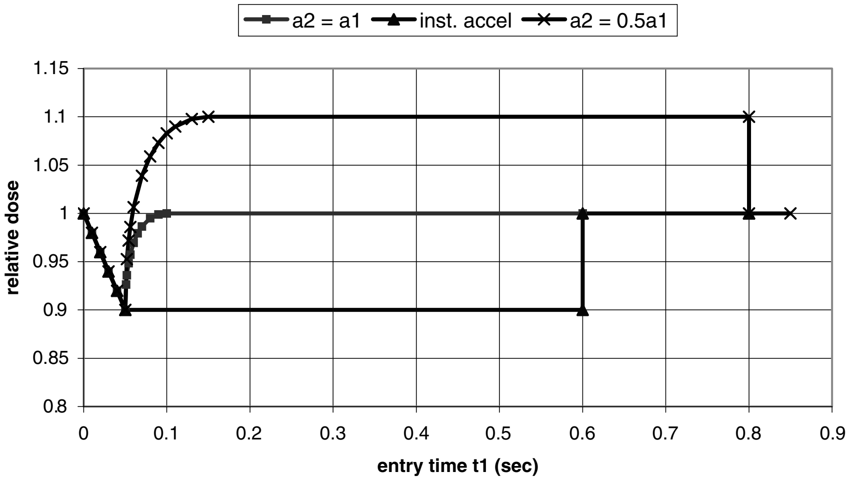

Figure 11-13. Relative dose profiles versus product time of entry for several different restart conditions.

it should be realized that the assumption of a square beam profile is somewhat artificial; the actual beam profile is likely to have Gaussian wings because of scattering in the exit window. Consequently, it is often possible to reduce the dose deficiency by further delaying the conveyor restart, letting the wings of the beam profile fill in the region of reduced dose. The downside of this strategy is a further increase in the maximum delivered dose.

11.7. SUMMARY

In this chapter we have considered several different topics related to dose variations produced by variations in key system parameters. In particular, a linearization procedure was used to calculate the variations in the electron depth-dose profile resulting from small changes in the kinetic energy. A comparison of the results of this procedure for a 10-MeV electron beam were shown to agree well with detailed TIGER Monte Carlo calculation results for kinetic energy variations over the range of −5% to +5% about the nominal 10-MeV value.

Having validated the analytical procedure, its results were then used to assess the impact of kinetic energy variations on the dose uniformity (max:min ratio) and the energy utilization efficiency for both single- and double-sided irradiation configurations. For single-sided irradiations, at an absorber thickness of 3.8 g/cm^2, corresponding to the maximum utilization efficiency condition (68%), a 1% change in kinetic energy produces a dose change of about 2.7%. Thus, for absorber thicknesses less than 4 g/cm^2, variations in kinetic energy of −3% to +5% about the nominal 10-MeV value will still result in high process integrity. If the maximum absorber thickness were restricted to 3.7 g/cm^2, the lower energy limit could be further reduced to −5%.

In contrast, the double-sided irradiation scenario is much less forgiving. For areal densities in the range of 8.0–8.8 g/cm^2, variations in kinetic energy of −3% to +3% cause marginally acceptable variations in dose uniformity (max:min ratio <2) and utilization efficiency. For areal densities outside this range, the limits on kinetic energy variations tighten considerably, especially for negative energy variations and thick absorbers. Further, decreasing the energy variation limits to +/−2% provides only a marginal increase in the allowable range of areal densities, to about 7.9–8.9 g/cm^2. In terms of process integrity for this double-sided irradiation scenario, it is far more important to hold the areal density at 8.4 g/cm^2, +/−0.4 g/cm^2, than it is to keep the energy limits at +/−0.2 MeV.

A linearization of the equations that control dose, together with the accelerator load line, provide an estimate of the allowable limits on key system parameters for both electron and x-ray irradiation configurations. For accelerator systems in which both the beam current and kinetic energy depend on the modulator voltage, the modulator voltage should be stabilized to typically $+/-2\%$ to ensure that dose variations do not exceed $+/-10\%$. For situations in which variations in kinetic energy must be tightly controlled, the gun current must be controlled independently to compensate for source power variations. In such cases it is possible to maintain a nearly constant dose by feedback control of the conveyor speed.

While certain critical parameters must be tightly controlled to ensure the dose integrity of the irradiation process, if these limits are set too tightly, the possibility for machine faults produced by spurious signals can rise dramatically. Based on a simple example of a process interrupt, a general conclusion is that the maximum percent decrease in delivered dose is approximately equal to the distance that the conveyor moves following the beam interruption, divided by the beam width. As a consequence, for low-dose electron beam irradiation applications (small beam width and high conveyor speeds), the dose variation is usually too large and product must be discarded. At the other extreme, for the large beam widths and slower conveyor speeds associated with x-ray irradiations, dose variations resulting from a process interrupt are usually not a problem.

REFERENCES

1. C. J. Karzmark, C. S. Nunan and E. Tanabe, **Medical Electron Accelerators**, McGraw-Hill, N.Y. (1993).
2. ISO/ASTM Standard **E 1649**, Practice for Dosimetry in an Electron Beam Facility for Radiation Processing at Energies between 300 keV and 25 MeV.
3. J. A. Halblieb, R. P. Kensek, T. A. Mehlhorn, G. D. Valdez, S. M. Seltzer and M. G. Berger, ITS Version 3.0: The Integrated TIGER Series of Coupled Electron/Photon Monte Carlo Transport Codes, **SAND91-1634** (1992).
4. R. B. Miller, G. Loda, R. C. Miller, R. Smith, D. Shimer, C. Seidt, M. MacArt, H. Mohr, G. Robison, P. Creely, J. Bautista, T. Oliva, L. M. Young, and D. DuBois, “A High-Power Electron Linear Accelerator for Food Irradiation Applications, Nucl. Instrum. Meth. in Sci. Res. **B 211**, 562–570 (2003).

APPENDIX A

DOSIMETRY TECHNIQUES

A1. INTRODUCTION

The effects of ionizing radiation in food processing applications are best characterized in terms of the amount of ionizing energy absorbed per unit mass of material; i.e., the absorbed dose. Consequently, reliable techniques for accurately measuring this quantity, generally termed dosimetry, are essential for ensuring the integrity of the irradiation process. In this Appendix we discuss the general topic of dosimetry, including the various classes of dosimeters and those dosimeter characteristics most useful for routine food processing applications (doses in the range of 0.1–10 kGy). Of special relevance for this topic are the dosimetry standards prepared for radiation processing applications by the American Society for Testing and Materials (ASTM),[1] and publications by the International Atomic Energy Agency,[2] and the International Commission on Radiation Units and Measurements.[3] These sources also cite numerous authoritative references.

A2. CLASSES OF DOSIMETRY SYSTEMS

Dosimeters and dosimetry systems are generally classified into four categories, according to their intrinsic accuracy and usage: (1) primary standards; (2) reference standards; (3) transfer standards; and (4) routine dosimeters. **Primary standards** are those dosimeters whose responses can be predicted from basic scientific principles, and thus do not require calibration against other standards. The two most common examples are gas-filled ionization chambers and calorimeters. National standards laboratories use these dosimeters for calibrating ionizing radiation environments. Typical (2σ) measurement accuracies are in the range of 1–2%.[4]

The dosimeters commonly used for dose mapping and process monitoring in irradiation applications are termed **routine dosimeters**. They are typically the least accurate, but are easy to use, low in cost and available in relatively large quantities. Ideally, they also have good pre-irradiation shelf life, and acceptable post-irradiation stability. Notable examples are the various plastic dosimeters (dyed and undyed) and the radiochromic film dosimeters. Typical (2σ) measurement accuracies are in the range of 5–10%, although care must be exercised to avoid large systematic errors due to environmental factors.[4]

Reference standard dosimeters provide high quality dose measurements, but may require calibration by comparison to primary standards. They can be used to calibrate less accurate routine dosimeters, or they may be used as routine dosimeters themselves when high quality measurements are necessary. Important examples of reference standard dosimeters include electron spin resonance in alanine, and various liquid chemicals that can form stable radiolytic byproducts with yields proportional to the absorbed dose. Measurement accuracies (2σ) achievable with reference standard dosimeters are generally 3% or better.[4]

Transfer standards are dosimeters used for transferring dose information from an accredited standards laboratory to an irradiation facility to establish traceability. Most reference standard dosimeters and some routine dosimeters can be used as transfer standards.

To illustrate the use of the various dosimeter systems, consider the following example. A national standards laboratory would use a primary standard, perhaps an ionization chamber, to calibrate a radiation field.[5] A food irradiation facility would then contract with the national standards laboratory to supply several reference standard dosimeters, such as alanine pellets, that had been exposed to the calibrated field at several different dose levels. After certification of the dose levels by the standards laboratory, the dosimeters would then be sent (transferred) to the irradiation facility, where they would be used to calibrate a local electron spin resonance (ESR) spectrometer. Alanine reference standard dosimeters and routine dosimeters (such as radiochromic film dosimeters) would then be simultaneously exposed at the food irradiation facility, and the dose readings of the reference standards would be used to calibrate the routine dosimetry system under field use conditions. In this way, the calibration of the routine dosimeters would be directly traceable to the accredited national standards laboratory. With this example in mind, the dosimetry systems required by the food irradiation facility include both reference standards and routine dosimeters. In the next section we examine those characteristics of reference standard and routine dosimeters of most relevance for food irradiation applications.

A3. DOSIMETER CHARACTERISTICS DESIRABLE FOR FOOD IRRADIATION APPLICATIONS

The typical applications for which dosimeters are used in a food irradiation facility include installation qualification, dose mapping, process qualification, and routine process control. During the initial installation the performance of the accelerator system must be determined under well-defined operating conditions. The necessary measurements include a determination of the electron kinetic energy, the height (width) and uniformity of the scan, the uniformity of the dose in the direction of conveyor motion, and a determination of depth dose distributions throughout the irradiation volume using homogeneous (phantom) absorbers with densities that correspond to the range of densities of the products to be processed.

Once the performance characteristics of the accelerator system have been determined, it is necessary to perform dose-mapping studies of representative product samples to determine the positions of minimum and maximum dose. These data can then be used to determine how the product should be configured on the conveyor system for highest throughput efficiency, while satisfying minimum and maximum dose requirements.

After the irradiation process has been qualified for a particular product set, it is necessary to periodically monitor the dose given to product during routine operations. This is typically accomplished by placing dosimeters in a convenient location on, or immediately adjacent to the product, and relating the dose measurements to the dose ratios established during the dose-mapping studies performed for process qualification.

With these typical applications in mind, it is apparent that the dosimeters should be small and easy to use, and should be insensitive to environmental influences (e.g., temperature, humidity, ambient light, etc.). Thorough dose-mapping studies can consume many dosimeters in a short time, so good availability at reasonable cost is highly desirable. Also, the unpredictable timing of new product introductions implies that a long pre-irradiation shelf life is desirable, and good post-irradiation stability of the dose is desirable for archival purposes. Finally, the dosimeters should give accurate dose measurements with small variability for the applicable dose and dose rate ranges for both electrons and x-rays. For food irradiation applications, doses are typically in the range of 0.1–10 kGy, while dose rates can range from 10 Gy/s to 10 kGy/s, depending on the conveyor speed and whether x-rays or electrons are used to deliver the dose.

The relatively high dose rates that may be encountered discourage use of ionization chambers that saturate at high dose rates, and dose-rate sensitive liquid chemical dosimetry systems. Calorimeters can be used at high doses and dose rates, but are more bulky and usually unsuitable for dose mapping studies. Also, the readings are not post-irradiation stable. Consequently, the dosimeters and dosimetry systems of most current interest for food irradiation applications are plastic dosimeters that can be formed into small pieces, various radiochromic dosimeters, and alanine films and pellets. Important examples of these dosimeters are discussed in more detail in the following section. Their salient features are summarized in Table A1.

A4. ROUTINE AND REFERENCE STANDARD DOSIMETERS FOR FOOD IRRADIATION APPLICATIONS

A4.1. Plastic Dosimeters

The first commonly used plastic dosimeters were based on the discoloration of pure polyvinyl chloride and the bleaching of blue cellophane when exposed to ionizing dose. Because of their sensitivity to environmental conditions, these materials have been largely replaced by the clear, colorless polymer polymethyl methacrylate (PMMA), commonly known as Lucite, Plexiglas, acrylic or Perspex. PMMA dosimeters, made in both dyed and undyed varieties, undergo a color change when exposed to radiation that can be accurately measured using a spectrophotometer. The increased absorption is the result of radiation-induced free radicals that initially react with oxygen present in the polymer to give peroxy radicals.[5] These dosimeters still exhibit some sensitivity to humidity and UV exposure and should be sealed in aluminum foil. When sealed, they have long shelf life, and exhibit good dose-rate independence. However, the absorption spectrum tends to change as the result of post-irradiation reactions, and the absorbance can fade as oxygen diffuses into the material (by several percent over a few days). Consequently, fading is typically less pronounced if the dosimeters are kept in their sachets until reading; the fading is also worse for higher doses. PMMA dosimeters should be handled by their edges only, and should be inspected for imperfections (scratches) prior to reading. Also, PMMA dosimeters do display some sensitivity to high dose rates and irradiation temperature variations.

As examples of PMMA dosimeters, Harwell Dosimeters Ltd. manufactures three types containing certain dyes that become darker on irradiation, Red 4034, Amber 3042 and Gammachrome YR.[6] These are produced in the form of optically transparent strips that are individually hermetically sealed in laminate sachets consisting of an inner layer of polyethylene and an outer layer of aluminum foil. The response curve of the Gammachrome YR dosimeter at a wavelength of 530 nm is shown in Figure A-1 as an example. Standard practice for the use of these dosimeters in given in ASTM Standard E1276.[1]

A4.2. Radiochromic Dosimeters

Various radiochromic dyes that become colored on exposure to ionizing radiation have been successfully developed as dosimeters. The most common of these are based on aminotriphenyl-methane dyes that gradually change from clear to a deep blue with increasing absorbed dose, and dyes based on pararosaniline cyanides which change from clear to deepening shades of red and purple with increasing dose. The dyes can be used in either liquid form or incorporated in or on polymer films

Table A1. Characteristics of Selected Routine and Reference Standard Dosimeters

Characteristic	Alanine Pellets	Alanine Films	Rad-Chr (B3)	Rad-Chr (FWT-60)	Optical WGs (FWT-70)	Perspex (Amber 3042)	Perspex (Gamma-chrome)
Instrument	ESR Spectrometer	ESR Spectrometer	Spectro-photometer	Spectro-photometer	Spectro-photometer	Spectro-photometer	Spectro-photometer
Size/shape	50 mg pellets	5.6875″ × 0.15625″ × 0.014″	1 cm × 1 cm × 20 μ	1 cm × 1 cm × 50 μ	3 mm dia × 5 cm	3 × 1.1 cm^2 × 3 mm	3 × 1.1 cm^2 × 1.7 mm
Precision (2σ)	<2%	<3%	5–10%	5–10%	5–10%	5–10%	5–10%
Shelf life	Excellent	Excellent	Very Good	Very Good	Very Good	Very Good	Very Good
Stability	Excellent	Excellent	Very Good	Very Good	Very Good	Good	Good
Dose (kGy)	0.1–100	0.5–100	2–80	1–200	0.1–20	1–30	0.1–3
Dose Rate	Excellent	Very Good	Very Good	Very Good	Very Good	Fair	Fair
Handling ease	Good	Excellent	Tweasers	Tweasers	Good	Tweasers	Tweasers
Environmental factors	Very Good	Very Good	Humidity, UV	Humidity, UV	Humidity, UV	Humidity, UV, irrad. temp.	Humidity, UV, irrad. temp.
Availability	Good	Good	Excellent	Excellent	Excellent	Excellent	Excellent
Cost	Expensive	Expensive	Inexpensive	Inexpensive	Inexpensive	Inexpensive	Inexpensive

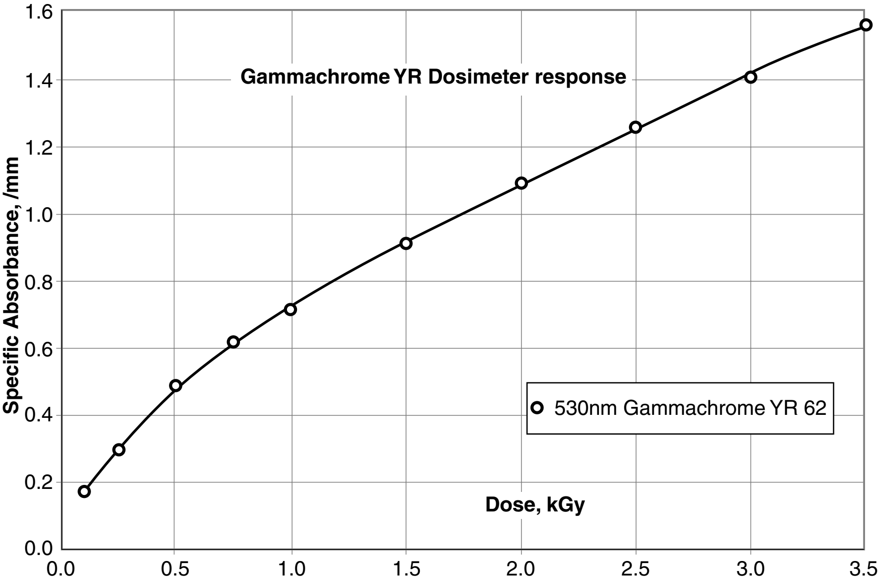

Figure A-1. Specific absorbance vs dose at 530 nm for the Harwell Gammachrome YR Perspex dosimeter.

to form solid dosimeters. They typically have long shelf lives, are relatively independent of dose-rate, and have a simple, accurate read-out procedure using a spectrophotometer. In the case of solid films, the irradiation temperature dependence is relatively small. However, these dosimeters must be protected from UV light and humidity changes, and should therefore be hermetically sealed in light-tight pouches. The optical surfaces of the solid films should not be touched or scratched, and they must be dust or lint free for the optical density readings to be accurate. Color build-up is not immediate and can take hours and days in some cases. Incubation at elevated temperatures can significantly reduce the color development time. Once full color has developed, the dose stability is relatively good in comparison with PMMA dosimeters. Standard practice for use of radiochromic film dosimetry systems is described in ISO/ASTM Standard 51275.[1]

Radiochromic dosimeters are readily available from commercial sources. For example, the pararosaline cyanide dye is used by the GEX Corporation as the basis for their B3 radiochromic dosimeters.[7] These consist of thin (<20 micron) plastic squares (approximately 1 cm × 1 cm) mounted in cardboard backing for relatively easy handling using tweasers. They are packaged in 3-mil poly-foil laminate pouches for protection against humidity and UV light. It is recommended by the manufacturer that these films be incubated for 15 minutes at 60 °C following the irradiation before making the optical density measurement in the spectrophotometer (at a recommended wavelength of 554 nm). The suggested dose range is 2–80 kGy, although accuracy and variability tend to worsen below about 5 kGy.

The radiochromic dye hexa(hydroxyethyl) aminotriphenylacetonitrile is used by Far West Technology, Inc. as the basis of their FWT-60 series of thin film dosimeters.[8] They are available individually (1000 pieces per box, for example), or packaged in aluminum laminated pouches to protect against stray light (especially UV). The nominal dose range is 1–200 kGy, although they too lose precision below a few kilogray. Their response is relatively constant when used above 0 °C.

The same dye is also used by Far West in their FWT-70 Opti-Chromic dosimeters, which are designed for radiation processing at the lower dose levels especially appropriate for food processing

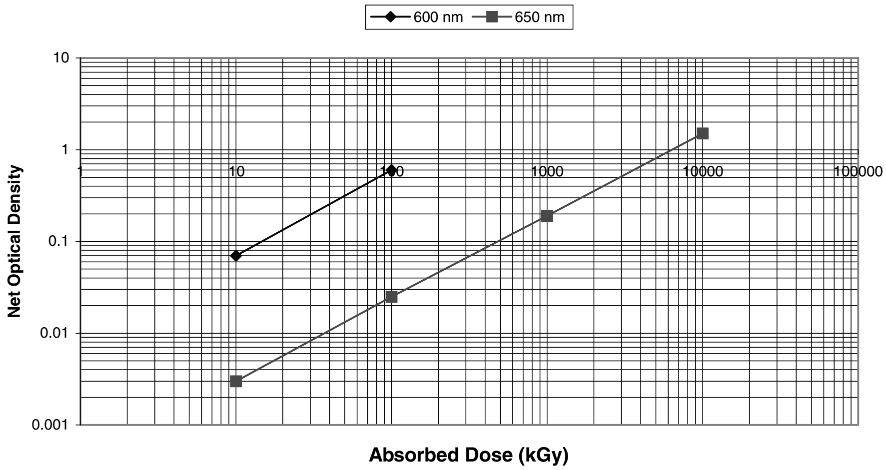

Figure A-2. Optical density vs dose for FWT70-83M Opti-Chromic dosimeters determined at two different wavelengths, 600 nm and 656 nm.

(in particular, 0.1–20 kGy).[8] These dosimeters are small optical waveguides (3 mm dia × 5 cm in length). The shelf life is claimed to exceed two years when stored at a temperature of 4 °C. The typical response curves for the FWT70-83M dosimeters are given in Figure A-2 for two different wavelengths, 600 nm and 656 nm. Standard practice for the use of a radiochromic optical waveguide dosimetry system is described in ISO/ASTM Standard 51310.[1]

A4.3. Alanine Pellets and Films

As described in Chapter 1, the interaction of ionizing radiation with organic compounds forms free radicals, which are very reactive species having unpaired electrons. The concentration of such free radicals can be measured using electron spin resonance (ESR) spectroscopy, also called electron paramagnetic resonance (EPR) spectroscopy. Consequently, free radical production can serve as the basis for a high-quality dosimeter, provided that the concentration is precisely related to the absorbed dose, and does not change appreciably with time following the irradiation. These circumstances have

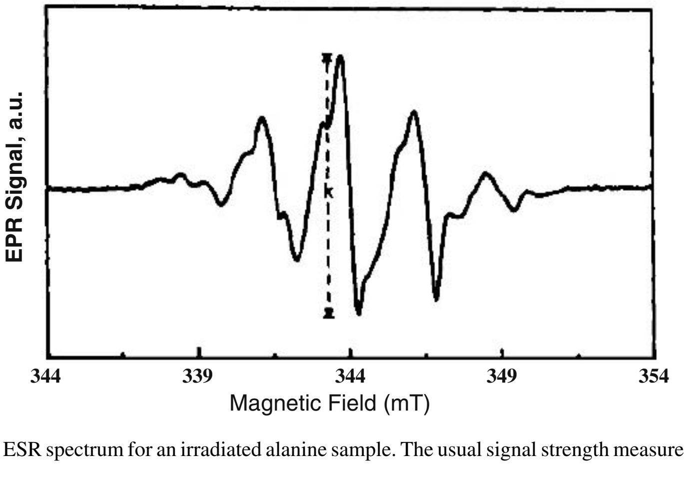

Figure A-3. A typical ESR spectrum for an irradiated alanine sample. The usual signal strength measurement (k) is indicated.

Table A2. Comparison of Dosimetry Approaches

Dosimeter	Advantages	Disadvantages
Alanine Pellets (Gamma Services/ Harwell)	1. can be read immediately 2. most accurate (2%) 3. dose stable with time 4. not affected by handling 5. excellent shelf life 6. good availability 7. excellent dose range	1. expensive 2. clumsy extraction from Bruker microwave cavity 3. good availability 4. not easily used for energy measurements 5. read time of approximately 40 sec per pellet at low doses
Alanine Film (Kodak)	1. easiest to use 2. not affected by handling 3. can be read immediately 4. good accuracy (3%) 5. good availability 6. suitable for energy measurements 7. Bar Code allows certain identification of each dosimeter	1. most expensive at present, but re-usable 2. reduced accuracy at doses below 1 kGy
B3 Radiochromic Film (GEX)	1. inexpensive 2. easily used for energy measurements 3. excellent availability	1. decreased accuracy (5–10%) 2. significant development time unless incubation is used 3. should be handled with tweasers 4. requires care in storage 5. should not be used below 2 kGy
FWT-60 Radiochromic Film (Far West)	1. inexpensive 2. easily used for energy measurements 3. excellent availability	1. decreased accuracy (5–10%) 2. significant development time unless incubation is used 3. should be handled with tweasers 4. requires care in storage 5. should not be used below 1 kGy
FWT-70 Optical Waveguides (Far West)	1. inexpensive 2. excellent dose range 3. excellent availability	1. decreased accuracy (5–10%) 2. significant development time unless incubation is used 3. unsuitable for energy measurements 4. requires care in storage
Perspex Gammachrome (Harwell)	1. inexpensive 2. easily used for energy measurements 3. excellent availability 4. good dose range	1. decreased accuracy (5–10%) 2. tends to fade at high dose rates 3. should be handled by edges 4. requires care in storage

been found to occur for the crystalline amino acid α-alanine (CH_3-CH(NH_2)-COOH). In particular, the free radical concentration remains unusually stable because of trapping in the crystalline lattice.[9] Both stereoisomers of α-alanine are suitable for dosimetry, although L-α-alanine is used most commonly. Since ESR spectroscopy is nondestructive, this dosimetry technique is suitable for archival purposes. Standard practice for the use of alanine ESR dosimetry systems is described in ISO/ASTM Standard 51607.[1]

Good introductions to ESR spectroscopy are readily available.[10] A typical spectrum of the predominant alanine free radical is shown in Figure A-3.[11] It consists of several peaks due to the hyperfine splitting of the unpaired electron with the N- and H- atoms. The signal strength is usually represented by the difference between the minimum and maximum of the central peak. To correct for fluctuations in spectrometer sensitivity, a reference sample having a noninterfering ESR signal is usually read simultaneously with the irradiated alanine sample. $MgO:Mn^{2+}$ is commonly used for this purpose.

Alanine dosimeters are usually prepared by compressing pure alanine powder with a suitable plastic binder. They are available commercially in both pellet (Gamma Services[12] and Harwell[6]) and plastic film versions (Kodak's Biomax Alanine Dosimeters[13]). Both types of dosimeters can be conveniently read using the E-Scan ESR spectrometer manufactured by Bruker Biospin Corporation.[14] The films are bar-coded and are especially easy to use. Problems with humidity have now been solved, and the dose precision provided by the films is nearly as good as that of the pellets, which is excellent. The only drawback with this approach in relation to the other routine dosimetry systems previously discussed is cost. For example, the Bruker spectrometer is roughly an order of magnitude more expensive than a good spectrophotometer (a few $K), and both the films and pellets are approximately $1 each (although for low dose increments they can be used multiple times). The signal strength depends on the amount of alanine in the sample. The pellets contain significantly more alanine, and their low dose limit is <0.1 kGy. The lower dose limit of the film samples is continually improving, but is currently limited to about 0.5 kGy.

A4.4. Discussion and Applicability of Routine Dosimeters

A summary of the advantages and disadvantages of the various dosimetry techniques is given in Table A2. Beyond these general characteristics, there are a few particular comments that can be made:

1. For situations in which high quality dose measurements are essential, alanine dosimeters are the clear choice.
2. For situations in which lower quality dose measurements are acceptable, the lower cost radiochromic dyes and PMMA dosimeters are more appropriate.
3. Alanine pellets and the optical waveguides are not well suited for electron kinetic energy measurements.
4. The optical waveguides should not be used for dose mapping with electron beams. (They are suitable for dose mapping with x-rays, however.)
5. Only alanine pellets, optical waveguides and Perspex gammachrome dosimeters cover the entire range of doses appropriate for all food processing applications.

REFERENCES

1. **Standards on Dosimetry for Radiation Processing**, RADPR0, ASTM International, West Conshohocken, PA, USA (2002).
2. **Dosimetry for Food Irradiation**, Tech. Report Series no. 409, IAEA, Vienna (2002).
3. **Radiation Dosimetry: Electron beams with Energies between 1 and 50 MeV**, ICRU Rept. 35, International Commission on Radiation Units and Measurements, Bethesda, MY (1992).
4. A. Miller, P. Sharpe and R. Chu, "Dosimetry for Industrial Radiation Processing," **ICRU News**, International Commission on Radiation Units and Measurements, Bethesda, MY (2000).
5. R.J. Woods and A.K. Pikaev, **Applied Radiation Chemistry: Radiation Processing**, Wiley and Sons, NY (1994).
6. Harwell Dosimeters Ltd., Oxfordshire, UK.
7. GEX Corporation, Centennial, Colorado, USA.
8. Far West Technology Inc., Goleta, California, USA.

9. W.W. Bradshaw, D.G. Cadena, G.W. Crawford and H.A.W. Spetzler, “The use of alanine as a solid dosimeter,” Radiation Research **17**, 11 (1962).
10. J.A. Weil, J.R. Burton, and J.E. Wertz, **Electron Paramagnetic Resonance; Elementary Theory and Practical Applications**, John Wiley and Sons, NY (1994).
11. D.F. Regulla and U. Deffner, Appl. Radiat. Isot. **33**, 1101–1114 (1982).
12. Gamma Service Produktbestrahlung GmbH, Leipzig, Germany.
13. Biomax Alanine Dosimeter Films, Eastman Kodak Company, Rochester, NY, USA
14. Bruker Biospin GmbH, Rheinstetten, Germany.

APPENDIX B

ELECTRON KINETIC ENERGY MEASUREMENTS USING THIN FILM DOSIMETERS

As discussed in Chapter 11, for direct electron irradiation applications the in-product depth-dose profile is energy dependent, and for indirect x-ray irradiation applications the efficiency of the x-ray generation process depends on the electron kinetic energy. Consequently, it is necessary to have a simple, accurate method for determining the beam kinetic energy. Such a method is provided by the depth-dose profile in a homogeneous material, as discussed in ASTM Standard E 1649.[1] In this Appendix we discuss certain features of this method, making specific recommendations for improved accuracy and ease-of-use.

For a monoenergetic 10-MeV beam normally incident on a water absorber, the characteristic depth-dose profile is shown in Figure B-1 as an example.

There are several electron ranges and depths that have been defined using this characteristic profile:

1. Optimum thickness (R_{opt}) – the depth at which the dose equals the surface dose. From Fig. B-1, $R_{opt} = 3.8$ g/cm^2.
2. Half-value depth (R_{50}) – the depth at which the absorbed dose is 50% of its maximum value. From Fig. B-1, the maximum dose is about 2.5 MeV-cm^2/g, so $R_{50} = 4.2$ g/cm^2.
3. Practical range (R_p) – the depth at which the tangent at the steepest point (the inflection point) on the almost straight descending portion of the depth-dose distribution curve meets the depth axis. This is nearly 5 g/cm^2, from Fig. B-1.

For pure aluminum (with a density of 2.7 g/cm^3), the accepted R_p and R_{50} ranges for a monoenergetic 10-MeV beam are 2.00 cm and 1.59 cm, respectively; for a monoenergetic 5 MeV beam, the corresponding quantities are 0.971 cm and 0.741 cm, respectively.[1]

The energy spectra of the beams produced by microwave electron accelerators are usually quite good, but they are not precisely monoenergetic. A typical energy spectrum of an rf linac is shown in Figure B-2. It consists of a tight, nearly Gaussian peak, superimposed onto a low energy tail. The most probable energy (the peak of the spectrum) is denoted by E_p, while the average energy is designated by E_a. For such spectra it is always the case that $E_p > E_a$.

Various empirical equations have been devised to infer the electron energy using the range estimates of the depth-dose characteristic. Since the practical range is based on the deepest part of the depth-dose curve, the energy inferred using R_p is most closely associated with the most probable energy of the spectrum. On the other hand, the R_{50} range depends on the maximum of the depth-dose profile, and is therefore most closely identified with the average energy of the spectrum. In particular, for an aluminum absorber over the energy ranges of interest (1–10 MeV), first and second

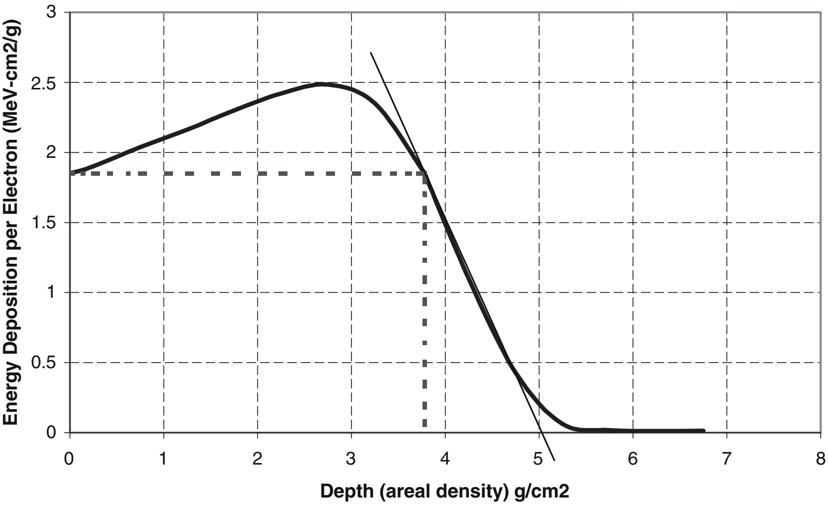

Figure B-1. The characteristic energy deposition profile for 10-MeV electrons in water.

order estimates[1] of E_p and E_a are summarized below:

First Order: $$E_p(\mathrm{MeV}) = 0.2 + 5.09\,R_p \tag{B1}$$

$$E_a(\mathrm{MeV}) = 6.20\,R_{50} \tag{B2}$$

Second Order: $$E_p(\mathrm{MeV}) = 0.256 + 4.91\,R_p - 0.0248\,R_p^2 \tag{B3}$$

$$E_a(\mathrm{MeV}) = 0.297 + 6.61\,R_{50} - 0.325\,R_{50}^2 \tag{B4}$$

If the values for R_{50} and R_p from the monoenergetic 5 and 10 MeV spectra are substituted into the first and second order equations, the results shown in Table B1 are obtained. There is little disagreement between the second order estimates, but the discrepancy between the first order results

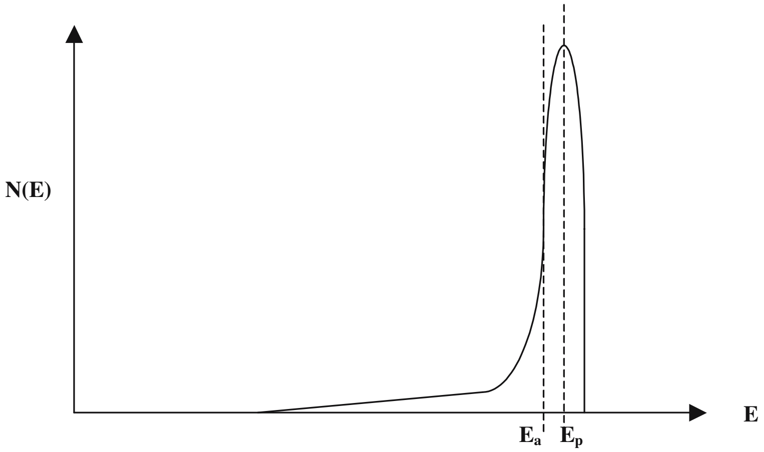

Figure B-2. Characteristic shape of the energy spectrum typical of a microwave linac.

Table B1. Comparison of Inferred Electron Energies for a Monoenergetic Spectrum

Electron Energy (MeV)	First Order E_a	First Order E_p	Second Order E_a	Second Order E_p
5.00	4.59	5.14	5.02	5.00
10.00	9.86	10.38	9.98	9.98

is over 500 kV for both cases. Consequently, for best accuracy, **only the second order equations should be used to infer E_a and E_p**.

ASTM Standard E 1649 describes two different energy measurement approaches based on the depth-dose profile.[1] The first uses a stack of thin plates interleaved with thin film dosimeters; the second uses two wedges stacked together to form a rectangular block, with a dosimeter strip placed along the center of the sloping surface between the wedges. The stacked plate method is virtually foolproof, as long as the thickness of the thin plates is accurately known, and provided that the irradiation pattern uniformly covers the plate stack. With the wedge, considerable care is required to ensure that the position of the film strip is accurately known. **Consequently, the stacked plate method is recommended over the wedge method for routine use in a production environment**.

Radiochromic film dosimeters are quite convenient to use with the stacked plate technique, but their greater inaccuracy (relative to alanine films, for example) can lead to greater uncertainty in the energy measurement. Consequently, **use of alanine film dosimeters is recommended**.

To illustrate this point further, consider the ideal normalized depth-dose profile in aluminum for 10-MeV electrons. From the values of R_{50} and R_p, the equation of the straight-line approximation in the vicinity of the half-maximum dose point is

$$D = -1.22\,R + 2.44 \tag{B5}$$

Suppose there is an error of +5% (typical of radiochromic film dosimeters) in the maximum dose measurement. From Eq. (B5) this error will give a −4.1% error in the R_{50} range. Taking differentials of Eq. (B4) about the R_{50} point gives

$$(dE_a/E_a) = 0.89(dR_{50}/R_{50}) \tag{B6}$$

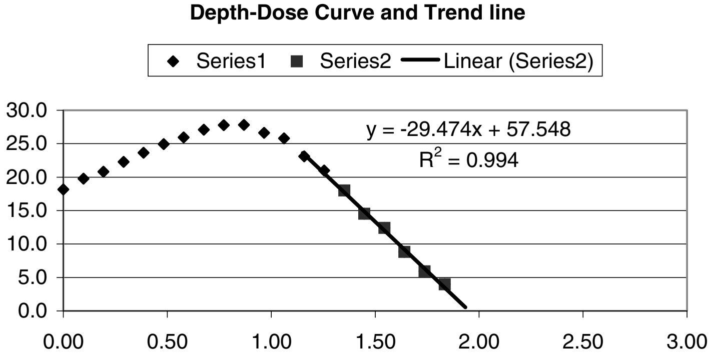

Figure B-3. Depth-dose profile using stacked aluminum plates with alanine film dosimeters: $R_{50} = 1.48$, $R_p = 1.93$ cm; $E_a = 9.35$ MeV, $E_p = 9.46$ MeV.

Therefore, the +5% error in the maximum dose measurement will give an error in the value of the average energy of approximately −3.65%, or an estimated average energy of 9.635 MeV instead of 10 MeV. For this reason, **it is recommended that the maximum dose always be obtained from a good curve-fitting routine if radiochromic film dosimeters are used.**

An example of the high quality data that can be obtained using the more accurate alanine film dosimeters in an aluminum plate stack is shown in Figure B-3. The data are nearly an exact match to the theoretical curve. For these more accurate dosimeters a +2% error in the maximum dose would result in only a −1.46% error in the average energy, which is usually acceptable. Further use of a curve fitting routine with the alanine film dosimeters will generally lower the error in the energy measurement to less than 1%.

Use of the alanine film strips for measuring the electron kinetic energy is further facilitated by constructing the stacked plates in the form of a stepped wedge. Small cutout pockets then permit easy insertion and extraction of the film strips.

REFERENCES

1. ISO/ASTM Standard E 1649, Practice for Dosimetry in an Electron Beam Facility for Radiation Processing at Energies between 300 keV and 25 MeV.

APPENDIX C

INDUCED RADIOACTIVITY IN FOOD BY ELECTRON AND X-RAY IRRADIATION

C1. INTRODUCTION

Following the recommendations of a Joint FAO/WHO/IAEA Expert Committee, all countries actively involved in food irradiation applications have (until recently) adopted kinetic energy limits of 10 MeV for direct electron irradiation and 5 MeV for indirect x-ray irradiation to avoid inducing radioactivity in food.[1] Subsequent detailed calculations and measurements have indeed shown that if these limitations are satisfied, induced radioactivity in food cannot be detected, even at very high dose levels. In particular, beef has been irradiated with 10 MeV electrons at doses in the range of 200–300 kGy without any evidence of measurable induced activity.[2] In a similar study, pepper was irradiated at doses up to 100 kGy with 10-MeV electrons without any detection of radioactivity.[3]

For x-ray irradiation the 5-MeV limit was established largely on the basis of the high-power electron accelerator technologies available at the time,[4] and on supporting theoretical calculations and electron irradiation experimental results.[5] Recent measurements and calculations indicate that this is a very conservative limit.[6] In fact, the last cited study was prompted by a FAO/IAEA report that a limit of 7.5 MeV would be safe with respect to induced radioactivity in food.[7]

This issue is of no small consequence. With the limited penetration depth afforded by electron beam irradiation, x-ray irradiation would greatly increase the types of products that could be processed. However, the inefficiency of the x-ray generation mechanism substantially increases treatment costs and requires significantly more powerful machines to realize reasonable throughput rates. As seen from Chapter 4, increasing the kinetic energy limit from 5 MeV to 7.5 MeV would improve the x-ray generation efficiency by 50%, and would also decrease the radiation cone angle thereby increasing the effective penetration depth. As a result, regulatory bodies were petitioned to raise the kinetic energy limit for x-ray processing from 5 to 7.5 MeV.[4] In a recent ruling, the US FDA has approved the 7.5 MeV limit, provided that the high-z material used in the converter is either tantalum or gold.[8]

C2. ESTIMATES OF INDUCED ACTIVITY

To explore this issue in more depth, the methodology developed for analyzing an explosive detection concept using energetic bremsstrahlung[9] is used as a starting point to provide a comparison with previous calculational results.[10]

The geometry of interest is shown in Figure C-1. An electron accelerator produces a beam of current I and kinetic energy E_o that is scanned vertically over a converter of height H. Homogeneous product of density ρ moves horizontally at velocity v through the bremsstrahlung x-ray field. There are two important mechanisms that could induce radioactivity, both of which are caused by the

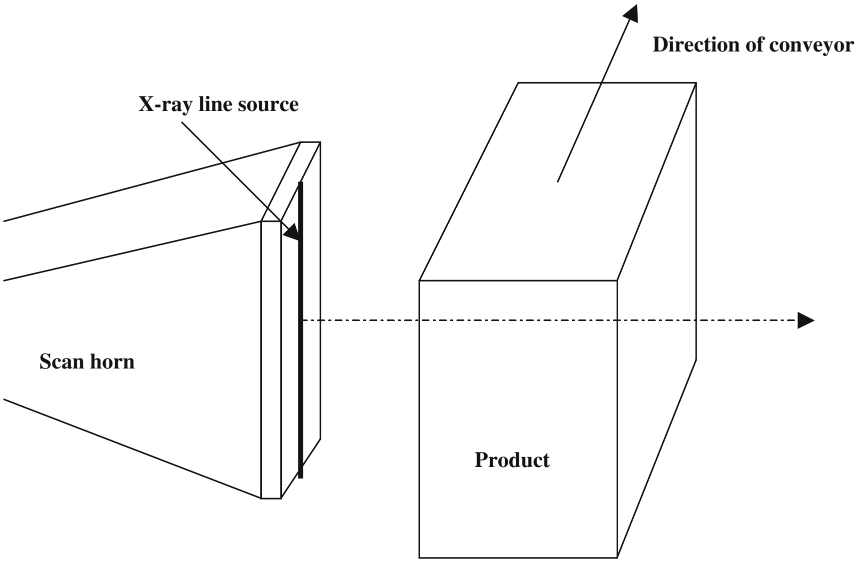

Figure C-1. X-ray irradiation configuration. The electron beam is scanned vertically over the converter producing an x-ray line source. Product is conveyed through the irradiation zone in a direction perpendicular to the scan.

energetic photons produced by the bremsstrahlung process. The first type is a (γ,x) reaction in which a photon interacts with a nucleus, resulting in ejection of a secondary particle (x), leaving an excited nucleus that subsequently undergoes radioactive decay. The second mechanism is that of neutron activation following the release of neutrons by the (γ,n) process just mentioned.

To evaluate contributions from these mechanisms it is first necessary to identify the elements that comprise foods, and to determine the nuclear activation thresholds and corresponding interaction cross-sections. The elemental constituents of foodstuffs are considered to be nearly identical to that of the human body, as shown in Table C1.[11] It is apparent that the human body is mostly water, with the addition of proteins, carbohydrates and fats.

For the elements listed, there are only three stable isotopes, ${}_1H^2$, ${}_8O^{17}$ and ${}_6C^{13}$, that have (γ,x) thresholds less than 5 MeV,[12] and all daughter nuclei are stable.[13] (All of these are (γ,n) reactions.) Increasing the energy limit to 7.5 MeV adds a few naturally occurring isotopes, as shown in Table C2. (Only the (γ,n) reactions are shown; the daughter nuclei are all stable, as are the daughter nuclei produced by a few (γ,p) reactions.) In addition to these reactions, there are three isotopes of tungsten that have (γ,n) reactions with thresholds less than 7.5 MeV. It is therefore assumed that the high-Z converter uses tantalum (with a reaction threshold of 7.62 MeV), in order to eliminate neutron production in the converter.

On the basis of these analyses, radioactivity cannot be induced by direct (γ,n) reactions because all daughter nuclei are stable. Therefore, the only pathway is that of neutron activation following the (γ,n) reactions in the foodstuffs. To evaluate this mechanism requires an estimate of the neutron source strength, which implies knowledge of the (γ,n) cross-sections, the bremsstrahlung spectrum, the neutron absorption cross-sections for the elements listed in Table C1, and the decay rates of the resulting daughter nuclei.

The number density of a particular isotope n_x per gram of product is determined by the weight fraction w, the atomic weight A and the relative abundance R according to

$$n_x = 6.02 \times 10^{23}\ (wR/A) \tag{C1}$$

Table C1. Average Composition of the Human Body

Element	Weight Fraction
Oxygen (O)	0.65
Carbon (C)	0.18
Hydrogen (H)	0.10
Nitrogen (N)	0.03
Calcium (Ca)	0.015
Phosphorus (P)	0.01
Sulfur (S)	0.0025
Potassium (K)	0.002
Sodium (Na)	0.0015
Chlorine (Cl)	0.0015
Magnesium (Mg)	0.0005
Iron (Fe)	5.7×10^{-5}
Zinc (Zn)	3.3×10^{-5}
Rubidium (Rb)	1.7×10^{-5}
Strontium (Sr)	2.0×10^{-6}
Copper (Cu)	1.4×10^{-6}
Aluminum (Al)	1.4×10^{-6}
Lead (Pb)	1.0×10^{-6}

The number densities of the isotopes listed in Table C2 are given in Table C3. Selected (γ,n) cross-section data are shown in Figure C-2.[14] It is apparent that the cross-sections are very small. Given the relatively high thresholds, very low cross-sections and low weight fractions, contributions from lead, zinc and magnesium are neglected in further calculations. Note, however, that the cross-section for lead rises very rapidly above 7 MeV. Consequently, lead should not be used as a primary shielding material in 10-MeV electron beam installations.

The number of electrons striking the converter per unit time is (I/e), where e is the unit of electron charge. Therefore, the number of photons generated in the converter per unit time is given by

$$(dN_p/dt) = (I/e) \int S(E)\, dE \tag{C2}$$

where S(E) is the energy-dependent, forward-directed bremsstrahlung spectrum, normalized to a single electron. Assuming for conservatism that *all* of these photons are directed toward product of depth d, then the number of neutrons generated per unit time by photonuclear reactions with isotope

Table C2. Thresholds for (γ,n) Photonuclear Reactions

Isotope	% Nat. Abundance	Threshold (MeV)
${}_1H^2$	0.015	2.23
${}_8O^{17}$	0.037	4.14
${}_6C^{13}$	1.11	4.95
${}_{82}Pb^{207}$	22.6	6.73
${}_{30}Zn^{67}$	4.11	7.05
${}_{12}Mg^{25}$	10.13	7.33

Table C3. Number Density of Selected Isotopes

Isotope	R	w	n_x (per gm)
$_1H^2$	1.5×10^{-4}	0.1	4.5×10^{18}
$_8O^{17}$	3.7×10^{-4}	0.65	8.5×10^{18}
$_6C^{13}$	1.1×10^{-2}	0.18	9.2×10^{18}
$_{82}Pb^{207}$	2.3×10^{-1}	10^{-6}	6.7×10^{14}
$_{30}Zn^{67}$	4.1×10^{-2}	3.3×10^{-5}	1.2×10^{16}
$_{12}Mg^{25}$	1.0×10^{-1}	5×10^{-4}	1.2×10^{18}

X is approximately given by

$$(dN/dt) = (\rho n_x d)(I/e) \int S(E)\sigma_x(E)\, dE \tag{C3}$$

The integral in Eq. (C3) is termed the activation integral, and requires the energy-dependent x-ray spectrum and cross-section data for evaluation. Bremsstrahlung spectra for 5-MeV and 7-MeV electrons normally incident on optimized x-ray converters are shown in Figure C-3. Guided by these results, for photon energies greater than 2 MeV, the bremsstrahlung spectrum is crudely modeled as

$$S(E) = 0.4 \exp[-4.9(E/E_o)] \tag{C4}$$

in which E is the photon energy and E_o is the energy of the incident electrons.

Below 5 MeV, the only reaction of any consequence is that with deuterium. In the range of 5–7.5 MeV, O^{17} and C^{13} are also considered. Crude approximations for these cross-sections are provided by

$$\begin{aligned} \sigma(\text{mb}) &= 2.0; & E &> 2.5\,\text{MeV}; & {}_1H^2 \\ &= 0.2 \exp[0.28(E-5)]; & E &> 5.0\,\text{MeV}; & {}_6C^{13} \\ &= 0.02 \exp[0.92(E-5)]; & E &> 5.0\,\text{MeV}; & {}_8O^{17} \end{aligned} \tag{C5}$$

With these analytical approximations, values of the various activation integrals are shown in Figure C-4 as a function of the incident electron kinetic energy.

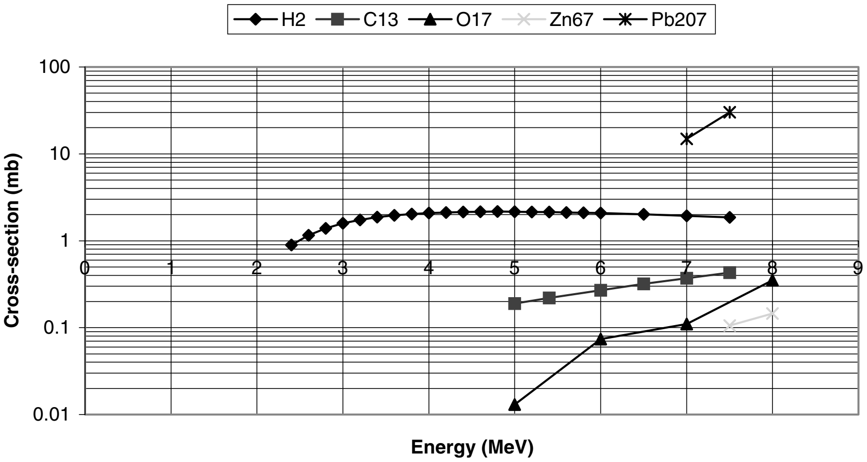

Figure C-2. (γ,n) cross-section data for selected isotopes.

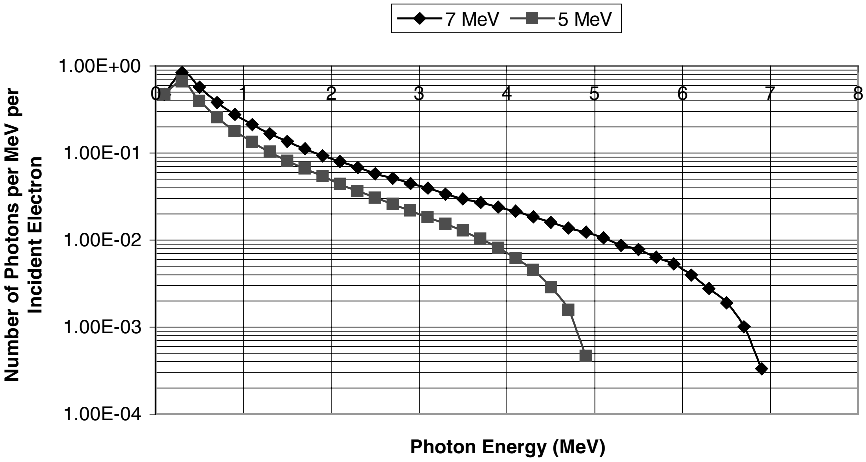

Figure C-3. Energy spectra of the forward-directed bremsstrahlung for 5- and 7-MeV electrons.

The number of neutrons generated per incident electron f_{en} in unit density product with a slab thickness of $d = 20$ cm is just the sum over the different species (x), according to

$$f_{en} = \sum \left[(n_x d) \int S(E)\sigma_x(E)\, dE \right] \tag{C6}$$

This quantity is graphed in Figure C-5 as a function of electron kinetic energy. For a fixed beam power of 100 kW, the number of neutrons generated per second is approximately 7.25×10^8 at 5 MeV, increasing to 1.8×10^9 at 7.5 MeV.

Combining Eqs. (C3) and (C6), $dN/dt = f_{en}\,(I/e)$. Rewriting the beam current in terms of the beam power and kinetic energy gives

$$dN/dt = f_{en}[P/(eE_o)] \tag{C7}$$

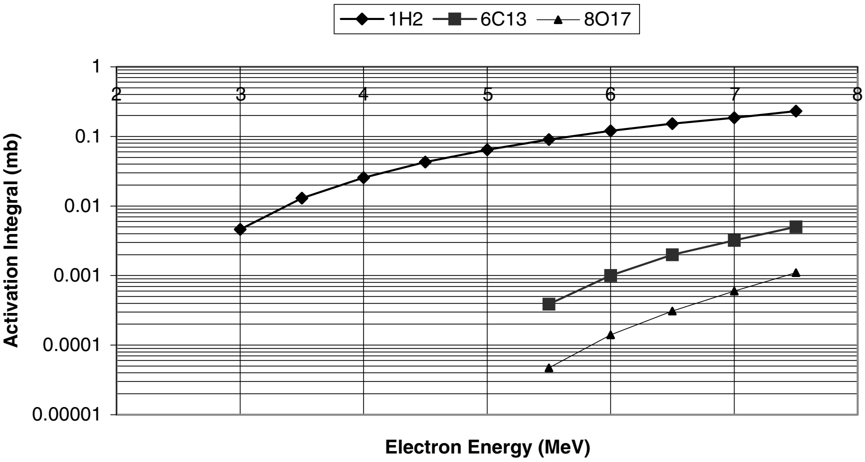

Figure C-4. Values of the activation integrals as a function of incident electron energy.

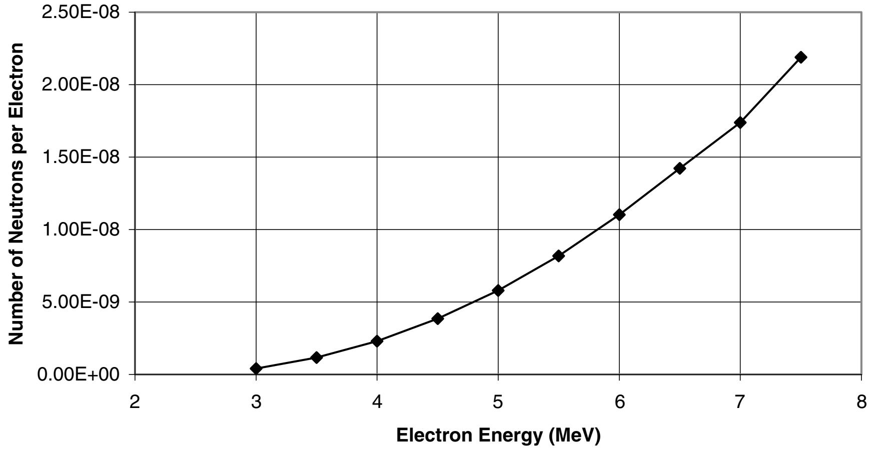

Figure C-5. Neutron source strength per incident electron.

The mass throughput rate of product (dm/dt) can be estimated using Eq. (C8),

$$(\mathrm{dm/dt}) = \eta \mathrm{P/D} \tag{C8}$$

where η is the throughput efficiency and D is the minimum dose. With D in kiloGray and power in watts, the mass throughput is in units of g/s. Reflecting the linear increase in bremsstrahlung efficiency with energy, the throughput efficiency is modeled as $\eta = 0.03(E_o/5)$ with E_o in MeV, in which case Eq. (C8) becomes explicitly

$$(\mathrm{dm/dt}) = [0.03(E_o/5)]/D \tag{C9}$$

Dividing Eq. (C7) by Eq. (C8) and keeping track of units, the neutron production per unit mass of material N_m is given as

$$N_m = 1.04 \times 10^{15}\, f_{en}\, D/(eE_o^2) \tag{C10}$$

with E_o in MeV. Therefore, the increase in neutron production with increasing kinetic energy is nearly offset by the faster mass processing rates. For a fixed dose of 1 kGy, the number of neutrons produced per gram of product processed is graphed in Figure C-6. Over the energy range of 5–7.5 MeV, the number of neutrons produced per gram of material increases by less than a factor of two.

Since the product is considered to be mostly water, the neutrons will be slowed by scattering interactions with hydrogen. A reasonable estimate for the slowing-down length is 6 cm in unit density materials,[10] which is significantly less than the slab thickness of unit density product that might be processed using x-rays (about 20 cm). Therefore, as a conservative approximation we assume that **all** neutrons generated in the product are captured in the product. In this case the probability p of production of a particular daughter specie by a captured neutron is the atomic density n of the parent isotope multiplied by its nuclear cross-section (the macroscopic cross-section), divided by the sum of all macroscopic cross-sections; i.e.,

$$p = n\sigma \Big/ \sum n_i \sigma_i \tag{C11}$$

A useful estimate[10] for the total macroscopic cross-section $\Sigma n_i \sigma_i$ is 2.2×10^{-2} cm^{-1}; that of hydrogen alone, with a cross-section of 0.33b, is about 2.0×10^{-2} cm^{-1}.

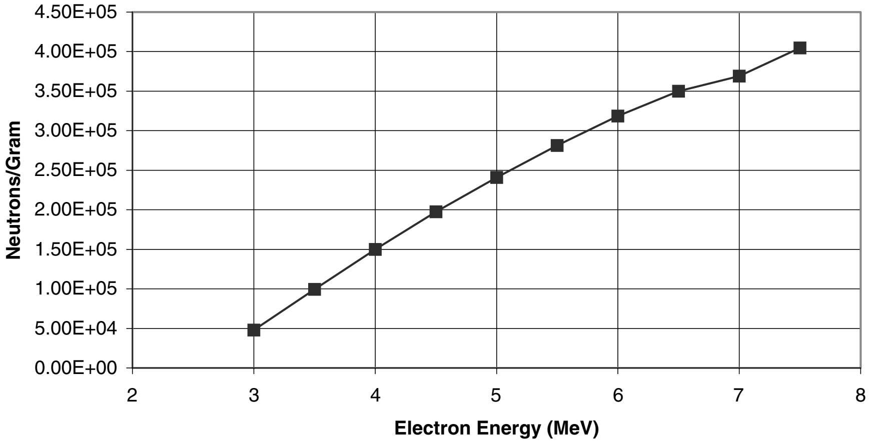

Figure C-6. Number of neutrons produced per gram of product processed at an irradiation dose of one kiloGray.

If τ is the half-life of the ith radioactive specie, then the activity A_i of this specie (disintegrations per second) as a function of time is given by

$$A_i(t) = n_i^*(0.69/\tau)e^{-0.69t/\tau} \tag{C12}$$

It is apparent that short-lived species (<30 minute half-lives) will disappear so quickly that they will not be a concern. On the other hand, species having very long half-lives (>1 year) will not be a problem because their activity will be too low. In particular, for the plentiful elements oxygen, carbon, hydrogen and nitrogen, the predominant neutron capture reactions produce daughter nuclei that are either stable, or have very short half-lives ($_7N^{16}$, $_8O^{18}$), or have very long half-lives ($_6C^{14}$, $_1H^3$). Finally, the weight fractions of the elements below magnesium in Table C1 are so small that they cannot contribute any significant activity. Consequently, interest is concentrated on those isotopes listed in Table C4. Also shown are the predominant decay modes and the capture probabilities from Eq. (C11), assuming a total macroscopic cross-section of $2.2 \times 10^{-2}\,\text{cm}^{-1}$.

Based on these data, the initial activity levels resulting from these capture reactions per gram of product are summarized in Table C5 for a dose of 1 kGy at an electron kinetic energy of 5 MeV. (One milliBecquerel (mBq) corresponds to 10^{-3} disintegrations per second.) The levels from calcium and sulfur are too low to be considered further. The initial high activity level due to Cl^{37} decays relatively rapidly, leaving phosphorus, potassium and especially sodium as the major contributors. The decrease in activity with time for these sources is shown in Figure C-7.

Table C4. Isotopes of Interest for Neutron Capture

Isotope	σ_n(b)	Daughter	$\tau_{1/2}$	Decay (MeV)	$p = n\sigma_i/\Sigma n\sigma_i$
Ca^{44}	1.1	Ca^{45}	165 d	β^- (0.25)	2.15×10^{-4}
Ca^{46}	0.25	Ca^{47}	4.53 d	γ (0.67)	4.4×10^{-6}
P^{31}	0.19	P^{32}	14.3 d	β^- (1.71)	1.6×10^{-3}
S^{34}	0.20	S^{35}	88 d	β^- (0.16)	1.7×10^{-5}
K^{41}	1.2	K^{42}	12.4 hr	β^- (3.42)	1.2×10^{-4}
Na^{23}	0.40	Na^{43}	15 hr	β^- (1.39)	7.1×10^{-4}
Cl^{35}	0.17	S^{35}	88 d	β^- (0.16)	1.5×10^{-4}
Cl^{37}	0.43	Cl^{38}	37 m	β^- (4.81)	1.2×10^{-4}

Table C5. Initial Activity Level following Irradiation at 1 kGy

Isotope	Activity (mBq)
Ca^{44}	0.0026
Ca^{46}	0.0019
P^{31}	0.23
S^{34}	0.000039
K^{41}	0.46
Na^{23}	2.3
Cl^{35}	0.0034
Cl^{37}	9.3

The activity levels summarized in Table C5 and Figure C-7 are quite low in comparison with the naturally occurring levels of radioactivity in most foods resulting from K^{40}, C^{14}, Ra^{226}, and Th^{232} decay.[15,16] The K^{40} activity levels of a few representative foods are presented as examples in Table C6.[16] The naturally-occurring activity level of red meat is also shown on Figure C-7 for comparison. The estimated yearly radiation dose resulting from naturally-occurring radioactivity in food is about 20 mr.

C3. SUMMARY

In conclusion, the level of induced radioactivity arising from food irradiation using x-ray sources has been estimated. The activity is primarily the result of (γ,n) reactions with deuterium. The resulting neutrons slow down and are captured by the various isotopes. Major contributors to the induced activity include the elements phosphorus, potassium, chlorine and especially sodium. For a dose of 1 kGy, a conservative (high) estimate is an activity level of a few mBq per gram of product, in comparison with naturally-occurring radioactivity levels that are typically in the range of 15–250 mBq/g. For the same beam power, increasing the electron kinetic energy from 5 MeV to 7.5 MeV increases the activity by only a factor of two. The US FDA approval of the 7.5-MeV limit appears to be wholly justified.

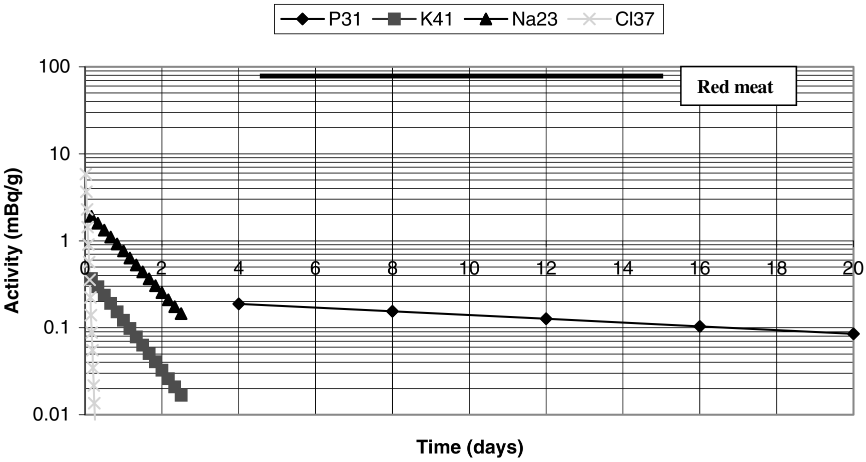

Figure C-7. Induced activity per gram of product vs time after irradiation for a dose level of 1 kGy. The approximate activity level of red meat is shown for comparison.

Table C6. Naturally-Occurring Radioactivity (K^{40} only) in Common Food Groups

Food	Activity (mBq/g)
Dairy products	28–56
Grain products	26–71
Fruits and vegetables	23–165
Meats and Fish	34–168
Nuts	130–237
Beverages	15

With these results in mind, it is also easy to see why electron irradiation at 10 MeV produces no measurable radioactivity in foods, even at dose levels of hundreds of kGy. Although there are several additional (γ,n) reactions between 7.5 and 10 MeV, the cross-sections are typically very small. More importantly, a consideration of the electron depth-dose profile indicates that only a small fraction (a few percent) of the dose delivered to product is due to x-ray absorption. In addition, the product depth that can be treated with electron beams is typically only a third or less of the depth for x-rays; a significant fraction of any neutrons created in the product will escape without capture. Consequently, the level of induced activity is so low that it cannot be detected in the presence of the naturally occurring background.

REFERENCES

1. Joint FAO/IAEA/WHO Report on the Wholesomeness of Irradiated Food, WHO Technical Report, **Series No. 659**, JECFI (1981).
2. A. Miller and P.H. Jensen, “Measurement of induced radioactivity in electron and photon irradiated beef,” Appl. Radiat. Isot. **38**, 507 (1987).
3. M. Furuta, T. Katayama, N. Ito, A. Mizohata, H. Toratina and A. Takeda, “Re-evaluation of induced radioactivity in 10-MeV electron-irradiated pepper for public acceptance,” Radiat. Phys. Chem. **35**, 349 (1990).
4. M. Cleland, Private Communications (2003).
5. H.W. Koch and E.H. Eisenhower, in **Radiation Preservation of Foods**, Amer. Chem. Soc., p. 87 (1967).
6. J. Meissner, M. Abs, M.R. Cleland, A.S. Herer, Y. Jongen, F. Kuntz and A. Strasser, “X-Ray treatment at 5 MeV and above,” Rad. Phys. Chem. **57**, 647–651 (2000).
7. FAO/IAEA Consultants Meeting on the Development of X-ray Machines for Food Irradiation, Vienna (1995).
8. Federal Register Vol. 69, No. 246, 76844–76847, Dec. 23, 2004.
9. K.W. Habiger, J.R.Clifford, R.B. Miller and W.F. McCullough, “Explosives dectection with energetic photons,” Nucl. Instr. Meth. in Phys. Res. **B56/57**, 834–838 (1991).
10. H. Leboute and S. Aucouturier, “Theoretical evaluation of induced radioactivity in food products by electron or x-ray beam sterilization,” Radiat. Phys. Chem. **25**, 233 (1985).
11. **Protection Contre Les Rayonnements**, Recommendations de la Commission International de Protection Radiologique, Gauthier-Villar (1959).
12. R.J. Howerton, D. Braff, W.J. Cahill and N. Chazan, “Thresholds for Gamma-Induced Reactions,” Lawrence Radiation Laboratory, University of California (1964).
13. **Handbook of Chemistry and Physics**, CRC Press, Boca Raton, FL, USA.
14. IAEA Photonuclear Data, International Atomic Energy Agency, Vienna.
15. Radiation in the Environment, US Dept. of Energy, Washington, DC.
16. **Handbook of Environmental Radiation**, A.W. Klement, ed., CRC Press, Boca Raton, FL, USA.

APPENDIX D

OZONE GENERATION BY IONIZING RADIATION

The toxic gas ozone is produced when ionizing radiation (e.g., electrons and x-rays) passes through oxygen. Because of its high chemical reactivity (equipment corrosion and personnel safety), the permissible threshold limit value for ozone is only 0.1 ppm,[1] a level that is easily detected by smell. In this Appendix, the factors that determine the amount of ozone that might be produced, and the resulting concentration levels are analyzed for both electron and x-ray irradiation facilities.

The ozone production rate p, in units of liters/sec, depends on the amount of dose deposited in the air, multiplied by the radiolytic yield, i.e., the number of ozone molecules formed per unit of energy deposited. Ozone decomposes spontaneously, with an effective decomposition time that depends on room size, wall material, temperature and impurities. Ozone can also be removed by ventilation. A simple rate equation for the ozone concentration C (in dimensionless units of liters/liter) that reflects these concepts is

$$dC/dt = p/V - C/T_e \tag{D1}$$

in which V is the volume of the region under consideration, typically in units of liters, and T_e is the effective ozone removal time. Integration of Eq. (D1) gives the time-dependent ozone concentration as

$$C(t) = (pT_e/V)[1 - \exp(-t/T_e)] \tag{D2}$$

For the worst-case assumption of poor ventilation, the effective removal time is just the characteristic decomposition time, which is usually taken to be of the order of 50 minutes.[2] In the limit of long irradiation times, the steady-state concentration level is

$$C_s = pT_e/V \tag{D3}$$

In air an efficient charge transfer mechanism ($N_2{}^+$ ions to O_2) enhances the O_3 yield, with the number of O_3 molecules produced per 100 eV of energy deposited varying between 7.4 and 10.3, depending on the rate of energy deposition.[3,4] (Note that these levels imply that more than one ozone molecule is formed for every electron-ion pair (34 eV) produced.) The lower number is associated with lower specific energy deposition rates characteristic of bremsstrahlung, while the higher number is associated with energy deposition by electron beams. Both situations are analyzed in the following paragraphs.

D1.1. Electron Beams

The energy lost by an electron in traversing an air volume of depth L is just

$$\Delta E = (dE/dx)\, L \tag{D4}$$

(dE/dx) is the familiar stopping power, for which a useful approximation is

$$\begin{aligned} (dE/dx)/\rho &= 2\,\text{MeV-cm}^2/\text{g}, \quad \text{or} \\ (dE/dx) &= 2.58 \times 10^3 \text{eV/cm} \end{aligned} \tag{D5}$$

assuming an air density of 1.29×10^{-3} g/cm^3.

The total energy deposition rate is given by multiplying Eq. (D4) by the total number of electrons traversing the pathlength L per unit time. Denoting the average beam current by I, then

$$\begin{aligned} [d(\Delta E_t)/dt](\text{eV/sec}) &= [2.58 \times 10^3 \text{eV/cm}]\, L(\text{cm})[6.25 \times 10^{18}\, I(\text{amps})] \\ &= 1.61 \times 10^{22}\, L(\text{cm})\, I(\text{amps}) \end{aligned} \tag{D6}$$

Assuming a radiolytic yield of 10.3 ozone molecules per 100 eV of deposited energy, and using the conversion factor of 22.4 liters per Avogadro's number (6.02×10^{23}) of ozone molecules finally gives the ozone production rate for energetic electrons as

$$p\ (\text{liters/sec}) = 6.28 \times 10^{-2}\, L(\text{cm})\, I(\text{amps}) \tag{D7}$$

As a numerical example, the average electron current of a 10 MeV/15kW electron facility is 1.5×10^{-3} amperes. Taking a nominal value of L = 10 cm, a decomposition time of 50 minutes, and a volume V of 100 cubic meters (10^5 liters), the estimated saturated ozone concentration from Eq. (3) is

$$C = 2.83 \times 10^{-5}$$

or 28.3 ppm. This level exceeds the threshold limit value by over two orders of magnitude. While under no circumstances are personnel permitted to enter the irradiation cell when the beam is on for radiation safety reasons, a good ozone ventilation system would be required to permit early entry into the cell after the beam has been turned off, as well as to limit corrosive damage to equipment surfaces.

D1.2. X-rays

For x-rays it is again necessary to estimate the total energy deposition rate in the air gaps between the converter target and the product positions. It is assumed that the x-ray installation operates at the maximum permissible electron kinetic energy of 5 MeV with an average electron beam power P. At 5 MeV, only about 8% of the electron beam energy is converted into useful forward-directed x-ray energy. Also, the effective absorption mean free path in air for the 5-MeV bremsstrahlung spectrum is about 100 meters. Therefore, the approximate rate of x-ray energy absorption in the air is given by

$$P_a = 0.08\, P(L/10^4) = 8 \times 10^{-6}\, P(W)\, L(\text{cm}) \tag{D8}$$

where L is the effective x-ray path length in air (usually the distance between the converter and the product). Assuming 7.4 ozone molecules per 100 eV of deposited energy, the corresponding ozone production rate is therefore given by

$$\begin{aligned} \text{p(ltrs/sec)} &= 8 \times 10^{-6}\,\text{P(W)}\,\text{L(cm)}(6.25 \times 10^{18}\text{eV/j}) \\ &\quad \times (7.4/100)(22.4/6.02 \times 10^{23}) \\ &= 1.40 \times 10^{-10}\,\text{P(W)}\,\text{L(cm)} \end{aligned} \tag{D9}$$

Again assuming that L = 10 cm and V = 10^5 liters, the saturated ozone concentration in an (unventilated) irradiation cell of a nominal 15 kW facility is estimated to be C = 0.62 ppm, which is only a few times higher than the threshold value. If the x-ray pathlength does not significantly exceed 10 cm, then only minimal ozone ventilation would be required.

For some x-ray irradiation installations, in which the x-ray converter is external to the scan horn, the electron beam must propagate in air before reaching the converter. In this case ozone generation by the electron beam will usually exceed that of the bremsstrahlung, as previously discussed.

REFERENCES

1. Occupational Safety and Health Standards, OSHA, US Department of Labor, Washington, DC, **Federal Register 39:125** (1974).
2. Radiological Safety Aspects of the Operation of Electron Linear Accelerators, IAEA **Technical Report Series No. 188**, Vienna (1979).
3. J.T. Spears and J.W. Sutherland, "Radiolytic formation and decomposition of ozone", J. Phys. Chem. **72** 4, 1166 (1968).
4. A.F. Hollavay and D.V. Cormack, "Radioactive and toxic gas production by a medical linear accelerator," Health Physics **38**, 673 (1980).

INDEX